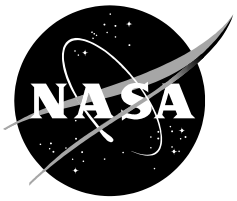

46th Aerospace Mechanisms Symposium

Edward A. Boesiger, Editor
Lockheed Martin Space Systems Company, Sunnyvale, California

Jonathan P. Wood, Editor
Lockheed Martin Space Systems Company, Sunnyvale, California

Proceedings of a virtual symposium
Hosted by the NASA Johnson Space Center and Lockheed Martin Space
Sponsored and Organized by the Mechanisms Education Association

May 11-13, 2022

National Aeronautics and
Space Administration

Johnson Space Center
Houston, Texas 77058

May 2022

PREFACE

The Aerospace Mechanisms Symposium (AMS) provides a unique forum for those active in the design, production and use of aerospace mechanisms. A major focus is the reporting of problems and solutions associated with the development and flight certification of new mechanisms. Sponsored and organized by the Mechanisms Education Association, responsibility for hosting the AMS is shared by the National Aeronautics and Space Administration and Lockheed Martin Space.

The 46th AMS was scheduled to be held in Houston, Texas but unfortunately, the worldwide COVID-19 pandemic led us to holding the symposium virtually on May 11-13, 2022. These proceedings are published to provide these lessons learned and mechanism design information to the mechanism community. Topics included instrument mechanisms, release devices, sensors, tribology, actuators and cubesat mechanisms.

The high quality of this symposium is a result of the work of many people, and their efforts are gratefully acknowledged. This extends to the voluntary members of the symposium organizing committee representing the eight NASA field centers, Lockheed Martin Space, and the European Space Agency. Appreciation is also extended to the session chairs, the authors, and particularly the personnel at JSC responsible for the symposium arrangements and subsequent cancellation and the publication of these proceedings. A sincere thank you also goes to the symposium executive committee who is responsible for the year-to-year management of the AMS, including paper processing.

CONTENTS

Symposium Schedule viii

Symposium Organizing and Advisory Committees xiv

Design of a Deployable Vacuum Seal Cover for the Europa Clipper's MASPEX Instrument 1
John Gordon, Scott Christiansen & Charles Lazansky

Laterally Unconstrained Magnetic Joint for Pointing, Scanning, and Steering Applications 17
Vlad Krylov & Aaron Castillo

Design, Manufacturing, and Testing of Precision Space Flight Qualified Single Degree of Freedom Flexure Based Linear Actuators / Mechanisms …….. 27
Brandon Schneider, Todd Jackson, Jesse Booker & Kevin Kelman

Active Thermal Architecture Cryo Cooler Mechanical Characterization and Thermal Performance Assessment including Practical Considerations of Exported Force and Torque Testing 39
Bill Zwolinski, Pascal Erne, Lucas Anderson, Joel Mork & Ian McKinley

X2B Wide Angle Steering Mirror 49
Miroslaw Ostaszewski, Tim Quackenbush, Alix Carson & Jamin Hershberger

Advances in Bending Flat Plate Shape Memory Alloy Actuation Modeling: Prediction of Actuation Behavior 61
Michael Halvorson, Jonathan Coleman, Logan Williams, Bryan Hardaker, Frank Brown, Noah Cargile, Hayden Patteson & Eric Bradshaw

Cost Efficient Space Micro-Switches Based on Contactless Eddy Current Sensors 75
Gérald Aigouy, Sylvain Duc, Mathieu Castruccio, Aurore Loubet, Olivier Sosnicki & Frank Claeyssen

Design and Qualification of a Restrain-Release Mechanism for a 600-kg Deployable Panel Array 85
Horacio Quiroz, Gustavo Di Pasquale, Leonel Garategaray, Alberto Martín Ghiselli & Juan Ignacio Casais

NEA Mini for Low Load Applications – Development and Qualification 99
Ruben Betancourt & Jason Nave

Application of Ballistic Modeling and Quasi-Static Severance Testing in the Design of a Bolt Cutter 111
Jason Kozmic, Michael Rapp & Hobin Lee

Scan Mechanism Design for Large Deployable Reflector 121
Christian Hehr, Daniel Schmalholz & Cristovao Cardoso

Development of a Thrust Vector Control Mechanism for Deorbitation System 135
Ewa Majewska, Michał Ranachowski, Witold Wąsowski, Damien Pawluk, Filip Czubaczyński, Adam Kmak & Piotr Palma

Engineering Design of a Thruster Pointing Mechanism (TPM-250) for Deep Space and IOS Nanosats 143
Emilia Wegrzyn, Aitor Estarlich, Artur Fouto & Alberto Garbayo

The GRASS Gravimeter Rotation Mechanism for ESA Hera Mission Onboard Juventas Deep-Space CubeSat 159
Matthias Noeker, Birgit Ritter, Ozgur Karatekin & Emiel Van Ransbeeck

From PSYCHE PAM30 to Large Scale Free-Space Optical Communication 173
Gérald Aigouy, Etienne Betsch, Augustin Bedek, Nicolas Bourgeot, Anthony Baillus, Hugo Grardel, Pierre Personnat, Jean-Marc Nwesaty, Xavier De Lepine, Thomas Maillard & Frank Claeyssen

Developing a Plunger-Based Liquid Propellant Delivery System for CubeSat Propulsion..... 185
Pilar Gonzalez Rueda Flores, Raul A. Cuevas, Javier Madrid, Andre Molina, Hiram A. Lopez, Amelia D. Greig, Joel Quintana, & Ahsan R. Choudhuri

Flat Pack HDRM for Low Load Applications 191
Jason Nave & Ryan Klecka

Updated Phenolic Ball Bearing Retainer Testing for Space/Vacuum Environments..... 201
John Renaud

Preventing the “Brown Sugar” Lubricant Phenomenon: The Relationship Between PFPE Chemical Compositions and their Susceptibility to Lewis Acid-Catalyzed Degradation..... 211
Amanda Stubbs & Jason Galary

Performance of MoS_2 Coated Gears Exposed to Humid Air During Storage (Study Number Two) 223
Tysen Mulder, Timothy Krantz, Claef Hakun, Zachary Cameron, Iqbal Shareef & Michael Dube

Bearing Starting Torque Measurements Down to –100°C..... 237
Kim Aaron, Duval Johnson, Shana Worel & Frank Tao

Project Orion Crew Impact Attenuation System (CIAS)..... 249
Dale Kennedy, Nicholas Williams, Richard Koelsch, Evan Siracki & Charles Herrmann

First Steps to Develop a Triboelectric Wind Turbine for Mars Exploration 261
Borja Pozo, Iban Quintana, Ewelina Ryszawa, Iñigo Muñoz, Lionel Galliard & Erlatnz Fernandez de Gorostiza

Mars Sample Handling End-Effector Breadboarding..... 275
Isacco Pretto, Mario Esposito, Tharek Mohtar, Stefano Scutti, Alessandro Bursi, Massimo Lucia, Andrea Rusconi, Guido Sangiovanni, Davide Nicolis & Philippe Schoonejans

Efficacy of Lead Naphthenate for Wear Protection in High Vacuum Space Mechanisms 287
Dorota Budzyń, Eoin Tuohy, Natan Garrivier, Timon Schild, Aidan Cowley, Reuben Cruise, Masato Adachi, Hossein Zare-Behtash & Andrea Cammarano

Establishment of a Lunar Surface Docking/Mating System Standard 301
James Lewis & Stanley R. Donahoe

Remote Diagnosis and Operational Response to an In-Flight Failure of the Drill Feed Mechanism Onboard the Mars Science Laboratory Rover 309
Ryan Kinnett, Thomas Green, Douglas Klein & Megan Richardson Lin

Radial Loading of Hydrodynamic Bearings due to Magnetic Variation..... 323
Warrick Leigh, Flora S. Mechentel, Sehyun Oh & Michael Underhill

Conceptual Design of an Extendable Rope-Inspired Module Space Orbit Arm for Maneuvering: ERM- SOA..... 337
Bhivraj Suthar & Seul Jung

SWOT and NISAR Boom Ground Deployment Test Challenges & Resolution..... 351
Paul Lytal, Jeff Waldmann & Kyle C. Waters

Flatness Adjustment in the Design and Integration of a 35-m^2 Space Deployable SAR Antenna 365
Leonel Garategaray, Juan Casais, Alberto Martin Ghiselli, Horacio Quiroz & Gustavo Di Pasquale

SYMPOSIUM SCHEDULE

WEDNESDAY, 11 May 2022

7:00 PDT: INTRODUCTORY REMARKS
Edward Boesiger, General Chairman, Lockheed Martin Space, Sunnyvale, CA
Brandan Robertson, Host Chairman, NASA Johnson Space Center, Houston, TX

7:15 SESSION I – INSTRUMENTS
Session Chair: Jonathan Wood, Lockheed Martin Space, Sunnyvale CA

- Design of a Deployable Vacuum Seal Cover for the Europa Clipper's MASPEX Instrument
  John Gordon, Scott Christiansen & Charles Lazansky, Sierra Space, Louisville, CO

- Laterally Unconstrained Magnetic Joint for Pointing, Scanning, and Steering Applications
  Vlad Krylov & Aaron Castillo, Light Steering Technologies, Manchester, NH

- Design, Manufacturing, and Testing of Precision Space Flight Qualified Single Degree of Freedom Flexure Based Linear Actuators / Mechanisms
  Brandon Schneider, Todd Jackson, Jesse Booker & Kevin Kelman, Danbury Mission Technologies (DMT), Danbury, CT

- Active Thermal Architecture Cryo Cooler Mechanical Characterization and Thermal Performance Assessment including Practical Considerations of Exported Force and Torque Testing
  Bill Zwolinski, Kistler Instrument Corp, Amherst NY; Pascal Erne, Kistler Instrumente AG, Winterthur, Switzerland; Lucas Anderson & Joel Mork, Utah State University, Logan, UT; Ian McKinley, NASA Jet Propulsion Laboratory, Pasadena, CA

- X2B Wide Angle Steering Mirror
  Miroslaw Ostaszewski, Tim Quackenbush, Alix Carson & Jamin Hershberger, Ball Aerospace & Technologies Corp., Boulder, CO

- Lubrication Concept Evaluated for Geared Actuators under Starved Conditions
  Erik Nyberg & Ichiro Minami, Luleå Tekniska Universitet, Luleå, Sweden; Jonny Hansen, Scania CV AB, Södertälje, Sweden

9:45 PDT: Break

10:00 PDT: SESSION II – COMPONENTS & RELEASE MECHANISMS
Session Chair: Adam Dokos, NASA Kennedy Space Center, Kennedy Space Center, FL

- Advances in Bending Flat Plate Shape Memory Alloy Actuation Modeling: Prediction of Actuation Behavior
  Michael Halvorson, University of Alabama in Huntsville, Huntsville, AL; Jonathan Coleman, Logan Williams, Bryan Hardaker, Frank Brown, Noah Cargile, Hayden Patteson & Eric Bradshaw, Auburn University, Auburn, AL

- Cost Efficient Space Micro-Switches Based on Contactless Eddy Current Sensors
  Gérald Aigouy, Sylvain Duc, Mathieu Castruccio, Aurore Loubet, Olivier Sosnicki & Frank Claeyssen, Cedrat Technologies, Meylan, France

- Design and Qualification of a Restrain-Release Mechanism for a 600-kg Deployable Panel Array
  Horacio Quiroz & Gustavo Di Pasquale, National Atomic Energy Commission, Buenos Aires, Argentina; Leonel Garategaray, Alberto Martín Ghiselli & Juan Ignacio Casais, National Commission for Space Activities, Buenos Aires, Argentina

- NEA Mini for Low Load Applications – Development and Qualification
  Ruben Betancourt & Jason Nave, Ensign-Bickford - NEA Electronics, Inc., Moorpark, CA

- Application of Ballistic Modeling and Quasi-Static Severance Testing in the Design of a Bolt Cutter
  Jason Kozmic, Michael Rapp & Hobin Lee, Chemring Energetic Devices, Downers Grove, IL

12:10 PDT: Break

12:30 PDT: SPECIAL PRESENTATION – ARGOS
Joshua Sooknanan, NASA Johnson Space Center, Houston, TX
The Active Response Gravity Offload System (ARGOS) is designed to simulate reduced gravity environments such as Lunar (1/6G), Martian (1/3G), or microgravity (0G). ARGOS achieves six degree of freedom motion using an active XYZ system similar to a bridge crane whereas rotational degrees of freedom are passively managed by a gimballing mechanism at the payload interface. ARGOS' control system continuously tracks and offloads of a percentage of a human or robotic payload's weight during a wide range of partial gravity and microgravity activities. The facility supports surface operation studies, suit and vehicle requirements development, suit and vehicle design evaluation, robotic development, mass handling studies, and crew training with both suited and shirt-sleeved subjects.

1:15 PDT: End of Day 1

THURSDAY, 12 May 2022

7:00 PDT: SESSION III - ACTUATORS & GIMBALS
Session Chair: Ben Nickless, NASA Langley Research Center, Hampton, VA

- Scan Mechanism Design for Large Deployable Reflector
  Christian Hehr, Daniel Schmalholz & Cristovao Cardoso, Airbus Defence and Space GmbH, Friedrichshafen, Germany

- Development of a Thrust Vector Control Mechanism for Deorbitation System
  Ewa Majewska, Michał Ranachowski, Witold Wąsowski, Damien Pawluk, Filip Czubaczyński & Adam Kmak, Łukasiewicz Research Network - Institute of Aviation, Warsaw, Poland; Piotr Palma, Astronika, Warsaw, Poland

- Engineering Design of a Thruster Pointing Mechanism (TPM-250) for Deep Space and IOS Nanosats
  Emilia Wegrzyn, Aitor Estarlich, Artur Fouto & Alberto Garbayo, Added Value Solutions, Oxford, Great Britain

- Mars 2020 Motor Bearing Failure, Investigation and Response
  Dave Suffern, Jeff Mobley & Stephen Smith, Sierra Nevada Corporation, Durham, NC

8:45 PDT: Break

9:00 PDT: SESSION IV – CUBESAT HARDWARE
Session Chair: Landon Moore, NASA Johnson Space Center, Houston, TX

- The GRASS Gravimeter Rotation Mechanism for ESA Hera Mission Onboard Juventas
  Deep-Space CubeSat
  Matthias Noeker & Birgit Ritter, & Ozgur Karatekin, Royal Observatory of Belgium, Brussels, Belgium; Emiel Van Ransbeeck, VRE Consultancy, Royal Belgian Institute for Space Aeronomy, Brussels, Belgium

- From PSYCHE PAM30 to Large Scale Free-Space Optical Communication
  Gérald Aigouy, Etienne Betsch, Augustin Bedek, Nicolas Bourgeot, Anthony Baillus, Hugo Grardel, Pierre Personnat, Jean-Marc Nwesaty, Xavier De Lepine, Thomas Maillard & Frank Claeyssen, Cedrat Technologies, Meylan, France

- Developing a Plunger-Based Liquid Propellant Delivery System for CubeSat Propulsion
  Pilar Gonzalez Rueda Flores, Raul A. Cuevas, Javier Madrid, Andre Molina, Hiram A. Lopez, Amelia D. Greig, Joel Quintana, & Ahsan R. Choudhuri, University of Texas at El Paso Center for Space Exploration and Technology Research, El Paso, TX

- Flat Pack HDRM for Low Load Applications
  Jason Nave & Ryan Klecka, Ensign-Bickford - NEA Electronics, Inc., Moorpark, CA

10:45 PDT: BREAK

11:00 PDT: SUPPLIER SESSION – *A rapid fire session of invited suppliers showcasing their latest and greatest products. Each supplier will give their best 3-minute pitch and of course contact information will be available for attendees to follow up.*
Session Chair: Ed Boesiger, Lockheed Martin Space, Sunnyvale, CA

- Artemis Space, Geoff Carter, https://artemis-space.com

- BEI Precision, John Beasley, https://beiprecision.com/

- Diamond-Roltran, Jeffrey Gilling, https://diamond-roltran.com

- Cobham Advanced Electronic Solutions, Boz Sharif, https://caes.com/

- Ensign-Bickford Aerospace & Defense, Jason Nave, https://www.ebad.com/

- Kistler Instrument Corporation, Bill Zwolinski, https://www.kistler.com/en/

- Blue Line Engineering, Greg Ames, https://www.bluelineengineering.com/

- Spinner Rotary Joints, Kevin Cody, https://www.spinner-group.com/

- ThinGap, Incorporated, John Baumann, https://www.thingap.com/

- Arquimea, Marcello Collado, https://www.arquimea.com/aerospace-and-defence/

- Ducommun Incorporated, Francis Castelo, https://ducommun.com/

- Gurley Precision Instruments, Martin Gordinier, https://www.gurley.com

11:45 PDT: Break

12:00 PDT: SESSION V – THE STU LOEWENTHAL TRIBOLOGY SESSION
Session Chair: Stu Loewenthal, Lockheed Martin Space (Retired), Sunnyvale, CA

- Updated Phenolic Ball Bearing Retainer Testing for Space/Vacuum Environments
  John Renaud, The Timken Corporation, Keene, NH

- Preventing the "Brown Sugar" Lubricant Phenomenon: The Relationship Between PFPE Chemical Compositions and their Susceptibility to Lewis Acid-Catalyzed Degradation
  Amanda Stubbs & Jason Galary, NYE Lubricants, Inc., Fairhaven, MA

- Performance of MoS_2 Coated Gears Exposed to Humid Air During Storage (Study Number Two)
  Tysen Mulder & Timothy Krantz, NASA Glenn Research Center, Cleveland, OH; Claef Hakun & Zachary Cameron, NASA Goddard Space Flight Center, Greenbelt, MD; Iqbal Shareef, Bradley University, Peoria, IL; Michael Dube, NASA Langley Research Center, Hampton, VA

- Bearing Starting Torque Measurements Down to −100°C
  Kim Aaron, Duval Johnson, Shana Worel & Frank Tao, Jet Propulsion Laboratory, Pasadena, CA

1:45 PDT: End of Day 2

FRIDAY, 13 May 2022

7:00 PDT: SESSION VI – SPACE EXPLORATION
Session Chair: Louise Jandura, Jet Propulsion Laboratory, Pasadena, CA

- Project Orion Crew Impact Attenuation System (CIAS)
  Dale Kennedy, Safe Inc., Tempe, AZ; Nicholas Williams, Northrop Grumman, Chandler, AZ; Richard Koelsch, NASA Johnson Space Center, Houston, TX; Evan Siracki, Lockheed Martin Space, Littleton, CO; Charles Herrmann, NASA Glenn Research Center, Cleveland, OH

- First Steps to Develop a Triboelectric Wind Turbine for Mars Exploration
  Borja Pozo, Iban Quintana, Iñigo Muñoz & Erlatnz Fernandez de Gorostiza, Tekniker, Gipuzkoa, Spain; Ewelina Ryszawa & Lionel Galliard, ESA-ESTEC, Noordwijk, The Netherlands

- Mars Sample Handling End-Effector Breadboarding
  Isacco Pretto, Mario Esposito, Tharek Mohtar, Stefano Scutti & Alessandro Bursi, OHB Italia S.p.A., Milano, Italy; Massimo Lucia, Andrea Rusconi & Guido Sangiovanni, Leonardo S.p.A., Nerviano, Italy; Davide Nicolis & Philippe Schoonejans, ESA ESTEC, Noordwijk, The Netherlands

- Lunar Dust: Its Impact on Hardware and Mitigation Technologies
  Dorota Budzyń, Hossein Zare-Behtash & Andrea Cammarano, University of Glasgow, Glasgow, Scotland; Eoin Tuohy, Natan Garrivier, Timon Schild & Aidan Cowley, European Space Agency, European Astronaut Centre, Cologne, Germany; Reuben Cruise, Imperial College London, London, United Kingdom; Masato Adachi, Kyoto University, Kyoto, Japan

- Establishment of a Lunar Surface Docking/Mating System Standard
  James Lewis & Stanley R. Donahoe, NASA Johnson Space Center, Houston, TX

- Design and Test of the Orion Crew Module Side Hatch
  Lance Lininger, Lockheed Martin Space, Denver, CO; Kyle Gotthelf, Honeybee Robotics, Longmont, CO

9:35 PDT: BREAK

9:50 PDT: SESSION VII – ANOMALY & FAILURE ANALYSIS
Session Chair: Lukasz Wisniewski, Astronika Sp. z o.o., Warsaw, Poland

- Remote Diagnosis and Operational Response to an In-Flight Failure of the Drill Feed Mechanism Onboard the Mars Science Laboratory Rover
  Ryan Kinnett, Thomas Green, Douglas Klein & Megan Richardson Lin, Jet Propulsion Laboratory, Pasadena, CA

- Radial Loading of Hydrodynamic Bearings due to Magnetic Variation
  Warrick Leigh, Flora S. Mechentel, Sehyun Oh & Michael Underhill, Jet Propulsion Laboratory, Pasadena, CA

10:45 PDT: BREAK

11:00 PDT: SESSION VIII – DEPLOYMENT
Session Chair: Jared Dervan, NASA Marshall Space Flight Center, Huntsville, AL

- Conceptual Design of an Extendable Rope-Inspired Module Space Orbit Arm for Maneuvering: ERM- SOA
  Bhivraj Suthar & Seul Jung, Chungnam National University, Korea

- SWOT and NISAR Boom Ground Deployment Test Challenges & Resolution
  Paul Lytal, Jeff Waldmann & Kyle C. Waters, Jet Propulsion Laboratory, Pasadena, CA

- Flatness Adjustment in the Design and Integration of a 35-m^2 Space Deployable SAR Antenna
  Leonel Garategaray & Juan Casais, National Commission for Space Activities, Buenos Aires, Argentina; Alberto Martin Ghiselli, Horacio Quiroz & Gustavo Di Pasquale, National Atomic Energy Commission, Buenos Aires, Argentina

12:20 PDT: BREAK

12:35 PDT: SPECIAL PRESENTATION – NASA Astronaut Don Pettit, who is a veteran of two long-duration stays aboard the International Space Station, one space shuttle mission, and a six-week expedition to find meteorites in Antarctica.

1:20 PDT: TECHNICAL SESSIONS CONCLUSION
Jonathan Wood, Lockheed Martin Space, Sunnyvale, CA
- Herzl Award Presentation

1:30 PDT: End of Day 3

SYMPOSIUM ORGANIZING COMMITTEE

Host Chair – Brandan Robertson, NASA JSC

General Chairman - Edward A. Boesiger, Lockheed Martin Space
Deputy Chairman - Stuart H. Loewenthal, Lockheed Martin Space (retired)

Earl Daley, NASA ARC
Damon C. Delap, NASA GRC
Jared A. Dervan, NASA MSFC
Adam G. Dokos, NASA KSC
Michael J. Dube, NASA NESC
Carlton L. Foster, NASA MSFC (retired)
Lionel Gaillard, ESA/ESTeC
Claef F. Hakun, NASA GSFC
Christopher P. Hansen, NASA JSC
Louise Jandura, JPL
Alan C. Littlefield, NASA KSC (retired)
Ronald E. Mancini, NASA ARC (retired)
Fred G. Martwick, NASA ARC
Donald H. McQueen, Jr., NASA MSFC (retired)
Robert P. Mueller, NASA KSC
Benjamin J. Nickless, NASA LaRC
Joseph W. Pellicciotti, NASA HQ
Minh Phan, NASA GSFC
Joseph P. Schepis, NASA GSFC
Donald R. Sevilla, JPL
James E. Wells, NASA LaRC
Jonathan P. Wood, Lockheed Martin Space

Design of a Deployable Vacuum Seal Cover for the Europa Clipper's MASPEX Instrument

John Gordon*, Scott Christiansen* and Charles Lazansky*

Abstract

The Mass Spectrometer for Planetary Exploration (MASPEX) instrument on the Europa Clipper Spacecraft required a deployable mechanism to hold vacuum and maintain a leak rate less than 1E-8 Pa*l/sec (1E-10 mbar*l/sec) throughout ground operations, launch, and interplanetary travel until commanded to deploy. This custom-designed vacuum cover mechanism utilized a metallic H-seal to meet stringent leak and cleanliness requirements. The cover also relied on a significantly scaled-down version of heritage clamprings to provide retention of the high seal loads prior to deployment. Due to the fine measurement capability of the MASPEX instrument, a hermetic actuation device and minimal non-metallic components and finishes were used.

This paper addresses the driving requirements, design, integration, and lessons learned for use of a deployable knife-edge seal. Design challenges of developing a miniature clampring (approximately 12.7 cm (5.0 in) outer diameter), incorporating micro-switches, limiting weight, and designing a mechanism with minimal non-metallic components are included. Additionally, the mechanism design path, from trade studies through successful protoflight testing, including a late system requirement change leading to the need to add redundant non-evaporable getter (NEG) pumps to the critical sealing component, is explored.

Introduction

The Europa Clipper spacecraft is planned to launch in 2024 to determine if Jupiter's moon Europa harbors conditions suitable for life [1]. The spacecraft will orbit Jupiter and make 40 to 50 passes over the moon's surface [2]. One of the instruments on the Europa Clipper is the Mass Spectrometer for Planetary Exploration (MASPEX) instrument. This instrument will sample and analyze gases from the plumes venting to space from Europa's surface to study the moon's ocean surface and atmosphere [3]. As the MASPEX instrument has a mass resolution hundreds of times finer than any hardware previously sent to space, all surrounding components were selected to minimize the use of non-metallic materials to limit outgassing near the instrument aperture [3]. In order to protect the instrument before space flight use, a deployable cover is to be mounted onto the instrument's antechamber (at instrument aperture) that can hold the required hermetic seal. Design, manufacturing, and test of the vacuum cover mechanism was performed at Sierra Space (Sierra Nevada Corporation) for Southwest Research Institute (SwRI).

Design Requirements

The deployable vacuum seal cover for the MASPEX instrument was a custom design due to several unique and challenging requirements. The cover is required to complete a single deployment in flight following interplanetary travel upon command. It is rated for 12 years of spaceflight operation as well as 12 years of ground use. The design driver for this mechanism was the sealing requirement of < 1E-8 Pa*l/sec (1E-10 mbar*l/sec) helium leak for ground, launch, and flight environments before release. This leak requirement is equivalent or greater than the best commercially available static seals, and is at the noise floor of most helium leak detectors. The MASPEX cover is required to maintain a hermetic seal to ensure that the instrument remains free of contaminants to protect the sample for subsequent error-free analysis. For similar reasons, materials were selected for a metallic seal and related internal chamber surfaces to avoid contaminants like dissolved hydrogen, nitrogen and argon gases. Any internal surfaces containing

* Sierra Space, Louisville, CO; John.Gordon@sncorp.com

dissolved gasses would outgas and negatively impact the instruments analytical results. All components of the cover mechanism were required to be retained below the instrument aperture following release, in order to not occlude the aperture, limiting the input into the instrument. Additional requirements include application of redundant heaters and springs (for cover open), as well as a mass limit less than .86 kg (1.90 lb).

Finally, due to the instrument and mechanism's position on the spacecraft (cantilevered away from the spacecraft) and functional requirement to maintain seal throughout environmental loading, the operational temperature and vibration requirements were key design drivers. Vibration, (X-Axis, perpendicular to aperture and sealing surface) was high at 26.1 gRMS. Cover operational (flight) temperatures ranged between -60°C to 80°C with a mechanism bakeout requirement of 220°C.

Flight Mechanism Design

The flight design evolved from a series of developmental design and test iterations as test results revealed new information and requirements evolved. Although the final flight design deviated from the prototype concept, the functionality of the cover as a whole remained consistent. The main structural components of the mechanism, including the rings, clampring, seal plate, and hinge structure were composed of Titanium 6AL-4V.

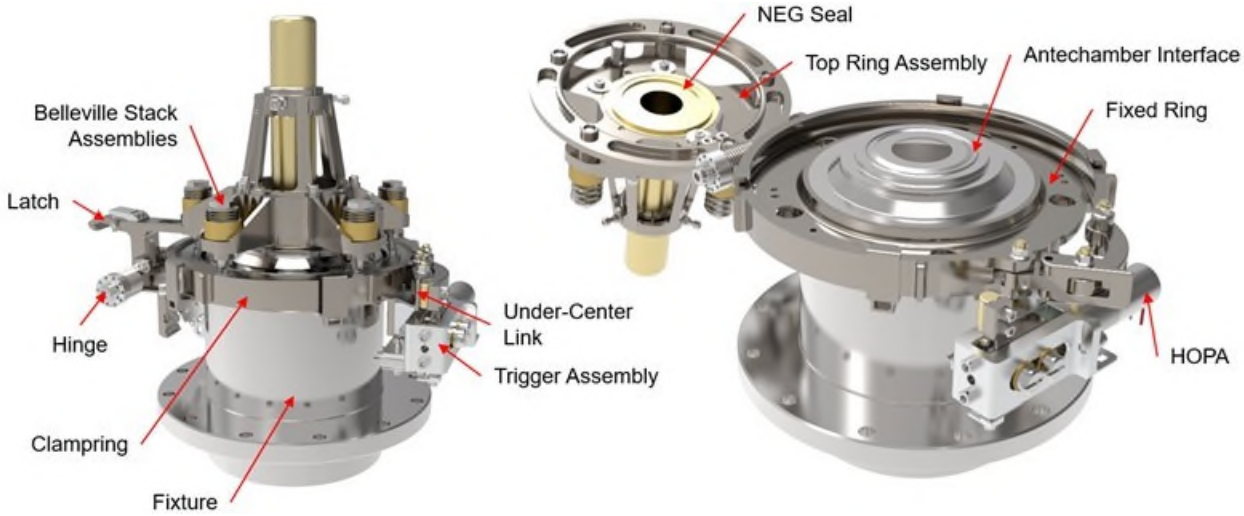

Figure 1: Component positions on cover mechanism (Left) Stowed rendering of flight mechanism mounted on antechamber, (Right) Deployed rendering. Credit: Sierra Space Corporation

The mechanism incorporates a modified Bostec capped H-seal to achieve the 1E-8 Pa*l/sec helium leak requirement. The seal is made from a C107200 copper alloy, with a gold-sputtered finish for corrosion resistance. C107200 copper was selected due to its CTE similarities to the instrument interface. Additionally the material, in conjunction with the H-seal design, had an acceptable force to load, and did not require any non-metallic components to retain the required leak rate. The seal was loaded perpendicularly to the surface with a GSE fixture. Hinge compliance (in-plane as well as axial rotation degrees of freedom) was incorporated to allow for proper loading and alignment of the seal. The design insured the seal remained parallel and did not arc down onto the knife-edge interface on the instrument prior to the engagement load event. For deployment, the cover rotates on a hinge line with 1.27 mm (0.050 in) of axial pin clearance to account for component tolerances and seal loading travel. The seal is designed with an extension to support redundant NEG pumps, which are required to mitigate outgassing during vacuum pump down of the instrument. This extension is supported by a structure that had three clamps surrounding the extension, preventing displacement of the seal during vibrational loading of the mechanism. These clamps are specifically designed with recessed features to ensure two lines of contact each onto the seal. This ensures the seal will not fail due to the attached support structure reaction loads during exposure to the vibration environment.

The top ring assembly is held in place using a miniaturized clampring with built-in shoes. The clampring, approximately 12.7 cm (5 in) diametrically, holds the top and fixed rings in place. Tension in the clampring, approximately 1780 N (400 lbf), is held with an under-center latch and trigger assembly. The clampring tension was derived to react the engagement loads required to set the cover seal. In accordance with heritage design, the clampring is machined in a free state larger than the radius of the band catchers, and its stowed state, such that upon deploy, the clampring is held under its own elastic forces. The catchers hold the clampring in place for the remainder of the spacecraft's operations, preventing microphonic excitation. The geometry of the linkage is designed to prevent the under-center link from reaching the over-center condition, thus ensuring the clampring always wants to open. The trigger assembly holds the latch in place until actuated using a Sierra Space High Output Paraffin Actuator (HOPA) mechanism. The trigger is held preloaded, before actuation, via compression springs housed in the trigger assembly. The trigger slides along a mounting bracket with redundant bushings. The HOPA used, an EH-3525 model, is hermetically sealed and provides 222 N (50 lbf) upon command using redundant heaters [5].

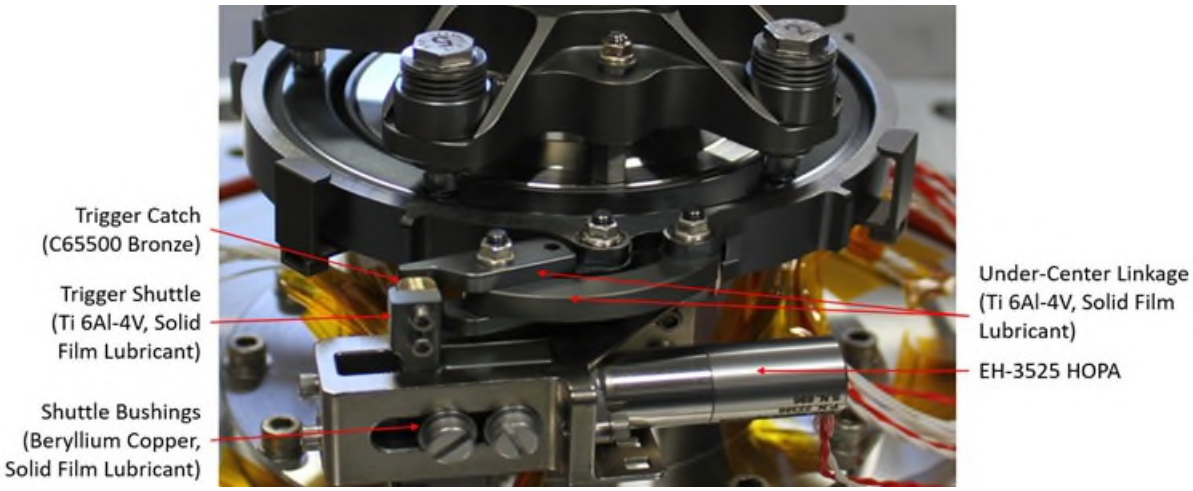

Figure 2: Stowed clampring and under-center latch on flight mechanism. The under-center latch assembly required use of components with different materials and the use of non-evaporable lubricants. Credit: Sierra Space Corporation

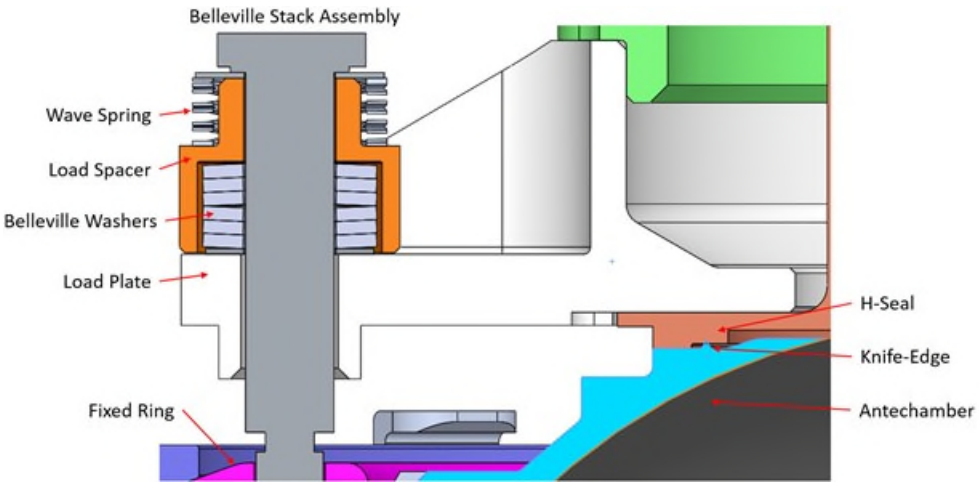

Figure 3: Belleville stack assembly isometric cut view. Also shown is the knife-edge cut into the H-seal from the antechamber sealing interface. The sealing interface is preloaded for flight by five Belleville washer stacks. Credit: Sierra Space Corporation

The seal is engaged onto the knife-edge antechamber via an external ground support equipment (GSE) fixture that loads the seal through the load plate. The seal protects an aperture slightly larger than 20.3 mm

(0.80 in). Following engagement of the seal, the seal is retained onto the antechamber with approximately 13.3 kN (3000 lbf) via five Belleville stacks. Each stack was characterized prior to integration and shimmed to ensure the desired preload when torqued to a hard stop. The Belleville stacks provide force through the load plate, and are retained by threading into the top ring, and constrained before deployment with a clampring. Each stack also has a wave spring, which upon clampring deployment, acts to pull the top ring away from the interface surface ensuring the top ring assembly clears the clampring (Ref Fig. 3).

Actuation of the HOPA is confirmed with a micro switch located on the trigger assembly. The switch is closed and snubbed into place during launch operations and rides along a cam during mechanism release.

Upon release of the clampring latch, the top ring assembly is released from the fixed ring and moves to the deployed state via two redundant torsion springs reacting at the hinge line. These springs are aided by a kickoff plunger, oriented 180 degrees from the hinge line, to mitigate any stiction of the seal onto the antechamber. Testing of the mechanism indicated that stiction and the force to release the seal was negligible. When fully deployed, the top ring assembly contacts a diving board hard stop. The diving board hard stop acts to react the deployment force from the torsion springs and kickoff plunger. Additionally, the top ring assembly is preloaded against the diving board and latched into place following seal deployment. A micro switch is located on the hinge line, to indicate when the cover is clear of the clampring towards the deployed condition. The switch is closed during stowed operations and rides along a cam as the top ring assembly deploys.

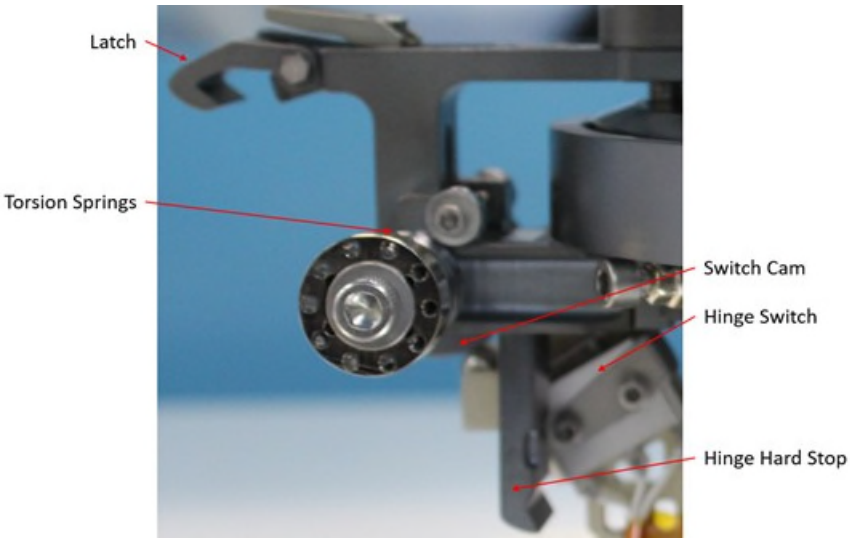

Figure 4: Hinge and latch assembly in stowed state. Latch assembly prevents rebound of cover and locks the upper ring assembly below the instruments aperture following mechanism deployment. Credit: Sierra Space Corporation

Due to the sensitive nature of the MASPEX instrument, careful consideration to all non-metallics and use of dissimilar metals was taken for the cover mechanism. No non-metallic materials were used in the sealing interface, which is exposed to the instrument aperture. For sliding surfaces of the mechanism, Dicronite solid-film lubricant was used. For the hinge line, the structural components of the mechanism, composed of titanium 6AL-4V, rotated on a 15-5 stainless steel hinge pin (undersized to provide compliance for seal loading), with the rotating surfaces separated by beryllium copper washers. The loading surfaces of the clampring and rings were also lubricated with the Dicronite solid-film material. Care was taken to properly burnish the rings and clampring before integration, and visual inspections were conducted after all functional testing to ensure that the surfaces were not degrading under the clamping loads. The solid-film coating was used on the prototype, EDU, and flight builds, and did not show degradation during functional and environmental testing. Additionally the under-center latch (Dicronite coated titanium 6Al-4V) component is loaded on the trigger assembly, and slides along a C65500 bronze shuttle when deployed.

The trigger shuttle rides on beryllium copper bushings along structural surfaces coated by Dicronite solid-film lubricant (Ref Fig. 2). More on this topic is discussed in the Trade Study section.

Although the cover mechanism was a unique custom design, several heritage components and concepts were incorporated. The cover design is based on an optical cover for NASA's Thermos-Spheric Temperature Imager. This design was updated to integrate the H-seal and to mount on the MASPEX instrument antechamber. The retention method is a modified clampring, based on a heritage clampring and HOPA mechanism for Cassini's Plasma Spectrometer, flown on the Cassini orbiter. The EH-3525 HOPA has significant flight heritage as a part of Sierra Space's paraffin actuator product line with over 20 years of spaceflight heritage. Bostec H-seals also have NASA flight heritage.

Mechanism Developmental History

A number of trade studies and engineering development units proceeded the final flight design. The following describes the history behind this cover mechanism's development. The initial concept for the cover mechanism incorporated a yet to be determined vacuum seal retained by a clamped interface to the MASPEX instrument's aperture. Design started around retaining the seal with a marman type clampring, however a pyro release of the clampring (commonly used) would have to be replaced with a lower shock release mechanism. This door cover was to be driven by torsion springs to move the door from the stowed to deployed state.

Trade Studies

The cover system design evolved from a series of trade studies to investigate potential seals capable of meeting the system leak requirement. This seal was originally required to meet a <5.0 E-10 Pa*l/sec helium leak requirement, without the use of non-metallic components with all surfaces free of dissolved hydrogen, nitrogen, and argon. The leak requirement was later relaxed to "just" 1E-8 Pa*l/sec helium leak. Further limiting design options was the deployable aspect of the seal cover. Design considerations were evaluated against required seal load (engagement and retention) as well as seal separation dynamics. Low engagement sealing force was critical to ensure the cover's mount (antechamber/ thermalizing chamber) would not be overloaded during mechanism integration. Additionally, potential seals were assessed for reusability, flight heritage, and cost/lead-time.

The seals investigated during this phase of the trade study were Bostec H-seals (cap, engaged exclusively on one side, and standard, engaged on two sides), conflat seals, delta seals, and metallic O-/C- rings. The H-seals, and the conflat seals were the highest scoring seals following the initial trade study. These seals scored the best because of effective performance in two key areas: leak rate and material composition (i.e., minimal leak rate and nonmetallic material composition). The H-seals also exhibited lower sealing force characteristics compared to other seals investigated. They function by engaging a knife-edge into a recessed flat surface on the seal. Load is taken through a positive stop on the seal to prevent overload of the seal once the knife-edge is fully engaged into the sealing surface [4] (Ref Fig. 3). The geometry of the knife-edge cut into the sealing surface is different than that of a conflat seal, and results in a lower necessary seal engagement load as compared to conflats.

Following initial trade studies, the capped H-seal was selected for additional helium leak checks. Note that these seals are typically used statically for vacuum tubing. The seal was tested under multiple configurations to determine the optimal seal material and interface engagement for the cover mechanism. Seal materials tested including 1100 aluminum, 200 nickel, and C107200 copper. Engagement depth of the knife-edge was characterized (.127 to .203 mm (.005 to .008 in)). This engagement depth study was critical and helped establish materials that required low engagement force while minimizing leak rate.

The seal configurations were subjected to thermal environments (25°C to 180°C) to ensure that the leak rate of the seal did not violate the leak requirement during thermal extremes or transitions between hot and cold. The seal configuration was set up in an enclosed chamber following seal loading, subjected to vacuum

on one side of the seal, and helium pressure (up to 689 kPa (100 psi)) on the other (Ref Fig. 11). Helium background checks and internal calibration of the leak detector were conducted before and after helium pressurization of the enclosure.

Trades and testing determined that nickel and copper H-seals exhibited the best sealing characteristics. CTE differences between the aluminum seal and the antechamber resulted in unacceptable leaks. Nickel and copper seals showed minimum leak rates when the knife-edge engagement of the seal was .178 to .203 mm (.007 to .008 in). Seals predominantly met the sealing requirements with knife-edge engagement of .127 mm (.005 in). There was a singular test event with the nickel seal at the maximum temperature that violated the leak requirement for the nickel seal. Further investigation into the leak suggested that this was due to a GSE error. It is critical to ensure all joints, valves, and interfaces in the test setup were correctly sealed to ensure that any leak detected could be accurately attributed to the seal being tested.

Following trades and testing, the copper seal proved to provide the best overall characteristics and was chosen for the mechanism for several reasons. First, it offered lower initial engaging loads. Second, copper is a better CTE match with the A286 antechamber interface. Additionally, it was determined that the copper seal would be sputtered with a gold plating to mitigate concerns about copper corrosion during spaceflight.

During testing, sealing performance of the seal flat and knife-edge interfaces were highly dependent on surface condition and proper loading. Components needed to be highly controlled to eliminate burrs, cuts, scratches and other surface defects. Any damage to the sealing surface resulted in reduced capabilities to hold leak at the required level. Load being applied perpendicular to the sealing interface proved critical. This load needed to be applied evenly around the knife-edge interface. The knife-edge cut into the H-seals needs to be crisp (Ref Fig. 5); rounded cuts due to uneven loading of the seal did not result in acceptable sealing interfaces. Following the conclusion of leak testing it was noted that negligible force was required to release the seal from the antechamber interface.

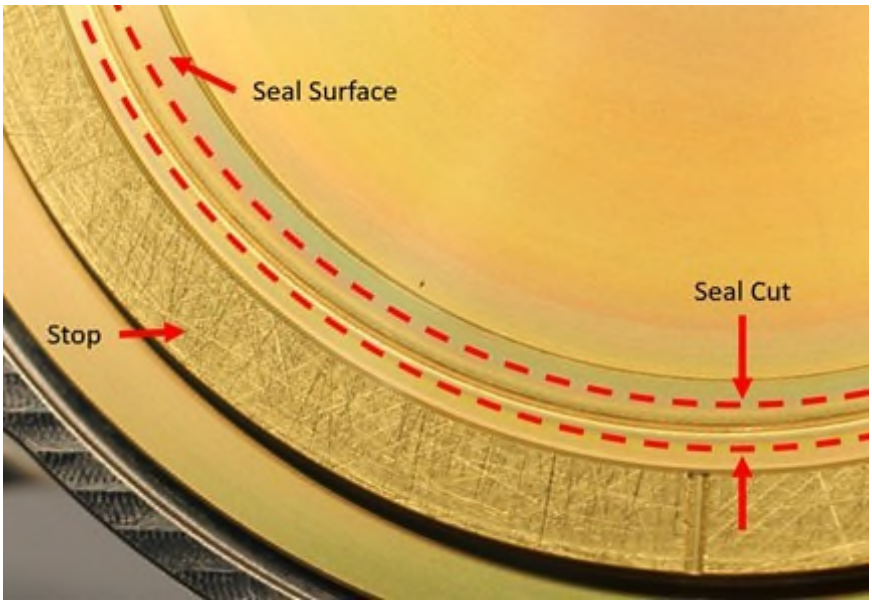

Figure 5: Desired cut from knife-edge onto capped H-seal. Cut is concentric relative to stop and sealing surfaces. The resulting cut is clean with not nicks or blemishes. Credit: Sierra Space Corporation

In addition to evaluating seal design, a trade study was conducted into potential actuation devices for the cover mechanism. Different models of heritage Sierra Space's HOPAs were compared for cleanliness (hermetically sealed), stroke and power output, mass, input power required, and redundancy for internal heater circuits. Trade study results indicated that the EH-3525 HOPA would best meet the mass and linear force actuation requirements for the cover release mechanism. The EH-3525 HOPA is hermetically sealed

via welded bellows with sufficient stroke and output force for use on the cover. The EH-3525 HOPAs operational power required (5 W @ 28VDC) and mass (<35 g) were minimal, and met system requirements.

Lubrication choice for the sliding surfaces of the mechanism also posed a unique problem. Given the mechanism's location very near to and around the instrument aperture, a low outgassing lubricant was needed. As this requirement eliminated all wet and binder based lubricants, it pointed toward a sputtered lubricant such as MoS_2 or WS_2. Because key requirements for this mechanism included very low outgassing, sliding contact, very low cycle life, and the need for a very thin coating, Dicronite (sputtered WS_2) was selected over MoS_2 [6]. Previous space industry experience also indicated that rigorous application and handling practices were required to successfully use Dicronite in a spacecraft mechanism. All lubricated components were coated exclusively at approved vendors, with 100% visual inspection upon receipt. During assembly, contacting interface surfaces were appropriately burnished, and these surfaces were inspected and monitored during subsequent assembly and test to ensure that degradation or exessive wear did not occur.

Prototype and EDU Development/Testing

The initial cover mechanism for the prototype and engineering development units was designed following the trade studies. This cover incorporated a copper capped H-seal and the EH-3525 HOPA. These non-flight builds were intended to prove out the cover concept to the TRL6 level to show that the cover met the sealing requirements through preliminary vibration levels and thermal cycling, and that it could functionally deploy following environmental testing. The cover was designed around the capped H-seal, which was clamped into place on top of the surrogate antechamber using a load plate. This load plate was fixed in place by two rings (one fixed onto the antechamber, one free to release) which were secured by a clampring. The clampring was held in position using an under-center latch, released by a trigger assembly actuated by the EH-3525 HOPA. Following the paraffin actuated unlatching event, the cover opens along a hinge line powered by redundant springs, and preloads it against a set of leaf spring to dampen the impact loads.

Given the material requirements for the mechanism, wet lubricants and the binder-based MoS_2 dry-film lubricants were not acceptable for use on the cover due to outgassing concerns and their propensity to produce particulates. A solid-film lubricant, Dicronite, was selected for use on the cover.

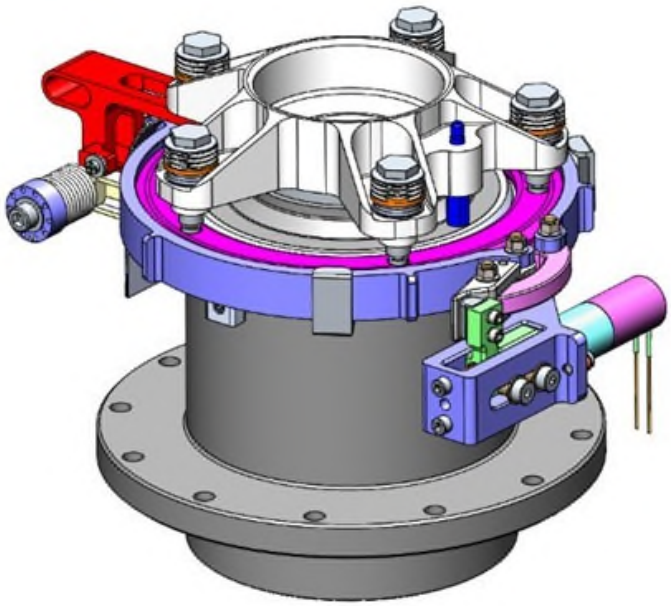

Figure 6: Prototype vacuum cover mechanism concept. Credit: Sierra Space Corporation

Clampring tension adjustability was designed into the mechanism trigger at the end of travel for the under-center latch (a new method of retaining a clampring). Initial loadings of the clampring (with or without the rings) showed that these shims provided negligible adjustability for the tension in the clampring. Further testing showed that by the time the under-center link reached the end of travel, as designed for the mechanism, adjustments in angle correlated to limited changes to the clampring tension; the greatest change in tension to link angle occurred significantly before the transition point between over and under-center. This resulted in a design modification to the under-center linkage for the prototype being slotted at assembly to achieve the desired tension in the clampring. Clampring tension was confirmed with force testing at the linkage and gap testing of the rings.

Retention load on the seal, before release, was set with five pre-configured sets of Belleville washers. These Belleville stacks were combined with wave springs to pull the top ring away from the clampring when the mechanism was deployed (Ref Fig. 3). Additionally the load plate featured a kick-off plunger to release the cover under any stiction events. The plan for this cover was to load the seal using the five Belleville stacks. The stacks threaded thru the top load plate into the free ring. These stacks were to be loaded incrementally in a star pattern in order to ensure the seal came down evenly. The required seal impregnation load was designed to be 17.8 – 22.2 kN (4500 – 5000 lbf). This load value accounted for the minimum engagement load measured during trade studies, with margin added to ensure complete engagement of the seal. Following initial impregnation of the capped H-seal, the retention load for the seal was only required to be approximately 13.3 kN (3000 lbf) (value also heavily margined to ensure proper preload during environmental exposure).

The design of this mechanism was a delicate balance between creating a cover that could keep a hermetic seal and then fully release upon command. Testing during the initial build of the first unit (TRL6 testing) revealed several functional issues that required design updates. The first issue involved the capped H-seal seal. Although the H-seals are capable of handling minor positional misalignments, it is critical that the seal is guided onto the knife-edge interface [4] (Ref Fig. 5). It is also critical to ensure that nothing interferes with the positive stop of the seal. The initial design had the capped H-seal secured in place using a clamp around the OD of the seal. Unfortunately, compliance built into the hinge that allowed the seal to engage properly was not enough to allow the top ring assembly to seat correctly on the antechamber. This drove a design change to replace the original seal securing ring with less obtrusive retention features.

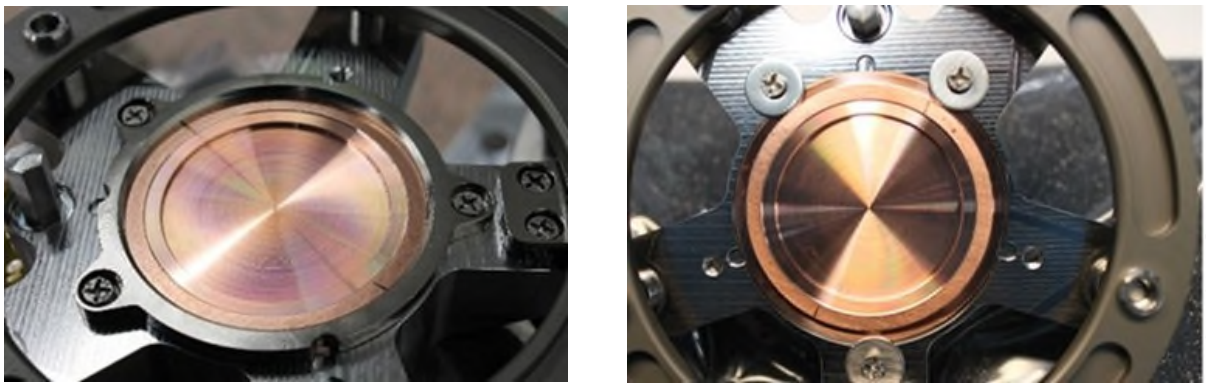

Figure 7: (Left) Original seal retention method (Right) Updated seal retention method. The original seal retention method did not give proper clearance to the antechamber to allow for the seal to be loaded correctly, and prevented proper deployment of the cover. Credit: Sierra Space Corporation

Following the change to the seal retention, the cover mechanism was loaded. Care was taken to ensure that the seal flat was properly oriented onto the knife-edge surface after the first operational loading resulted in a seal that was only 75% engaged on the sealing surface due to a concentric misalignment. The seal was biased in the load plate to counter the load plate being biased by the torsion springs. Once that was corrected, integration and test resulted in proper concentricity of the knife-edge cut onto the seal. Following

several stow and load cycles of the prototype cover, it was noted that the cut into the seal was rounded at the top, which resulted in undesirable sealing conditions. Further investigation into the loading procedure found that incrementally loading Belleville stacks was insufficient to ensure proper penetration of the knife-edge into the seal. To remedy this, the mechanism was loaded using an arbor press to depress the load plate, ensuring that the knife-edge seal engaged the mating interface of the surrogate antechambers knife-edge perfectly perpendicular to the seal. A GSE fixture was developed to ensure proper load application of the seal. This fixture mimics the functionality of the arbor press through two power screws, torqued simultaneously to load the cover. The GSE loading fixture mounts on the fixed ring and loads the seal through the load plate.

Following several confidence test deployments of the prototype unit, the front band catcher for the clampring showed significant yielding, to the point where it was no longer functional. Analysis of the high-speed video showed the under-center latch and clampring system resulted in more energy input into the catcher than anticipated. This resulted in a catcher material (Aluminum 6061 to Titanium 6Al-4V) and thickness change. Subsequent deployments confirmed that the new catchers functioned as-designed without deformation.

Characterization of the Belleville stacks for the prototype build also resulted in a desired change to the mechanism. The prototype mechanism relied on previously characterized spring stacks to be torqued to a certain height with gauge blocks indicating deflection located on either side of the stack. This was a needlessly tedious process with potential to not be as reliable as desired; every .025 mm (.001 in) deflection of the stack resulted in significant load changes for the stack. It was determined that all future designs should have a hard stop feature around the stacks to ensure consistent retention loading of the seal. To make the stacks adjustable, shims were placed inside the sleeve to allow for the desired load to be dialed in during Belleville characterization.

Loading of the EDU clampring showed that the under-center linkage needed to be slotted differently than the prototype build, in that additional slotting was needed. Further inspection of the rings being clamped by the clampring showed the rings were minimally greater in their outer diameters as compared to the prototype unit. Further testing with varying sizes of rings, showed that the final tension of the clampring was highly dependent on the size of the outer diameter of the rings. This resulted in the tolerance of the outer diameter feature for the rings being tightened for all subsequent builds.

Updates to the mechanism design and loading procedure resulted in a prototype cover that was sealing properly during functional/confidence testing. The prototype build was then exposed to vibration in all axis and subjected to thermal cycling (-45°C to 175°C). The cover mechanism was helium leak checked continuously during each environmental test. The prototype cover successfully passed all environmental testing while maintaining the required sealing interface throughout. Following environmental testing, the cover was successfully deployed. The cover design was updated with the lessons learned from the prototype build and released at the non-flight level. Environmental testing was repeated on the EDU cover proving the concept and giving high levels of confidence in the design.

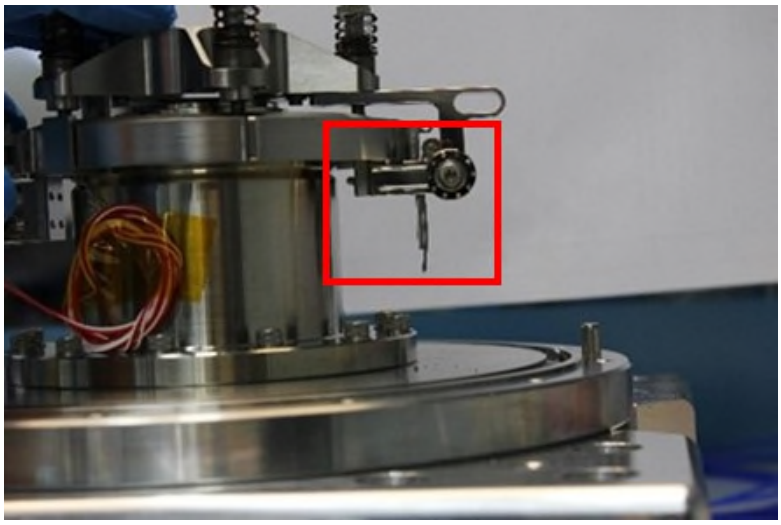

Figure 8: Yielding of leaf springs following deployment of the cover. The leaf springs on the prototype cover yielded following multiple test deployments. Credit: Sierra Space Corporation

Following the EDU test campaign, two updates were needed for the flight mechanism. The first was to update the stop for the top ring assembly following release. Multiple undesirable features were noted with the leaf spring stop. Following multiple deployments, the leaf springs began to yield. Further testing of the mechanism (including over 50 releases into the leaf springs) showed that the yielding stabilized after the first 5-10 deployments, however, a more robust stop and capture system was determined to be necessary for the flight built. Additionally, the leaf spring stop did not absorb enough energy of the cover after contact, causing the cover to bounce back over the instruments aperture. The cover would eventually rest on the leaf springs as designed. Although the door bouncing did not violate any requirements, it was determined that the flight build must retain the cover in place following deployment without the cover re-entering the aperture of the instrument to prevent any damage to the antechamber (surrogate or flight) for future units.

Additional lessons were learned during the development of the test fixture. Initial base readings showed that background helium could be sensed by the LACO Titan Test Machine (LACO) if not properly vented. This was isolated following gradual increases in helium being detected by the machine throughout prototype vibration testing. The LACO was blanked off; following reset and pump down of the system, the helium leak detected had climbed significantly above what had been detected during previous background calibrations. It was determined that the helium from previous pressurizations had built up in the smaller (than the manufacturing floor) test room. This was mitigated by opening the test room during helium purge events, and piping the LACO exhaust outside the testing area. Additionally, it should be noted that each interface in the test set up presented a potential leak point. Each of the interfaces had to be meticulously secured and checked (using a Helium sniffer bottle) to ensure that the cover mechanism would be isolated as intended.

EDU to Flight Design Build and Test

Before updating the development design of the vacuum cover mechanism to flight, a system-level requirements change was levied against the mechanism. It was determined that redundant NEG pumps were necessary to counter outgassing inside the instrument. The NEG pumps, and subsequent housing, could not be attached directly to the antechamber due to the antechamber's function as the MASPEX instrument input component. The cover's H-seal was determined to be the only location to attach the NEG pumps. This added a new wrinkle in the challenge of designing a deployable interface that could maintain a hermetically sealed chamber. Additional design iterations were required to accommodate the seal growth into the cover, hopefully without a complete re-design of the cover mechanism.

Even though the NEG pumps represented a relatively minor mass increase, the offset cantilevered nature of the housing components, and related heating requirements drove a design change to the seal and surrounding structure. For the NEGs to function, they need to be heated to over 500°C for 10 minutes. Because antechamber vacuum must be pulled prior to NEG activation, NEG heating was required after the cover system was sealed onto the instrument's antechamber. Due to the risk of the seal failing from rapid CTE changes, NEG activation was required to occur away from the critical seal interface with enough distance to create an effective heat sink. This drove a design change to attach a structural extension to the H-seal that offset the NEG pump approximately 9.5 cm (3.75 in) away from the seal interface, deviating significantly away from the original flat seal design.

Several design updates accommodated the extension change to the critical sealing component. A bore was added to the load plate for the NEG seal to pass through. Additionally, the extension in the H-seal had a marginal fillet at the extension point (1.9 mm (0.075 in) radius), which resulted in a high-stress point. It was analytically determined that launch loads would break the NEG extension off of the H-seal if not properly supported. A "tree" support assembly was integrated into the cover to properly support the seal. This support structure is attached to the load plate to offload the mass of the NEG extension under launch loads and to prevent related deflection from compromising the seal. This assembly features three radially adjustable clamps. Each clamp has a recessed feature to ensure two lines of contact per clamp on the extension in order to reduce associated Hertzian contact stress (Ref Fig. 9). These clamps were lightly snugged against the seal extension, and then locked into place. The support structure is designed to be installed on ground prior to launch following activation of the NEGs.

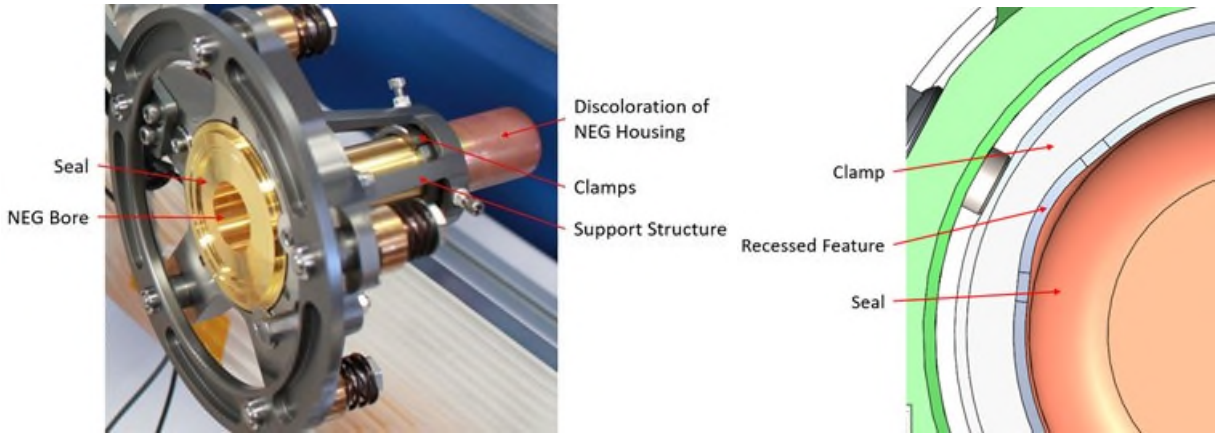

Figure 9: (Left) NEG Seal following activation with support fixture installed. The support fixture was required to prevent deflection of the NEG pump seal housing. The NEG seal was discolored following activation where it was heated to 500°C for over 10 minutes. (Right) Clamp interface onto seal. Cut in clamp ensures two lines of contact on seal to limit Hertzian stresses. Credit: Sierra Space Corporation

In addition to the NEG support flight design update, the stop design for the cover was improved and a latch was added. As the original stop design on the prototype and the engineering development units exhibited significant bounce back of the cover into the instruments aperture, the leaf spring stack up was replaced with a single flexure (diving board). The new design was analyzed to optimize thickness, avoiding over stress (yield), while maintaining adequate force and deflection parameters for force attenuation following deployment. A latch was incorporated to prevent the deployed cover interfering or damaging the instrument aperture; it was designed to activate with the inherent hinge compliance and catch underneath the diving board to secure the cover following deployment (Ref Fig. 4).

It was also determined that two telemetry switches were necessary. The first switch was required to indicate actuation of the HOPA. The switch was added underneath the trigger holding the under-center link and guided along a cam which activated the switch once the link was released. The second switch was required to indicate the cover opened clear of the clampring and was integrated into the hinge components of the

cover. This switch was placed alongside the diving board and was depressed with a cam attached to the hinge line, toggling when the cover was released and significantly routed towards its stowed condition.

Finally, minor improvements were also made to the kickoff plunger to replace a retention ring with a nut and washer hard stop. Additional band catchers were also placed around the mechanism to ensure the clampring was fully retained following deployment, and would not rattle during interplanetary travel to meet a new microphonics requirement.

Flight Cover Testing

Following implementation of design changes to the EDU unit, development testing was conducted to validate design changes. Before environmental testing, to validate the NEG seal activation process, the NEG seal was sealed and activated. An induction heater was positioned around the NEG and a heat sink was connected to the seal. Thermocouples were placed at the base of the seal to monitor temperature changes ensuring that the knife-edge interface would not be damaged during the activation process. The thermocouples showed that the base temperature did not notably increase. This result greatly alleviated concerns that NEG pump operations would compromise the seal and fail the helium leak requirement.

Helium leak checks were conducted with a LACO TitanTest machine. This machine was calibrated such that the minimum detectable helium leak rate in the ultra-fine vacuum mode was at the leak requirement (at the time) for mechanism (<5.0 E-10 Pa l/sec). Leak tests were conducted by placing the mechanism, stowed and sealed on a surrogate antechamber, underneath an enclosed top hat (Ref Fig. 11). The surrogate antechamber was connected to the LACO machine and pumped down to vacuum. The top hat was then pressurized with helium. This enclosure was mounted on a vibration table or in a thermal chamber with helium leaks being monitored by the LACO during all tests. Standard calibration and background levels were conducted/recorded before and after each test to ensure accurate leak measurements.

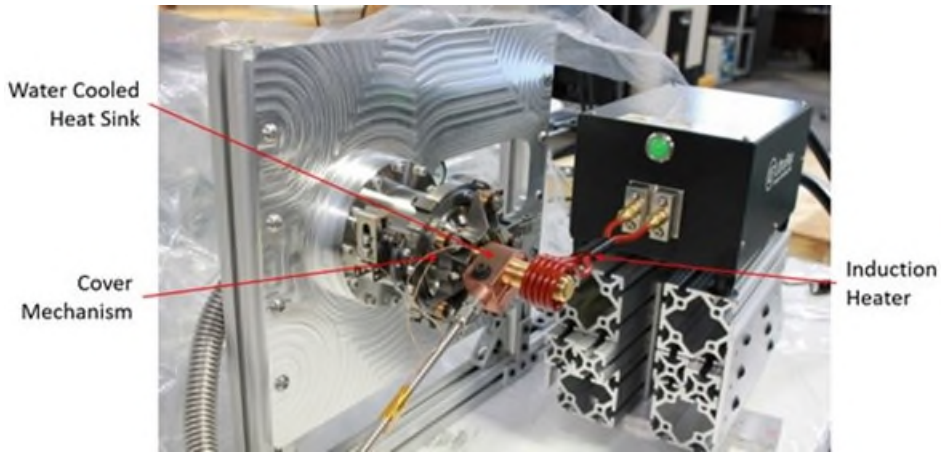

Figure 10: NEG activation and heat sink. NEG activation involved an induction heater heating the NEG pumps to 500°C. A water cooled heat sink was mounted to the NEG seal to prevent damage to the critical sealing interface. Credit: Sierra Space Corporation

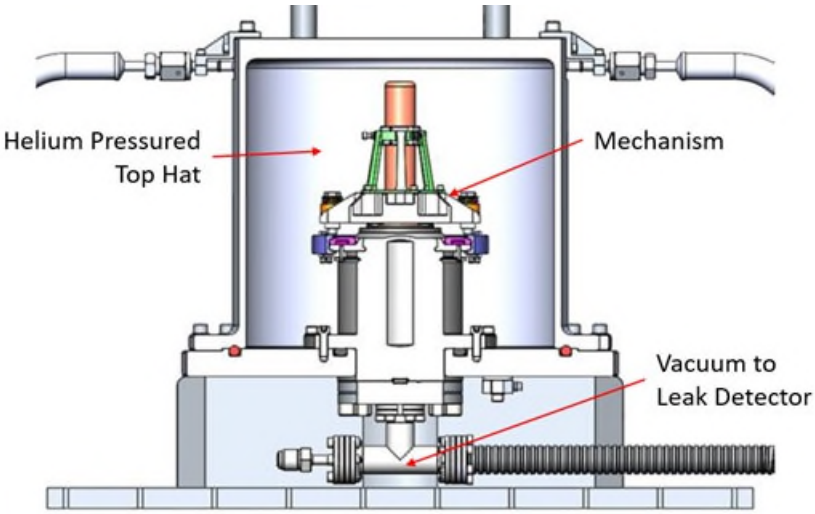

Figure 11: Leak chamber for cover mechanism. Helium was backfilled into a top hat, with a leak detector pulling vacuum on the other side of the seal, monitoring for He leak. Credit: Sierra Space Corporation

The leak requirement levied on the mechanism was at the noise floor of what could be detected using commercial vacuum/leak detector machines. It was noted during initial trade study testing that when the LACO was measuring at the noise floor, background (artificial) spikes were being detected. This posed problems for validating the sealing interface of the mechanism as these background spikes (although consistent both in size and frequency) occasionally violated the system level leak requirement. Additional data refinement was required to ensure that these background spikes were not artificially “failing” the mechanism interface.

Measurements were taken before all vibration and temperature cycling to develop background values to determine if any potential delta in leak rate was recorded during environmental testing. This method was developed during the trade study phase, and used throughout the remainder of the program.

Following NEG activation, the updated engineering development unit was environmentally tested to the updated flight vibration and thermal levels to ensure functional compliance. Fortunately, with the design changes implemented, the updated EDU mechanism was able to pass all environmental test (vibration and thermal cycling) and functionally deploy, clearing the way to move to the final flight build. The flight design was then built and tested to the updated environmental conditions. A full visual inspection was conducted on the seal following release to confirm that no yielding occurred and that no particles (from the NEG assembly) were generated during testing. The successful completion of these tests moved the mechanism to the TRL-8 level, and the flight configuration was shipped to Southwest Research Institute (SwRI) for final integration onto their instrument.

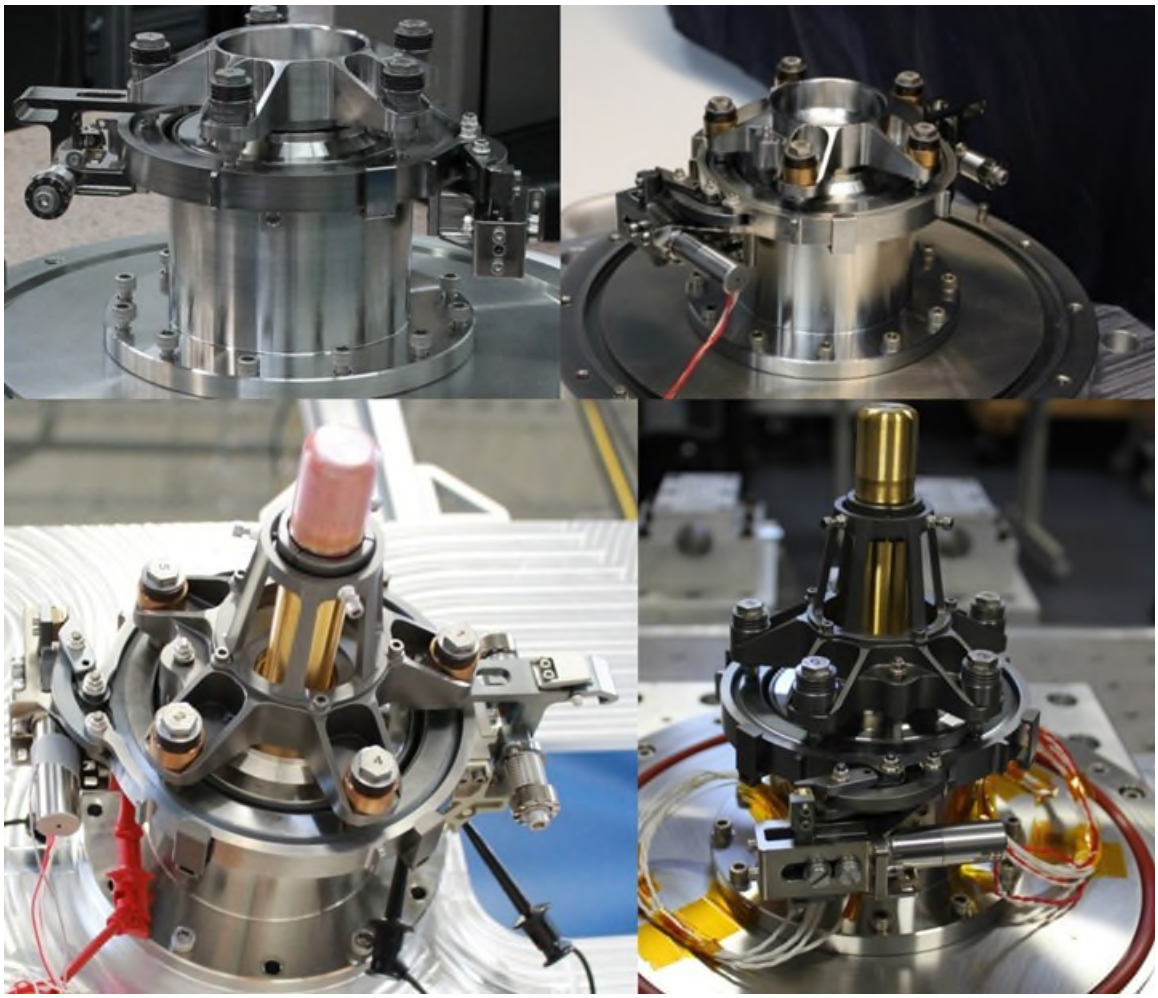

Figure 12: Cover mechanisms developed for MASPEX Instrument: (Top Left) Prototype Stowed, (Top Right) EDU Stowed, (Bottom Left) EDU (NEG) Stowed, (Bottom Right) Flight Delivery Unit. The cover design changed dramatically away from the previously tested prototype and engineering development units following the addition of NEG pumps attached to the critical sealing component. Credit: Sierra Space Corporation

Lessons Learned

Several lessons were learned during the development of a deployable cover capable of holding a hermetic seal from prototype to flight.

Hermetic Sealing

- H-seals and conflat seals are ideal for hermetically sealing interfaces, especially when metal on metal interfaces are required.
- It is critical that the sealing surface of H-seal and knife-edge interface are pristine surfaces free of burrs, nicks, and markings.
- Knife-edge interfaces need to be able to fully engage with the sealing surface.
- When loading H-seals onto a knife-edge, the seal needs to come down consistently perpendicular to the surface plane. The seal cannot be rocked or unevenly engaged onto knife-edge during loading.
    - For deployable mechanisms, this means compliance for the seal to come down perpendicular, and not on an extended radius from a hinge line (if applicable).

Clampring

- When tensioning a clampring with an under-center link, the majority of loading occurs during the initial movement of the linkage. There is limited load adjustability once the under-center linkage is near its end of travel towards the over-center condition.
- Variability in ring ODs, even by .025 mm (.001 in), greatly affects the final tension in the clampring. Those features need to be very tightly controlled to get repeatable results between mechanisms.

Helium Leak Testing

- It is critical to minimize all potential interfaces when testing minimal levels of Helium in the system.
- Excess background helium needs to be cleared from the immediate area of a leak detector
- The leak detector needs to be in pristine condition to measure at noise floor. Any undesirable particulates in the machine will prevent the system from pumping down and reading at the absolute floor.

Conclusion

A unique cover mechanism was required for the MASPEX instrument on the Europa Clipper Spacecraft that was capable of deploying a hermetically sealed contamination cover. Following trade studies and a non-flight build, a flight cover concept was built, functionally tested, and validated for all environmental loads and effects. System-level requirement updates necessitated design changes to the primary sealing interface late in the program. The updated design passed all helium leak checks, sealing to levels <1*10^-8 Pa*l /sec helium leak throughout all environmental tests. Several challenges were overcome throughout the development of this hermetically sealed cover system including management of deployable sealed interfaces, integrating miniaturized clamprings, minimal use of non-metallics, and application of under-center linkages. All these challenges resulted in invaluable technology advancement that can be applied to future flight designs and related space missions.

Acknowledgements

The authors wish to express appreciation to the MASPEX team at SwRI for their collaboration in the mechanism development and test. Specifically, Chip Beebe and Tim Brockwell's (SwRI) contributions and collaborations with the team at Sierra Space allowed this mechanism to make it through flight design and test. Development of the mechanism was made possible with the team's collaboration, frank discussions, and dedication to supporting development of a suitable cover for their MASPEX instrument.

References

1. Europa, https://europa.nasa.gov
2. Europa Clipper Mission, https://europa.nasa.gov/mission/about
3. Mass Spectrometer for Planetary Exploration/Europa (MASPEX), https://europa.nasa.gov/spacecraft/instruments/maspex,
4. H-Seal® Metal Gaskets: Developed for Small Footprint UHV, https://bostecengineering.com/index.php?page=prodHSeal
5. Sierra Space Product Catalog, EH-3525 High Output Paraffin (HOP) Actuator, pg 39
6. Anderson M.J., Cropper M., Roberts E.W., “The Tribological Characteristics of Dicronite”, Proc. 12th ESMATS, 2007

Laterally Unconstrained Magnetic Joint for Pointing, Scanning, and Steering Applications

Vlad Krylov* and Aaron Castillo*

Abstract

Laterally unconstrained magnetic joints enable a novel mechanism for tip-tilt and piston platform actuation. The mechanism is useful in applications where angular orientation of the platform in three-dimensional space needs to be controlled over a typical angular range of ±20 degrees. This mechanism comprises three linear actuators traveling along parallel axes and a platform supported by three joints at the ends of the actuators. The lack of a rigid lateral constraint within the magnetic joint enables the capability of platform to change orientation via the point contact interfaces. In this paper, the mechanical properties of the laterally unconstrained magnetic joint and their impact on tip-tilt platform performance are discussed.

Introduction

Tip-tilt actuation of a platform is a common task in many applications, especially flat mirror actuation in optical systems. Conventional mechanisms such as gimbal mounts, hexapods, and others are frequently pushed towards higher performance. Typical performance parameters include actuation range, speed, pointing accuracy, and cost.

The actuation speed of all mechanical systems is fundamentally limited by the moving mass of the payload and the actuation mechanism. A major advantage of the laterally unconstrained magnetic joint is the minimization of the parasitic moving mass required to actuate the platform. This in turn results in a higher actuation speed and lower cost. Increased reliability may be achieved through simplification and reduced component count.

Laterally Unconstrained Magnetic Joint

A practical implementation of the laterally unconstrained magnetic joint (the joint or the magnetic joint) consists of a permanent magnet having a flat surface interfacing and a ferromagnetic stainless-steel part having a spherical surface as shown in Fig. 1. The flat surface of the magnet may have nickel or other types of corrosion protective coatings, or a thin sheet of a bearing material, such as a sapphire disk. The bearing material creates a magnetic gap between the permanent magnet and the ferromagnetic metal.

The two interface surfaces within the magnetic joint have a point contact throughout the actuation range. The magnetic field produced by the interaction between the joint components results in an axial preload force and a lateral centering force. The axial force acts through the point of contact between the two surfaces perpendicular to the flat surface of the magnet. The lateral centering force is present when the two joint components are misaligned. Within the operating range, the lateral centering force magnitude increases with joint component misalignment.

The magnet and steel parts are both axially symmetric and have the same diameter. This configuration produces the fastest increase in the lateral centering force which is the desired property in tip-tilt platform attachment applications.

* Light Steering Technologies, Inc., Manchester, NH

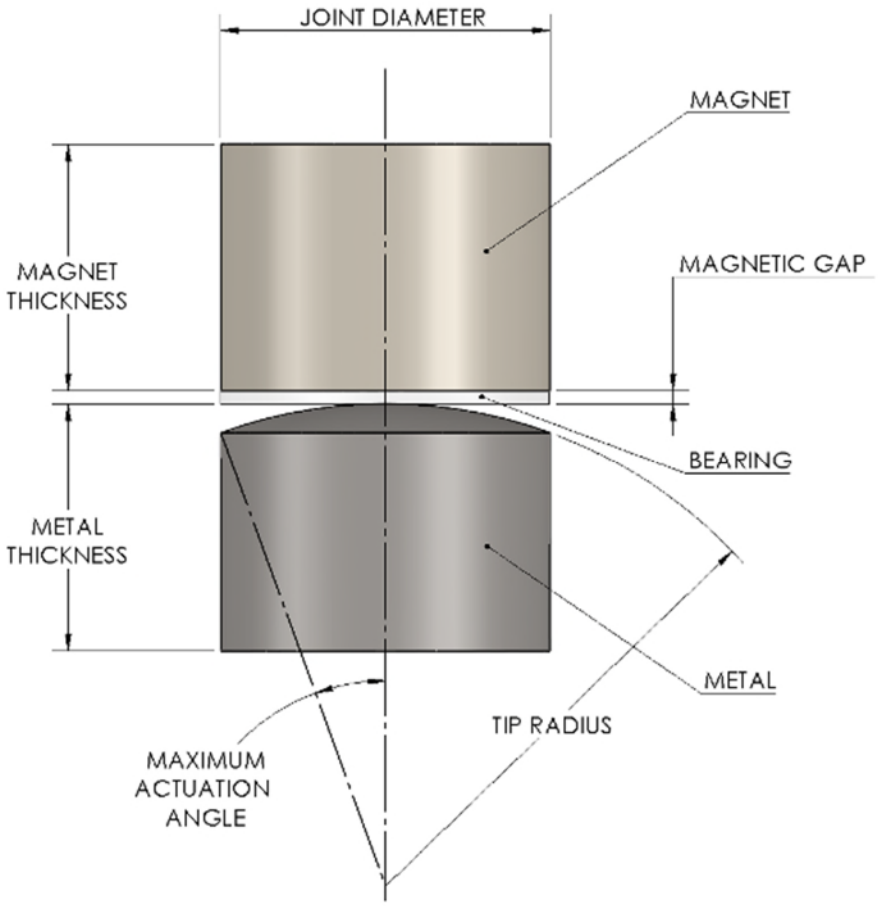

Figure 1. Basic Geometry of the Laterally Unconstrained Magnetic Joint

Other configurations of the magnetic joint, such as having both parts made from a permanent magnet or using another type of a convex surface, are possible; however, these are outside of the scope of this paper.

Nomenclature

Throughout this paper the following nomenclature may be used for brevity:

Joint: Laterally unconstrained magnetic joint

Magnet: The first component of the laterally unconstrained magnetic joint made from a permanent magnet material. In most applications it is a high grade of Neodymium Iron Boron magnet, which offers the highest force for expected operating temperature range.

Metal: The second component of the laterally unconstrained magnetic joint made from a ferromagnetic material. In most applications it is 416 or 430 stainless-steel, based on the trade between hardness and machinability. In environments where corrosion is not a concern other steel alloys may be used.

Bearing: A non-magnetic material rigidly attached to the magnet. In most cases it provides the magnet with corrosion protection and improve the joint bearing properties.

Tip Radius: Spherical radius of the second mating surface of the joint.

Piston-Tip-Tilt Platform Application of the Magnetic Joint

Efficient actuation of a tip-tilt platform is the most common application of the laterally unconstrained magnetic joint. The magnet component is attached to the platform side. The bearing surfaces of the three joints form a planar surface. In optical applications where the platform is a front surface mirror, the planar surface formed by the three joint bearings is parallel to the mirror. Such a configuration ensures that the lateral motion of the platform does not affect its pointing.

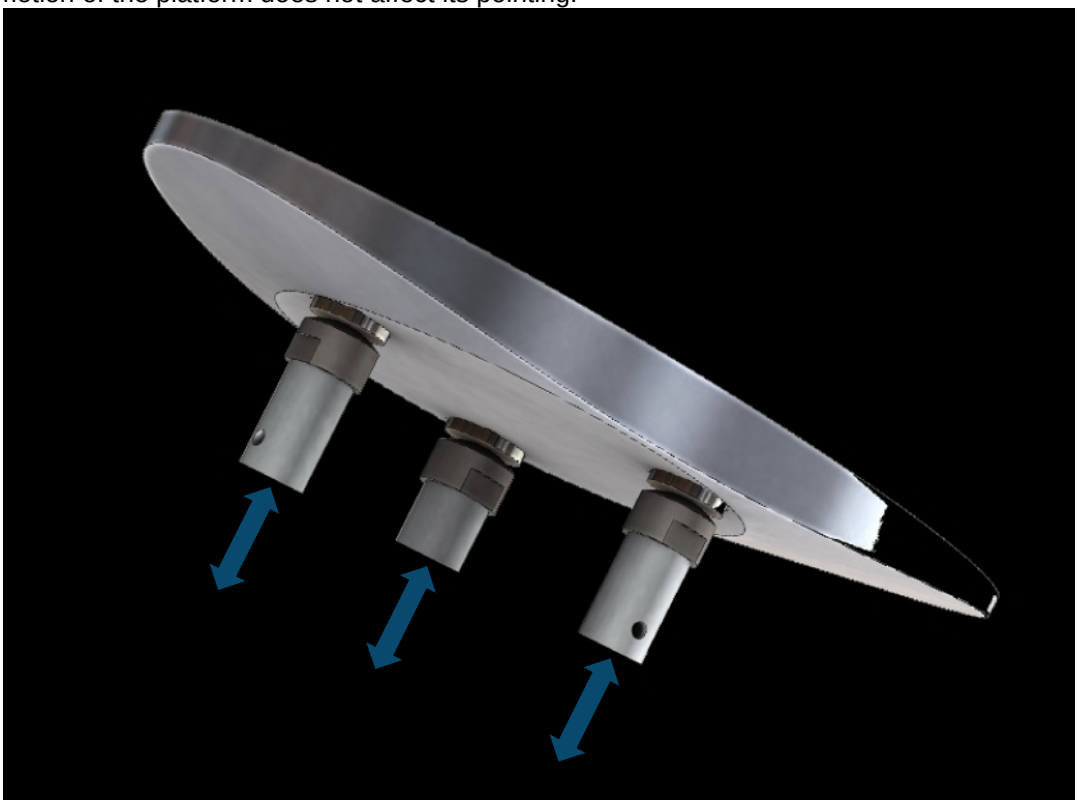

Figure 2. Tip-Tilt Platform Application of the Laterally Unconstrained Magnetic Joint

The mating joint component – metal tip – is attached to a linear actuator. The spherical radius of the metal tip and the bearing surface of the magnet interface through a point contact. This contact is preloaded by the magnetic force produced between the magnet and the metal tip.

The distance between the contact points of each actuator pair changes throughout actuation range, see Figure 3. The lack of rigid lateral constraint within the joint accommodates this change and allows the platform to float on the three metal tip points. The lateral magnetic force within the joint increases with de-centration of the magnet and metal tip thus maintaining the integrity of the system within the range of operating conditions.

The lack of rigid mechanical constraint in the platform mount has other potential benefits. In environments with large temperature variations, the platform can expand and contract independently from the base of the system to which actuators are attached. In optical applications this allows for a lighter mirror as the requirement for the structure rigidity is reduced. The modal frequencies of the system are also higher due to decoupling of the platform and actuators in all but one degree of freedom simplifying the control and improving the bandwidth in high frequency applications.

Figure 3. Tip-Tilt Platform Actuation Enabled by the Laterally Unconstrained Magnetic Joint

Joint Geometry

The parameters of the joint geometry such as diameter, thickness of each component, and the spherical radius of the tip are optimized based on application requirements. This optimization is focused on achieving the axial and lateral magnetic attraction forces that support the platform weight in the dynamic operation, actuation angle, environmental shock and vibration the system is required to withstand.

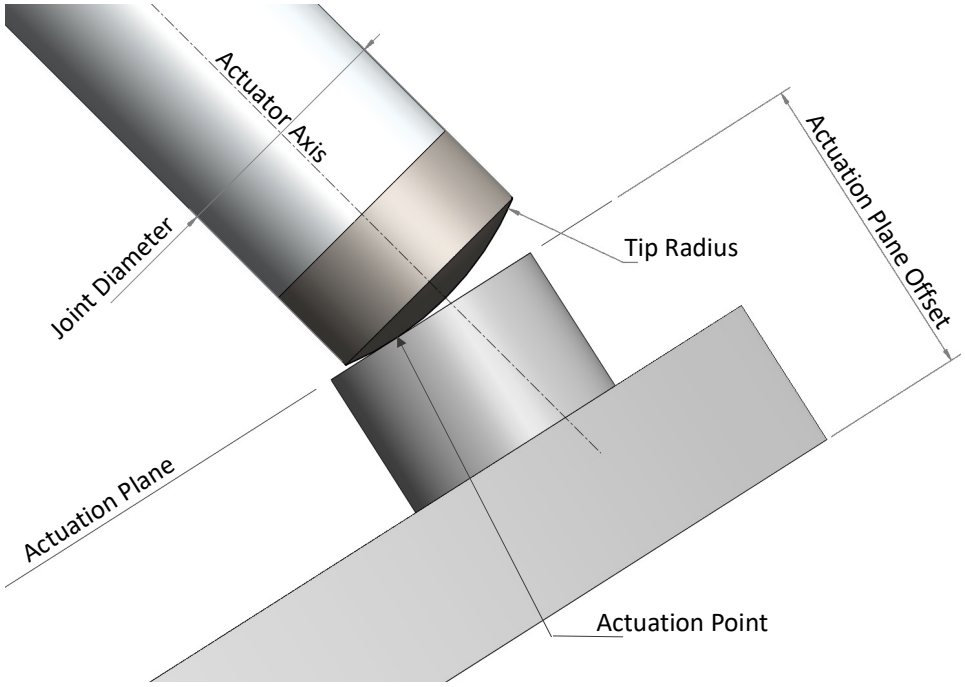

Figure 4. Impact of the Application Constraints on the Joint Geometry

The spherical radius of the metal tip is selected to accommodate the maximum actuation angle. Radii smaller than the maximum would compromise the joint attraction force in favor of lesser lateral displacement over the actuation range.

The minimum diameter of the joint is based on the actuation geometry and the maximum actuation angle. The joint diameter accommodates the travel of the point contact on the magnet bearing surface resulting from the change in the distance between the metal tips. The joint diameter is also a function of the required attraction force driving the size of the joint components. In practical applications we find the joint diameter being 2 – 3 times greater than the minimum for tip/tilt angle of 20 degrees.

Material Selection

Currently, the strongest known magnet type is Neodymium Iron Boron (NdFeB). There are multiple grades of NdFeB magnets, each with a specific B-H curve. The strongest commonly available grade is N52, which would be used in most implementations of the joint, except applications requiring an operating temperature above 80°C. In latter cases, magnet strength will be traded for higher demagnetization temperature. Fig. 5 shows a representative difference in the joint axial attraction force for two common NdFeB magnet grades for a specific joint geometry.

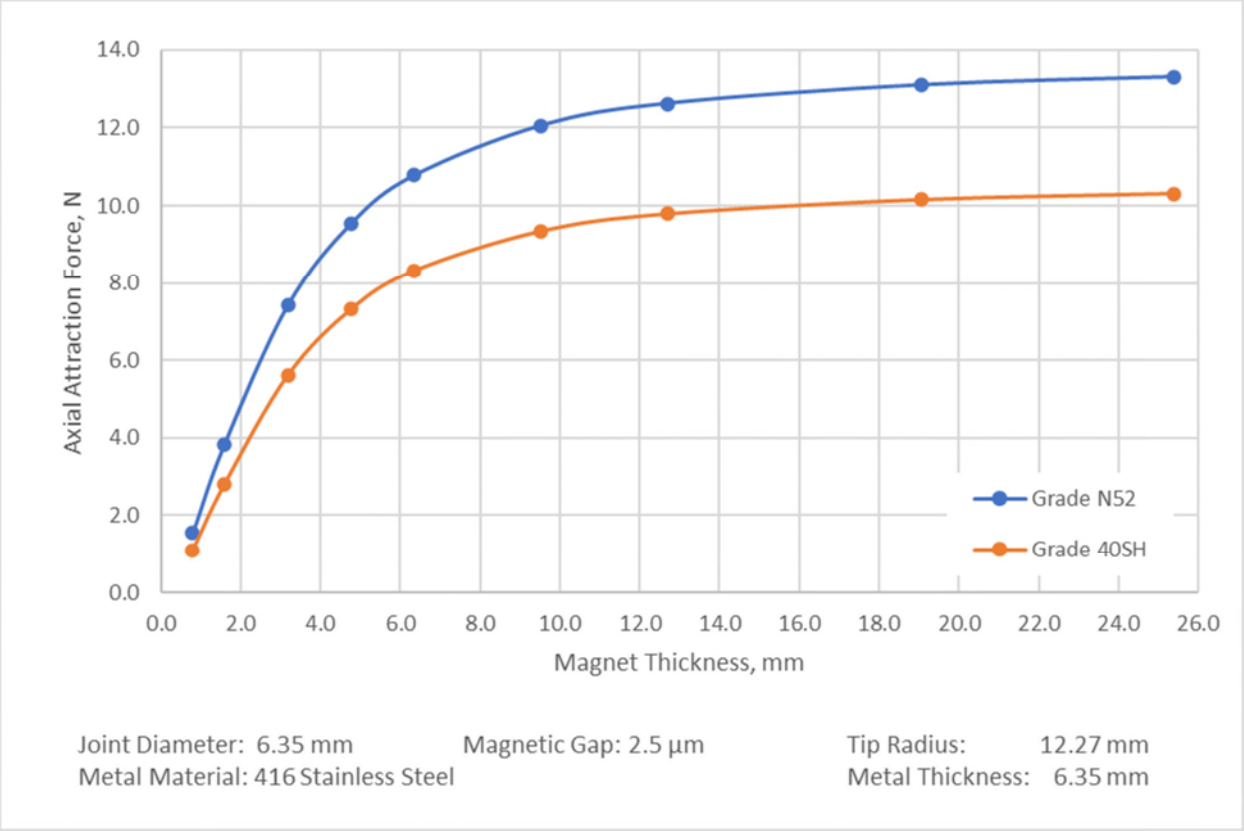

Figure 5. Axial Attraction Within the Joint for Common NdFeB Grades

Due to corrosion, in most expected application environments, ferromagnetic stainless steel would be the preferred material for the metal. There is no appreciable joint axial attraction force difference between common 400 Series ferromagnetic stainless steels, such as 416, 430, or 455.

Bearing material depends on the joint applications. For lighter platforms without demanding accuracy requirements, a polished nickel coating of the magnet ranging in thickness between 2.5 µm and 25 µm could be sufficient. When higher precision of motion is required, a 75 µm to 200 µm thick sapphire disk is bonded to the magnet.

Axial Attraction Force

Axial attraction force is the primary characteristic that defines the performance of the magnetic joint in an application. The optimization of the joint geometry is done based on achieving the axial attraction force required by the weight of the platform or other payload, dynamics of the application, and the environment.

This paper presents the results of simulation of axial attraction force for an aligned joint using commonly available sizes of cylindrical NdFeB magnets from 1.6 mm to 19 mm diameter.

To optimize the joint geometry, two derived parameters are considered:

- Joint attraction force per unit weight (N/g)
- Maximum axial acceleration (m/s^2) with a specific payload

Magnet thickness and metal thickness can be optimized for desired retention force based on joint diameter, tip radius, maximum deflection angle, magnetic gap, and materials. Fig. 6 shows an example of optimization for a 10 N attraction force.

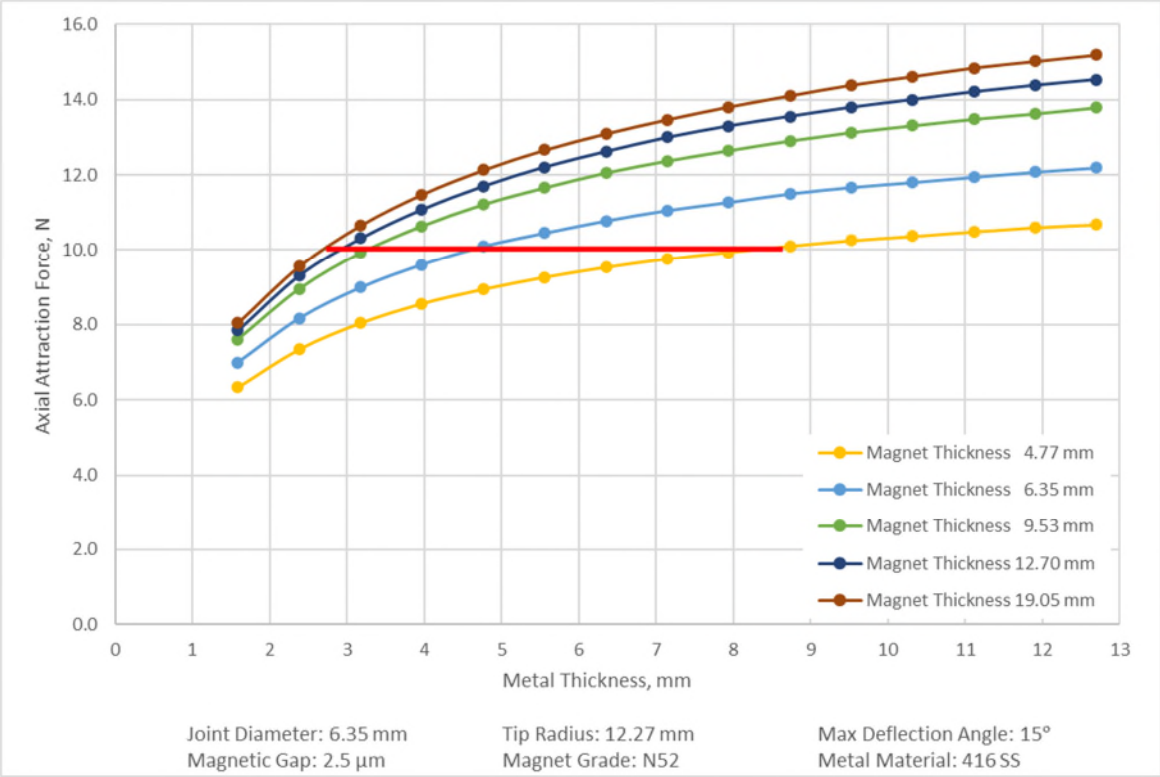

Figure 6. Axial Attraction Force as a Function of Component Thickness

From the attraction force plot alone, it is not clear which combination of magnet and metal thickness is the best choice. Fig. 7 shows the attraction force per unit weight for the same geometries. The red line represents the 10-N force selection. The attraction force per unit weight plot, when analyzed together with the attraction force plot, shows the preferred combination of the joint component thicknesses which offer the lowest joint weight and thus the best dynamic performance.

The maximum axial acceleration with the selected payload determines the acceleration at which the axial attraction force of the joint can no longer overcome the separating force of the mass consisting of the magnet, bearing, and payload. Fig. 8 shows the maximum axial acceleration for the same set of geometries and a payload mass of 75 grams. Red triangles show the 10-N force points.

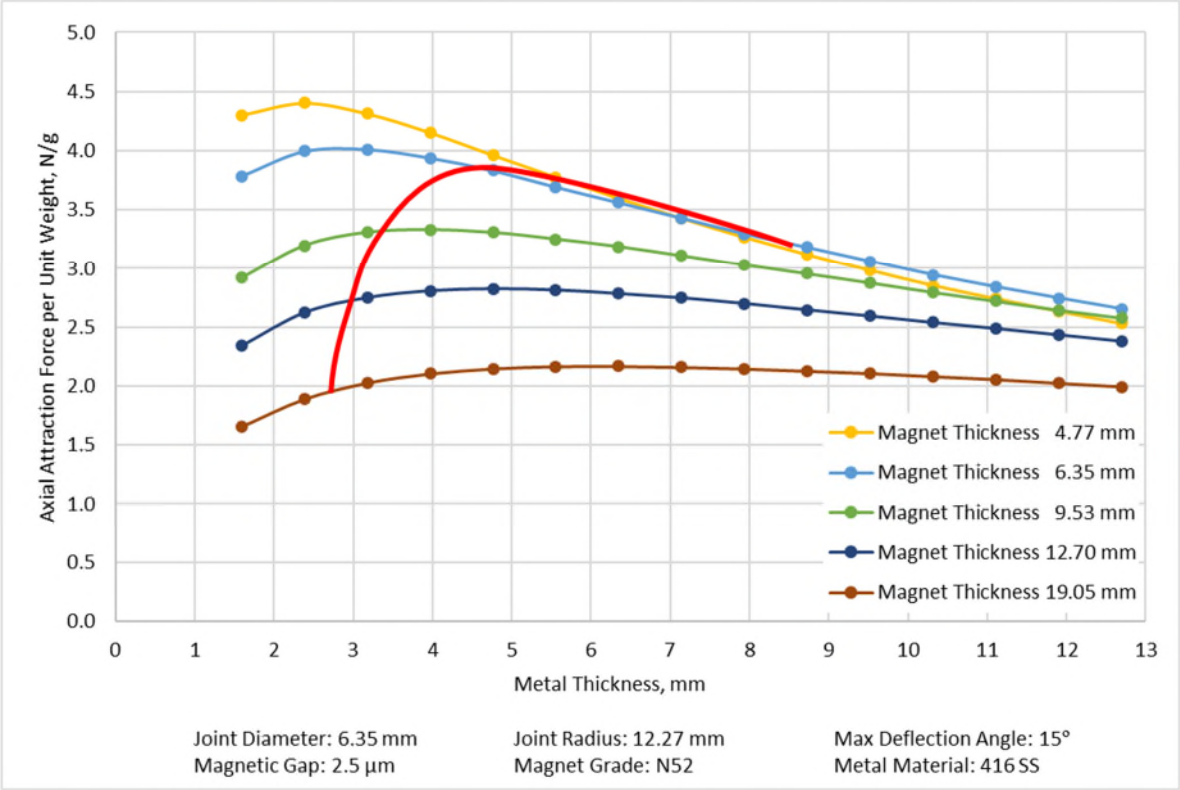

Figure 7. Axial Attraction Force per Unit Weight as a Function of Component Thickness

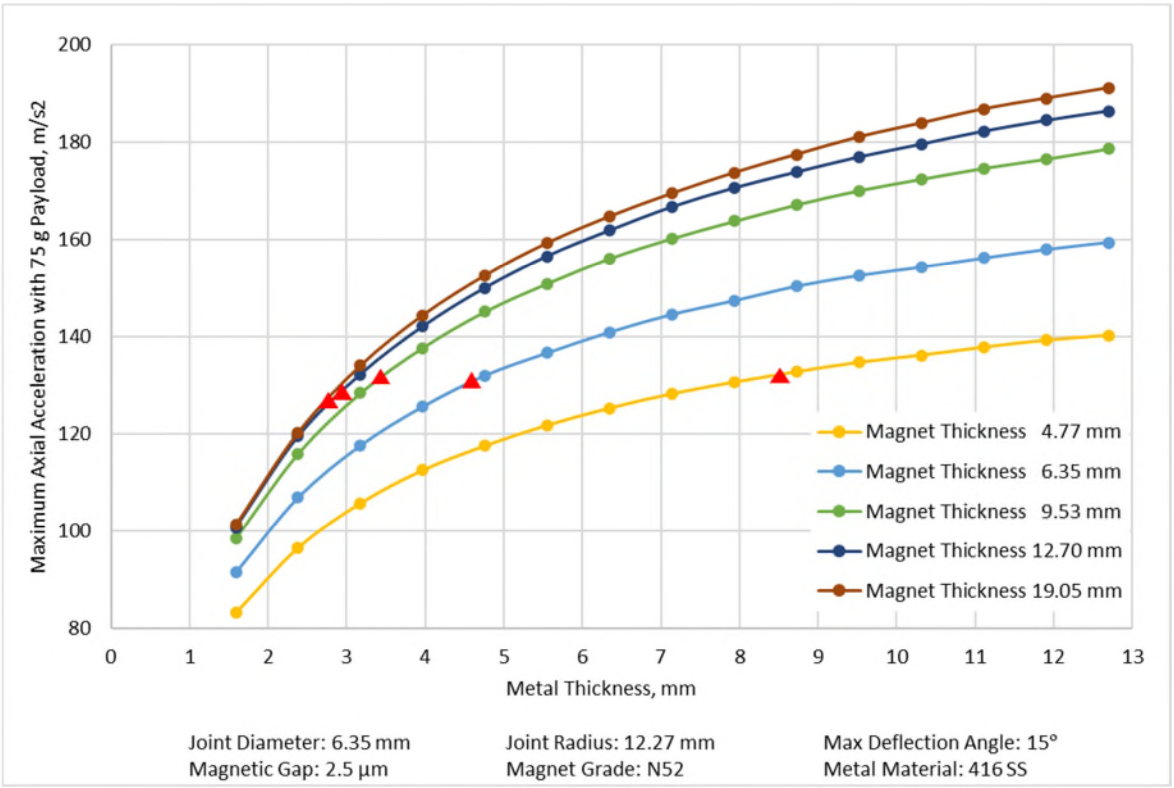

Figure 8. Maximum Axial Acceleration as a Function of Component Thickness

While the axial acceleration plot shows that the joint having magnet thickness of 9.53 mm and a metal thickness of ~3.3 mm slightly outperforms the joint having magnet thickness of 6.35 mm and a metal thickness of ~ 4.6 mm, this comes at a cost of greater weight, and actuator capabilities would need to be considered as part of the geometry selection. If actuator performance is one of the limiting factors, the latter joint geometry may offer the better overall system performance.

The air gap between the joint components depends on the tip radius. Smaller tip radii increases the air gap and thus lowers axial attraction force. In most joint applications, the radius is optimized to achieve the desired actuation angle, however, in some applications it may be beneficial to reduce the joint radius which would also minimize lateral displacement of the joint contact point over the actuation range.

Fig. 9 shows a typical dependence of the axial attraction on the tip radius. Data labels show the corresponding maximum actuation angle of the joint. In advanced joint applications, the gap between the joint components can be filled with ferrofluid to increase the axial attraction force at larger metal tip radii.

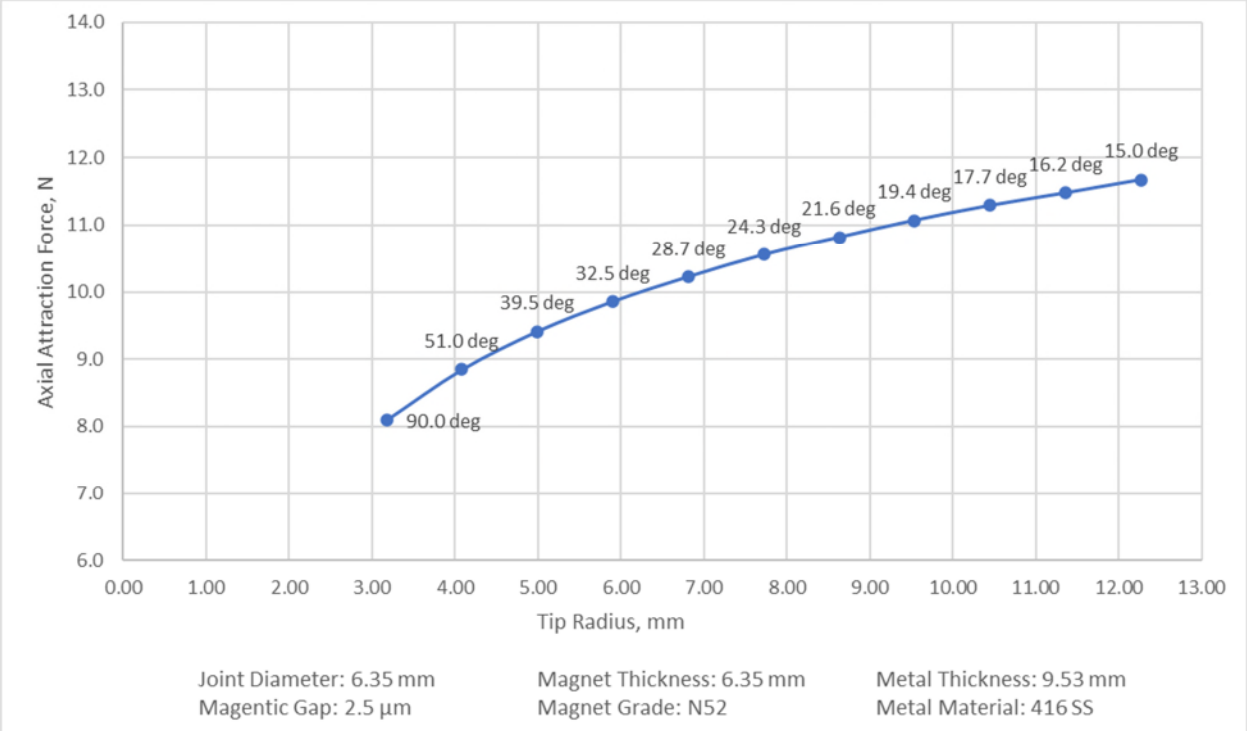

Figure 9. Axial Attraction Force as a Function of Metal Tip Radius

The attraction force within the joint reduces as magnetic gap increases. Typical implementation of the joint minimizes the thickness of the bearing material. An example of this dependence between magnetic gap and attraction force is shown in Fig. 10.

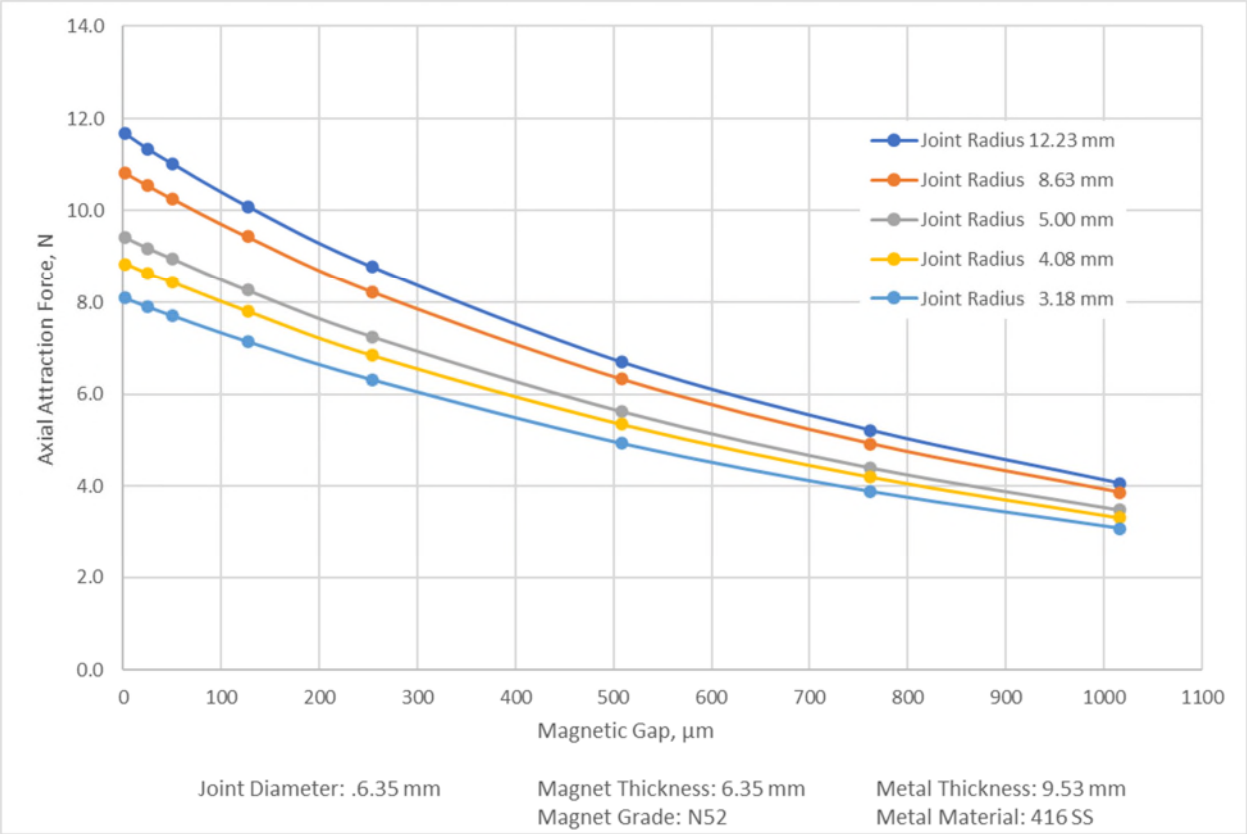

Figure 10. Axial Attraction Force as a Function of Magnetic Gap.

Conclusions

A novel magnetically coupled mechanism with a laterally unconstrained magnetic joint, and its application in tip-tilt platform actuation was introduced. A common application, optical flat mirror actuation over an extended pointing angle, was also described. The paper outlined the considerations and optimization process for the geometry of the joint components. The results of a Finite Element Analysis study on the axial attraction force within the joint were presented.

References

1. Krylov, Vladimir and Castillo, Aaron “Multi-axis Scanning Pushes Next-Generation Steering Performance.” *Laser Focus World* (September 2021)
2. Krylov, Vladimir G. *Magnetic Joint and Optical Mount Using the Same* (U.S. Patent No 10,685,771). U.S. Patent and Trademark Office.
3. Krylov, Vladimir G. *Laterally Unconstrained Magnetic Joint for Tip Tilt and Piston-Tip-Tilt* mounts (U.S. Patent No 10,830,988). U.S. Patent and Trademark Office.

Design, Manufacturing, and Testing of Precision Space Flight Qualified Single Degree of Freedom Flexure Based Linear Actuators / Mechanisms

Brandon Schneider*, Todd Jackson*, Jesse Booker*, and Kevin Kelman*

Abstract

This paper describes the design, manufacturing, and testing of a range of high-reliability, space-qualified single degree-of-freedom (1-DOF) linear actuators used to position optics to a high degree of precision. Danbury Missions Technologies, LLC (Danbury) has developed a series of single-stage linear actuators, which provide extremely repeatable and deterministic nanometer scale output motion with near zero backlash or hysteresis over extended ranges. This paper highlights the design architecture of these actuators, which utilize flexures to transform rotary input motion into precise linear output motion and meet the rigorous demands of launch and space environments. The paper also touches on the key areas of manufacturing and test required to assemble and qualify these actuators including representative test results.

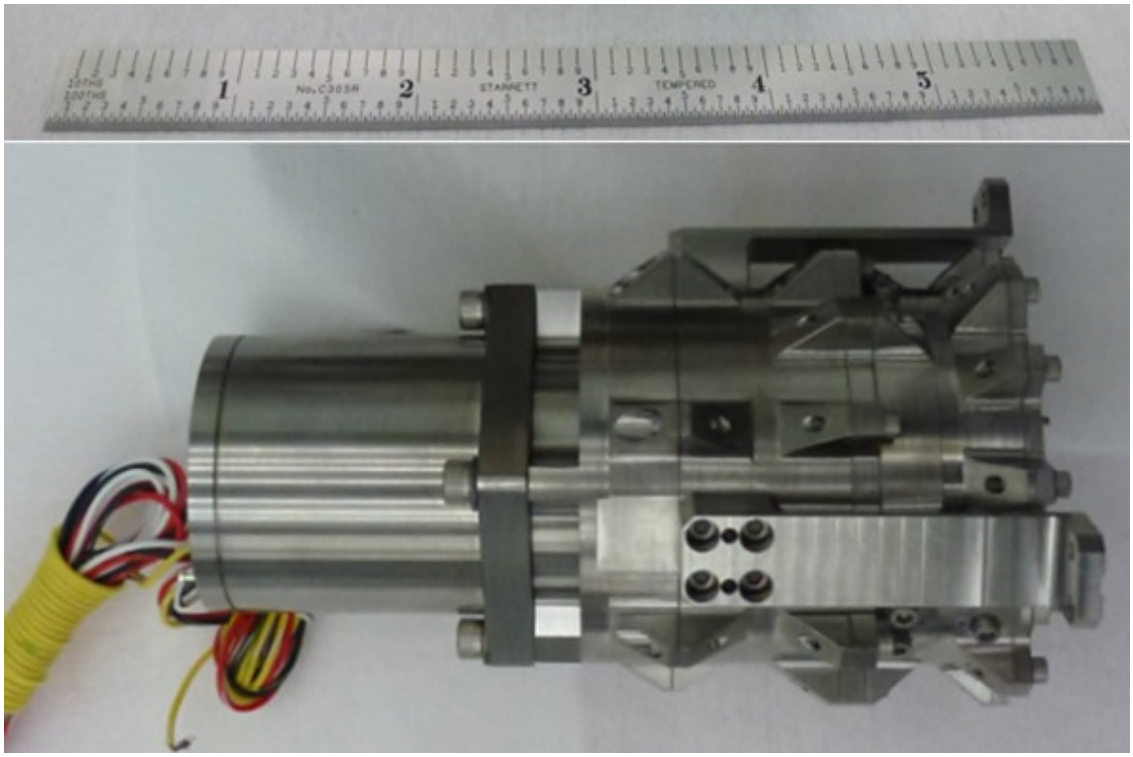

Figure 1. Representative Danbury Flexure-Based Linear Actuator Provides Precision Motion Without Need for Separate Launch Locks

* Danbury Mission Technologies, LLC, Danbury, CT; Brandon Schneider bschneider@dmtllc.org, Todd Jackson tjackson@dmtllc.org, Jesse Booker jbooker@dmtllc.org, and Kevin Kelman kkelman@dmtllc.org

Introduction

Advanced space-based optical systems require the ability to locate and maintain optical surfaces relative to each other with extreme precision, within the optical frame of reference. The need to precisely position/reposition optics remotely on-orbit typically results from some combination of:

- Active focal correction as a function of range to an image
- Optical misalignments or shifts due to launch
- Optical metering structure dimensional changes due to seasonal thermal effects, and composite on-orbit dry-out.

Additionally, as optical systems continue to increase in size, there becomes a point where there is a need to segment the mirror to achieve the best balance of performance and cost for the optical system. These mirror segments must be precisely aligned to produce a coherent image. This creates yet another demand to precisely reposition optics relative to each other. To achieve the proper mirror surface geometry, the surface figure and rigid body positions of mirror segments must by dialed in by precise actuation to induce the desired precision wavefront quality.

To address the needs for on-orbit optical correction, Danbury has developed a series of compact modular single-stage linear actuators, which range in size with the ability to be tailored for specific applications. These actuators can be used standalone providing 1-DOF or in a system where up to six degrees of freedom (6-DOF) can be achieved in a hexapod arrangement. To achieve demanding system requirements of positioning highly sensitive optics, each actuator is designed to have the following characteristics:

- High positional precision and accuracy with minimal backlash and hysteresis over large actuation ranges
- High stiffness and load/moment capability acting as a stressed member of the optical metering path
- Ability to withstand launch loads without the need for separate launch locks
- Athermalization to minimize the impact of thermal effects (bulk and gradient) on the optical metering path length
- The ability to maintain precise position unpowered
- High reliability
- No lost motion or missed steps such that the actuator can be used without positional feedback (open-loop),
- Minimal motion biproducts in the non-actuated axes
- Minimized SWaP (size, weight, and power).

This paper focuses on one of Danbury's most recent and most challenging actuators to design, build, and test. This single-stage flexure-based linear actuator, termed the Testbed Actuator (TBA), was developed to challenge the envelope on the competing requirements of range and resolution. We also integrated real-time motor position and output force feedback devices into the TBA to further increase capability and to broaden the list of potential applications. We highlight the design, assembly, test setup, and test results of the actuator. We also discuss key lessons learned and follow-on work being performed to continue to advance the design of precision linear actuators.

Actuator General Design

Each of our flexure-based linear actuators are composed of three main sections which work in concert to be compliant with the demanding list of requirements. These sections are modular such that they can be tailored for each application to optimize range, resolution, and SWaP. The three main sections are depicted in Figure 2:

1. The Motor → typically a unipolar or bipolar stepper motor
2. Harmonic Drive (HD) → single or multiple stage drive gear reducer transmission
3. Rotary to Linear Output Assembly (RLOA) → flexure-based arrangement converting rotary motion from the output of the harmonic drive to linear motion [1]

As noted, the TBA described in this paper also includes an integrated optical encoder for motor position feedback and load cells on each of the flexure athermalized mounting feet to provide force output feedback. A functional diagram of the actuator is illustrated in Figure 3.

Figure 2. Testbed Actuator General Design

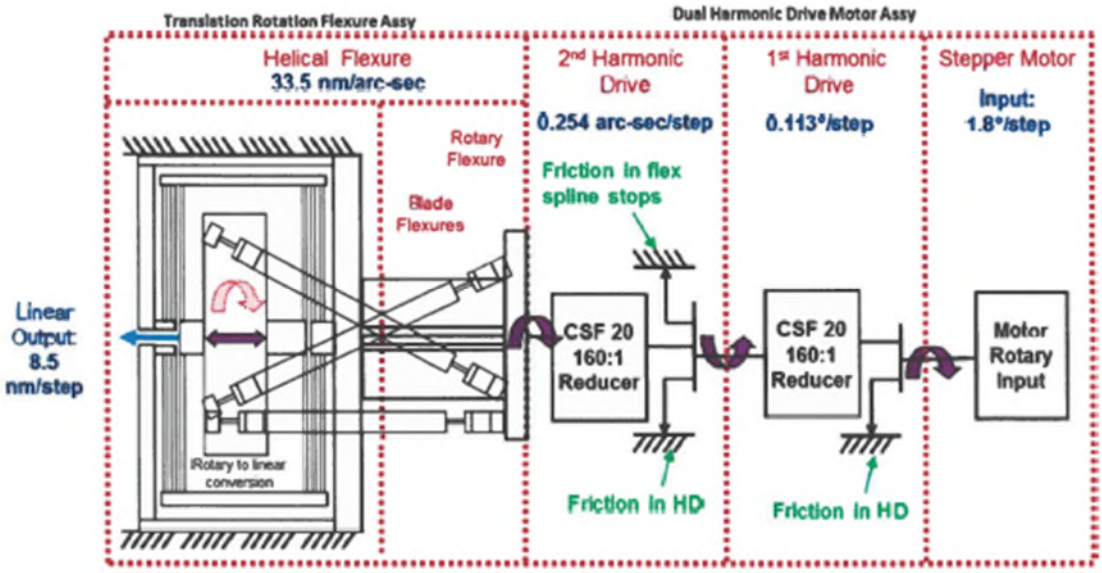

Figure 3. TBA Actuator Functional Diagram

Actuator Motor

Brushless DC 2-Phase Unipolar or Bipolar Stepper Motors are used to drive the linear actuator since they can be driven open loop, minimizing complex and expensive feedback electronics when compared to a servo motor-based actuator. Also, stepper motors provide the benefit of providing an unpowered holding torque due to the motor step detent amplified through the transmission. Unipolar motors are used for applications that do not require image capture during actuation. Bipolar motors are used for applications that require smooth motion outputs during imaging, requiring more sophisticated drive electronics that microstep the motors and current shape as required.

Actuator Harmonic Drive

Harmonic drive(s) gear reducers are used for the actuator transmission to increase the actuator resolution and amplify the motor output torque. Harmonic drives are chosen for their compact size, high gear output ratios, and minimal backlash / hysteresis, which are all key elements to meet the actuator design requirements. In some instances, a series of two harmonic drives are used in actuators that require very high output resolution.

Actuator Rotary to Linear Output Assembly (RLOA)

The key element to our linear actuator design is a highly engineered rotary to linear output assembly. This completely flexure-based design takes the rotary output motion from the final harmonic drive and translates it into pure linear motion. A fully flexure-based design is used such that the output motion is extremely repeatable, and deterministic being void of any effects due to friction, and lost motion / deadband. The RLOA is designed and analyzed using linear and non-linear finite element analyses (FEA), optimized for range and resolution, while ensuring positive margins for stress and buckling throughout the actuator range. Material choices in the RLOA assembly are critical for optimal actuator performance. The RLOA is responsible for properly constraining and balancing internal forces such that a pure axial motion is output from the actuator. The RLOA is also responsible for providing the actuator with the required load and moment capacities.

Optional Feedback Devices

The modular actuator design allows for optional feedback devices to be integrated if the application requires. It should be noted that feedback devices are not required for standard operation since each actuator is driven using stepper motors, which output through a harmonic drive(s) transmission, and flexure-based RLOA to provide exceptional repeatability without suffering from lost motion. But for instances where feedback is desired, the following options are available:

- High sensitivity radiation hardened optical encoders with 28-bit capability can be integrated to the harmonic drive output to measure absolute angular input into the RLOA. The optical encoder is polled, and position is averaged over a predetermined number of samples. The actuator is commanded to achieve the desired displacement, and the optical encoder is polled again to establish a differential measurement of the motor shaft displacement.
- We have also developed the capability for our actuators to have the option to include strain gages on the RLOA diaphragm to provide correlated (strain to displacement) linear output measurements.
- Finally, the actuators have the option to provide force feedback with integrated force gages installed at the three flexurized mounting interfaces. This option is typically employed for actuators which are used in mirror figure control applications.

Actuator Assembly Overview

Spaceflight actuators and mechanisms are assembled in our cleanroom facilities which are class 10k or better per FED-STD-209E. All cleaning, surface preparation, priming, barrier film applications, and impregnation / lubrication processes are performed internally.

Key design features of the actuator include integral alignment features which aid in assembly, as shown in Figure 4, reduce the risk of misalignment / assembly error, and significantly reduce the need for special complex tooling.

Figure 4. Fixturing and Integral Alignment Features Utilized to Assemble Actuator

Actuator Testing Plan

Each space flight actuator design goes through a full qualification program. The flow of our component flight actuator testing is shown in Figure 5. An initial performance test is performed after the actuator is assembled and baked-out. This is followed by a dynamic characterization in three orthogonal axes to determine the modal frequencies of the actuator, to provide correlation to the FEM, and the data is used for setting up the control constraints during vibration testing. A run-in test is performed for 5% of mission life to ensure the mechanism is running correctly and to properly distribute lubrication prior to Baseline Performance Testing.

Comprehensive Baseline Performance testing fully characterizes the actuator against all performance requirements and provides a baseline set of measurements for all subsequent tests. Environmental testing includes vibration testing, which consists of random vibration and sine-burst in three orthogonal axes enveloping the launch environments and providing workmanship assurance. Thermal Vacuum (TVAC) testing is performed after vibration testing where the unit under test is subjected to numerous thermal cycles including testing over the operational temperature ranges and survival thermal cycling, which properly envelopes the worst case expected on-orbit conditions.

Intermediate Performance Testing is performed after each environmental test to ensure no changes have occurred as a result of being subjected to prior environmental testing. During component qualification testing 2X Life Testing is also performed under vacuum conditions to simulate on-orbit operational environments. At the conclusion of environmental testing, a comprehensive Final Performance Test is performed assessing the actuator against all performance requirements and comparing the test results to those taken during Baseline Performance Testing.

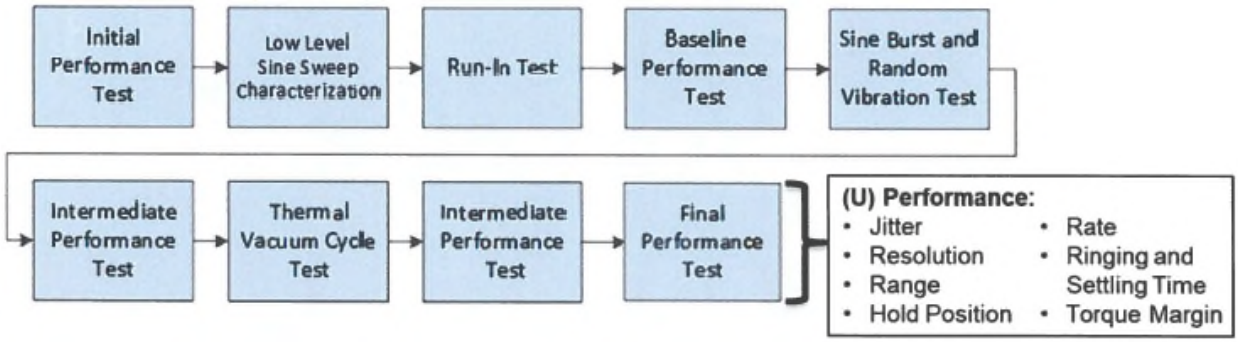

Figure 5. Flight Actuator Testing Flow Chart (Note for Qualification Units a 2X Life Test in Included Prior to Final Performance Testing)

Actuator Performance Test Setup

Performance testing is typically one of the most challenging aspects of the mechanism program for high precision actuators where output resolution is measured in the single digit nanometer range. Very high sensitivity sensors and a test environment, which is both extremely thermally stable and has near zero external disturbances, is required to properly measure the actuator output performance with regards to resolution, accuracy, range, and jitter. We have been successful in providing appropriate test conditions with the use of sensors specifically fixtured for this unique application with appropriate environmental conditions. These fixtures generally include very stiff and well damped interfaces mounted on an isolated granite bench in a room with better than 0.1˚C temperature control. Figure 6 and Figure 7 show a block diagram of the performance test set-up along with an example of a test station utilized to measure 6 DOF.

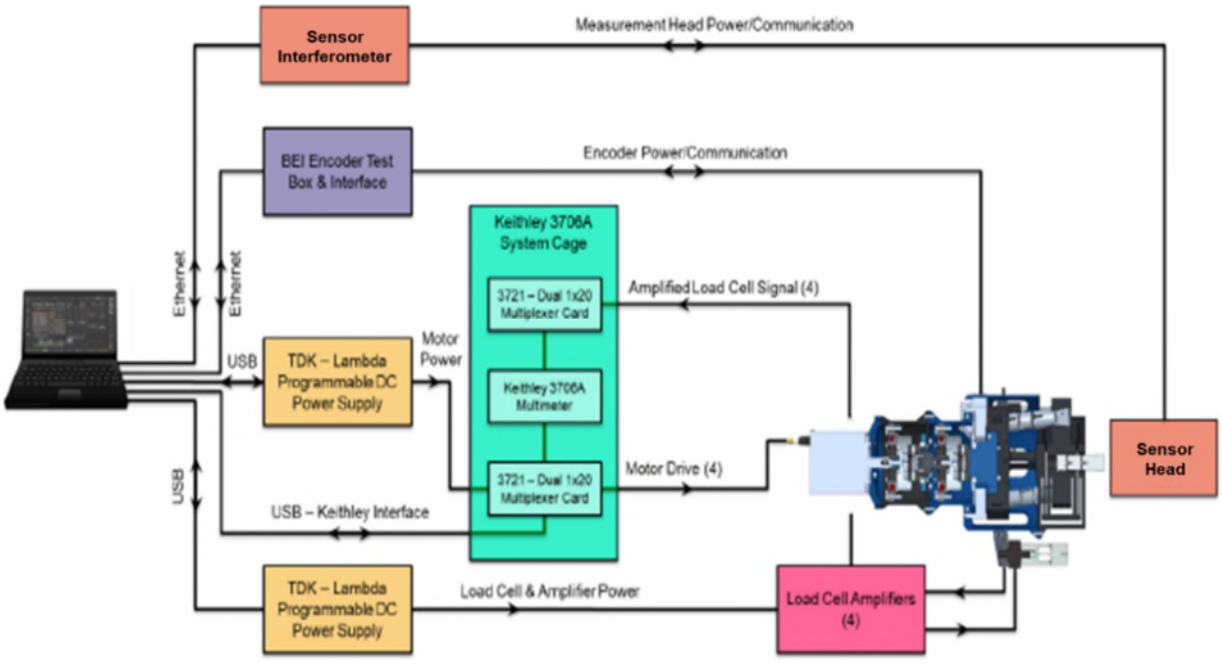

Figure 6. Performance Test Set-Up Block Diagram

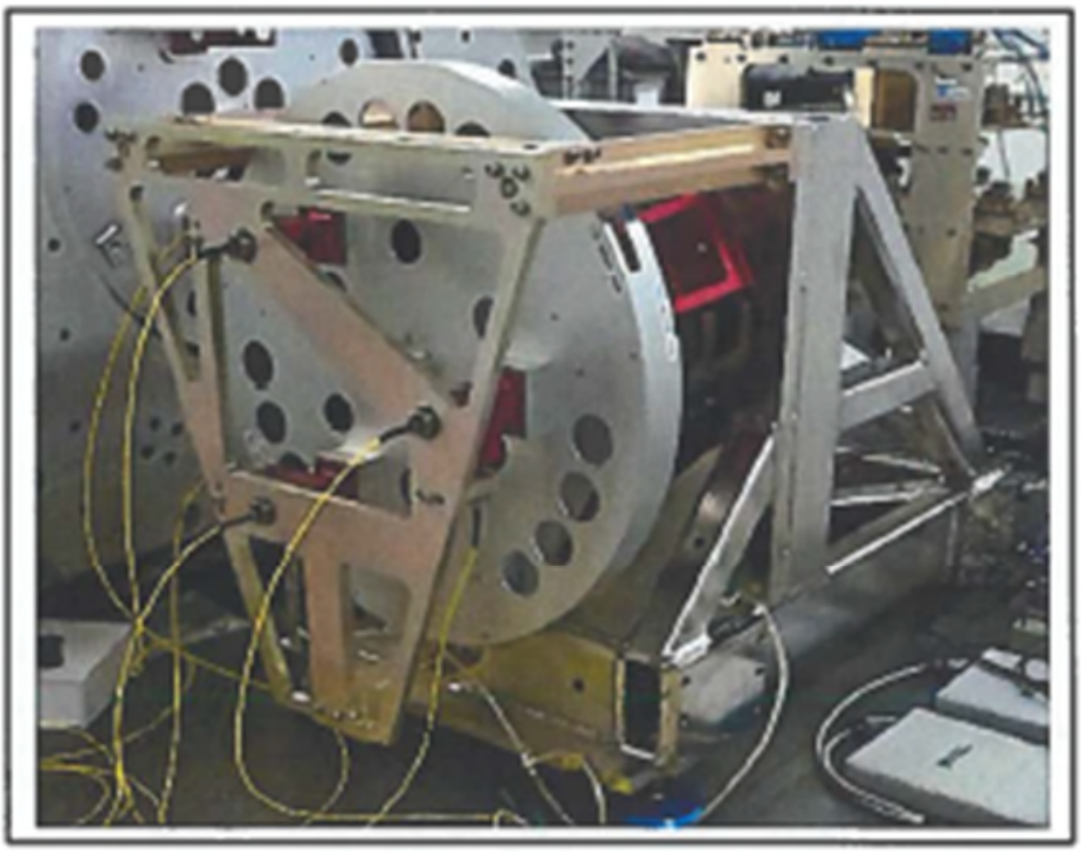

Figure 7. Actuator Performance Test Station Measuring 6 DOF

Actuator Test Results

Table 1 compares design goals to measured test results from the pathfinder high performance pre-production Testbed Actuator, which pushes the state of the art on single-stage flexure-based linear actuation with regards to range and resolution. Subsequent graphs (Figures 8 – 12) provide examples of measured data.

Table 1. TBA Performance Bettered Design Goals for all Requirements.

TBA Performance Parameter	Design Goals	Tested Results	Units
Total Range	≥ ±500	> ±650	μm
Resolution (avg. over range)	≤ 10	6.5	nm
Rate	≥ 700	compliant	nm/sec
Settling Time	≤ 300	compliant	msec
Accuracy	≤ 5	< 3	nm
Backlash over full range	≤ 10	< 3	nm
Hysteresis over full range	≤ 10	< 1	nm
Stepper Motor Torque Margin (per AIAA-S-114A-2020)	≥ 150	compliant	%
1st Mode w/supported mass	≥ 150	compliant	Hz
On-Orbit Life	10	compliant	years
Life Cycles (Full Range)	≥ 10,000	compliant	cycles
Encoder Resolution	≤ 1	< 1	motor step(s)

Non-Linear FEA Output

A non-linear FEA analysis was performed to simulate the input angle from the motor to linear output displacement through the rotary flexure design. The results of the analysis show expected non-uniform step size change about the zero location (the zero location is defined by the initial assembled location). As the input angle increases, the step size decreases in a non-linear fashion until an inflection point is reached where the flexural arrangement effectively causes the step size to go to zero. The reverse direction produces an increase in step size, in a slightly less non-linear fashion as compared to the positive direction, until the maximum displacement is achieved. The maximum displacement is limited by stress, such that a factor of safety of 1.5 on the material yield strength is achieved for the flexural components. The non-linear behavior in step size variation over input angle is due to the cylindrical flexures changing angle with respect to ground. Although the step size is non-linear, the behavior is repeatable and can be characterized during performance testing.

Displacement vs Input Angle test

Figure 8 shows the output data of the Displacement vs. Input Angle test. The graph shows a portion of the test starting at the negative most displacement through the positive most displacement with respect to the zero location. The graph shows a total displacement of the mechanism of 1.4 mm, with a much larger displacement in the negative direction than the positive direction. The non-uniform displacement with respect to the zero location is associated with the non-linear behavior of the actuator.

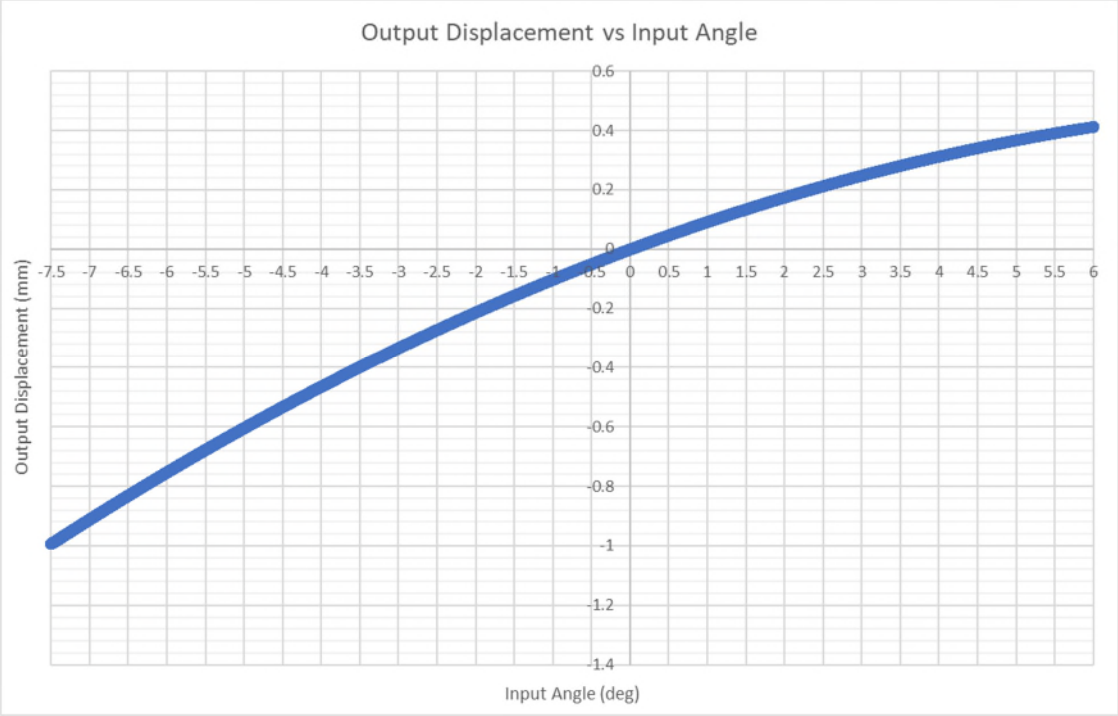

Figure 8. TBA Displacement vs. RLOA Input Angle

Resolution (step size) test

The resolution test shows the step size at the zero location of the mechanism. The test was performed by commanding the mechanism to perform a series of steps in a (+10, -10; -10, +10) pattern. Shown in Figure 9 is a portion of the test. The graph shown is data with the initial ringing of each step removed and the noise in the data removed over the multi-second dwell time. This test shows the average step size at the zero location is 6.8 nm. The steps deviate approximately ±1 nm from the 6.8 nm average over the test.

Figure 9. TBA Resolution over Range Data Showing Desired Step Size of 6.8 ± 1 Nanometer.

Step Resolution and Encoder Feedback

Figure 10 shows the encoder feedback (orange dashes) overlayed on the step resolution test. The encoder shows a strong correlation to the measured step size. The encoders ideal resolution is about 52 counts per step of the mechanism. The data shows an encoder deviation of ± 3 counts on average with some outliers being off by 7 counts. At the center of travel, where the step size is approximately 6.8 nm, the average encoder deviation equates to ± 0.4 nm, which is within 6% of the step size. The results of this test show that the encoder strongly correlates to the step resolution of the actuator over the range of the actuator.

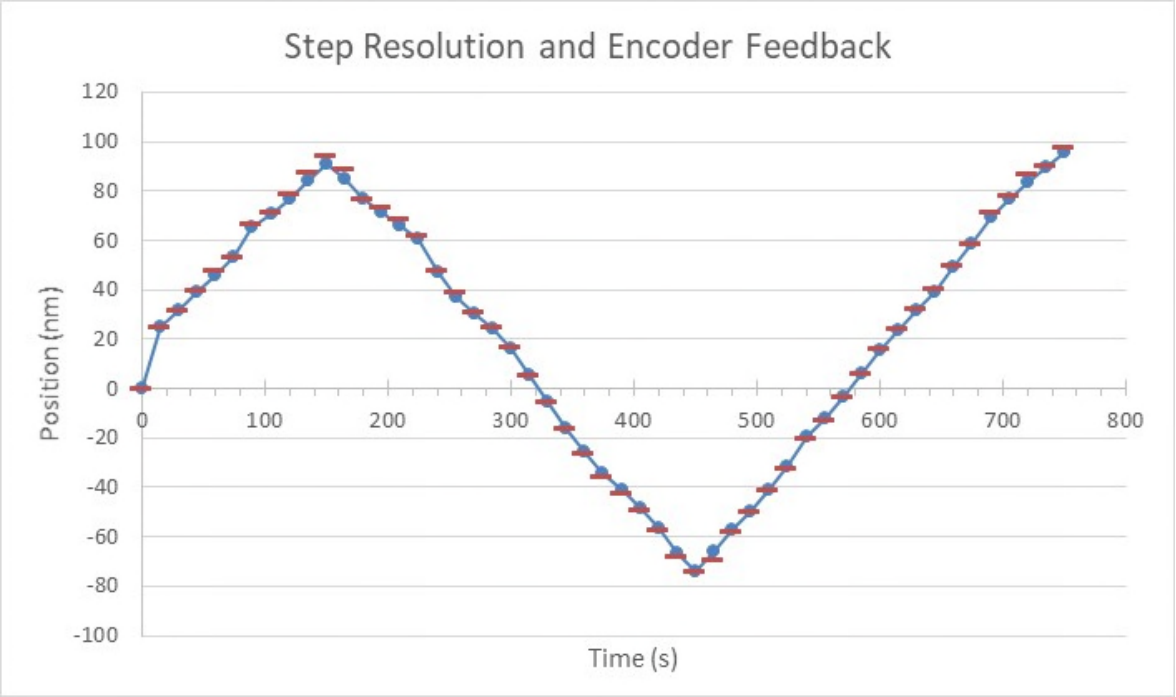

Figure 10. TBA Step Resolution compared to Optical Encoder Data

Hysteresis Test and Backlash Testing

Figure 11 and Figure 12 show the results of the hysteresis and backlash tests. The tests were performed in multiple iterations of positive and negative step transitions to observe what motion was lost due to change in directions. For the hysteresis test, we repeated a ± 40 steps over several ranges. The average loss from reversing direction per step was 0.27 nm. For the backlash testing, we repeatedly changed direction with different numbers of steps before returning to a net 0 step position. After multiple iterations of motion, the total loss of position was 1.7 nm. The step positions for each test, were an average over a multi second dwell at each step.

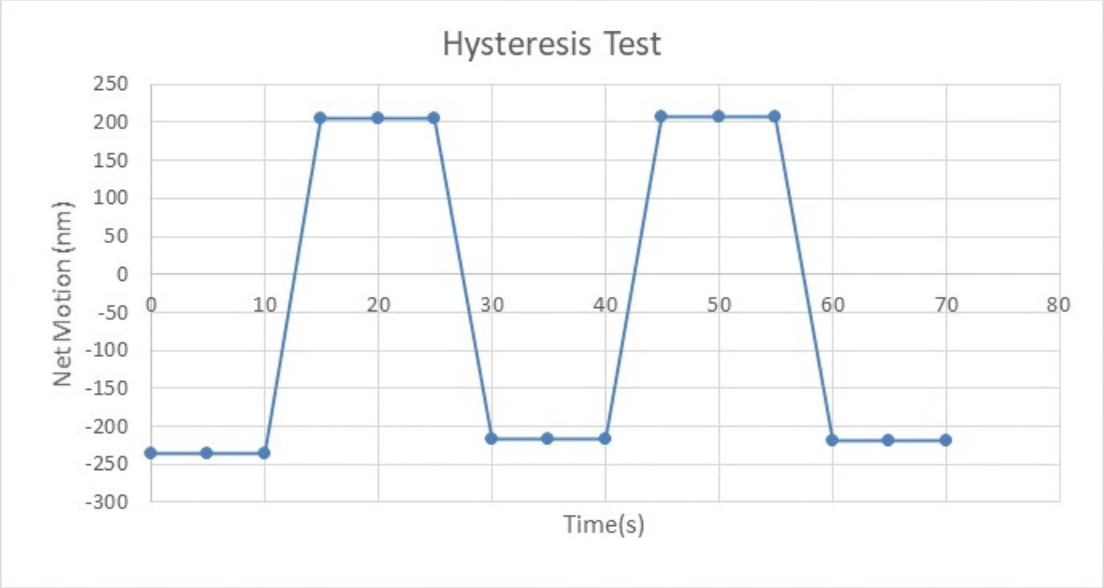

Figure 11. TBA Hysteresis Test Results Show Excellent Performance

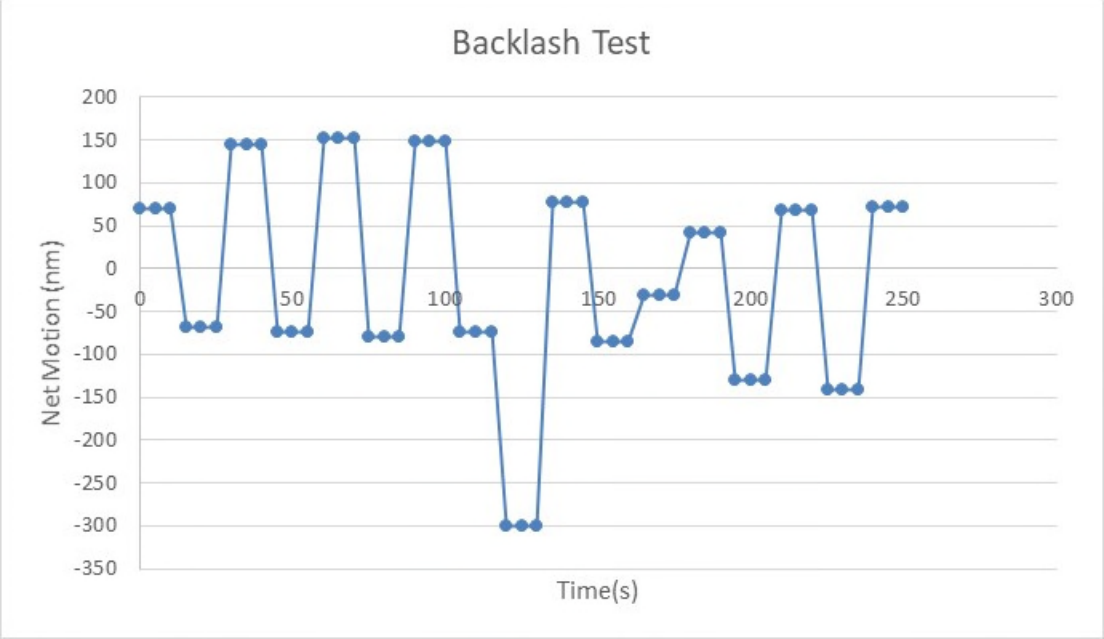

Figure 12. TBA Backlash Test Result Show Near Zero Actuator Backlash

Conclusion

The mechanism performed as expected and made repeatable (to single nanometer) steps. The design and configuration of this actuator provided a plethora of range (1.4 mm of travel) with nanometer level precision. The encoder follows the motion of the mechanism to within 6% of each step taken (resulting in an average encoder deviation of ± 0.4 nm). The backlash and hysteresis tests show there is little to no backlash from the dual stacked harmonic drives and very little hysteresis in the system. The range and resolution of this actuator, in combination with its deterministic and repeatable behavior and stiffness capabilities, has pushed the boundaries and capabilities of what is possible. Going forward we would like to better optimize the center of motion of the mechanism and reduce the change in step size over the range.

References

1. Booker, Jesse W. (2017). *Actuator device and method of converting rotational input to axial output with rotary flexure mechanism*. (US 9787157 B2). United States Patent Office.

Measurement Considerations for Exported Force and Torque Testing of the Ricor K508N Cryocooler

Bill Zwolinski[*], Pascal Erne[**], Lucas Anderson[***], Joel Mork*** and Ian McKinley[****]

Abstract

This paper presents a review of the practical design considerations in the mechanical characterization of micro-vibrations via Exported Force and Torque (EFT) testing. The concepts of piezoelectric force measurement will be discussed along with vibration fixture design, sensor mounting, signal conditioning, and data acquisition. The Active Thermal Architecture (ATA) system will be used as an application example for the EFT characterization of micro-vibrations from a COTS Ricor K508N cryocooler. The ATA employs passive vibration isolation technologies to minimize the impact of vibrational jitter on a suspended kevlar isolated detector. The ATA's use of a Kistler Force Dynamometer, three-axis force transducer, and accelerometer to characterize the multicomponent forces generated by the K508N will be explored and performance benchmarks for the ATA's passive vibration isolation technologies given.

Introduction

Commonly used spacecraft mechanisms span a wide range of applications including cryocoolers for EO/IR imaging, reaction wheels/control moment gyros for attitude control, robotics subsystems as well as actuators, motors, latches and clamps for antennas and positioning/release mechanisms. Exported forces and torque (EFT) resulting from mechanism operation can affect spacecraft mission performance. As such, these disturbances can be continuous vibration or short-term transient depending on the mechanism function. For example, the attitude determination and control system corrects the spacecraft orientation due to exported disturbances without the use of fuel thus creating stable pointing/positioning. Characterization of such EFT-related flight disturbances typically utilizes force dynamometers for multi-component force measurement to characterize micro-vibration disturbances to the spacecraft in 6-components (*Fx, Fy, Fz, Mx, My, Mz)*.

Practical considerations of multi-component force measurement include vibration fixture design, sensor mounting, signal conditioning and data aquisition. For example, factors such as sensor alignment, preloading and checkout/calibration of force test fixtures need to be considered in the design. Force dynamometers are comprised of several sensors where design considerations such as load bearing surface materials, preparation and tolerances as well as mass loading effects are considered for fixture design. Multicomponent force sensor terminology addresses performance parameters such as linearity, hysteresis, cross talk and stiffness to provide an awareness of design considerations as well as FEA and experimental results. As low-level disturbances are to be measured, it is critical to isolate the EFT measurement system from seismic inputs and acoustic noise sources as well as ensuring table resonances are outside the frequency band of interest. As such, measurement noise can be comprised of electrical and environmental effects where noise characterization as a function of analog bandwidths/frequency has to be taken into account. Lastly, depending on the mechanism, vacuum EFT testing may be required to assess mechanism operation where best practices are considered for low outgassing. The results are aimed at achieving a compact design, high frequency, high resolution, and the required dynamic range to characterize the mechanism under test.

[*] Kistler Instrument Corp., Novi, MI bill.zwolinski@kistler.com
[**] Kistler Instrumente AG, Winterthur, Switzerland pascal.erne@kistler.com
[***] Utah State University, Logan, UT lucas.anderson@usu.edu
[****] NASA JPL, Pasadena, CA ian.m.mckinley@jpl.nasa.gov

The Active Thermal Architecture (ATA) system is a sub 1U two-stage, single-phase Mechanically Pumped Fluid Loop (MPFL) active thermal control technology targeted at 6U CubeSat platforms and above. The ATA's first stage comprises a micro-pump-driven MPFL, connecting an internal heat exchanger to a deployable tracking radiator through a two-axis rotary fluid hinge. A COTS Ricor K508N cryocooler forms the second stage and provides cryogenic cooling to a custom Kevlar detector mount. The ATA system utilizes advanced 3D fabrication techniques such as Ultrasonic Additive Manufacturing to miniaturize and simplify the MPFL by directly embedding the working fluid channels into the CubeSat chassis. The ATA system includes passive vibration isolation and damping technologies such as wire rope isolation, particle dampers, and flexible (TMT) pyrolytic graphene thermal straps to mechanically isolate the active components from the CubeSat and payload and to minimize the impact of micro-vibrations on mission success. [1]

Funded by the NASA Small Spacecraft Technology Program, the ATA project is a joint venture between the Center for Space Engineering at Utah State University and the NASA Jet Propulsions Laboratory. It is a continuation of the Active CryoCubeSat Project project. The ATA technology as been selected for demonstration on the Active Cooling for Multi-spectral Earth Sensors (ACMES) mission scheduled to launch in late 2024. The ATA will act as thermal support for the University of Hawaii's Hyperspectral Thermal Imaging instrument (HyTi). This flight is funded through the In-Space Validation of Earth Science Technologies (InVEST) program and the Earth Science Technology Office (ESTO). [2]

Piezoelectric Force Technology - Concept of Operation

Piezoelectric (PE) sensors make use of the piezoelectric effect of single crystals such as quartz (SiO_2), in which the charge released is proportional to the applied load. Because natural quartz crystals contain too many imperfections, use is made of quartz grown artificially under precision-controlled conditions. Quartz crystals are grown artificially in autoclaves as illustrated in Figure 1. [3], [4]

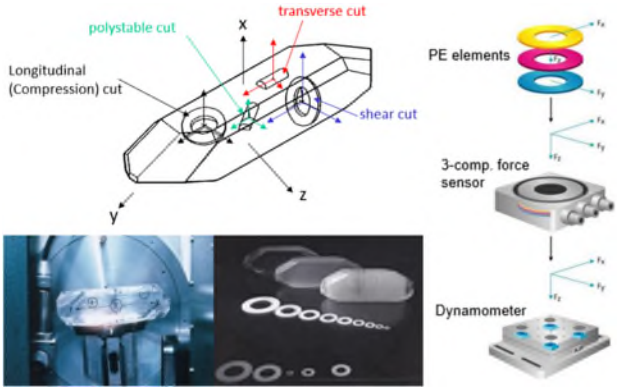

Figure 1: Illustration of Quartz Crystal and use in 3-Component Force Sensors and Force Dynamometers

Quartz sensors provide high stiffness and quasi-static to high-frequency operation nature demonstrates that the sensitivity of quartz remains extremely stable: natural quartz that is over one million years old retains the same pC/N sensitivity, with virtually no sensitivity shift over its lifetime. Kistler also grows its own high-performance crystals known as PiezoStar®, which has higher sensitivity and higher operating temperature compared to quartz.

Piezoelectric Terminology

PE sensors do not have internal electronics, so they require an external charge amplifier to convert the electrical charge signal into a proportional voltage. An IEPE (Integrated Electronic Piezoelectric) sensor, however, does have internal electronics powered by a constant current supply, thus providing a voltage output. Figure 2 compares the properties of PE and IEPE sensors. EFT systems commonly use PE technology.

	PE (pC/mu) - Piezoelectric	IEPE (mV/mu) - Integrated Electronics Piezo Electric
Electronics	External charge amplifier	Internal charge to voltage converter, powered by IEPE constant current supply
Cable	High impedance	Standard cable
Temperature	Very wide range	Limited with integrated electronics
Rangable	Yes.	No.
Measurement	Quasi-static (long TC) as well as highly dynamic measurements possible	Only dynamic.
Reset/Measure	Tares the measurement to remove static loads from the dynamic range	Not possible
TEDS	n.a. (retrofit only)	Yes

Figure 2: Comparison of PE and IEPE Piezoelectric Sensors Types

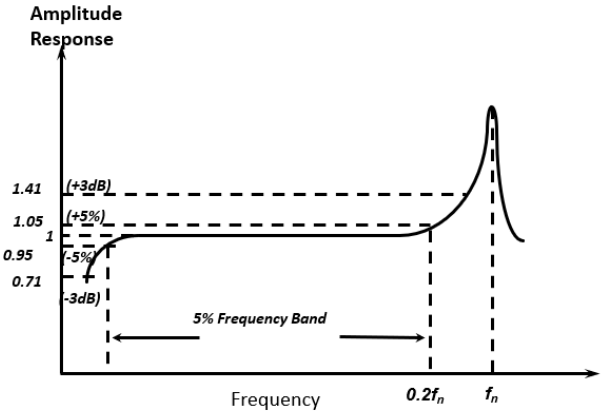

Approximation for PE Sensors

$f_{5\%} \sim f_n/5$; $f_{10\%} \sim f_n/3$; $f_{3dB} = f_{+41\%} \sim f_n/2$

Figure 3: Typical Frequency Response of a PE Sensor

Piezoelectric Sensor Frequency Response

A PE sensor can be described as a lightly damped second-order system at medium to high frequencies, and as a single-order high-pass characteristic at low frequencies, as illustrated in Figure 3.

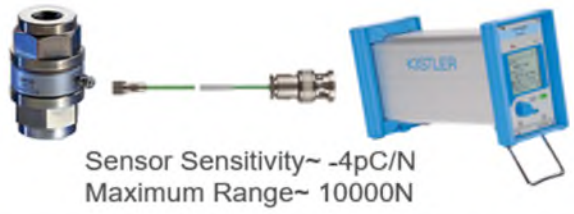

Full Scale Range (FSR = 10V)	Output Scale Factor (N/V)	Broadband Noise rms	Broadband Noise rms
1 N	0.1 N/V	0.0045 Vrms	0.00045 Nrms
25 N	2.5 N/V	0.0012 Vrms	0.003 Nrms
1000 N	100 N/V	0.0006 Vrms	0.06 Nrms
10000 N	1000 N/V	0.0006 Vrms	0.6 Nrms

Figure 4: PE Measuring Chain Rangeability Example

Piezoelectric Measuring Chain Rangeability

The PE measuring chain is rangeable using an external charge amplifier where noise (resolution) scales as a function of the selected measuring range. Figure 4 shows an example of the noise (resolution) as a function of the selected range. The rms (root mean square) noise is the integration of noise power spectral density over operational frequency range. The Reset/Measure function of the amplifier also allows taring of the measuring chain from a static mass acting on it.

Design of PE Force Dynamometers

Non-axial forces applied to an individual force sensor create moment loads which at best degrade accuracy and, at worst, can break the sensor. A PE force dynamometer comprises an array of force sensors mounted between thick metal plates. Important parameters to be considered and related to performance are the parallelism of the cover and base plate, flatness, strength and stiffness. The better these parameters are, the better the frequency response will be. A certain minimum tensile strength is necessary so that the top and bottom plate can withstand the large forces from the preloading bolt.

Figure 5: Example of a Ceramic Micro-Vibration Dynamometer Type 9236A2

Force dynamometers absorb non-axial loads and distribute moment loads by differential force reactions within the force sensor array; they can be of various shapes and sizes – square, triangular, rectangular, or circular. A PE force dynamometer measures the magnitude and direction of *Fx, Fy, Fz* acting on the dynamometer, but it does not measure their spatial location on the top plate. [5]

A search for new materials for the top plate found ceramic offers highly advantageous properties for EFT, low specific gravity and a high modulus of elasticity. Finite element method calculations show that natural frequencies are increased by 40% for ceramic top plates

with the same dimensions as steel. This is especially important for large test articles and corresponding large dynamometers.

Typically, four force sensors are used between two parallel plates to calculate the 6 components forces and moments. A typical dynamometer geometry is shown in Figure 6. As shown a, b is the vertical and horizontal separation relative to the force sensor center to dynamometer center line respectively.

$$F_x = F_{x1+2} + F_{x3+4} \quad (1)$$

$$F_y = F_{y1+4} + F_{y2+3} \quad (2)$$

$$F_z = F_{z1} + F_{z2} + F_{z3} + F_{z4} \quad (3)$$

$$M_x = b * (F_{z1} + F_{z2} - F_{z3} - F_{z4}) \quad (4)$$

$$M_y = a * (-F_{z1} + F_{z2} + F_{z3} - F_{z4}) \quad (5)$$

$$M_z = b * (-F_{x1+2} + F_{x3+4}) + a * (F_{y1+4} - F_{y2+3}) \quad (6)$$

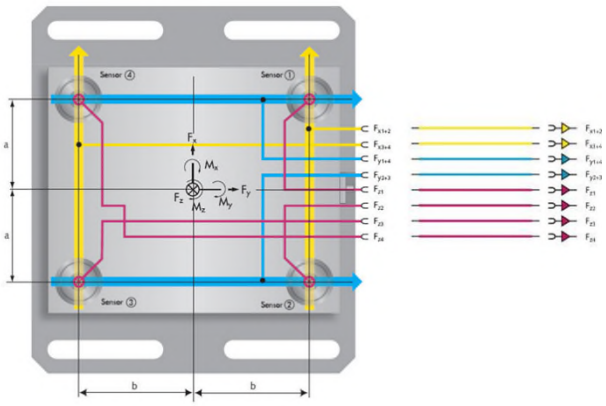

Figure 6: *Dynamometer Geometry with 4x 3-Component Force Sensors Resulting in 6-Component Equations for Fx, Fy, Fz, Mz, My, Mz*

A PE dynamometer can be represented as a simple spring mass model consisting of:

- A base plate
- A top plate with mass *m*
- A spring with stiffness k_f
- A damper with damping coefficient *D*

PE sensors and dynamometers usually have very low damping (0 < *D* < 0.01). The large cross-section of the quartz plate sensing elements for the 3-component sensor results in very high stiffness which supports high-frequency measurements. Even with an additional mass, the natural frequency of a PE dynamometer remains high due to the equivalent stiffness. The dynamometer exhibits the same behavior as a lightly damped second-order system (see Figure and Figure). Added mass acts to reduce the natural frequency, as illustrated. [6]

$$f_r = \frac{1}{2\pi} \cdot \sqrt{\frac{k_f}{m}} \quad (7)$$

$$f_{r,red} = \frac{1}{2\pi} \cdot \sqrt{\frac{k_f}{m + m_2}} \quad (8)$$

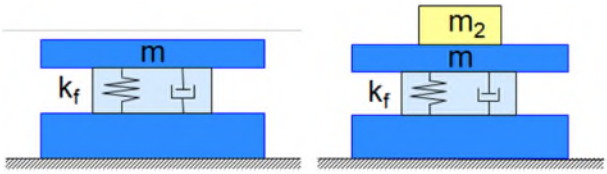

Figure 7: Spring Mass Model of PE Dynamometer

m: mass of top plate
k_f: stiffness of spring
m_2: added mass
$f_{r,red}$: reduced resonance frequency

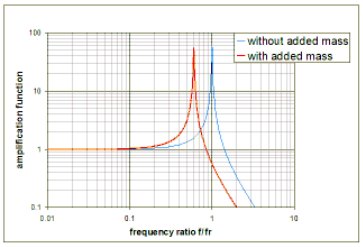

Figure 8: Natural Frequency of Spring Mass System

<u>Analog bandwidth considerations relating to measurement</u>

For PE force measurement the charge amplifier determines lowest and highest frequencies that can be measured. The test article and application define the required frequencies of interest and associated resolution. However, the test stand, fixtures and mass acting upon the PE force dynamometer determine the highest possible measurement frequency. As the amplitude response tolerances can be expressed as a function of natural frequency the 5%, 10%, 3 dB bandwidths can be selected to make the measurement.

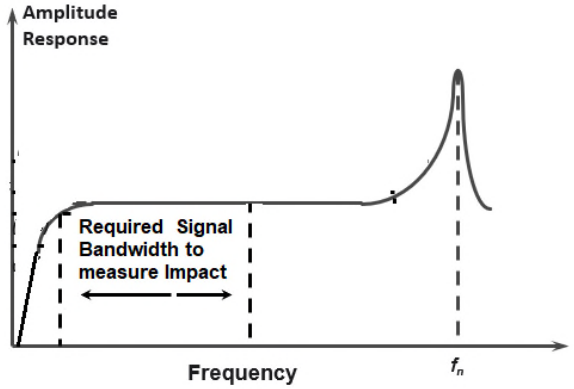

Figure 9: Illustration of Required Signal Bandwidth and Force Sensor Natural Frequency

Design Drivers for Operational Performance Testing of Reaction Wheels

With reaction wheel testing, the magnitude and frequency of a wheel's EFT is characterized. A reaction wheel test dynamometer consists of four 3-component force sensors. The output of each of the sensors are summed in *Fx*, *Fy* and *Fz* for the resulting impact forces where moments can be calculated as described in equation (4) - (6). The PE force dynamometer has a very large measurement range and is rangeable allowing for measurements for very small reaction wheels. As a result, one PE dynamometer size will fit all measurement requirements. High natural frequency, also in shear direction is required where the dynamometer must also provide a stiff interface with easy mounting possibilities. Lastly the PE dynamometer uses a charge amplifier for rangeability, high dynamic range and high signal fidelity.

Typical dynamometer installation guidelines

As shown in Figure 10, the dynamometer is hard-mounted on the seismically isolated table and the test article is hard-mounted on top of the dynamometer. The top adapter plate is typically made of aluminum; it mates with the hole pattern of the dynamometer and has the hole pattern required for the test article. The bottom adapter plate mates with the hole patterns of the table and of the dynamometer. Maintenance of 0.01 mm flatness and parallelism of the adapter plates is recommended for the best frequency response. The bottom adapter plate can sometimes be eliminated if the table has the same mounting hole pattern as the dynamometer: direct mounting is then possible. Again, the table surface should be flat and parallel to within 0.01 mm. Granite or optical tables provide a stiff and rigid mounting surface so that resonances are minimized, ideally remaining outside the measurement frequencies of interest.

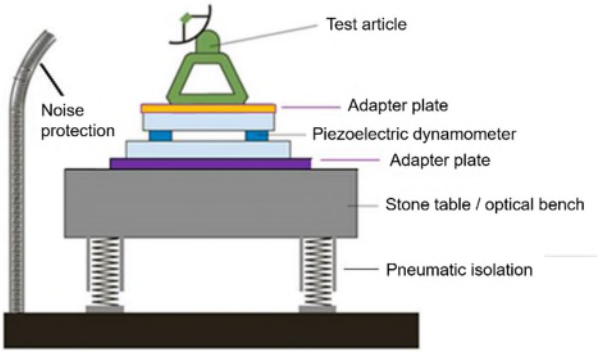

Figure 7: Typical Installation of Dynamometer for EFT Testing

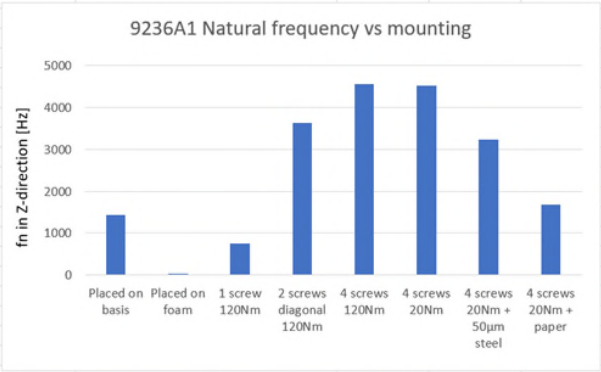

Figure 8: Effect of Frequency Response for Various Mounting Parameter such as Torque, Flatness, and Number of Fasteners

For granite or stone tables, the general rule is that the mass mounted on the test bench is less than 10% of the table's mass. As mentioned above, acoustic noise protection is also recommended for the installation. The background vibration (noise) for the facility/table setup can be determined by running an ambient noise test once the dynamometer is connected and the overall setup is completed.

As Figure 11 shows, it is more important to ensure flatness, parallelism, and an adequate number of fasteners than to achieve the highest preload. In the ideal mounting configuration, the dynamometer is fastened on the base with four screws (measurement 5). The effect of mounting torque is small (there is almost no difference between 120 N·m and 30 N·m torque for mounting screws). Since fewer fasteners

and less surface flatness can degrade the frequency response, any configurations other than measurement 5 are not recommended.

Data Acquisiton

Depending on the signal to be measured, AC coupled, or DC coupled data acquisition is used. EFT charge amplifiers are typically set up in short or medium time constant as EFT is an AC coupled measurement. With today's 24-bit data acquisition systems, the resulting measurement resolution is usually far greater than is required for the signal measurement. Bandwidth is the difference between the upper and lower frequency in a continuous band of frequencies; theoretically, the minimum sample rate is two times the maximum signal frequency but in practice, 5 to 10 times is used to avoid aliasing. For this purpose, the natural frequency of the complete system (including force sensors and fixtures, etc.) must be considered.

Noise consideration

Noise consists of unwanted random fluctuations that degrade signals and limit the minimum signal level that can be measured. The total noise from multiple random (white) noise sources can be described as:

$$\sigma_{rms} = \sqrt{{\sigma_1}^2 + {\sigma_2}^2 + \cdots + {\sigma_N}^2}. \qquad (9)$$

Filtering reduces noise and enhances the signal quality but can affect the overall analog bandwidth of interest.

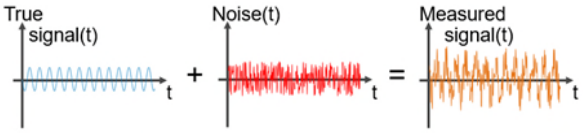

Figure 9: Schematic of a Measurement Signal Affected by Noise

Electrical noise can adversely affect the measurement noise. Use of ground-isolated measuring chains is preferred to avoid ground loops where one common ground for the measurement chain is provided. EFT Dynamometers are typically ground isolated complementing low noise measurement.

Avoiding strong electromagnetic fields (e.g., electromagnetic interference (EMI)) in the area of the instrumentation/cables is best practice, as is the use of 360°-shielded cables. The battery power of the signal conditioner and amplifiers can often show an improvement in both noise level and 50 Hz/60 Hz harmonics due to the AC-DC power conversion process, which is not a perfect process. Lastly, analog bandwidth is proportional to root mean square (RMS) noise.

Multi-channel charge amplifiers with internal summing calculators generate some additive electrical noise to the measured 6-components. Using software (such as DynoWare) to compute the six component signals from the component signals results in no additive noise compared to the internal summing calculator. Additional noise error sources originating from the environment include HVAC inputs with airflow on structures under test, acoustics, structure-borne noise, structural response of the test rig or transmissibility of seismic inputs to the sensors performing the measurement; we will not discuss these sources in this paper, but they must nevertheless be taken into account.

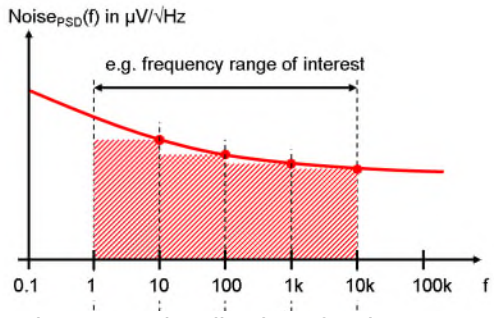

Figure 10: Visualisation of Noise Power Spectral Density

Noise power spectral density

The noise power spectral density describes the signal's power content versus frequency. It allows the noise to be estimated as a function of bandwidth/filtering. Fast Fourier Transform (FFT) is effectively narrowband filtering of the signal of interest. Narrowband FFT processing can support higher resolution and signal-to-noise ratio on a frequency bin basis, where the frequency bin width is related to the number of FFT points and sample rate. The noise RMS can be calculated as:

$$\text{Noise}_{rms} = \sqrt{\int_{f_L}^{f_H} [\text{Noise}_{PSD}(f)]^2 df}. \qquad (10)$$

Calibration

Calibration not only provides information about the functionality of the measuring equipment, but also precisely determines characteristics such as sensitivity, linearity, hysteresis, crosstalk and drift, and thus contributes significantly to the overall accuracy of the measurement. Only a fully calibrated measurement chain can provide the necessary confidence in the measurement equipment.

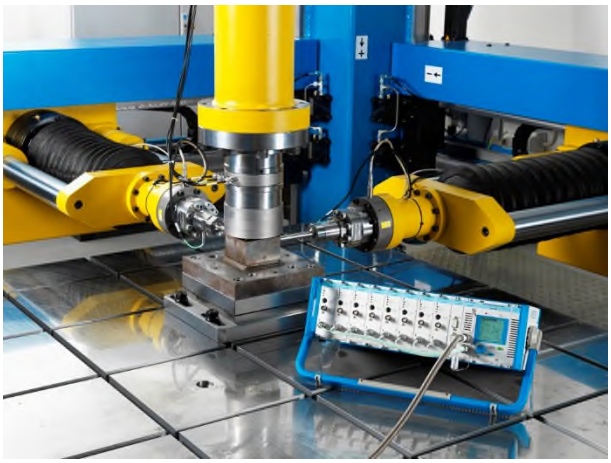

Figure 12: 3-Component Force Dynamometer with 5080A charge amplifier at Calibration

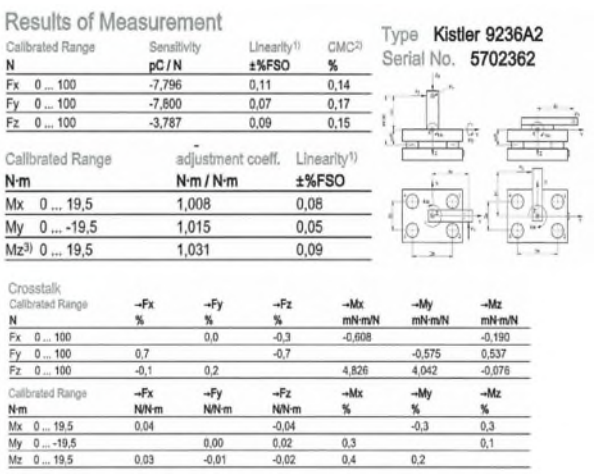

Results of Measurement

Type Kistler 9236A2
Serial No. 5702362

Calibrated Range N	Sensitivity pC / N	Linearity[1] ±%FSO	CMC[2] %
Fx 0 ... 100	-7,796	0,11	0,14
Fy 0 ... 100	-7,800	0,07	0,17
Fz 0 ... 100	-3,787	0,09	0,15

Calibrated Range N·m	adjustment coeff. N·m / N·m	Linearity[1] ±%FSO
Mx 0 ... 19,5	1,008	0,08
My 0 ... -19,5	1,015	0,05
Mz[3] 0 ... 19,5	1,031	0,09

Crosstalk

Calibrated Range N	→Fx %	→Fy %	→Fz %	→Mx mN·m/N	→My mN·m/N	→Mz mN·m/N
Fx 0 ... 100		0,0	-0,3	-0,608		-0,190
Fy 0 ... 100	0,7		-0,7		-0,575	0,537
Fz 0 ... 100	-0,1	0,2		4,826	4,042	-0,076

Calibrated Range N·m	→Fx N/N·m	→Fy N/N·m	→Fz N/N·m	→Mx %	→My %	→Mz %
Mx 0 ... 19,5	0,04		-0,04		-0,3	0,3
My 0 ... -19,5		0,00	0,02	0,3		0,1
Mz 0 ... 19,5	0,03	-0,01	-0,02	0,4	0,2	

Figure 11: Example of a Calibration Certificate incl. Crosstalk and Linearity

Figure 14 shows the calibration test stand where calibration is performed using a multi-component press for high loads as illustrated below. In each axis there is a strain gage sensor to control the applied force and a PE force sensor to quasi-statically calibrate the PE dynamometer in *Fx, Fy* and *Fz*. Figure 15 shows the calibration results indicating very low crosstalk and highly linear operation of the multicomponent PE force platform.

Application – Ricor K508N Micro-Vibrations for the ATA system

Understanding the impact of micro-vibrations on spacecraft structures and payloads can be mission critical. For example, micro-vibrations, or jitter, can cause excitation of the support structures for optical elements during imaging operations, this can result in severe degradation of image quality due to smearing and distortion for Earth observation satellites. A prime example of this is the inclusion of miniature cryocoolers for sub-cooled electro-optical instrumentation on CubeSat platforms. Stirling cryocoolers in particular rely on a dynamic compression stage which can induce high amplitude frequency dependent vibrations that can be detrimental to sensitive optical instruments. The ATA system features an integrated Stirling based Ricor K508N miniature cryocooler. The K508N is a long life tactical cryocooler based on a high-speed rotary compression cycle (reciprocating vibration) and as such generates micro-vibrations. Cryocooler's generally impart body vibrations throughout the satellite structure, as well as cold tip vibration, which can be passed directly to sensitive instrumentation. To mitigate the impact of this jitter on critical systems, the ATA technology features several of passive vibration isolation technologies. Including wire rope spring isolation of the entire ATA system, a cold tip particle damper, and a Pyrolytic Graphene Sheet (PGS) thermal link to mechanically isolate the cryocooler cold tip from the detector assembly. The ATA K508N cryocooler is shown in Figure 16 with industry standard coordinate directions labeled.

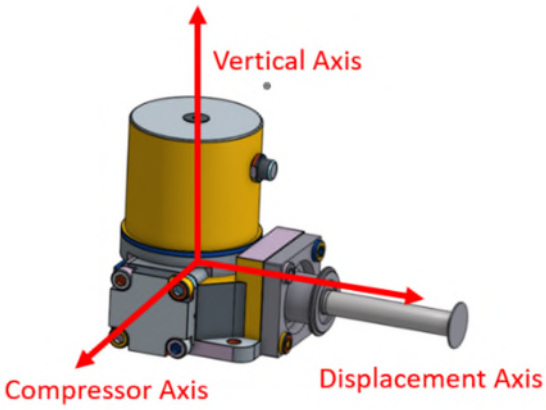

Figure 16: Ricor K508N cryocooler CAD model with common coordinate axis

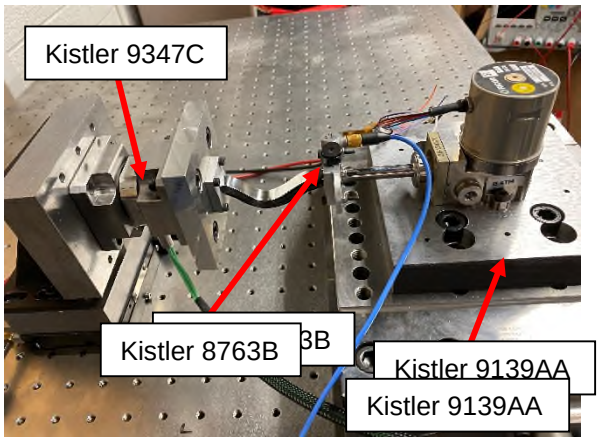

Figure 17: Kistler EFT test setup for the characteriztion of the ATA Ricor K508N micro-vibrations

The ATA K508N cryocooler was simultaneously characterized for body EFT, cold tip exported triaxial force, and acceleration. The integrated K508N cryocooler was mounted to a Kistler 9139AA multi-component dynamometer that provided 6-component equations. Three-axis orthogonal force and three-axis moment measurements. The cryocooler cold tip was attached to a horizontally mounted Kistler 9347C triaxial force transducer. Which directly measured the exported force of the cold tip while an 8763B Kistler low noise accelerometer was also mounted to the cold tip and recorded the triaxial acceleration. Figure 17 shows the ATA cryocooler mounted to the Kistler dynamometer with the Space Dynamics Laboratory TMT PGS thermal link attached to the force transducer. Each of these Kistler EFT sensors were fed into a quasi-static 5080A multi-channel charge amplifier to integrate, convert, and amplify the measurement signal. Four parallel 5165A LabAmp data acquisition cards recorded the frequency dependent multi-component micro-vibration signals from each Kistler instrument at 20 MHz. Kistler DynoWare was used to interface and collect the various signals and process the data to text files. A custom MATLAB code was used to post process the data. The data was low pass filtered and analyzed via Fourier transform. The ATA heat exchanger plate, shown in Figure 18, has four ITT Enidine CR2400BM wire rope isolators attached at each corner. Gold anodized mounting posts are used to lock the heat exchanger down.

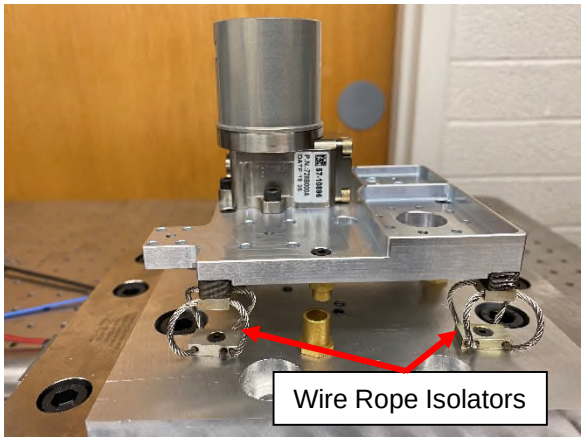

Figure 18: Wire rope isolation of the ATA K508N cryocooler

The ATA K508N cryocooler exhibits a strong vibration peak at approximately ~80 Hz. This can be seen as the first peak in Figures 19 & 20 for the hard mounted case. This first peak corresponds to the Stirling cycle drive frequency of the K508N and is similar for all cryocoolers tested by the ATA project. From this point, higher order harmonics dominate until close to 1000 Hz. When high frequency noise, likely caused by internal rubbing washes out the signal with white noise. The CR2400BM wire rope isolators have resonant peaks at ~85 Hz (Compressor axis), ~120 Hz (Displacer), and ~400 Hz (Vertical). Unfortunately, the 80-Hz driving signal of the K508N amplifies the wire rope isolator's compressor axis resonance. Therefore, the vibration isolation of the WRI's sees a sharp peak near 80 Hz, in the compressor and vertical axis, and then a rapid damping of all higher-order harmonics and noise. Overall, the wire rope isolators show a significant (several orders of magnitude) reduction in the overall amplitude of the exported force for the K508N EFT.

The PGS thermal strap exhibits a roll off frequency between ~20 & 500 Hz. Higher and lower frequencies do not appear to be dampened as much. The PGS thermal link shows the highest damping in the displacer axis and vertical axis, which corresponds to the directions of most flexibility. Figures 19 & 20 show the exported triaxial force of the cryocooler body and cold tip as measured by the Kistler 9139AA dynamometer and 9347C force transducer. Micro-vibration signals are referenced to hard mounting the cryocooler body and cold tip, as opposed to mechanical isolation via wire rope isolation and PGS thermal link. Further information on the vibrational characterization of the ATA Ricor K508N can be found in Ref [1].

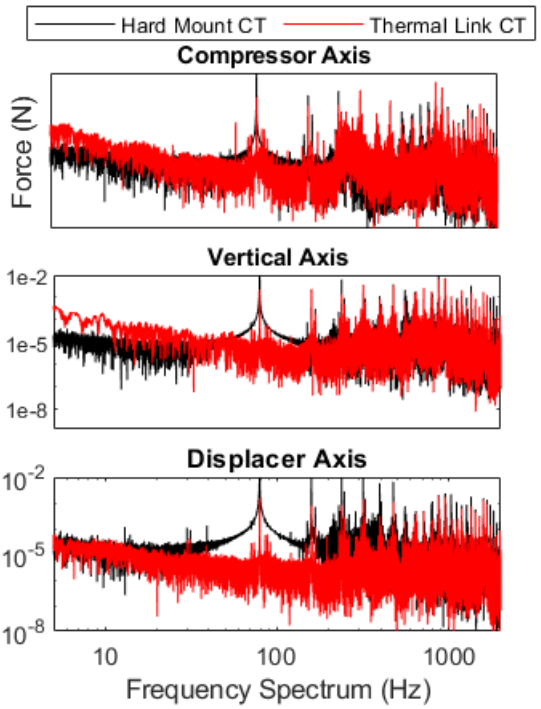

Figure 19: Exported cold tip force for the Ricor K508N. Force comparison of the cold tip hard mounted vs. mechanically isolated via PGS thermal link

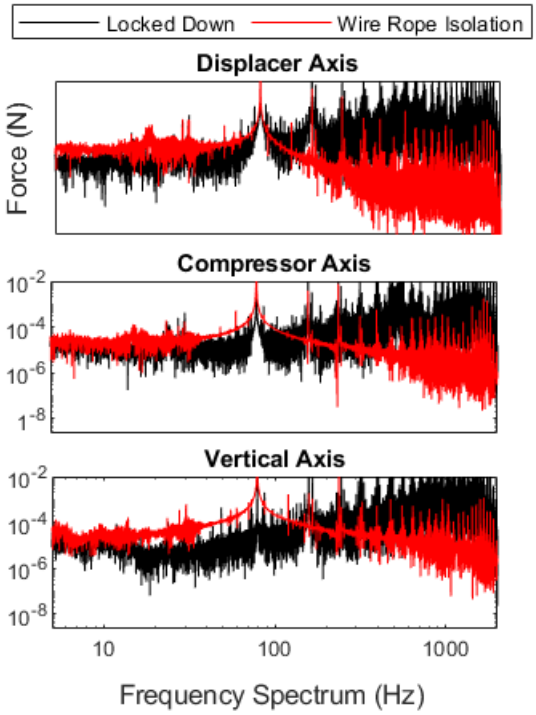

Figure 20: Exported body EFT for the Ricor K508N. Force comparison for hard mounted vs. mechanically isolated via wire rope isolators

Conclusions

Practical considerations for the mechanical characterization of micro-vibrations via Exported Force and Torque testing included vibration fixture design, sensor mounting, signal conditioning, and data acquisition. The Active Thermal Architecture system used a COTS Ricor K508N cryocooler employed passive vibratoin isolation technologies to minimize the impact of vibrational jitter. The EFT system utilized a Kistler Force Dynamometer, three-axis force transducer, and triaxial accelerometer to characterize the multicomponent forces generated by the K508N. The ATA's passive vibration isolation technologies provided an effective method to reduce EFT.

References

[1] L. Anderson, C. Swenson, R. Davidson, A. J. Mastropietro, E. Maghsoudi, S. Luong, S. Cappucci, and I. Mckinley "CubeSat active thermal management in support of cooled electro-optical instrumentation for advanced atmospheric observing missions", Proc. SPIE 10769, CubeSats and NanoSats for Remote Sensing II, 1076907 (18 September 2018); https://doi.org/10.1117/12.2321959
[2] Lucas Anderson, Joel Mork, Charles Swenson, Bill Zwolinski, A. J. Mastropietro, Jonathan Sauder, Ian McKinley, and Mason Mok "CubeSat active thermal control in support of advanced payloads: the active thermal architecture project", Proc. SPIE 11832, CubeSats and SmallSats for Remote Sensing V, 1183203 (2 August 2021); https://doi.org/10.1117/12.2594375
[3] Bill Zwolinski, Pascal Erne (2021). Practical Consideration in multicomponent force measurement for mechanism exported force and torque (EFT) testing
[4] Force Sensors, Kistler, 960-350e-4.0 © 2019 Kistler Group https://www.kistler.com/files/download/960-262e.pdf
[5] Christof Sonderegger (2017). Tracking Micro-vibrations. Micro-vibration testing. Showcase 2017. Aerospacetestinginternational.com, pp 78-81.
[6] Paul A. Tipler and Gene Mosca. “Physik – Für Wissenschaftler und Ingenieure" (2004): pp. 246
[7] L Anderson1 , J Mork1 , C Swenson1 , B Zwolinski2 , A J Mastropietro3 , J Sauder3 , I McKinley3 and M Mok3 “Random vibration, exported vibration, and passive isolation testing of the Ricor K508N cryocooler” Cryocooler Engineering Conference, CEC, 2021

X2B Wide-Angle Steering Mirror

Miroslaw Ostaszewski*, Tim Quakenbush*, Alix Carson* and Jamin Hershberger*

Abstract

Ball Aerospace developed the Wide-Angle Steering Mirror model X2B-WASM with aggressive performance capability and lower cost value. The design of X2B-WASM will be presented along with lessons learned throughout the manufacturing, assembly, integration, and test of this miniaturized fast steering mirror. Engineering/Breadboard/Development testing was completed to verify key performance parameters: ±3 deg of rotation in two axes, greater than 1.0 kHz closed loop bandwidth, and jitter less than 2 μrad.

Overview

The mechanism is comprised of a 26 mm (1.02 in) x 26 mm (1.02 in) mirror that mounts to a Cross Flexure (US Patent US10598924B2) suspension that can achieve ±3 deg of rotation in two axes. Figure 1 shows the CAD model of the X2B-WASM identifying major components: moving mirror assembly with Voice Coil Actuator (VCA) magnets, VCA coils, and proximity position sensor heads mounted to the base assembly.

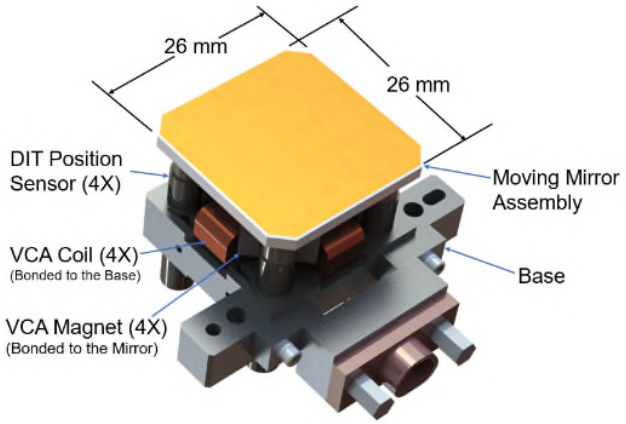

Figure 1. X2B-WASM CAD Model

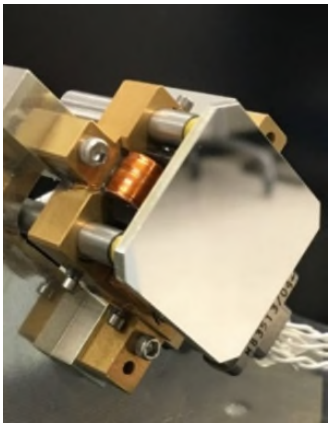

Figure 2. Completed X2B-WASM

The Mirror Moving Assembly tip-tilt motion is driven by a VCA assembly as shown in Figure 3. Four magnets are bonded to the underside of the mirror configured in a magnetic loop with the polarity of magnets as shown. Four coils are bonded to the stationary base and placed in the gaps between magnets. Lorentz force is generated at each coil location with two coil pairs acting in push-pull fashion to produce torque on the moving assembly. The four-coil actuator configuration allows large angular motion within the small volume constraint of the mechanism.

The tip-tilt angle position of the mirror is sensed by a Differential Impedance Transducer (DITs) system. Each DIT sensor head has electrical impedance from the interaction of itself and eddy current in the mirror substrate. The impedance is a function of separation between the sensor head and mirror. The DIT electronics subtracts, demodulates, and amplifies the signals from each pair of sensor heads that are mounted across the center of mirror rotation to give an output signal proportional to mirror angle. DITs angle sensors are common for this type of application and available from several suppliers.

* Ball Aerospace & Technologies Corp., Boulder, CO

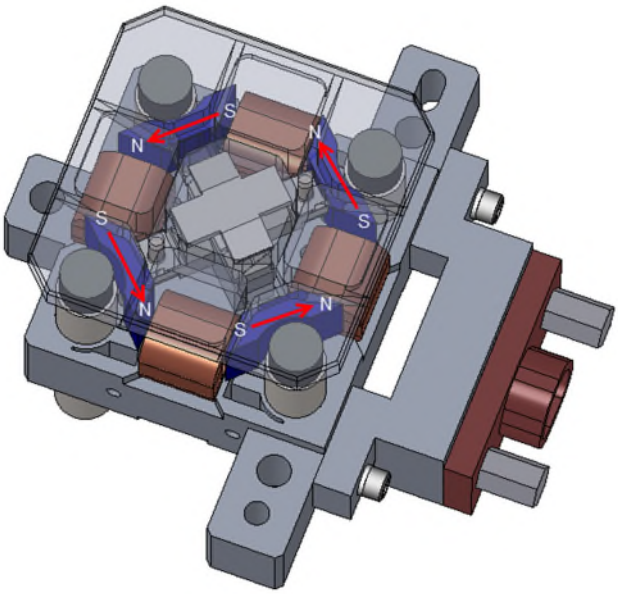

Figure 3. X2B-WASM Magnetic Loop VCA Configuration

Figure 4 shows the two-axis, tip-tilt titanium monolithic flexure; the thin blades in X configuration allow rotation in each axis while being rigid in all translations. The flexure is mounted to a rigid base structure with two 00-90 fasteners and a pin interface that provides precise flexure location on the base. The flexure interface to the mirror with two 00-90 fasteners with mounting locations as shown. Figure 5 shows the small size of the flexure as compared to a penny.

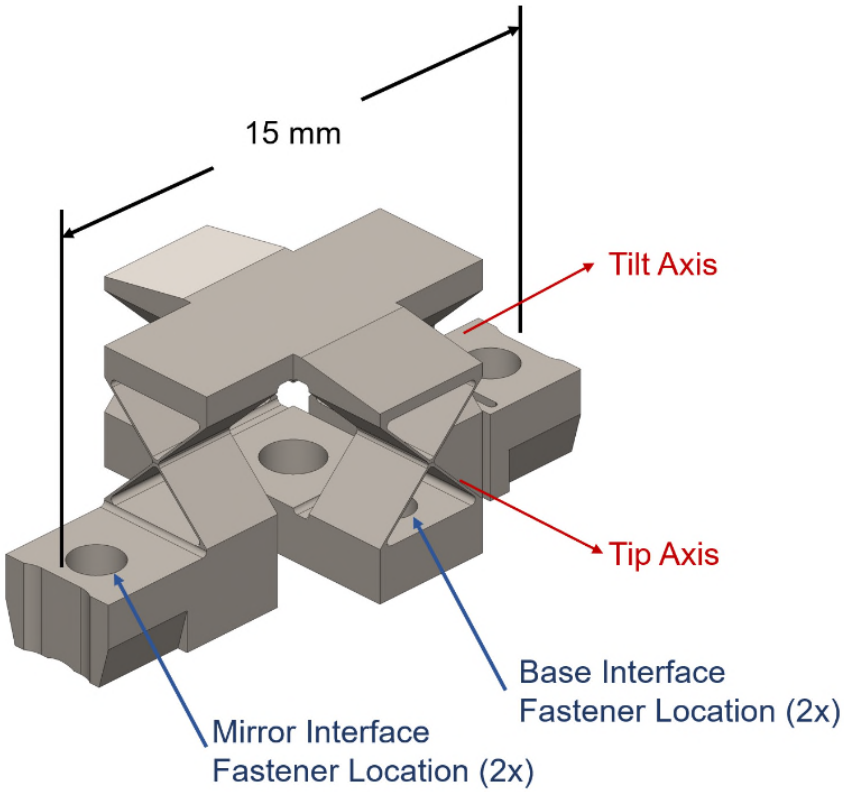

Figure 4. X2B Cross Flexure CAD Model

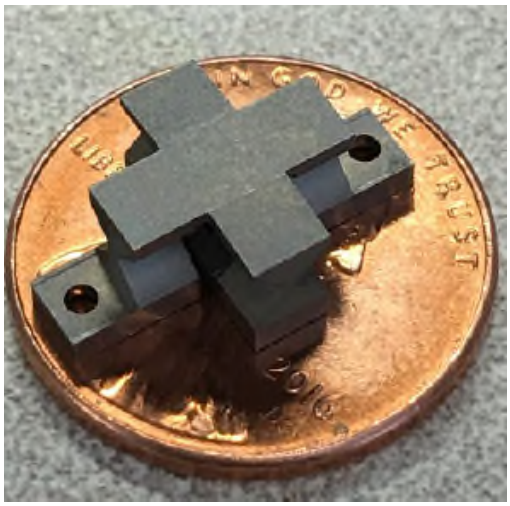

Figure 5. X2B Cross Flexure on a Penny

Table 1. X2B-WASM Performance

Property	Performance
Maximum Range of Travel (Tip, Tilt)	± 3 deg
Residual Mirror Jitter	1.0 µrad RMS
Closed Loop Bandwidth (CLBW) (-3dB)	≥ 1.0 kHz
Mirror Clear Aperture	20.1 mm (0.791 in)
Mirror Surface Figure Error (RMS)	< 23 nm
Rotation Center to Mirror Surface	≤ 4.65 mm (0.183 in)
Total Mass (Mechanism)	Less than 48 gm.
Motor Power at Max Mirror Angle	≤ 2 watts
Launch Load (Static)	100 G axial, 75 G lateral
Launch Loads (Random Vibration)	21.1 G (RMS) overall axial 14.9 G (RMS) overall lateral
Launch Load (Shock)	672 G

Table 2 is a list of measured values for built X2B-WASM units that are referenced throughout this document. Serial numbers that end with the letter “a” indicate values in that row were measured before the unit’s flexure was replaced and “b” designates measurements after flexure replacement. Serial numbers with no letter suffix did not have the flexure replaced. The table is sorted by date to support the flexure design and manufacturing changes that will be described.

Assembly Integration and Test

Maintaining manufacturability of the compact X2B-WASM while ensuring performance metrics were met presented several challenges that required design updates and tooling changes. The serial numbers X2WM1001 - X2WM1005 were built with components using typical tolerances between 0.05 mm (0.002 in) and 0.13 mm (0.005 in). Difficulties during procurement, assembly, integration, and test, led the team to reassess the design from both a manufacturability and producibility standpoint.

Table 2. History of flexure blade thickness effect on 1st & 2nd mode and lifetime.

Build Date yyyy-mm	WASM Serial#	1st Mode (Hz)	2nd Mode (Hz)	CLBW (Hz)	Phase Margin (deg)	Notes
2017-07	X2WM1001	80	950	1200	42	Prototype
2018-07	X2WM1002	18	1110	940	46	Flexure failed in 2020-03 and scrapped.
2020-03	X2WM1003a	16	3500	1180	38	Flexure failed in 2020-12
2020-03	X2WM1004a	18	460	1240	37	Flexure failed in 2020-12
2020-03	X2WM1005a	9 (X) 20 (Y)	560	530	38	Flexure crack suspected
2021-05	X2WM1004b	9	720	1030	40	Updated flexure not available
2021-05	Updated flexures received					
2021-05	X2WM1006	51	1320	590	44	CLBW per system requirements
2021-08	X2WM1003b	43	3500	1030	38	Installed updated flexure
2021-11	X2WM1005b	48	1340	500	39	Installed updated flexure. CLBW per system requirements.

The initial X2B drawings, used for X2WM1001 - X2WM1005, focused on maintaining mirror alignment and optimizing the magnet – coil gap to achieve high motor efficiency across the full range of motion. Actuator performance studies were run on the operational range of travel of the VCAs but did not consider the effect of tolerance stack up. The assembly process relied on complex tooling that proved to be impractical for bond control and produced inconsistency in gap size. For serial numbers X2WM1002a - X2WM1005a the magnet – coil gap resulted in contact between the adjacent magnets and coils. This limited the mechanism range of travel as a magnet face would contact a VCA coil before reaching the hard stop. Additionally, the contact threatened to scratch insulation from coil wires (see Figure 6).

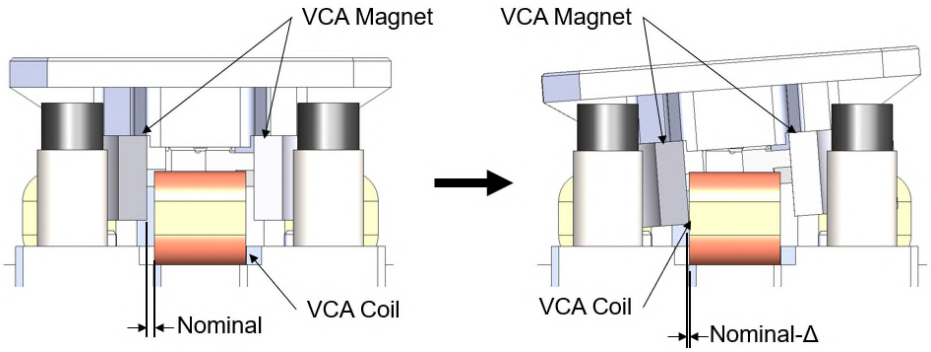

Figure 6. Actuator Gap Across Range of Motion

To investigate the required motor gap to meet performance, a parametric study was devised to analyze the actuator orientation in operation, distances from magnets to VCA coils, and the resultant implied moment on the system. Figure 7 shows the impact of the actuator gap on VCA performance. The nominal gap of 0.51 mm (0.02 in) shows peak performance with larger gaps showing degradation in performance.

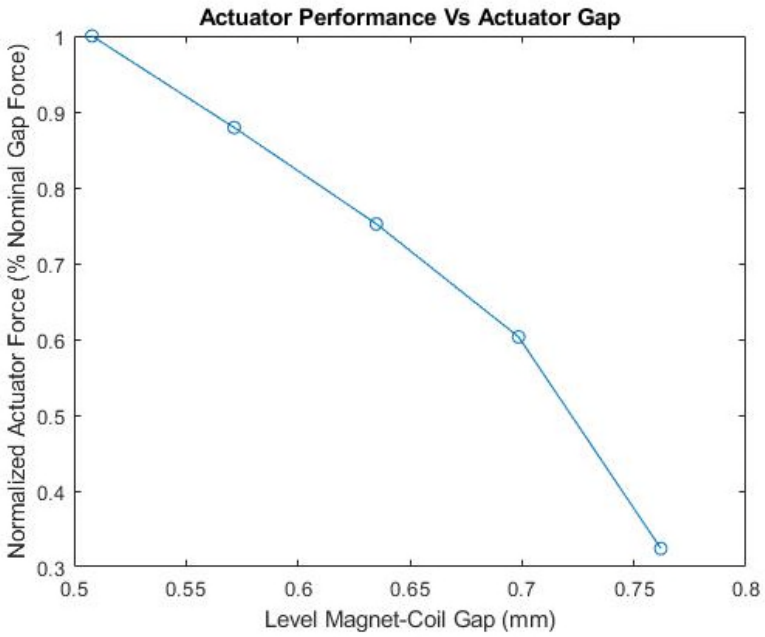

Figure 7. Actuator force vs. magnet-coil gap (mm)

A study of mirror motion found that the assembly required a minimum of 0.33 mm (0.013 in) of clearance between the coils and the magnets at the 0 deg tip and tilt position to allow for full rotation of the mirror. In addition, it was found the assembly could tolerate up to 0.64 mm (0.025 in) of VCA gap before VCA performance degraded to 75% of nominal. A nominal designed gap of 0.51 mm (0.020 in) was selected.

The design was revaluated through a tolerance analysis to assess how the required magnet – coil gap should be controlled. The mechanism is broken into two modular sub-assemblies: the Baseplate Assembly (BA) consisting of the Baseplate, VCA coils and DITs, and moving mirror assembly (MMA) consisting of the Mirror, Flexure and VCA magnets. The interface between these two sub-assemblies consists of a locating emboss and two screws. It was determined that if both the pattern of mirror magnets on the MMA and pattern of VCA coils on the BA were controlled during assembly, then the interface between the MMA and BA could be adjusted at final assembly to achieve the correct VCA gap size. The pattern of VCA coils is controlled by tight position tolerances on the pattern of slots the coils are bonded to in the baseplate. The mirror magnet pattern is controlled via bond tooling, which allows for the pattern to be measured and adjusted prior to bonding. At final assembly, the MMA can be adjusted rotationally relative to the BA until the desired gap size is achieved for all VCA gaps in the system. This is accomplished with simple go/no-go shim stock.

To improve tooling, a cross functional collaboration took place between engineers and technicians to validate a new procedure. Rapid prototyping was used to print mock-ups of new tooling designs, as well as an actual mechanism assembly. This allowed for quick feedback and design iteration to finalize new tooling and assembly procedures that met cost, reduced in touch-labor time, and increased repeatability for gap control.

Figure 8 shows one iteration of the magnet bonding tooling. Note the shims used to set each magnet gap. It is important to state that the magnets have a strong attraction. During the first brass board unit builds, it was observed that magnets shifted during the bond cure. To reduce this behavior, magnets are bonded sequentially and then secured in place by setscrews to restrict movement during cure. Figure 8 shows the final magnet bonding tooling and the magnets being secured in place by nylon tip set screws.

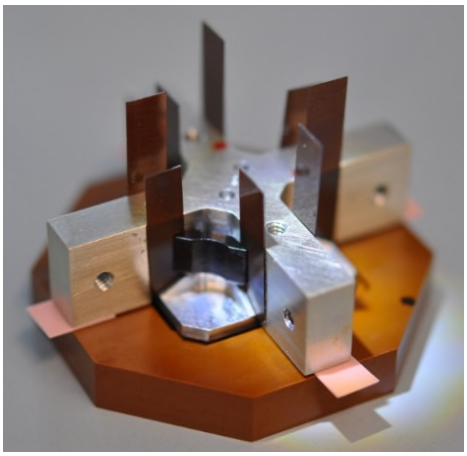

Figure 8. Magnet Bond Tooling

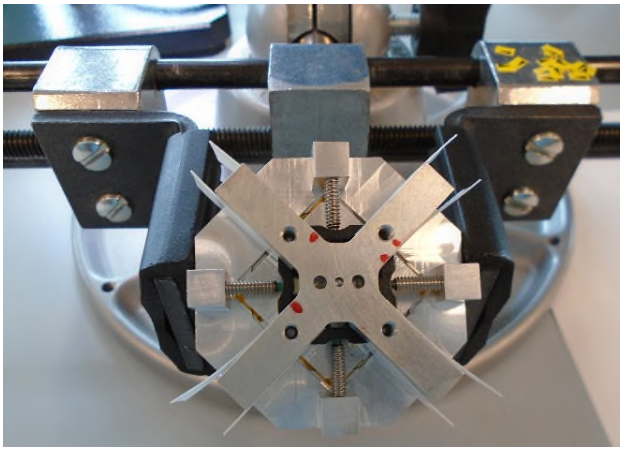

Figure 9. Magnet Bond during Cure

The initial X2B-WASMs also exhibited extremely fragile flexures with cross blades approximately one-third the thickness of a sheet of printer paper, 0.0381-mm (0.0015-in) thick. To assemble the flexure onto the mirror substrate, two fasteners are tightened in an alternating pattern, see Figure 10. Due to the flexure's susceptibility to damage, it is important to ensure that the flexure mounting pads are flat against the mirror substrate mounting pads before torquing the fasteners. There is limited visibility to confirm the flexure position after torquing the fasteners.

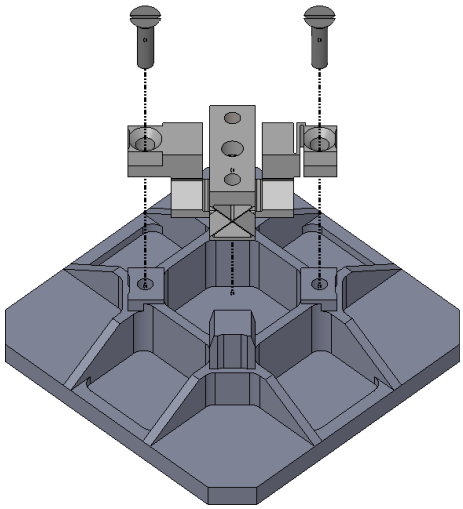

Figure 10. Mirror Substrate and Flexure Subassembly

If the flexure is not mounted with its pads flush to the mirror pads, the flexure is at an increased risk of breaking at the higher assembly. The MMA is pulled onto the baseplate assembly using two fasteners that thread onto the flexure through the baseplate, see Figure 11. Again, this operation has no visibility of the flexure to confirm the condition of the cross blades after assembly. It is during this assembly that a misaligned flexure's cross blades are at a greater risk of yielding due to the tension from threading a fastener into the flexure. The risk of flexure failure during assembly led to a design analysis of the flexure blade thickness to attempt to increase the structural integrity of the design.

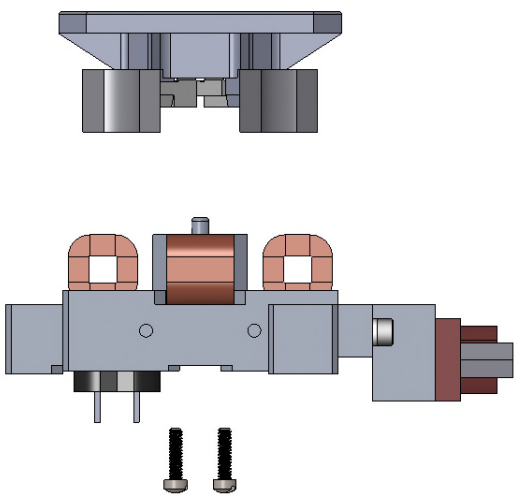

Figure 11. Moving Mirror Subassembly and Baseplate Assembly Integration

Due to the packaging constraints, 00-90 fasteners are necessary to attach the flexure to both the mirror and baseplate. The 00-90 fasteners represent a hurdle for procurement as they are non-standard fastener per ASME B18.3. Certified supply for these fasteners is not reliable. During assembly of serial numbers X2WM1002a - X2WM1005a, the original supplier discontinued their production of these fasteners. An order for certified 00-90 fasteners was placed with a new supplier for future flight builds. The brass board development units were completed with non-flight 00-90 fasteners that could be procured quickly and met the needs of the brass board test plan. These types of substitutions may not be palatable for flight programs. For future flight builds, ample procurement time is necessary to ensure the availability of flight rated hardware.

Flexure Design and Analysis

The titanium (TI-10V-2FE-3AL) cross flexure fits in a 15.2 mm (.598 in) X 88.9 mm (3.5 in) X 5.46 mm (.215 in) volume. The key parameters considered for the flexure design were first mode frequency of the MMA and the mechanism power consumption. The desired first mode frequency is 40-50Hz to achieve the 1-kHz bandwidth and the max angle power budget of 2 W. The flexure is manufactured by Electrical Discharge Machining (EDM) processing, followed by an etch bath for recast removal. To validate the process, the supplier provides a coupon that is used to examine surface finish, recast removal, and final cross blade thickness. The recommended minimum tolerance for wire EDM and recast removal is .005 mm (.0002 in).

The first mode frequency and power consumption of the mechanism are driven by the thickness of the cross blades. A thicker cross blade increases the blade stiffness, increasing the first mode frequency and power needed to hold the mirror at the maximum angle of travel. The initial design set the flexure blade thickness to 0.0483 mm (.0019 in) ± 0.0025mm (.0001 in), a thickness that proved to have reliability and manufacturability concerns. The design pushed beyond the limit of repeatable wire EDM and etching capabilities, and three flexures built in the first lot ended up being only 0.0381-mm (.0015-in) thick. With blades that thin, the mechanism assembly was unstable during calibration and vulnerable to damage during assembly and test. Once assembled, visual inspection is not possible to identify a damaged flexure; failure is identified during X2B-WASM calibration and testing. A damaged flexure often presents a lower first mode frequency, shifted mode frequencies at larger angles of travel, or a null pointing position offset at calibration.

Lab vibration testing was performed on two of the units. The mirror-flexure subassemblies sheared off the baseplate. The post-mortem inspection started the effort to enhance the design to improve reliability,

manufacturability, and minimize risk. It is believed that the flexures were damaged during assembly and buckled during testing.

The second-generation cross flexure aimed to improve the design by analyzing the optimal blade thickness to maintain the desired first mode frequency, meet power requirements and survive assembly, integration, and test. To find the optimal blade thickness to meet frequency and power requirements, a program was developed in MATLAB to relate first mode frequency and power consumption. To predict first mode frequency for a given blade thickness, a structural analysis was completed to determine an approximate first mode. The flexure blade thicknesses of 0.0381 mm (0.0015 in), 0.0483 mm (0.0023 in), 0.0635 mm (0.0025 in), and 0.0686 mm (0.0027 in), were selected for analysis. Figure 12 plots a linear curve fit of the predicted first mode frequency against flexure blade thicknesses.

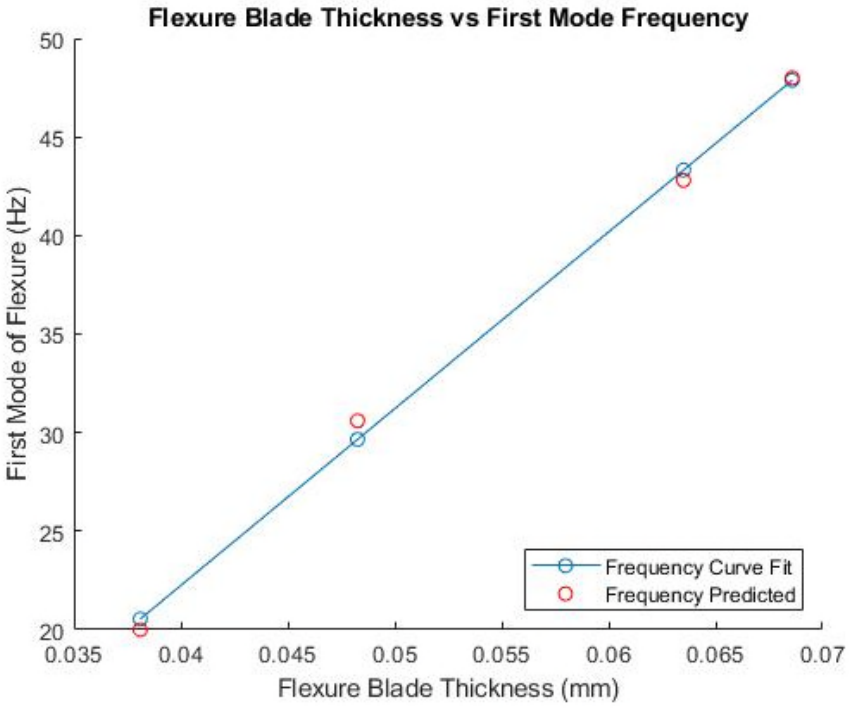

Figure 12. Flexure Blade Thickness (mm) vs First Mode Frequency (Hz)

To predict power consumption for a given blade thickness, the power consumed by the X2B-WASM serial numbers X2WM1003a, X2WM1004a, and X2WM1005a from Table 2 were interpolated to create a polynomial curve fit that could predict power consumed for a given blade thickness. To find the predicted power for the analyzed blade thicknesses, the first mode frequencies determined from the structural analysis are used to find the spring rate, and therefore holding current, needed to maintain the maximum angle of travel. The power is then calculated by multiplying the square of the holding current by the resistance of the four coils. Figure 13 plots the predicted first mode frequency against the predicted power needed for maximum angular travel for the selected flexure blade thicknesses. After running the MATLAB program, the flexure blade thickness 0.0635 mm (0.0025 in) had a predicted first mode frequency of 42.8 Hz and a max angle power consumption of 2.07W. This met the target for those two parameters. The predicted values can be compared to the actual measurements provided for X2WM1003b defined by Table 2 and Figure 17 for a percent error of roughly 12% for the first mode frequency and 18% for the power budget. Given the small sample size for analysis, it is not unexpected to have a percent error greater than 10%.

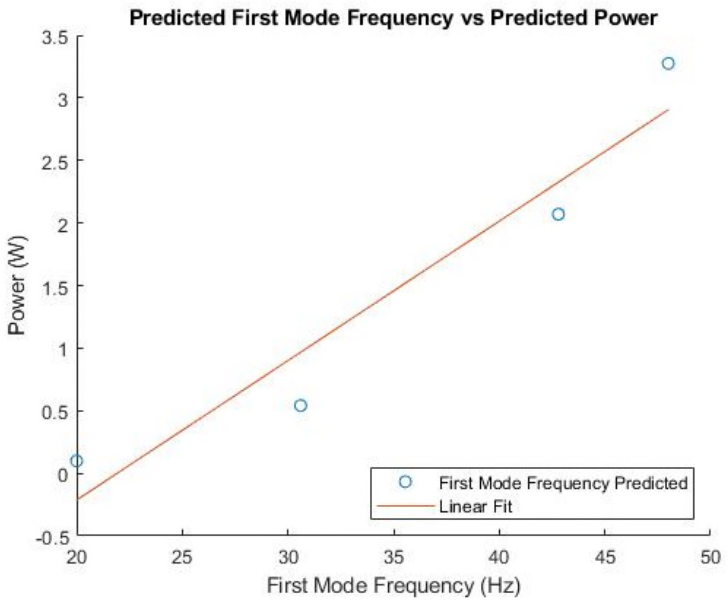

Figure 13. First Mode Frequency (Hz) vs Predicted Power (W)

After down selecting to the 0.0635-mm (0.0025-in) blade thickness, the performance for the 0.0635-mm (0.0025-in) and 0.0381-mm (0.015-in) flexures were evaluated in a simulated vibration environment. The flexures were analyzed at a random vibration of 0.44 g^2/Hz, shock at 672 G, and tilt of 3 deg to determine maximum stress along the flexure axis. Table 3 compares the analyzed stress on the flexures under the defined environments. It is expected to see a higher stress for the thicker flexure due to mirror tilt as the thicker flexure will be stiffer, making the blade less compliant to bending.

Table 3. Structural Analysis Margin of Safety Parameters

Flexure	Max Stress due to 1G Shock (along flexure axis)	Max Stress due to Random Vibe (All Axis)	Max Stress Due to Mirror Tilt (3 deg)
.0381 mm (.0015 in)	3.3 MPa (0.48 ksi)	141 MPa (20.5 ksi)	119 MPa (17.2 ksi)
.0635 mm (.0025 in)	2 MPa (0.29 ksi)	140 MPa (20.3 ksi)	197 MPa (28.6 ksi)

The analysis predicted the 0.063-mm (0.0025-in) thick flexure blade to have improved stress for random vibration and shock with buckling at 0.29 G^2/Hz (see Figure 14), which met the outlined mechanism performance. This flexure blade thickness also met the target first mode frequency and max angle power budget.

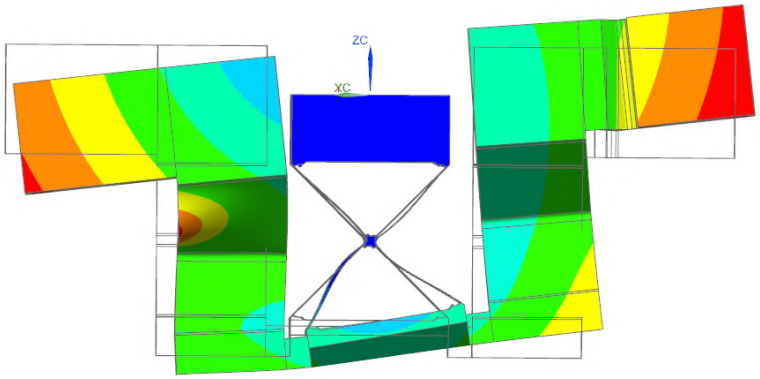

Figure 14. Flexure Blades Begin to Buckle at 0.29 G^2/Hz

Measured Performance

The X2B-WASM is designed to exceed 1-kHz bandwidth with good stability margins. The batch of flexures with blades made too thin had reduced performance because of vibration modes that change with mirror angle (see WASM serial numbers 1002, 1003a, 1004a and 1005a in Table 2). As each flexure failed during lab testing, they were replaced with correctly manufactured flexures (see WASMs with build dates after May 2021 in Table 2). The exception is serial number X2WM1001, which has the first prototype flexure that is slightly different than all the other steering mirrors in the table.

A primary limitation to closed loop bandwidth is the second vibration mode type and frequency. If the vibration mode is mechanically between the motors and sensors, the plant transfer function phase shift will be negative and is more likely to cause stability problems. If that mode frequency is too close to the desired open loop crossover, notch filters will not help, and the crossover (and bandwidth) will need to be reduced.

The X2B-WASM second vibration mode is more forgiving. The phase bump is very small, moves in a positive direction, and has frequency much higher than the open loop crossover (see 1200-Hz mode in bottom of Figure 15). The magnitude and frequency also have minimal change over mirror angle range. This means the high bandwidth (1030 Hz in Figure 15) is achievable without additional notch or low pass filters. Small signal bandwidth higher than 1200 Hz is possible by designing electronics and compensator to reduce the phase loss at frequencies above 1000 Hz, using a flexure with higher first mode frequency, and incorporating possible notch filters to attenuate and problematic vibration modes.

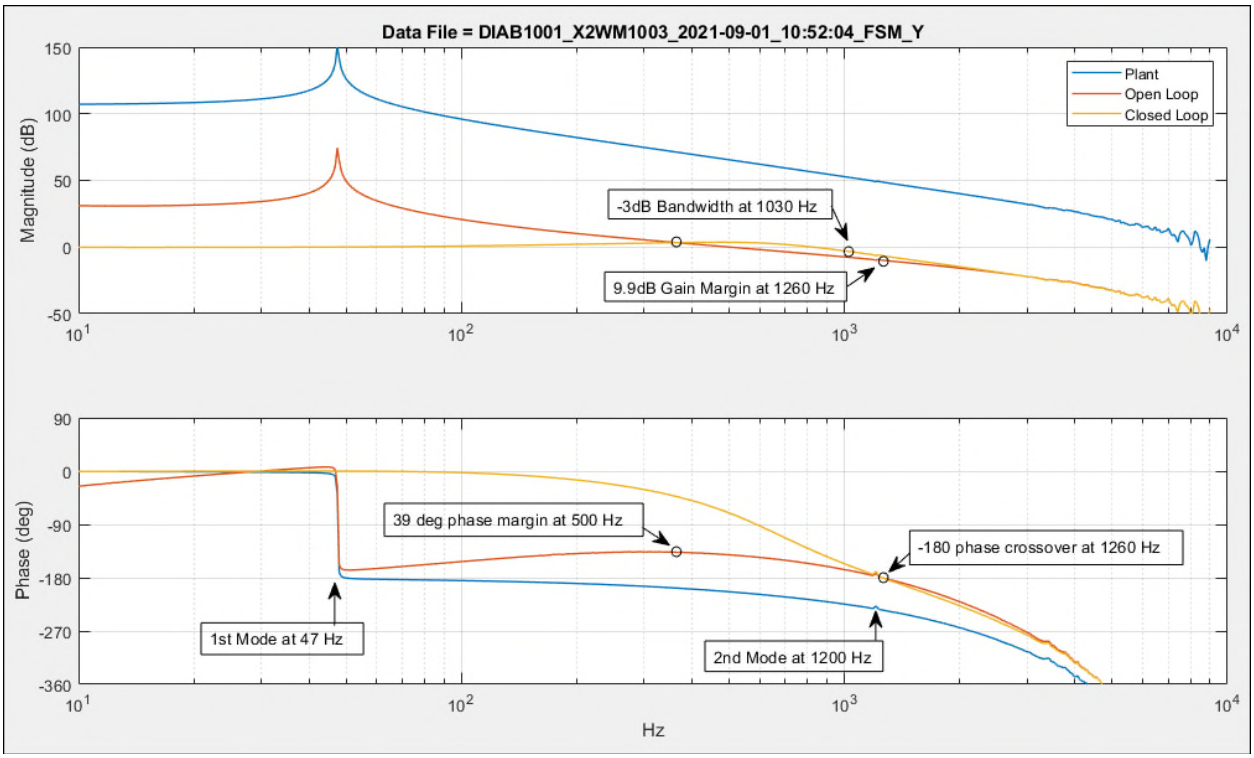

Figure 15. Transfer functions of X2WM1003 with updated flexure design

Figure 16 shows the measured estimate for residual jitter is 1 µrad RMS for serial number X2WM1003b. The jitter estimate starts with blocks of time series data that were recorded at 49 different mirror positions across the range of travel. The sample rate, and compensator update rate, was 20 kHz. A power spectral density (PSD) curve was calculated from each time series block. The top graph in Figure 16 is the mean of all the PSD curves and the bottom graph is the forward RMS sum curve. The forward sum at 10 kHz in Figure 16 is 1.8 µrad RMS and the largest of the 49 forward sum curves is 2.05 µrad RMS.

Previous comparison of steering mirror position data with mirror angle measured with a 3-axis interferometer revealed that mirror residual jitter can be approximated by integrating the PSD curve up to the mechanism closed loop bandwidth. That point is indicated by a red circle in the bottom curve of Figure 16 with coordinate values 1030 Hz and 1.0 µrad RMS.

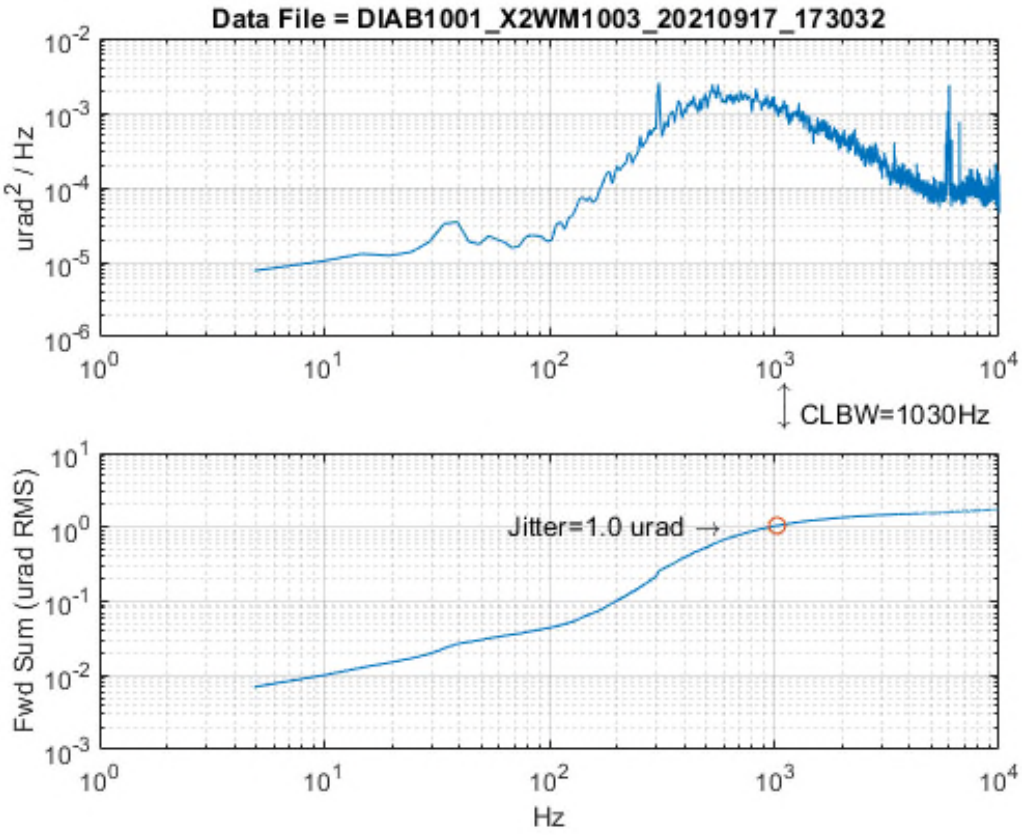

Figure 16. PSD curve (top graph) and forward RMS sum of mirror angle signal (bottom graph)

Figure 17 is a graph of motor power calculated from motor resistance and motor current data recorded during angle calibration of serial number X2WM1003b. This reflects the power to hold against the flexure spring constant. Mechanism power will be larger when rejecting base motion disturbance and performing continuous scan profiles.

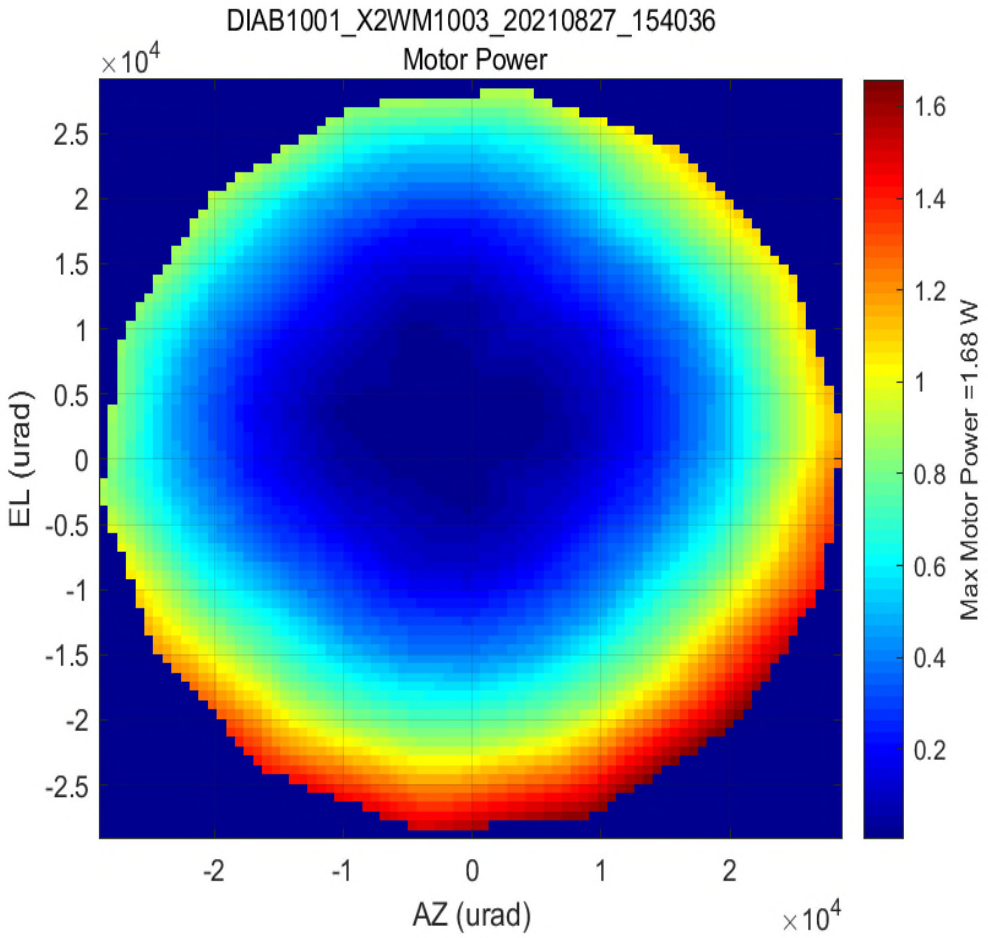

Figure 17. Motor power vs. angle for X2WM1003b

Conclusion

The compact Wide Angle Steering Mirror, X2B-WASM development presented many challenges during assembly, integration, and test. Assembly of the small mechanism required thoughtful tooling design to ease assembly, improve alignment, and maintain performance. In designing a miniature mechanism, one key takeaway is to focus on modularity of the system. Modularity allowed there to be more visibility during assembly of each piece part which led to simplified assembly processes, lower risk of piece part damage, and reduction of in-touch labor. Additionally, one must identify the gating manufacturing processes early in the design phase. The ideal design for performance may never be achievable due to manufacturing limitations. Failure of the key component, the two-axis cross flexure, due to manufacturability, required detailed analysis and test to converge on an optimal solution. Testing of the optimized development unit showed the mechanism capable of ±3 deg of rotation travel in two axes with 1.0-kHz closed loop bandwidth and residual jitter under 2 µrad RMS. The redesign efforts of the X2B-WASM resulted in a robust design that meets the desired performance parameters.

Advances in Bending Flat Plate Shape Memory Alloy Actuation Modeling: Prediction of Actuation Behavior

Michael Halvorson*, Jonathan Coleman**, Logan Williams**, Bryan Hardaker**, Frank Brown**, Noah Cargile**, Hayden Patteson** and Eric Bradshaw**

Abstract

A predictive model for the actuation of bent, flat nitinol plates was created with thermomechanical, kinematic, and constitutive relations; bent nitinol plates representing hinge actuators for deployable solar arrays with large moments of inertia were fabricated, shape trained, and actuation tested to evaluate performance against model behavior predictions. Model results were highly sensitive to nitinol residual stress and critical stress constant, parameters that may differ for fabricated nitinol specimens even within the same specimen batch, but model results were in excellent agreement with test results overall. The model assumed nitinol transitioned from fully detwinned martensite to austenite, and neither full detwinning nor a lack of nitinol rhombohedral or glass transition phases could be accurately determined by differential scanning calorimetry in the utilized specimens. Therefore, despite comparison of predictive model results to empirical test results, the model is considered to be neither verified nor validated; limited consideration is provided for test results. The predictive model is characterized fully.

Introduction

Shape Memory Alloys (SMA) such as nitinol are among the highest energy density actuators [1-2], with nitinol displaying controllable properties during use. Significant research has been performed to characterize the actuation of linear nitinol systems [3-6], but accurate prediction of flat plate SMA actuation under bending conditions has been limited in both scope and application [7-9]. A framework was developed to predict the bending actuation of flat plate nitinol SMA under non-standard geometric conditions yielding rise time of the actuating system. The framework includes a heat treatment procedure to prepare the material for actuation, a geometry-specific heat transfer model including phase change, conduction, convection, and radiation, a Finite Element Analysis (FEA) of mechanical bending stresses, and a kinematic model to simulate actuation across the bend region. This model is an improvement on the single-node bend framework presented in Halvorson et al. [10]. A single flat plate actuating to a deployed angle of 135° is shown in Figure 1, and the full test apparatus with three flat plates is shown in Figure 2.

Three flat nitinol plates were fabricated by water jet cutting and mounted to the test apparatus shown in Figure 2. Each SMA strip was 15-mm wide by 80-mm long by 0.5-mm thick with the bend line centering at 27-mm length. SMA material outside the minimum bending radius was for Patch Heater (PH) or bracket mounting purposes only. The plates were heat treated and shape trained to ensure desired deployment geometry. A HK6900 polyimide flexible PH from Minco was layered above and below with electrically insulating Kapton® film; the PH and Kapton assembly was tie-mounted to the SMA strip using heat-resistant Kevlar® thread. Both Kapton and Kevlar are registered products of DuPont; neither are shown on Figure 2. The SMA bend line was directly to the left of the PH in Figure 2; the PH was placed directly after the bend line to avoid stretching or compressing the PH during SMA acutation. The SMA was mounted via fasteners to a stationary base plate and rotating plate with controllable moment of inertia; the rotating plate was manually rotated into the non-deployed U-shape prior to actuation. Upon powering the PHs to heat the

* University of Alabama in Huntsville, Huntsville, AL; mch0043@uah.edu

** Auburn University, Auburn, AL

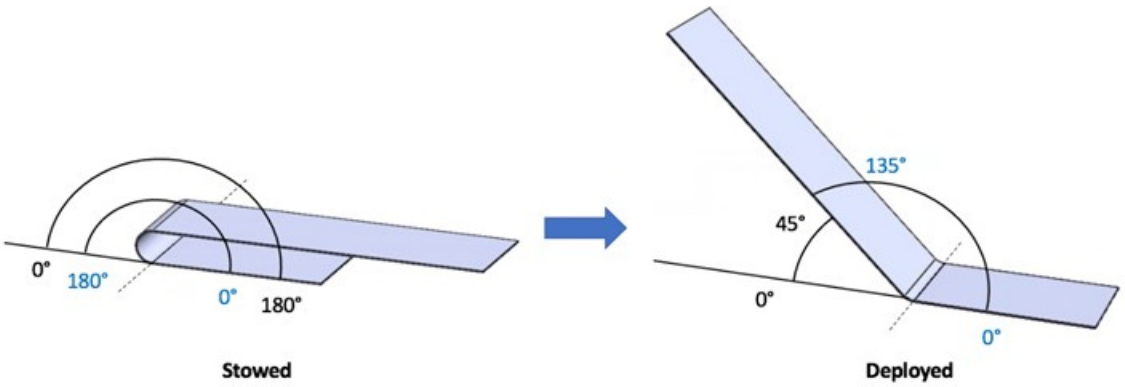

Figure 1. Single nitinol strip deploying to 135 ° representing a non-standard deployment geometry

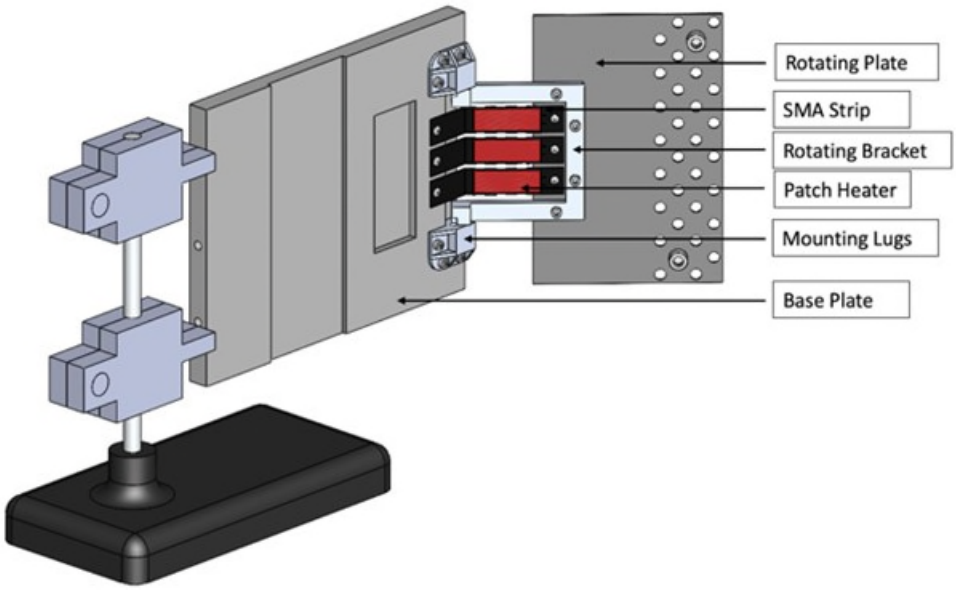

Figure 2. CAD representation of test apparatus

plates, the SMA experienced phase transformation resulting in bracket and plate rotation to the 135° deployment configuration. After full actuation, a locking pin in the mounting lugs secured the rotating hinge to a fixed position. SMA bend line temperature was measured during actuation using LabView and type K thermocouples attached laterally to the bend line via Kapton tape, and hinge rotation angle was measured using MATLAB's image processing toolbox and a downward-facing camera tracking a binary visual target on the top of the rotating plate. This actuation procedure was repeated ten times and compared to predictive model results; test results are not provided because compliance to the model's phase transition predicate, that pre-actuation nitinol phase is fully detwinned martensite without the presence of Rhombohedral phase (R-phase) or glass transition phase, could not be verified. This fully detwinned martensite phase preparation can be accomplished via SMA heat treatment resulting in twinned martensite and subsequent mechanical deformation of the SMA resulting in detwinned martensite at the bend line. While Differential Scanning Calorimetry (DSC) testing of the nitinol samples showed clear martensite-to-austenite phase transition, R-phase and glass transition phases were present. The presence of R-phase did not appear to affect actuation or actuation repeatability, but model verification by test is not assumed to be complete.

SMA Training

The SMA training and heat treatment profile ensures geometry-specific actuation fidelity and repeatability, though imprecise nitinol manufacturing techniques impart inconsistent phase characteristics to nitinol specimens even within the same batch of specimens. The authors observed phase inconsistencies in specimens from a variety of nitinol vendors and nickel contents; it is therefore imperative to DSC test all mechanism-utilized nitinol before heat treatment, after heat treatment, and after detwinning via mechanical deformation to ensure appropriate phases and phase transition temperatures exist for the intended operational environment and to determine martensite-to-austenite transition start, peak, and finish temperatures as inputs to the predictive model. All nitinol considered in the present work was 55.75% nickel by mass procured from Kellogg's Research Labs.

To set the desired actuation shape, a nitinol sheet was constrained in the 135° deployment configuration within an oven or furnace and subjected to high temperatures dependent on the SMA nickel content and actuator geometry. The furnace temperature was then ramped down to adjust the SMA transition temperatures, or the temperatures at which the SMA transitions from detwinned martensite to austenite and vice versa. There exist distinct temperatures for phase transition start, peak transition, and transition finish for each phase transition [4]. Immediately following furnace heat treatment, the sample was subjected to an ice water quench, a high thermal gradient, which causes the martensite-to-austenite transition temperatures and austenite-to-martensite transition temperatures to delineate, reducing phase overlap in the SMA. Once the nitinol has been quenched, it is in a twinned martensite phase that is unpredictable during actuation and easily fatigued, resulting in an actuator lacking repeatability or predictable actuation [11]. Detwinned martensite is an aligned and predictable form of the martensite phase; options for detwinning twinned martensite include manual or mechanical cold work and load frame tensile cycling. Bending the nitinol with any method will achieve partial detwinning, but localized twinned areas may present as opposed to fully detwinned martensite as detwinning occurs at the atomic lattice level. Performing X-Ray Diffraction on a detwinned sample would provide clarity on the level of detwinning after a deformation process. Consecutive tensile cycling, meaning programmed, cyclical loading and unloading on a load frame would be a rigorous, more repeatable detwinning process but requires a load frame and clamps specific to the geometry of the SMA to prevent slipping during tensile cycling operations. For the purposes of preliminary model validation, repetitive rotation of the SMA plates in the test apparatus, nominally 100 rotations, resulted in SMA that displayed slight sporadic behavior during acutation signifying pockets of twinned martensite but did not display actuation fatigue inherent to fully twinned martensite. Again, comparison of model results to test results are not presented here due to the model's phase predicate violation; an example DSC result is provided in Figure 3 characterizing the violation.

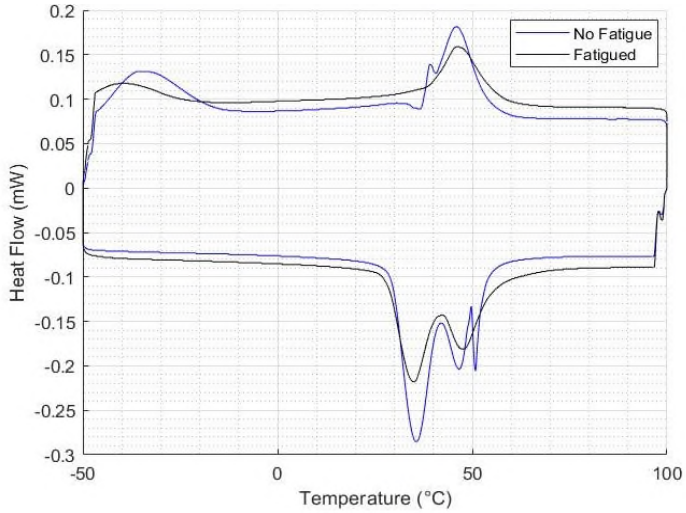

Figure 3. DSC results for a 55.75% nickel SMA sample treated at 550°C for 30 min, ramped down to 400°C at a rate of 5°C/min, and treated at 400°C for 15 min

The SMA in Figure 3 was secured in a mold and placed into a furnace at 550°C for 30 minutes. It was then ramped down to 400°C at a rate of 5°C/min. Once at 400°C, it was aged for 15 minutes. Lastly, both the SMA and mold were quenched in an ice water bath. SMA directly after ice quenching is labeled “No Fatigue”, signifying twinned martensite, and SMA after mechanical work in the test apparatus is labed as “Fatigued”, signifying partial to full martensite detwinning. Instead of smooth, single-peaked transitions from martensite to austenite (heating from bottom left to bottom right) and back (cooling from top right to top left), the phase transitions in this sample contained both R-phase and glass transition phases. The bottom left plateau is martensite, and both the bottom right and top right plateaus are austenite. During the heating phase transition in the non-fatigued martensite, multiple peaks and a “spike” pulse is visible, indicating multiple material phases. Multiple phases are seen in the cooling profile as well. The spike phase and multi-peak transitions smooth out after mechanical work to detwin the martensite, but determination of a clear martensite start, peak, and finish temperature was not possible with this specimen. The top left plateau is at least partially R-phase because another phase transition occurs near -40°C, presumably from R-phase to detwinned martensite. If the test specimen was transitioning from detwinned martensite to austenite upon heating and from austentie to a mix of martensite and R-phase upon cooling, the test could not be considered repeatable, and the predicate of the model is violated. While the model strongly correlates with physical principles and expected actuation behavior, training SMA to transition from only detwinned martensite to austenite at a specific temperature is non-trivial.

Methods exist to remove the spurious phases, though more testing is warranted on purchased specimens with consistent material properties. An increase in the initial furnace temperature leads to a shorter and less pronounced R-phase plateau [12]. In Halvorson et al [10], spike phases were postulated as effects of quenching in liquid nitrogen instead of an ice bath; this has been determined to be incorrect. Multiple DSC test iterations with an ice water quench resulted in spike phases occurring where R-phase is expected near the Austenite finish temperature. The evolution to R-phase to glass phase is poorly documented in literature. It is asserted that the spike phases are glass transition phases; glass phases can occur ranging from 12%-82% nickel by mass [13].

Predictive Actuation Model

The thermal, constitutive, and kinematic behavior of the SMA actuation process was modeled with a MATLAB simulation code divided into three elements: a heat transfer model, a thermo-mechanical model, and a kinematic model. SMA transient thermal response to PH operation in the bending region was determined using a quasi-3D, finite-difference heat transfer model with simulated conduction, convection, and radiation heat transfer effects corresponding to lab and PH input conditions. The thermo-mechanical model employed actuation criteria from Zhou, Yoon, and Leng [14]; the provided temperature distribution at each geometric node and time step was used to determine the transient stress and phase distribution per node. The kinematic model computed a motion-inducing stress relaxation from the thermo-mechanical model at each time step and used this relaxation to determine kinematic parameters such as warm-up time, rise time, and angular velocity. The combination of geometry-specific thermal response, thermo-mechanical stress, and kinematic motion fully characterizes the bending flat plate behavior during phase change.

Thermomechanical Model

The SMA geometric profile was first discretized into an array of rectangular elements called nodes. A single non-linear equation was written for each node using the First Law of Thermodynamics. Each equation was a function of location-specifc heat inflows and outflows present at the node as well as any property variations borne from changes in phase or geometric thickness. Thermal conductivity and specific heat were linearly phase-dependent for SMA and temperature-independent for Kapton, Kevlar, and PH material; radiative emissivity was a function of surface material and was assumed constant with respect to phase and temperature. The average convective heat transfer coefficient for a lab environment was calculated

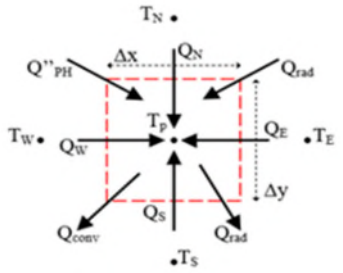

Figure 4. Internal SMA node containing material from patch heater, Kevlar, Kapton, and SMA

using the procedure in Awibi [15], and incident radiation from the walls and lights in a lab environment were modeled using the method outlined by Omori et al. [16]. It is possible to simulate a cold space environment by negating the convective heat transfer coefficient and the input environment radiation, taking the environment temperature to be 2.7 K to represent the Cosmic Microwave Background [17], and adjusting the initial condition to suit a colder space environment. The solution process for deriving the nodal equations begins with an energy balance. The example node in Figure 4 represents an internal node on the rotating section of the SMA flat plate with SMA, Kapton, Kevlar, and PH materials included. The generalized conservation of energy equation is defined in Eq. 1 without internal heat generation.

$$\frac{dE_{sys}}{dt} = \Sigma \dot{E}_{in} - \Sigma \dot{E}_{out} \tag{1}$$

Converting E energy values into Q heat values in Eq. 2, heat inputs were from nodal conduction, a constant heat flux from the PH Q''_{PH}, and radiation $Q''_{rad,in}$ when present. Heat outputs were from convection Q_{conv} and radiation $Q_{rad,out}$.

$$Q_{Transient} = \left[\Sigma Q_{cond,nodal} + \left(Q''_{rad,in} + Q''_{PH}\right) \cdot A\right]_{in} - \left(Q_{conv} + Q_{rad,out}\right)_{out} \tag{2}$$

Nodal areas A were divided into ΔX, ΔY, and ΔZ components representing discretized distances between nodes with only one node in the Z-direction, signifying a quasi-3D model. Conduction terms were replaced with Fourier's Law of Conduction whereas PH and incident radiation heat flux were left as generalized flux terms. The mounted sections of the SMA were assumed to be exposed to convection and radiation heat transfer on one side only. The thermal capacitance of combined Kapton, Kevlar, SMA, and PH material or any combination therein was found using a weighted average by material thickness; SMA specific heat included a term for latent specific energy of phase transformation L_{pc} multiplied by the change of phase per change in temperature $\frac{\partial \xi}{\partial T}$. This term was zero until phase change begins, non-zero during actuation, and zero upon phase change completion; it caused a plateau in the temperature field during phase change as expected. A breakdown of the terms comprising Eq. 2 is shown in Eqs. 3-6; the inputs $Q''_{rad,in}$ and Q''_{PH} were constants. Parameter k represents thermal conductivity, T temperature, ϵ emissivity, σ_{sbc} the Stefan-Boltzmann constant, h convective coefficient, ρ density, c specific heat, z thickness, and t time. Subscripts E, W, N, S represent node directionality with S being the stationary section direction in Figure 2 and N the rotating section direction. Subscript p represents the current node, and i represents the current timestep. The calculation of node-specific thermal conductivity k is geometry-dependent average weighted by thickness and is not provided. Convective coefficient h was constant for the top and bottom.

$$\sum Q_{cond,NB} = \Delta X \cdot \Delta Z \cdot \left(k_N \cdot \frac{T_N - T_{p,i}}{\Delta Y} + k_S \cdot \frac{T_S - T_{p,i}}{\Delta Y}\right) + \Delta Y \cdot \Delta Z \cdot \left(k_E \cdot \frac{T_E - T_{p,i}}{\Delta X} + k_W \cdot \frac{T_W - T_{p,i}}{\Delta X}\right) \tag{3}$$

$$Q_{rad,out} = \Delta X \cdot \Delta Y \cdot \left(\epsilon_{top} + \epsilon_{bottom}\right) \cdot \sigma_{sbc} \cdot \left(T_{p,i}^4 - T_{surr}^4\right) \tag{4}$$

$$Q_{conv} = \Delta X \cdot \Delta Y \cdot \left(h_{top} + h_{bottom}\right) \cdot \left(T_{p,i} - T_\infty\right) \tag{5}$$

$$Q_{Transient} = \Delta X \cdot \Delta Y \cdot \Delta Z \cdot \left[\frac{\rho_{PH} \cdot c_{PH} \cdot z_{PH}}{\Delta Z} + \frac{\rho_K \cdot c_K \cdot z_K}{\Delta Z} + \frac{\rho_{Kevlar} \cdot c_{Kevlar} \cdot 2 \cdot z_{Kevlar}}{\Delta Z} + \rho_{SMA} \cdot \frac{z_{SMA}}{\Delta Z} \cdot \left(c_{SMA} - L_{pc} \cdot \frac{\partial \xi}{\partial T}\right)\right] \cdot \frac{\left(T_{p,i} - T_{p,i-1}\right)}{\Delta t} \tag{6}$$

Eq. 2, when written in the form specified by Eqs. 3-6, is divided by the nodal volume $\Delta X \cdot \Delta Y \cdot \Delta Z$, and $T_{p,i}$ terms are collected on the Left-Hand Side (LHS). The remaining like terms are combined on the Right-Hand Side (RHS) to produce Eq. 7.

$$\left[\frac{C_{total}}{\Delta t}+\frac{k_N+k_S}{(\Delta Y)^2}+\frac{k_E+k_W}{(\Delta X)^2}\right]\cdot T_{p,i}=\frac{k_N\cdot T_N}{(\Delta Y)^2}+\frac{k_S\cdot T_S}{(\Delta Y)^2}+\frac{k_E\cdot T_E}{(\Delta X)^2}+\frac{k_W\cdot T_W}{(\Delta X)^2}+\frac{Q''_{rad}+Q''_{PH}}{\Delta Z}-\frac{(\epsilon_{top}+\epsilon_{bot})\cdot\sigma\cdot\left(T_{p,i}^4-T_{surr}^4\right)}{\Delta Z} \quad (7)$$

$$-\frac{(h_{top}+h_{bot})\cdot(T_{p,i}-T_\infty)}{\Delta Z}+C_{total}\cdot\frac{T_{p,i-1}}{\Delta t}$$

where the effective volumetric thermal capacitance C_{total} is given by,

$$C_{total}=\frac{\rho_{PH}\cdot c_{PH}\cdot z_{PH}}{\Delta Z}+\frac{\rho_K\cdot c_K\cdot z_K}{\Delta Z}+\frac{\rho_{Kevlar}\cdot c_{Kevlar}\cdot 2\cdot z_{Kevlar}}{\Delta Z}+\rho_{SMA}\cdot\frac{z_{SMA}}{\Delta Z}\cdot\left(c_{SMA}-L_{pc}\cdot\frac{\partial\xi}{\partial \mathrm{T}}\right) \quad (8)$$

In preparation for a Tri-Diagonal Matrix Algorithm (TDMA) solution, Eq. 7 may be written as Eq. 9,

$$a_P T_{p,i}=a_N T_N+a_S T_S+a_E T_E+a_W T_W+S \quad (9)$$

Where the coefficients a_N, a_S, a_E and a_W form the off-diagonal coefficients shown in Eq. 10.

$$a_N=\frac{k_N}{(\Delta Y)^2};\ a_S=\frac{k_S}{(\Delta Y)^2};\ a_E=\frac{k_E}{(\Delta X)^2};\ a_W=\frac{k_W}{(\Delta X)^2} \quad (10)$$

It can be shown that the diagonal coefficient a_P is the coefficient of $T_{P,i}$ in Eq. (7). The source term S is comprised of everything that remains after the off-diagonal coefficients are assigned. The nodes adjacent to a rivet were taken to be a Dirichlet constant temperature boundary condition; this was imposed by setting all off-diagonal coefficients at the node to zero, the diagonal coefficient to one, and the source term to the desired temperature. This ensured the solution process will arrive at the boundary temperature. The Neumann constant heat flux boundary conditions were imposed by setting the boundary-side, off-diagonal coefficient to zero and updating the volumetric thermal capacitance term to reflect the reduction in cross-sectional area. Deriving the nodal equations for all nodes yields a large, nearly tri-diagonal set of linear equations suited for a TDMA solution [18]. The inherent non-linearity associated with radiation heat transfer necessitates an iterative approach to ensure the simulation arrives at the correct temperature distribution. Thus, once a solution was obtained from the TDMA, the resulting temperature field was used to re-calculate the source term, and the TDMA was again applied. This process continued until the maximum change in the output temperature field fell below a pre-defined tolerance, ensuring that the resulting temperature field satisfied the heat conduction equation and thus an overall energy balance. Depending on the time step and spatial resolution selected, the system memory requirements of the above heat transfer model can become very large. For this reason, variables defined as a function of both space and time (and initialized as 3D matrices) were written as functions of space alone (2D matrices) and updated each time step. By saving only the needed time steps of these variables, the memory requirements of the heat transfer model were significantly reduced. Any efforts to parallelize the simulation should be focused on the finite-difference TDMA solver as the simulation spends substantial runtime in this section of the predictive model.

Constitutive Model

Three stresses are present in the SMA hinge actuator: stress due to thermal strain σ_{TH} induced by a temperature difference and dependent on the coefficient of thermal expansion α, stress due to pseudoelastic strain σ_{PE}, which is a function of residual strain ε_r and martensite phase fraction ξ, and stress due to mechanical bending σ_{MECH}, which is relaxed during phase transformation. $E(\xi)$ represents the modulus of Elasticity. Thermal and pseudoelastic stress are defined in Eq. 11 and Eq. 12, respectively.

$$\sigma_{TH}=E(\xi)\cdot\alpha\cdot(T-T_o) \quad (11)$$

$$\sigma_{PE}=E(\xi)\cdot\varepsilon_r\cdot\xi \quad (12)$$

Mechanical bending stress has historically been obtained for flat plate geometries by beam theories (such as Euler-Bernoulli beam theory) that typically assume small deflections [19]. Because bending stress calculations that do not violate the small-angle assumption for flat plate geometries are not readily available, mechanical stresses at discrete bending angles were simulated using FEA in Siemens NX. Ten simulations were conducted at angular increments of 15° between the 0° and 135° values depicted in Figure 2 to obtain a mechanical stress distribution that varies with bend angle and martensite phase fraction. For each bend angle, all phase-dependent solid properties were taken to be linear functions of martensite phase fraction,

which was assumed to vary linearly with the hinge bend angle, e.g., an angle of 45° was 33% austenite. The number of bending nodes required to represent the entire bending region is dependent on the material minimum bending radius MBR, the sma thickness z_{sma}, and the lengthwise grid resolution n_y used in the MATLAB heat transfer and kinematic models. This relationship is shown in MATLAB parlance in Eq. 13,

$$n_{bend} = floor\left(\frac{MBR \cdot \pi \cdot n_y}{z_{sma}}\right) + 1 \tag{13}$$

The bending region was divided into twelve nodes to characterize the actuation behavior of the system around the bend line. The "floor" function was employed to ensure the number of bending nodes remained an integer. All discrete bending nodes were evenly distributed above and below the pre-defined center bend line specific to the application geometry. For each finite element simulation, probes were placed at locations corresponding to the y-position of each of the twelve discrete bending nodes; the MATLAB simulation featured the same 12 nodes for the mechanical bending stress distribution and kinematic joints. With this configuration, each of the ten finite element simulations yielded a mechanical stress distribution represented by twelve mechanical stresses in a 10x12 matrix. The deployment angle, which the SMA was trained to deploy to, was considered to be zero mechanical stress at all locations; the maximum stress for a bend line node constrained in the initial U-shape was 806 MPa. Mechanical stresses are provided in the Appendix.

In the MATLAB simulation, the mechanical stress at each set of bend line nodes in the length direction was obtained via linear interpolation of the FEA mechanical stress distribution per the phase fraction found by the heat transfer model and averaged over the bend line. Due to the uneven martensite fraction distribution along the bending region width, the MATLAB simulation will not find a mechanical stress distribution that is identical to one found in the finite element simulation unless the phase fraction distribution is uniform at the bending region. Having obtained values for the mechanical, pseudoelastic, and thermal stresses, the total equivalent stress is calculated for each node using Eq. 14.

$$\sigma_{total} = \sigma_{MECH} + \sigma_{PE} + \sigma_{TH} \tag{14}$$

Using the temperature distribution obtained from the heat transfer model and the stress distribution calculated above, the martensite fraction was determined for each node at each time step. The martensite to austenite transition criteria are found in Eqs. 15-17 using the original nomenclature where A is temperature [14]. The austenite transition start A_s, peak A_p, and finishing temperature A_f were determined by DSC testing. Eqs. 18-20 characterize the transition from detwinned martensite to austenite.

$$\sigma_s^A = (T - A_s) \cdot C_A \tag{15}$$

$$\sigma_p^A = \left(T - A_p\right) \cdot C_A \tag{16}$$

$$\sigma_f^A = \left(T - A_f\right) \cdot C_A \tag{17}$$

$$s_{a1} = \frac{\pi}{2 \cdot \left(\sigma_p^A - \sigma_s^A\right)} \tag{18}$$

$$s_{a2} = \frac{\pi}{2 \cdot \left(\sigma_f^A - \sigma_p^A\right)} \tag{19}$$

$$\xi_s = \begin{cases} \xi_{s0} \cdot \left\{\frac{s_{a2}}{s_{a1}+s_{a2}} \cdot \cos[s_{a1} \cdot (\sigma_{tot} - \sigma_s^A)] + \frac{s_{a1}}{s_{a1}+s_{a2}}\right\} & for\ \sigma_p^A \le \sigma_{tot} \le \sigma_s^A \\ \xi_{s0} \cdot \left\{-\frac{s_{a1}}{s_{a1}+s_{a2}} \cdot \sin\left[s_{a2} \cdot \left(\sigma_{tot} - \sigma_p^A\right)\right] + \frac{s_{a1}}{s_{a1}+s_{a2}}\right\} & for\ \sigma_f^A \le \sigma_{tot} \le \sigma_p^A \end{cases} \tag{20}$$

Kinematic Model

The equation of motion describing the actuation dynamics of a flat plate SMA geometry is defined in Eq. 21 as a function of mass moment of inertia I_{tot}, stiffness coefficient K, and kinematic torque τ_{bend}. The motion of the system is independent of the angular velocity at each bending node. While the gravitational body force was neglected in the kinematic formulation due to the orientation of the testing apparatus, it could be

incorporated in the kinematic model by adding the cross product of the gravitational force vector and the vector extending from the bending region to the system center of mass to the equation RHS. The stiffness and torque change in response to a change in martensite fraction; this produces a smooth actuation without the oscillation pattern that is normally expected from an Ordinary Differential Equation (ODE) of this form.

$$I_{tot} \cdot \ddot{\theta} + K \cdot \Delta\theta = \tau_{bend} \tag{21}$$

The coefficient I_{tot} represents the mass moment of inertia of the rotating portion of the system and was obtained via the parallel-axis theorem to calculate the inertia of each system component about the rotation axis. The system response time is a strong function of inertia; care should be taken to ensure it is calculated accurately. The stiffness coefficient K is calculated by Eq. 22, where $E(\xi)$ is Young's Modulus as a function of martensite fraction averaged across the bend line, J is the area moment of inertia of the SMA cross-section, and L_{bend} is the length from the center of the bending region to the top edge of the SMA [20]. The $\Delta\theta$ in the stiffness term represents the angular deflection of the bending node from its standard equilibrium point, which was taken to be the angle state at the previous time step to prevent the stiffness term from being non-zero when the torque is zero.

$$K = \frac{E(\xi) \cdot J}{L_{bend}} \tag{22}$$

The input torque τ_{bend} drives the motion of the system and is calculated by Eq. 23. The parameters A_C and z_{SMA} represent the SMA cross-sectional area and thickness, respectively.

$$\tau_{bend} = \sigma_{PH} \cdot A_c \cdot z_{SMA} \tag{23}$$

The phase relaxation stress σ_{PH} can be calculated using one of two variations; without formal model verification by test it is unclear which is correct. Eq. 24 characterizes the relaxation stress as a function of both mechanical (bending) stress and pseudoelastic stress, while Eq. 25 shows the relaxation stress as a function of mechanical stress alone. Either approach could be valid and the distinction between the two is a major point of investigation. The desired relaxation stress behavior (zero→non-zero→zero) occurs regardless of the form of the relaxation stress. Thermal stress was neglected in the calculation of the relaxation stress due to its small magnitude relative to the other stress modes present in the system.

$$\sigma_{PH} = \frac{d\sigma_{MECH}}{dt} \cdot \Delta t + \frac{d\sigma_{PE}}{dt} \cdot \Delta t \tag{24}$$

$$\sigma_{PH} = \frac{d\sigma_{MECH}}{dt} \cdot \Delta t \tag{25}$$

At each time step, all phase-dependent properties and stresses were averaged across each discrete bending node. Eq. 21 was then evaluated at each bending node using the implicit Backward Euler method to determine the angle state and angular velocity for the time step. The Backward Euler method was selected for this application due to its lack of reliance on the previous angle state, which is needed to model the stiffness term in Eq. 21 accurately. An effect of the form of the ODE shown in Eq. 21 is that the system will not halt motion once phase change has completed. It is necessary to set individual angular displacements and angular velocities to zero once they reach the trained angle state.

Predictive Actuation Results and Model Sensitivity

The parameters employed for the reference case study are summarized in the Appendix. The predictive model was run with varied inputs against a reference case; the results were compared to the reference study to determine the sensitivity of the system to the input parameters. Additionally, the model was run with and without the influence of pseudoelastic stress in the torque calculation and in the phase fraction comparison to determine the effect of these parameters on the actuation dynamics of the system. The results of the sensitivity study indicate that the patch heater power, critical stress constant C_A, mass moment of inertia, and the maximum residual strain have the greatest impact on the dynamic response of the system. A change in any of these variables yielded a comparatively large change in the warm-up time and rise times of the system. Tables 1-4 show the influence of these variables in determining the system rise times. All other parameters adhere to reference case parameters provided in the Appendix.

Table 1. Effect of patch heater power on system rise times

Patch Heater Power, [% of Total]	Warm-Up Time, [s]	10% Rise Time, [s]	90% Rise Time, [s]
75%	40	60	90
100%	27	46	66
150%	15	33	51
200%	11	28	45

Table 2. Effect of critical stress constant on system rise times

C_A, [MPa/K]	Warm-Up Time, [s]	10% Rise Time, [s]	90% Rise Time, [s]
9.85	Did not actuate – required temperature too high		
35	27	35	27
50	23	50	23
100	19	100	19

Table 3. Effect of mass moment of inertia on system rise times

Mass Moment of Inertia, [kg-m^2]	Warm-Up Time, [s]	10% Rise Time, [s]	90% Rise Time, [s]
4.72·10-4	27	31	50
5.60·10-4	27	31	50
6.64·10-4	27	46	66
6.96·10-4	27	93	145

Table 4. Effect of residual strain on system rise times

Residual Strain, [%]	Warm-Up Time, [s]	10% Rise Time, [s]	90% Rise Time, [s]
1.0%	27	46	66
3.0%	37	54	77
5.0%	49	66	94
6.7%	Did not actuate – required temperature too high		

Table 5 shows the effect of residual stress on the actuation behavior of the system. The increase in equivalent stress brought on by residual stress allows the relaxation stress induced by phase change to be much larger. Thus, systems including residual stress tend to actuate faster than those without .

Table 5. Effect of pseudoelastic stress inclusion to relaxation stress on system rise times

	Warm-Up Time, [s]	10% Rise Time, [s]	90% Rise Time, [s]
Pseudoelastic Stress	28.0	46.0	66.0
No Pseudoelastic Stress	28.0	59.0	88.5

Figure 5 shows the temperature and martensite fraction contours at 45 seconds and after the system has reached steady state. It is clear the thermal behavior of the hinge does not limit the size of the bending region in any way, as the system achieves the required actuation in the entire bend line at steady state. It can be observed from the martensite fraction contours in Figure 5 that phase change at the bending region does not occur uniformly but from the outside in; the stress required to achieve phase change is larger in the center of the bending region than in the sides. Since the center of the bending region has a higher "critical stress" σ_{tot} than the rest of the bending region, it requires a higher temperature to actuate; nodes do not actuate in order of proximity to the patch heater.

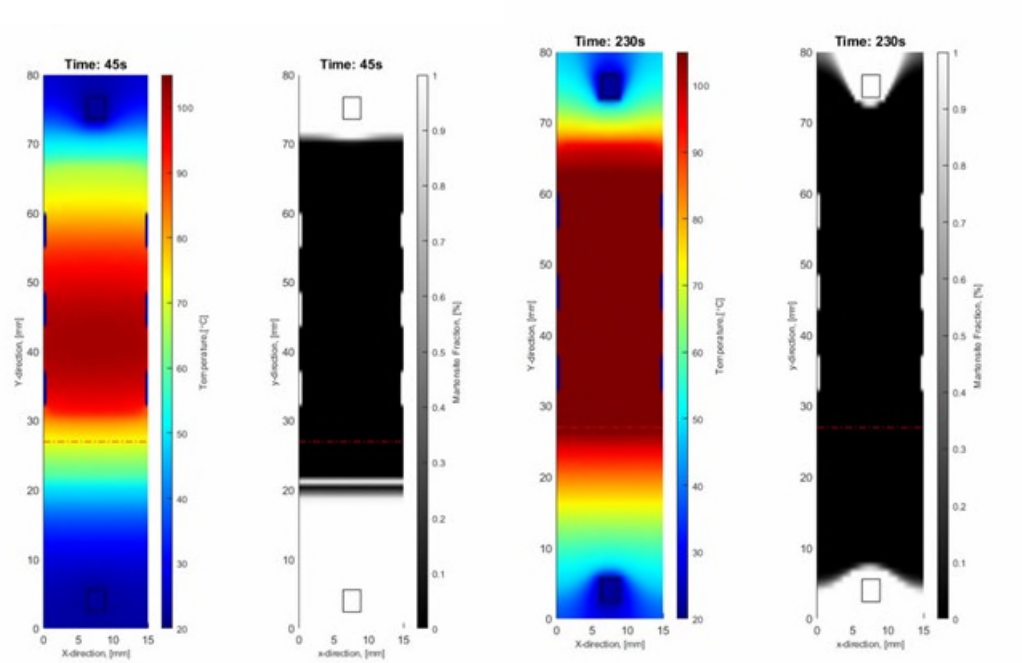

Figure 5. (left) Temperature and phase distributions at 45 s actuation time, (right) Temperature and phase distributions at steady state. The central bend line is shown dotted in red.

Figure 6 shows the kinematic behavior of each discrete bending node as well as the composite bend angle. Each bending node exhibits roughly uniform behavior, but actuation order is dependent on nodal σ_{tot}. This results in a system actuation profile where behavior near the trained deployment angle is greatly dependent on the stress distribution of the hinge. A maximum stress at a node that is much greater than stresses of neighboring nodes will result in additional time needed for bending actuation. This behavior can be mitigated with an increase in the critical stress constant C_A or a decrease in maximum residual stress.

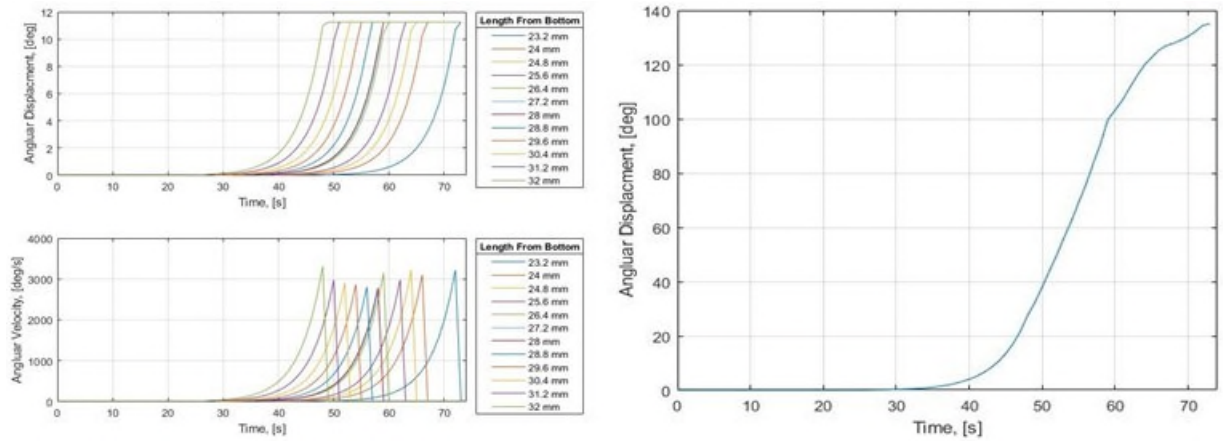

Figure 6: Discrete bend angles (top left), discrete angular velocities (bottom left), and total bend angle (right) vs. time

As is true of all material phase changes, thermal energy can be converted into phase change energy if energy requirements are met. Figure 7 depicts the full actuation of the system until the hinge geometry reached steady state. Evident is the temperature plateau indicating phase change energy conversion.

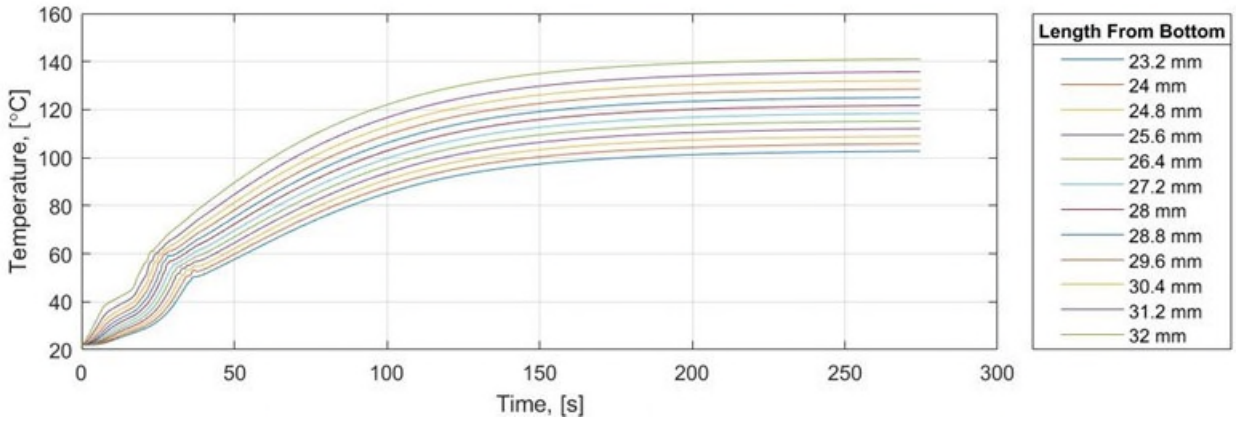

Figure 7: Temperature per node as a function of time until steady-state is reached

Conclusions

The actuation of flat plate SMA that is shape trained into a non-standard deployment geometry, heat treated to twinned martensite phase, and mechanically worked to detwinned martensite phase can be modeled using thermomechanical, constitutive, and kinematic relations yielding valuable mechanism considerations such as rise time. While the shape training aspect of heat treatment is achieved simply by constraining the plate in the intended deployment geometry using a mold, any thermal recipe to convert untrained SMA into detwinned martensite SMA must be specific to both the SMA manufacturing process and pre-treatment DSC results due to the presence of material phases other than martensite and austenite. Model verification by test was performed for the considered model, but the model predicate of phase transition from solely detwinned martensite to austenite could not be verified by DSC test in the SMA actuation test specimens due to the persistent presence of R-phase and glass transition phases. Test results, while informally in good agreement with model results, were therefore not included in this work for comparison to predictive model results; the model is considered unverified and unvalidated yet scientifically rigorous.

Residual stress is included in the equivalent stress actuation criteria via the pseudoelastic stress term, but it is unclear if torque-inducing relaxation stress should be a function of pseudoelastic stress without formal verification by test. Including residual stress in the stress relaxation term decreases actuation rise time because the hinge torque increases. However, if too much residual stress exists in the SMA after heat treatment, the system will not actuate because the critical stress criteria is not met to initiate actuation even if the SMA is above its actuation temperatures. Rise times are also heavily dependent on critical stress constant, which is a change in internal unit stress per change in unit temperature and has wide disparity in reported values. Critical stress constant determination may vary per SMA manufacturer and may require manufacturer input.

Prediction of kinematic parameters such as rise time was enabled by high-fidelity thermal modeling using geometry-specific nodal energy balances and TDMA solution methodologies. While nodal temperatures increased over time with controlled heat input from the mounted patch heater and expectedly plateaued as phase change occurred at each node, an unexpected yet legitimate discovery was that the plate changed phase from the outside-in on the non-rotating section of the SMA due to mechanical bending stresses present at that near-bend line location. Away from the bend line, the SMA actuated as the nodal temperature exceeded the actuation temperature. Near the bend line, the mechanical stresses prevented actuation until the nodal temperature exceeded the actuation temperature inversely proportionate to the value of the critical stress constant. If the critical stress constant is low, the bend line temperatures must greatly exceed actuation temperatures for the system to actuate, sometimes unrealistically so. If this scenario is unavoidable in a given geometry, it is possible to accommodate for a low critical stress constant by heat treating the SMA during shape training to lower actuation temperatures.

Acknowledgements

The authors would like to thank the Alabama Space Grant Consortium for its continued support in all aspects of workforce development in the commercial space sector. Dr. L. Dale Thomas is thanked for his direction and leadership of the consortium and the Complex Systems Integration Lab at the University of Alabama in Huntsville. Dr. David Beale is thanked for championing shape memory alloy research in the state of Alabama.

References

[1] Eschen, K., Granberry, R., & Abel, J. (2020). Guidelines on the design, characterization, and operation of shape memory alloy knitted actuators. Smart Materials and Structures, 29(3), 035036.

[2] Reynaerts, D., & Brussel, H. V. (1997, December 22). Design aspects of shape memory actuators. Mechatronics, 8(6), 635-656. doi:10.1016/s0957-4158(98)00023-3

[3] Mohd Jani, J., Leary, M., & Subic, A. (2017). Designing shape memory alloy linear actuators: A review. Journal of Intelligent Material Systems and Structures, 28(13), 1699-1718.

[4] Zhou, B., Liu, Y., & Leng, J. (2010). A macro-mechanical constitutive model for shape memory polymer. Science China Physics, Mechanics and Astronomy, 53 (12), 2266-2273. doi:10.1007/s11433-010-4163-2

[5] Jayender, J., Patel, R., Nikumb, S., & Ostojic, M. (2008). Modeling and Control of Shape Memory Alloy Actuators. IEEE Transactions on Control Systems Technology, 16(2), 279-287. doi:10.1109/tcst.2007.903391

[6] Brinson, L. (1993, April). One-Dimensional Constitutive Behavior of Shape Memory Alloys: Thermomechanical Derivation with Non-Constant Material Functions and Redefined Martensite Internal Variable. Journal of Intelligent Material Systems and Structures, 4(2), 229-242. doi:10.1177/1045389x9300400213

[7] Stroud, H., & Hartl, D. J. (2020). Shape memory alloy torsional actuators: a review of applications, experimental investigations, modeling, and design. *Smart Materials and Structures*. 5-7

[8] Soother, D. K., Daudpoto, J., & Chowdhry, B. S. (2020). Challenges for practical applications of shape memory alloy actuators. *Materials Research Express*, 7(7), 073001.

[9] Mertmann, M., & Vergani, G. (2008). Design and application of shape memory actuators. *The European Physical Journal Special Topics*, 158(1), 221-230.

[10] Halvorson, Michael c., et al. “A Bending Flat Plate Shape Memory Alloy Model for CubeSat Solar Array Deployment with Thermomechanical, Constitutive, and Kinematic Relations.” *AIAA Scitech 2021 Forum*, 2021, doi:10.2514/6.2021-1792.

[11] Sreekumar, M., et al. “A Compliant Miniature Parallel Manipulator with Shape Memory Alloy Actuators.” *2006 IEEE International Conference on Industrial Technology*, 2006, doi:10.1109/icit.2006.372370.

[12] Duerig, T.W. “Some Unsolved Aspects of Nitinol.” *Materials Science and Engineering: A*, vol. 438-440, 2006, pp. 69–74., doi:10.1016/j.msea.2006.05.072.

[13] Aliaga, L.C.R., et al. “Selection of Good Glass Former Compositions in Ni–Ti System Using a Combination of Topological Instability and Thermodynamic Criteria.” *Journal of Non-Crystalline Solids*, vol. 354, no. 17, 2008, pp. 1932–1935., doi:10.1016/j.jnoncrysol.2007.10.018.

[14] Zhou, Bo, Sung-Ho Yoon, and Jin-Song Leng. "A three-dimensional constitutive model for shape memory alloy." *Smart Materials and Structures* 18.9 (2009): 095016.

[15] Awbi , H. B., “Calculation of convective heat transfer coefficients of room surfaces for natural convection,” Energy and Buildings, vol. 28, 1998, pp. 219–227.

[16] Omori, T., Taniguchi, H., & Kudo, K. (1990). Monte Carlo simulation of indoor radiant environment. International Journal for Numerical Methods in Engineering, 30(4), 615-627. doi:10.1002/nme.1620300405

[17] Fixsen, D. J. (2009). THE TEMPERATURE OF THE COSMIC MICROWAVE BACKGROUND. *The Astrophysical Journal*, *707*(2). https://doi.org/https://doi.org/10.1088/0004-637X/707/2/916

[18] Versteeg, H. K., & Malalasekera, W. (2011). Solution of discretised equations. In *An Introduction to Computational Fluid Dynamics: The Finite Volume Method* (2nd ed., pp. 212–242). essay, Prentice Hall.

[19] Ugural, A. C., & Fenster, S. K. (2020). Bending of Beams. In *Advanced Mechanics of Materials and Applied Elasticity* (6th ed., pp. 242–300). essay, Pearson.

[20] Crews, J. H., & Smith, R. C. (2013). Quantification of parameter and model uncertainty for shape memory alloy bending actuators.*Journal of Intelligent Material Systems and Structures*,25(2), 229-245. doi:10.1177/1045389x13490842

Appendix

Table 6: Mechanical bending stresses at each node along the bend line as a function of node location and coupled bend angle and martensite fraction

ξ_{Def}	σ_M (MPa)	σ_M (MPa)	σ_M (MPa)	σ_M (MPa)	σ_M (MPa)	σ_M (MPa)	σ_M (MPa)	σ_M (MPa)	σ_M (MPa)	σ_M (MPa)	σ_M (MPa)	σ_M (MPa)	Θ (°)
0	0	0	0	0	0	0	0	0	0	0	0	0	45
0.11	39	57	74	82	90	111	116	125	120	117	109	89	60
0.22	55	78	92	118	129	137	158	166	159	150	131	108	75
0.33	86	112	152	188	199	204	207	208	204	196	172	151	90
0.44	102	140	173	197	204	226	238	249	246	237	214	181	105
0.56	199	246	270	301	309	322	330	332	329	321	304	298	120
0.67	208	265	277	311	358	369	374	415	397	380	371	345	135
0.78	239	287	335	368	436	526	574	586	572	567	553	526	150
0.89	281	318	333	382	428	529	574	619	596	578	567	560	165
1	307	319	327	393	426	532	755	806	802	799	796	781	180
Y (mm)	22.29	23.07	23.86	24.64	25.43	26.45	27.00	27.79	28.57	29.36	30.14	32.00	

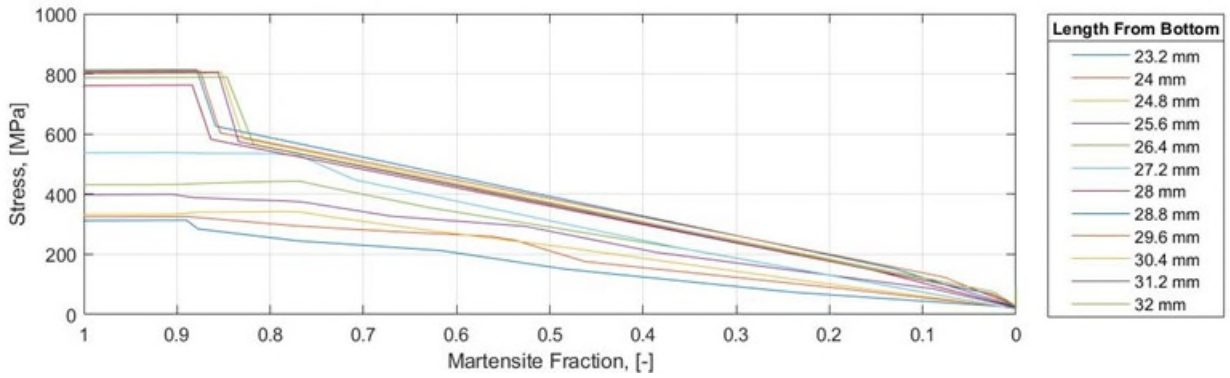

Figure 8: Discrete mechanical bending stresses as a function of martensite fraction

Table 7: Model inputs used as the reference case. Subscript M indicates martensite; subscript A indicates austenite.

Parameter	Value	Unit	Description
n_x	101	node	Number of nodes in the x-direction
n_y	101	node	Number of nodes in the y-direction
ΔX	1.5e-4	m	Nodal dimension in the x-direction
ΔY	8.0e-4	m	Nodal dimension in the y-direction
ΔZ	Variable	m	Nodal dimension in the z-direction
Δt	1	s	Discrete time step
E_M	28	GPa	Elastic modulus of martensitic nitinol
E_A	75	GPa	Elastic modulus of austenitic nitinol
α_M	6.6e-6	1/K	Coefficient of thermal expansion of martensitic nitinol
α_A	11e-6	1/K	Coefficient of thermal expansion of austenitic nitinol
ρ_{SMA}	6,500	kg/m^3	Density of nitinol
ρ_{PH}	2,329	kg/m^3	Density of patch heater
ρ_{kapton}	1,420	kg/m^3	Density of Kapton
ρ_{kevlar}	1,000	kg/m^3	Density of Kevlar
z_{SMA}	0.5e-3	m	Thickness of nitinol
z_{PH}	0.4e-3	m	Thickness of patch heater
z_{kapton}	0.2e-3	m	Thickness of Kapton
z_{kevlar}	0.1e-3	m	Thickness of Kevlar
k_M	8.6	W/m·K	Thermal conductivity of martensitic nitinol
k_A	18	W/m·K	Thermal conductivity of austenitic nitinol
k_{PH}	68.8	W/m·K	Thermal conductivity of patch heater
k_{kapton}	0.12	W/m·K	Thermal conductivity of Kapton
k_{kevlar}	0.04	W/m·K	Thermal conductivity of Kevlar
$C_{p,M}$	451	J/kg·K	Specific heat capacity of martensitic nitinol
$C_{p,A}$	500	J/kg·K	Specific heat capacity of austenitic nitinol
$C_{p,PH}$	710	J/kg·K	Specific heat capacity of patch heater
$C_{p,kapton}$	1,090	J/kg·K	Specific heat capacity of Kapton
$C_{p,kevlar}$	1,420	J/kg·K	Specific heat capacity of Kevlar
$Q''_{rad,in}$	7	W/m^2	Environmental incident radiative heat flux
Q''_{PH}	11,400	W/m^2	Patch heater conductive heat flux
ε_{SMA}	0.2	-	Emissivity of nitinol
ε_{kapton}	0.72		Emissivity of Kapton
h	8	W/m^2·K	Environmental convective coefficient
T_∞	295	K	Ambient temperature
L_{pc}	20,652	J/kg	Latent specific energy for martensite-to-austenite phase change
A_s	318.15	K	Austenite transition start temperature
A_p	320.65	K	Austenite transition peak temperature
A_f	323.15	K	Austenite transition finish temperature
C_A	35	MPa/K	SMA critical stress constant
ε_r	1.0	%	Residual strain
I_{tot}	6.64e-4	Kg·m^2	Mass moment of inertia of the rotating matter
J	1.56e-13	m^4	Area moment of inertia in the SMA cross-section
A_c	7.5e-6	m^2	SMA cross-sectional area
L_{bend}	0.048	m	Length from the center of the bending region to the top edge of the SMA

Cost Efficient Space Micro-Switches Based on Contactless Eddy Current Sensors

Gérald Aigouy*, Sylvain Duc*, Mathieu Castruccio*, Aurore Loubet *, Olivier Sosnicki *
and Frank Claeyssen*

Abstract

Micro-switches are frequently used in space mechanisms to provide telemetry or to provide positive indication of the achievement of a desired position or function such as open, close, ready-to-latch, latched, end of travel, reference position, and for different mechanism applications.

Current switches that rely on electro-mechanical technology are not very reliable and are sensitive to mounting orientation, to thermal gradients, and have a limited number of operational cycles, which is a problem for long life application, launch vibrations and shock loads.

Micro-switches relying on contact, as well as relay reeds, provide additional resistive torque that has to be overcome by the mechanism actuator, having a negative impact on the motorization margins.

In this paper, CEDRAT TECHNOLOGIES presents the design and tests results of contactless micro-switch devices, based on Eddy Current Sensors (ECS) technology, and with embedded conditioning space-grade electronics. This development was achieved under an ESA R&D space program, in order to develop micro-switch devices not affecting reliability of mechanisms, not adding extra mass nor any resistive torque, and with the major objective of achieving very high cost efficiency for space applications with large quantities, such as for New Space constellations.

The design has been achieved for two sensing configurations, one for axial motion, and the second for tangential motion. The test results of a batch of Engineering Qualification Models are presented for sensing precision, space environmental temperature conditions, launch vibrations and shock tests, spacecraft Electro-Magnetic Compatibility (EMC) tests, and radiation environmental tests up to 300 Krad.

Introduction

For many years, CEDRAT TECHNOLOGIES (CTEC) has been developing and qualifying miniature sensor technologies in the field of space fine pointing and positioning applications, based either on strain gauges for piezoelectric mechanisms, or Eddy Current Sensors (ECS) for magnetic ones.

ECS sensor technology is currently a major topic of interest, especially in the field of scan mirror mechanisms, fast steering mirrors (FSM), fine pointing mirrors, and in the field of reference sensor for proximity detection such as micro-switching and tachometer sensors, for either ambient or cryogenic space temperatures.

For the last few years, the field of new space applications such as giant constellations requiring very large quantities, with both high reliability and high cost efficiency, has led to the increase of ECS technologies development for proximity detection in deployment mechanisms. The maturation of CTEC ECS technology in that field was first started under CNES funding, and is then being continued under ESA funding for micro-switching applications.

* CEDRAT TECHNOLOGIES, Meylan, France ; actuator@cedrat-tec.com

Figure 1. ECS-Based Micro-Switch Sensor

Micro-Switch Sensor Design Description

Design and Integration Concept Overview

Two micro-switches have been designed in order to provide either axial detection or tangential detection, both having the same housing and interface design, and each having a dedicated sensor head configuration.

The sensing head is located at the tip of a cylindrical body which provides an M16 fastening interface over the complete body length, and which also provides the housing for the embedded conditioning electronics. This design has been proposed in order to provide cost efficiency, as well as simple integration onto structures with precise sensing clearances adjustment, and easy electrical connection to a distant power source without requiring any remote signal conditioning.

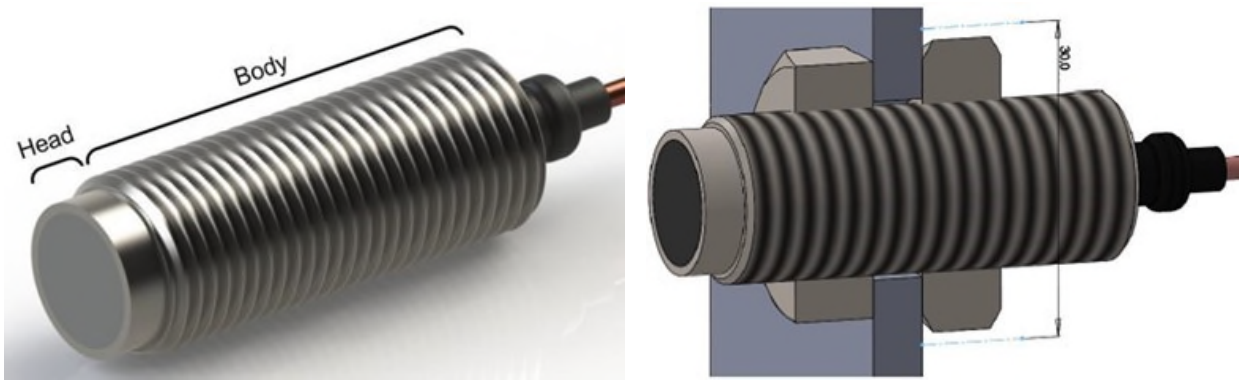

Figure 2. Micro-Switch Design and Integration Concept

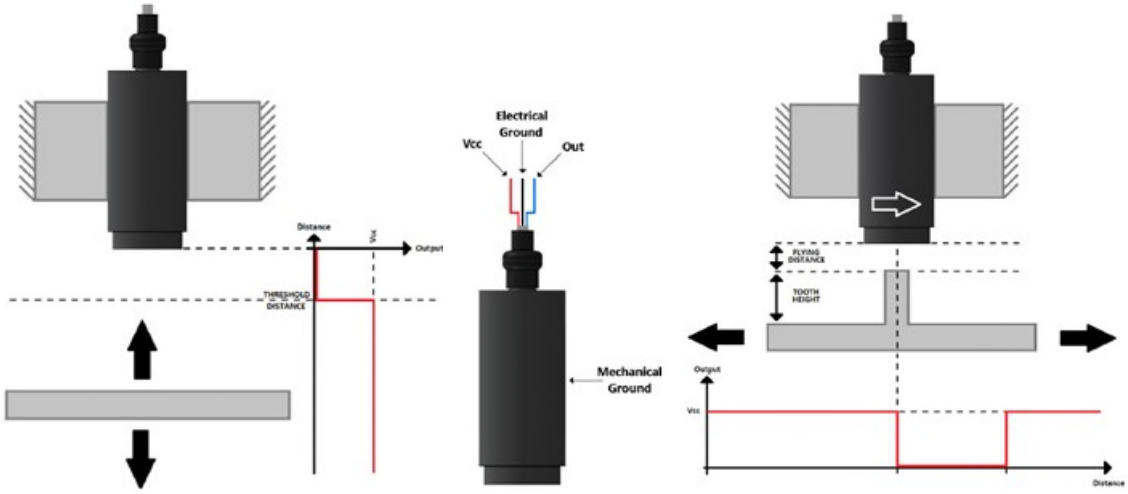

Figure 3. Axial motion micro-switch design (left) and tangential motion micro-switch design (right)

The sensor operates with a push-pull voltage output, which provides a digital output indicating the proximity of a target located onto a moving part. A high level (VOUT = VCC) means that the target is far from the sensor and a low level (VOUT = GND) means that the target close to the sensor.

The approach of a high output level when the target is far from the sensor was defined for safety concerns, in case of sensor failure. If a failure does occur, the output is set to low level, as if indicating the proximity of the target is in front of the sensor, in such a way that the mechanism motion can be stopped to avoid a collision, in order to activate a redundant sensor.

Figure 4 illustrates the clearances to be adjusted at integration (red colors), at end of stroke of mechanism i.e., at mechanism motion stopping, thanks to the M16 fastening / positioning interface.

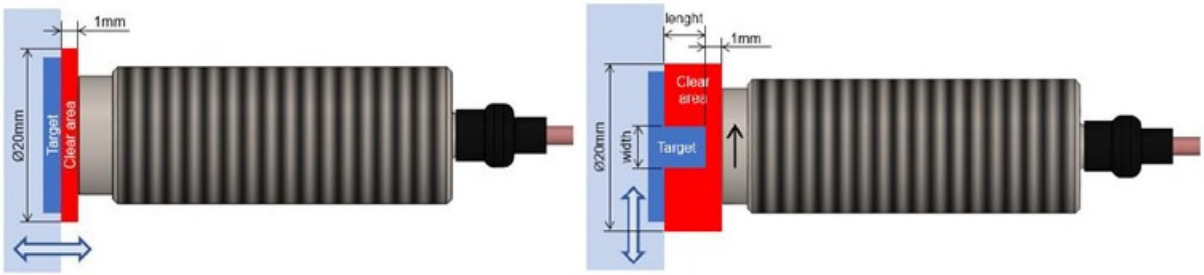

Figure 4. Micro-Switch proximity clearance for axial motion (left) and tangential motion (right)

The cylindrical body of the sensor which serves as the fastening interface also provides the housing for the conditioning electronics, which will detect and quantify the inductance and resistance variations difference between two measurement coils, based on differential measurement principle. The void volume of the housing all around the electronics Printed Circuit Board (PCB) is filled with potting, in order to avoid any air entrapment, and to provide thermal heat sinking toward mechanical interfaces.

The major advantage of the differential measurement approach between two coils is the insensitivity to thermal variation of the environment, as the thermal drift is applied to the two coils with the same effect, and cancelled by differential subtraction. Figure 5 illustrates the architecture of the embedded conditioning electronics.

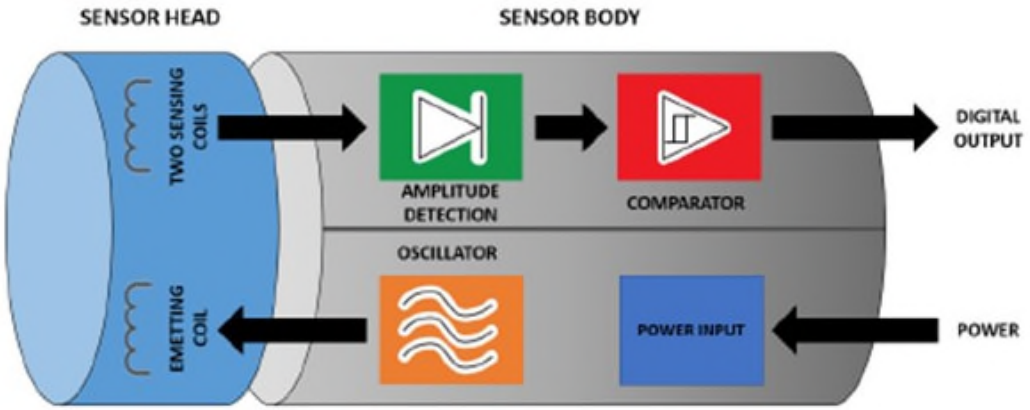

Figure 5. Micro-switch embedded conditioning electronics

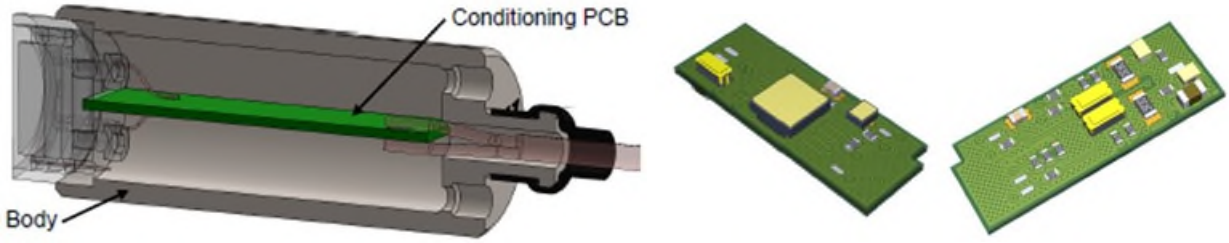

Figure 6. Micro-switch embedded space-grade conditioning PCB design

The sensor head, body, and conditioning electronics are independent prior to final assembly, and can be modified separately. This feature enables multiple sensor configurations without impacting outer design or dimensions, in order to provide either tangential or axial motion detection of a distant target located on a moving part.

With same mechanical design configuration, other sensing heads and conditioning electronics can be customized to fit with customer requirements, in order to provide specific threshold distances, and specific operational conditions from high to cryogenic temperatures.

Axial and Tangential Sensing Heads Configurations

The sensing principle of the micro-switches proposed are based on the eddy current measurement principle, requiring emitting and sensing coils implemented onto a space PCB. The emitting coil generates eddy currents on a distant target surface, with a small electrical excitation at high frequency, typically adjustable between 500 kHz to 5 MHz. This signal is based on Colpitts oscillator, the emitting coil being part of the current tank in such a way that the emitting function requires a very low power to provide the required high frequency magnetic field oscillation.

According to Lenz's Law, the direction of the eddy currents induced on the target conductor by the oscillating magnetic field generates an opposite magnetic field opposing to the emitted one in such a way that variations are observed in the sensing coil inductance values as function of the distance to the target.

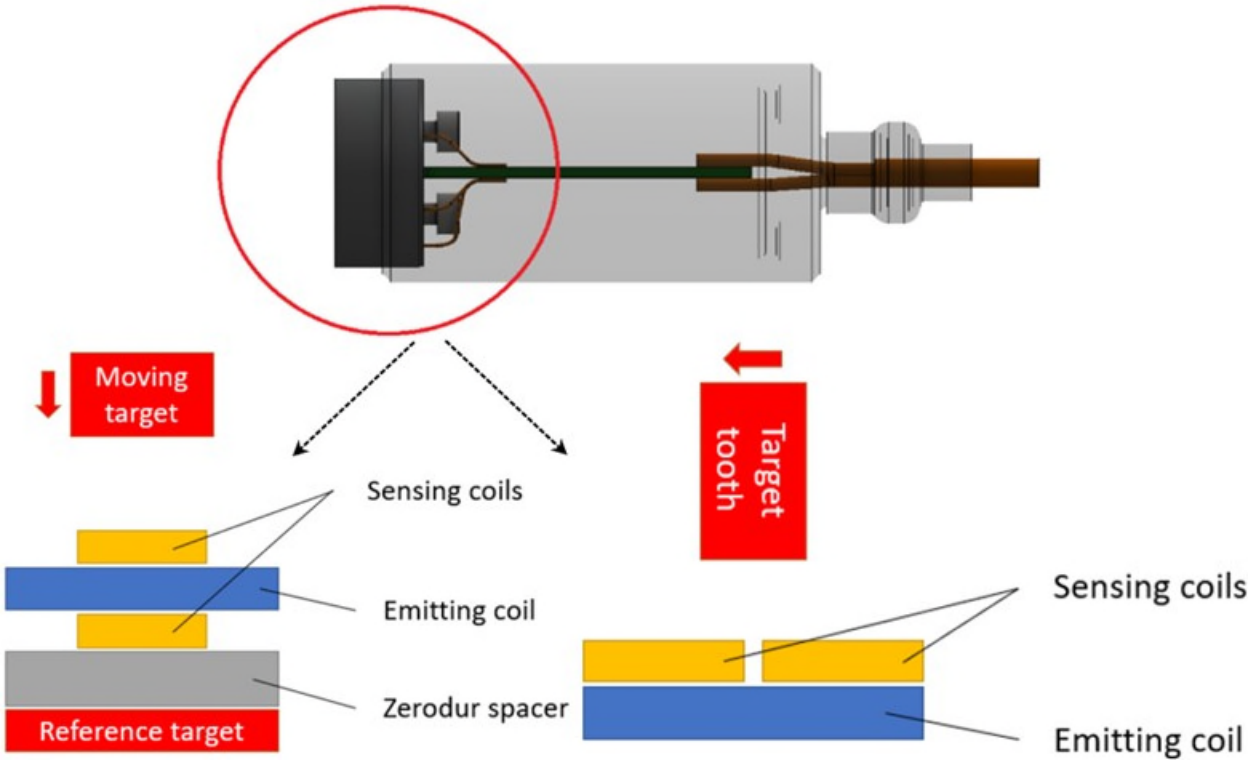

Figure 7. Emitting Sensing & Sensing coils configurations, axial (left) and tangential (right)

Manufacturing of Engineering Qualification Models (EQM)

The project which is still ongoing has allowed the manufacturing of a batch of four Engineering Qualification Models, two in axial motion detection, and two in tangential. Figure 8 shows the space design achieved, with the space design of embedded conditioning electronics.

Figure 8. Batch of Four Engineering Qualification Models

The embedded conditioning electronics were designed and manufactured according to space-grade standards, considering the PCB applicable design rules as well as materials. All active components included in the PCB are space Engineering Models.

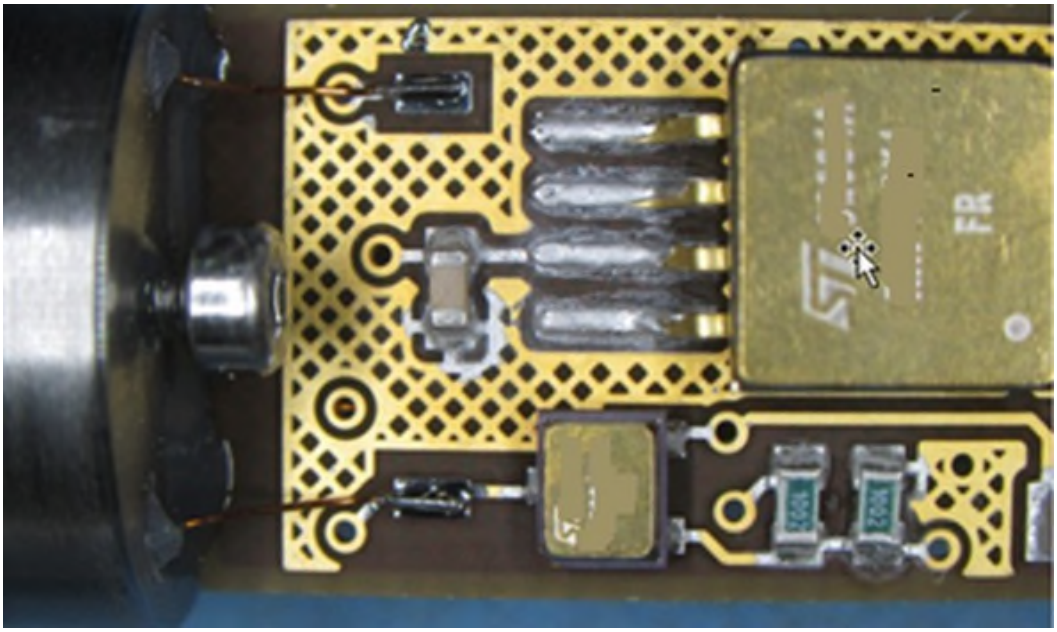

Figure 9. Space Grade EQM Embedded Conditioning Electronics

The performance test bench was realized based on a commercial reference position sensor and the use of a voice coil actuator implemented onto flexure bearings, in order to simulate a proximity motion of a moving part without friction.

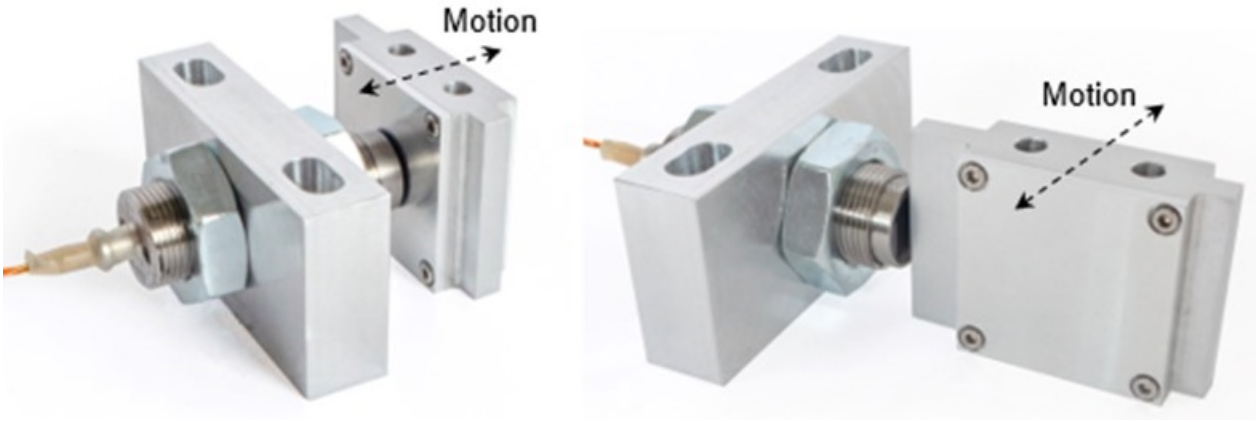

Figure 10. Sensing motion test bench principles, axial (left) and tangential (right)

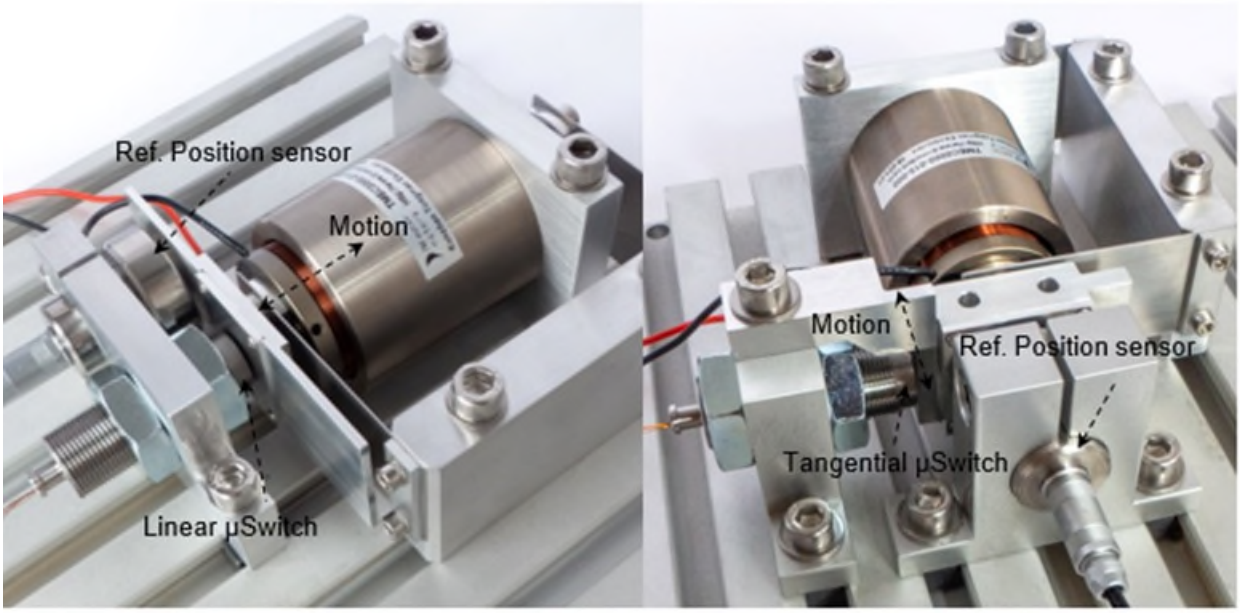

Figure 11. Sensing performance test bench, axial (left) and tangential (right)

At the time of the current publication, the proximity detection principle has been successfully tested, with accuracy demonstrated lower than 50 µm. The hysteresis error during cyclic forward and backward motions has also been evaluated to about 20 µm, but this does not need to be taken into account when using the micro-switch to detect end of stroke in such applications as deployment mechanisms.

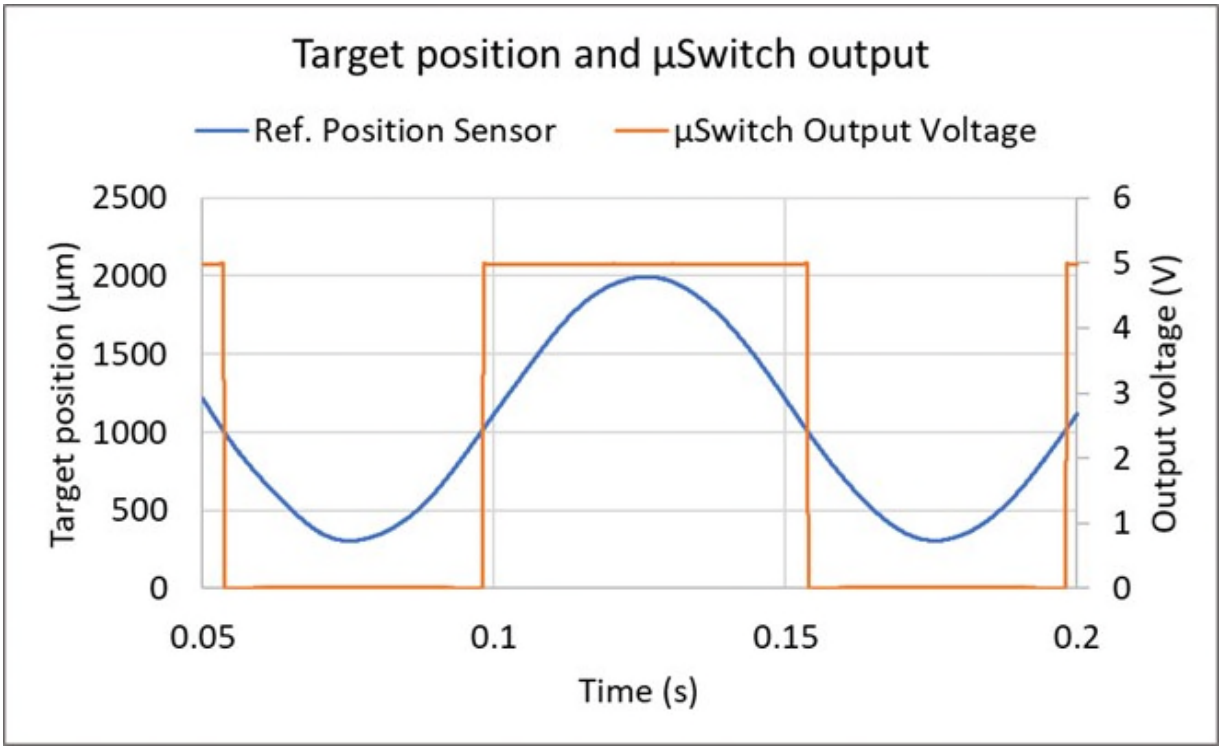

Figure 12. Sensing Test Results – Proximity Detection

Figure 13. Sensing test results – Forward / backward hysteresis threshold

The qualification test campaign shall be completed by the end of 2022 to fully demonstrate all environmental requirements by test.

Table 1 summarizes the performances expected of the proposed micro-switch design, as well as expected recurrent cost which is a key driver of this technology in new space applications.

Table 1. Micro-Switch functional performances & recurring costs summary

Contactless Threshold distance	1 mm
Switching Function	Push-pull
Switching level - High	Power supply
Switching level - low	GND
Power supply	3.3 or 5V DC
Power consumption	<100 mW
Electrical interface	Pigtail with leads
Repeatability	≤10 µm
Accuracy	≤50 µm (1)
Response time	<1 ms
Mechanical interface / Overall dimensions	Ø16 x 50 mm
Mass	37 g
Operating temperature	-50°C to +90°C
Non-operating temperature	-60°C to +100°C
Radiative environment	100 - 300 Krad
Detection cycles	> 500 000
On / Off cycles	> 1000
Lifetime	< 22 years
Outgassing	TML <1%, CVCM<0.1%
1st mechanical resonance	> 200 Hz
Mechanical random vibration	0.5 g²/Hz 60 Hz to 400 Hz
Mechanical shock	1500 g's 1000 Hz to 10000 Hz
Reliability	> 0.9999 with a confidence level of 95%
Recurring cost per unit	< 6k euros for 10 units < 4k euros for 100 units

(1) Depending on calibration reference sensor accuracy. Repeatability ≤ 10 µm is to be considered as most relevant performance.

Conclusion and Acknowledgments

The proposed micro-switch design has shown successful preliminary performance, not yet fully qualified, but which should ensure a space commercial exploitation at the end of the project. Qualification runs will cover functional tests at ambient and operational temperatures, vibrations and shock environments, EMC and radiation tests.

The maturation of CTEC space ECS technology was possible thanks to CNES and ESA support funding, which have allowed the development of relevant and compact sensing solutions in the field of fine pointing and fine positioning applications, which are currently being launched as off the shelf space products. The reader is invited to evaluate the application of CTEC ECS sensors technologies in the proposed references, especially in the field of new space applications, large size constellations, and pointing mirror mechanisms.

References

1. CEDRAT TECHNOLOGIES, Gerald Aigouy “P-FSM150S & M-FSM45 For Large Scale Free-Space Optical Communication”, *OPTRO 2022*
2. CEDRAT TECHNOLOGIES, Gerald Aigouy “P-FSM150S & M-FSM45 For Large Scale FSO Constellations”, *ESMAT 2021*
3. CEDRAT TECHNOLOGIES, Frank Claeyssen “Magnetically actuated fast steering mirrors”, *ACTUATOR 2021*
4. CEDRAT TECHNOLOGIES, Frank Claeyssen “Large Stroke Fast Steering Mirror for Space Free-Space Optical communication”, *OPTRO 2020*
5. CEDRAT TECHNOLOGIES, Gerald Aigouy “Large Stroke Fast Steering Mirror”, *ICSO 2020*
6. CEA Paris-Saclay, Jean-Christophe Barriere, Olivier Corpace. " Qualification of Euclid near infrared Spectro photometer cryomechanism - An application of CTEC ECS." *ESMAT 2017*
7. CEDRAT TECHNOLOGIES, Olivier Sosnicki “Eddy current sensors on Printed Circuit Board for compact mechatronic application”, *SENSOR & TEST 2010*

Design and Qualification of a Restrain-Release Mechanism for a 600-kg Deployable Panel Array

Horacio Quiroz*, Leonel Garategaray**, Gustavo Di Pasquale*, Alberto F. Martín Ghiselli* and Juan Ignacio Casais**

Abstract

The SAOCOM satellites have a Synthetic Aperture Radar (SAR) instrument with a distributed electronic architecture. This concept resulted in two arrays of deployable panels for the antenna with a mass of approximately 600 kg each. To support the deployable panels of the antenna during launch, each assembly has six restrain-release mechanisms. Both satellites deployed the SAR antenna panels in orbit succesfully. This paper presents the design constraints for these restrain-release mechanisms, the characteristics of the adopted solutions for the design, and the steps and results of the qualification campaign.

Introduction

The SAOCOM Mission (Satélite Argentino de Observación Con Microondas) is a program defined, managed and operated by CONAE (Comisión Nacional de Actividades Espaciales), Argentina's Space Agency. It is composed of a twin satellite constellation, SAOCOM 1A and SAOCOM 1B, each carrying a polarimetric L-band SAR instrument operating at 1.275 GHz with a spatial resolution between 10 and 100 meters as regards to the acquisition mode and the observation angle. The main driver of the mission is to generate soil moisture maps and both satellites are in orbit and operative. The satellites were launched in 2018 and 2020 respectively, and now are in full operating mode in a polar sun synchronous frozen orbit at 619 km with a 98° mean inclination. Figure 1 shows the SAOCOM satellite in flight configuration with the solar panels and SAR antenna deployed.

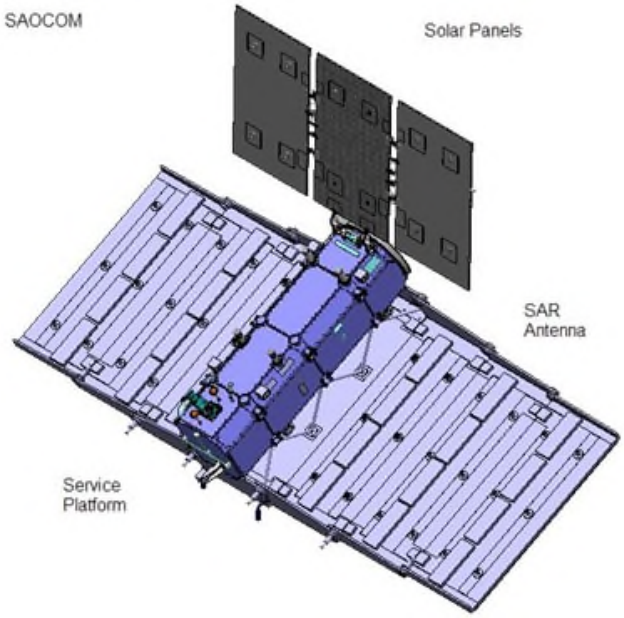

Figure 1. Flight configuration of the SAOCOM satellite.

* National Atomic Energy Commission, Buenos Aires, Argentina
** National Commission for Space Activities, Buenos Aires, Argentina

The SAR antenna structure and deployment mechanisms were designed and manufactured by the Comisión Nacional de Energía Atómica (CNEA), while the assembly, integration and tests were conducted together with CONAE.

The SAR antenna has a distributed electronic architecture, so the front-end electronics of the instrument are mounted on the antenna. The SAR antenna consists of seven panels whose structure is made of an aluminum honeycomb core sandwiched between high-modulus carbon fiber laminated facings. The electronic boxes and radiofrequency front-end electronics are mounted on the backside of this structure, and the radiating modules are mounted on the frontside. With all hardware mounted, each panel weighs approximately 200 kg and the smaller panels are 1.5-meters long and 4.0-meters wide. The total radiant surface is 35 m^2 at 10-meters long by 3.5-meters high. The SAR antenna has a structural configuration with one central panel fixed to the Service Platform of the satellite by means of a dedicated interface structure, and two symmetrical wings with three deployable panels each. Each wing has a mass of approximately 600 kilograms. During launch, each wing is folded and retained with an array of dedicated mechanisms. Once in space, each wing is released and then deployed by stepper motors via ground commands, reaching its final position after six deployment stages.

To support the panels of the antenna wings during launch, each assembly of three panels has six restrain-release mechanisms, which were designed not only to meet their mechanical and functional requirements, but also those of the integration. They are able to absorb misalignments between panels to guarantee the flatness of the antenna once deployed.

The restrain-release mechanism also prevents the folded panels from hitting each other during launch and transfers all structural loads supported by the antenna during launch to the satellite Service Platform (SP). The location and available space for the mechanisms in each folded panel has to comply with certain requirements imposed by the electromagnetic design of the radiating elements of the antenna.

Mechanism Design

The design of the restrain-release mechanisms for the SAR antenna had constraints related to the required electromagnetic characteristics and design of the antenna. The location and available space for the holes required in each structural panel to fix the mechanism must comply with certain requirements imposed by the radiating elements in the electromagnetic design.

The holes in the radiating surfaces could have a maximum diameter of 75 mm and any two holes should be made between successive rows of eight radiating slots and, in each panel, between the second and third circular slots and between the sixth and seventh circular slot of the row. The resulting position of a hole for the restrain-release mechanims, according to these requirements is shown schematically in Figure 2.

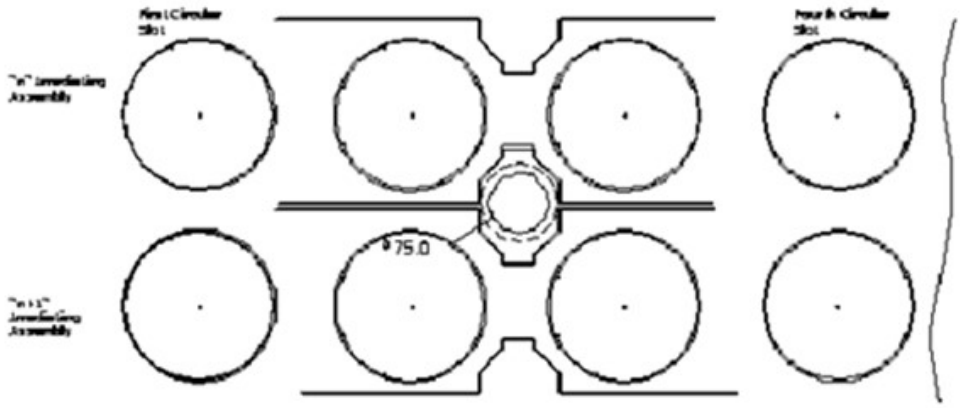

Figure 2. Available space and location for the restrain-release mechanisms holes in the radiating surface.

The restrain release structure must have a smaller diameter (less than 75 mm) to avoid mechanical contact with the radiating elements to accommodate mounting tolerances and to allow the alignment of the mechanisms with the folded panels. These requirements limit the maximum diameter of the restrain-release structure to 67 mm in the area where it crosses the radiating elements of the antenna.

Also, in order not to affect the emission and reception characteristics of the antenna, it is required that no metallic element protrudes from the radiating plane of the panels in their unfolded configuration. Therefore, the separation surface of the restrain release parts shall be below the radiating surface in each panel.

This requirement, together with the maximum diameter of the mechanism structure in this area, limits the area of the support and separation surfaces of the restrain-release parts in each panel, restricting the loads that each mechanism can transmit and support. This load limitation, together with the one supported by the chosen release device, determine the minimum number of mechanisms required and their distribution in each set of folded panels, which must be placed according to the loads produced by the launch vehicle.

The selection of a six-mechanism configuration for the array of panels resulted from the previous requirements and the need to reduce the bending moments generated on them and, as described in the following paragraphs, to limit the preload of the mechanisms. Considering this arrangement of mechanisms distributed on the surface of the folding panels, the load cases foreseen for the launch indicate that each of the mechanisms must withstand a minimum of 55 kN (12,365 lb) of compression load to avoid loss of preload and panel separation.

To comply with these requirements and constraints, the adopted design of the restrain-release mechanism is an assembly of tube sections located on each folded structural panel and on the primary structure of the Service Platform (SP). These tubes are joined by male and female cup and cone type sections to transfer the forces, bending moments and torques that the antenna supports during launch to the SP structure. Inside this tube a preload rod maintains the contact between tube sections and assure the load transfer.

A release device located on the outer panel supports the preload of the rod and, when operated, releases the rod and allows the latter wing deployment. A redundant assembly of helical springs retracts the rod into the SP to avoid interferences during the deployment operation. To stop the movement, the rod has a shock absorber located just beside the release end. A scheme of the restrain-release mechanism is shown in Figure 3 in both configurations, i.e., with restrained and released panels.

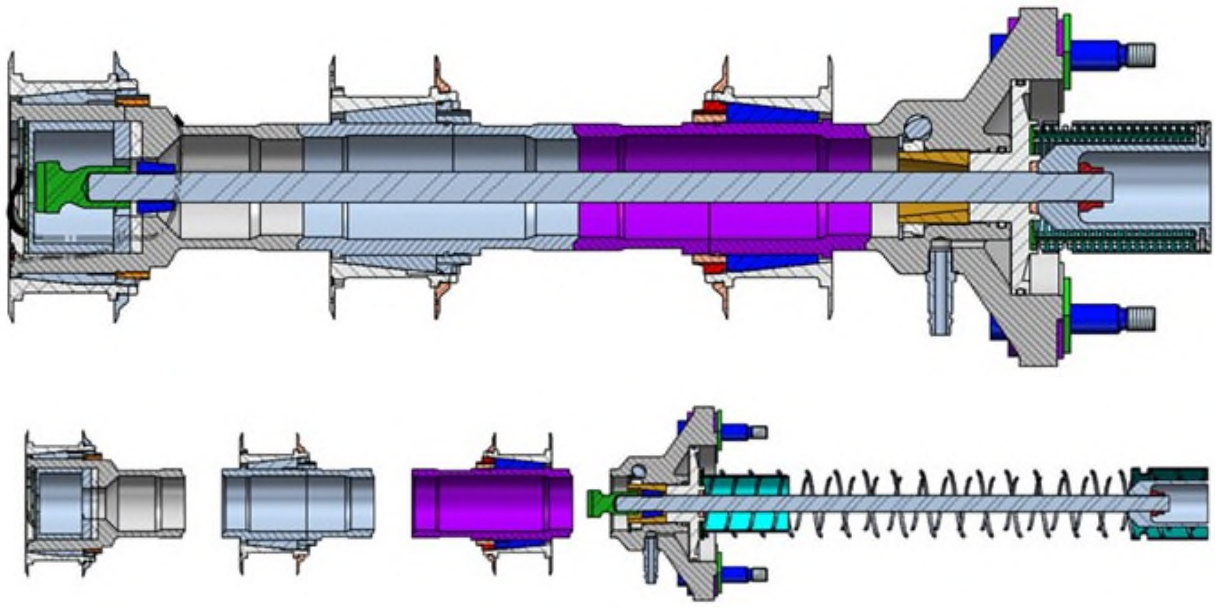

Figure 3. Restrain-Release Mechanism.

All the tubular parts, the flange mounted on the SP, and the preload rod of the restrain-release mechanism are manufactured from a titanium alloy (Ti5Al4V) due to its high strength and low mass. This alloy's low coefficient of thermal expansion also avoids the generation of high tensions between the carbon fiber structural panels and the fixed part of the mechanisms due to thermal stresses produced by differential expansion between components.

The pullback springs are made of stainless steel, the pneumatic piston is made of a titanium alloy and the shock absorber is made of Delrin®. The cup and cone type contact surfaces of the tube sections incorporated a surface coating to avoid cold welding that could be produced by the preload and vacuum conditions that the mechanism must withstand in orbit before activation. The coating used on these surfaces is a multi-layer chrome nitride coating with a few microns of thickness applied by means of a PVD (Plasma Vapor Deposition) process developed and qualified in-house.

The selected release device is an electromechanical separation nut based upon patented split-spool and fuse wire technologies from NEA Electronics Inc. (USA, model 9106B-3, shown in Figure 4, with a load carrying capability of up to 148 kN).

In addition to a lightweight design, the release device provides extremely low shock – orders of magnitude below pyrotechnic devices, is fast acting, releasing in milliseconds, can operate over a wide temperature range, and provides misalignment capability of up to 15 degrees. The design is a fully redundant configuration, both mechanically and electrically.

It should be noted that the manufacturer of the release device recommends using a preload rod made of Custom 465® stainless steel in order to use the entire preload allowed by the device. During development, a requirement was generated indicating that the use of magnetic materials inside the satellite SP should be avoided and therefore, as the preload rods of these mechanisms are housed inside the SP after the mechanisms are activated; it was necessary to change their material to a non-magnetic titanium alloy that could withstand preloads of up to 75 kN.

Figure 4. NEA Release Device.

To reach the preload on the internal rod of the mechanism during the integration process, a disc or piston operated pneumatically (using compressed dry nitrogen, vented at the end of the maneuver) produces the load and then a nut is pressed close against the disc of the piston to maintain the preload. The use of the pneumatic device to preload the rod reduces the required size of the nut and the volume and mass required for the mechanism. Figure 5 shows a cross-section of the described mechanism mounted into the tube section located on the SP.

The dimensions of the structural panels of the antenna and the distribution of the six restrain-release mechanisms therein require their precise alignment during the integration of the array of folded panels. To facilitate the integration tasks, both the tubular sections of the mechanisms and the parts located on the satellite SP have mechanical devices that allow the precise alignment of the parts, thus ensuring the proper transfer of both the preloads of the mechanism as well as the loads that are generated during the launch.

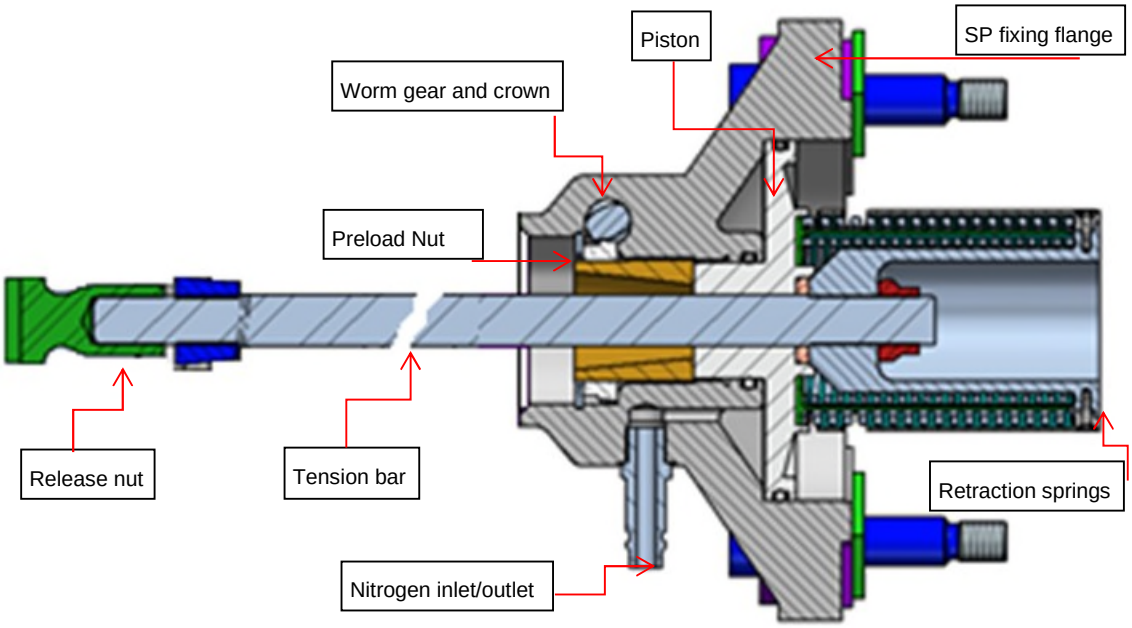

Figure 5. Detail of the pneumatic drive device.

Each mechanism is fixed to the structural panels using large titanium inserts. Inside these inserts, a set of conic elastic eccentrics and nuts are mounted to allow the radial and axial position of the assembly to be adjusted. Also there are eccentric bushings on the fixing points of the flange to align the mechanism in the SP. Figure 6 shows a view of the mechanism assembly which shows the three metal inserts that fix it to the panels and a detail of the alignment mechanism mounted on these inserts can be seen.

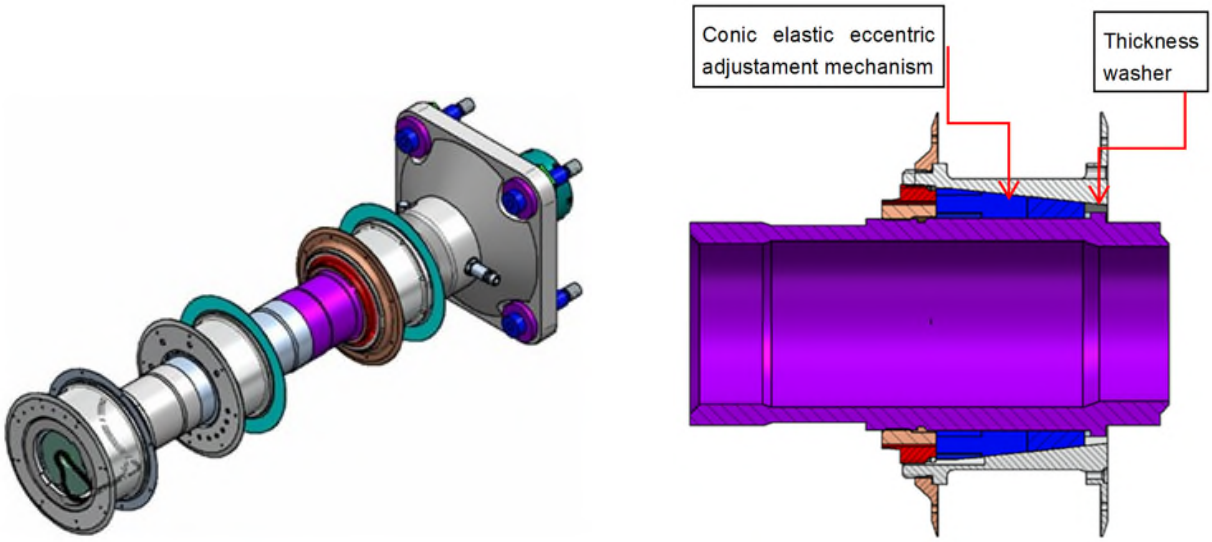

Figure 6. Restrain release assembly and detail of the alignment device.

The total mass of each mechanism, including the inserts that fix it on the panels and the parts mounted on the satellite SP, is approximately 15.6 kg.

Qualification Process

The qualification process of these mechanisms involves environmental and functional tests. Functional tests were performed before and after the sequence of the environmental tests following the guidelines of the NASA document of Reference [1].

The qualification units consisted of the Mechanisms Qualification Model, the SAR Antenna Structural Model (integrated to the Satellite Structural Model), and the Satellite Proto-flight Model (the first flight model).

The Mechanism Qualification Model was prepared to conduct a complete campaign of environmental mechanical and thermal tests with qualification level and functional tests in order to qualify all the mechanisms involved in the deployment of the antenna. This functionality was tested with simulated on-orbit thermal environment conditions using a thermo-vacuum chamber, after a successful first release and deployment of the model carried out before the vibration test.

This model included a structural support assembly for the mechanisms to be tested, consisting of a mock-up of sandwich panels with similar characteristics to those used in the antenna and a fixed aluminum panel to represent the support of the satellite SP. On this mock-up, two prototypes of the latch mechanism (to fix the relative position between succesive deployed panels), two prototypes of the hinge mechanisms (to allow the deployment of the panels using a stepper electrical actuator), a prototype of the restrain-release mechanism and two prototypes of the devices for the passing through of harness between antenna panels were assembled.

The SAR Antenna Structural Qualification Model (SQM) was prepared to be integrated with the satellite's SQM and to carry out a complete mechanical and functional qualification test campaign. This model of the SAR Antenna included the fixed central panel and the Interface Structure, a main assembly of three deployable panels, composed of flight-like strcutures and mechanisms, and a dummy representing the other main assembly of panels with the same inertia and stiffness properties. The deployable panels and the central panel had all the Radiating Modules and the corresponding deployment mechanisms integrated and included a set of six restrain-release mechanisms.

The Proto-flight Model (PFM) was the SAOCOM 1A satellite and was subjected to a complete campaign of functional and environmental vibration and acoustic tests with qualification levels. The test campaign included a SAR antenna release and deployment test before and after the environmental tests with the corresponding actuation of the release devices. For these tests two sets of NEA separation nuts were employed.

Qualification Results

The main objective of the thermo-vacuum test on the Mechanisms Qualification Model was to qualify the SAR antenna mechanisms against thermal loads. The different components were analyzed for the most unfavorable temperatures that will be experienced during the release and deployment in flight. Figure 7 shows the model integration to the thermo-vacuum chamber and the deployment performed.

The restrain-release mechanism would be successful if the interruption of the release device circuit is electrically verified, and the retraction of the preload rod inside the thermo-vacuum chamber is observed. If the retraction of the preload rod is successful, the mechanism must allow the correct separation of the set of movable panels with respect to the flange of the mechanism fixed to the SP dummy.

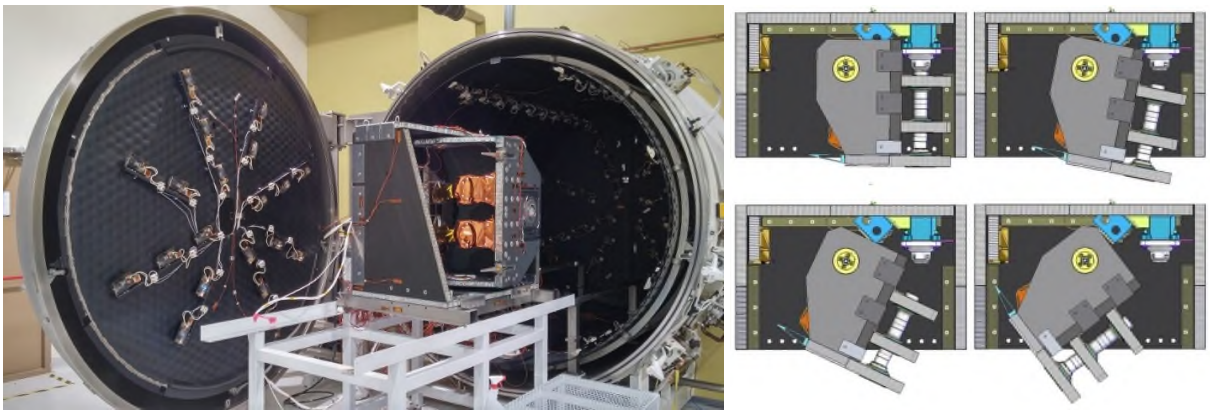

Figure 7. Integration of the Mechanisms Qualification Model to the thermo-vacuum chamber.

The release device circuit had an LED lamp connected to the Electrical Ground Support Equipment in arming mode so, at the moment of release, it would turn off indicating that the circuit was interrupted. This ensures that the drawn current correctly triggers the restrain-release mechanism. The retraction of the preload rod and the panel deployment were visually verified through a window in the chamber.

The actuation of the mechanism and the deployment of the model inside the chamber were performed after the qualification thermal cycling with the release device at a temperature of +45°C. The employed thermal cycling is shown in Figure 8 and it should be noted that, unlike other mechanisms such as deployment actuators or hinges between panels, the restrain-release mechanism did not have active temperature control.

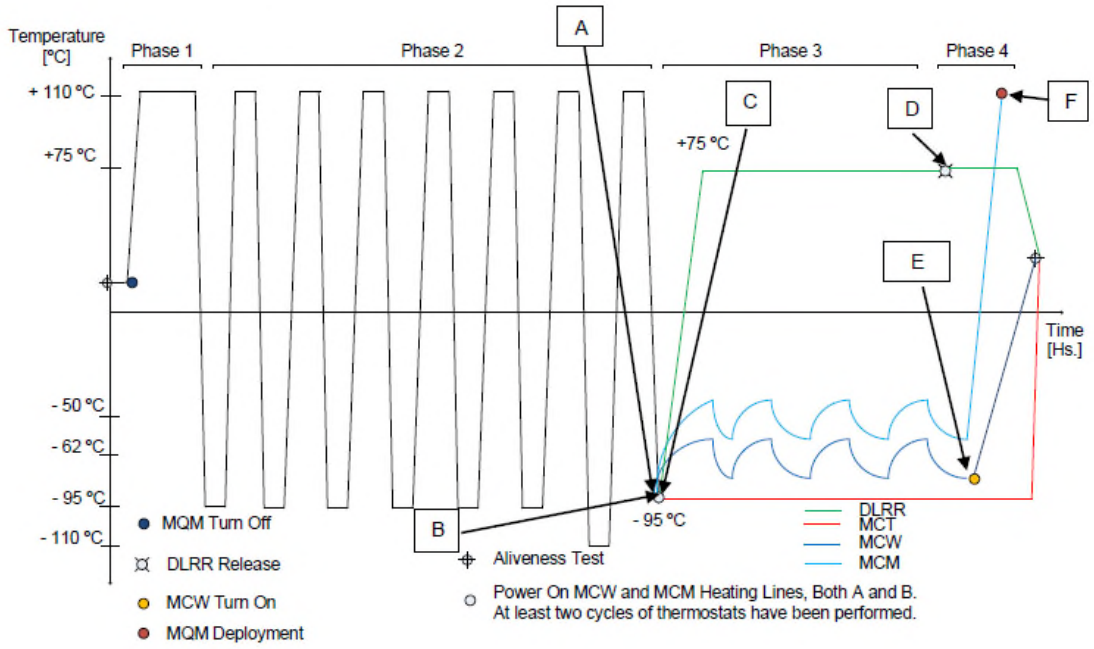

Figure 8. Thermal cycling of the Mechanisms Qualification Model, temperature evolution of the release device (in green) and release of the mechanism (point D).

The next step in the mechanism qualification was the SQM with a complete set of six mechanisms integrated to a complete array of deployable panels. Two actuations of these mechanisms were performed during the test campaign. The first one before the vibration tests and the second one after the acoustic test.

In the SQM, the restrain-release mechanisms' tubes were instrumented with a set of strain gages in order to characterize the preload applied by means of the pneumatic system. The value of preload or minimum axial force required to assure the contact of the cup and cone surfaces was set at 70 kN and is transmitted through the preload rod, which is subjected to traction. The mathematical model results showed that the required preload needed a pneumatic pressure of 8.0 MPa.

The distribution used for the instrumentation was four strain gages placed on the outer surface of the tubes as shown in the development model of Figure 9. This allows bending stress at the junction of the tubes to be ignored and for the minimum compression component to be measured. The compression component of the stress is required by the mechanism to ensure the transfer of loads between the panels of the antenna model during the vibration tests.

Unidirectional grid strain gages were used for these tests, which were fixed to the tubes of the mechanism using an epoxy-type adhesive. For each mechanism, the strain gages were placed on the tube closest to the flange located on the SP, which is the location requiring the highest stress according to the analysis carried out on the mathematical models. A total of 24 strain gages were installed, oriented at 90º to each other, each one with its grid aligned in the direction of the longitudinal axis of the mechanism.

Each strain gage was connected to the data acquisition system in a ¼ bridge configuration and without compensation for temperature variations. Data acquisition is performed using three Vishay amplifiers (strain indicator) and three switch & balance units.

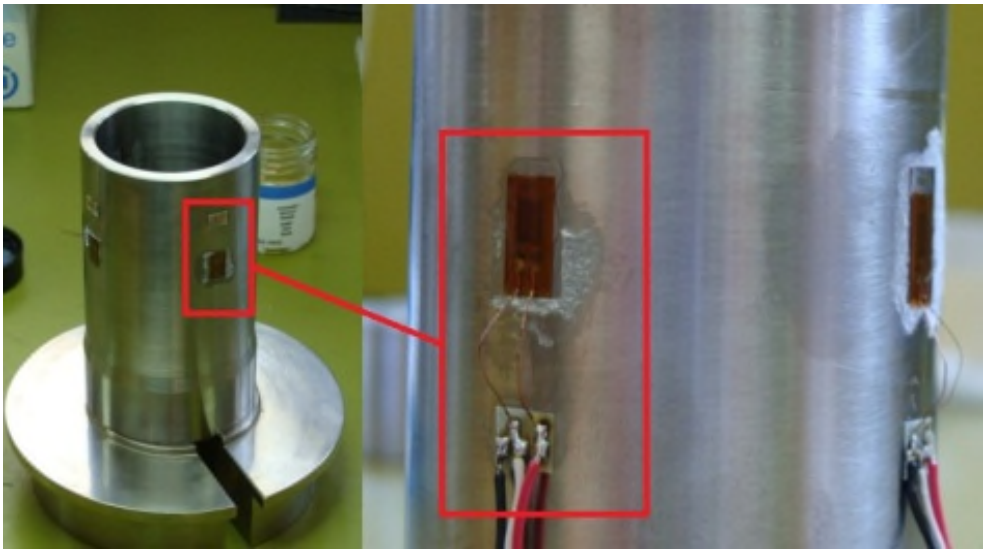

Figure 9. Strain gages for preload characterization located on the development model.

Once the deformation in each strain gage has been obtained, the determination of the bending moments in each axis and the axial force that the tube supports were estimated, being the latter the one that is transmitted to the preload rod. Table 1 shows an example of the strain measurements and preload obtained using a pneumatic pressure of 8.0 MPa in the mechanisms. The results were similar in all the preload operations performed on the SQM and showed that the required preload was obtained with a maximum 2.2% variation respect to the nominal value.

This procedure made it possible to qualify the preload process of the restrain release mechanisms by applying a pneumatic pressure of 8.0 MPa to them. In this way, it was established that it would not be necessary to repeat the instrumentation on the tubes of these mechanisms in the flight models of the antenna.

Table 1. Strain measures and preload obtained applying 8.0 MPa.

Mechanism ID	SG1 [µs]	SG2 [µs]	SG3 [µs]	SG4 [µs]	Preload [N]
4	-617	-710	-668	-610	-70585
3	-622	-1089	-521	-318	-69095
6	-512	-453	-904	-767	-71425
2	-845	-519	-459	-736	-69339
5	-866	-553	-527	-683	-71236
1	-644	-601	-715	-684	-71642

During the qualification campaign, the restrain-release mechanisms had to comply with two specific requirements. The first one required a complete retraction of the preload rods after the release in order to avoid mechanical interferences during panel deployment. The second one specified that the shock due to antenna release should not introduce shock spectrum in excess of Figure 10 in the most loaded leg of antenna mounted electronic equipment in order to not affect their functionality.

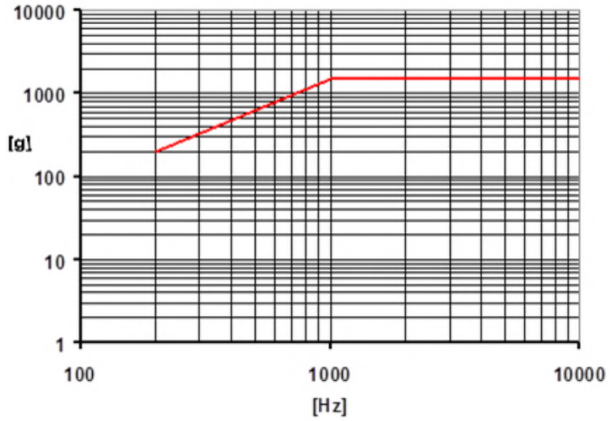

Figure 10. Maximum shock spectrum requirement during the antenna release.

To evaluate the shock due to the panels' release, an array of accelerometers distributed on the structural panel that has the assembly of the mechanism with the release device were employed. The time signals of these accelerometers during the activation of the restrain release mechanism were recorded and processed using the recursive algorithm introduced in Reference [2] to obtain the shock response spectrum (SRS) showed in Eq. 1:

$$SRS_{(f_s)} = \max\left(\left|Real\left[\frac{1}{N}\sum_{k=1}^{N}\left\{H_{(f_s,f_k)}\cdot\sum_{j=1}^{N}y(j)e^{-\frac{2\pi i(j-1)(k-1)}{N}}\right\}e^{-\frac{2\pi i}{N}}\right]\right|\right) \qquad \text{(Eq. 1)}$$

$$\text{with} \quad H_{(f_s,f_k)} = \left(\frac{{f_s}^2+i\frac{f_s f_k}{Q}}{{f_s}^2-{f_k}^2+i\frac{f_s f_k}{Q}}\right) \text{ as the transfer function}$$

f_x, are the frequency values, Q is the quality factor and $y(j)$ are the acceleration values measured along the test.

Figure 11 shows the accelerometers distributed on the panel near the release devices and also near some electronic front-end boxes and other mechanisms as the latch devices. Figure 12 shows the time signals obtained during the 50-second sequence of release device activation with peak values around 6000 g, and Figure 13 shows the SRS obtained from the accelerometers located near the position of the release devices. The shock waves are attenuated by the structure of the panel, and near the electronic boxes the obtained SRS complied with the requirement. It is shown in the SRS of Figure 14 that measurements near two of the transmision-reception assemblies with values one order of magnitude below the requirement.

The test also allowed for activation time verification of the release devices within the operating parameters indicated by the manufacturer. The activation time was 25 milliseconds and the frequency spectra obtained presented amplifications around 5 kHz, which also matches with the response spectrum of the release devices provided by their manufacturer.

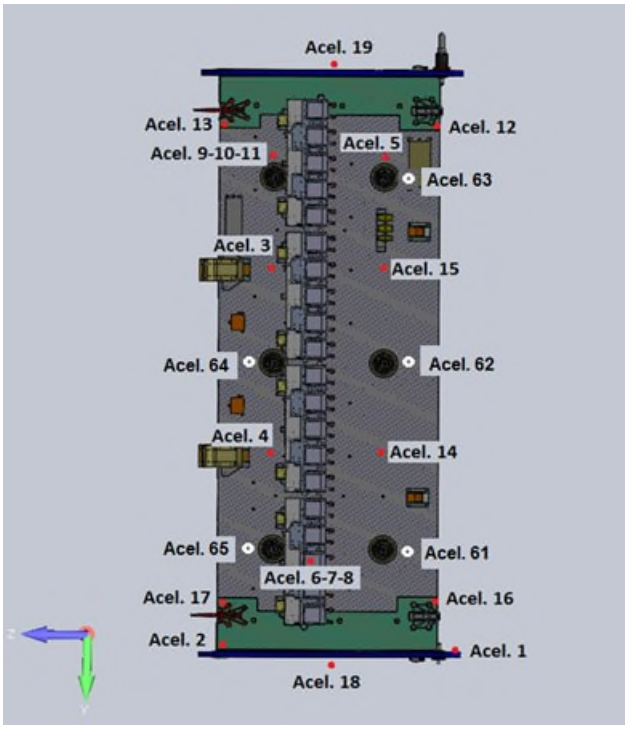

Figure 11. Accelerometers installed on the antenna panel for the qualification campaign.

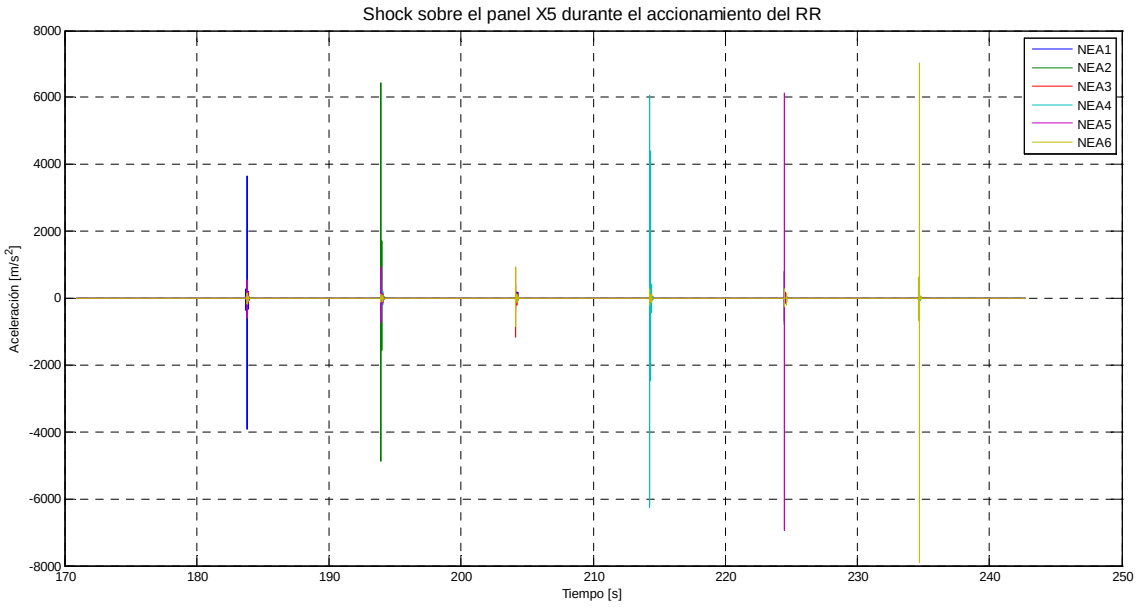

Figure 12. Time signals of the accelerometers located near the release devices during the activation of the mechanisms.

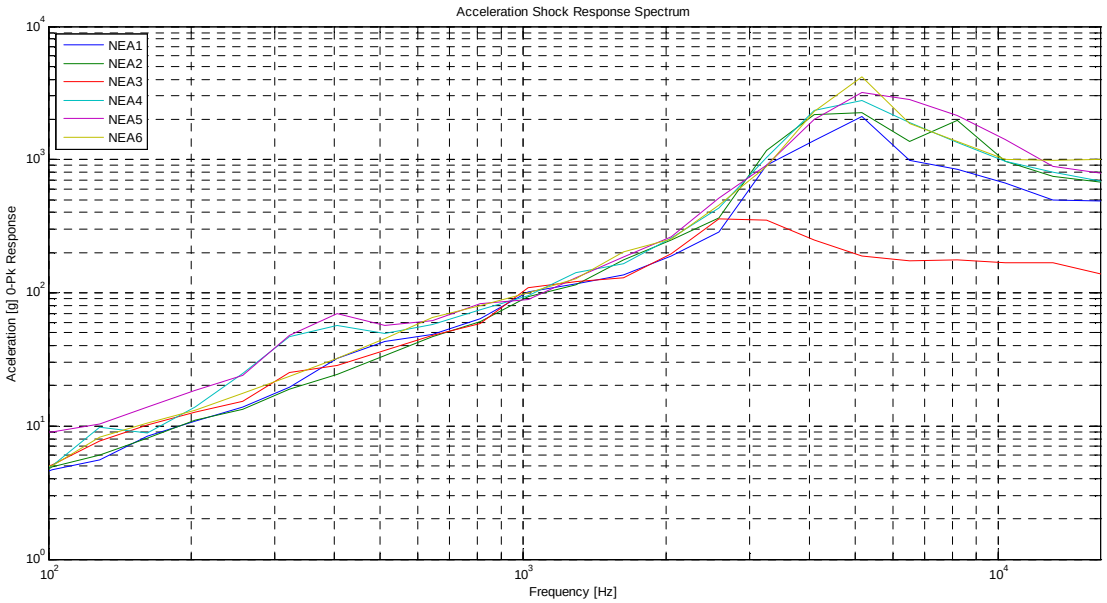

Figure 13. SRS of the accelerometers located near the release devices during the activation of the mechanisms.

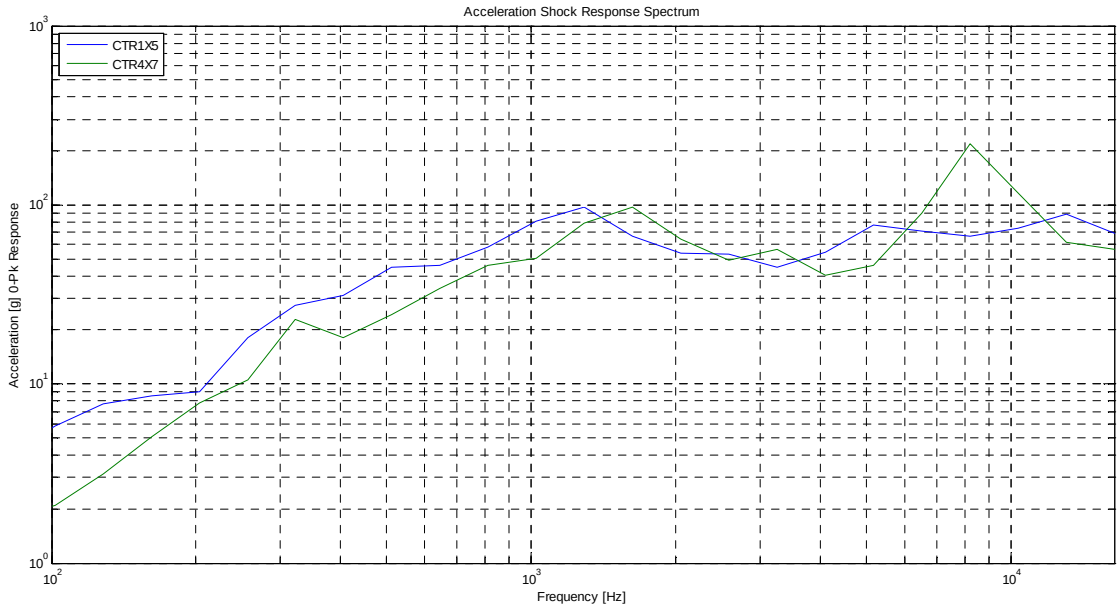

Figure 14. SRS of the accelerometers located near two of the electronic boxes during the activation of the mechanisms.

The mechanisms verification in the SQM also included the analysis of the possible geometric interference in the areas of least clearance that was between two restrain-release mechanisms and the support legs of the hydrazine tank located inside the SP. This possible interference would occur when the preload rods of the mechanisms, once released, retract inside the SP as a result of the action of the springs. If interference occurs, it would lock the mechanism without reaching its expected final position, preventing the deployment of the antenna panels.

In order to evaluate if there are geometric interferences, witness guide surfaces were placed along the path of the mechanism, so that when it was activated it would be possible to assess for any interference beyond the assigned volume.

To fulfill this function, the guide surfaces were painted with an ink for tooling that allows, after the test, to determine if there was contact between the parts during the actuation of the mechanism. Figure 15 shows these painted surface guides installed inside the structural model of the SP in the planned route of the preload rods and the location of the support leg assemblies of the hydrazine tank.

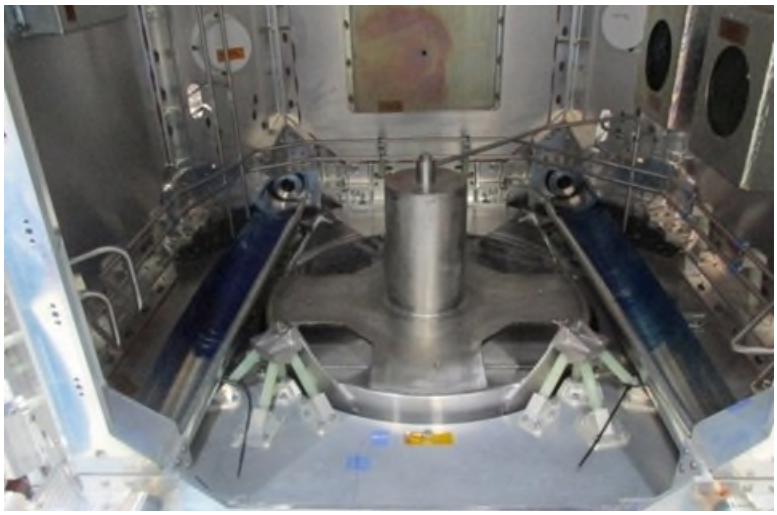

Figure 15. Array of surface guides installed inside the SP model to evaluate geometric interferences between the restrain-release mechanisms and the hydrazine tank supports.

For the test to be conservative, these guide surfaces for the rods were formed by a 0.5-mm thick section of tube and were placed above the possible points of contact (fixing screws and surface of the supports of the hydrazine tank) and the parts that form the end of the preload rod had a diameter of 76 mm compared to the 70 mm for the flight model's mechanisms, which increased the radius of the possible geometric interference by more than 3 mm.

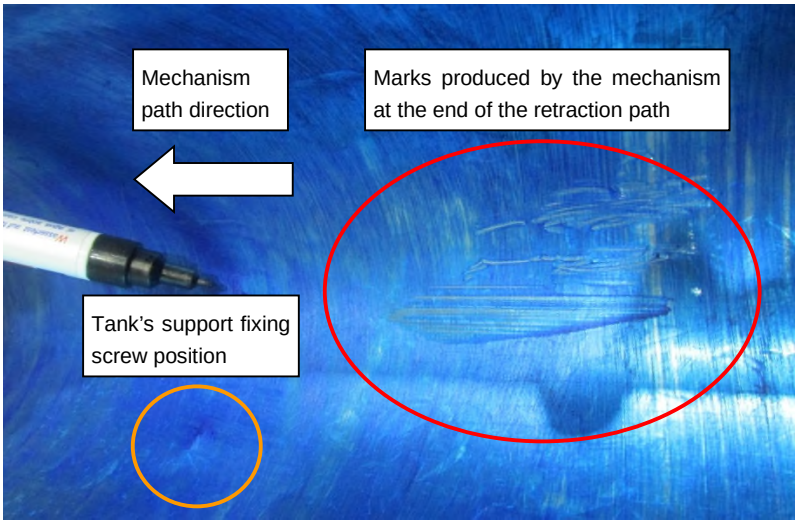

Figure 16. Details of the marks produced by the release of the rods on the guide surfaces.

Figure 16 shows a detail of the marks produced by the release of the rods on the guide surfaces. The inspection showed the areas where the sliding of the end tube of the mechanism occurred. These marks appeared in both cases before where the hydrazine tank supports are located, which indicates that there was no interference or collision between the mechanism and these supports of the fuel tank. Also the contact of the end of the mechanism on the guide surface occurred at the end of the rod's travel. Given that the marks are at the end of the rod's path and that they were found on the lower area of the guide surface,

it was concluded that the rod made its entire path centered and without an angle with respect to the bushing located on the flange of the mechanism. And when it stops, it rests on the guide surface due to the effect of gravity.

The release and deployment tests verified the complete retraction of the mechanisms preload rods inside the SP as shown in the example of the visual inspection performed in Figure 17 (left) after the successful panels' deployment of the PFM.

Also, during the PFM qualification test campaign, the visual inspection reveals that 3 of the 12 rods didn't retract completely as shown in Figure 17 (right). In those cases, it was possible to record that the rods with retraction incomplete overhang with respect to the flange of the mechanism by approximately 32 mm, while the design value is 22 mm. However, the maximum admissible limit that geometrically allows the correct deployment of panels is 85 mm. This value was obtained from the most unfavorable condition with respect to the regulation of the panel position by the hinge mechanisms and in the position closest to the panel rotation axis. After the visual inspections and the detection of the rods with incomplete retraction, it was also observed that due to gravity, these rods were in an oblique position with respect to the flange axis, and when aligned, the axis friction forces are minimized and fully retracted it to the design position due to the preload still existing in the springs of the mechanism. Therefore, it was concluded that in the absence of gravity, the rods should retract to their designed position without problems.

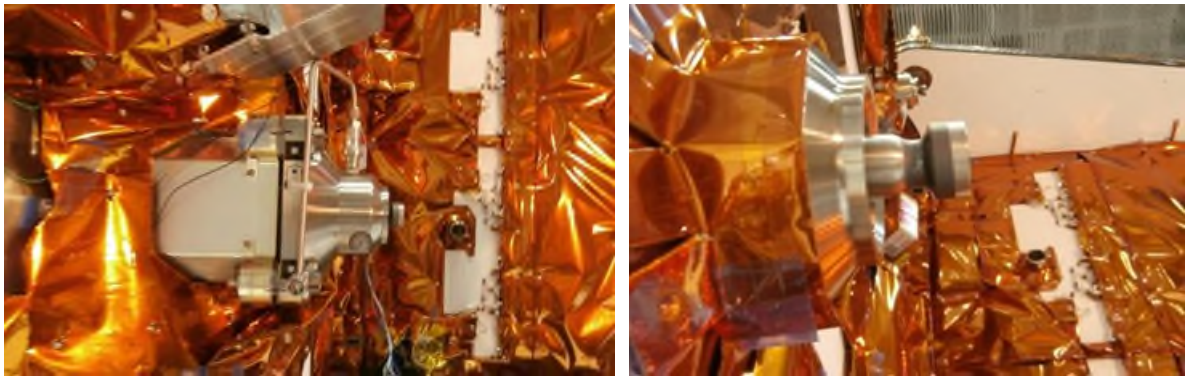

Figure 17. Visual inspection of the preload rod complete retraction (left) and preload rod incomplete retraction after the panels' deployment.

During the Flight Model (FM) SAOCOM 1B acceptance test campaign, a comparison was made between the time signals acceleration recorded during the release tests of the SAR antenna panels, after the environmental vibration tests of the PFM and FM satellites, to analyze the particular case of one of the restrain-release mechanisms in order to identify differences and evaluate their possible causes.

Figure 18 presents a comparison of both time signals synchronized with the firing signal and showing an important difference between the maximum amplitude recorded during the actuation of the corresponding release devices of each model. The maximum amplitude recorded during the FM release test is approximately 82% lower than the amplitude recorded during the same PFM test. The analysis of the signals in Figure 12 also showed that the time of flight of the rods, between release and impact on the shock absorber, was 4 milliseconds longer in the case of the PFM, in addition to not being able to be identified in the latter case, neither the start of the burning of the release device with a duration of 20 milliseconds, nor the pulse that occurs at the moment of panels separation.

These differences can be explained as the result of the absence of preload in the mechanism of the FM, since none of the accelerometers installed in the vicinity of the mechanism registered a significant amplitude pulse immediately after the 20 milliseconds of burning the release device that could indicate the separation of the panels. This analysis concluded that the environmental vibration tests of the FM were performed with one of the restrain release mechanisms without the design preload. The evaluation of the tests showed that there was no gap between panels and the inspection of the mechanisms showed that there was no

degradation of the contact surfaces between the parts of the mechanism located in the different panels. This problem, which occurred during the FM tests, showed the important design margins of the restrain release mechanism configuration adopted.

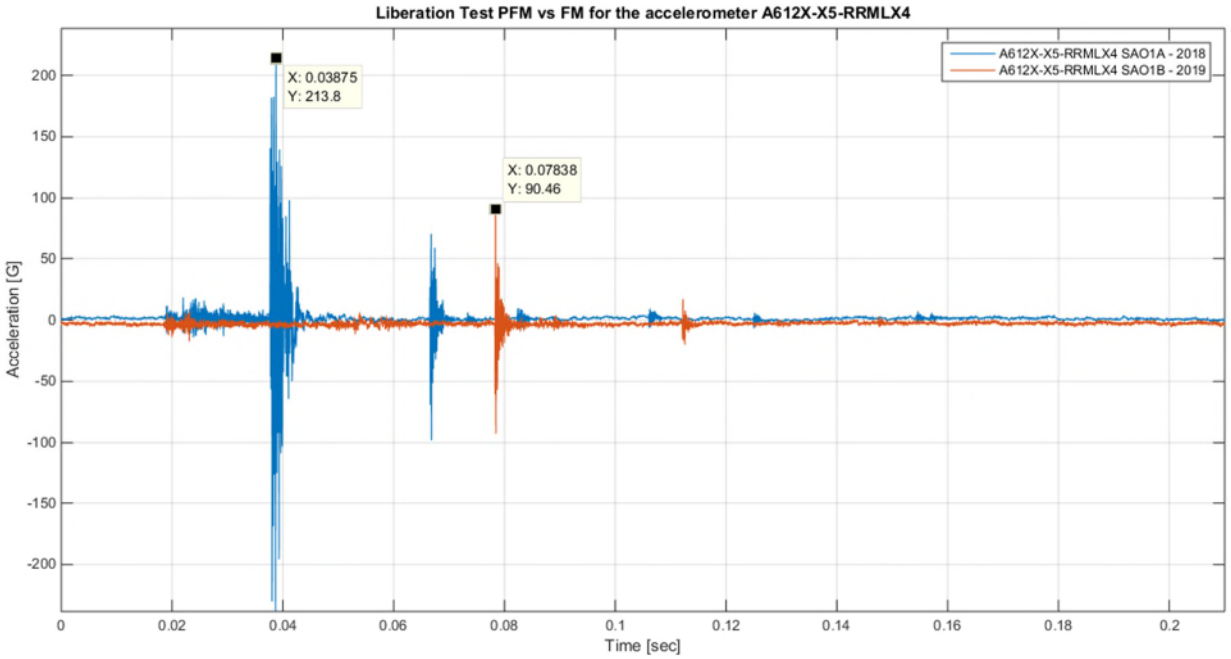

Figure 18. Synchronized time signals for the release of the same mechanism on Proto Flight Model and Flight Model.

Concluding Remarks

The tests performed over the different models during the qualification process of the restrain-release mechanisms for the SAR Antenna of the SAOCOM satellites showed that the adopted concept has design margins to withstand higher loads, originated both in a set of panels of greater mass and in a launcher with a greater acceleration envelope.

In addition to the multiple tests carried out during development and qualification phases of the project, the reliability of the restrain-release mechanisms designed in this case was confirmed by the successful performance on-orbit of a total of 24 units between the two launched satellites.

The qualification campaign of these mechanisms demonstrated the correct choice of a pneumatic preload system, which provided in-family preload values in all the mechanisms of each model and the fast and reliable performance of this task.

References

1. NASA GFSC-STD-7000, General Environment Verification Standard (GEVS) For GSFC Flight Programs and Projects.
2. NASA Technical Reports Server (NTRS) - “On the Shock-Response-Spectrum Recursive Algorithm of Kelly and Richman”, Justin N. Martin, Andrew J. Sinclair, and Winfred A. Foster. Aerospace Engineering Department, Auburn University.

NEA® Mini for Low Load Applications – Development and Qualification

Ruben Betancourt* and Jason Nave*

Abstract

EBAD published a paper in the 2018 AMS proceedings [1] describing the development of the NEA® Mini hold-down and release mechanism (HDRM) for low load applications. This design was born from the popularity of small, inexpensive Nichrome burn wire solutions in the small satellite community, coupled with some associated failures of those devices that revealed the opportunity for a more reliable solution. EBAD adapted our GEO NEA® battery bypass switch into an HDRM for small sat applications, built and tested an initial prototype. These devices have the advantages of being small, light, low power, low shock, and high reliability. The 2018 paper described the series of load and shock output tests that validated the HDRM as a potential product for typical low-load release mechanism applications. This paper describes the further development and qualification of the NEA® Mini HDRM for spacecraft and satellite applications.

Introduction

The NEA® Mini (EBAD part number SSD9040) design is an integration of our design expertise with high-reliability bypass switches and high-load/low-shock release mechanisms. The release mechanism in the bypass switch (Figure 1) is similar in operation to our standard release mechanisms and utilizes the same patented fuse wire technology. This combination resulted in the development of a scaled down version of the HDRM that is less than a cubic inch (16 mL) in volume, yet capable of holding a functional load of at least 1110 N (250 lbf) while producing the same low shock characteristics expected of EBAD's NEA® HDRMs.

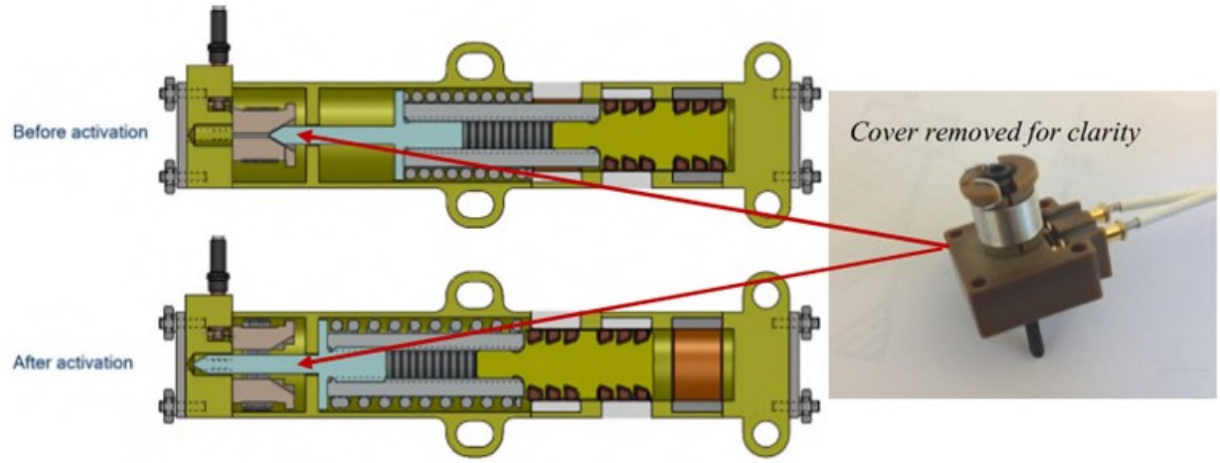

Figure 1. NEA® Switch Components Repurposed for the Mini HDRM

An initial prototype was built with common switch components and a #1 fastener size release rod. This unit was tested for load and shock output characteristics [1] and provided the baseline for further development described in this paper.

* Ensign-Bickford Aerospace & Defense, Moorpark, CA; rabetancourt@ebad.com

NEA® Mini Design

The design evolved from the initial proof of concept presented at the 2018 AMS to a DVT-level design, then finally to the Qual-level design, with lessons learned at each phase. See Figure 2 for a representation of the DVT and qualification-level designs. The envelope is virtually unchanged between the two.

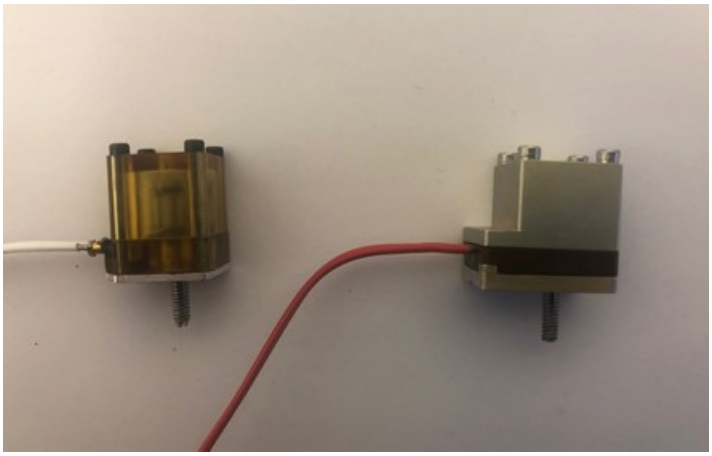

Figure 2. DVT (left) and Qualification NEA® Mini HDRM

At the heart of the Mini design is the split-spool technology used in all EBAD NEA® HDRMs. These HDRMs are electrically initiated, one-shot release mechanisms that have the ability to carry a very high tensile preload until commanded to release. The preload is applied through a release rod held in place by two separable spool halves which are in turn held together by tight winding of restraining wire. The restraining wire is typically held in place by redundant electrical fuse wires, where actuation of either circuit allows release. When sufficient electrical current is applied, the restraining wire unwinds, allowing the spool halves to separate and release the release rod and the associated preload.

Unlike the vast majority of EBAD's NEA® release mechanisms, the Mini has a single actuation circuit (non-redundant) and is not refurbishable. Based on the low price point of the unit, it is just as cost effective to replace the unit than to refurbish it.

Figure 3 shows the unit that was developed for qualification testing and Figure 4 illustrates its interface dimensions. The prototype test results were very promising in terms of load, functionality, and emitted shock. EBAD implemented several changes in the qualification model design that improved its performance. Chief among the design updates was to increase the functional load capacity of the initial prototype from 445 N (100 lbf) to a minimum of 1110 N (250 lbf) by incorporating metal spools, a primary component that holds the load in the device.

To maintain the increased load without yield or creep throughout environments, the unit base was upgraded from plastic to aluminum. Additionally, to increase load margin on the release rod, as well as make the unit easier to assemble and install, the release rod was increased from a #1 size fastener thread to a #4-40.

The change from a #1 size fastener to a #4-40 was based on a lesson learned from various manufacturing issues and prototype tests. The original design utilized a #1 thread in an attempt to machine it from a standard #1 size fastener, in order to reduce cost and lead times. However, this led to various challenges. Both internal and external machine shops had difficulties working with a #1 size thread on high strength material while holding tight tolerances on a relatively long component. It also meant that all test hardware would need to have a corresponding #1 thread, and would need to be made from high strength material, with tight tolerances. We learned in test that small errors in the setup utilizing a #1 thread could lead to significant load drops, or high stress points. Changing to a #4-40 thread eliminated most of these issues. A #4-40 thread was much easier to machine, and since the stress was lower, the material did not have to be

as high strength, and tolerances could be loosened. Paying a bit of a premium for custom 4-40 threaded rod led to a reduction in cost of other associated components and much more robust design. It also made the testing process easier, saving additional labor.

Changing the base and spools from plastic to aluminum created a potential ground path between the actuation circuit wires and the unit housing through these and other metal components in the assembly. To address this concern, the bases and the spools are coated with high dielectric space-qualified coatings. The coatings provide a measured insulation resistance consistently above 50 MΩ.

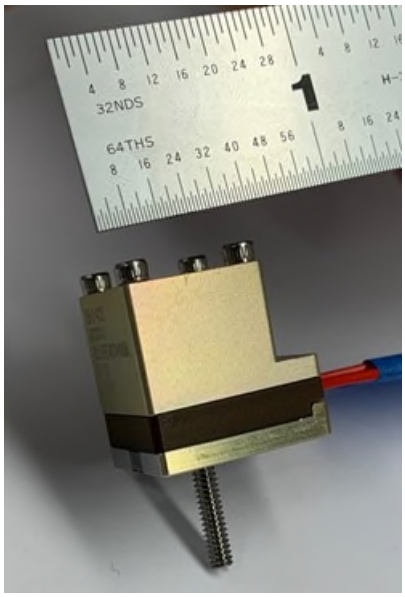

Figure 3. Qualification-level Mini HDRM

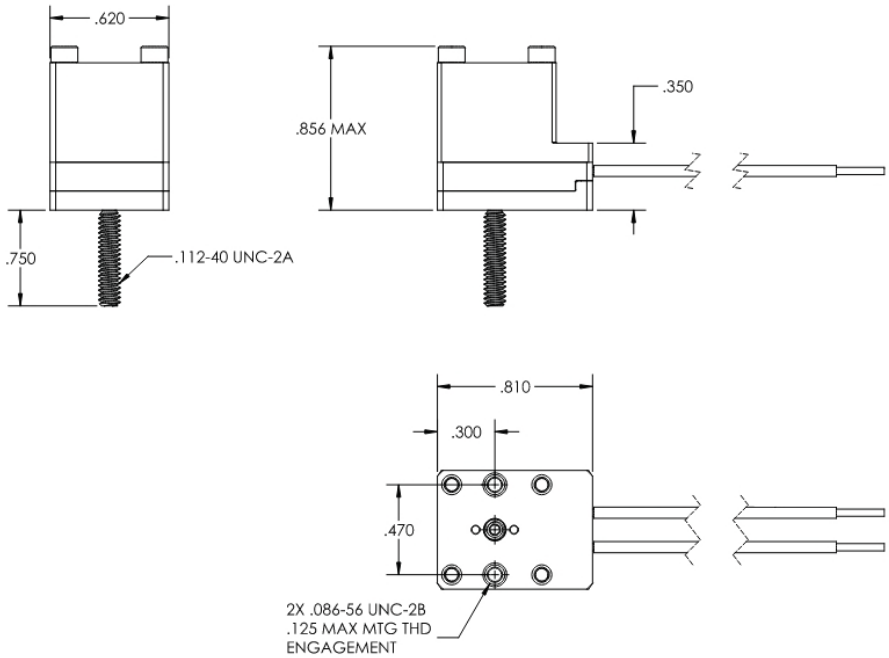

Figure 4. Mini HDRM Interface dimensions

NEA® Mini Testing

The DVT and Qualification test sequence is shown in Table 1. This sequence is common for NEA® HDRMs of all sizes. The DVT phase of testing was completed in 2021 and internal Qualification testing was performed in 1Q2022. The test levels selected were based on worst-case intended use cases and parameters previously used for similar NEA® HDRMs of larger size but similar material components.

Table 1. Mini Qualification Test Sequence.

Sequence	Test Type	Unit 1	Unit 2	Unit 3	Unit 4
1	Visual & Dimensional Inspection	X	X	X	X
2	Mass Evaluation	X	X	X	X
3	Circuit Resistance	X	X	X	X
4	Dielectric Strength	X	X	X	X
5	Insulation Resistance	X	X	X	X
6	Proof Load	X	X	X	X
7	Preload	X	X	X	X
8	Functional Test	X	X	X	X
9	Unit Rebuild	X	X	X	X
10	Circuit Resistance	X	X	X	X
11	Dielectric Strength	X	X	X	X
12	Insulation Resistance	X	X	X	X
13	No-Fire Testing	X	X	X	X
14	Proof Load	X	X	X	X
15	Circuit Resistance	X	X	X	X
16	Preload for Environments	X	X	X	X
17	Random Vibration	X	X	X	X
18	Input Shock	X	X	X	X
19	Thermal Cycling	X	X	X	X
20	Functional Testing - Cold	---	---	X	---
21	Functional Testing - Hot	---	---	---	X
22	Output Shock	X	X	---	---

Initial Tests

Test sequence numbers 1 through 6 are intended to confirm compliance to design requirements and workmanship standards to proceed along to the full functional test sequence. The four test units passed all of these tests and moved on to be functioned.

The units were proof-loaded to 1335 N (300 lbf), then preloaded to a test plate to 1110 N (250 lbf). The setup is shown in Figure 5. All units were actuated successfully and rebuilt for the remaining test sequence. Note that this is a one time use device. The parts were refurbished to save time in qualification. Dielectric coatings need to be replaced after actuation. This process would be cost prohibitive for production devices.

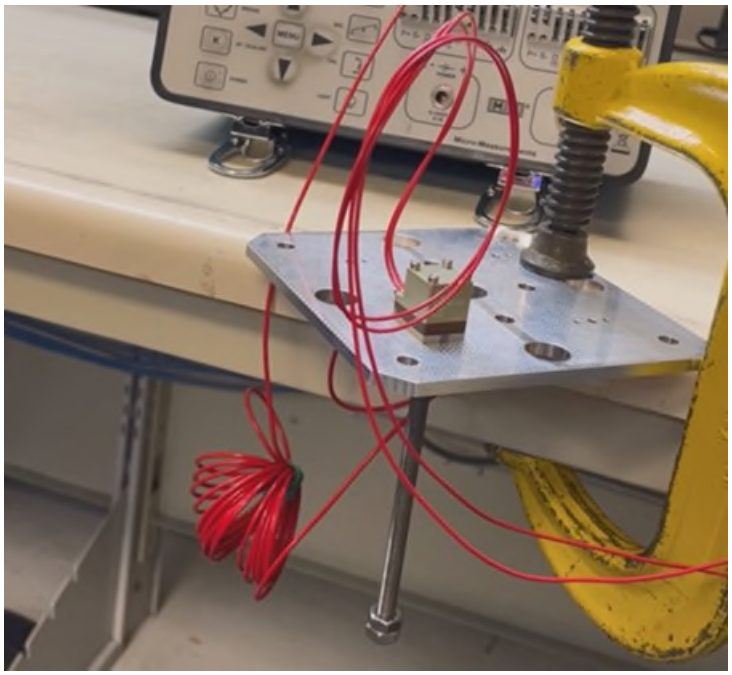

Figure 5. Mini HDRM Initial Actuation Setup

Random Vibration

After rebuild, the test units were preloaded to 1110 N (250 lbf) on a vibration test plate, as shown in Figure 6. The test parameters are shown in Figure 7. No mechanical issues, visible damage, or degradation were observed, with minimal preload change in-line with other NEA® HDRMs. The units were left installed on the test plate and moved on to input shock testing.

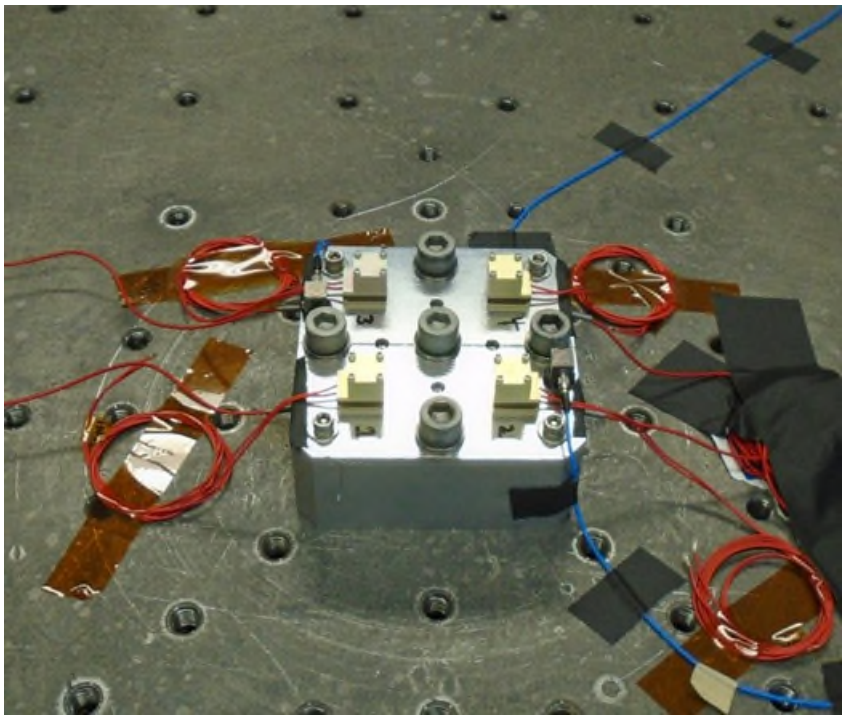

Figure 6. Mini HDRM Random Vibration Test Setup

Direction	Frequency (Hz)	PSD (G^2/Hz)	GRMS
X,Y, & Z	20	0.8	50.9
	50	2	
	600	2	
	2000	0.6	
Test Duration: 6 minutes/Axis			

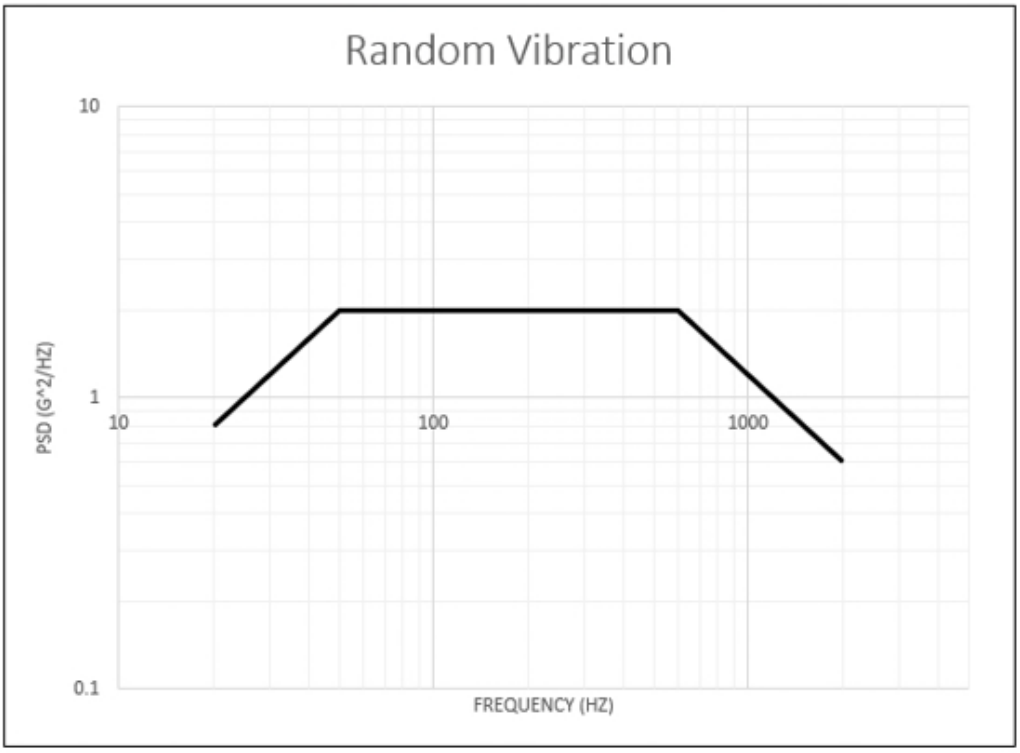

Figure 7. Mini HDRM Random Vibration Test Parameters

Input Shock

The units remained preloaded from the vibration test setup and were installed onto the drop tower for input shock testing. No mechanical issues, visible damage, or degradation were observed, with minimal preload change in-line with other NEA® HDRMs. The units were left installed on the test plate and moved on to thermal vacuum cycling. The input shock test setup and parameters can be seen in Figure 8 and Figure 9, respectively.

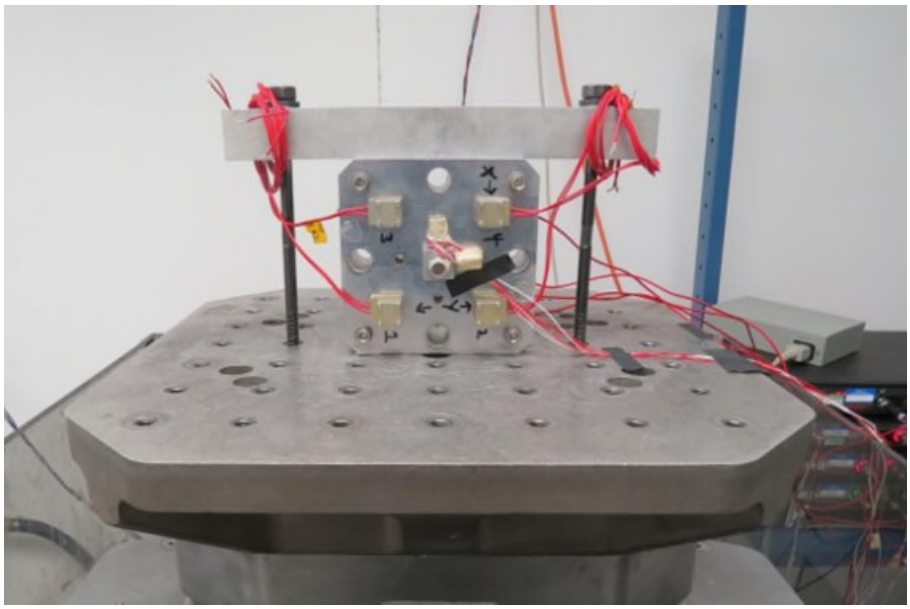

Figure 8. Mini HDRM Input Shock Test Setup

Frequency (Hz)	Shock (G)
100	100
700	1000
2000	2500
10000	2500
Shocks/ Axis =1	
Shock Spectrum Q=10	

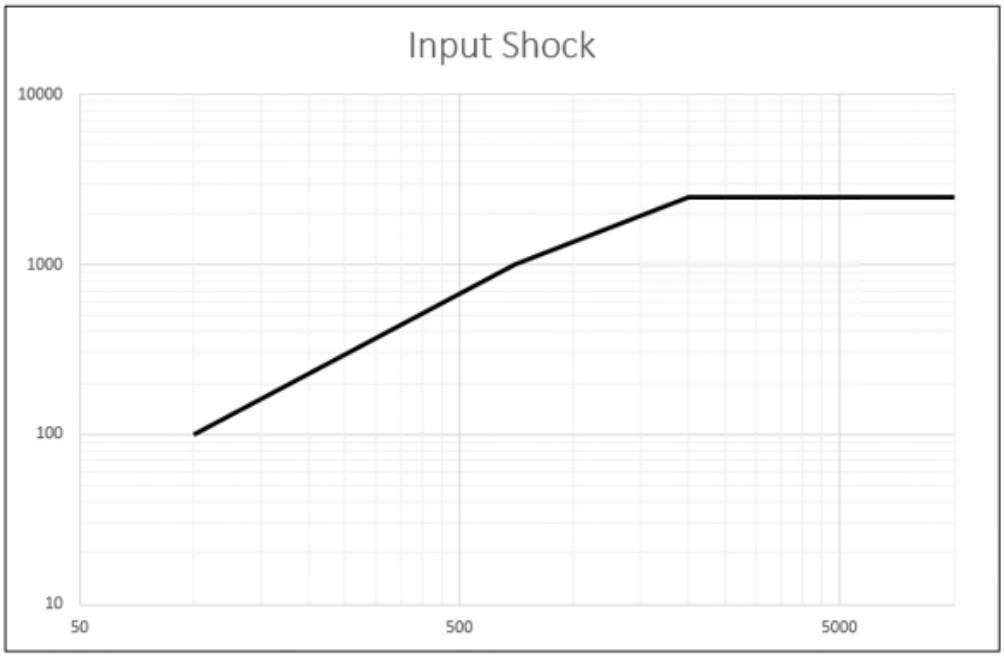

Figure 9. Mini HDRM Input Shock Test Parameters

Thermal Vacuum (TVAC) Cycling

The pre-loaded units remained on their test plate and were moved from shock input testing to TVAC cycling. They were subjected to 10.5 cycles in a thermal vacuum environment (<1.33E-3 Pa) from -135°C to 135°C. The TVAC cycling test setup and thermal cycle plot can be seen in Figure 10 and Figure *11*, respectively.

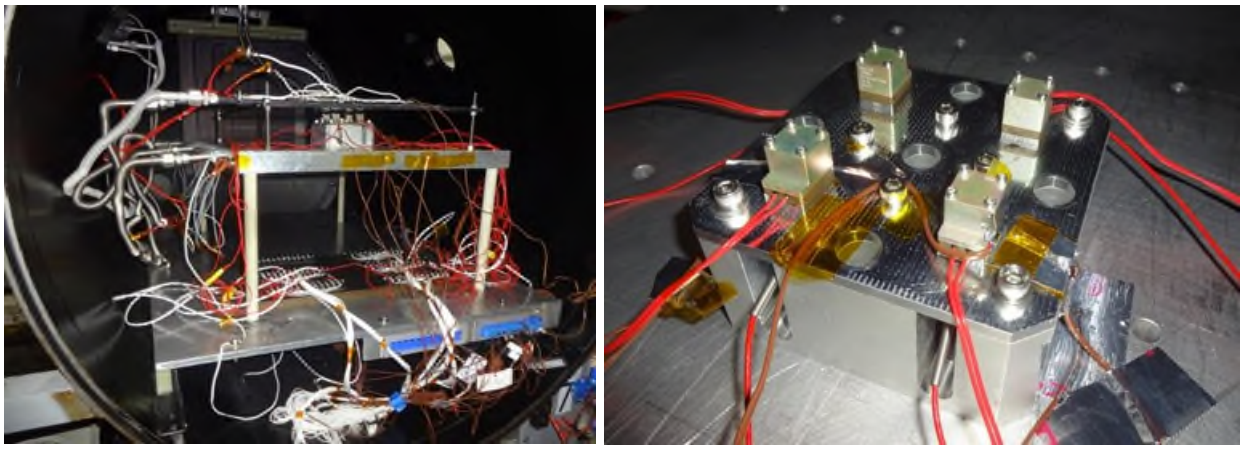

Figure 10. Mini HDRM TVAC Test Setup

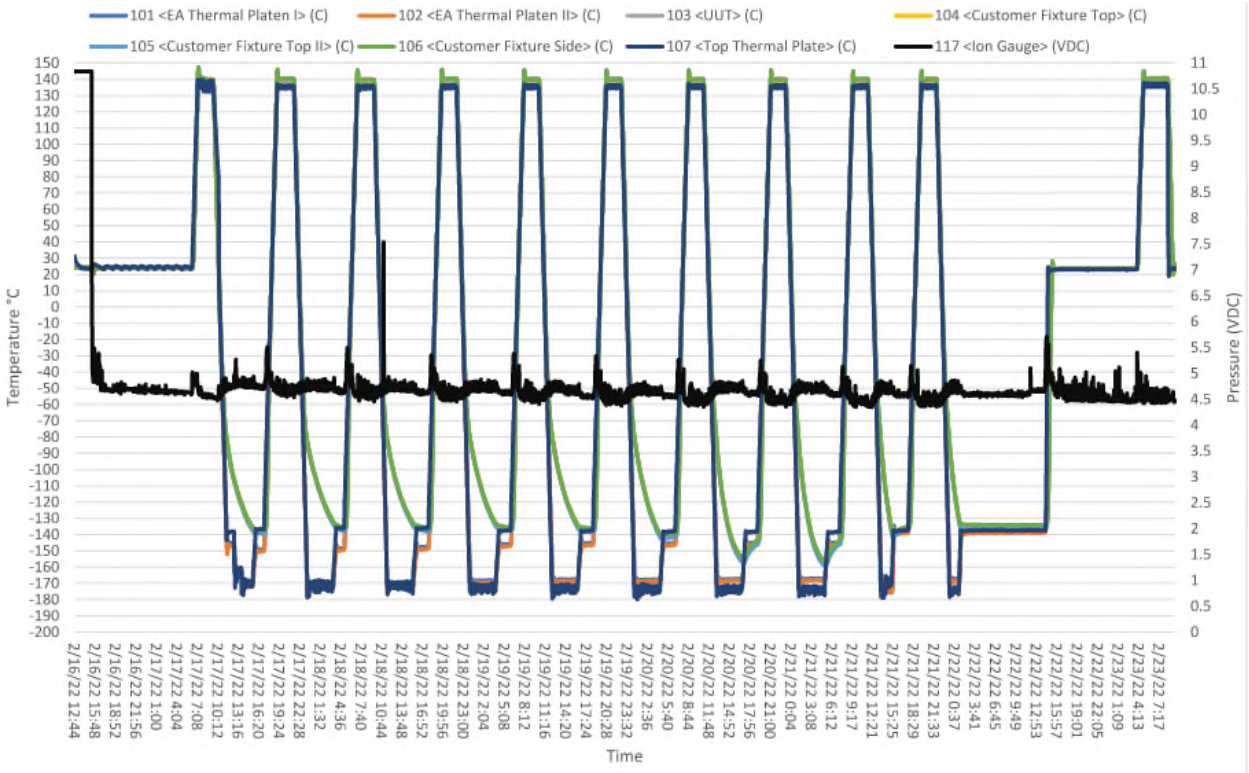

Figure 11. Mini HDRM TVAC Cycling Plot

The units experienced an out-of-tolerance extreme temperature on two cold cycles, where they reached as low as -159°C. This was deemed acceptable for the purpose of this testing, in which the units would be actuated following the TVAC cycling. There was no apparent impact to the units due to the thermal cycling or the out-of-tolerance test condition.

Two units were actuated at Cold temperature (-135°C) and two at Hot temperature (135°C). Both fired successfully. See Table 2 for conditions and actuation times.

Table 2. Mini TVAC Actuations.

Serial Number	Temperature (°C)	Firing Current (A)	Actuation Time (ms)
1	135	3.0	32
2	135	3.0	26
3	-135	3.0	38
4	-135	3.0	40

Output Shock

Two test units were actuated and the resulting output shock was measured. See Figure 12 for the test setup parameters and Figure 13 for a photo of the setup. Figure 14 shows the test result data. Each unit had an output shock <250g for the full measurement range of 10,000 Hz.

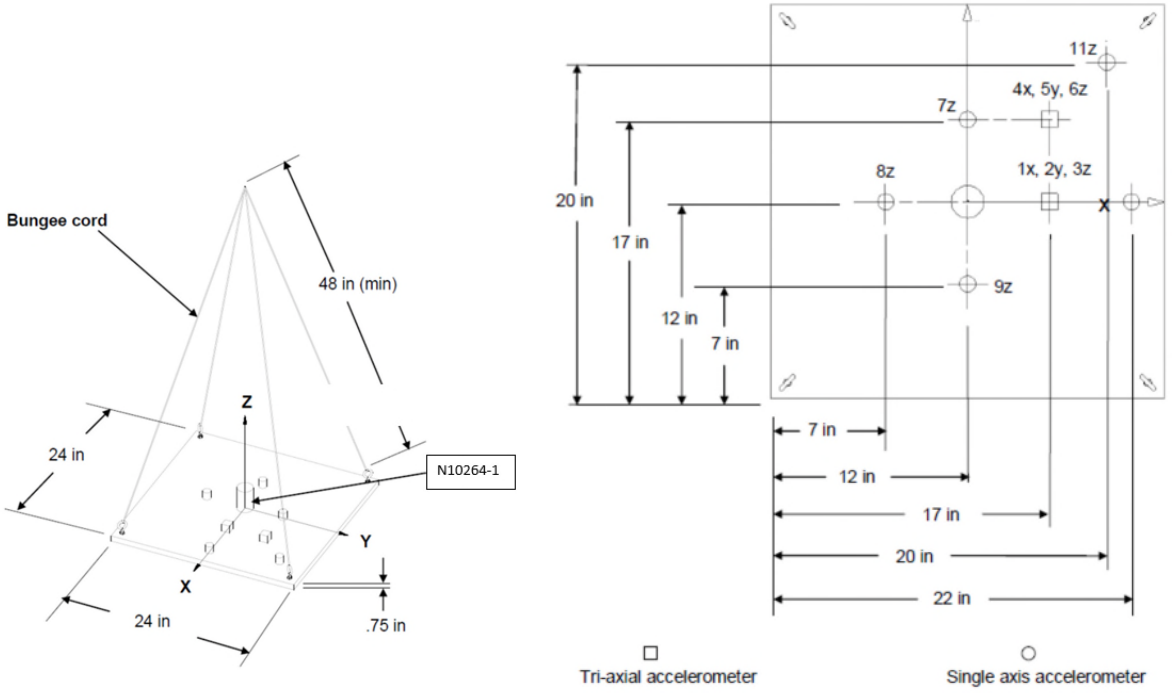

Figure 12. Mini HDRM Output Shock Test Setup Parameters

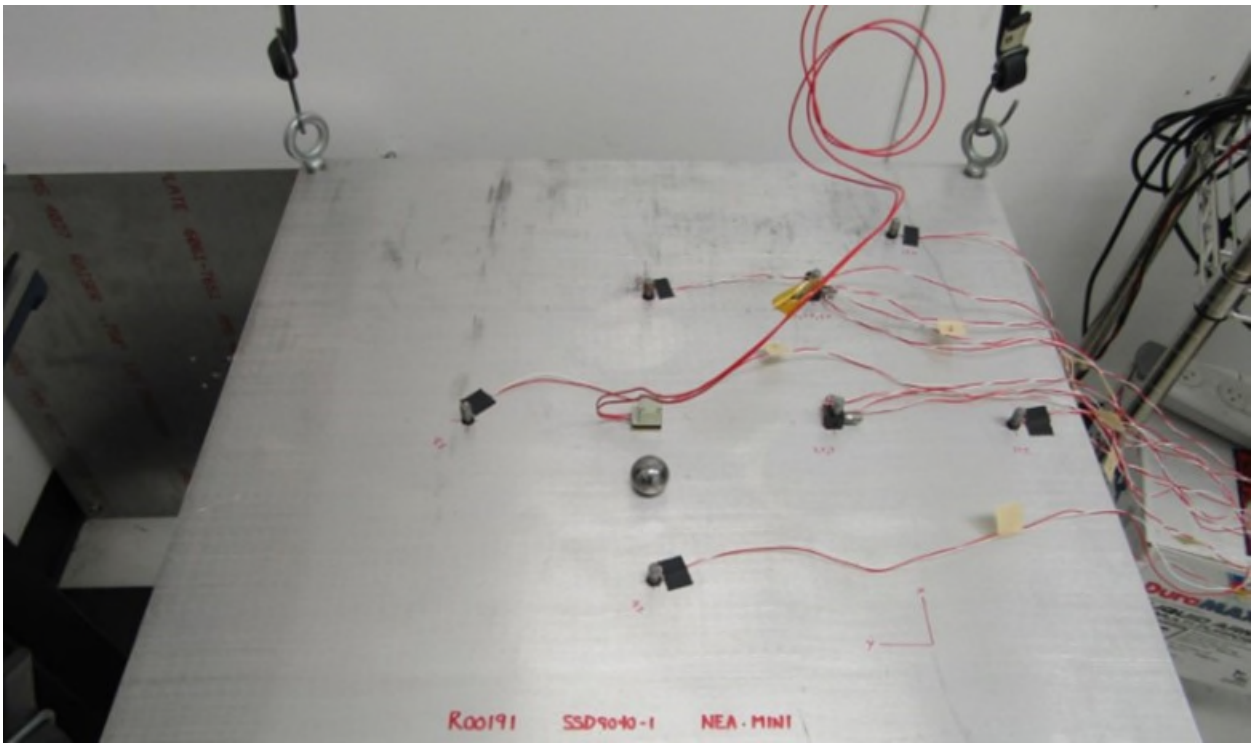

Figure 13. Mini HDRM Output Shock Test Setup Photo

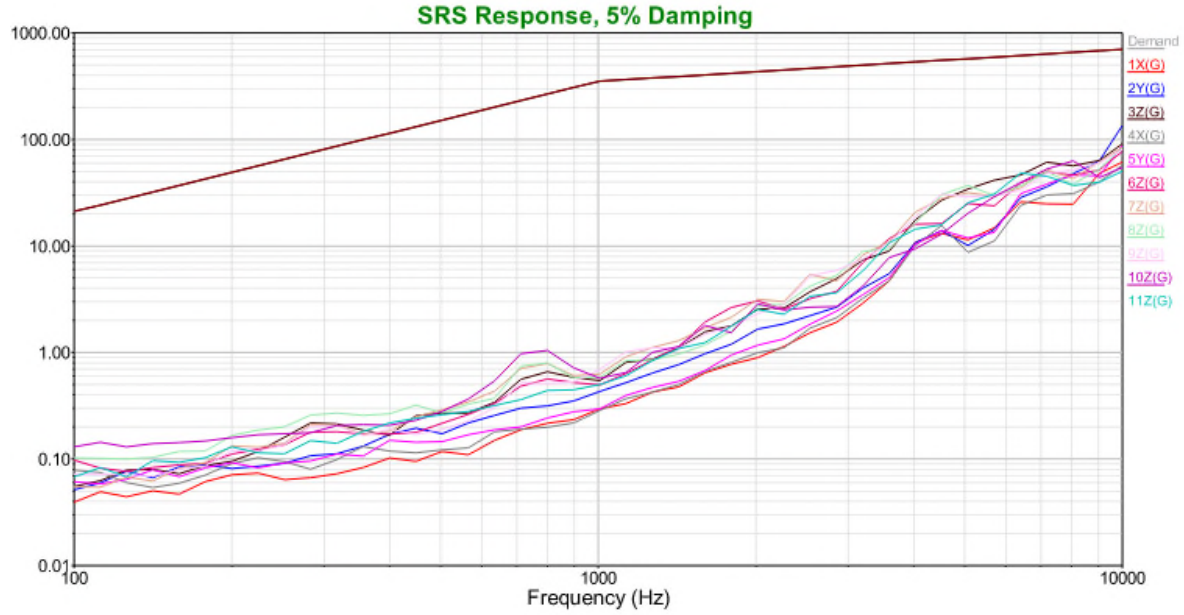

Figure 14. Mini HDRM Output Shock Test Results

Conclusions and Lessons Learned

The design, build, and test of the NEA® Mini HDRMs resulted in a number of lessons learned, as listed below.

1. Functional loads of at least 250 lbf are achievable with the updated Mini design.
2. Shock Output of the mechanism is well below expectations and industry standards.
3. The Mini devices successfully operate in extreme heat and cold space environments.
4. Miniature size mechanisms in general present manufacturing and test challenges that require special tooling and fixturing.
5. Very small fasteners (#1) present issues in machining, assembly, and test. The release rod was therefore upsized to a #4-40.
6. Upgrading to metallic parts from plastic increased the load and thermal capabilities of the device with minimal impact to cost.
7. Upgrading to metallic parts introduced a ground path that needed to be mitigated.
8. Units with no ground path mitigation function as designed.

References

1. Sudick, John and Geoff Kaczynski. "Development of the NEA® Mini for Low Load Applications." *Proceedings of the 44th Aerospace Mechanisms Symposium*, May 16-18, 2018, pp. 233-238.

Application of Internal Ballistic Modeling in the Design of a Bolt Cutter

Jason Kozmic*, Michael Rapp* and Hobin Lee*

Abstract

Utilization of an internal ballistic modeling tool combined with strategic characterization testing was shown to significantly aid the development and qualification of a pyrotechnic cutter. A quasi-equilibrium model was used to simulate the interdependencies between the thermodynamic and mechanical variables of the pressure cartridge, the cutter and the target. The cutting force dynamics, or the interaction between the cutter's blade and the target material, was considered to have the greatest design impact. To reduce the risk, a quasi-static cutting force model of blade force vs. target penetration was generated by running simple tests. The full performance model including the quasi-static cutting force estimation was shown to provide a high degree of accuracy and predictability for the actual cutting event and proved to be beneficial in accelerating the concept to development and qualification cycle.

Nomenclature

P	=	pressure
v	=	specific volume
b	=	covolume
R	=	gas constant
x	=	mass fraction
λ	=	linear burn fraction
a	=	burn rate coefficient
n	=	burn rate exponent
r	=	linear distance to achieve complete burn
m	=	gas mass
w	=	initial charge weight
$f(\lambda)$	=	propellant form function, fraction of mass burnt as function of linear burn fraction
T, T_0	=	temperature and initial temperature
q_{burn}	=	heat released by propellant burning
q_{loss}	=	heat lost through heat transfer
W_b	=	boundary work
h, u	=	specific enthalpy and energy
h_c	=	convection coefficient
SA	=	surface area
Ma	=	orifice throat mach number
γ	=	specific heat ratio
c_dA	=	orifice throat area with discharge coefficient
P_b	=	pressure acting on blade

* Chemring Energetic Devices, Downers Grove, IL; jkozmic@ced.us.com

Introduction

Internal ballistic modeling of pyrotechnic devices early in the development phase is an important tool to help understand design sensitivities and aid in the selection of critical design parameters. When the device requires predictable fracture or permanent deformation of structural elements, the dynamics and non-linear responses of the structural elements play a significant role in the overall performance of the pyrotechnic device. Examples of such devices are pyrotechnic cutters and pyrotechnic valves. For the pyrotechnic cutter, the material responses of the blade and the target, and for the pyrovalve, the fracturing of the material to open up the flow passage, have significant impact on the overall design of the device. These material responses are highly non-linear and transient so detailed strength and fracture models for such events are often not available. However, simplified models grounded in strategically designed engineering tests can often be a valuable substitute when timelines do not support obtaining specific high fidelity material models. Furthermore, there are many design factors that influence variability and cutting performance, including blade and anvil material, hardness, and geometry which can be captured in such tests. It was suggested by H. Lee [1] that a quasi-static (QS) cutting test could be a potentially useful means to characterize the complex cutting action. It is the goal of this work to demonstrate the applicability of this idea.

Chemring Energetic Devices (CED) has recently designed and qualified the pyrotechnic bolt cutter depicted in Figure 1 to reliably sever a 6.35 mm (0.250 inch) diameter custom 455 H1000 steel target rod. Internal ballistic modeling of the device was performed and supplemented with a simple, attainable fracture model tailored to the specific target being severed. The simple fracture model testing was performed early in the development phase knowing it would have major implications in the cutter design. The ballistic model and the fracture model were then used to help select critical design features such as the shear pin size and required propellant charge.

Figure 1. Qualified Pyrotechnic Bolt Cutter

Cutter Description and Analytical Model

The pyrotechnic bolt cutter is a guillotine style cutter designed to sever a 6.35-mm (0.250-inch) diameter custom 455 H1000 steel rod. The cutter includes an inert cutter body with a hardened blade secured within the body using a shear pin and an anvil which reacts to the target during cutting forces and prevents the blade from exiting the cutter body following completion of target severance. The cutter body is powered by a hermetically sealed pressure cartridge containing a main charge (RDX-based composite propellant) and is initiated using redundant initiators each primarily containing a $BKNO_3$ ignition charge. A conceptual layout is provided in Figure 2.

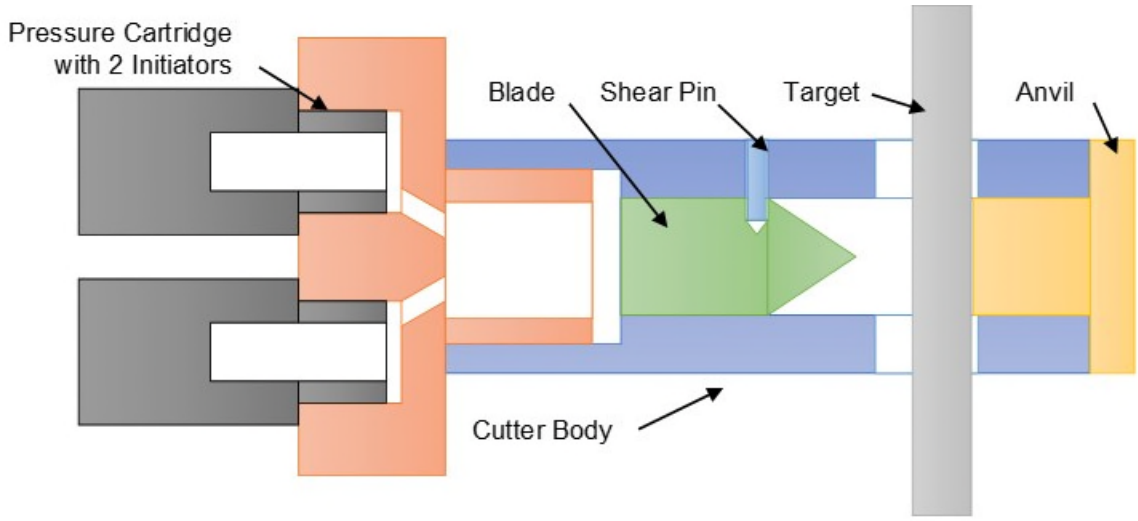

Figure 2. Conceptual Layout of Pyrotechnic Bolt Cutter

Upon receiving the all-fire stimulus, the $BKNO_3$ ignition charge within each initiator produces high temperature products of combustion which flow through small passages connecting the pressure cartridge initiator ports to the main charge chamber. These products ignite the main charge, which produces high pressure and high temperature gases behind the cutter blade. When the cutter body pressure reaches a sufficient pressure, the shear pin restraining the cutting blade fractures and the blade begins traveling toward the target. As the blade penetrates the target, resistive cutting forces oppose blade motion until uncontrolled crack propagation occurs and fractures the remaining target section, at which point there is little resistance to motion and the blade completes the stroke, striking the anvil.

The internal volume inside the cutter body and pressure cartridge initiator ports, the main charge, shear pin fracture force, and free stroke between blade tip and target are critical design parameters. These values require careful selection to ensure successful severance of the target. An analytical model was created to study these parameters and drive the design and charge selection.

Analytical Model

CED's internal ballistic model (called CIBAC, CED Internal Ballistics Analysis Code) captures the pertinent physics occurring within the cutter including propellant burning (solid to gas conversion), thermodynamics, the mechanics of the cutting blade's motion, high speed gas flow between internal chambers, heat losses, and resisting forces associated with target severance. At its core, CIBAC is a lumped parameter model in which all solid propellant is converted to an inert working fluid that flows between control volumes and performs boundary work through volume expansion. CIBAC is described by the following equations where index i specifies the gas species (igniter product, output charge product, or initially present gas) and index j specifies the control volume (CV, three total in the device presented herein), and index k specifies the orifice (2 total in the device presented herein).

$$P_j\left(v_j - \bar{b}_j\right) = \bar{R}_j T_j \tag{1}$$

$$\bar{R}_j = \sum_i x_{i,j} R_i \tag{2}$$

$$\bar{b}_j = \sum_i x_{i,j} b_i \tag{3}$$

$$\dot{\lambda}_{i,j} = \frac{a_i P_j^{n_i}}{r_i} \tag{4}$$

$$\dot{m}_{burn_{i,j}} = w_{i,j} f_i'(\lambda_{i,j}) \dot{\lambda}_{i,j} \tag{5}$$

$$\dot{m}_{i,j} = \dot{m}_{in_{i,j}} - \dot{m}_{out_{i,j}} + \dot{m}_{burn_{i,j}} \tag{6}$$

$$\dot{T}_j = \sum_i \left[\dot{m}_{burn_{i,j}} q_{burn_{i,j}}\right] - q_{loss_j} - \dot{W}_{b_j} + \sum_i \left[\dot{m}_{in_{i,j}} \left(\hat{h}_{in_{i,j}} - u_{i,j}\right)\right] - \sum_i \left[\dot{m}_{out_{i,j}} \left(\hat{h}_{i,j} - u_{i,j}\right)\right] \tag{7}$$

$$q_{loss_j} = h_{c_j} SA_j \left(T_j - T_{w_j}\right) \tag{8}$$

$$\frac{T_{w_j} - T_{0_j}}{T_j - T_{0_j}} = erfc(0) - e^{\frac{h_{c_j} \alpha_j t}{k_j^2}} erfc\left(\frac{h_{c_j} \sqrt{\alpha_j t}}{k_j}\right) \tag{9}$$

$$Ma_p = \min\left\{\left(\left(\left(\left(\frac{2}{\gamma_p + 1}\right)^{-\frac{\gamma_p}{\gamma_p - 1}}\right)^{\frac{\gamma_p - 1}{\gamma_p}} - 1\right)\left(\frac{\gamma_p - 1}{2}\right)^{-1}\right)^{\frac{1}{2}}, 1\right\} \tag{10}$$

$$\dot{m}_p = c_{d_p} A_p Ma_p \sqrt{\gamma_p R_p \frac{T_p}{1 + \frac{\gamma_p - 1}{2} Ma_p^2}} \left(\frac{1}{1 + \frac{\gamma_p - 1}{2} Ma_p^2}\right)^{\frac{1}{\gamma_p - 1}} \tag{11}$$

$$P_b A_b - F_c = m_b \ddot{X}_b \tag{12}$$

Equations (1) – (3) describe the equation of state for the products of combustion assuming Amagat's Law of Partial Volumes for the gas mixture. Equations (4) and (5) describe the rate of solid propellant to gas conversion (burning). Equation (6) expresses continuity for the gaseous products and Equation (7) expresses conservation of energy for each CV. Equation (8) and (9) describes convective heat losses within the device assuming an infinite plane wall and Equations (10) – (11) describe isentropic nozzle flow through the orifices connecting CVs. Equation (12) expresses conservation of momentum for the cutter blade. The cutting force, Fc which appears in the momentum equation is the major unknown which this work addresses through the use of a simplified quasi-static cutting force profile. This model was implemented in MATLAB and used to evaluate the cutter and to drive critical design decisions.

Cutter Force Characterization

The main energy and power requirement for the cutter is driven by the resistive cutting force; therefore, a reasonable analytical model is necessary to build a useful performance model. The high speed cutting event is complex and the cutting force depends not only on the target's quasi-static (QS) stress versus strain characteristics (of which the data are typically available in public domain), but also on the materials strain rate hardening and thermal softening behavior as well. Additionally, the fracture criteria of the target is complex and the detailed failure criteria for the target (Johnson-Cook failure or similar) is not readily available. Such lack of detailed material characteristics including the fracture criteria is not uncommon in typical design and development of these devices. In reality, schedule demands often preclude the raw material characterization required to obtain high fidelity strain rate and temperature dependent material models. In lieu of a detailed cutting force model, a simple model based on the quasi-static cutting force versus cutting distance was selected as alternate approach. The model is conceptually illustrated in Figure 3 and assumes an increasing force resists increasing blade penetration until a critical cutting depth is achieved leading to uncontrolled crack propagation through the remaining cross section at which point the target is fully severed. Such a model is admittedly less accurate than an explicit material model or fracture model, but is quick and easy to determine.

Figure 3. Illustration of Cutting Depth Leading to Uncontrolled Crack Propogation

The quasi-static model was determined by severing three (3) 6.35-mm (0.250-inch) custom 455 H1000 sample targets using a representative cutter. The blade was forced against the target using a hand pumped hydraulic ram while hydraulic pressure was monitored and ram stroke measured using an linear variable differential transducer. The collected data provided a cutting force vs distance curve which was enveloped using a piecewise linear lookup table for use in the internal ballistic model. A photo of the test setup and the resulting cutting force vs distance model is provided in Figure 4. In each of the three (3) samples, the blade penetrated the target between 3.56 mm (0.14 inch) and 3.81 mm (0.15 inch) before fracture occurred with uncontrolled crack propagation through the remaining section of the target. Within the context of the simple quasi-static cutting force model, this was used as the critical cutting distance to achieve fracture and the cutting force was reduced to zero once this was reached.

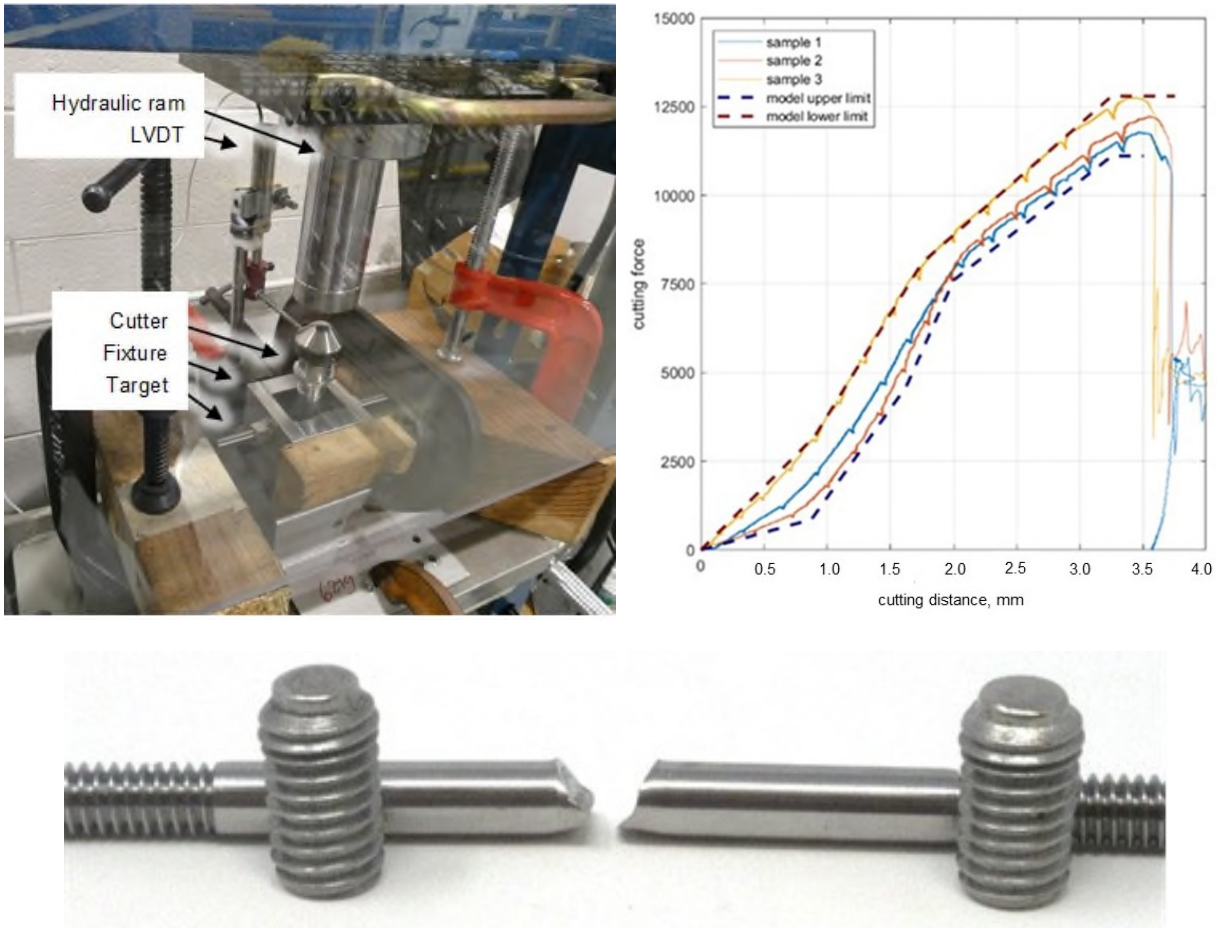

Figure 4. Cutting Force Measurement Setup (left); QS Cutting Force Model (right); Severed Target (bottom)

Model Validation

The analytical model parameters were continuously modified and validated as data was collected during the development phase of the program. Closed bomb (2 cm^3) testing, depicted in Figure 5, was performed to characterize the pressure cartridge output in a small volume and to ensure the main propellant modeling characteristics (burning form function, linear burning rates, impetus, etc.) were representative of the propellant lot being used. The analytical model previously described is readily tailorable to a closed bomb configuration by turning off mass flow through all orifices and fixing the blade such that no boundary work is performed by the gas products. Results of a typical closed bomb trace and model prediction is presented in Figure 6 and demonstrate a satisfactory match, indicating the model accurately captures the burning and gas generation characteristics of the pressure cartridge.

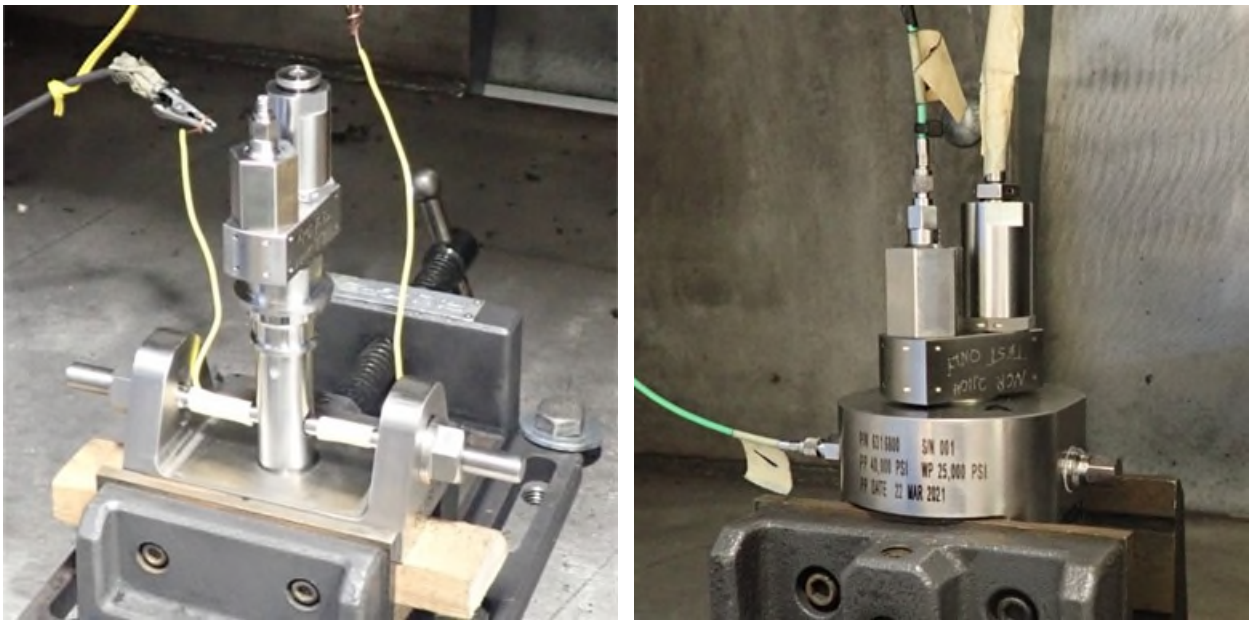

Figure 5. Functional Test Setup (left) and 2-cm^3 Closed Bomb (right)

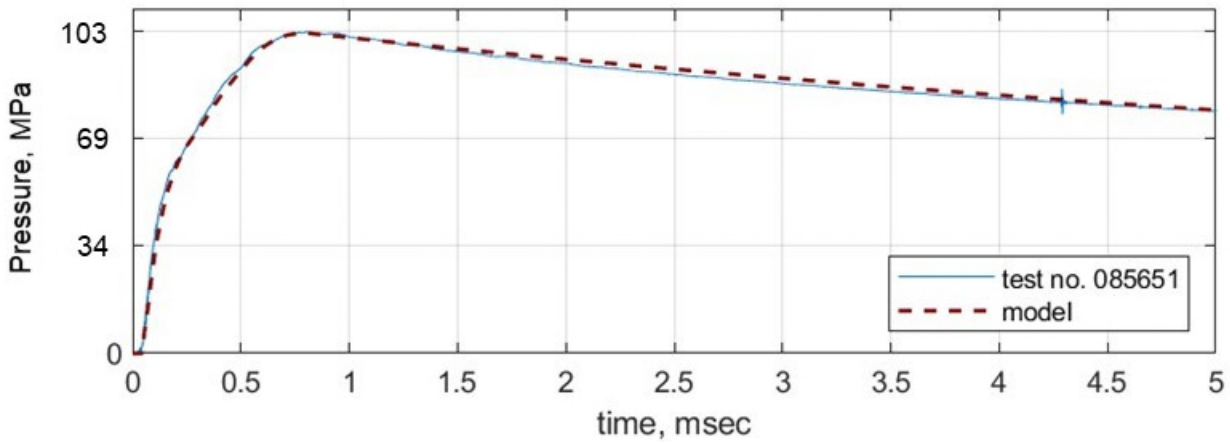

Figure 6. 2-cm^3 Closed Bomb Model Comparison

The analytic model of the cutter was evaluated on an on-going basis as part of CEDs charge development program and was used to drive subsequent charge development loadings. The purpose of the charge development program was to determine the critical charge above which the cutter would successfully sever the target and below which the target would not be fully cut. An initial charge was selected using the analytic model setup based on the developed quasi-static severence mode, 2-cm^3 closed bomb test results, and initial engineering estimates for other model parameters. Initial baseline functional tests were performed (see Figure 5 for test configuration) and the model was refined based on the results then used to generate additional trial charges. The charge development effort is summarized in Table 1 with the loaded charge expressed as a fraction of the final determined production charge. Note that no peak pressure is reported for tests performed with 2 initaitors as pressure was measured in the redundant initiator port and a second initaitor precluded measurement.

Table 1. Charge Development Test Results

Unique Test No.	No. Initiators	Loaded Charge/ Final Charge	Test Temp	Peak Pressure	Target Severence
085653	1	109%	Amb	79 MPa	Pass
085654	2	110%	Amb	-	Pass
085883	1	101%	Amb	*Not Captured*	Pass
085884	1	94%	Amb	78 MPa	Pass
085885	1	86%	Amb	73 MPa	Pass
085886	1	77%	Amb	71 MPa	Pass
085887	1	69%	Amb	63 MPa	Pass
085945	1	61%	Amb	65 MPa	**Fail**
085946	1	53%	Amb	61 MPa	**Fail**
085949	2	152%	Amb	-	Pass
085950	2	160%	Amb	-	Pass
085951	2	120%	Hot	-	Pass
085952	2	136%	Hot	-	Pass
085953	1	80%	Cold	65 MPa	Pass
085954	1	70%	Cold	64 MPa	Pass

The analytic model output for test numbers 085887 and 085945 are presented in Figure 7 along with the measured test pressure. These two test conditions represent critical cases as the charge used in test number 085887 succesfully severed the target and a small reduction in charge, test number 085945, failed to fully cut the target. These cases therefore represent a critical test of the analytic model's usefulness, namely the ability to accurately predict the critical charge.

The analytic model correctly captures full severence of the target in simulation of test number 085887 and failure to fully cut in test number 085945. Post-function measurements of blade penetration without severence from test number 085945 indicated the blade had penetrated the target 3.45 mm (0.136 inch) prior to the blade momentum being halted without target severence and agree well with analytic model predictions. Overall peak pressures and secondary peak pressures (occurring after blade reaches end of stroke) from the model agreed well with measurements (within 5%) although the model predicts a slightly longer action time (approximately 0.2 ms). Examination of the pressure curve indicates the initial pressure rise may be predicted too long and could be a result of flake breakup resulting in a different form function than that which was implemented based on 2-cm^3 closed bomb testing. Despite this timing difference, the

model was determined to be sufficient for engineering application based on the overall agreement in peak pressures, successful prediction of total blade penetration, and overall time scale accuracy being well within the device's required function time.

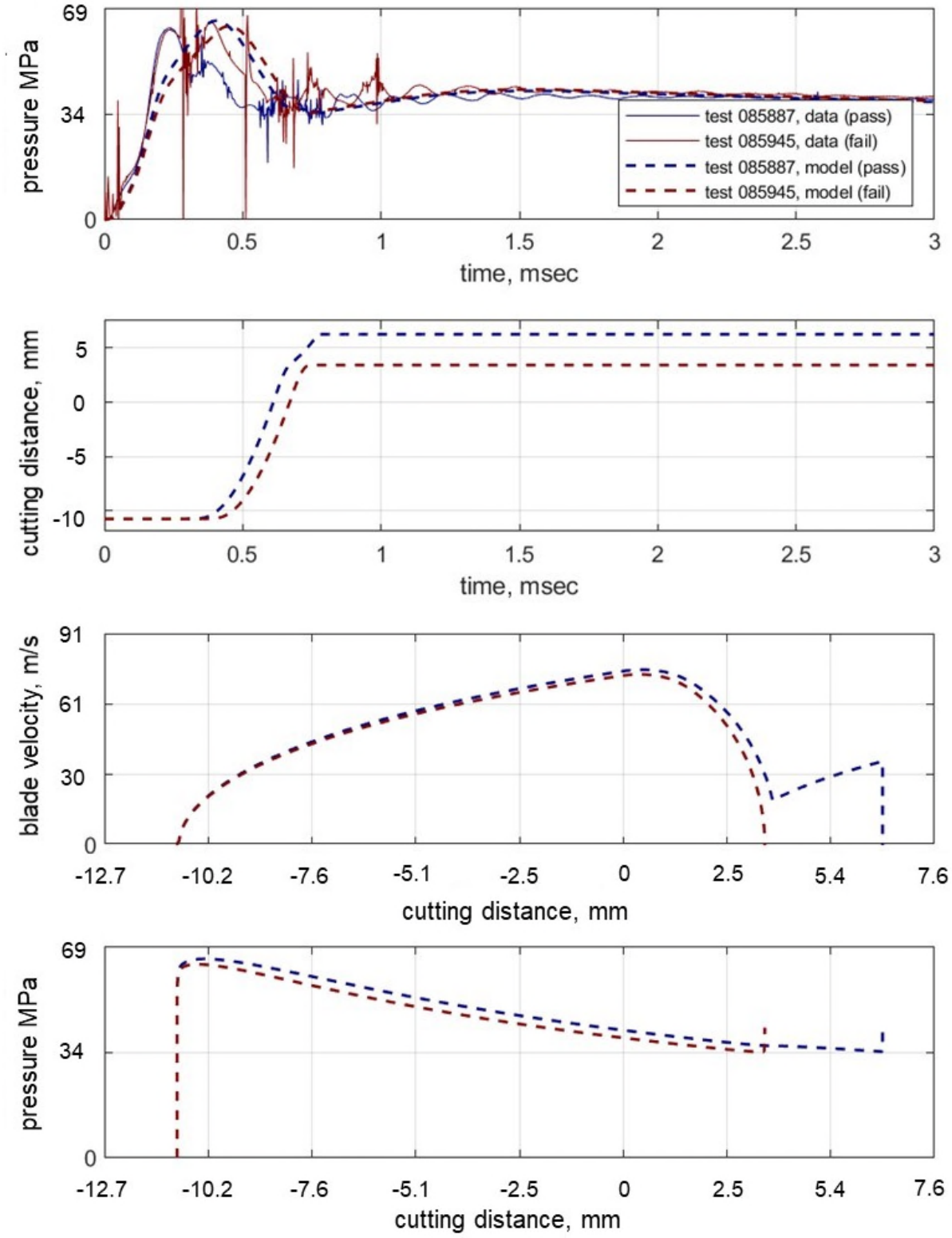

Figure 7. Cutter Model Comparison with Measured Pressure Data (top) and Additional Model Output

Cutter Distance Observations

The effect of increasing charge on the cutting depth prior to uncontrolled fracture is depicted in Figure 8 and is plotted as a function of the charge to nominal charge ratio in Figure 9. The depth of cut prior to uncontrolled fracture was estimated using a microscope and imaging software. Quasi-static samples exhibited a smooth cut and clean transition from blade penetration to uncontrolled crack propagation with approximately 3.68 mm (0.145 inch) of the severance occurring as a result of blade penetration. Charge ratios from zero (quasi-static data) up to approximately 110% of nominal resulted in very similar blade penetration depth prior to uncontrolled fracture and maintain the clean transition between penetration and crack propagation. At higher charge ratios (>140% of nominal charge weight) which resulted in higher pressures and cutting speeds, a dramatic reduction in blade penetration depth occurred and the clean transition from blade penetration to crack propagation was lost. Based on these results, it is believed that the quasi-static cutting model with a failure criteria based solely on blade penetration was a reasonable model choice for the cutting speeds encountered during a typical cutter firing, but would have been a poor choice for higher charge (cutting speed) conditions.

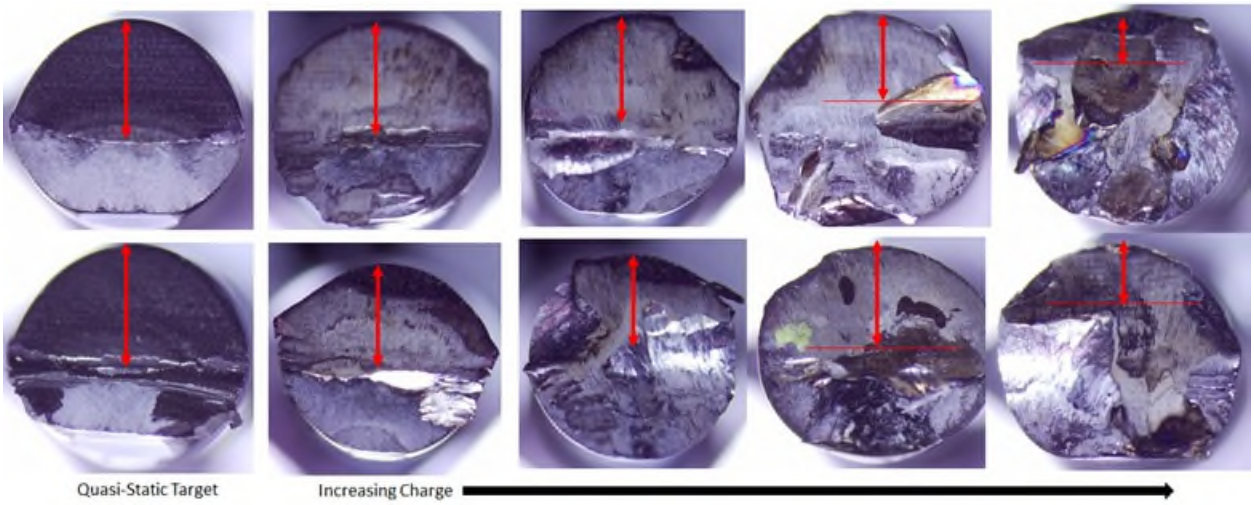

Figure 8. Effect of Cartridge Charge on Cutting Depth/ Surface

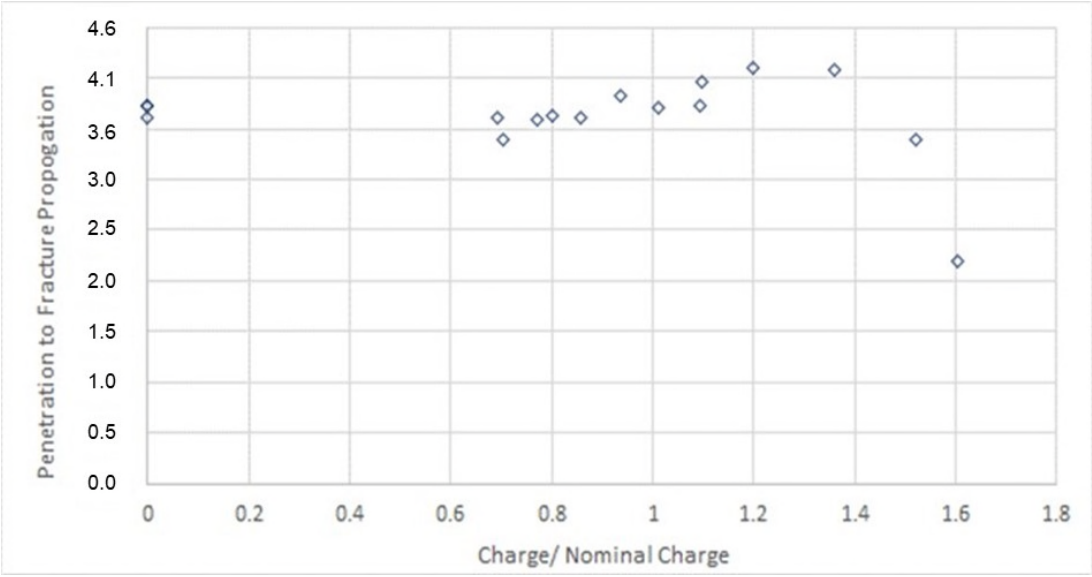

Figure 9. Cutting Depth to Achieve Uncontrolled Fracture Propagation as Function of Charge Ratio

Suggested Extension of Work

The presented model can be readily extended to cutters of differing size or target materials where the accuracy is tied to the fidelity of the cutting force estimation. When developing pyrotechnic cutters such as that presented in this paper, it is recommended that the quasi-static cutting force test be performed on the target samples. If target samples or representative cutter blades for testing are not available, then it may be reasonable to scale the results based on size and strength of target relative to available QS data. CED has not yet evaluated the accuracy of scaling results, although future work could include an assessment of scalability to determine if a linear scaling is appropriate or a more complex scaling scheme is required.

While the subject of this work was a pyrotechnic cutter, there are many other pyrotechnic devices that require the fracturing of structural members. Modeling of these devices can be improved by performing similar force versus stroke characterization testing. The physics of pyrotechnic or ballistic events are such that that the propellant burning, the thermodynamics, and the mechanical responses are highly interdependent. Therefore, having a good starting point model of the resisting force profile is critical to build a useful model that captures the structural elastic/plastic response and the failure criteria. As with the discussed cutting depth as a function of charge (or the cutting velocity), an assessment of the QS applicability would be needed on a case by case basis to verify that a reasonable model is obtained.

Conclusion

Internal ballistic modeling of pyrotechnic devices used to reliably fracture or sever structural members can be supplemented with simple-to-obtain quasi-static force versus stroke characterization. It was shown to significantly help with the selection of design parameters and then predict performance under different design cases. An example of how this can be accomplished was provided for a recently qualified bolt cutter but this work can be extended to other devices with similar requirements. It is important to compare the quasi-static results with high speed functional results to determine if the fracture event occurs on a time scale at which the quasi-static force versus stroke curve gives a reasonable approximation or if more complex material strength and fracture models are warranted, such as during a detonation driven event. Future work may include development of a method to scale 6.35-mm (0.250-inch) diameter target bolts to different sized targets or different materials.

References

1. Lee, H., "Underwater Performance Characterization of A ballistic Guillotine Cutter at Operating Temperature Extremes" *50th AIAA/ ASME/ SAE/ ASEE Joint Propulsion Conference*, July 2014

Scan Mechanism Design for Large Deployable Reflector

Christian Hehr*, Daniel Schmalholz* and Cristovao Cardoso*

Abstract

Airbus Defence and Space GmbH Germany is developing the Scan Mechanism (SCM) for the instrument of the Copernicus Imaging Microwave Radiometer (CIMR) Satellite. The CIMR mission will carry a wide-swath conically scanning multi-frequency microwave radiometer to provide observations of sea-surface temperature, sea-ice concentration and sea-surface salinity. Uniquely, it will also observe a wide range of other sea-ice parameters.

The SCM will rotate the Large Deployable Reflector. Its size is approximately 8-m diameter with an arm of approximately 8 m. This results in significant rotating mass, inertia and unbalance which needs to be handled by the SCM in combination with extremely high pointing requirements. This combination is considered unique for the space business. A similar NASA Mission with SMAP[1] (Soil Moisture Active/Passive) is available however with a smaller reflector size of 6 m[1] which is approximately 56% of CIMR reflector surface area.

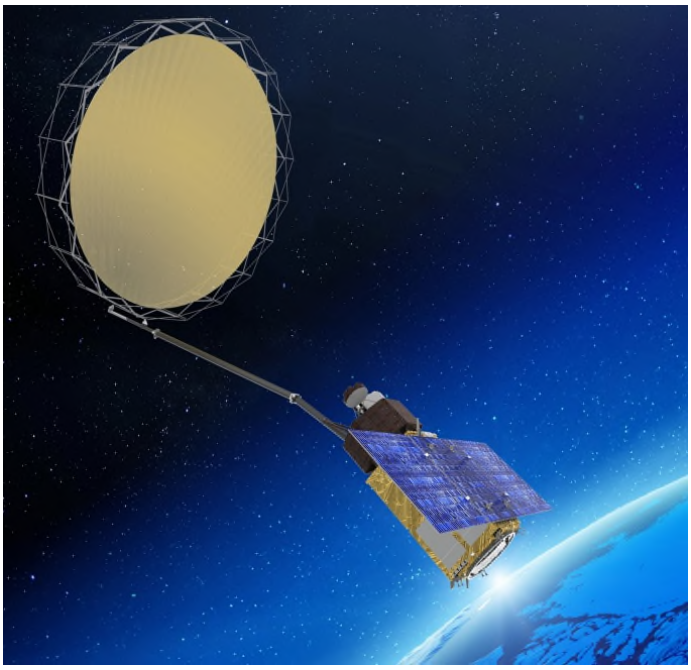

Figure 1: CIMR Image (ESA Homepage, 2021)[2]

Introduction

Many years of experience exists for design development, manufacturing verification and orbit feedback of Scan Mechanisms[3,4,5,6,7] with different requirements. Key requirements are high speed accuracy, specific rotating mass properties, low micro vibration emission, high pointing accuracy and long lifetime. Thanks to

* Airbus Defence and Space GmbH, Friedrichshafen, Germany;
Christian.Hehr@airbus.com; Daniel.Schmalholz@airbus.com; cristovao.cardoso@airbus.com

the modular design, adaptation is manageable; however, the CIMR requirements cause some challenges which are shared in this paper. Furthermore, a design adaptation for the new mission allows implementation of the lessons learned from several Scan Mechanisms of previous MetOP Second Generation projects.

The Scan Mechanism (SCM) is the rotating mechanical and electrical link between the CIMR Platform with the arm and the Large Deployable Reflector. The SCM design consists of a Drive Unit, a Launch Offloading Device (LOD) and a Power and Data Transfer device (Roll-Ring). The LOD is required to decouple the Instrument load from the SCM during launch. The design of the SCM is based on a standardized drive unit design that has been flown on previous missions, such as MHS, MWRI, ADM and which also formed the design baseline for the MWI, ICI, MWS and METImage scanning mechanisms for MetOp-SG and MWRI for FY-3. The main components of the standard drive unit are ball bearings, a brushless DC motor, and a digital encoder. To meet the CIMR requirements, several modifications of the standard design were performed, which are outlined herein. The SCM drives a heavy instrument with the reflector resulting in an angular momentum of maximum 1090 Nms. The scan performance is achieved by the closed control loop included in the Scan Drive Electronics.

Scan Mechanism (SCM)

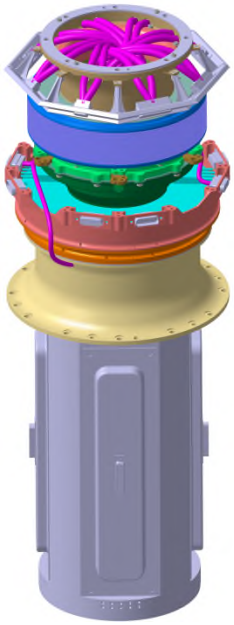

Figure 2: SCM

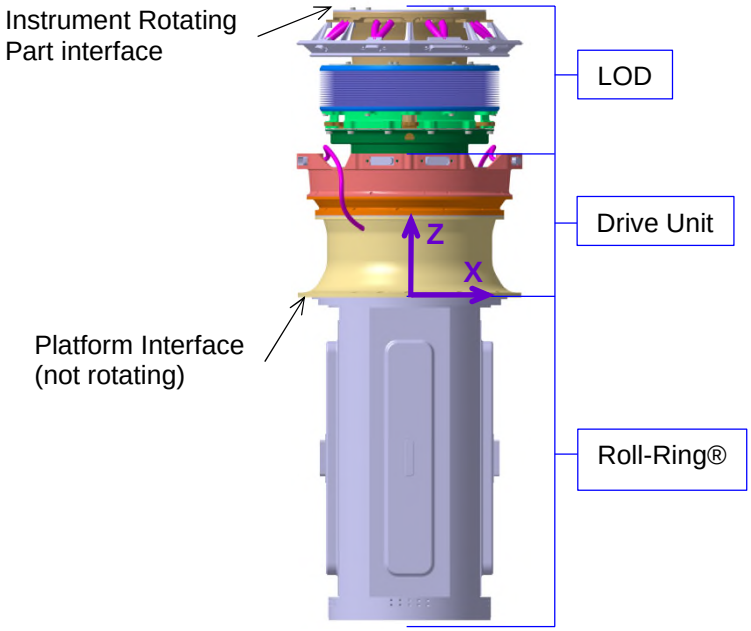

Figure 3: SCM main components and coordinate system

Major design adaptations for CIMR

During the mission, the heavy rotating mass introduces high disturbance moments into the Scan Mechanism mainly due to static and dynamic unbalance, orbit pulsation, and orbit maneuver. High angular stiffness is required for pointing performance of the Scan Mechanism due to the described disturbance and also to achieve the required Eigen frequency of the orbit configuration. In order to increase SCM stiffness, pointing performance and load capability, considerable changes have been done on the drive unit, although maintain applicable previous heritage. For the LOD, the design is upgraded and breadboard activities are currently ongoing for TRL6 demonstration within B2 phase.

Lessons Learned from previous projects

A power and data transfer device is used to transfer the power from the stator to the rotating instrument and the exchange of data between instrument and platform. The data are transferred via Low Voltage Differential Signaling. In the previous project, the selected technology was a Roll-Ring®[1] from Diamond Roltran LLC based on an outcome of a pre-development study. The aim of the study was to evaluate its performance and to demonstrate the feasibility of achieving the required performance over the lifetime and in a representative environment prior to MetOp SG start. The study was successfully completed. Airbus gained a lot of experience during the MetOp SG Project with the Roll-Ring®.

This next generation slip-ring provides low resistance noise, low debris, and long lifetime. The reason is the use of electrical rolling contacts instead of sliding contacts. The life test has shown that the required performance for power and signal is achievable after more than 230 million life qualification revolutions. However, the PDTD development during MetOp SG was not free of issues, which will be described in this paper with improvements implemented for the CIMR Mission in the life test section.

Drive Unit Design Changes for CIMR

To take advantage of heritage, the drive unit uses the same two bearing pairs as in previous MetOP Second Generation projects. Each bearing pair is in an X configuration and supported by a flexible membrane on the housing side. These membranes deliver the required flexibility to handle the misalignment between bearing pairs and thermal induced strains, maintaining the bearing stresses under acceptable values.

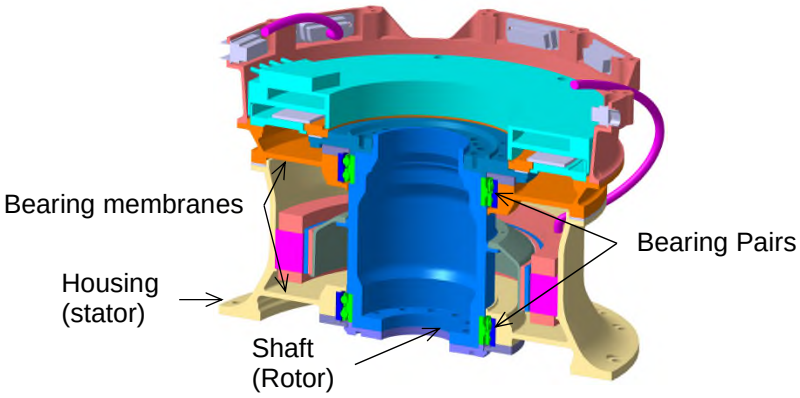

Figure 4: Drive Unit.

On the other hand, high angular bending stiffness is required to achieve the pointing performance of the Scan Mechanism while coping with disturbance torques, and also to achieve the required Eigen frequency of the orbit configuration. Disturbance moments during mission are caused by the heavy rotating mass with static and dynamic unbalance, orbit pulsation, and orbit maneuver. In CIMR project, the rotating mass is 4-times and the inertia 180-times larger than in previous MetOP Second Generation projects.

The following goals:

1. Low axial stiffness between bearing pairs,
2. High angular stiffness of the SCM (extremely challenging to reconcile with previous goal),
3. Acceptable bearing loads (also under wide temperature range and considerable thermal gradients),
4. Low mass,

are expected to be achieved with the following modifications to the previous design:

[1] Roll-Ring® is a registered trademark of Diamond-Roltran LLC

- o Considerable increase of distance between bearing pairs (this increased SCM angular stiffness without changing stiffness between bearing pairs)
- o Increase of diameter and thickness of bearing membranes. This increases the X and Z translation stiffness at each bearing pair, with low change on Z translation and X/Y rotation stiffness, contributing for the reconciliation of goals 1 and 2.
- o Change of shaft and housing material from titanium to stainless steel (this eliminated bearing stresses due to wide temperature range; also allowed to achieve high stiffness in the bolted joints of the shaft where space is the limiting factor)
- o Straightening and shortening of load paths
- o Condensation of functionalities in a reduced number of parts, reducing interfaces in the load path (leading to more complex geometries and demanding manufacturing)

The estimation is an angular stiffness increased of a factor 9 regarding the previous MetOP Second Generation projects, with a mass increase of only factor 1.6 on the parts in the load path (orbit configuration). A trade-off has been performed at requirement level between stiffness and mass and finally the mass and stiffness optimized design is achieved with some effort.

LOD

Concept and challenges

The patented LOD is a coupling which is open during launch and is closed in orbit. The purpose is to interrupt the load path, and so avoid that the launch loads of the instrument rotating part go thru the SCM with the bearings.

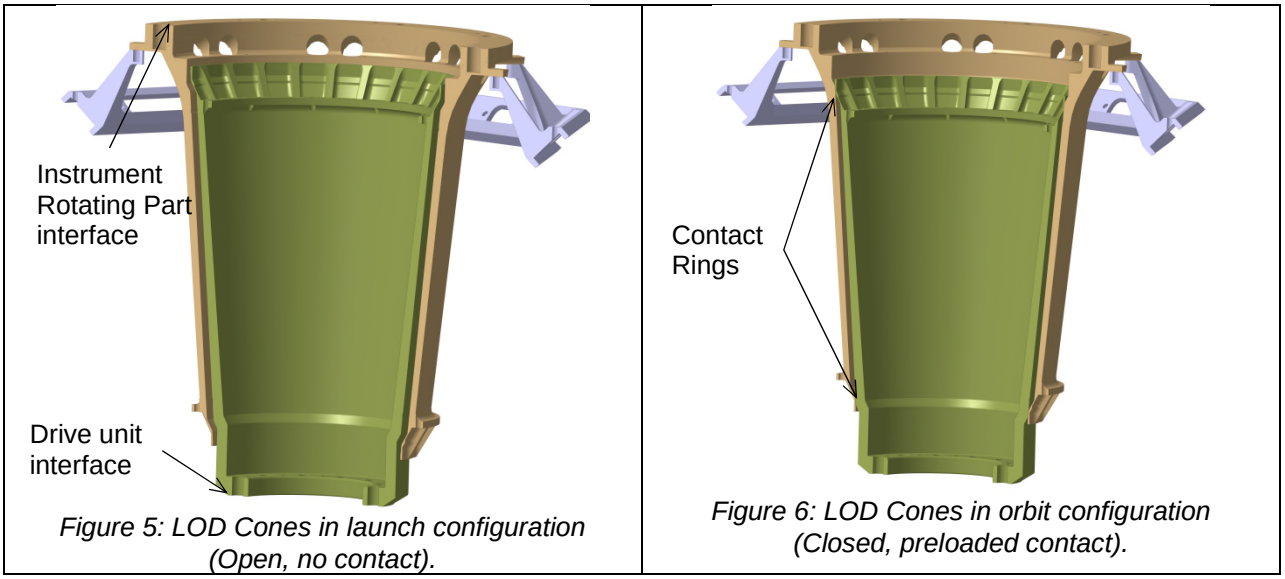

Figure 5: LOD Cones in launch configuration (Open, no contact).

Figure 6: LOD Cones in orbit configuration (Closed, preloaded contact).

The main requirements for the LOD are:

1. Enough clearance during launch, so that no loads are transferred to the Drive Unit (6 DOF free)
2. Reliable transition from launch to orbit configuration (avoid failure modes like getting stuck halfway due to friction or unforeseen clashes, capability to achieve orbit configuration independently of starting conditions)
3. Low energy release during configuration change (the kinetic energy of transition will bend the bearing membranes, and if more than the acceptable values, will cause a clash on the glass encoder disc)
4. 6 DOF locked at orbit configuration, with high load capacity to handle maneuver loads
5. High repeatability (to achieve required pointing performance)

6. High angular stiffness (X and Y), to achieve pointing performance and first Eigen frequency in orbit

Low local stiffness for high repeatability and high SCM stiffness

The current design is the result of assessing several concepts and performing many design-analysis iterations. The cones with 2 contact rings create an over-constrained coupling. This is not ideal because when tolerances are different than absolute zero, it will lead to having contact on one ring only, meaning that: repeatability, load capacity and stiffness will not be achieved.

The way to ensure contact on both contact rings is to elastically deform the contact regions to overcome the manufacturing tolerances. For this, low stiffness in the contact regions and high preload are desired.

To be highlighted the following challenging reconciliations:

a. low stiffness in the contact regions, with high LOD angular stiffness (X and Y),
b. High preload, with low energy release during configuration change (avoiding active components like motors and sensors).
c. Low stiffness in the contact regions, narrow manufacturing tolerances.

Reconciliation “a” is achieved by tuning the contact stiffness value and directions. The idea behind the current geometry is to reduce axial stiffness in the tangential direction (easy change of perimeter), while minimizing the losses of wall bending and shear stiffnesses.

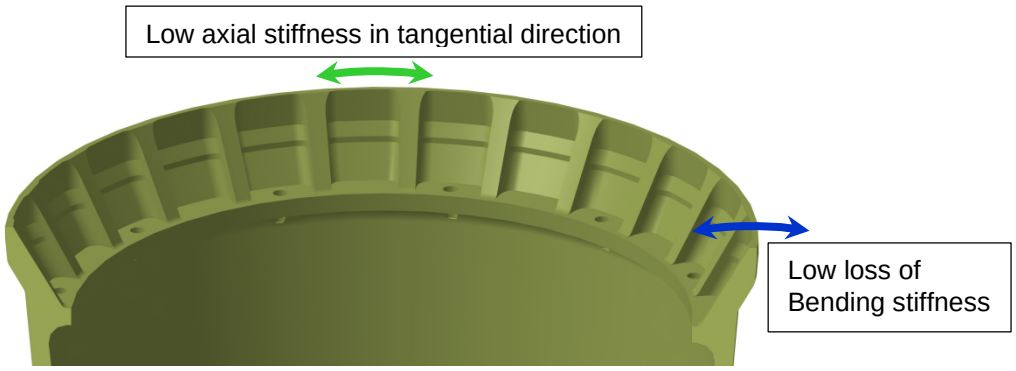

Figure 7: Cone contacts local stiffnesses.

Reconciliation “b” is achieved by actuating the configuration change with a spring delivering low force, as constant as possible thru the stroke (low stiffness spring). In parallel, permanent magnets are used to increase the closing force at the end of the stroke.

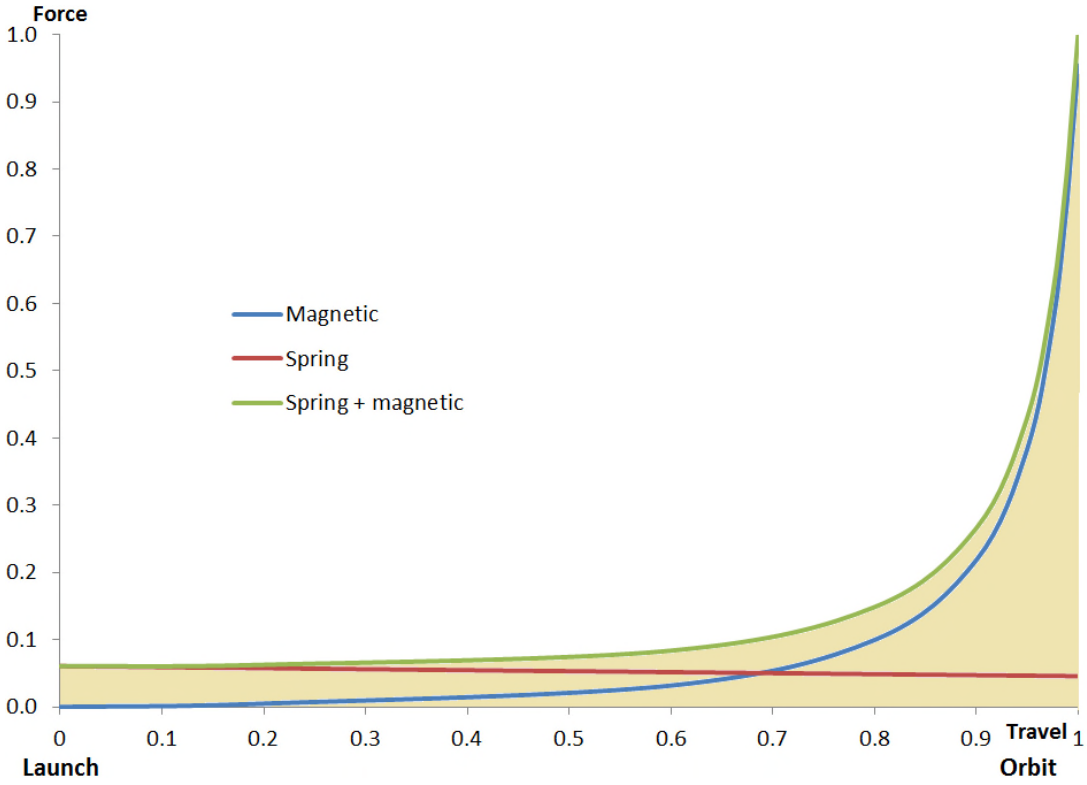

Figure 8: The energy released for the actuation is the area under the green curve (presented values are adimensional).

Reconciliation "c" is challenging because the low stiffness in the contact regions leads to considerable local deformations under cutting loads during machining. These deformations make it almost impossible to achieve well defined dimensions and geometries. The expectation is this reconciliation with a correct tuning of stiffness and machining parameters.

LOD Dynamic analysis

Dynamic simulations were made to predict the configuration change. The main parameters modeled were:

- Masses and inertias of: S/C non rotating part; SCM rotor; Instrument rotating part.
- Most relevant stiffnesses: cones coupling; bearing membranes …
- Actuating forces: spring; magnetic,
- Friction on contacts
- Damping; bearings, material.

Some results are presented in Figures 9 and 10.

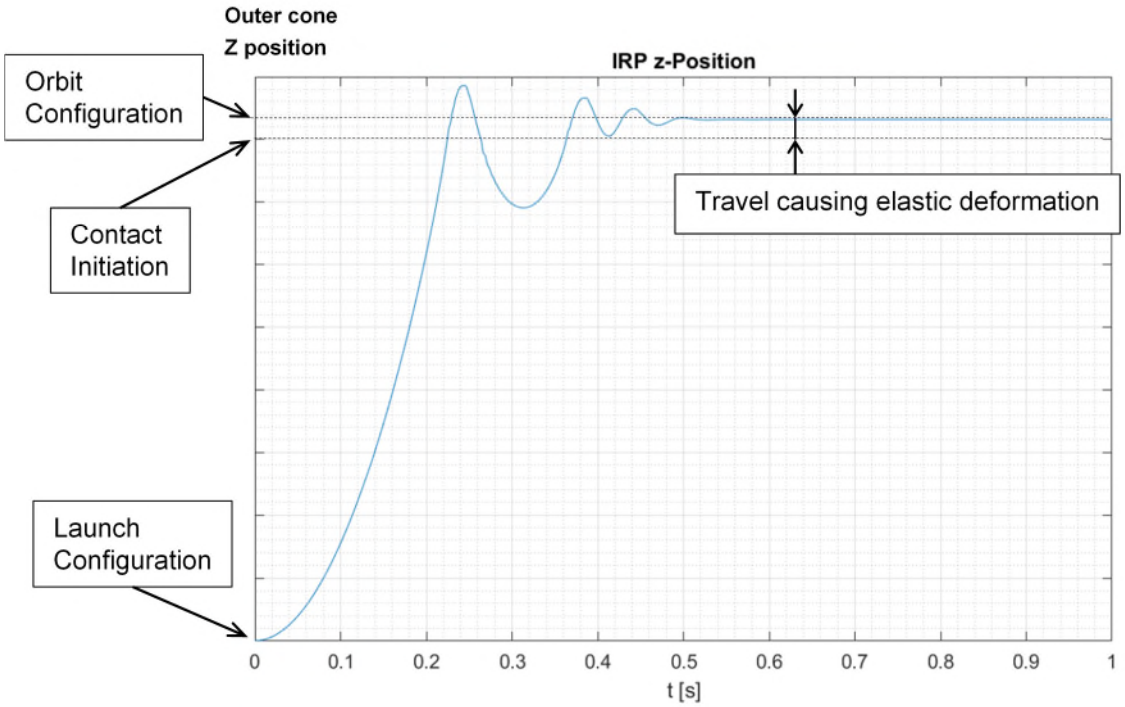

Figure 9: Configuration change travel (axial direction).

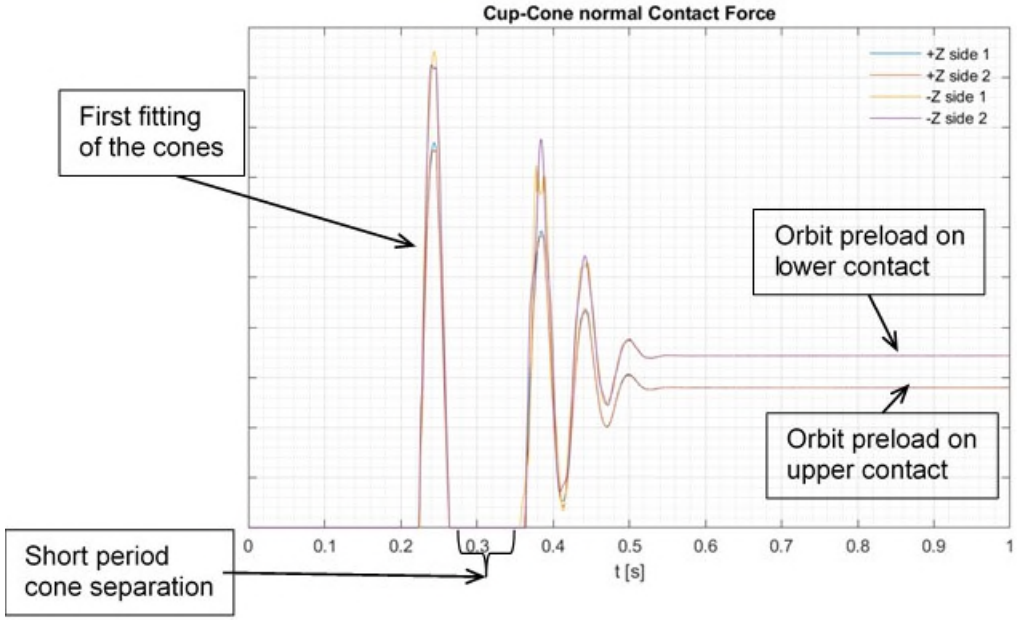

Figure 10: Contacts normal force during configuration change.

It is curious to see that the cones separate during a short period, after the first fitting. This is explained by the low friction in the contacts, relatively high fitting angle, and the considerable amount of energy bounced back by the bearing membranes.

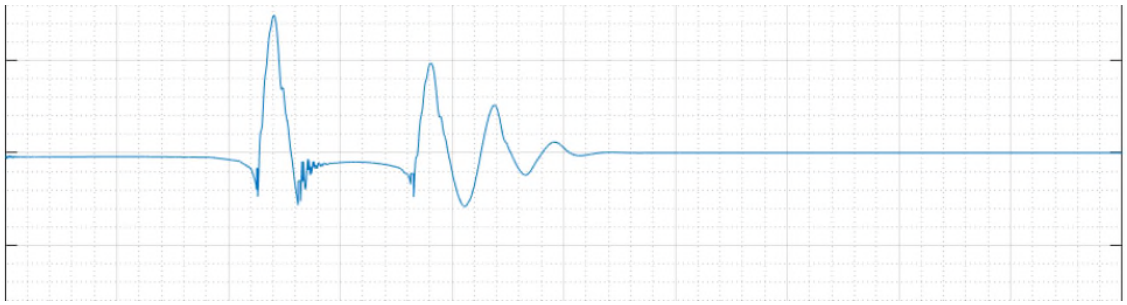

Figure 11: Axial force on bearings.

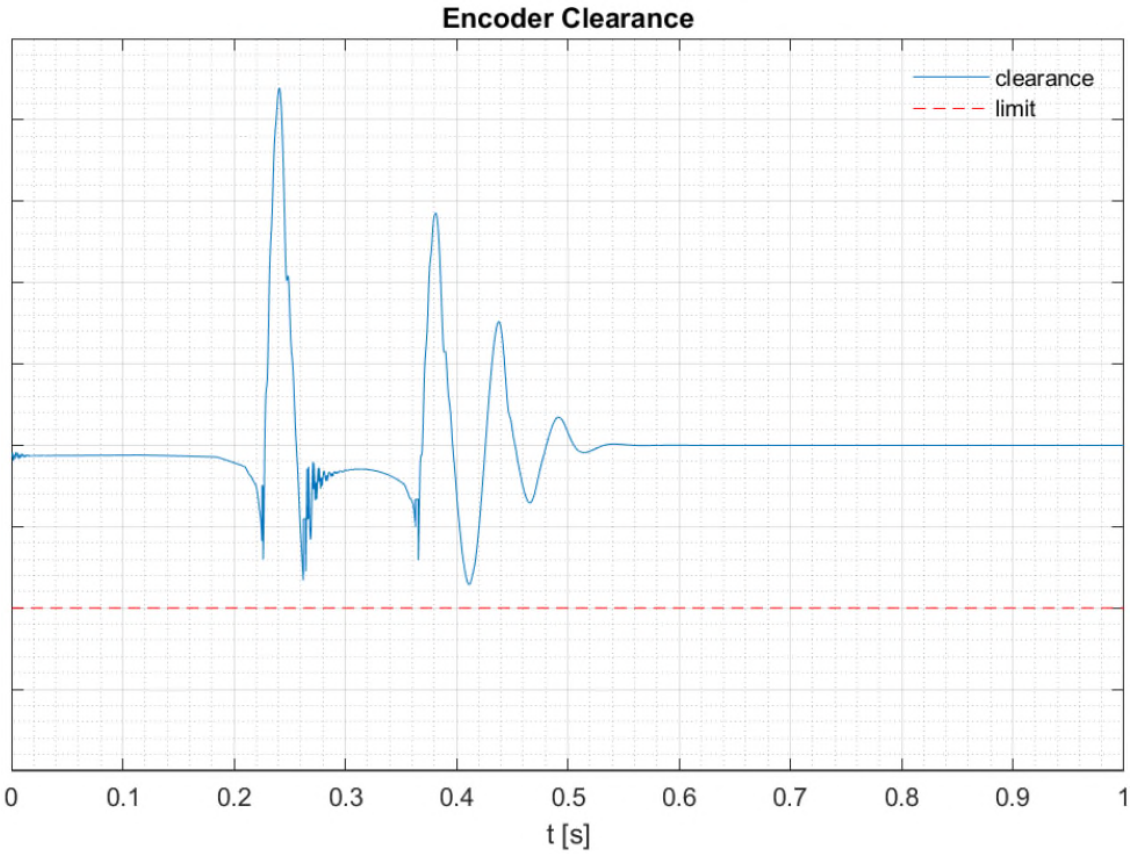

Figure 12: Encoder clearance during configuration change.

To be noticed the following relations of the graphics:

- Sliding on the cones contacts <-> Variation of contact normal force <-> Z force on the bearings (Sliding on the cones causes deformation of the contact regions and force changes on the contact due to stiffness, Z bearing force and inertial forces push and pull the contacts)
- Z force on the bearings <-> Encoder clearance (due to bearing membrane elastic deformation)

LOD Breadboard (BB)

Multiple requirements apply to this device i.e., high load transfer, high stiffness and high pointing repeatability. Many effects are contributing to the performance of the LOD, being that some of them are rather difficult to predict. Therefore, a Breadboard test program is the most efficient way to determine / verify / reduce uncertainty of several parameters. Table 1 presents the main effects to be studied during a BB test campaign, as well as the main requirements affected by these parameters.

Table 1: Breadboard goals

Parameter / effects	Goal at BB level	Source requirement	Uncertainty preventing determination by analysis
LOD position and orientation repeatability	To be measured	Pointing performance;	Manufacturing tolerances, Friction
LOD angular stiffness	To be measured	On orbit stiffness	contact on the cones (with low preloaded when compared to bolted interfaces)
Cones fitting force	To be measured	Reliable cone fitting	Manufacturing tolerances, Friction
Kinetic energy transferred to the bearing membranes	To be indirectly measured	Survivability encoder disc	Friction, other damping sources
Magnetic force along transition travel	To be measured (reduce margins)	Pointing performance; On orbit stiffness;	Material properties; Model verification;

The test setup concepts for two tests are presented in Figures 13 and 14.

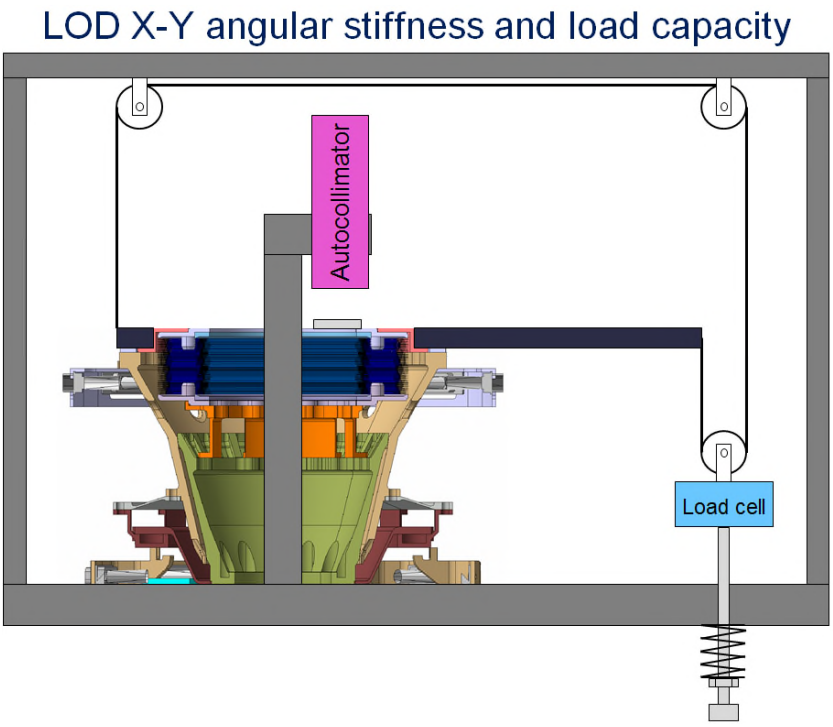

Figure 13: X-Y LOD angular stiffness, static measurement.

The concept is direct, to apply a torque and measure the angular displacement. Complementarily a dynamic test will be done in the shaker to measure the first Eigen frequency.

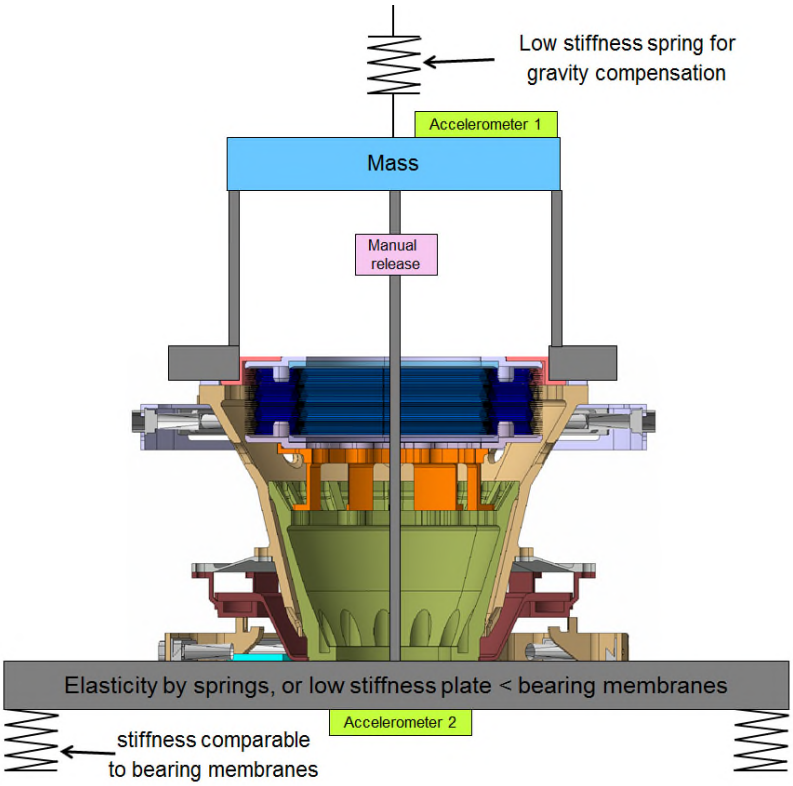

Figure 14: Kinetic energy transferred to the bearing membranes during configuration change.

The concept is to execute the configuration change with gravity compensation in order for the test to be energy representative. The stiffness of the support will be measured during the test measuring the first Eigen frequency and using the previously measured oscillating mass. With the stiffness of the support and amplitude measured by accelerometer 2, the energy can be calculated and compared with the predicted in the dynamic simulations.

Life Test

Scan Mechanisms usually operating during the entire mission. The required life revolutions depend on mission time and speed and can be usually several hundred million revolutions. Therefore, the lifetime qualification needs specific attention and a good preparation since the test validation takes a long duration even in accelerated condition and introduces a notable risk to the project with respect to schedule and effort in case of failure.

A usual approach is (if representative) to perform a life test in accelerated condition to have the test validation available prior FM manufacturing. However, the orbit condition representativeness cannot be easily demonstrated, as some parameters are different like speed, lubrication regime, heat dissipation, temperature gradients, motion etc.

On the previous MetOP SG project, the life test has shown an issue with some Roll-Ring channels which haven't performed in the expected way. A detailed investigation has been performed. A Build Fixture, which was used for the Roll-Ring assembly was not sufficiently accurate, causing a malfunction that allowed the Coupler to move outside of the ring. Furthermore, an investigation was performed to predict if such an error can be due to an accelerated speed of over 225 rpm, which is a factor of 5 times faster than the orbit speed. No reliable calculation method was found for a clear relation between speed factor and degradation factor, but negative effects couldn`t be excluded.

As with any electrical rotating interface, circuit resistance performance is degraded somewhat due to moisture effects and the test setup requires at least two parallel circuits to be measured together which makes it difficult to isolate areas of concern.

Complicating the situation, an Instrument Unit was designed with a very sensitive under voltage protection, supplied by power via the roll-ring. Therefore, the concern was raised about the resistance peaks within millisecond range.

These challenges led to a specific resistance measurement and measuring equipment with the following characteristics:

- Continuous resistance recording of all roll-ring channels at the same time
- Continuous current transfer of the power lines during lifetime
- Resistance sampling rate of 25 kHz of all channels (well above industry standard)
- EGSE noise level < 0.0005 ohm (well above industry standard)
- Resistance recording during entire life test sampled for trend analysis
- Resistance recording with high data rate at a specific event (versus a threshold value)

This specific ground support equipment was manufactured and is under operation to perform monitoring of the Roll-Ring under real environmental conditions.

The Roll-Ring technology demonstrates inherent low dynamic resistance noise levels over extended periods of time. Humidity can impact the noise level which is usually higher after long term storage (under clean room conditions) but quickly improves with nitrogen purging or in a vacuum condition. The dynamic resistance noise level also varies in relation to the shaft speed. Figure 15 shows the Roll-Ring dynamic resistance noise measurement with a sampling rate of 25 kHz. No filter is applied to the measurement data, and this sampling rate is well above industry standard, but used here for our purposes. The resistance measurement was performed in ambient condition.

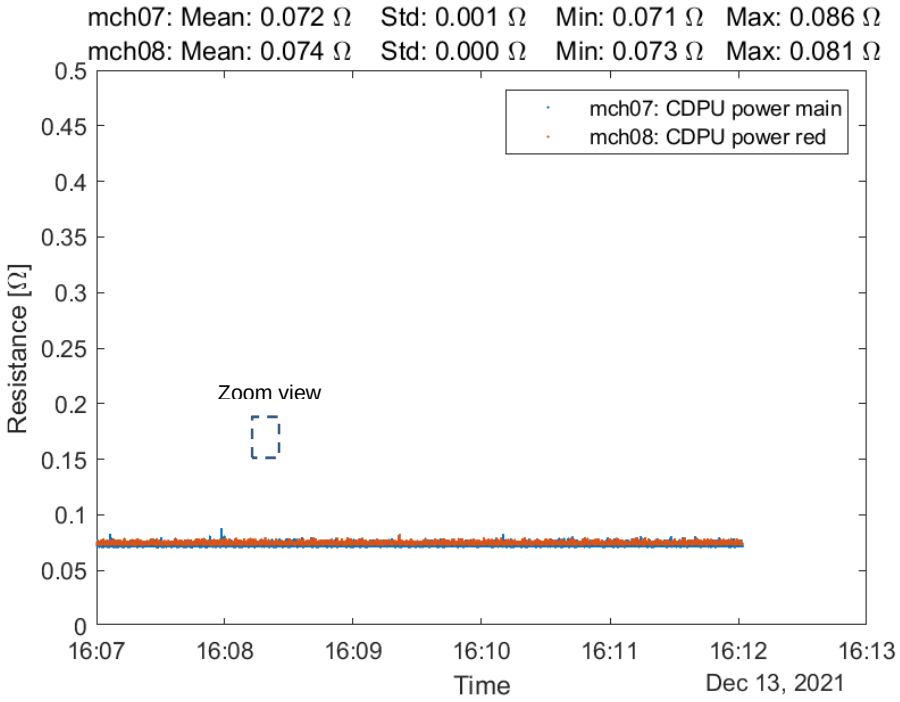

Figure 15: PDTD Resistance noise with 25 kHz sampling rate

Figure 16 is a zoom view of Figure 15 with short resistance peaks in a millisecond range. There are many possible reasons for this, to include moisture effects, contamination, or irregularity in contact surface.

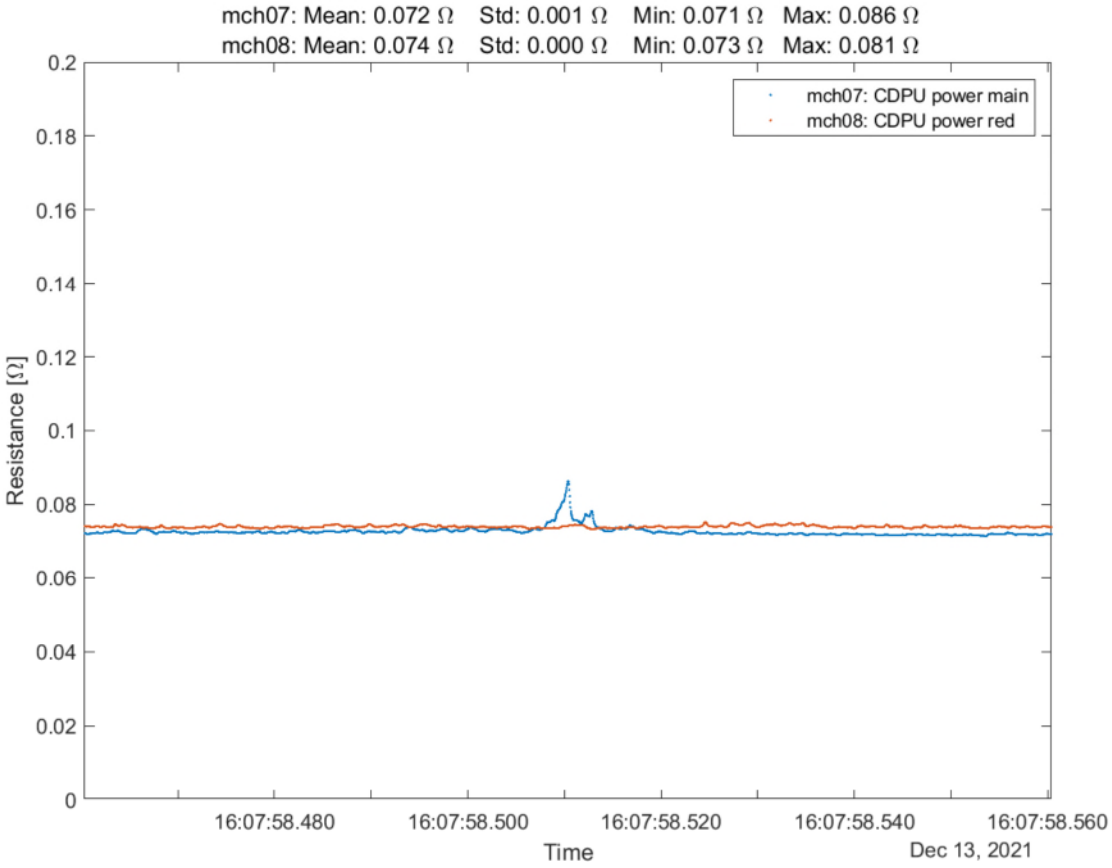

Figure 16 Zoom view

Figure 17 shows the nomenclature of the Roll-Ring items. Electrical contacts are between the inner Ring and Coupler and between the Coupler and the outer Ring.

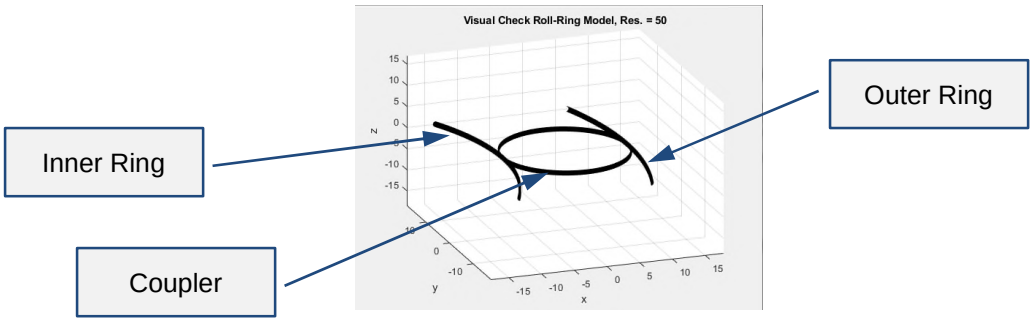

Figure 17: Roll-Ring® nomenclature

Figure 18 shows the Roll-Ring characteristics which were helpful for failure detection. The plot represents the measured 4 Channels with two in series at a sampling rate of 25 kHz, again without any filter. The plot shows the measured value in the frequency domain. There are typical peaks at specific frequencies which are clearly linked to the three contact surfaces for Inner Race, Outer Race and Coupler.

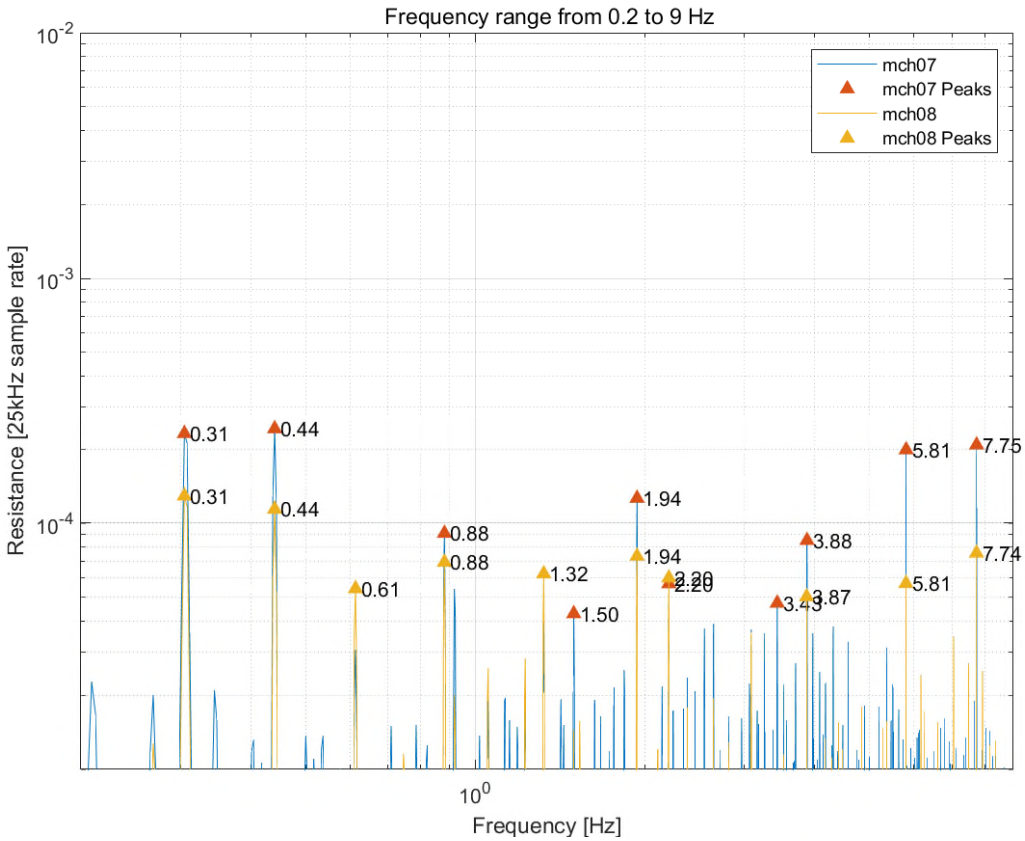

Figure 18 Fast Fourier Transformed resistance data

The Roll-Ring supplier has made improvements to ensure a robust solution that will operate with a misaligned build fixture and at accelerated speed with sufficient margin. With all the experience of the previous life test, the Roll-Ring supplier has implemented the knowledge gained to all design and manufacturing standards.

<u>Therefore, the following are key lessons learned</u>

Customer levels:

- The envelope should be defined by means of feasible design concepts with sufficient margin.
- Best practice selection process does not allow envelope iteration with the bidders. Therefore, the envelope should be defined as a goal and not as a hard requirement to make different design concepts possible for best selection.
- Electrical dynamic contacts cause resistance noise. Power regulation and under voltage protection must be adapted accordingly.
- Adequate planning with successful life testing is warranted.

Supplier level:

- Accuracy of the build fixture must be verified by test, preferably with and without the installed device.
- Be aware that an envelope change becomes more difficult as the project progresses.
- Design must be sufficiently robust against manufacture tolerances and accelerated life test speed.

The robustness of the CIMR PDTD design is significantly improved against manufacture and alignment tolerances compared with the previous design. Early confidence test verification has been implemented to verify the assumptions prior to SCM Life test with the following aim:

- Margin verification with respect to accelerated speed
- Margin verification with respect to manufacture tolerances
- Margin verification with respect to rated and de-rated current transfer
- Confidence life test at PDTD level prior to SCM life test

In summary, the issues experienced have led to advanced understanding and robustness improvements. The Roll-Ring provides excellent resistance noise levels over extended time periods and is therefore considered the best choice in high performance data and power transfer for long life applications.

Acknowledgement

The authors would like to thank the members of Diamond-Roltran (Jeff Gilling, Laura Dion, James Squires) for their effort performed in failure investigation, the support and possibility of the missions to the members of Airbus, OHB Italia S.p.A., Thales Alenia Space Italia S.p.A. and the final customer European Space Agency (Philipp Eggers) and Eumetsat.

References

1. Kent Kellogg, Eni Njoku "NASA’s Soil Moisture Active and Passive (SMAP) Mission" https://ntrs.nasa.gov
2. ESA Homepage retrieved 10 8, 2021, from ESA Homepage: https://www.esa.int/Applications/Observing_the_Earth/Copernicus/Copernicus_Sentinel_Expansion_missions
3. Scanning System Development and Associated Bearing Cage Instability Issue (Manfred Schmid, Christian Hehr), AMS 2008
4. Antenna Despin Mechanism for BepiColombo (Manfred Schmid, Tatsuo Kawamura, Christian Hehr, Udo Rapp), ESMATS 2009
5. Scanning Mechanism of the FY-3 Microwave Humidity Sounder (Manfred Schmid, Li Jing, Christian Hehr), AMS 2010 (NASA/CP-2010-216272)
6. Design and verification status of the Scan Mechanism assembly for MWI/ICI Instruments in the frame of Metop-SG Program (Stefan Dittenhauser, Christian Hehr), ESMATS 2019
7. Design, Development and Verification of the METimage Scanner and Derotator Mechanisms (Sebastian Rieger, Armin Jago), AMS 2020

Development of a Thrust Vector Control Mechanism for Deorbitation System

E. Majewska*, Michał Ranachowski*, Witold Wąsowski*, Damien Pawluk*, Filip Czubaczyński*, Adam Kmak* and Piotr Palma**

Abstract

The following paper details development of design features employed within the Thrust Vector Control (TVC) which is a part of deorbitation propulsion system based on a Solid Rocket Motor (SRM). The main purpose of TVC mechanism is to increase the controllability of the deorbitation system. The TVC design incorporates outside flaps working as deflectors, moved in and out of the exhaust stream of a nozzle at the exit plane. Deflection of the flaps produces a lateral force relative to the direction of axial thrust, resulting in a moment with regards to the vehicle's center of gravity, which results in a turn. The paper presents the design process, accompanying analysis and ablation test results with lessons learned and conclusions.

Introduction

The TVC described herein was designed as a part of the development of a deorbitation system based on an SRM. The paper focuses on the mechanism adding necessary details concerning SRM performance.

After over 60 years of the space age, there is an urgency to think about protection of the space environment: to prevent continuous growth of debris and to prevent orbits from becoming entirely inhospitable. This is especially true with a space private sector growing rapidly and offering new technologies and approaches which result in a revolution with regards to the costs of spacecraft launch and payload capabilities. Those implications are going to be reflected in the design philosophy – less conservative design, accepting larger risk, and introducing technologies with no space heritage. Commercializing space by competing entrepreneurs brings a lot of new possibilities, but it also results in a rapid increase in the number of space vehicles (including large constellations) which generates space traffic, especially at low-Earth orbit and geostationary orbit regions. Non-operating satellites need to be removed from orbits to make space for newcomers. Hence, a reliable end-of-life strategy has to be implemented as soon as possible. One of the most effective methods to mitigate the risk of new space debris generation is its end-of-life utilization. A deorbiting SRM with a TVC system is one potential solution. The main advantages of using a dedicated deorbiting system based on an SRM are: relatively high density performance, low system complexity, storability and autonomy [1] [2]. By adding TVC to an SRM, a deorbiting system gains better control over an end-of-life maneuver: its attitude and orientation, ensuring that the final trajectory would be performed accurately and safely. The TVC system should compensate trajectory misalignments and uncertainties resulting from spacecraft's center of mass, inertia, flexibility of appendages, sloshing, thrust variation from motors and different burning time in order to correctly set the spacecraft's position during the deorbitation maneuver. The proposed design can be optimized precisely, depending on satellite needs and deorbiting requirements. The mechanism presented herein is focused on increasing capabilities in terms of thrust deflection angle, which is an angle defining how thrust is inclined with regards to the axis of the SRM. According to the analysis, it is possible to obtain ~10° for thrust deflection.

Concept

The selected concept using outside flaps has been chosen based on a thorough trade-off, preceded by a detailed state-of-the-art research including thrust vectoring methods from missiles, launchers and aircrafts.

* Łukasiewicz Research Network – Institute of Aviation, Warsaw, Poland

** Astronika, Warsaw, Poland

The trade-off included four different, preliminarily selected TVC concepts: gimbal, outside flaps, supersonic split line [3] and movable nozzle. It took into consideration 17 driving attributes/selection criteria chosen based on the application purpose, and main coinstraints coming from the SRM design (i.e., long-storage capabilities, operation duration, envelope size, test capabilities, or thrust losses). The outside flap solution scored the highest in the trade-off for the particular application. At the later stage of the concept investigation, attention was paid to the kinematics of the solution and envelope size. The chosen concept is a variation of a Fowler mechanism, commonly used in aviation wing design. It benefits from the kinematics: flap slides backwards before hanging inwards. This setup allows less volume for the mechanism, as the geometry of the design can be circumscribed to the maximum diameter of the SRM. Moreover, in a stowed position it does not elongate the axial dimension (that could be problematic in terms of configuration onto a satellite having in mind the SRM parameters). Also, in terms of steering and control the design should benefit as the variable-ratio design could be adjusted according to specific needs. The system is rather lightweight (unlike a gimbal where the entire motor needs to be moved). Moreover, the method requires only minor changes in the SRM design – adding aditional mounting features on the nozzle part (unlike the movable nozzle where the motor design is highly affected by incorporating a TVC). The main disadvantage is axial force (thrust of SRM) reduction required to achieve the desired vectored thrust. The thrust reduction is proportional to the deflection angle.

The SRM provides a maximum thrust of 250 N and it weighs 53 kg (including 31 kg of propellent). Total lengh is 1500 mm and maxium diameter 215 mm. It operates for approximately 300 s. The currently proposed TVC design weighs 7.5 kg (four independently driven actuation units supporting 4 flaps).

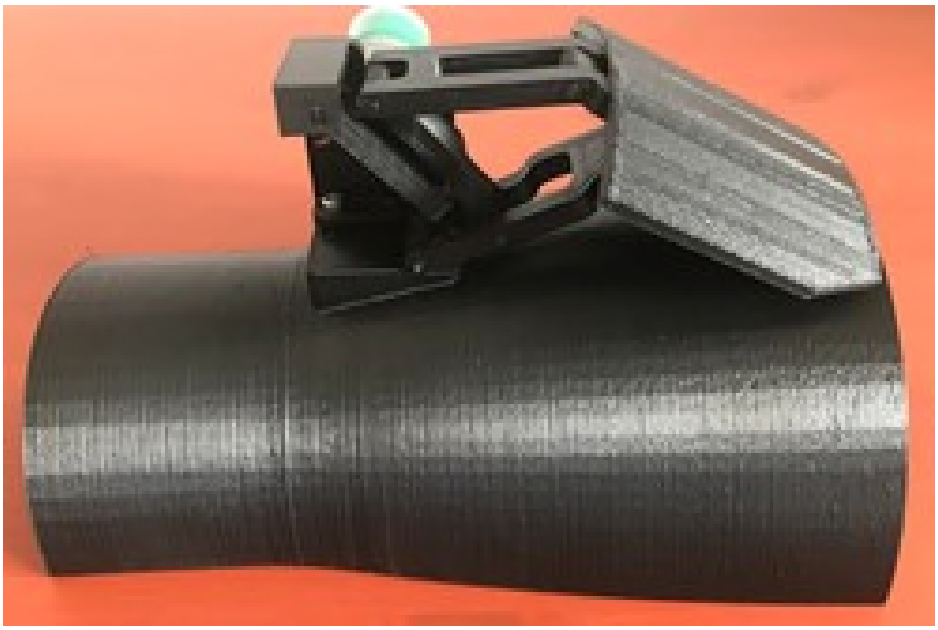

Figure 1. Thrust Vector Control mechanism – 3D printed prototype

Analysis

The complete analysis logic used for the purpose of TVC sizing is shown in Figure 2. In order to properly investigate the performance of the proposed concept, a set of analyses was prepared. Results obtained from CFD analysis helped to estimate the loads on the flap generated by the outflow of exhaust gases from the SRM. The dimension and location of a flap (its length, chamfer, radii and position with regards to the exit plane) was strictly related to CFD iterations. The most promising results from the CFD analysis served as an input for the next stage of analysis, namely the multibody simulation. This stage was aimed at calculating the torque of the electric motor required to overcome the aerodynamic loads, friction torque and

inertia. The results dictated the size of the driving unit (stepper motor with planetary gearbox). The sizing task (motorization margin) was done in accordance with the ECSS standards and recommendations for margins to be applied and features to be taken into account [4]. The above-mentioned analyses showed the use of a COTS solution for the actuator unit would be acceptable.

The CFD analysis was the first and critical part of the mechanism design. At this stage, the optimization direction had be set and driving requirements needed to be frozen. In the scope of the project, the deflection angle was selected to be the driving parameter. However, it has to be noted that depending on the specific mission needs, the concept can be adjusted. During the CFD anaysis, 44 iterations of the flap were investigated. The effects of 6 variables associated with flap dimensions and position with regards to the SRM were examined. The interesting finding was that the flap insertion does affect not only plumb, as was expected, but also the flow inside the nozzle. The presence of the flap creates a set of shock waves. Those located close to the nozzle inner wall create a high pressure zone near the exit plane causing an additional lateral force component acting in the motor nozzle. This could positively influence the thrust deflection (similar behavior described in [3]).The additional component (even up to 15% of lateral force in the case of a flap with double curvature) interacts with the SRM directly – it does not load the flap, hence does not influence the actuator sizing (it does not enlarge the stepper motor which drives the mechanism).

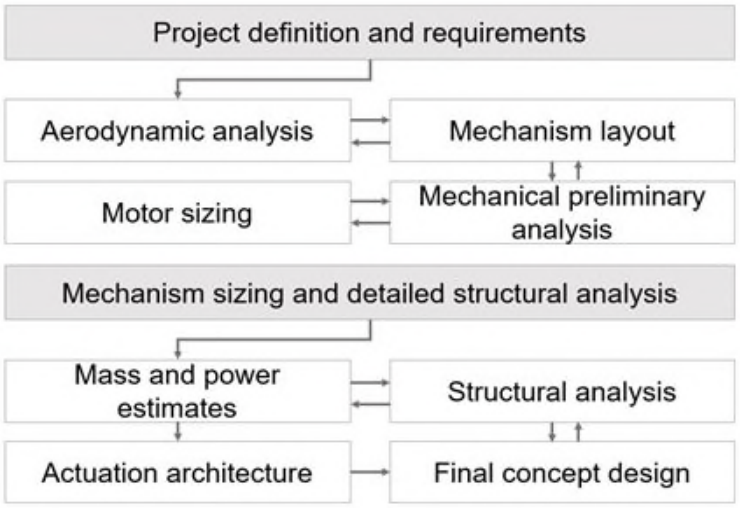

Figure 2. Analysis logic

Forces and torques coming from aerodynamic loads were a contribution for the next step of the analysis, the multibody analysis of the mechanism. The purpose of this analysis was to investigate and understand how the mechanism moves and operates under the influence of force (forward dynamic exercise). It allowed better understanding of the dynamics and kinematics of the variable ratio. Therefore, the analysis was a step towards motor sizing (motorization margin calculation in accordance with [4]). As a result of the multibody analysis, it was possible to obtain data used in motorization margin coming from:

- Aerodynamic loads,
- Friction,
- Inertia of the mechanism.

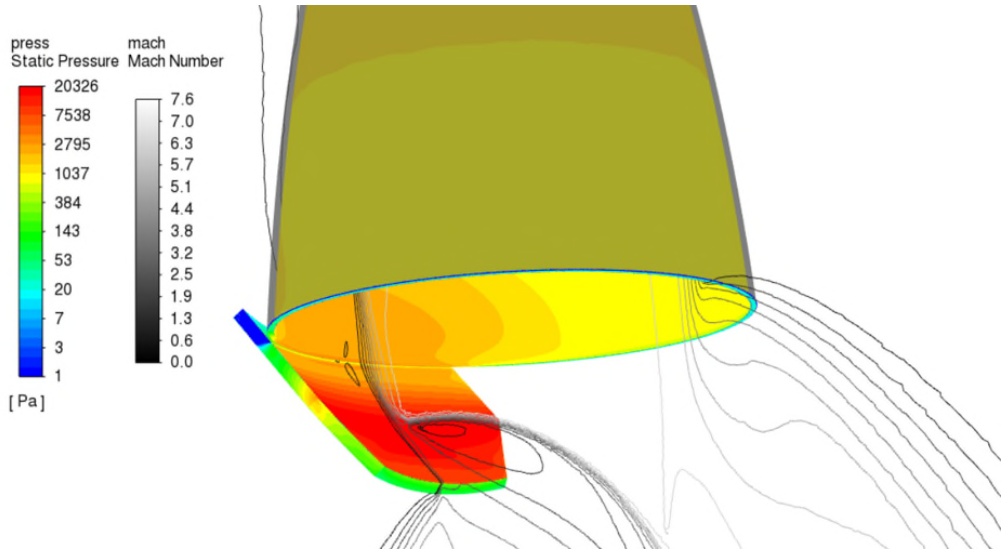

Figure 3. CFD results: static pressure and Mach number distribution around the flap

Based on the model prepared in MATLAB-Simscape, a stepper motor with an integrated low backlash planetary gearhead was chosen as best suiting the design requirements. The key reasons why this was considered adequate for the TVC application are:

- Long-term non-operational period in orbit in high vacuum favors a solution which is not using any brushed commutation;
- Control simplicity for a stepper motor allows for smaller, less complex driver than a brushless direct current motor;
- The relatively small diameter of the actuator comprised of a motor and gearhead under 43 mm allows to optimally use space around the SRM which is the baseline location for the actuators.

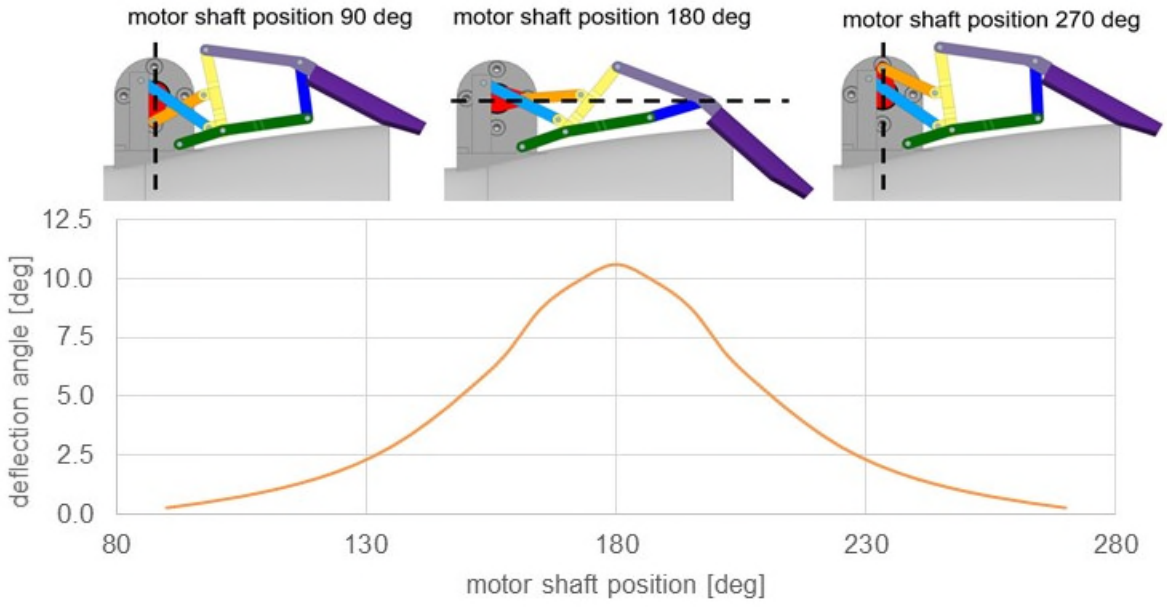

Figure 4. Flap insertion and thrust deflection angle with relation to motor shaft position

Ablation Tests

Ablations tests were conducted, considered to be one of the main elements of the overall test campaign. Based on the previous investigation, three materials were selected which seemed to be suitable for the application: tungsten copper alloy (W80Cu20), tantalum (Ta) and silicon nitride (Si_3N_4).

Tungsten-copper alloy was selected mainly due to the fact that it is also used for the throat insert in the SRM design. Having in mind the critical flow parameters, the throat area is exposed to more severe conditions than any other part of the motor in terms of temperature, pressure and erosion. Tests conducted as a part of the motor development project (30 seconds motor burn in atmospheric conditions) showed almost negligible erosion of the throat insert. However, the main disadvantage of W80Cu20 is its density. A material similar to tungsten-copper is tantalum – both in terms of thermal and erosion properties as well as in terms of density. The last candidate was silicon nitride – a ceramic that is characterized by low density, low erosion rate, and good thermal properties.

The ablation tests were conducted on a stand designed according to the standard ASTM E285-08 [5]. The test method determines the relative thermal insulation effectiveness when a squared specimen is placed in an environment of a steady flow of hot gas provided by an oxyacetylene burner. Hot combustion gases are directed along the normal to the sample. Each material was represented by 5 specimens which were flat, square panels with dimensions 101.6 +0.0/-0.71 mm wide and 6.35 ±0.41 mm thick. A thermocouple, aligned with the center of the torch tip, measured the back-face temperature of the sample. Due to the material properties of the candidates, the parameters and conditions described in the standard needed to be adjusted in order to get representative results. The heat flux described in the standard was too high – the temperature was rising too rapidly to allow the data acquisition system to collect usable information. Sampling frequency and thermal inertia of thermocouple were the main reasons for the adjustments. In order to extend the test time, it was decided to reduce the flow of gases and increase the distance between the torch tip and the specimen – both resulted in longer tests. The heat flux, measured before each test on a dedicated cold-wall calorimeter, was 340-380 W/cm^2, flow of oxygen was set to 23.9-25.0 liters/min, and acetylene 19.7–20.9 liters/min. Temperature was measured in range: ambient to ~660˚C.

In total 15 specimens were examined – one cracked during the test execution. Figure 5 shows the test results: W80Cu20 is the most promising in terms of thermal insulation properties, tantalum and silicon nitride show very similar behavior.

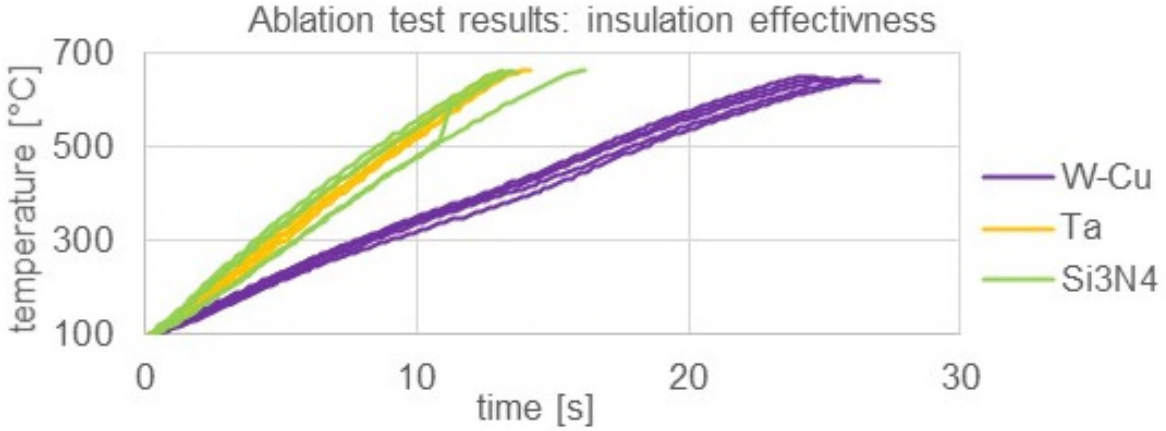

Figure 5. Ablation test results – insulation effectivness

One silicon nitride specimen was poorly manufactured – a bare-eye inspection showed some imperfections before the test. Polishing, as a part of the final sample preparation, probably helped to expose those imperfections which resulted in two spots. Despite the flaws, it was decided to still subject it to the evaluation. It cracked during the test. It occured most probably when the temperature at the back surface

was around 500˚C. The thermocouple was destroyed. However, this sample showed how imperfections on ceramics might be severe in terms of results. Non-destructive inspection can be consided in order to investigate the quality of samples/components.

Specimens of silicon nitride did not bear any visual signs of the conducted tests. The samples before and after the tests looked almost the same (apart from the cracked sample). Whereas the W80Cu20 and Tantalum had circle-like shapes concentrated around the axis of the torch.

Figure 6. Ablation test stand and samples: silicon nitride (cracked), tantalum, tungsten-copper

The next tests intended to destroy the specimens, testing until burned-through is achieved. The heat flux, measured before each test, was 840-920 W/cm^2, flow of oxygen was 52.5-54.1 liters/min, and acetylene 43.2-44.7 liters/min. The first specimen tested was W80Cu20. However, after ~90 s of test, problems with the test stand occurred. Aluminum profiles of the stand, shields and water-cooling pipes started to fail. It was decided to stop the test for safety reasons. Similarly, but after ~60 s, the same happened with the Ta sample. Also those two materials started to melt. Melted metal drops, in orbit, could easily become space debris. Having that in mind, that the deorbitation system should not generate any additional debris in orbit, it is recommended to reconsider those options. A sample of silicon nitride cracked after ~8 s. In order to make sure it was not caused by material imperfections, 3 more samples were tested. All of them broke within 8-10 s in similar way: crack occurred vertically. It is believed that it was due to thermal expansion of the two steel mounting slots that held the sample during the test. Rapidly increasing the temperature caused dimensional change and as a result some extra compressive load was introduced which caused a crack. It is recommended to repeat the silicon nitride tests, but with a different sample mounting. In all cases, the back side of the sample reached the maximum temperature of the thermographic camera (~1500°C) before a crack happened.

Lessons Learned

Based on the current development of the project, the following conclusions can be drawn:

- Design driving requirements must be cleary defined at the beginning of the project – the Fowler mechanism with variable-ratio can be optimized precisely depending on the exact satellite needs and deorbiting requirements;
- The CFD anaysis showed that the selected method based on the outside flaps generates a reduction of thrust that is proportional to the deflection angle of exhaust gases;
- A well-optimized flap geometry is able to increase the thrust deflection by up to 15% by creating a high pressure zone, causing an additional lateral force component acting in the motor nozzle;
- W80Cu20 provided the best performance among the tested materials in terms of thermal insulation effectiveness, however, like tantalum, it melted on a test stand during the burn-through test. The deorbitation system should not generate any additional space debris, therefore, it is recommened to reconsider those materials. Silicon nitride cracks, most probably due to mounting frame thermal expansion – the test stand needs to be re-design and tests have to be repeated.

Conclusion

The most suitable method of thrust vectoring for a deorbitation propulsion system based on the SRM is a concept with outside flaps. The proposed mechanism, inspired by a Fowler mechanism used commonly in aviation to extend flaps on a wing, is a promising concept. The design introduces a number of benefits, i.e., relatively low envelop size, adjustable design (potential for optimization for different driving parameters) and necessity to actuate only flaps and associated levers (unlike a gimbal where entire motor needs to be moved).

Ablation tests were conducted for three candidates for the flap: tungsten copper alloy (W80Cu20), tantalum (Ta) and silicon nitride (Si_3N_4), with the first one having the best properties in terms of thermal effectivness. However, like Ta, it melts potentially causing a creation of new space debris (which shall be avoided). Ceramic material does not melt, but during tests, it breaks – probably due to thermal expansion of a holding frame. Tests need to be repeated on a different sample mounting.

Acknowledgements

The work described was performed with funds from the European Space Agency under contract Solid Propellant Rocket Motor Thrust Deflection System No. RFQ 3-16437/20/NL/MG/rk. The authors would like to thank all the team members that contributed to the project and also all ESA technical and contractual officers.

References

1. Okniński, Adam “Solid rocket propulsion technology for de-orbiting spacecraft.” Chinese Society of Aeronautics and Astronautics, Elsevier Ltd, 2021.
2. Schonenborg, R. A. C. and Schöyer H. F. R. “Solid propulsion de-orbiting and re-orbiting.” Proceedings of the 5th European Conference on Space Debris, Darmstadt, Germany, 2009.
3. Orbekk E. "SuperSonic Split Line TVC Technology and Testing at Nammo Raufoss AS." 42nd American Institute of Aeronautics and Astronautics, Joint Propulsion Conference & Exhibit, Sacramento, California, 2006.
4. European Cooperation for Space Standardization ECSS-E-ST-33-01C Rev.2 Space engineering: Mechanisms, 2019.
5. Oxyacetylene Ablation Testing of Thermal Insulation Materials (E285-08), 2015.

Engineering Design of a Thruster Pointing Mechanism (TPM-250) for Deep Space and IOS Nanosats

Emilia Wegrzyn*, Aitor Estarlich*, Artur Fouto* and Alberto Garbayo*

Abstract

This paper presents preliminary the design of the Thruster Pointing Mechanism (TPM-250) for electric propulsion thrusters for nanosats. The work described in the paper covers the most critical requirements, trade-off and design description, along with plans for the future development. Project will continue until the development and the acceptance of the Thruster Pointing Mechanism Flight Model for the ESA M-Argo mission. A breadboard and an engineering model will be built during 2022, including the control electronics, allowing us to reach TRL 6 towards the end of 2022 or early 2023.

AVS is a worldwide leader in the development of complex instrumentation for Science and Space applications. The background of AVS in vacuum engineering, high-precision mechanisms and mechatronic systems has led us to become one of the only few specialized and EN9100-approved Space mechanisms suppliers in Europe. AVS and its subsidiary URA Thrusters are also one of the most active players in the in-space propulsion field, and will use this specific development as the stepping stone to develop a wide variety of TPM products for a wide set of missions, platforms and application, from nano or micro-satellites, to large GEO spacecraft.

In particular with the M-ARGO's TPM, the system design is challenging due to the typical nanosatellite volume (in this case half 1U), power, and mass constraints. At the same time, the requirement to fit the tubing and harness inside (particularly possible connectors from thrusters) is limiting space inside the allowable volume. Likewise, it is creating additional resistive torque terms, which are quite difficult to assess at initial stage without testing.

Introduction

The aim for the project was to design a pointing mechanism for electric thruster propulsion for nanosat, for the development of a miniature pointing mechanism (TPM250) compatible with standard nanosatellite requirements, to enable deep space missions, inter-planetary exploration or rendezvous with a Near Earth Objects using CubeSat platforms. Due to the limited resources of CubeSats in terms of power, mass and volume, thrust vector control needs to be implemented to enable efficient use of all on-board resources, including the propellant.

AVS plans to develop a product able to compete against current TPM commercial solutions, by offering commercial TPM systems by 2025, not only for CubeSat platforms, but also for larger satellites and complex institutional missions. The project is being funded by European Space Agency General Support Technology Programme.

The paper covers description of the main design drivers, the technical trade-off that resulted from it, the selected solution and final budgets. Plans for further development are presented at the end of the paper.

* Added Value Solutions, Oxford, UK; ewegrzyn@a-v-s.uk

Technical Requirements

The main design requirements for the TPM are presented in Table 1.

Table 1. TPM main requirements

ID	Description
Req-1	TPM shall accommodate payload with external dimensions of 80 mm diameter, height 70 mm, CoM (Center of Mass) at 54 mm from IF (Interface) plane and mass of 0.5 kg
Req-2	TPM shall withstand maximum operating thruster temperature of 100°C
Req-3	The TPM shall accommodate the tubing and harness required for the ETPM from the spacecraft.
Req-4	The TPM shall fit into half of 1U Cubesat volume (100x100x50 mm)
Req-5	The TPM-Thruster assembly shall comply with the provided Tuna-can dimensions in launch configuration.
Req-6	The mass of the TPM, including all features (possible HDRM, required harness…) shall be lower than 280 grams, including maturity mass margin factors (20% currently considered).
Req-7	The TPM shall enable a positioning within a resolution of 0.05 degree at each axis
Req-8	The TPM shall provide a range of ±5 degrees around each axis
Req-9	The TPM shall consume no more than 2.4 Watts at its maximum power setting (+20% margin currently considered)
Req-10	The TPM shall withstand, with no degradation of functionality nor performance, a maximum duration of 5 years in orbit, and no less than 3 years.
Req-11	The TPM shall enable 500 full range cycles during in-orbit operation.

Technical Trade-off

State of the art

An analysis on the current State-of-the-art systems related to TPM has been carried out, which includes other possible variations such as Thruster Orientation Mechanisms or Electric Propulsion Pointing Mechanisms. Although most of the systems are adapted to larger thrusters compared to the current one considered, those same ones are used mainly for Electric Propulsion. There are several types of architecture considered for the TPM, the concepts are described further in the paper.

The requirements that have been established by the TPM of this proposal are relatively demanding, mainly regarding the available volume and the limited mass. Based on analysis of various systems of the current State of the Art, with many different configurations that have been designed for specific thruster assemblies with their own requirements, some conclusions can be drawn focusing on the following specific features:

- Joint/motion type. There is a large tendency to use gimbal-based systems. They present the advantage of reduced joints, similarity between structural elements, and a “direct” rotary actuation, without having relative motion transformation.
- Number of actuators: All studied concepts include two actuators. Gimbal systems have theirs assigned directly to each rotation axis, while the linear actuator concept studied provides a hinged platform so one actuator can be removed and control the platform with only two motors.
- Range: The usual required range that the systems need to fulfil is low, ranging between 5 to 7 degrees, similar to the established range of 5-degree half cone to the current TPM proposed.
- Actuator type: The use of stepper motors is predominant within the concept actuation. Stepper motors provide a relatively robust, low-cost solution, and accurate positioning in open-loop control configuration. Their inherent detent torque coupled with a high gear ratio provides the possibility of holding a position while the actuation is unpowered.

- Thruster tubing/harness: Leaving a central gap on the TPM and connecting the thruster from the platform through the thruster mechanical interface is a common feature in some concepts. A helical configuration for the tubing reduces its resistive torque when the thruster is rotated.

In this paper, following the state of the art analysis and other mechanism analysis, two subsystems have been the main focus of further study: the actuation, that translates into the type of motor considered, and then the mechanism concept, which drives the structure, transmission system and thruster interfaces, among other critical sides of the TPM.

Actuation type selection

Following the state-of-the-art analysis, stepper motors are the preferred choice for most of the concepts analyzed so far. In determined applications within some of them, piezoelectric motors and Brushed DC motors are mentioned as well. These actuators (and similar ones) are analyzed for its possible use in the TPM.

Piezoelectric motors have been undergoing an increasing demand in more uses. Their accuracy and operation method makes them robust and adaptable to many applications. As of characteristics of interest for this application besides their accuracy, they provide high detent torque at small sizes, moving only when powered. However, they present some disadvantages. They usually require relatively high voltages to enforce their motion, sometimes translating in high power. Their electronics are usually custom made for the specific actuator and application, incurring higher costs, and are not supported with the large heritage of stepper motor electronic components.

Brushed and Brushless DC motors could be considered as well. Brushed ones present a simple, low-cost choice, with many different products available. However, their use is limited due to the constant wearing, their efficiency is low, and they present poor thermal characteristic in vacuum, among other disadvantages. Brushless DC motors are an improved version of the brushed ones, providing high torque at high speeds, doubling the output compared to them. They are vacuum compatible and have an improved heat dissipation. However, their cost, mainly related to the required electronics, is higher and of more complexity. They usually require closed-loop position control and positioning sensors, and their unpowered torque is lower than the stepper's.

For the application at hand, then, where a simple system with high positioning accuracy, low speeds and high holding and detent torque is required for long periods, the stepper motor is the baseline selected, although other options could be considered in the future.

Mechanism Trade analysis

The initial mechanism trade analysis provides a final selection among different traded general concepts, developed and filtered using the previous analysis performed as baseline. "General concepts" is referred to the mechanism and motion type, without having specific components related to each concept. Some assumptions are therefore placed before preparing the Figures of Merit and providing the concepts with scores based on them. Following the State-of-the-Art Analysis in TPMs, the same actuation based in stepper motors will be baselined for each option.

- For concepts using direct rotary motion, a gearbox is assigned. The ratio considered will be 100.
- The baselined leadscrew is a Stainless Steel 5-mm diameter and 0.5-mm pitch one, assumed from an analysis on lead/ball screws that suppliers like Reliance can provide.
- Being almost negligible in mass and volume, all joints are considered with the same mass and volume, although the required DOFs for each of them will be included in the trade. A stainless steel, 5mm rod-end characteristics are baselined
- The "thruster platform", or the thruster support, is the same for all concepts
- The structural material used for all concepts is Aluminum 7075-T6.

The trade-off was intended to provide orientation on which concept to select. Moreover, rather than choosing a specific one, the result was meant to limit many choices to just some of them and give insights on which kind of mechanisms could be better suited for the TPM.

Concepts: Description

The considered concepts are shown and described in Table 2. Each concept has a depiction through a simple, conceptual drawing to understand the mechanism's function. The specific position of the actuators, shape and volume of the joints and other features are not representative.

Table 2. Description of the concepts considered for the Trade-off

CONCEPT	DESCRIPTION
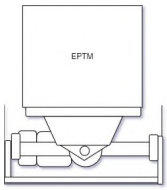 (GRM)	**Gimbal Ring miniaturized concept** • Based on the Gimbal Ring concept. • Gimbal joint type mechanism. • Thruster platform is not connected with the primary structure. • 2 actuators. • Direct rotation actuation. • The first actuator rotates the gimbal ring with reference to the lower bracket, while the second actuators rotate the upper bracket with reference to the gimbal ring.
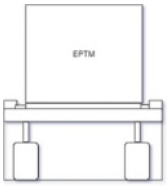 (VAG)	**Vertical Actuation Gimbal concept** • Concentric Gimbal joint type mechanism. • Thruster platform and middle platform are connected to primary structure through two joints. • 2 actuators. • Linear motion actuation. • Two concentric plates, with their hinges perpendicular to each other, are pushed by 1 actuator each to provide the required rotation.
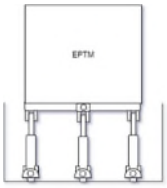 (GS3)	**Gough-Stewart 3 actuator platform** • Based on the Gough-Stewart platform. • Thruster platform is not connected to the primary structure. • 3 actuators. • Linear motion actuation. • The orientation is given by adjusting the lengths of the 3 actuators, allowed with the 3 DOF joints that unite the structure with the thruster platform.
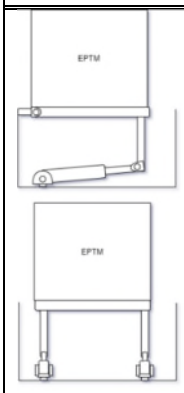 (HAL)	**Horizontal Actuation Lid concept** • Based on the Austrian Aerospace TPM concept. • Thruster platform is connected to a primary structure through one hinge. • 2 actuators. • Parallel linear motion actuation. • The horizontal linear actuators, already inclined in resting position and with the required joints to allow their movement, pull and push the vertical arms connected to the thruster platform. Independently actuated, they can provide 2 axis rotation

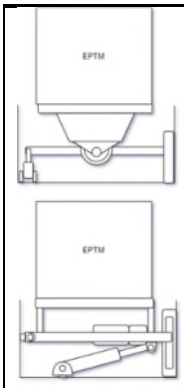 (LRS)	**Linear-Rotary in Series concept** • Combination of base concepts. • 2 platforms. One hinged to the structure, while the thruster platform is connected to the first one. • 2 actuators. • Linear motion followed by rotary motion • Linear motion actuation for 1 axis, while a direct rotation is applied for the other, similar to the GRM concept. The linear actuator provides a rotation with reference to the hinge, supported by a prismatic joint on the other side to keep alignment, while the second rotation is performed by a motor.
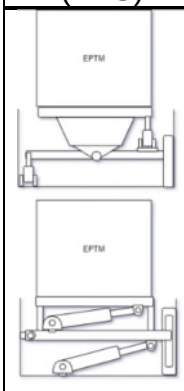 (LLS)	**Linear-Linear in Series concept** • Similar to the HAL concept but with actuators in series. • 2 platforms. One hinged to the structure, while the thruster platform is connected to the first one. • 2 actuators. • Linear motion followed by linear motion • Linear actuation for both axes. The first actuator provides a rotation with refence to the hinge, supported by a prismatic point on the other side to keep the alignment, while the second linear actuator creates the rotation of the thruster platform

Figures of Merit: Rationale

The Figure of Merits (FoM) finally selected for the concept trade-off have been selected following the requirements and critical characteristics that would define the further design of TPM.

- PTA (Pointing Accuracy) Proportionality: Inverse, Accounts for the accuracy that the system can achieve;
- MVL (Mass & Volume) Proportionality: Inverse, Accounts for the expected total mass/volume of the mechanism, which are related for the trade-off;
- HER (Heritage) Proportionality: Direct, Accounts for the heritage that the mechanism type has had, be it in space or in other known applications;
- NAC (Number of actuators) Proportionality: Inverse, Accounts for the number of actuators that the system requires, Number of actuators can also be used as a representative of power consumption and complexity, amount of TPM harness. The scoring is straightforward;
- NJN (Number of Joints) Proportionality: Inverse, Accounts for the number of joints of the mechanism, considering also their DoF;
- LLD (LLD requirement) Proportionality: Direct, Accounts for the possible requirement of a Launch Locking Device or a HDRM to support the TPM during launch;

Weight factors

Once the FoM are defined, their prioritization, and therefore the applied weight to each of it, has been made by a priority matrix, where each Figure has been compared to the others, establishing a ranking. The results on the weights are shown on the visual pie chart, Figure 1.

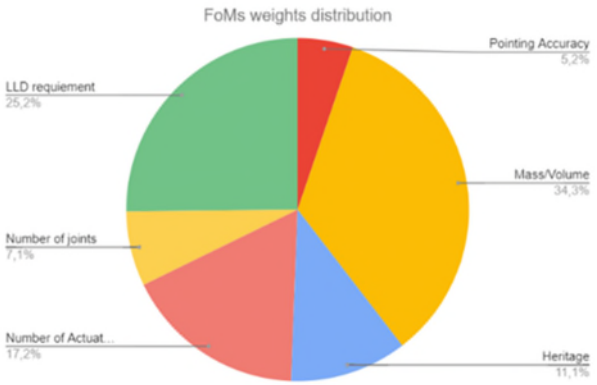

Figure 1. FoM weight distribution pie chart

As critical requirements for a mission like M-Argo where the considered spacecraft is a Cubesat, limiting the mass and the volume is critical for every system included within it. MVL therefore would obtain the highest weight with 0.343. The addition of an LLD would imply an increase in complexity, mass and volume that is rather reduced or avoided, and therefore it ranks second with a 0.252, followed by the number of actuators. Although, as mentioned before, heritage is crucial when systems for the space industry are developed, the requirements of the M-Argo mission, where the TPM will be used as TVC and its integration requires the downsizing of many components, provide an opportunity for innovative solutions that are not specifically required to mimic the current system, but either include reliable components and materials for their application in space. Following the number of joints in second to last position, Position Accuracy is the FoM with the lowest weight, with 0.052.

Concept Scoring and selection

Considering each concept with the aforementioned figures of merits, the results obtained are represented on Figure 2. The trade-off results show a rather clear tendency toward the gimbal ring (GRM) and the vertical actuation, concentric gimbal joint (VAG) concepts. The GS3 is heavily punished due to its extra actuator and “free” thruster platform mainly, although it does not perform badly in the Mass/Volume FoM. LRS and LLS obtain very similar scores, since their noticeable differences are more related to the FoM that are lower ranked. Finally, the HAL obtains high scores in the MVL, first on the ranking, but performs rather poorly in the rest of them.

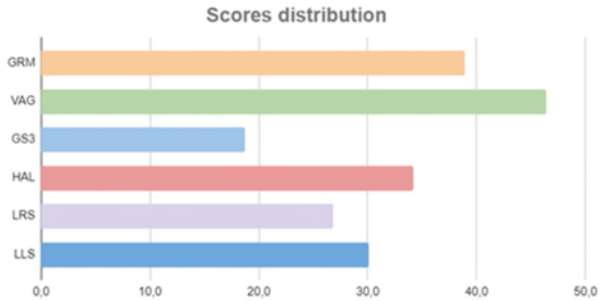

Figure 2. Bar chart with final score visualization

Further design has followed the result of the trade-off and focused primarily on the Vertical Actuation Gimbal concept. Besides the result, the VAG provides a potentially lightweight, simple system with low number of joints, and with the consideration of having the concentric platforms attached to the primary structure by more than one hinge, a robust and compact TPM can be developed.

Design Description

Overview

The preliminary design proposed by AVS UK is shown in Figure 3 along with the designation of the main components.

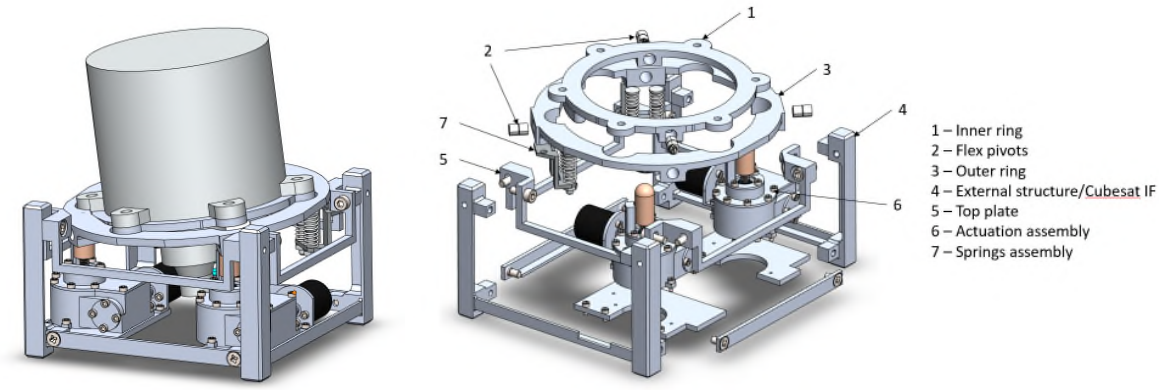

Figure 3. TPM assembly with Thruster (left)/ Exploded view of TPM with component list

Functional description

The TPM connects the thruster to the spacecraft structure, with the main function of orientation control. It provides a ±5-degree cone, with its rotation axis lateral to the flight direction. A two independent axis configuration has been implemented, where each actuation subassembly provides a rotation around one of the axes. While the actuation is fixed to the TPM structure, both axes include two supporting points via two opposed flex pivots. To take advantage of the space available in the corners of the assigned volume, the axes are in an “X” configuration with respect to a typical 12U Cubesat body’s dimensions, as shown in Figure 4.

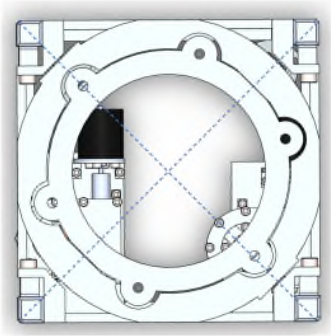

Figure 4. Top view with marked rotation axes

The system is controlled in an open-loop mode, and relies on high accuracy sensors to provide a homing function for the actuators. It also includes the required electric and fluidic interfaces for the thruster coming from the spacecraft. The actuation (per axis) is formed by a motor-transmission assembly and a pair of redundant springs placed opposite to each other, in a perpendicular direction to the rotation axis. The primary actuation has a nut with a push contact with the moving ring and rotates the platform counteracting the spring force. An initial preload of the springs allows for the rotation in the opposite direction, so when the nut is retracted, the spring pushes back, keeping constant contact with it and overcoming the resistive torques of the system. Both active actuation assemblies are in a fixed position, but the pair of springs corresponding to the thruster ring are connected to the outer ring to ensure a perpendicular contact with the first one. The actuation of the inner ring, although fixed to the structure, is positioned so the nut and the ring make contact in the line formed by the rotation axis of the outer ring. This way, although there is some relative rotation of the outer ring, the rounded tip of the nut presents no opposition to this rotation and can push the inner one vertically.

The system includes end-stops to limit the movement of the rings, as an added value to the functional end-stops provided by the maximum compression of the spring and the maximum retraction travel of the nut.

Structure

The main structural element is the 100 mm x 100 mm outer square-shaped plate. In its center, two round, concentric elements are the two rotation rings actuated for the thruster rotation. The square plate has four perpendicular side parts connected to it, delimiting the volume, and will be the elements attaching the whole TPM to the platform. Actuation assemblies are attached to the opposite sides of the frame.

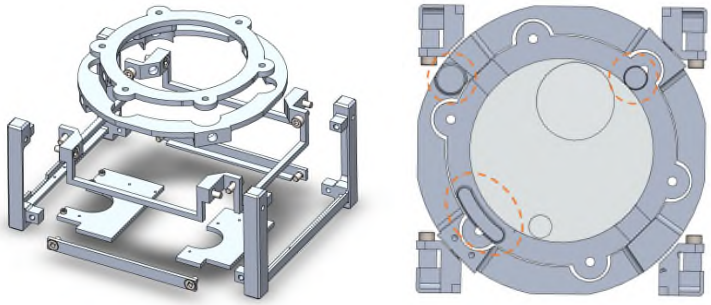

Figure 5. Bottom exploded view of TPM structural components (left)/ Bottom view with marked actuation contact features

The inner ring provides the mechanical interfaces for the thruster. In the outer side of the ring two flattened surfaces with a through hole each are included for the flex pivots that connect it to the outer ring. In the lower side, two specific extrusions are added, one to contact the actuation nut, and the other to contact the springs. Both surfaces will be hardened to avoid any possible deformations or undesired attachments due to temperature and stress (Figure 5).

The outer ring is similar to the inner one. Two through-holes are included to accommodate the flex pivots that connect it to the square plate, and two added extrusions with a hardened surface for its respective actuation nut and spring. The material baselined for the structural parts is Aluminum 7075-T6.

Active actuation

The actuation is an assembly made of a stepper motor and a transmission system, that includes a 2-stage transformation using worm gears and a lead screw. The baselined motor is a Faulhaber AM1524, a 2-phase stepper motor with 24 steps. This Faulhaber model provides motors suited for high levels of vacuum. Selected model of the motor will be suitable considering TRL 6 needs to be met. Based on the heritage of this motor series it is considered that the same line will likely be suitable for higher TRL levels, after some additional tests which we will conduct on the motor i.e., radiation resitance.

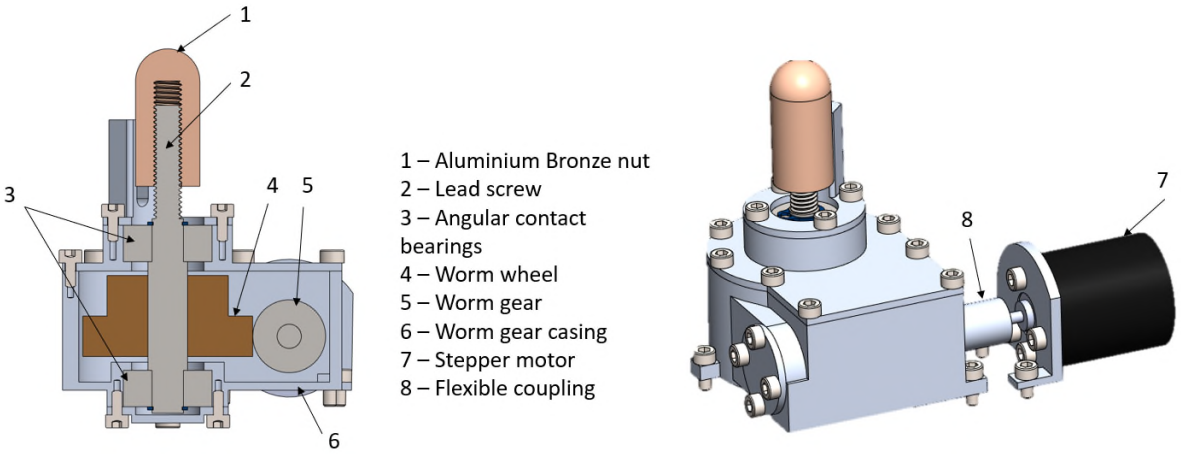

Figure 6. Cut view of active actuation assembly with main parts list

The 2-stage transmission system will be developed using a COTS miniaturized worm gear set provided by Reliance Precision. Current worm gear ratio is 1:40, increasing torque downstream of the system. The worm wheel is attached to the non-threaded part of the lead screw. The lead screw is supported by two angular contact bearing at two different points, providing a good support for the axial and radial forces. The rotation of the lead screw creates a linear displacement of the nut, which is hollowed and threaded inside, so it provides the 8 mm of stroke required to enforce the 5-degree rotation of the rings. The nut is guided using a pin running in the slot, which disables its rotation.

The baseline lead screw has a diameter of 3.6 mm and a fine pitch of 0.3 mm, which enables high resolution in the system rotation and enhances the required back-driving torque (already provided in worm gear), providing the system with a robust positioning when the system is unpowered. The current material for the nut is Aluminium Bronze. Its tip is rounded to provide a single-point contact, and in the case of the thruster ring, adapts to an initial perpendicular rotation the outer one may have before actuating it. Material considered for the gears set are Aluminium Bronze for the worm wheel and SS 304 for the worm.

The resolution reached for the solution utilizing motor with 24 steps, worm gear with ratio of 1:40 and lead screw with 0.3 mm lead is in the range of 0.00002° - complying with Req-7. Enough margin is considered for gear and lead screw backlash effect, although the constant load in the nut will greatly reduce the effect in the lead screw by a pre-loading provided mainly by the spring.

Passive actuation - Springs

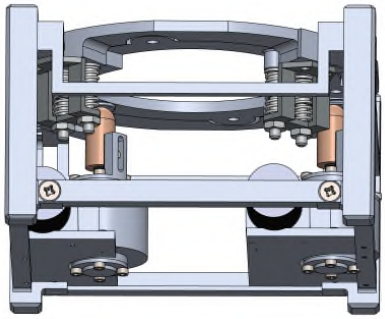

Figure 7. Side view. Spring assemblies on top right and left

At the opposite side of the active actuation contact point with the rings, the redundant springs provide the required force to keep the contact between the active actuation nut and the rings. Each spring is sized so that, when the nut is retracted and the system is rotated towards the active actuators, therefore reaching the minimum deflection, the force provided is enough to counteract all resistive torque trying to compress it. A determined pre-load is applied to enforce this condition.

While a pair of springs is attached to the square plate and therefore is static, the pair corresponding to the inner rings is held to the outer ring, always keeping a perpendicular position and not counteracting its rotation. The baseline attachment is a simple bracket that connects the plates and has a horizontal surface for the springs to contact on. The springs' inner space is filled with a shoulder screw to ensure spring assembly is robust and the outer and inner rings compress the spring through a contact with the screw. A nut is placed in its bottom after a through hole to keep the springs in place and, if needed, can be used to limit the decompression of the spring to a desired value.

Position sensors

Although absolute angular position can be extracted from the step counting, to enable the recalibration of the system, redundant homing position sensors are implemented. The BAUMER MY-COM F75/405600 is the baselined sensor. With a repeatability of less than 0.001 mm and no mechanical pre-run, it provides a high accuracy positioning. The switch is vacuum rated, and for future applications, RUAG has a similar end-switch qualified for space (RUAG Space MSwitch), reducing risk and development time of the system.

Preliminary position of the sensors is considered next to the actuation, with a similar shaped extrusion to contact them. They are precisely positioned so the end-stops can avoid overstressing them, but just enough to measure the position accordingly.

Materials

Aluminum alloy 7075-T6 is the baselined for the structure of the TPM. Used in applications that require high strength and temperature, including extrusions for aerospace, fittings and major structural components. It provides fatigue performance and fracture toughness at the low density of Aluminum.

In the transmission system the baselined material for the nut body is Aluminum Bronze. A proposed alloy is 2.0966. Although the nut/pusher is expected to always stay in contact with the pushed rings, due to their relative motion, to ensure a minimum of 500 HV is achieved, the tip would be substituted with a higher hardness material, and the rings surface will undergo a surface treatment to harden it. The baselined material for the worm gear wheel is Aluminum Bronze as well, and for the worm it is SS 304. End stop material used will be a dissimilar to the structure with suitable hardness for contact with the rings.

Tribology

To ensure low wear and friction over the required temperature range and lifetime of the components and interfaces, proper lubrication must be applied in relative motion areas.

The gimbal joints have to perform an oscillating motion, which is detrimental in conventional bearings, with an angular stroke between +5° and -5°. For a relatively small range, flex pivots offer many advantages: they do not need lubrication, are compact and their performance is not affected by the oscillating motion, and their working temperature range is wide, without significant performance variations. However, unlike conventional bearings, they provide a resistive torque that depends on the applied rotation. For the specific rotation range expected, though, the contribution is not of primary effect within the full resistive torque.

The passive actuation is also free of such issues, essentially having a similar working principle to the flex pivots, translated into linear motion instead of a rotary one. This is not the case for the active actuation, though. The motor and transmission system's angular range is higher. Considering the number of cycles with the applied ECSS corrective factors that the actuation needs to perform, the motor itself performs over 200,000 cycles. The mating surfaces of the worm gear will be lubricated by Braycote 601 grease. Worm gear set will be working in elasto-hydrodynamic lubrication regime, which is considered to have infite life providing enough film thickness on mating surfaces, which for our geometry had deemed to be possible (despite high number of cycles, contact loads are very low).

Harness and tubing routing

With the current configuration of the TPM proposed, there is central space available to include the propellant lines the ETPM will require.

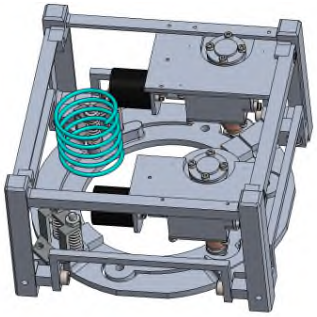

Figure 8. Bottom view with propellant line coil model

Required tubing consists of a 1/16-inch (1.6-mm) Stainless Steel tube. Due to the required rotation, placing the tube in a straight configuration from the spacecraft to the thruster would translate in high bending stresses, being a danger for the tube itself, as well as the added resistive torque that would affect the

required motor torque. The necessary flexibility can be obtained by increasing the length of the tube and manufacturing it in a helical shape, simulating a typical compression spring. Such a design can manage axial and lateral deflections, and the sizing can be made manipulating two parameters: the external diameter of the coil, and the number of coils set.

Control

Four modes have been identified for the TPM at the current stage, that will be used to estimate total power consumption.

- Off mode: All electrical systems are shut down on the TPM, and there is no power consumption coming from Stepper motors or homing sensors.
- Stand-by mode: Stepper are powered but no rotation is applied, maintaining the TPM position with the holding torque. This is a bridge mode, where the system is awaiting instructions. Sensors are not powered.
- Configure mode: Considering the mechanical precision end-switches baselined as homing sensors, they are temporarily powered, and motors are powered so the system rotates towards the end-switch, for re-calibration of the positioning accuracy.
- Aligment mode: Nominal movement of the TPM in open loop with step counting. Homing sensors are unpowered since homing is not required, and the motors are powered to orientate the ETPM towards the specified direction.

Motorization

A preliminary sizing of the required motor torque has been performed. Besides the already calculated resistive torques affecting the system, the resistive torques due to the payload and rings' inertias, the reaction force of the springs in maximum deflection and the losses associated with the drivetrain need to be sized.

Spring sizing

Being part of the actuation, the motorization uncertainty factors apply to the spring. All involved resistive torque related to the springs are gathered in the Table 3. The minimum required torque is calculated following the ECSS equation.

Table 3. Preliminary torque budget

Source	Type of contribution	ECSS Factored contribution (Nmm)
Flex pivots	Spring	7.73
Harness	Harness/others	35.04
Tubing	Harness/others	12.59
Orbital Dynamics	Inertia	0.042
Minimum torque (ECSS factor & MF))		55.4
Spring distance (mm)		37
Minimum force (N)		**1.49**

Since two flex pivots are applied for each rotation axis, the resistive torque is doubled. Following the left side of Figure 9, for clarification, the minimum force of the spring is the required force any of them has to provide in a position when the motor is fully retracted. The spring will then be at minimum compression, but still with enough preload to sustain all resistive torque trying to oppose it. The spring distance considered is based on the worst case scenario, which corresponds to the ETPM ring.

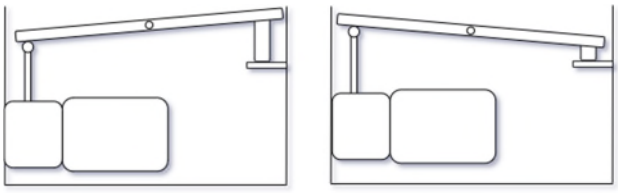

Figure 9. Schematics of two opposite positions.
Left: Spring minimally compressed. Right: Spring fully compressed

Assuming an initial deflection of 6 mm in that position, the required spring stiffness is 0.3 N/mm. This stiffness is used to calculate the maximum force exerted by the spring when the rings are rotated to the opposite side, as shown in the right side of the figure. The actuation needed to be able to provide enough force to compress the spring in order to reach that position, and since another spring has been included as redundancy, the resistive torque provided is doubled.

The maximum force opposing is calculated with the maximum deflection sustained by the spring, which is the addition of the vertical movement to the initial pre-load deflection.

$$F_{spring} = k_{spring} \cdot \left(6 + 2 \cdot d_{spring} \cdot \sin(5)\right) = 6.2\ [N]$$

where k_{spring} is the spring constant and d_{spring} the distance from the center of rotation to the spring. The value will be multiplied by 2 for its addition to the motor resistive torques.

Motor sizing

The value above is added to the list of resistive torques, and the induced acceleration is calculated. Since there is no requirement in speed, an initial value of 0.05 °/s at thruster level has been considered. Considering the lead screw pitch and the bevel gear ratio, the thruster rotation translates into a motor angular rate of 18.5 rpm. An assumed low angular acceleration of 0.5 rad/s^2 has been baselined for the motor. The properties of the Faulhaber AM1524 are shown in Table 4.

Table 4. Faulhaber AM1524 properties

Property	Value
Holding torque	6 N-mm
Detent torque	0.51 N-mm
Rotor inertia	0.045 kg-mm^2
Voltage	1.95 V

The efficiencies of the lead screw and worm gears have been established at a 21% and 28% value, respectively. Table 5 shows the new breakdown of resistive torques, and the minimum torque required for the worst-case scenario. Due to the 2-stage transmission system, the effects of the resistive torques are vastly reduced at motor level, compared to the spring motorization ones. However, their effect is noticeable when the calculation of the transmission losses is performed.

For the calculation of the detent torque (Table 6), the same resistive torques as in the table above will be applied to the system. For the worst case scenario possible, no holding contributors have been applied during the detent torque calculations. Since the M-Argo mission is not crewed and AVS UK has some experience in measuring uncertainty factors, high back-driving efficiencies have been considered for a 0.3-mm lead screw. These measured factors have been considered for the sizing of the resistive torques for the required detent torque estimation.

Table 5. Active actuation pull-in motorization margin

Source	Type of contribution	ECSS Factored torque contribution (Nmm)
Commanded acceleration inertia	Inertial resist torque	$5.56 \cdot 10^{-5}$
Flex pivots	Spring	$2.99 \cdot 10^{-4}$
Harness	Harness/others	$3.39 \cdot 10^{-3}$
Tubing	Harness/others	$1.22 \cdot 10^{-3}$
Orbital Dynamics	Inertia	$1.59 \cdot 10^{-6}$
Motorization springs	Spring	$1.18 \cdot 10^{-2}$
Leadscrew efficiency as losses	Friction	0.175
Worm gears efficiency as losses	Friction	1.47
Total resistive torque (ECSS factor and MF) (Nmm)		3.32
Total commanded torque (ECSS factors) (Nmm)		$5.56 \cdot 10^{-5}$
Minimum torque (pull-in) (MF included) (Nmm)		**3.32**
Motorization margin factor		2.06

Table 6. Active actuation detent torque motorization margin

Source	Type of contribution	Factored torque contribution (Nmm)
Flex pivots	Spring	$2.99 \cdot 10^{-4}$
Harness	Harness/others	$3.39 \cdot 10^{-3}$
Tubing	Harness/others	$1.22 \cdot 10^{-3}$
Orbital Dynamics	Inertia	$1.59 \cdot 10^{-6}$
motorization springs	Spring	$1.18 \cdot 10^{-2}$
Leadscrew efficiency as losses	Friction	$3.32 \cdot 10^{-2}$
Bevel gears efficiency as losses	Friction	$2.13 \cdot 10^{-2}$
Motor detent torque	Magnetic effects	$3.4 \cdot 10^{-4}$
Total acting torque (Nmm)		$1.37 \cdot 10^{-2}$
Total resistive torque (Nmm)		$3.94 \cdot 10^{-1}$
Motorization factor (MF)		2
Minimum detent torque (MF included) (Nmm)		**0.0004**
Ratio T_{mot_det} / T_{min_det}		13.4

Budgets

Current mass budget is given in Table 7.

Table 7. Preliminary mass budget

Part code	Part description	Mass
		g
1	Main top plate	18
2	Outer ring plate	26
3	Inner ring plate & ETPM interface	21
4	Cantilever flex pivots	8
5	Actuator holding bottom plate	17
6	Side plates	21
7	Actuation assemblies	156
8	Spring assemblies	8
9	Positioning sensors	24
10	Harness	12
Total		**311**

The initial power budget is presented in Table 8.

Table 8. Preliminary power budget

Mode	Off	Stand-by	Nominal
Component	**(W)**	**(W)**	**(W)**
Stepper motor 1	0	0	1.04
Stepper motor 2	0	0	1.04
End switches	0	0	0
Thermocouples	0	~ 0	~ 0
Total	0	0	2.1

Summary and Future plans

The work described in this paper is only the preliminary design of the current TPM, but this activity will continue until the development and the acceptance of the Thruster Pointing Mechanism Flight Model for the ESA M-Argo mission. A breadboard and an engineering model will be built during 2022, including the control electronics, allowing us to reach TRL 6 towards the end of 2022 or early 2023.

AVS is a worldwide leader in the development of complex instrumentation for Science and Space applications. The background of AVS in vacuum engineering, high-precision mechanisms and mechatronic systems has led us to become one of the only few specialized and EN9100-approved Space mechanisms suppliers in Europe.

AVS and its subsidiary URA Thrusters are also one of the most active players in the in-space propulsion field, and will use this specific development as the stepping stone to develop a wide variety of TPM products for a wide set of missions, platforms and application, from nano or micro-satellites, to large GEO spacecraft. As part of this endeavor, AVS UK is already working in the development of a fully industrialised, low-cost and compact TPM for the next generation of High Throughput Satellites (HTS) to be used with standard mid and high-power (3-10 kW) Electric Propulsion systems.

In particular with the M-ARGO' TPM, the system design is challenging due to the typical nanosatellite volume, power, and mass constrains. Furthermore, in this 12U M-ARGO CubeSat application, the propulsion system, including the TPM needs to be installed in half of the spacecraft unit, and therefore this TPM could be easily scalable down to a 6U CubeSat. At the same time, the requirement to fit the tubing and harness inside (particularly possible connectors from thrusters) is limiting space inside the allowable volume. Likewise, it is creating additional resistive torque terms, which are quite difficult to assess at initial stage without testing.

Acknowledgements

The project team would like to thank ESA for the financial support of this project. This work is part of the ESA GSTP funding associated with the contract No: AO/1-10571/20/NL/MG.

References

1. Mankaï, Sami. “Thruster orientation mechanism’’ ESMATS. Tolouse, 1999
2. B, Wood, Buff W y Delouard P. ‘’Smart-1 electrical propulsion steering mechanism (EPMEC) ‘’ ESMATS. Liege, 2001
3. Falkner, Manfred. ‘’Electric propulsion thruster pointing mechanism (TPM) for Eurostar 3000’’, 29th International Electric Propulsion. 2005
4. Asadurian, Armond. ‘’Design and development of a two-axis thruster gimbal with xenon propellant lines’’, 40th Aerospace Mechanisms Symposium. 2010.
5. Neugebauer, Christian. ‘’ Electric propulsion pointing mechanism for BepiColombo’’ ESMATS 2011. Constance.
6. ALMATECH. 2018, ‘’Novel thrust vectoring mechanism’’, https://almatech.ch/.
7. MOOG, 2021, ‘’Electric propulsion thruster gimbal assemblies (TGA)’’ https://www.moog.com/products/space -mechanisms/gimbals.html

The GRASS Gravimeter Rotation Mechanism for ESA Hera Mission On-Board Juventas Deep Space CubeSat

Matthias Noeker* **, Emiel Van Ransbeeck*** ****, Birgit Ritter* and Özgür Karatekin*

Abstract

The ESA Hera mission will follow the NASA DART mission to the binary asteroid system Didymos for detailed investigation of the asteroids and the impact crater caused by the DART spacecraft. The Hera spacecraft will release two CubeSats, Milani and Juventas. In the final mission phase, Juventas will attempt landing on the secondary, Dimorphos. Here, the GRAvimeter for small Solar System bodies (GRASS) will measure the surface gravity. In this work, we describe the design, fabrication and testing of the gravimeter rotation mechanism with its key components. Overall, a gear-motor rotates the sensor head by means of gear train and continuous electrical contact is ensured by a slip ring. The main design drivers were the harsh deep-space environment, especially the cold operating temperature limit of −30°C, and the limited mass (0.38 kg) and volume (1 CubeSat unit U = $(100\ mm)^3$) budgets available inside the 6U-XL-CubeSat. While here the presented mechanism is specific to the GRASS scientific payload, it could be used for other future instrument demanding sensor head rotation or pointing.

Introduction

This paper presents the design, development, manufacturing, integration, and functional tests of the rotating mechanism for the gravimeter on-board the nanosat platform to land on the surface of an asteroid. Juventas will carry the GRAvimeter for small Solar System bodies (GRASS) for surface gravimetry [1, 2] and is part of the ESA Hera mission, which is the first European planetary defense mission, targeting the binary asteroid system 65803 Didymos [3]. Together with the NASA Double Asteroid Redirection Test (DART) mission, it forms the Asteroid Impact Deflection Assessment (AIDA) international cooperation [4]. Here, NASA will perform a kinetic impact to the secondary of Didymos, called Dimorphos, to demonstrate the feasibility of deflecting an asteroid on collision course with Earth. ESA will then embark to visit the same asteroid system for detailed characterization of the system, with special attention to the artificial impact crater. This is necessary to complete the DART test, i.e., by determining the impact momentum transfer, mechanical surface strength, interior structure and asteroid mass. To support this, the Hera parent-craft will deploy two child-craft, the CubeSats Juventas [5] and Milani [6]. In their final mission phases, Juventas, and possibly Milani, will attempt landing on Dimorphos to perform additional surface measurements, most notably the GRASS surface gravimetric measurement.

The landing orientation of Juventas is uncontrolled [7] and the (precise) gravity vector orientation of Dimorphos is unknown. Unlike on Earth, and in absence of a complex levelling mechanism, a 3D-measurement is required for full gravity vector reconstruction. Two gravimeter axes, aligned orthogonally, and the rotation of the instrument sensor heads, in which the gravimeter spring is placed, realize this. The rotation of the spring also allows for instrument bias rejection, similar to the quasi-steady acceleration measurement (QSAM) instrument for spacecraft that inverted the measurement direction by 180° [8]. Therefore, the mechanism rotation is crucial to the experiments success. In this work, we present the GRASS mechanism as designed for flight on-board the Juventas CubeSat forming part in the ESA Hera mission. For this, the one-axis mechanism is presented in detail that is identical for the both combined axes. In addition, the combination of two mechanisms, forming the two-axes GRASS instrument, is described.

* Royal Observatory of Belgium, Brussels, Belgium; matthias.noeker@observatory.be
** Université catholique de Louvain, Ottignies-Louvain-la-Neuve, Belgium
*** VRE Consultancy, Mazenzele, Belgium
**** Royal Belgian Institute for Space Aeronomy, Brussels, Belgium

The instrument has passed the critical design review (CDR) and first pre-tests on the engineering-qualification model 1 (EQM-1) were successful. The whole instrument, including the mechanism, is designed for the harsh environmental conditions in deep space and on the asteroid surface, as well as for a long cruise phase of up to four years. At this project stage, no noteworthy changes are expected on mechanism level towards the flight model integration and delivery planned for late 2022. The here presented design, hardware and tests belong hence to the EQM, providing the reader with the latest status of the work.

This document first lists the mechanism requirements, followed by an introduction to the working principle of the GRASS mechanism. Next, the instrument architecture, the component selection, mechanism manufacturing, and integration is detailed. Lastly, functional tests with a focus on the cold temperature functionality is presented.

Mechanism Requirements

The requirements (REQ) for the GRASS instrument relevant to the rotation mechanism are formulated and numbered for reference as listed below. Some of them were already discussed in [9].

The first set of requirements considers the instrument accommodation, demanding an extremely compact instrument design, and the sensor head rotation:

- REQ-001: The overall instrument shall fit inside a volume envelope of one CubeSat unit (1U = $(100\ mm)^3$).
- REQ-002: The total instrument mass shall not exceed 380 grams including margins.
- REQ-003 The sensor head length must be maximized.
- REQ-004: The mechanism shall enable continuous, bi-directional and unrestricted rotation of the sensor head, with a safety factor of at least 3 for the torque.
- REQ-005: The mechanism shall accommodate the sensor head with diameter of 15 mm.
- REQ-006: The mechanical noise induced to the sensor head shall be minimized.
- REQ-007: The sensor head rotation shall allow slow rotation (<10 RPM) and incremental rotation.

The environmental requirements concern the mechanism regarding the temperature:

- REQ-008: The mechanism shall operate in the temperature range from −30°C to +50°C [243 K to 323 K].
- REQ-009: The mechanism shall comply with the non-operational temperature range from −30°C to +50°C [243 K to 323 K].
- REQ-010: The thermal contact between the gear-motor and the mechanism shall be minimized.

The lifetime of the mechanism is non-critical, as the rotation is only performed for the surface operation and maintenance:

- REQ-011: The mechanism shall have a minimum lifetime of 43,200 revolutions.

The requirement on the electric contact between rotor and stator remained unchanged from [9], but demanded two additional lines:

- REQ-012: The mechanism shall provide continuous, uninterrupted electrical connection between the instrument back-end electronics and sensor front-end electronics at 8 lines.

The angular position requirement was tightened compared to the prototype requirement [9], now reading:

- REQ-013: The mechanism shall provide continuous information about the absolute angular position of the sensor head, with an accuracy better than 0.5 degree and the rotation direction.

The instrument mounting requirements are not only concerned with fixing the instrument inside the spacecraft, but also with non-deformation of the instrument, the knowledge of the instrument orientation and the combination of two axes:

- REQ-014: The instrument shall be mounted with countersunk screws following the specified hole pattern.
- REQ-015: Two identical rotation mechanisms shall be combined orthogonally without inducing additional stresses to either mechanism.
- REQ-016: The mounting inside Juventas shall not influence the orientation of the two orthogonal instrument axes.
- REQ-017: The thermal contact between the instrument and the satellite shall be minimized.

With the mechanism requirements formulated above, the mechanism development is described in this work. As will be shown, it was possible to fulfill all of the formulated requirements.

Working Principle

This Section describes the mechanisms overall concept. A gear-motor is aligned in parallel with the sensor head and the torque is transmitted by a gear train (REQ-004). Continuous power and signal transfer from the instrument to the rotating sensor head (REQ-012) is realized with a slip ring.

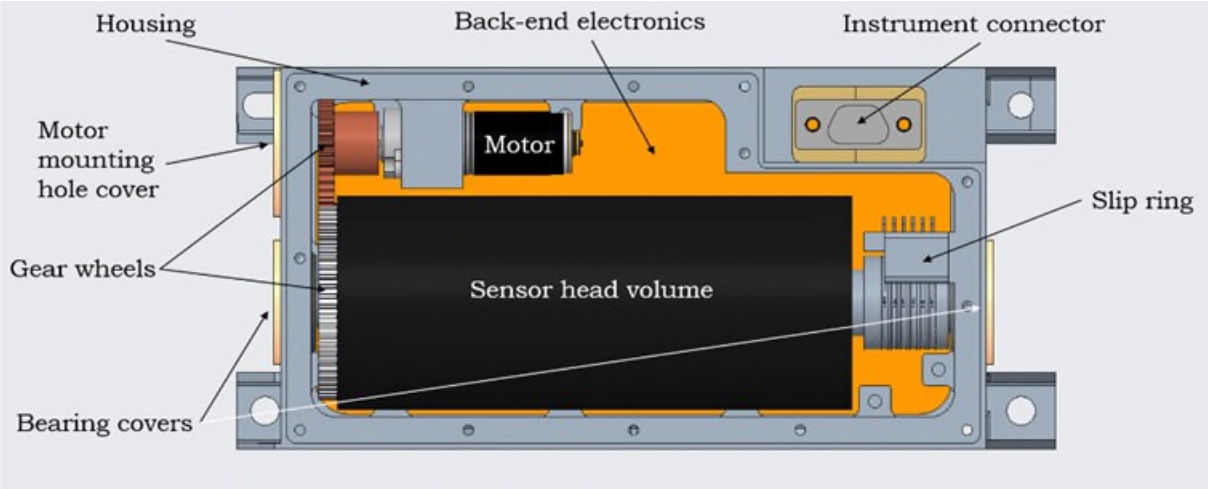

Figure 1. Working principle of the GRASS mechanism prototype, forming the basis of the here presented mechanism. Figure from [9].

The working principle of the spring-based GRASS gravimeter mechanism prototype was described in [9], which formed the basis for the continued development. The design included a large degree of adaptability, allowing to test a large range of gravimeter sensor head configurations (i.e., different bending springs, sensing electrodes, front-end electronics, etc.). The prototype consisted only of a single-axis instrument and the constraints on volume and mass were less strict than for the flight model design. Obviously, it is well possible to align two of these instruments orthogonally, e.g., by using a mounting plate as described in this work. The mechanism working principle is shown in Figure 1, allowing to retrace the subsequent development, strongly driven by the need of an extremely compact design, as described with the requirements REQ-001 and REQ-002.

Mechanism Development

The mechanism development consists of two parts. Firstly, the main part is the one-axis rotation mechanism description. Secondly, the orthogonal mating of two rotation mechanisms is described with special attention to REQ-015 and REQ-016. The used components are detailed in the next Section.

GRASS Rotation Mechanism

Before providing more details, the top-level mechanism architecture is described in the following as shown in Figure 2. Core element of the mechanism is the rotating sensor head (REQ-004 and REQ-005). Supported by two flanged bearings, the sensor head is rotated by a gear train connected to a gear-motor. The arrangement of the motor in parallel to the sensor head allows maximizing the sensor head length (REQ-003). Electric contact between the rotor and stator (REQ-012) is ensured by means of a slip ring, arranged in-line with the sensor head. The slip ring output harness is passed through protective harness bushes towards the inside of the housing for connection with the back-end electronics (BEE). The BEE also drive the mechanism by controlling the gear-motor, and receive the angular position data. This data is recorded by an absolute encoder (REQ-013), which monitors the angular position of the sensor indirectly, as it reads the position of the motor gear. For this, the encoder is positioned and clamped inside the housing and the encoder magnet is placed inside the motor gear. Driven by REQ-010, the motor mounting piece is machined in titanium and fixed with titanium fasteners. Furthermore, the contact area of the piece to the housing is minimized, all aiding to keep the motor warm in the cold temperature regime down to −30°C (REQ-008 and REQ-009).

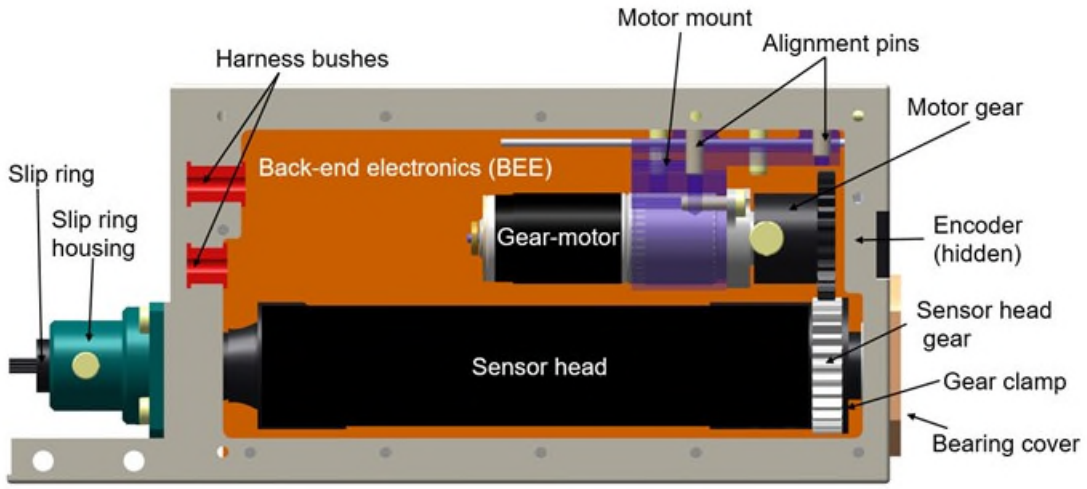

Figure 2. GRASS mechanism architecture. A global cover covers the open front and slip ring.

Two Axes Arrangement

For flight, two of the above presented mechanisms are required (for gravity vector reconstruction) as stated in REQ-015. We have accounted for the orthogonal combination of two identical mechanisms, forming the GRASS instrument. Looking at Figure 2, it is easy to imagine that two mechanisms can be combined by

flipping one upside down and merging them at the part of the slip rings. Like this, the two slip rings are stacked above each other at 90°, allowing to meet the maximum length constraint of 100 mm in both dimensions (REQ-001). This arrangement is shown in Figure 3. The second harness bush (Figure 2), allows the interior interconnection of the two instruments, e.g., making it possible to control the full instrument with only one set of BEE, while here the baseline design considers individual communication between spacecraft and each rotation mechanism. For this, each BEE is equipped with an individual connector for power and data connection. A global L-shaped cover on the outside closes the open side of the two mechanisms and the intersection with the two slip rings and harness (Figure 8). Like this, the instrument with its two mechanisms is fully enclosed.

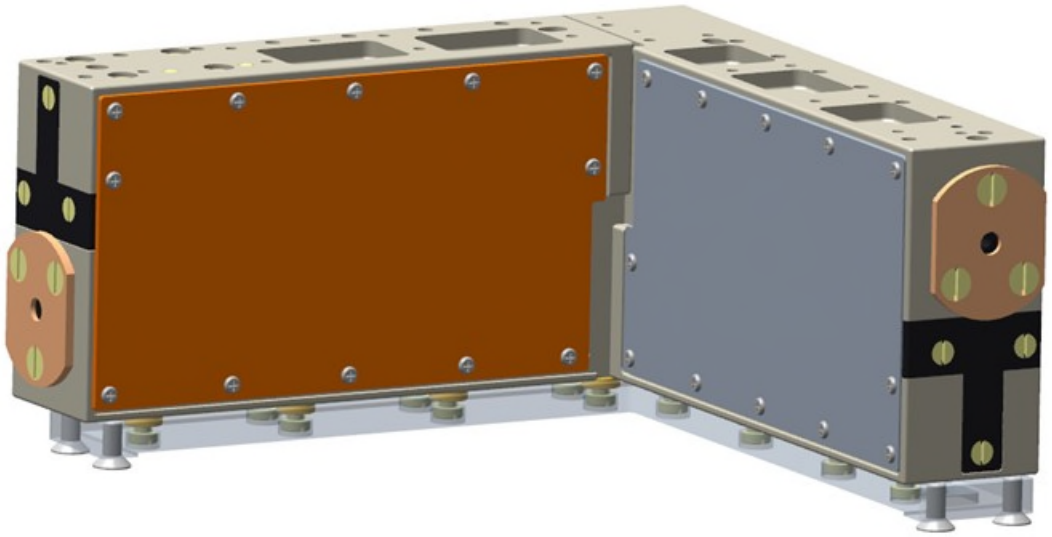

Figure 3. Combination of two GRASS gravimeters to form an orthogonal setting. Clearly, the instruments appear identical but stacked upside-down to allow maximizing the length of the instrument. The two axes can be differentiated by the back-end electronics shown in orange and grey, respectively. On the bottom, the common mechanical interface plate is shown with the considered mounting screws for the Juventas CubeSat.

In principle, the mechanism, single or double, can be directly mounted inside the spacecraft. However, the orientation between the two mechanism axes must not be altered (REQ-016), and no mounting stresses shall be induced to the mechanisms (REQ-015). Provided that countersunk screws are used (REQ-014), any misalignment in the screw holes on the housing or the spacecraft (even within the machining tolerances), will induce stress, as the countersunk screw heads force themselves into their sunk position. Therefore, an L-shaped mounting plate is used on which the two-axes mechanism setup is fixed using cheese head screws. This screw type does allow for some lateral play, absorbing any mounting stress (REQ-015 and REQ-016) by the counter sunk screws, used to fix this mounting piece. Furthermore, the thermal insulation of the instrument mechanisms is improved, as the mounting piece is made of titanium and the contact area towards the spacecraft is limited to the surrounding of the screw contacts. The thermal contact is reduced further by using again titanium screws between the mounting piece and the housings, and by using thermal Vespel-SP3 washers, avoiding direct contact of housing and titanium piece. These washers also compensate for the differential thermal expansion of titanium and aluminum. Bending along the mechanisms length is avoided by using shims during the satellite integration, if necessary.

Components

In this Section, the key (purchased) components forming part of the mechanism are presented together with applied customizations, where they were necessary. Starting here, we present lessons learnt of the presented work, indicated by a ➔ symbol.

Gear-Motor

The gear-motor (Figure 6) selected for the mechanism is the same as for the mechanism prototype [9], being the *CoograDrive® Space 10 mm - Type 6* from Micromotion GmbH. For the initial selection, a preliminary torque requirement with the required safety factor had been formulated together with limitations on mass and volume. This gear-motor, fulfilled all preliminary requirements without any problem for both the prototype and the design for the Juventas CubeSat and meets REQ-007. The extremely compact design (diameter = 10 mm, length = 36.15 mm, mass = 13 gram), did not drive the mechanism length or depth, as both are smaller than the sensor head (REQ-005), and the part delivers a high nominal torque of 15 mNm. As will be shown in the *Mechanism Verification* Section, this torque satisfies REQ-004. According to the supplier, the part has heritage in space, yet limited to geocentric orbits. Regarding the cruise phase in deep space, two solutions were implemented to minimize the lubricant creep and to ensure proper functioning of the motor, and therefore the mechanism, upon arrival in the binary asteroid system. Regarding a physical creep barrier, this option was discarded, as a well-functioning lubricant seal would come at the cost of torque, which was a critical motor selection criterion. Rather, the output bearing, gear components and motor bearing will be customized by applying epilamization[1], limiting the spreading of the lubricant inside the gear-motor. The second solution is the implementation of a mechanism maintenance procedure, described in detailed in Section *Mechanism Maintenance*. Regarding the minimum operating temperature, the gear-motor has a nominal value of −10°C, which is too warm considering the formulated requirement REQ-008. To verify the part's functionality at colder temperatures, a cold motor starting test is presented below in Section *Mechanism Verification*.

- ➔ The CoograDrive® Space gear-motors provide a very good Torque/(Volume×Mass) ratio for our application.
- ➔ To avoid lubricant spreading, the relevant surfaces should be treated with epilamization.

For performed trade-offs regarding this gear-motor, including the option to include an encoder or a slip clutch in the gear-motor, we refer to [9].

Slip Ring

The selection of the slip ring to realize electric contact (data and power) between mechanism rotor and stator was driven by similar factors as for the (gear-) motor. An extremely compact design in diameter and length was needed to not drive the instrument width, while limiting the increase on the total mechanism length, respectively. While for the motor a torque as large as possible was desired, the required torque for turning the slip ring had to be minimized. Furthermore, as discussed below in the *Integration* Section, the slip ring had to be without flange, and the harness were not to exceed the part's diameter-bound cylinder. When selecting a slip ring, the nominal torque values often lead to exclusion of candidates. Finally, we have selected the *MMC1189-S08* slip ring from Moflon. The version S08 provides the required 8 lines (maximum number of lines available). This slip ring has again an extremely compact design (diameter = 5.9 mm, length = 11.9 mm, mass = 3.8 gram). The nominal torque (data sheet) was 25 mNm (for 6 lines), which was also too large, but was found much lower in our testing (Section *Mechanism Verification*). This slip ring is sold as military grade, and the finally purchased parts were again customized, here by changing the housing material to aluminum and by adopting the bearing to space conditions by using a bearing without lubricating oil.

[1] http://www.epilamisierung.com/en/, accessed on 12.01.2022.

➔ Considering extremely compact slip ring designs, it is hard to find a motor meeting the nominal slip ring torque. However, measuring the torque can reveal that the actual torque requirements is (much) lower than the value stated in data sheets.

Encoder

Driven by REQ-013, positional knowledge only once per revolution as in the prototype [9] was no more an option. Rather, an absolute encoder was integrated in the mechanism design. Here, we use the *RM08 Miniature Rotary Magnetic Encoder* from RLS. The angular position is not measured directly over the sensor head, but rather over the motor gear wheel. As discussed in the next Subsection, the gear ratio is $i = 1$, thus the angular position translation is straightforward, while the measured rotation direction is obviously inverse. A section-view of the encoder setting is displayed in Figure 4. The gear was adapted to mount a (screw-fixed) magnet bush, in which the encoder magnet is glued. The nominal distance between the magnet and the encoder is 1.0 mm ±0.5 mm. The encoder is clamped with a dedicated encoder mounting bracket into the housing that also covers the encoder harness before it enters the housing. Encoder and magnet mass is <2 gram and 0.4 gram, respectively. The encoder accuracy is rated up to ±0.3°.

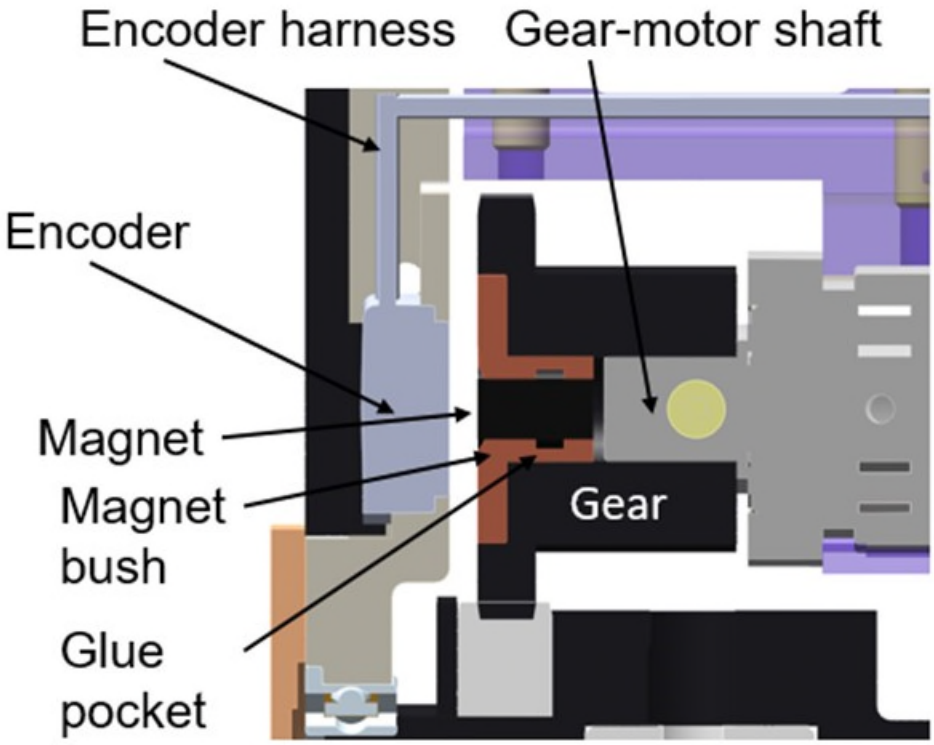

Figure 4. Section-view of mechanism encoder solution.

Gear Train

The gear motor torque is transferred by a gear train of two gear wheels to the sensor head. To avoid cold welding of the mechanism, the (gear-) motor gear is made of stainless steel 304L and the sensor head gear of Delrin®. The motor gear with the encoder magnet is visible in Figure 4. Regarding the sensor head gear, we increase the bore hole and mounted it over the sensor head. Initial mounting of this gear, screwing directly in the thermoplastic, lead to problems due to the proximity of the (countersunk) screw holes to the gear teeth profile. Therefore, an aluminum clamp to fix the gear (Figure 2) was added to the sensor assembly. The gear ratio i (output to input) is computed in Equation (1) and the module of the two parts is 0.50.

$$i = \frac{D_D}{D_S} = \frac{14mm}{14mm} = \frac{z_D}{z_S} = \frac{28}{28} = 1 \quad (1)$$

Where $D_{D/S}$ is the reference circle and $z_{D/S}$ the number of teeth of the Delrin (D) and stainless steel (S) gear, respectively. Like for the prototype [9], a gear ratio $i > 1$ would have been desired, however, a reduction of the motor gear was not possible due to the encoder magnet, and a larger sensor head gear would have increased the overall mechanism volume.

Bearings

The sensor head is supported by two identical flanged bearings that are assembled from the outside in the housing. The selected bearing cages are made of non-metallic BarTemp material and machined in one-piece. This material is very well suited for space applications, as it is dry-lubricated, not demanding conventional lubrication. For example, the operational temperature of these bearings ranges from −200°C to +100°C. Dry-lubrication means that the BarTemp cage material provides a lubricating dry-film to the bearing balls during their movement, lubricating both the balls and the raceway. While this is an excellent solution for space mechanisms, the loading on the bearings is limited due to the absence of conventional lubrication. Furthermore, this self-lubricating bearings should have an initial rotation of about 30° in order to distribute the dry-film in the bearing [10], which is another motivation for the mechanism maintenance, described below.

➔ BarTemp bearings provide unique properties for space mechanism, not demanding lubrication and being operational in a very wide temperature range, but they are generally not available off-the-shelf with a very long lead-time of nearly one year in our case.

Wave Washers

For structural reasons, the sensor head was made of titanium Ti-6Al-4V, while the housing is made in aluminum Al-7075-T7351. To compensate for differential thermal expansion between the two pieces, one wave washer (2 waves) has been added between each of the two bearings and the sensor head. This avoids axial play of the sensor head, e.g., in the warm case, when the housing thermally expands more than the sensor head. Furthermore, it avoids rigid contact from the sensor head to the bearing-housing assembly, aiding at reducing vibrations in the sensor head (REQ-006).

Helicoils

Preferably, titanium Helicoils Screwlock Tangfree should be used for fixing the mechanism, to reduce the thermal contact of the mounting, in support of the used titanium screws (REQ-017). However, we were not able to find a Helicoil supplier offering the pieces made in titanium, except one with a minimum order quantity (MOQ) of 5,000 with additional charges on the tooling, making it prohibitively expensive for the project budget.

➔ Titanium (or comparable material) Helicoils could be used in aerospace applications e.g. to further reduce thermal contact between bolted parts, but are currently hard to source on the market.

Manufacturing

Regarding the manufacturing of the mechanism hardware, this Section focuses on measures to minimize the mechanical noise induce in the sensor head (REQ-006). For this, the machined pieces shall ensure best possible alignment of the two bearing holes, and best parallelism of the two axes of sensor head and gear-motor. The latter reduces the noise within the gear train, with the additional condition that the axis distance is within the specified positive tolerance of $d = 14^{+0.03}_{+0.02}$ mm (accounting for thermal expansion).

For the bearing holes drilled in the one-piece housing, it is required to do all measurement and the machining with respect to the same reference surface. Like this, best alignment of the two bearings and therefore the sensor head rotation is ensured. Relative to the bearing holes, the hole for the encoder is

machined, ensuring good positioning of this component. Regarding the axes distance, the machining of the motor mounting piece is key (Figure 6). Here, the machining cannot be done independently from the machined housing. Rather, the machining is done with a positive tolerance on the distance from the motor mounting hole to the contact surface with the housing. Following this, the piece is screwed in the housing using additionally the alignment pins. This two-part assembly is then used for the measurement, focusing on the motor mounting hole *relative* to the bearing holes in the housing. If the distance is measured too small, or the axes alignment is not sufficient due to the geometric tolerances, the motor mount contact surface with the housing is re-machined by grinding. This process is repeated until the required specifications are met.

All aluminum (Al-7075-T7351) parts are treated with Alodine 1200, passivation is applied to stainless steel parts and the titanium (Ti-6Al-4V) parts experience blue anodization. The total instrument was found to have a mass smaller than 330 gram, leaving a margin of 15 % and fulfilling REQ-002.

- ➔ The iterative process of measuring two assembled parts and adapting one part as required, ensured meeting the assembly tolerances, and mitigated the risk when manufacturing and measuring both pieces individually.
- ➔ Adaptation of precision gears must be done by no other means than grinding to avoid burrs in the precision pieces.

Integration

The rotation mechanism integration is performed in two steps, firstly the two one-axis mechanism are integrated individually, followed by the orthogonal combination of the two mechanisms and the combination with the mounting plate. These two integrations are described in this Section.

Firstly, the *sensor head subassembly* is integrated, an in-line assembly of the *sensor head* with the *slip ring*, connected by the torque-transmissing *slip ring clamp*. The torque of the rotating sensor head is transmitted to the *slip ring clamp* by fins. Through this hollow piece, the sensor head harness arrives at the rotating shaft of the slip ring that is glued to the clamp. The custom-made precision sensor head gear and the associated gear clamp, as pictured in Figure 5 (it is referred to left/right as in this Figure), complement the assembly. This subassembly is realized to ensure the best in-line alignment of the assembly, e.g. when aligning and gluing the slip ring clamp. During the gluing process, the clamp is fixed with a setscrew to affix the position.

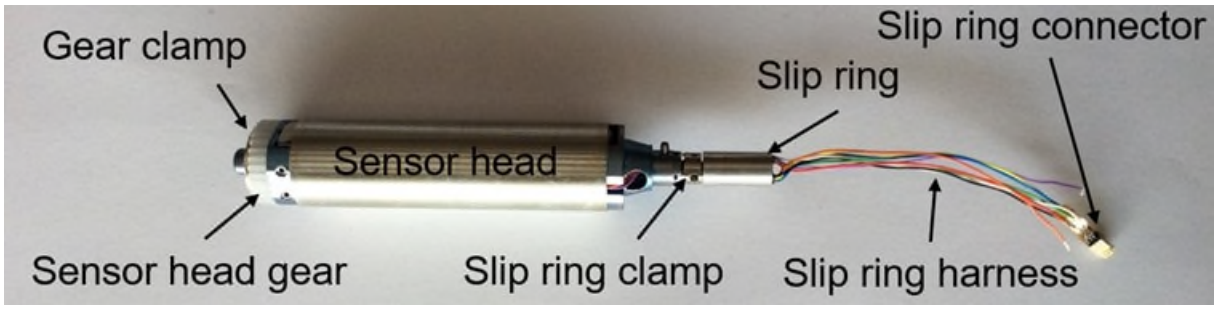

Figure 5. Integrated in-line "sensor head subassembly" for integration into the housing. Note that the slip ring clamp is not yet glued in the shown setup.

This pictured subassembly is then introduced into the mechanism *housing*. With the housing being in one piece, the design allows to introduce this setting laterally with the chamfered shoulder of the sensor head temporarily entering the bearing hole, thus allowing the leftmost shoulder to enter the second bearing hole. This assembly is then positioned with the two flanged bearings mounted from the outside. Here, it becomes clear why the slip ring outer diameter was limited, as the bearing is slid over the slip ring and its clamp to the sensor head bearing shoulder on the right. The left bearing is secured with the *bearing cover* and the

right bearing is secured by the *slip ring housing,* serving therefore twofold. The second purpose is the support of the slip ring stator, which is glued and screw-clamped in this housing. At this stage, the rotational torque of this subassembly is measured below in the *Functional Tests* Section.

After this, the second half of the one-axis mechanism assembly concerns the assembly of the *gear-motor* and the *encoder* setup. Firstly, the encoder is placed inside the housing and its harness enters the housing through the dedicated hole. Using the *encoder clamp*, the encoder is fixed in its position and the external part of the harness, as well as the harness hole are covered by this piece (Figure 6). Second, the *gear-motor assembly* is prepared as shown in Figure 6. The *encoder magnet* is glued inside the *magnet bush*, which in turn is screwed in the *motor gear*. The gear motor is put inside the *motor mount* and its gear is then screwed on the shaft of the gear-motor. This subassembly is then introduced into the housing, while the alignment is ensured using two alignment pins during the fixation (identical to the mounting during machining, see above).

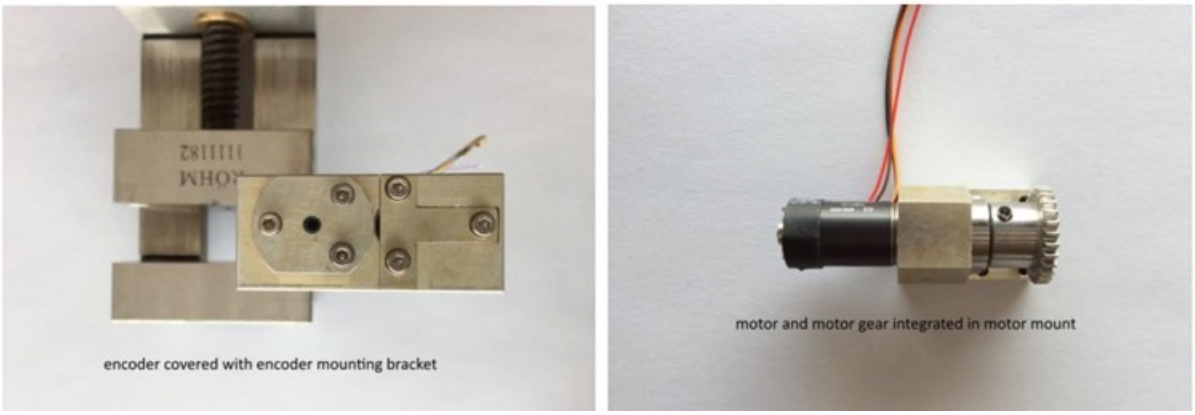

Figure 6. (Left) Bearing and encoder cover on side view of the mechanism. Note that countersunk screws have replaced the screws on the bearing/encoder covers. (Right) Motor mount with integrated gear-motor and motor gear.

As a last step, the *back-end electronics (BEE)* of the instrument are mounted, which closes the mechanism off on one side. The gear-motor and slip ring harness are connected to the BEE, while the latter harness is guided inside the housing through one of the harness bushes. For the BEE (and cover, introduced below) fixation, special SNZS pan head screws are used to limit the width of the mechanism. The fully integrated mechanism is shown in Figure 7.

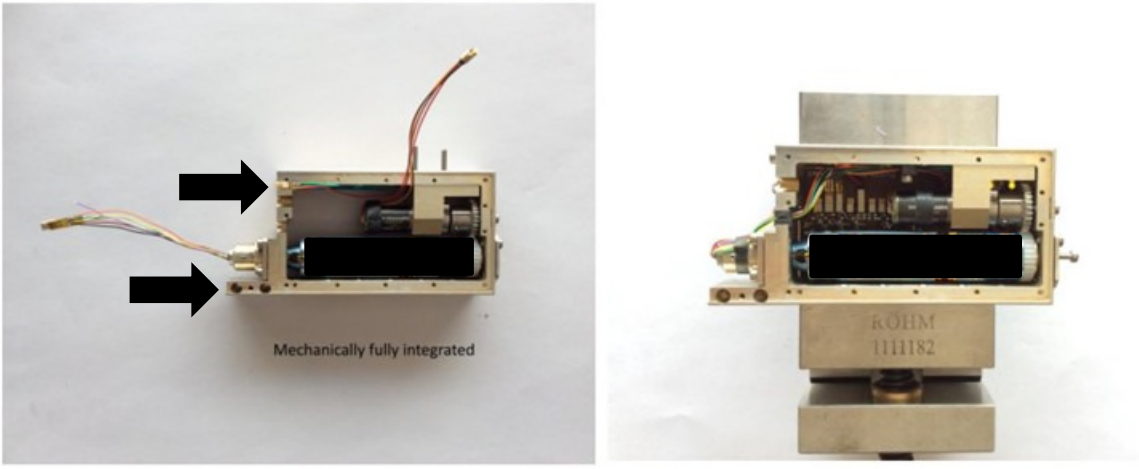

Figure 7. Manufactured and assembled EQM GRASS instrument showing the main characteristics of the payload mechanism. Black arrows indicate the interface for two-axes assembly.

The combination of the two individual mechanisms to form the orthogonal instrument mechanism (Figure 3) is straightforward. The two identical mechanisms are combined orthogonally by stacking the two instruments such that the rotation axes are skewed with the slip rings lying above each other (Figure 8). Per axis, two screws enter the respective other housing, as indicated in Figure 7. As shown in Figure 3, the inside of the instrument is closed off with the BEE, while the outside is covered with a L-shaped *global cover* made from a single sheet material bent at 90°. With this cover, the instrument is fully enclosed, including the junction with the two slip rings, aiding to avoid EMC problems and covering all moving parts of the mechanism(s). Finally, this setting is mounted on the Titanium *mounting piece* with *thermal washers* to complement the full instrument. After allowing for some stress relaxation time, the alignment of the two axes is measured by obtaining the orientation of defined reference planes that have previously been defined with respect to the sensor head rotation axis. This is a specific requirement coming from the gravity vector reconstruction, and might not be needed for other science payload applications. It allows further confirming that the alignment between the two axes was indeed not altered during the instrument mounting (REQ-016) as should be avoided due to the mounting piece.

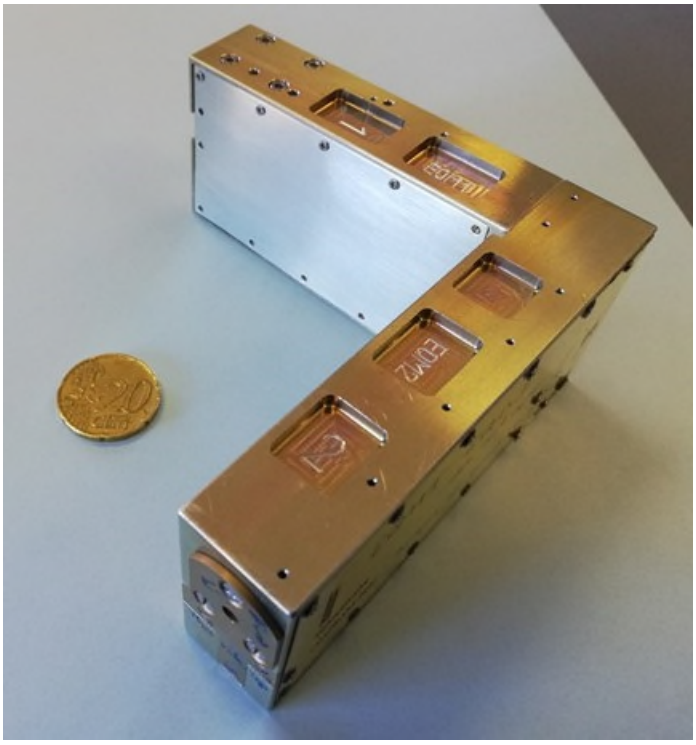

Figure 8. Integrated two-axes GRASS instrument (without satellite interface and dummy BEE on the inside). Engraving in the mass reduction pockets allows clear identification of the instrument axes (1 and 2), as well as the instrument version (here: EQM). In the front, the bearings and encoder covers are visible. 20 cent euro coin for size-reference.

Mechanism Verification

In order to verify the mechanism design, two functional tests regarding the sensor torque after integration, and the functionality at low temperatures have been performed. The qualification testing of the EQM at instrument level, thus including the mechanism, is ongoing and not reported in this paper. First pre-tests show favorable results regarding the here presented rotation mechanism. The below reported sensor torque test has been re-measured after a pre-vibration test, and no measurable increase in the torque was observed. Regarding REQ-011, no lifetime test was foreseen, as this requirement was found non-critical regarding all used components affecting the rotation (gear-motor, slip ring, bearing, and gear train) considering their individual lifetimes and recalling the low rotation speed (REQ-007).

Sensor Rotational Torque

In order to verify the safety factor of the torque (REQ-004), the torque of the sensor head sub-assembly (bearings, slip ring, moment of inertia) has been measured. The value of the tested torque $M_{T,start}$ for both directions, was found to be 1.2 mNm.

With the gear ratio i = 1 (Equation (1)) and an assumed gear efficiency for the precision gears of η = 0.9, the nominal input torque of the motor of 15 mNm yields an output torque at the sensor head as shown in Equation (2).

$$M_{T,out} = M_{T,in} \cdot i \cdot \eta = 15\ \text{mNm} \cdot 1 \cdot 0.9 = 13.5\ \text{mNm} \tag{2}$$

With this, the safety factor S can be computed as in Equation (3).

$$S = \frac{M_{T,out}}{M_{T,start}} = \frac{13.5\ mNm}{1.2\ mNm} = 11.25 > 3 \tag{3}$$

The safety factor of 11.25 is much larger than the minimum required value of 3, and therefore, no problems in the gear train are expected.

Cold Motor Start

One of the limiting factors of the mechanism in cold temperature was the minimum nominal operating temperature of the gear-motor. The supplier stated that this is due to the reduced viscosity of the lubricant and that additional testing would be required if the range could be extended for the minimum operating temperature of −30°C (REQ-008). For this, a cold motor start had been performed in a thermal vacuum chamber. Specifically for the cold motor start test, the ambient temperature was set to −35°C. After holding this temperature for about two hours, the motor was started at a temperature of about −29°C ± 1°C without problems. This was well confirmed by the encoder reading, clearly showing the expected gear-motor rotation. The delay in reaching the target temperature comes from the functioning of the thermal insulation of the gear-motor (REQ-010). Still, the result was very promising and showed a good behavior of the gear-motor below its nominal minimum working temperature. Additionally to this, the option to power the stepper motor coils, to perform preheating of the gear motor prior to a cold motor start, and the option to add an external heater are considered as additional measures. Based on future test results, it will become clear if these measures are needed. If in doubt, it will be possible to consider one or both options as backup solutions, provided that the mechanism rotation is indispensable to the experiment's success.

Mechanism Maintenance

Other than for Earth-orbiting mechanisms, the cruise phase of the here presented mechanisms can be up to four years. Additionally, the ground-storage phase of instruments on piggyback-spacecraft, i.e., a CubeSat deployed by a parent-spacecraft, is extended due to two deliveries (instrument to CubeSat, CubeSat to main spacecraft). Therefore, the idle time of the here presented mechanism will be extended. This poses a risk to the movability of the mechanism. Most specifically, it is possible that, despite the epilamization added to the gear-motor, the lubricant creeps and that it leaves the regions to which it has been applied. These are the internal bearings and the gears of the planetary gear forming part of the gear-motor. For this reason, and in discussion with the gear-motor supplier, it was proposed to include a mechanism maintenance to minimize the lubrication creep. This maintenance would exercise the rotation mechanism regularly, monthly, or at least bi-monthly during storage and cruise. In case that this exercise cannot be performed during certain periods, due care will be taken to place two additional exercises as late as possible before such interruption, and likewise as early as possible after the interruption. The rotation of the sensor head during cruise phase will induce a torque T on the spacecraft that needs to be compensated. However, given the small moment of inertia I_{xx} of the sensor head and the low angular acceleration $\ddot{\omega}$ of the maintenance mode, it is shown in Equation (4) that the induced torque is negligible (and that the mechanism cannot be used as backup reaction wheels).

$$T = I_{xx} \cdot \ddot{\omega} = 7 \cdot 10^{-7}\,\mathrm{kgm^2} \cdot 0.210\,\frac{1}{s^2} = 1.47 \cdot 10^{-7}\,\mathrm{Nm} \quad (4)$$

Additionally, this mechanism maintenance aids at maintaining the dry-lubrication film of the self-lubricating bearing cages on the bearing balls. Nevertheless, one initial rotation should be considered before entering the incremental rotation/pointing mode, if applicable and possible.

➔ Mechanisms for deep space exploration can be subject to (very) long storage times in cruise. Mechanism maintenance can increase the reliability of a mechanism upon arrival, yet mechanism exercise might not be possible for all kinds of mechanisms and it has to be agreed upon with the operations of the spacecraft.

Future Mechanism Utilization

While the here presented mechanism has been developed for the GRASS gravimeter and the Juventas CubeSat as part of the ESA Hera mission, it can be adapted to other use cases in space. For example, payloads likewise requiring sensor head rotation or pointing can make use of the here presented system. Together with the larger prototype design [9], a large range of sensor head sizes is covered, and the presented mechanism can be adapted or scaled for other sensor head dimensions. Further miniaturization of the presented CubeSat mechanism will be challenging, but achievable when identifying corresponding smaller solutions for dimension-drivers, e.g., the gear-motor, slip ring. The total mechanism length might be reduced for shorter sensor heads. The mechanism of one axis can work as a standalone instrument with minor modifications to the cover and mechanical interface. The orthogonal arrangement of two axes is the baseline presented in this paper, while other arrangements or a third orthogonal axis (potentially for redundancy) are possible, either with an adapted design or by using one one-axis and one two-axes mechanism in combination.

Conclusions

Here, we present the complete rotation mechanism for the GRASS gravimeter on-board Juventas CubeSat as part of the ESA Hera planetary defense mission. The requirements were introduced and the design is presented. Compared to the previous prototype development, the main difference is the need for an even more compact design, the compliance with the accommodation requirements in the CubeSat, and the orthogonal combination of the individual mechanisms forming the instrument.

The design drivers, choices as well as component and material selection have been presented in this work. Regarding the individual mechanism components, customizations were applied to the gear-motor and slip ring as adaptations to the space environment, and to prepare the mechanism for a long cruise phase in deep space. Functional tests showed a good mechanism performance and confirmed the presented design. The manufacturing description was focused on ensuring the proper tolerances, specifically concerning the gear train axes distance. Using an iterative machining-measurement process, best results were obtained. After this, a detailed description of the mechanism integration steps and their order has been presented. This was complemented by the description of two functional tests. Both showed satisfactory results with regard to the formulated requirements. Next, a procedure for mechanism maintenance, considering both the long ground storage and deep space cruise phase, has been presented for this mechanism. Lastly, possible future adaptations of the here presented mechanism to other science payloads have been discussed, opening a wide range of possibilities for future science missions demanding sensor head rotation or pointing.

The relevant lessons learned have been formulated throughout this paper in the relevant sections. Without repeating these in detail, it is worth highlighting two lessons learned that were developed specifically for this deep space mission: The gear motor was treated with epilamization to minimize lubricant creep, and

furthermore a maintenance procedure on mechanism level has been described. Both aspects address a specific challenge of mechanisms for space missions and might prove particularly valuable for future mechanism developments.

Acknowledgement

We thank the Royal Belgian Institute for Space Aeronomy (BIRA/IASB) technicians and engineers for their help and support in realizing the presented mechanism and the GRASS gravimeter. We would like to extend our thanks to the GRASS instrument team members. GRASS has been developed in collaboration between ROB and Embedded Instruments & Systems – Emxys. The authors acknowledge funding support from the PRODEX program managed by the European Space Agency (ESA) with help of the Belgian Science Policy Office (BELSPO) and from the European Union's Horizon 2020 research and innovation program within the NEO-MAPP project. M.N. acknowledges funding from the Foundation of German Business (sdw) and the Royal Observatory of Belgium (ROB) PhD grants.

References

1. Karatekin, Ö., Ritter, B., Carrasco, J., Noeker, M., Umit, E., Van Ransbeeck, E., Alaves, H., Tasev, E., Goli, M. and Goldberg, H., 2021, April. Surface gravimetry on Dimorphos. In EGU General Assembly Conference Abstracts (pp. EGU21-15901).
2. Ritter, B., Karatekin, Ö., Carrasco, J. A., Noeker, M., Ümit, E., Van Ransbeeck, E., Alaves, H., Tasev, E., Goli, M., Van Ruymbeke, M., 2021, Surface Gravimetry on Dimorphos with GRASS on Juventas. IAA-PDC-21-0X-XX. IAA Planetary Defense Conference – PDC 2021.
3. Michel, P., Küppers, M. and Carnelli, I., 2018. The Hera mission: European component of the ESA-NASA AIDA mission to a binary asteroid. 42nd COSPAR Scientific Assembly, 42, pp.B1-1.
4. Cheng, A.F., Rivkin, A.S., Michel, P., Atchison, J., Barnouin, O., Benner, L., Chabot, N.L., Ernst, C., Fahnestock, E.G., Kueppers, M. and Pravec, P., 2018. AIDA DART asteroid deflection test: Planetary defense and science objectives. Planetary and Space Science, 157, pp.104-115.
5. Karatekin, Ö., Le Bras, E., Herique, A., Tortora, P., Ritter, B., Scoubeau, M. and Moreno, V.M., 2021, September. Juventas Cubesat for the Hera mission. In European Planetary Science Congress (pp. EPSC2021-750).
6. Ferrari, F., Franzese, V., Pugliatti, M., Giordano, C. and Topputo, F., 2021. Preliminary mission profile of Hera's Milani CubeSat. Advances in Space Research, 67(6), pp.2010-2029.
7. Karatekin, O., Moreno Villa, V.M. and Goldberg, H., 2020, September. Preliminary investigation of the Juventas CubeSat landing on asteroid Dimorphos. In European Planetary Science Congress (pp. EPSC2020-683).
8. Hamacher, H., Jilg, R. and Feuerbacher, B., 1991. QSAM-A measurement system to detect quasi-steady accelerations aboard a spacecraft. Acta Astronautica, 24, pp.243-249.
9. Noeker, M., Van Ransbeeck, E., Karatekin, Ö. and Ritter, B., 2021, Development of a Compact Payload Mechanism enabling Continuous Motorized Sensor Head Rotation and Signal Transfer. 19th ESMATS, #18.
10. Hadley, H. (1980). in 14th Aerospace Mechanisms Symposium: Proceedings of a Symposium held at NASA Langley Research Center, Hampton, Virginia, May 1-2, 1980, vol. 2127 (NASA Scientific and Technical Information Office), vol. 2127, p. 101.

From PYSCHE PAM30 to Large Scale Free-Space Optical Communication

Gérald Aigouy*, Etienne Betch *, Augustin Bedek*, Nicolas Bourgeot*, Anthony Baillus*, Hugo Grardel *, Pierre Personnat*, Jean-Marc Nwesaty*, Xavier De Lepine*, Thomas Maillard* and Frank Claeyssen*

Abstract

New space giant constellations based on Free-Space Optical Communication are a new challenge from many perspectives. Considering the mandatory cost efficiency, with repeatability of performance, and reliability with no defect at customer integration, this requires an upheaval in space production and acceptance test methods when the quantities are beyond several thousands of units. Starting from the former PYSCHE PAM30 flight project heritage for Deep Space Optical Communication, CEDRAT TECHNOLOGIES (CTEC) presents the new design and test results of the P-FSM150S Fine Steering Mirror (FSM) Engineering Models developed under the ARTES project TELCO-B for future Free-Space Optical Communication constellations. The specific cost-efficient hardware design is presented, dedicated to very large quantities to be manufactured together with the performance test results over a preliminary batch of Engineering Model's production. The environmental test campaign for space qualification was passed and is presented, which includes launch vibration and shock tests, thermal vacuum tests, and high-frequency accelerated lifetime fatigue tests.

Introduction

The new P-FSM150S fine pointing mirror mechanism is the result of former CTEC space heritage in the field of mirror tilting piezo mechanisms and SiC substrate mirror design. The TELCO-B project was the opportunity to re-define the PSYCHE PAM30 design to future new space applications that require very high cost efficiency and very large quantities for giant constellation programs. A strong effort was applied to the design not only for achieving performance requirements, but also in the concept simplification for fast and reliable assembly processes, as well as qualification of a mirror supply chain with two different substrate technologies, i.e., SiC and SiSiC.

Figure 1. PSYCHE PAM30 (Left) and P-FSM150S (Right)

* CEDRAT TECHNOLOGIES, Meylan, France; gerald.aigouy@cedrat-tec.com

SiC Mirror Design and Manufacturing

One of the main design constraints of an embedded optics mechanism is to keep the mirror surface deformation to a minimum to limit the induced optical wave front error below the requirements. In this case, a maximum of 40-nm rms RWE at 0° mirror surface flatness is the target (corresponding to a 20-nm rms optical surface flatness). To ensure that the specification would be reached, CTEC used tools developed for previous space optical mechanisms projects. Specifically including evaluation of induced surface deformation caused by mechanical biases, thermal deformation, as well as optimization of mirror shape and dimensions.

The design optimization process included not only the mirror, but also an equally important part, the mirror support. The mirror support is the part providing the mechanical link between the actuators and the mirror. A specific mirror with flexible support design was performed. The support design aimed at reducing the operational optical surface deformation, while keeping the assembly stiff enough to withstand (mechanical stress considerations) environmental conditions (temperature, vibration) and mechanisms forces.

The mirror deformation induced by the mechanism was targeted to be under 20-nm rms RWE (at 0° angle of incidence), the mirror manufacturer was requested to deliver a coated mirror also under 20-nm rms RWE.

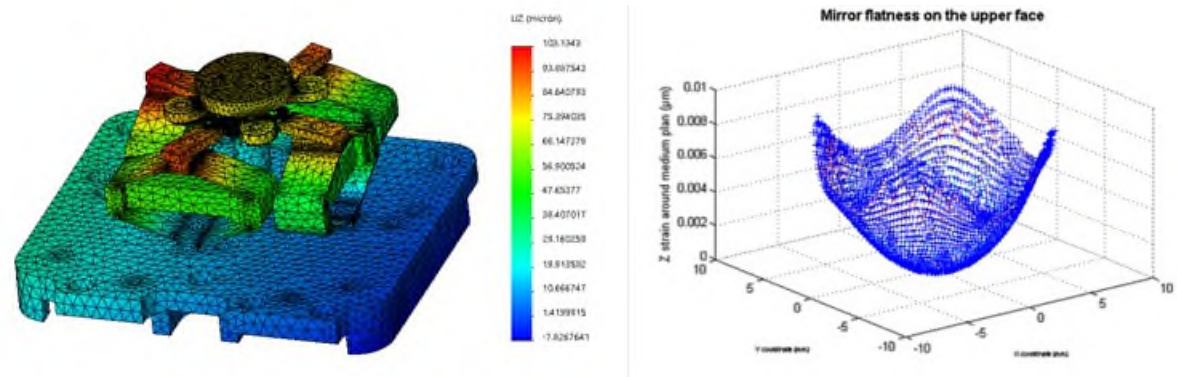

Figure 2. P-FSM150S WFE Simulation For a +60°C Temperature

Two mirror types were manufactured to be integrated onto the engineering models, i.e., SiC substrate with silver coating and SiSiC substrate with gold coating, from different suppliers and optical verifications were performed. Figure 3 shows the two mirror types and the RWE (reflected wave front error) measurement Zygo interferometer at CTEC laboratory.

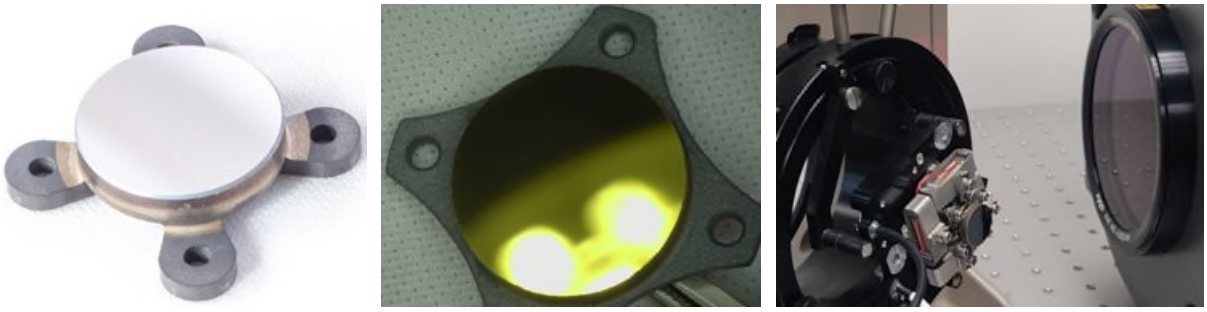

Figure 3. SiC Mirror (Left) SiSiC Mirrors (Middle) and RWE Test After Integration (Right)

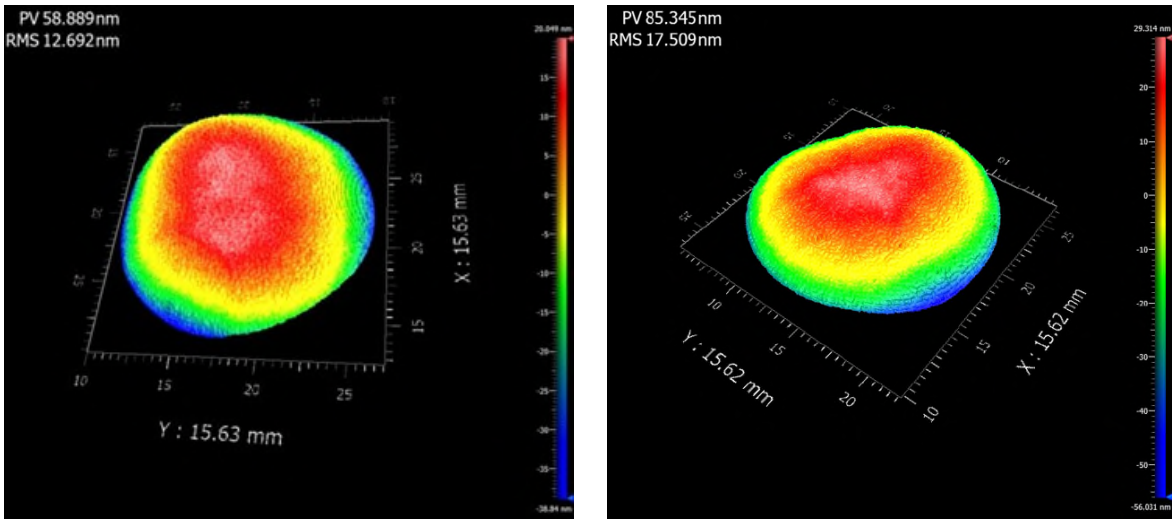

Figure 4. Mirrors RWE at 0° Test After Integration, Type1 (left) and Type2 (right)

The optical verification indicates that both mirror types are compliant with important margins in both free state and after integration (<40-nm rms was targeted).

Table 1. Mirror Optical Control Results (Specification: RWE < 40-nm rms at 45°)

	Type 1	**Type 2**
Mirror RWE at 0° before integration (nm rms)	10	14.2
Mirror RWE at 0° after integration (nm rms)	12.7	17.5

P-FSM150S Mechanism Design and Manufacturing

The main requirements for this mechanism were to ensure an angular stroke of ±7 mrad throughout the full operational temperature range of the mission (-10/+60°C) and a mirror surface flatness under 40-nm rms RWE (Reflected Wavefront Error) while remaining inside a very limited volume (especially less than 30-mm height) and surviving launch vibration.

Four P-FSM150S Engineering Qualification Models (EQM) have been assembled (EQM1 to EQM4). The integration process and assembly tooling were constantly improved as the operations were progressing. Even for prototypes one of the focus areas was to keep the time required to assemble the model as low as possible in anticipation with the plan to have this mechanism compatible with serial production.

Hence the number of steps, especially highly time-consuming ones like gluing, were reduced to the minimum required without impacting required quality. With that in mind, each integration step duration was monitored and the overall process time was analyzed in order to identify critical steps and room for process optimization.

<u>P-FSM150S Piezo Mechanism Design</u>

The piezo actuators are cabled in two push-pull configurations (one per axis) to allow a direct mirror rotation control, inheriting from PHARAO and ATLID tip-tilt mechanisms [3,4]. The P-FSM150S itself is composed of the following parts:

- A bracket baseplate (in aluminum): The APA® (Amplified Piezo Actuators) are fixed on it with screws.

- Four APA® (in stainless steel): They provide the required displacement and are fixed to the baseplate and to the mirror support. The APA® are equipped with SG sensors by a gluing process
- A flexible mirror support (in stainless steel) which holds the mirror. It includes flexible parts in order to ensure the limitation of the mirror deformation after integration (insulate the mirror surface from the mechanism bias)
- A flexure bearing (in stainless steel) soldered onto the central cylinder that stiffens the assembly.
- A Silicon Carbide (SiC or SiSiC) substrate-based mirror with either silver or gold coating.

The mechanism is composed of four APA®, deriving from CTEC standard APA120S. The existing CTEC actuators were either slightly too short in stroke or not stiff enough to ensure the mechanism survival during launch. Therefore, APA150S have been specifically designed for the application needs. A total of 25 APA® were assembled and tested; the measurements are detailed in Table 2.

Table 2. P-FSM150S Custom APA Measurement Results

	Full stroke (-20/+150V)	**1st coupled resonant frequency**
Units	µm	Hz
Average (measured)	187.3	4892.0
Standard deviation (measured)	0.9	22.9
Design value (worst case)	152.8	4783
Difference measurement/design value	+23%	+2%

P-FSM150S Strain Gauge Position Sensors (SG)

In order to be able to monitor the mirror angle, an indirect solution using strain gage placed on each piezo actuator is selected based space heritage from other projects, especially ATLID [4] on this matter, which enabled an important development on the SG assembly process.

The project used constantan, 350-ohm SG. There is one SG per piezo stack, mounted in one full Wheatstone bridge per rotation axis to maximize the sensitivity while minimizing thermal drift. All SG wires and PCB traces are the same length to limit offset drift.

Expected Reliability from OPTRONICS Recurrent Manufacturing CTEC Heritage

CTEC has a long heritage in the Optronic domain with the delivery of 3430 XY piezo stages based on similar push-pull piezo-mechanism and with fluctuating production rate from 200 to 500 per year (i.e., 20 to 50 per month).

Since 2005 this production has been delivered to several customers, with custom designs for each on interfaces, connectors, and optical components.

The production rate and test acceptance approach are based on this heritage to guarantee a zero defect at the customer level and 100% testing before delivery.

Over this historical quantity delivered, only one failure was observed and led to a customer service, which concluded the cause of failure to be a customer mistake at integration and not a hardware defect. The piezo stage was sent back to customer without modification.

Considering nonetheless this single event as a failure to be conservative, the following reliability analysis can be performed:

- Cumulated operational hours = 1.33 x10^7 at 20°C and average voltage @ 65 V
- Failures in Time (FIT) = 75 over 1 billion hours
- Reliability R= 0.992

P-FSM150S Test Results

Angle Stroke Test Results

As it was anticipated based on the good piezo actuator stroke performance (see Table 2), the P-FSM150S mirror tilt angle range is compliant with the requirements with notable operational margins. Hence the target stroke of ±7 mrad can even be reached (at ambient temperature) when supplied with a limited voltage range of 0/+130 V instead of -20/+150 V (23% less voltage).

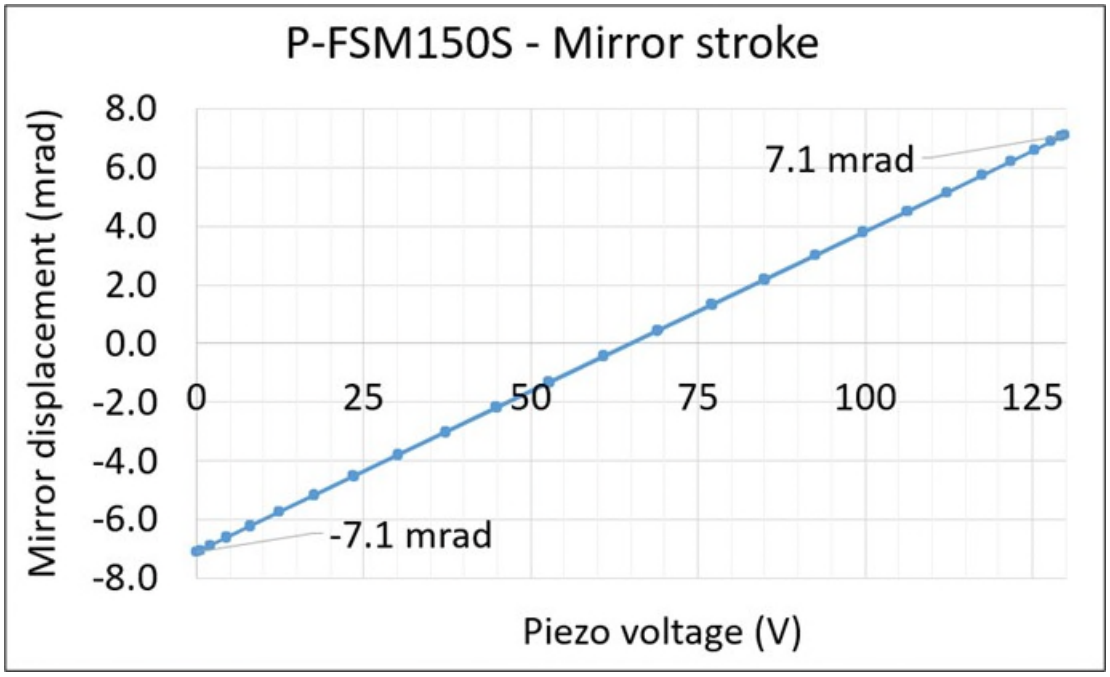

Figure 5. P-FSM150S Stroke Results with a 0/+130 V Supply

The actual full operational stroke could not be fully tested due to the limited range of the autocollimator instrument, but we can extrapolate that the P-FSM could reach a ±9.6-mrad stroke with a -20/+150 V supply, which should cover the slight stroke loss expected in cold operational temperature (around -5%) and the mirror integration offset compensation.

Modal frequencies test results

The mechanism stiffness and associated modal landscape is evaluated with an admittance sweep. With that method, only the piezo coupled modes are visible, hence the vertical pumping mode (cancelled from piezo point of view) is not visible.

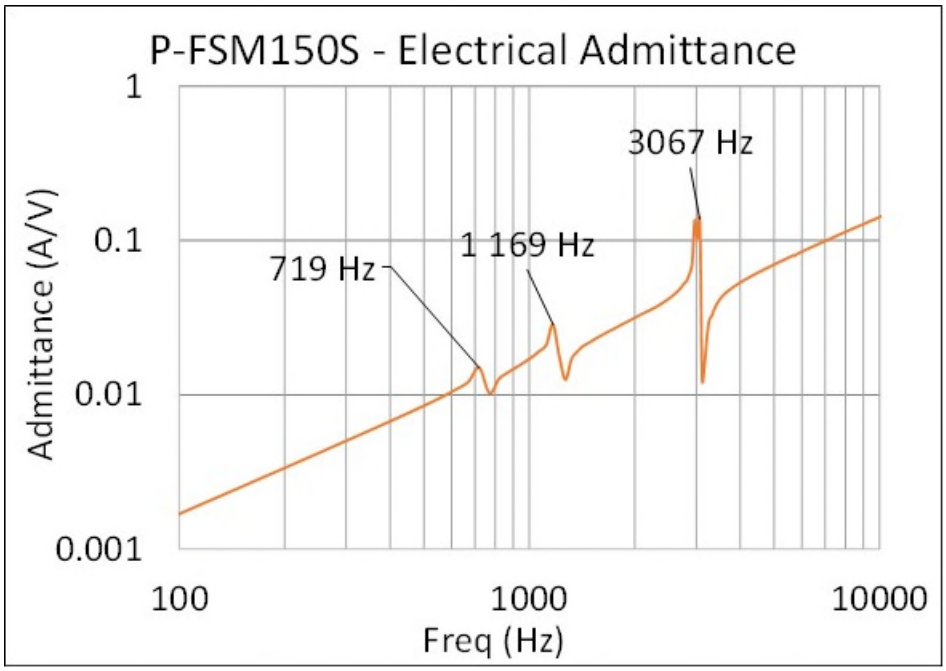

Figure 6. P-FSM150S EM1 X-axis Admittance Sweep

Pointing accuracy test results

The tests reveal a 0.1% cross coupling: ±10-µrad cross axis displacement with a ±7-mrad stroke which is a good result given the high amplification of the mechanism.

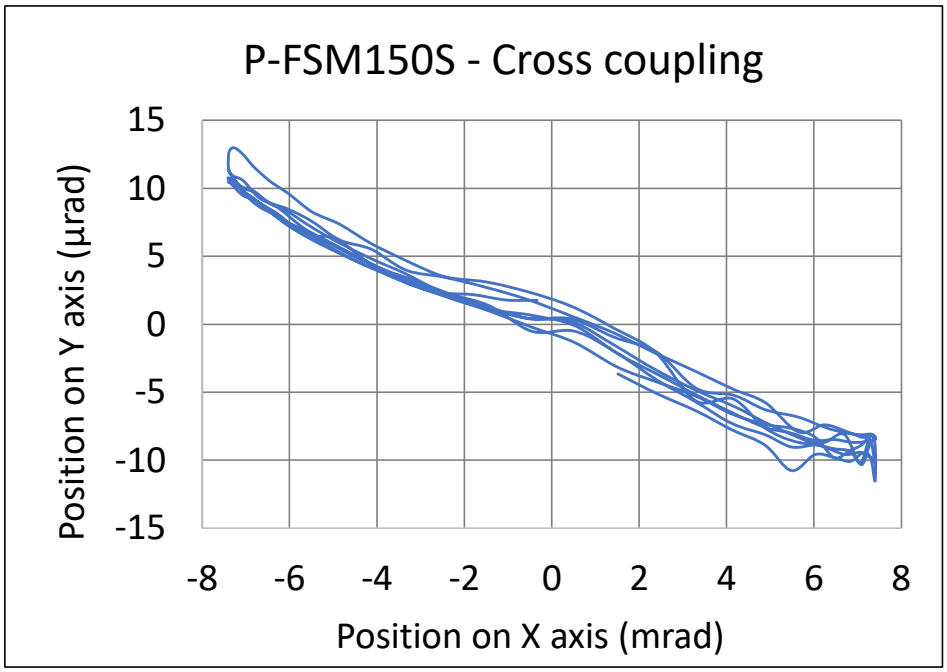

Figure 7. P-FSM150S Cross Coupling Measurement

With another test, it is demonstrated that the mechanism can generate ±1-µrad steps (0.01% mechanical resolution) using an external measurement for the mirror angle (autocollimator). The share of errors due to instruments measurement has still to be determined (especially for cross coupling) but measured resolution is already compliant with the ±1-µrad requirement.

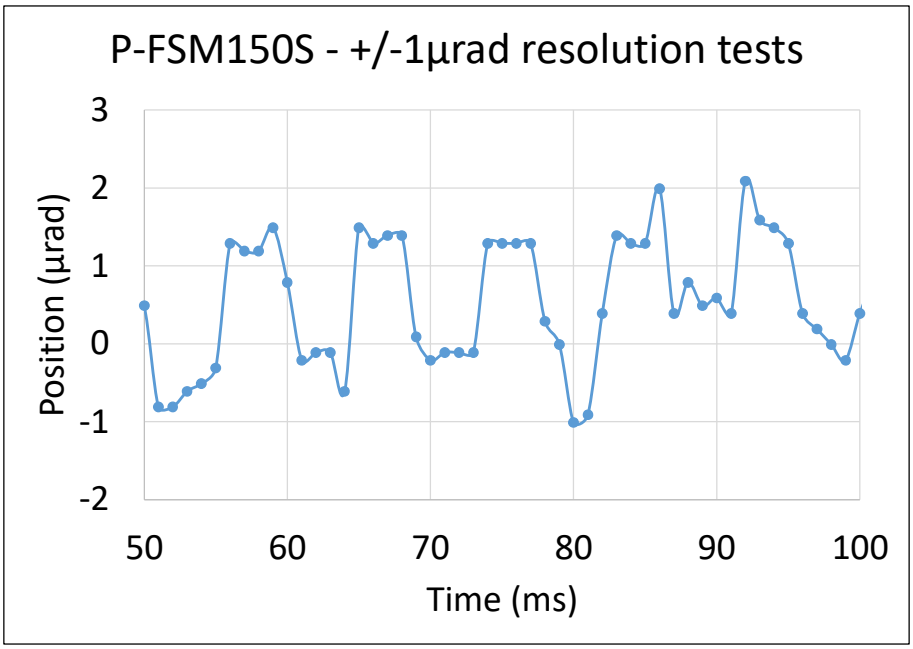

Figure 8. Mechanical Resolution Test

Fatigue lifetime tests

The EM1 is currently going through a lifetime test. The mechanism is actuated at full stroke (±7 mrad) in a diagonal direction (45° along X and Y axes) to excite both axes in fatigue. With a frequency of 100 Hz, 2.6e8 cycles are performed each month so the first billion cycles have been reached after the first four months of test. After that period, the test frequency was accelerated to 400 Hz, which has allowed to achieve at publication 4.7×10^9 cycles, with the test still ongoing. The lifetime test shall be continued up to failure and will be regularly interrupted to perform stroke and SG verification, to detect any deviation linked to lifetime evolution.

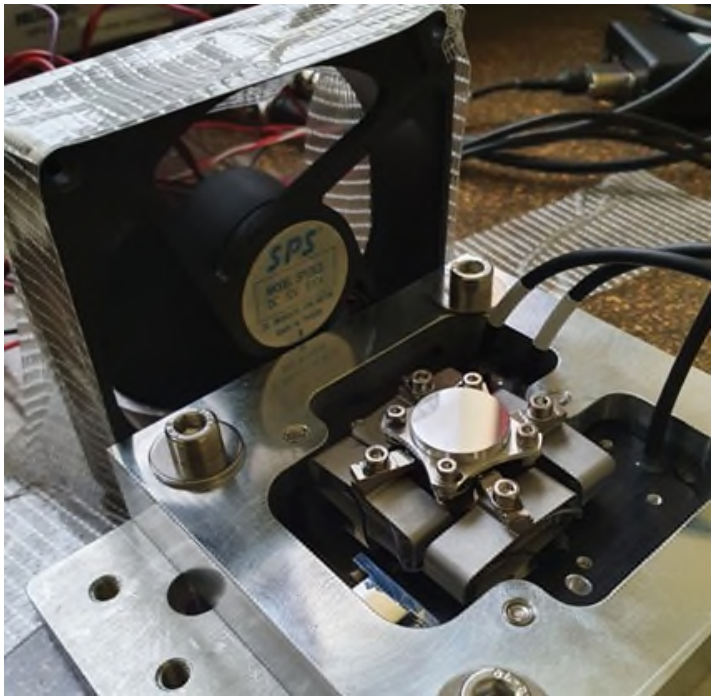

Figure 9. Lifetime Test Setup for P-FSM150S EM1

Vibration and shock tests

The P-FSM150S was tested in random vibration at 0.65-g²/Hz maximum level at its first structural resonance frequency at 720 Hz and with ISO8 clean condition packaging.

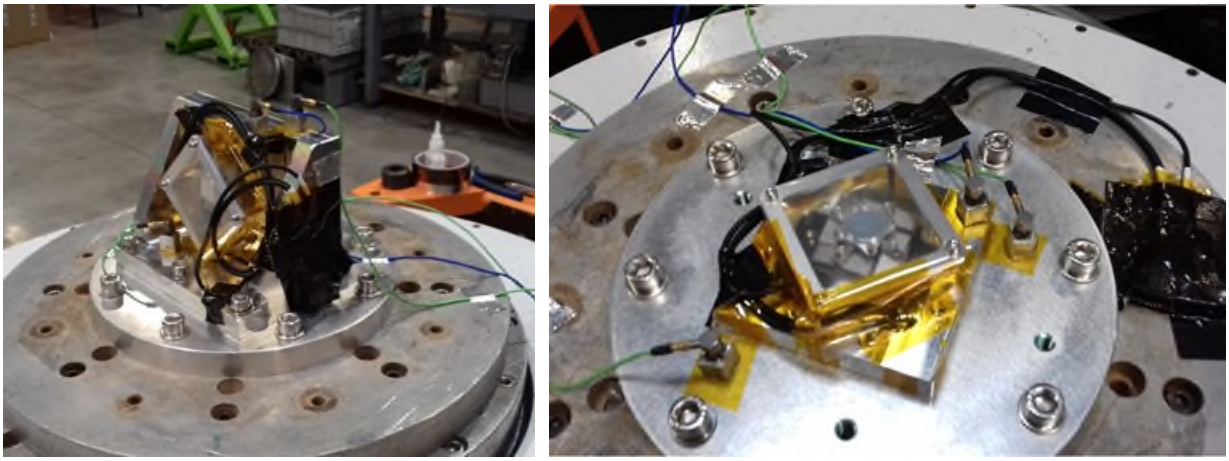

Figure 10. Random Vibration Test Setup in Clean ISO8 Condition

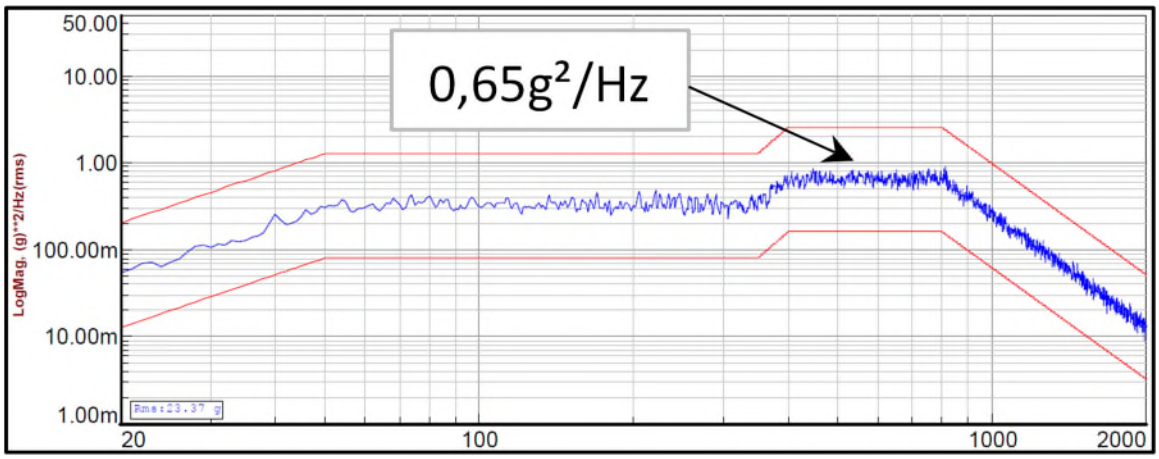

Figure 11. P-FSM150S 0.65-g²/Hz Random Vibration Test

The P-FSM150S was shock tested with a drop machine in order to test a 1000-g SRS shock input level at 800 Hz. In order to achieve the targeted test input all along the specified SRS frequency spectrum, the level was exceeded up to 1500 g at drop impact, as can be seen in shock the transient measurement at interface as shown in Figure 14.

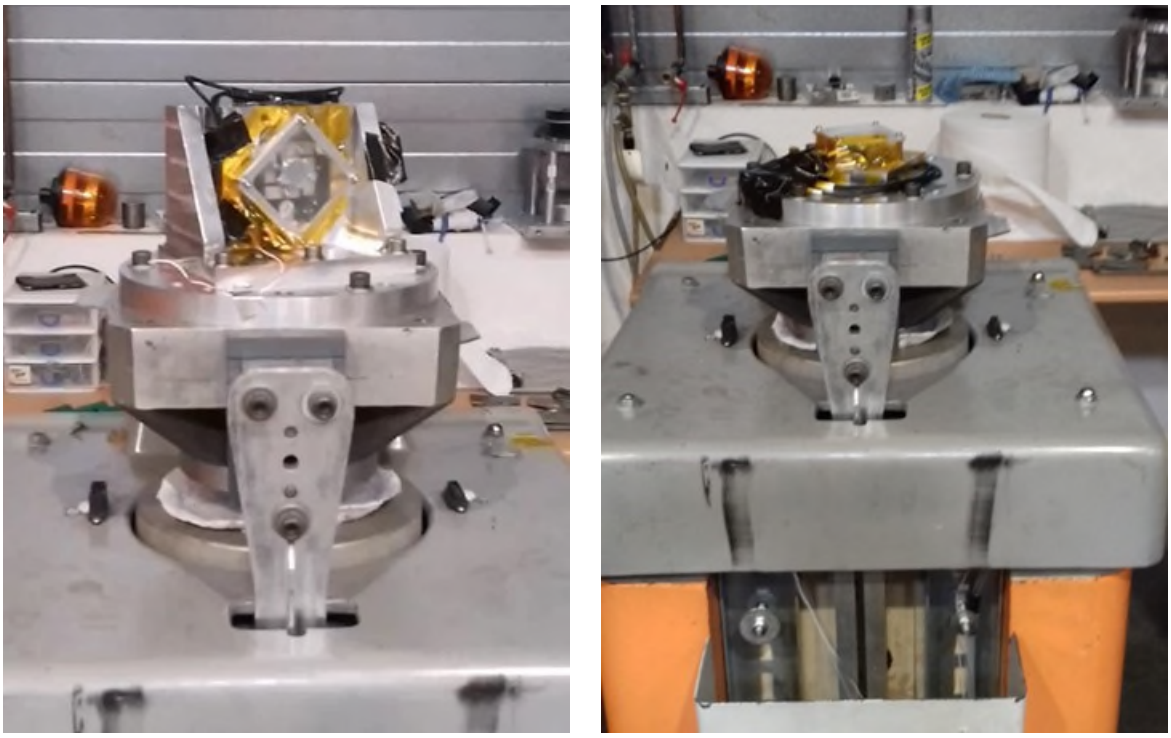

Figure 12. Shock Test Setup in Clean ISO8 Condition

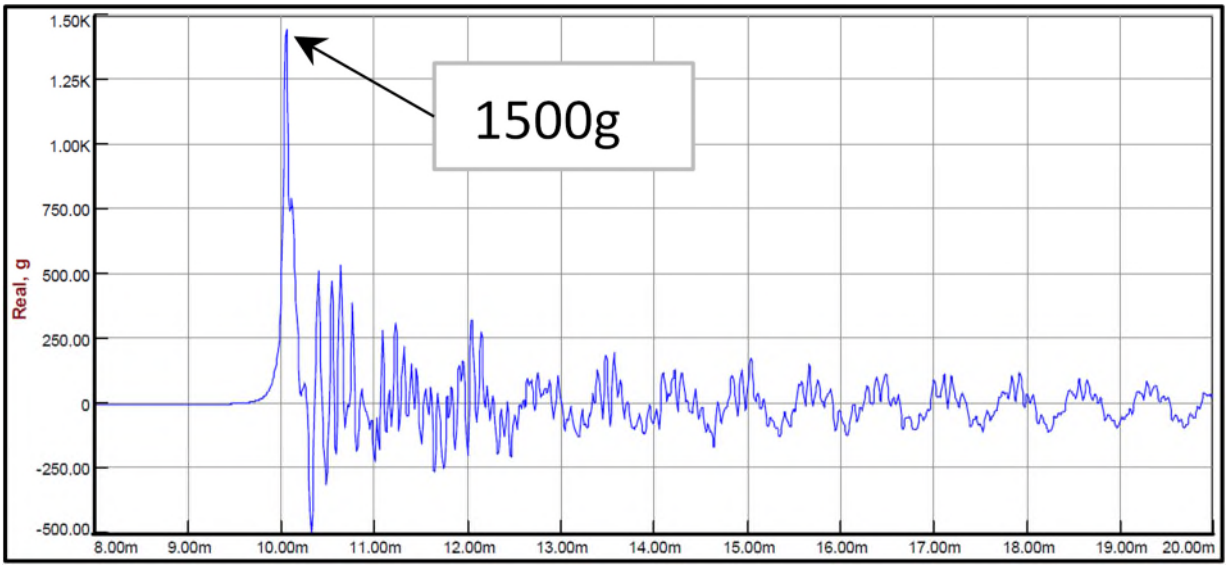

Figure 13. P-FSM150S 1500-g SRS Shock Test - Transient Measurement

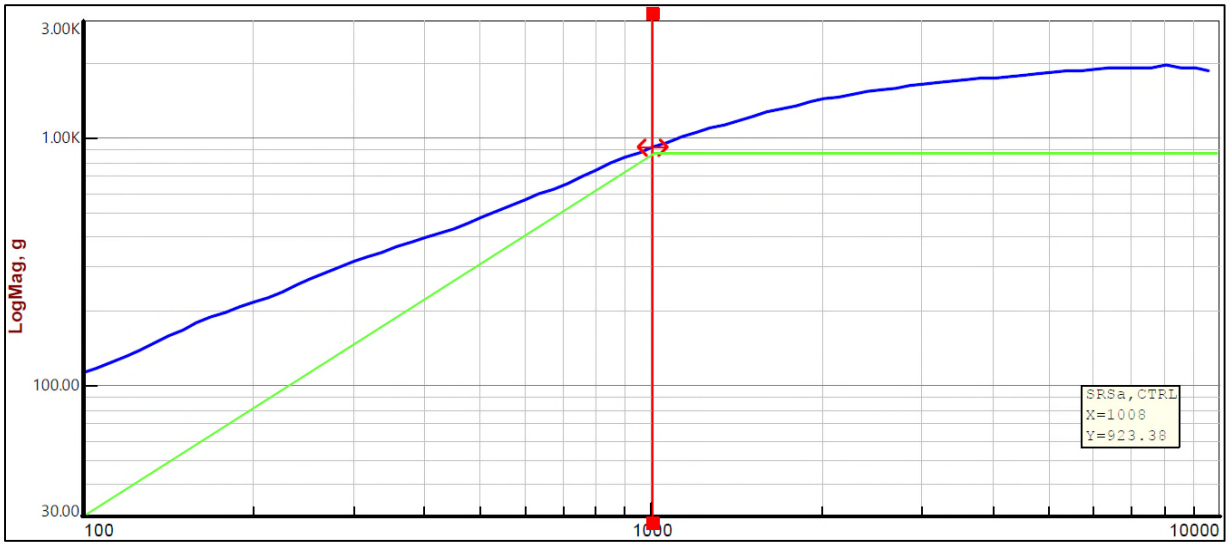

Figure 14. P-FSM150S 1500-g SRS Shock Test – SRS Analysis

Performance Summary Table

Table 3 summarizes the P-FSM150S performance as verified by test.

Table 3. P-FSM150S Design and Performance Summary Table

P-FSM150S	
Dimensions	65 mm x 60 mm; Height 30 mm
Mass	150 g
Stroke at [0V- 130V] voltage range	±7 mrad
Stroke at [-20V- 150V] voltage range	±9 mrad
Resolution with cots drive electronics (non space)	±1 µrad
Accuracy with cots drive electronics (non space)	±10 µrad
Embedded position sensors	Strain gauges
1st resonance frequency (Actuation)	720 Hz
Closed loop position control Frequency bandwidth	> 200 Hz for low speed fine pointing operation (*)
Mirror size	Ø17 mm with Ø15 mm clear aperture
Mirror substrate and coating (**)	SiC with Silver coating or SiSiC with Gold coating
Mirror mechanical interface onto support	Fastening (***)
Mirror RWE after integration on flexible support	< 20 nm rms @ 0° angle of incidence
Operational temperature	-10°C / +60°C
Random vibration level	0,65 g^2/Hz from 100 Hz to 800 Hz
SRS shock level	1000 g from 1000 Hz to 10000 Hz

(*) With basic proportional integral controller tuned for low frequencies fine pointing operation. Much higher frequency bandwidth is achievable with other tuning for fast steering operation.

(**) The mirror flexible support is compatible, with respect to WFE after integration, with other alternate metallic substrates, with same usable mirror mechanical drawing applicable

(***) Mirror gluing processes was avoided for fast and reliable assembly processes

Conclusion and Acknowledgments

The authors specifically thank CNES and ESA for the funding of TELCO-B project as well as THALES ALENIA SPACE for the close collaboration on requirements definition and performance evaluations.

References

1. G. Aigouy “P-FSM150S & M-FSM45 For Large Scale Free-Space Optical Communication”, Proc. OPTRO 2022
2. A. Guignabert, Point Ahead Mechanism for Deep Space Optical Communication for PSYCHE mission, Proc. ICSO, February 2021
3. A. Guignabert, Point Ahead Mechanism for Deep Space Optical Communication – Development of a new Piezo-Optical Tip-tilt mechanism, Proc. 45th AMS, Houston, May 2020
4. R. Le Letty, Miniature Piezo Mechanisms for Optical and Space applications, ACTUATOR Conf, Messe Bremen (G), June 2004, pp 177-180
5. F. Claeyssen, Beam Steering Mirrors from space applications to optronic solutions, Proc. OPTRO Conf, Paris, Feb. 2018
6. F. Claeyssen, Large-stroke Fast Steering Mirror for space Free-Space Optical communication, OPTRO 2020, n°0062, 28-30 Jan 2020
7. A. Guignabert, E. Betsch, G. Aigouy, Large stroke Fast Steering Mirror, Proc. ICSO, February 2021
8. W. Coppoolse, Dual-axis single-mirror mechanism for beam steering and stabilization in optical inter satellite links, Proc ESMATS conf, 2003
9. Y. Long, Design of a Moving-magnet Electromagnetic Actuator for Fast Steering Mirror, J. of Magnetics, Vol. 19 (3), 2014
10. JC Barriere, Qualification of Euclid-near infrared Spectro-photometer cryomechanism, Proc. ESMATS 2017

Developing a Plunger-based Liquid Propellant Delivery System for CubeSat Propulsion

Pilar Gonzalez Rueda Flores[*], Raul A. Cuevas[*], Javier Madrid[*], Andre Molina[*], Hiram A. Lopez[*], Amelia D. Greig[*], Joel Quintana[*] and Ahsan R. Choudhuri[*]

Abstract

The Aerospace Center at the University of Texas at El Paso is currently developing a low-cost 1-N propulsion module for use in 6U CubeSats. This module uses the liquid monopropellant AF-M315E. The fuel delivery system was identified as a subsystem that could be targeted for cost reductions. The current design, which is expected to be tested throughout Summer 2022, uses a plunger-based propellant delivery system instead of a pressurized fuel compartment. Challenges and solutions the team faced are outlined, starting with an overview of the design, then organized by the process of delivering fuel, thermal considerations, interaction with Attitude Determination and Control System (ADCS), material compatibility, ensuring sufficient fuel capacity is in the design, manufacturing, and avionics.

Introduction

CubeSats are a standard for small satellites developed by CalPoly, with each unit (or U) measuring 10 cm x 10 cm x 10 cm. Relatively low price and complexity of CubeSats have led to an increase of popularity in recent years. As their popularity continues to grow demand for propulsion systems with higher delta-V has increased to expand the capabilities of CubeSats. [1] Higher delta-V capabilities would be able to reach higher orbits and greatly increases the versatility of CubeSats. Hydrazine has been a commonly used monopropellant for small satellite propulsion but is known for its high toxicity. In response to the toxic nature of hydrazine, the Air Force Research Laboratory developed the green monopropellant called AF-M315E, also known as ASCENT. In addition to its lower toxicity, AF-M315E has a higher theoretical specific impulse and density than hydrazine. Its significantly reduced toxicity allows for easier storage and handling which could potentially reduce launch processing times and costs. [2] The Aerospace Center located at the University of Texas at El Paso is currently developing an AF-M315E based propulsion module for use on 6U CubeSats. This module, referred to as the Green Monopropellant Engine (GMPE), uses a 1-N thruster and a catalyst previously developed and tested by the Aerospace Center. Market research found that the high cost of propulsion modules is a major concern for universities and small institutions planning CubeSat missions, so the vision for the GMPE is to provide a lower cost solution for CubeSat propulsion.

About the GMPE

While the module's design is still in development, a central feature is the plunger-based fuel delivery system. A CAD image of the current GMPE design is shown in Figure 1, while Figure 2 shows a more detailed design from a previous iteration. Both figures show the fuel tank, electronics compartment, satellite bus interface, and thruster positioning. The outer walls are transparent in both figures to allow for a view of the internal cavities.

[*] The University of Texas at El Paso, El Paso, TX

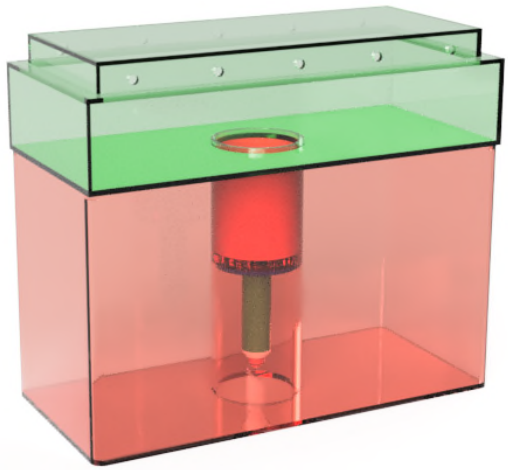

Figure 1. Rendered image showing layout of current GMPE design. The fuel tank is the red region, the electronics compartment and satellite bus interface are at the green region, and the thruster can be seen in the center of the module.

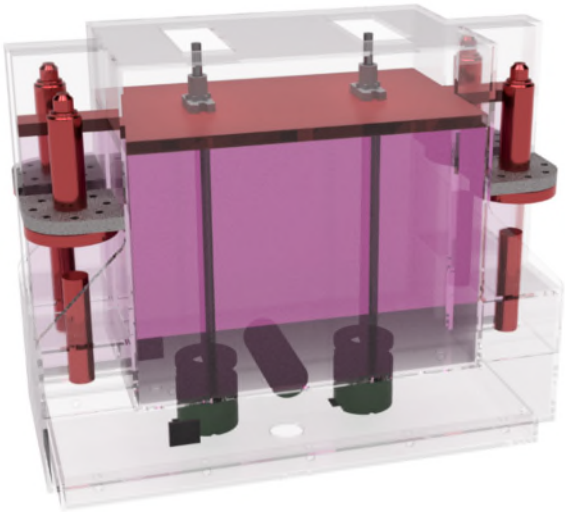

Figure 2. Rendered image of previous GMPE design with four thrusters. The plunger mechanism is shown in red, with AF-M315E being shown in magenta. Motors, valves, and electronics are shown in green.

Liquid propellants can be difficult to manage in micro-gravity, but a plunger-like fuel delivery system removes some of the challenges normally faced. For example, the plunger system does not require pressurant gas to move the fuel. Removing the need for a pressure vessel increases the space available for more fuel or additional equipment. Similarly, the fuel's flow rate and remaining volume can be easily monitored through the speed and location of the plunger. The plunger operates by using a motor driven piston to decrease the volume of the tank, while simultaneously forcing propellant through feed lines. The piston will be attached to two threaded rods which will be spun by the motors that raise or lower the piston, like how a 3D printer might raise and lower a gantry. Similar systems are commonly used on Earth in laboratory applications. They are particularly useful in applications requiring a well-controlled volumetric flow rate. As previously mentioned, using this system removes the need for flow meters and sensors monitoring remaining fuel in the module's tank simply by using an encoder on the lead screws. Thermocouples and pressure transducers allow for close monitoring the conditions inside the fuel tank. Although the GMPE team was unable to find literature regarding use of motor-powered piston-based fuel

delivery systems, previous laboratory testing successfully used a syringe pump for hot fire tests. A summary of major requirements for the GMPE are listed in Table 1.

Table 1. Summary of major requirements for the GMPE.

Requirement	**Notes**
The GMPE SHALL have fully autonomous operations.	The module will have communications with the satellite bus, but not with a ground station.
The GMPE SHALL be able to complete mission with ADCS tolerances of 0.2° to 6°.	Based off tolerances from commercially available CubeSat ADCS.
The GMPE SHALL raise the temperature of the satellite bus no more than 5°C at any time.	
The GMPE's tank SHALL keep the AF-M315E at a temperature between -80°C and 140°C at all times.	Range between glassing and autoignition for AF-M315E.
The GMPE SHALL provide a maximum Delta-V to a 6U CubeSat of 515 m/s.	

Additionally, a brief breakdown of expected costs for the testbed version of the GMPE by subsystem are listed in Table 2.

Table 2. Expected cost of testbed GMPE prototype by subsystem.

Subsystem	**Cost, USD**
Thruster	$2,000
Tank, fuel delivery	$2,300
Heater	$200
Electronics, sensors	$2,000
Thermal Insulation	$800
Total	$7,300

Fuel Delivery

One of the first concerns was that of cantilevering. If the plunger becomes uneven, not only would the predicted tank status become inaccurate, but there would also be the possibility of fuel leaking through a gap in the seal. This issue will be mitigated with the set of threaded lead screws controlling the plunger. One lead screw will be a right-handed screw while the other will be a left-handed screw. Because the lead screws are equidistant from the module's center of mass and will be moving at the same rate and timing, no net angular momentum will be generated from the movement of the lead screws.

Another issue that soon arose was that of possible hydraulic locking, also known as hydrolock. A few steps were taken to mitigate the possibility of hydrolock in the GMPE. First, the tank's total volumetric capacity was made to be larger than the maximum initial fuel volume that would be loaded into the tank. This additional volume was calculated by estimating the thermal expansion of AF-M315E at in the worst-case scenario of reaching 140°C, at which autoignition becomes the primary concern [3]. Then, by monitoring the temperature and pressure inside the fuel tank, adjustments can be made to the position of the piston to accommodate the expansion of the fuel.

Pressure drawdown was a major issue that arose when the team decided to remove pressurant gasses from the system. If the backside of the plunger is in a sealed space, the pressure drawdown from moving the plunger down would quickly overtake the force the motors could exert on the plunger. The team considered using a volatile fluid, such as acetone, to fill a buffer space above the plunger, as shown in Figure 3. As the volume in the buffer zone would increase, the fluid would evaporate and pressurize the buffer space, reducing the effect of the pressure drawdown. The team found that this solution would not entirely fix the drawdown issue. Instead, the backside of the plunger will be exposed to the vacuum of space. With this setup, the plunger will be working with the vacuum rather than against it during hot fires.

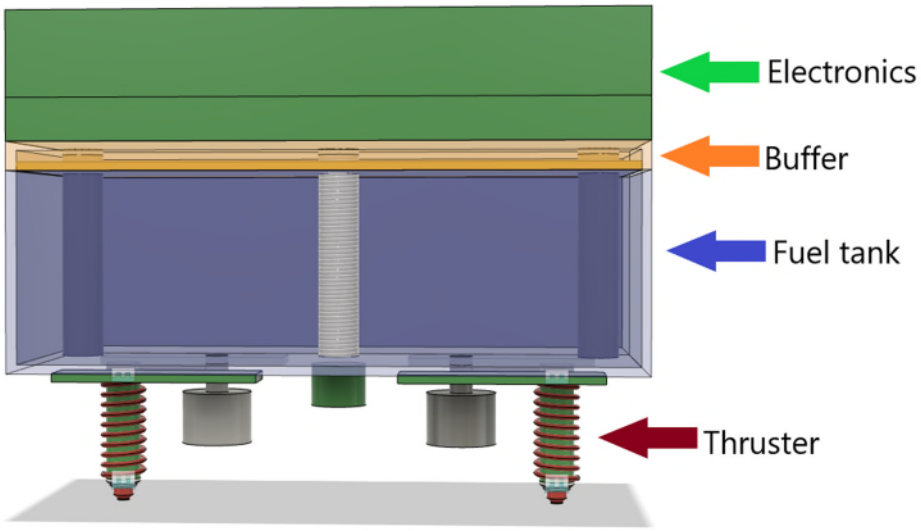

Figure 3. Diagram depicting the proposed buffer area in an earlier GMPE design.

Next, the team had to ensure that the motors controlling the lead screws would be able to provide sufficient torque to move the plunger. In addition to this, encoders on the motors would have to provide a high enough resolution so that the tank's status could be properly monitored. First, the motor's torque output, T, the diameter of the shaft, d, gear reduction, N, and efficiency, η were used to find the motor's force output, F. This was done using Eq. 1.

$$F = \frac{T}{d} N \eta \qquad \text{Eq. 1}$$

A higher gear reduction ratio reduces the maximum speed of the motor but allows it to provide a higher force to the plunger. To ensure the new speed of the motors would still be high enough to provide the necessary flow rate, the speed at which the plunger would need to move was found. The speed at which the plunger would need to move along the vertical axis, v_{va}, was found using the volumetric flow rate, $\dot{V}$, and the plunger's surface area, A, using Eq. 2.

$$v_{va} = \frac{\dot{V}}{A} \qquad \text{Eq. 2}$$

The conveying speed of the lead screws, v_c, was then used to find the maximum required rotations per minute, RPM, that the motors would need to provide. This was found with Eq. 3. The resulting RPM value was then compared to the manufacturer's specifications for the gearmotor in consideration.

$$RPM = \frac{v_{va}}{v_c} \qquad \text{Eq. 3}$$

Thermal Considerations

Because of the high temperatures at which AF-M315E decomposes, careful consideration was given to the thermal aspects of the design. First, an analysis using AGI's STK software was conducted to estimate the range of temperatures the GMPE might experience during a mission. Then, a thermal analysis of the module was conducted to find the maximum temperature it would reach with no thermal insulation. The setup to this problem is shown in Figure 4. Because the resulting tank temperature was above AF-M315E's autoignition temperature, layers of insulation were added to the design until a satisfactory maximum temperature was obtained. This was achieved with 15 layers of MLI, for a maximum temperature of around 32°C at the boundary between the MLI and wall.

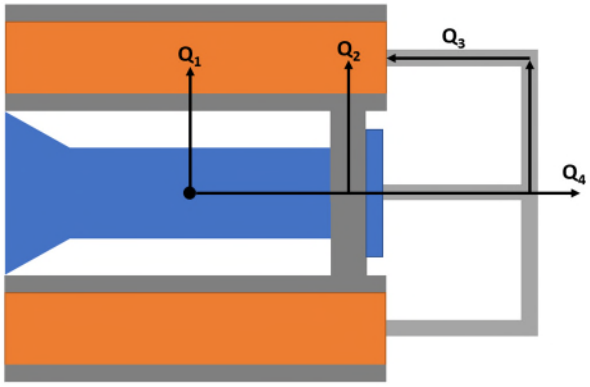

Figure 4. Setup for thermal analysis for the GMPE, seen in a cross-sectional view of the module. The propellant tank is shown in orange, while the thruster is shown in blue. Gray lines represent walls and fuel lines.

Other Considerations

Considering the small size of a CubeSat, saturation of the ADCS must also be taken into account. Due to the placement of the thruster, three different torque cases can arise due to misalignment. The first is the simplest case where no misalignment is present, and no torque is created as the force passes through the center of gravity. Misalignment in one plane (Figure 5) is referred to as "simple misalignment" while a misalignment in two planes is referred to as "complex misalignment." These misalignments are likely to occur as a result of slight imperfections during the manufacturing process. The exact extent of these misalignments will depend on the tolerances used when manufacturing the thruster, tank, flange, and feedlines.

Figure 5. Simple (left) and Complex (right) misalignment depictions

The torques created will depend on which case is encountered once the module is manufactured. Each case will result in different allowable firing durations. While users would be free to add additional equipment to the satellite bus for further desaturation to achieve longer firing durations, the module was designed with the assumption of only having the rotation wheels as a desaturation device.

Additionally, selection of materials is a crucial step in the development of the propulsion module. Two main sections can be identified: wet and dry. Wet interfaces refer to portions that will be in contact with the propellant, such as the propellant tank and feed lines. Since the propellant is corrosive, only certain materials can be used in this section. Proven compatibility of stainless steels series 300 and Ti 6Al-4V with the propellant can expedite the material selection process [4]. If the system requires a different material for any wetted components, it is highly recommended to avoid Fe, Ni, Cu, and some transitions metals, since these could decompose the propellant and hinder performance [3]. For any other dry component, depending on the mass budget, aluminum is an excellent choice due to its low density.

Manufacturing proved to be more difficult than initially expected. The nature of the design relies on a uniform and even tank design and any deviations could lead to increased resistance on the plunger mechanism or, with enough imperfections, a complete loss of function for the plunger. Another point of concern is the pointing accuracy of the thruster. Ideally the thruster is pointed axially such that it does not create any torque, as mentioned in the ADCS section, however this is extremely difficult and costly to achieve. The design must therefore carefully balance small tolerances with the available budget for manufacturing.

Conclusion

The development of a plunger-based propellant delivery system as opposed to a traditional pressurized propellant delivery system has led the development team to encounter a variety of important considerations. Issues such as hydraulic locking, cantilevering, ensuring sufficient motor torque, thermal management, and selection of compatible materials have been addressed. Additionally, although the plunger-based delivery system requires unique support equipment of its own, the team found it to be more compact than what as anticipated for a pressure-based fuel delivery system. As the prototype phase of the project approaches, these key lessons will be used to continue to improve the GMPE design.

References

1. Lin, W.-C., Chao, Y.-C., Chen, C.-A., and Hsu, H.-W., “Preliminary Dynamic Verification of Green Hydrogen Peroxide Monopropellant Thrusters for CubeSats with Simple Control System,” Jun. 2019.
2. Mohon, L., “Green Propellant Infusion Mission (GPIM),” NASA Available: https://www.nasa.gov/mission_pages/tdm/green/index.html.
3. Digital Solid State Propulsion Inc, “AF-M315E Safety Data Sheet” (Revised Feb. 2020).
4. B. Greene, P.R. Spencer, and P.F. Jones. *“Material Compatibility Study with AF-M315E: Supplementary Data for 60°C/ 32 Day Test Results (Draft)”* Manuscript in publication. United State Air Force Research Laboratory, Edwards AFB, CA

Thin Pack Hold Down and Release Mechanism for Low Load Applications

Jason Nave* and Ryan Klecka*

Abstract

Ensign-Bickford Aerospace & Defense (EBAD) is a provider of hold down and release mechanisms (HDRMs) to the space industry. Our devices are used in a wide range of load applications. Strong growth in the small satellite (SmallSat) market is driving the need for higher reliability, lower profile release devices. This paper describes the design and development of our third product offering for the SmallSat market, the Thin Pack HDRM (TH50). This new design offers all the advantages of our qualified Micro Latch design in a low profile package of less than 6.4 mm (0.25 in) height for ≤225 N (50 lbf) load cases.

Introduction

The first SmallSats started out using nichrome burn wire technology to perform releases. This technology is very simple and cost effective. Today, SmallSats are being used to perform high value missions and require higher reliability technologies. Well known SmallSat constellations such as Starlink, OneWeb, and Kuiper have driven the market to respond with new products that are not only lower cost, but also have higher reliability. With the increase in the demand for SmallSats, EBAD surveyed our customers and asked "How can we help?". The industry responded with a common answer: "We need a lower profile, resettable HDRM."

EBAD's existing resettable solution, the TiNi™ Micro Latch, leverages our ERM device heritage and has a taller design envelope that users say can cause some integration design challenges. Based on industry feedback, EBAD engineered our new TH50 Thin Pack release device. This new product provides a solution in the ≤225 N (50 lbf) load case in a low profile envelope (<6.4 mm / 0.25 in height). See Figure 1 for both the TiNi Thin Pack and Micro Latch products. This paper describes the design and development of the new Thin Pack device.

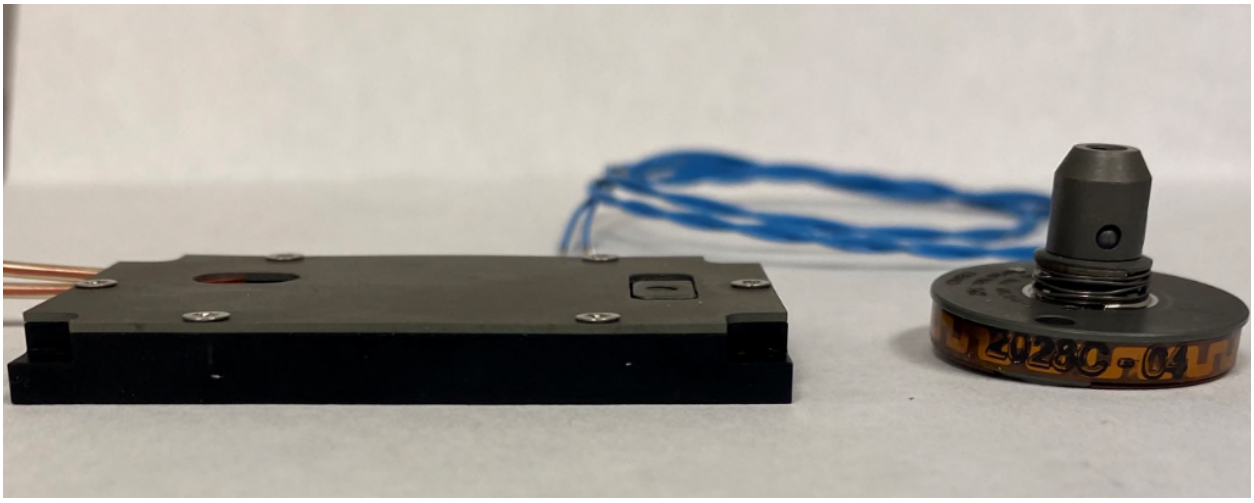

Figure 1. EBAD Thin Pack development unit (TH50, left) and Micro Latch (ML50).

* Ensign-Bickford Aerospace & Defense, Moorpark, CA; jcnave@ebad.com

Thin Pack Background

EBAD's Thin Pack uses our qualified Shape Memory Alloy (SMA) technology, which makes it field-resettable like all of our other TiNi devices and shares the same high reliability. The Thin Pack helps SmallSat designers improve space utilization and reduces integration costs for solar arrays, antenna reflectors, instruments, doors, sensors, and booms.

SMAs refer to a group of materials that have the ability to return to a predetermined shape when heated, illustrated in Figure 2 [1]. The shape memory effect is caused by a temperature dependent crystal structure. When an SMA is below its phase transformation temperature, it possesses a low yield-strength crystallography referred to as Martensite. While in this state, the material can be deformed into other shapes with relatively little force. The new shape is retained, provided the material is kept below its transformation temperature. When heated above this temperature, the material reverts to its parent structure, known as Austenite, causing it to return to its original shape.

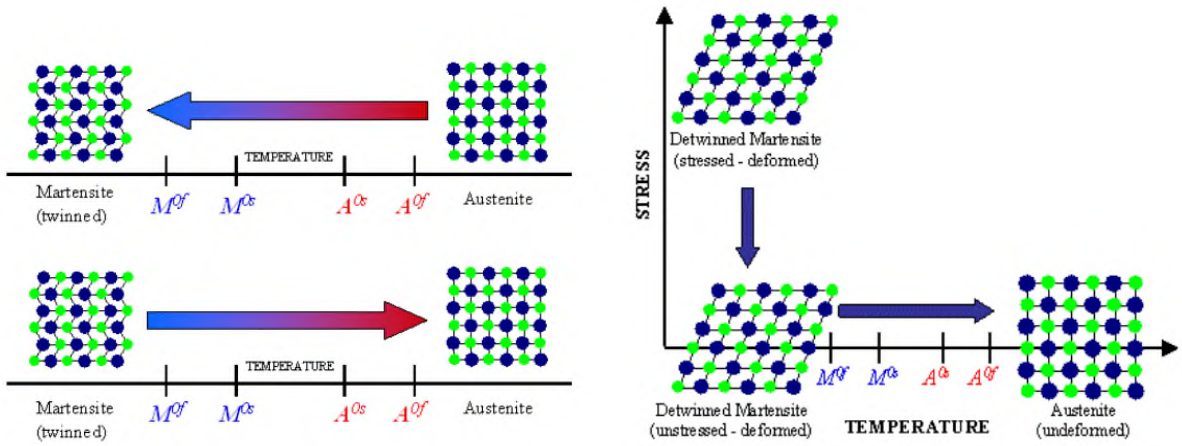

Figure 2. Shape Memory Alloy Phase Transformation [1]

The most widely used shape memory material is an alloy of Nickel and Titanium called Nitinol. This alloy is commercially available and has the following characteristics:

- Excellent mechanical properties
- Capable of long fatigue life
- May be joule heated
- High corrosion resistance

In actuator applications, it is capable of up to 4% strain and 345 MPa (50,000 psi) recovery stress, resulting in approximately 1 joule/g of work output. Nitinol is readily available in the form of wire, rod, and bar stock, with a transformation temperature in the range of -100°C to +100°C.

As with some other TiNi™ devices, such as ejectors and pin pullers, the Thin Pack utilizes the SMA wire as a trigger to actuate the unit. The Thin Pack interfaces with the load to be released via a #4-40 threaded release nut. The nut is held captive by a slider, which is retained by a rolling trigger. The Nitinol wire is attached on each end to a switch contact and routed through a bell crank that holds the position of the trigger. When sufficient current is applied to the external lead wires, the Nitinol wire is heated and shrinks, shifting the trigger and releasing the slider. This motion frees the release nut, allowing the payload to separate from the Thin Pack body.

Thin Pack Design

The interface dimensions of the Thin Pack are shown in Figure 3. The design's low profile makes it able to fit into small envelopes, particularly in applications with very low height requirements. It is manufactured using the same space-rated materials as all of our other space-qualified products. Commercially-available components were used as much as possible to help keep the price point of the device in line with other devices on the market. The Thin Pack generates no debris during its actuation, so it is compliant to applications where FOD is prohibited. When a nominal 1.8 A current is applied, the device actuates in approximately 50 ms. It is also equipped with a safety switch that automatically opens upon release and stops current flow through the SMA wire. This feature prevents excess current from damaging the SMA wire.

The Thin Pack is designed to have a minimum number of moving parts. This was a significant design challenge for a resettable device, as resettability inherently means the unit will have more parts. The Thin Pack also does not require disassembly or have replaceable or consumable parts in order to be reset. These factors increase the device's reliability substantially when compared to other devices on the market with a similar form factor.

The Thin Pack is designed to be reset without the need for a special tool. After actuation, the Thin Pack can be reset by threading a #2-56 screw or inserting a gage pin into the device. The Thin Pack is rated for at least 50 actuations, giving the user plenty of test cycles during development.

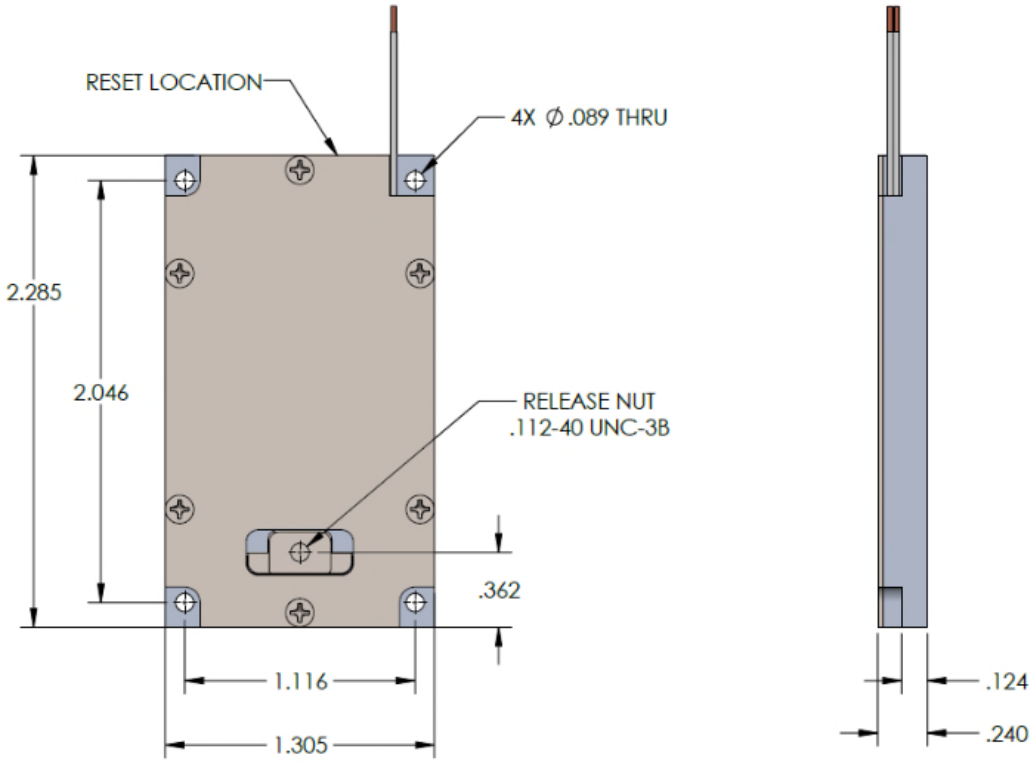

Figure 3. EBAD Thin Pack (TH50) Interface Dimensions

Design Challenges

The device's small size (see Figure 4 for reference) presented several design challenges to the team. Constrained to less than half the footprint of a credit card and thinner than a deck of playing cards, the device packs a number of space-grade components into a tiny body. With the small scale of the components, part tolerancing and assembly were continually reviewed.

The small size of the internal components presented the team with several assembly and handling challenges. The assembly process was developed in conjunction with the manufacturing team, with input from engineers and operators. Special handling fixtures and tooling were designed to aid in assembling the tiny components of this device, with a focus on ergonomics.

The Thin Pack is designed to have 2X margin on the force to release the payload nut. The device's release and reset energy is supplied via springs. The design of the springs compensates for sliding friction between internal components during release and reset. Initial development testing on a prototype test rig showed the frictional forces were higher than expected, impacting the 2X design requirement. Increasing spring size within the device would have grown the package size, which was not desirable. Therefore, the team opted to address the friction issue with smoother surface finish and coatings to reduce friction between moving components.

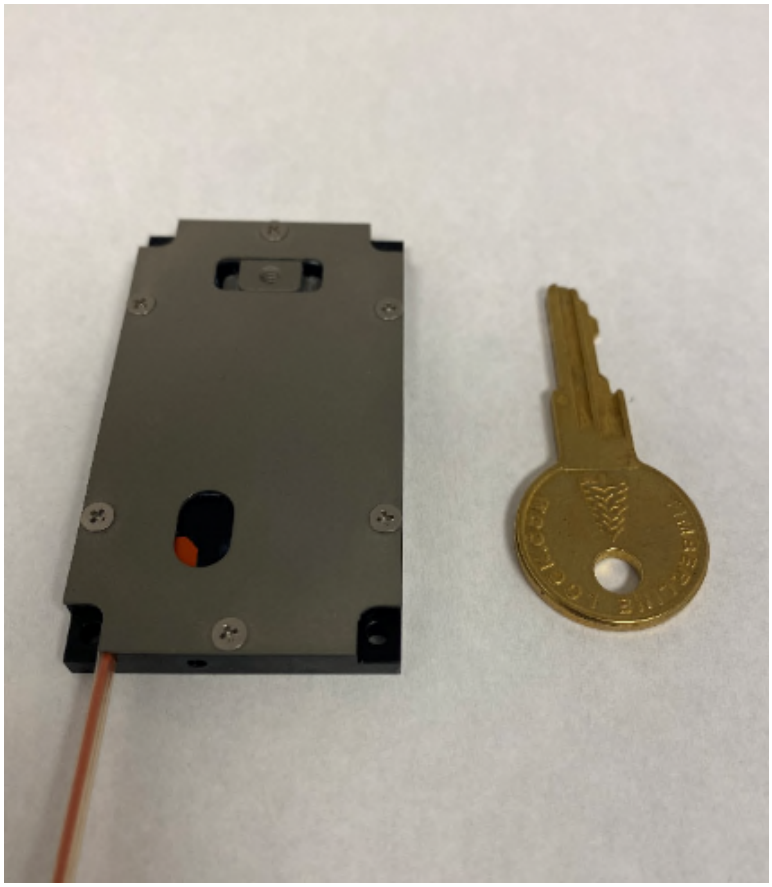

Figure 4. EBAD Thin Pack (TH50)

Prototype Testing

A prototype unit, shown in Figure 5, was built as a proof-of-concept device to demonstrate functionality and characterize baseline performance. The team was given a tight development timeline of nine months. A prototype device was fabricated using internal machining capability and quick-turn prototype shops. Testing of this initial iteration of the Thin Pack started with characterization with respect to basic design goals and expected use cases, consisting of:

1. Proof load test
2. Release test under full load
3. Force to release (actuation margin)
4. Self actuation limit for thermal environment
5. Vibration survivability

Figure 5. EBAD Thin Pack Prototype Unit.

A Mark-10 force tester was used to apply loads for the proof load, release test, and force-to-release tests. The proof load and release test setup can be seen in Figure 6, and the force-to-release test setup is shown in Figure 7. The unit was proof-load tested to 445 N (100 lbf) and release tested to 290 N (65 lbf). It was subjected to random vibration at the planned development test level of 26.0 G_{rms} in each of three orthogonal directions. No issues arose from these tests.

Since SMA devices are temperature-limited based on their transformation temperature, the Thin Pack was placed in a thermal chamber to determine its self-actuation limit. The temperature was gradually increased until the unit self-actuated. This action occurred at approximately 81°C, which is consistent with devices of similar materials and construction.

Using a test rig representative of the prototype design, the force to release was measured to be 22 N (5 lbf). This is the amount of force it took to shift the internal bell crank and release the payload nut, and accounts for the component interaction and friction within the device. When compared to the full force capability of the SMA wire, this gives an indication of the actuation margin in the system. The pull strength of SMA wire size used results in approximately 70% margin based on the prototype fixture test.

EBAD expects that the force to release can be reduced by minimizing the friction in the device through smoother surface finish, low-friction coatings, and the continued use of grease, which reflects the construction of the development units. This configuration will be assessed on a similar test rig, with the goal of demonstrating higher actuation margins. EBAD expects force-to-release margins in excess of 100% (compliant to the 2X design requirement) for this configuration based on similar historical data.

The prototype successfully completed all tests, indicating that the base design functionally met the design goals.

Figure 6. EBAD Thin Pack proof load and release characterization test setup.

Figure 7. EBAD Thin Pack force to release test setup.

Development Testing

Based on lessons learned from the build and test of the prototype unit, the design was updated for the development units. This included the component coatings, adding a damper to reduce actuation shock, and providing internal strain relief of the lead wires.

EBAD built and performed preliminary tests on five (5) development units. These tests consisted of electrical checks, proof loading, actuations, and output shock. A full set of development tests is planned for these units. The tests are described in the following sections.

Electrical Tests and Proof Load

Electrical tests were performed based on typical release device parameters and SMA characteristics. They are meant to confirm workmanship and compliance to the design. The tests, requirements, and test results (Pass/Fail) for the units are shown in Table 1.

Table 1. Thin Pack Development Unit Electrical Tests

Test	**Requirement**	**Test Result**
Circuit Resistance	5 to 6 Ω	Passed
Insulation Resistance	100 MΩ minimum, shorted lead wires to lid (@500 ± 50 V_{DC} for 15 seconds minimum)	Passed
No-fire Current	75 mA to 85 mA for 5 minutes	Passed

Proof load testing was performed using a Mark-10 force tester shown in Figure 6. All units held the proof load of 445 N (100 lbf).

Actuations

The units were successfully actuated and reset five times each. The planned cycle life for the Thin Pack is 50 actuations, which is consistent with TiNi™ devices that operate in a similar fashion. This requirement will be validated as part of the full development plan.

Output Shock

An output shock test was performed to characterize the shock emitted from the Thin Pack when actuated. As mentioned, a damper was incorporated into the development unit design to reduce this shock. The test utilized a typical 19 mm x 610 mm x 610 mm (0.75 in x 24 in x 24 in) plate with accelerometers installed 127 mm (5 in) away from the test unit, as shown in Figure 8. Output shock results were very consistent across all five units (<50g max up to 10,000 Hz), with a typical SRS plot shown in Figure 9.

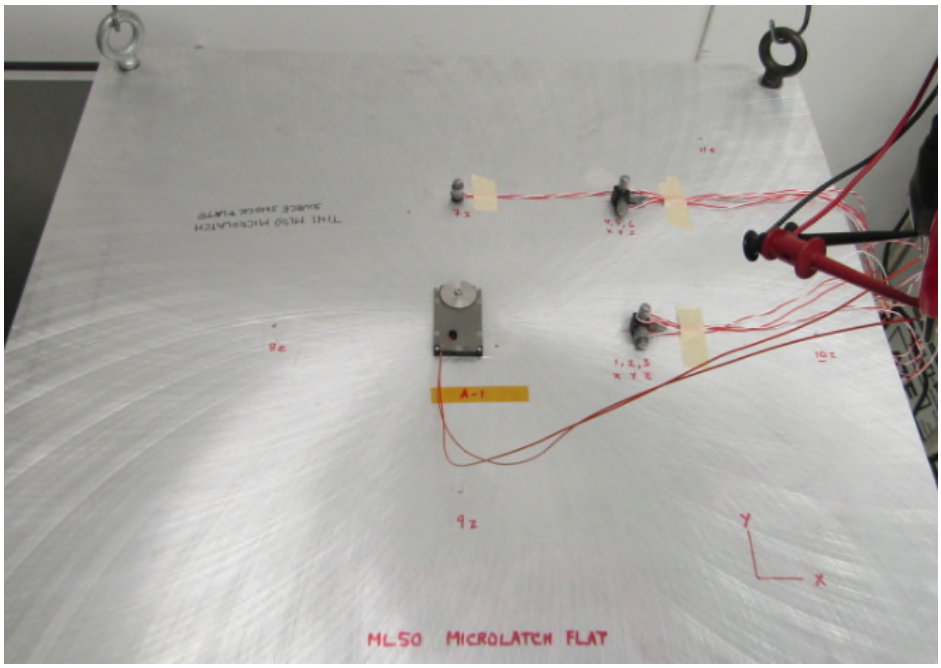

Figure 8. EBAD Thin Pack Output Shock Test Setup.

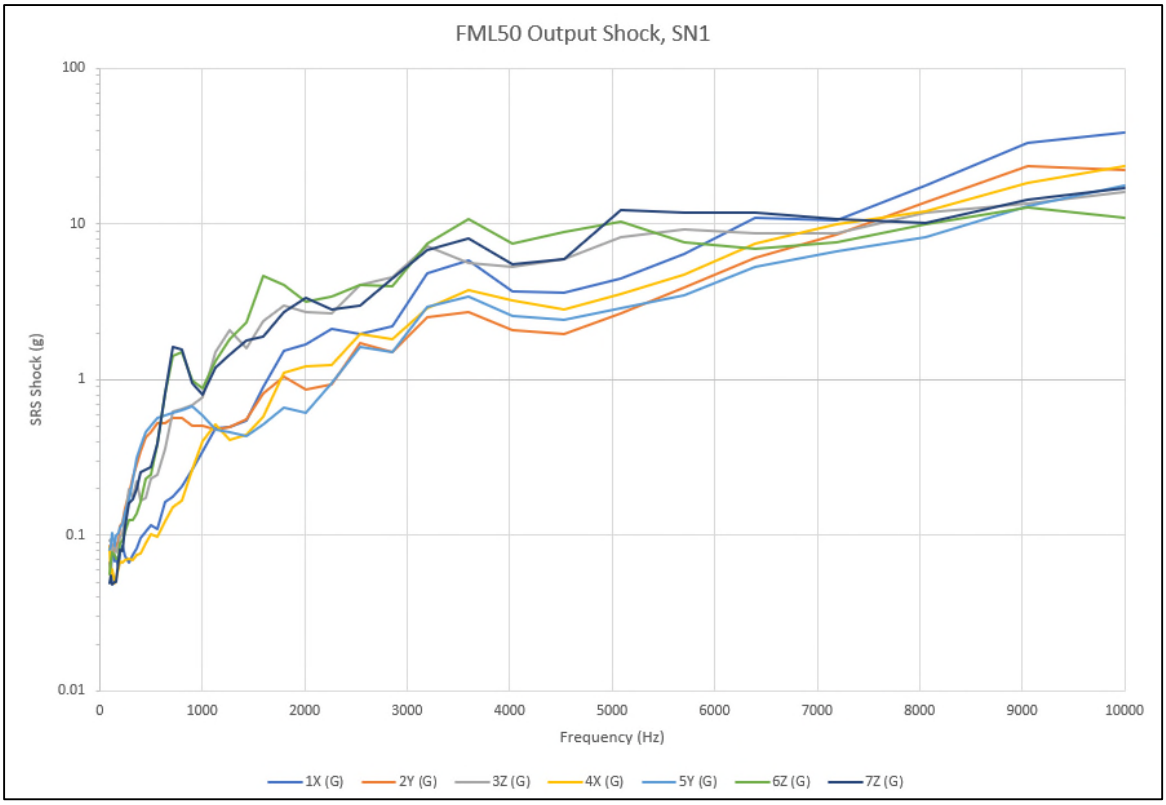

Figure 9. EBAD Thin Pack Output Shock Test Results.

Full Development Testing

After assessing the preliminary test results and design enhancement opportunities, EBAD will take the Thin Packs through a full development test sequence to validate the design and performance characteristics. The proposed test sequence is shown in Table 2. Items 1 through 4 and 8 have been performed on the current development units.

The units will go through environmental testing, including vibration, shock, and thermal vacuum cycling. They will be actuated after each environment, including during TVAC at hot, cold, and ambient temperatures, and at a range of actuation currents. Finally, additional actuations will be performed for a total of 60 planned actuations per test device. This quantity allows for margin above the 50 actuations expected to be part of the Thin Pack's specifications.

Throughout the test sequence, after each actuation the units will be preloaded (225 or 290 N), then have their circuit resistance measured to continually assess the device's health.

Additionally, as mentioned previously, the force to release the payload will be measured using a test rig representative of the development units.

Table 2. Thin Pack Development Test Sequence

Seq #	Test Name / Test Parameters
1	Electrical tests @ Reset State (Circuit Resistance, Insulation Resistance, No Fire Current) [Circuit Resistance re-checked throughout test sequence]
2	Actuation – No Load, Ambient (Low, Nominal, High Current)
3	Proof load – Max (445 N)
4	5X Actuations @ Load (Ambient, Nominal Current)
5	Random Vibration
6	Input Shock
7	Actuation @ Load (Ambient, Nominal Current)
8	Output Shock Test (Ambient, Nominal Current)
9	2X Actuations @ Load (Ambient, Nominal Current)
10	TVAC Cycling & Actuation @ Hot, Cold, & Ambient (Nominal Current)
11	No Fire Margin Tests @ Temp
12	47X Actuation @ Load (Ambient, Nominal Current)
13	Re-Characterize the Load vs Stroke for comparison to Pre-Test Data, No Fire Current Margin test, Transient Current susceptibility test

Lessons Learned

The design, build, and preliminary testing of the Thin Packs resulted in a number of lessons learned, as listed below.

1. The Thin Pack can hold and release loads of at least 225 N (50 lbf).
2. The Thin Pack output shock is extremely low at <50g max up to 10,000 Hz.
3. Units of this small size are inherently challenging to assemble.
4. Great care must be taken to balance the internal forces, including: the pull force of the SMA wire, spring forces to release the nut and reset the device, and frictional forces between sliding components.
5. To maximize the actuation margin, friction should be minimized through surface finish, component coatings, and grease.

References

1. Awan, Iqra Zubair and Abdul Qadeer Khan, "Fascinating Shape Memory Alloys." Journal of the Chemical Society of Pakistan, (Vol. 40, No. 1, 2018), 1-23.

Phenolic Ball Bearing Retainer Testing for Space/Vacuum Environments

John Renaud*

Abstract

This paper documents testing performed on recently produced lots of phenolic material and a review of historical testing and publications. The results of this testing could be used to update bearing retainer designs and risk mitigation practices for phenolic ball bearing retainers used in space flight applications.

Introduction

Cotton phenolic composite is a common material used for ball bearing retainers in a variety of high-precision applications, including applications used in a vacuum environment such as satellites working in space. The material is porous, allowing oil impregnation, and meets general requirements for space material out-gassing. In addition, the material has long-time heritage use in successful space flight mechanisms and is used extensively for these types of applications.

Phenolic composite material is known to change size due to moisture absorption, typically from humidity in ambient air. However, the space vacuum environment is devoid of humidity and moisture. A retainer fabricated and measured in a typical manufacturing environment shrinks when placed in a vacuum and expands with increases in humidity. If the bearing retainer shrinks sufficiently in the vacuum, along with thermal expansion and contraction, it can create an interference fit on the inner ring of the bearing. This condition can result in excessive bearing drag torque and in extreme case, possible cage failure.

Previous Publications

A commonly referenced publication for the phenolic material property of size change with humidity is Bertrand-and-Sinsheimer's 2002 article, "Humidity-Induced Dimensional Changes in Cotton-Phenolic Ball-Bearing Retainers" [1]. This report was based on testing of phenolic retainers performed by Bertrand of Aerospace Corp and Sinsheimer of TRW (now Northrop Grumman).

In summary, this testing found that a phenolic bearing retainer's size can change between 0.2% and 0.4% with humidity. These results were based on measurements of retainer bores using a tapered arbor. Measurements were taken both immediately upon removal from vacuum and also after multiple days of soaking at 52% and 87% relative humidity (RH) conditions.

Background

All material tested as part of this evaluation was compliant with the requirements of MIL-I-24768/13 [2] "FBE" material, which is the material specification typically used for spaceflight bearing applications. Previously collected, internally generated data (2012) regarding the size change of phenolic bearing retainers with exposure to humidity, largely aligned with published results across multiple size ranges. The data included results from testing two prominent manufacturers of phenolic material for this type of application. This data was used to define size requirements in relation to various humidity conditions, with good results.

However, recent testing of a thin section bearing system operating in a vacuum environment resulted in a torque anomaly that was determined to have been caused by a loss of retainer piloting clearance. This

* Timken Aerospace, Keene, NH

prompted a review of more recently produced materials to determine if design offsets needed to be revisited.

Test Details

A test plan was developed to classify the phenolic material for vacuum application using equipment readily available in the bearing production facility. This testing was performed in four steps as shown below. The testing compared the material in the as-machined condition to reference humidity conditions. The area of most concern/risk is the resulting cage piloting clearance when operating in a vacuum condition typical of space flight applications.

Test overview steps:

1. Define how to determine a truly “dry” state for the bearing cage to establish a low temperature bake process that would prevent any unwanted changes to material properties
2. Expose the retainers to ascending steps of humidity using a controlled humidity chamber to determine the size response of the material, and compare to historical testing.
3. Extrapolate the size response model to an assumed full vacuum condition.
4. Vacuum dry the retainers and test directly from the vacuum chamber for minimum size using a go-no go pin check to test the full vacuum state.

Four groups of retainers, 10 samples each, were obtained. Two groups were manufactured at The Timken Company bearing plant from “Manufacturer A” (MFR A) phenolic material, and two groups were produced at JPM of Mississippi using material produced from “Manufacturer B” (MFR B). All retainers were through-hole designs for use in angular contact thin section bearing typical of ABMA Standard 12 thin sections. The retainer groups included one design that was common across historic 2012 and current testing, as well as one alternate design from both material manufacturers for comparison. Figure 1 depicts an image of retainer Design 1 from MFR B material and Table 1 contains an overview of the retainer designs with approximate dimensions.

Table 1: Retainer design reference used in test

	Bore	OD	Width	Phenolic Material	Measurement Data Sets
Design 1 "3746"	64.3 mm (2.53 in)	67.1 mm (2.64 in)	5.8 mm (0.23 in)	MFR A and B	Historic 2012 data, current testing
Design 2 "2128"	37.3 mm (1.47 in)	39.9 mm (1.57 in)	5.8 mm (0.23 in)	MFR A	Current testing
Design 3 "3240"	55.4 mm (2.18 in)	57.9 mm (2.28 in)	5.8 mm (0.23 in)	MFR B	Current testing

Figure 1: Phenolic bearing retainer Design 1 from MFR B material

Establishing Vacuum Dry Condition

Vacuum drying was done in a ThermoScientific™ vacuum oven in the manufacturing clean room. Retainers were placed in vacuum of at least 28 in-Hg gage pressure. An elevated temperature well below the glass transition temperature of the phenolic resin was used to speed the process and limit other material factors from playing a role in the size testing. Vacuum dry testing was done using both of the current testing “MFR A” samples (Designs 1 and 2) to determine an adequate cycle for preparing samples of the full dry condition to use in later tests.

Mass measurements were taken immediately upon removal from the vacuum at specified time steps between two working days. Fitting a first order function to the mass-over-time data gives a correlation coefficient of 0.985, indicating a good fit. Using this function, it can be determined that both Design 1 and Design 2 retainers, when taken from ambient manufacturing conditions, will lose over 99% of their moisture mass after vacuum drying for 14 hours. This testing was also used to verify the mass condition of fully dried retainers that were vacuum-baked from a different starting point.

After the full dry condition was established various preservation methods were tested to keep parts dry between the vacuum drying process and the measurement process. Storing retainers in the controlled humidity cabinet at 10% (RH) resulted in a mass change with less variability from moisture absorption, equivalent to that obtained when using the best available dry purged packaging process. This 10% RH was used as the minimum humidity state for continuous bore and OD measurements for size modeling.

Measurement of Retainer Bore and OD with Humidity

The next step of testing was to measure and fit a model to the phenolic size change with humidity for each set of retainers. This was done by soaking the retainers at various levels of relative humidity and measuring bore and OD at each condition. An Electro-Tech Systems humidity cabinet utilizing a humidity sensor with a microcontroller (controlling a dry nitrogen supply and a deionized water humidifier) was used to actively control humidity. Retainer bore and OD measurements were taken using a TESA Visio V-300 vision system.

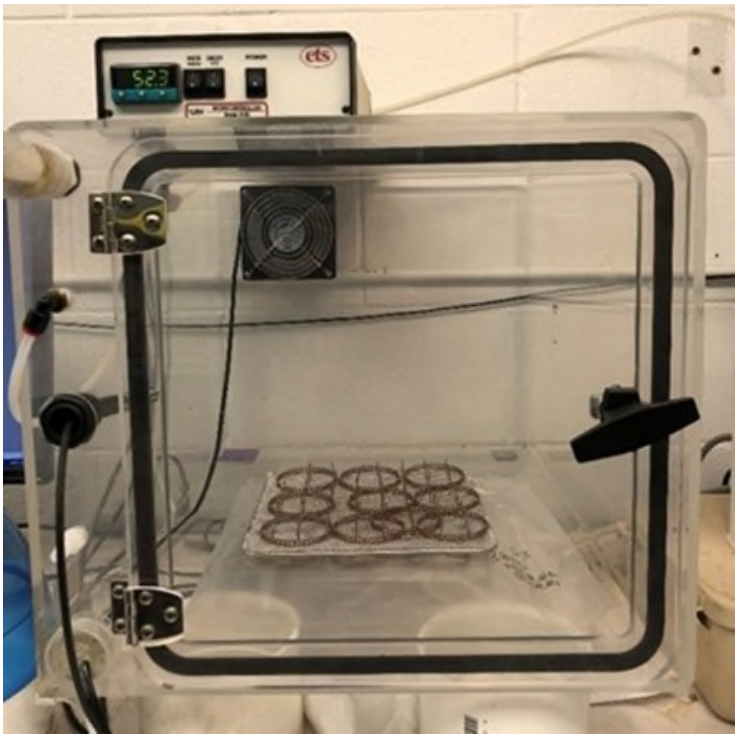

Figure 2: ETS humidity-controlled cabinet

This is a non-contact optical measurement system which fits an average size to hundreds of optical measurements via specific program for each retainer design. All measurements used in this paper including previous data from 2012, and current testing were done using the same humidity cabinet type and the same Visio measurement system. Each retainer was removed independently from the humidity chamber for each measurement taken on current testing. Previous 2012 data being used as a reference comparison, the exact procedure used for this testing was not fully documented at the time of testing. Humidity cabinet and measurement Bore and OD vision system are shown for reference in Figures 2 and 3. Both systems are immediately next to each other on a common work bench to limit time outside of the reference humidity conditions.

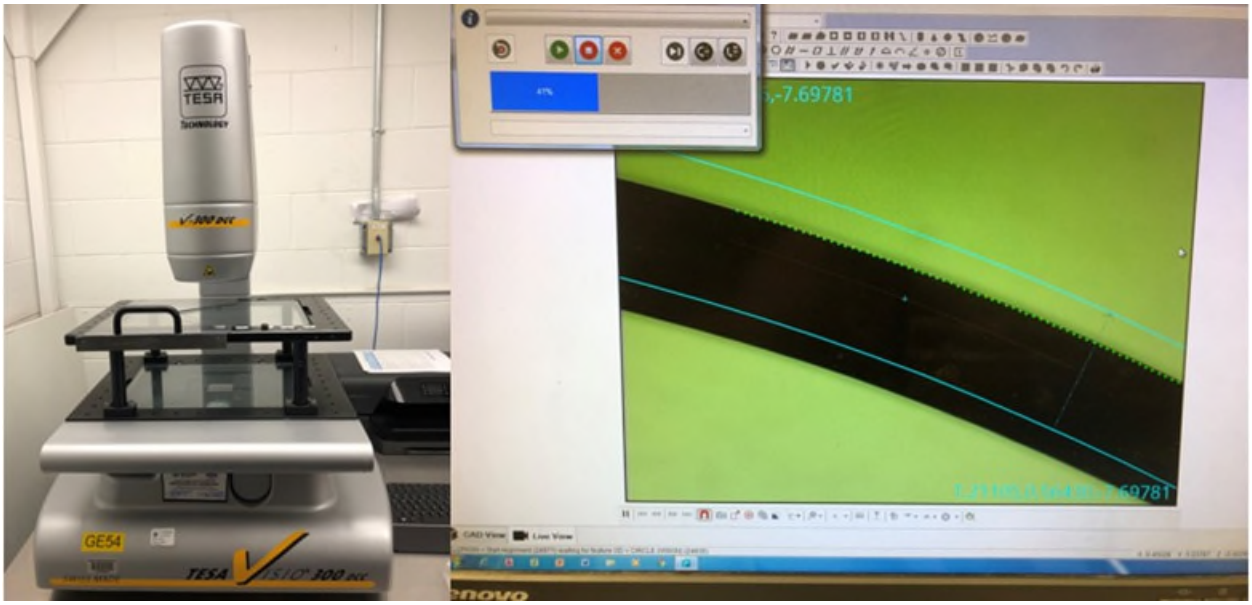

Figure 3: TESA Visio 300 optical vision measurement system

Previous reference data was available for retainer “design 1” using both MFR A and B material from 2012. Bore and OD sizes were available for 20%-40%-60%-80% Relative Humidity. The new retainer samples were all measured after soaking at the minimum set 10% RH condition as well as the same 20% RH steps from previous testing in ascending order to allow for a direct comparison using similar test conditions.

Bore and OD measurements were taken every 24 hours at each humidity step until a matched pairs comparison of the data set did not show a statistically significant change in average growth from the previous day. The humidity chamber was then increased to the next step of humidity and the process was repeated for each humidity step through 80% RH. Size data for each retainer design was normalized for comparison as a percentage size change from a reference condition. The reference condition used was the 40% RH measurement which is the closest data point to a typical “as manufactured” condition.

Bore and OD size change data is shown as Figures 4 and 5 respectively. The data is plotted along with the data collected in 2012 to determine if there was a difference in how the material changes in size with humidity between manufacturers or time of manufacture.

The size changes for both bore and OD appear linear, with a similar rate of change for each measurement set regardless of retainer design. The material is assumed to swell from moisture absorption, resulting in a higher rate of change for the OD compared to the bore, which is reflected in the measured data. The results of the 2012 data indicate both of the phenolic manufacturers’ materials grew at a similar rate. The new test data shows each manufacturer’s material grew at a similar rate between the two designs tested, but MFR A’s size change varied significantly from the 2012 data. The current MFR B material changed at a different rate but was not as significantly different from the 2012 data.

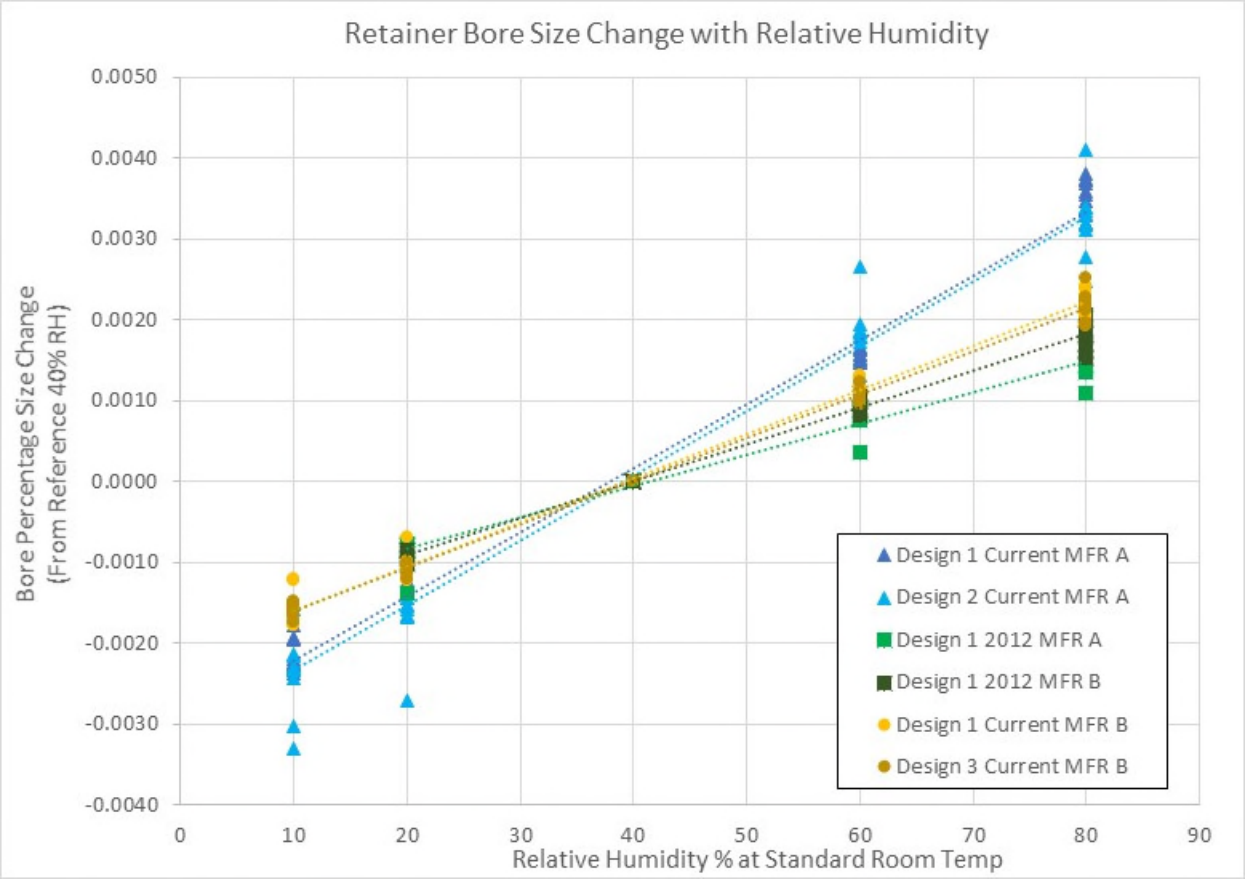

Figure 4: Bore size change of phenolic samples with humidity

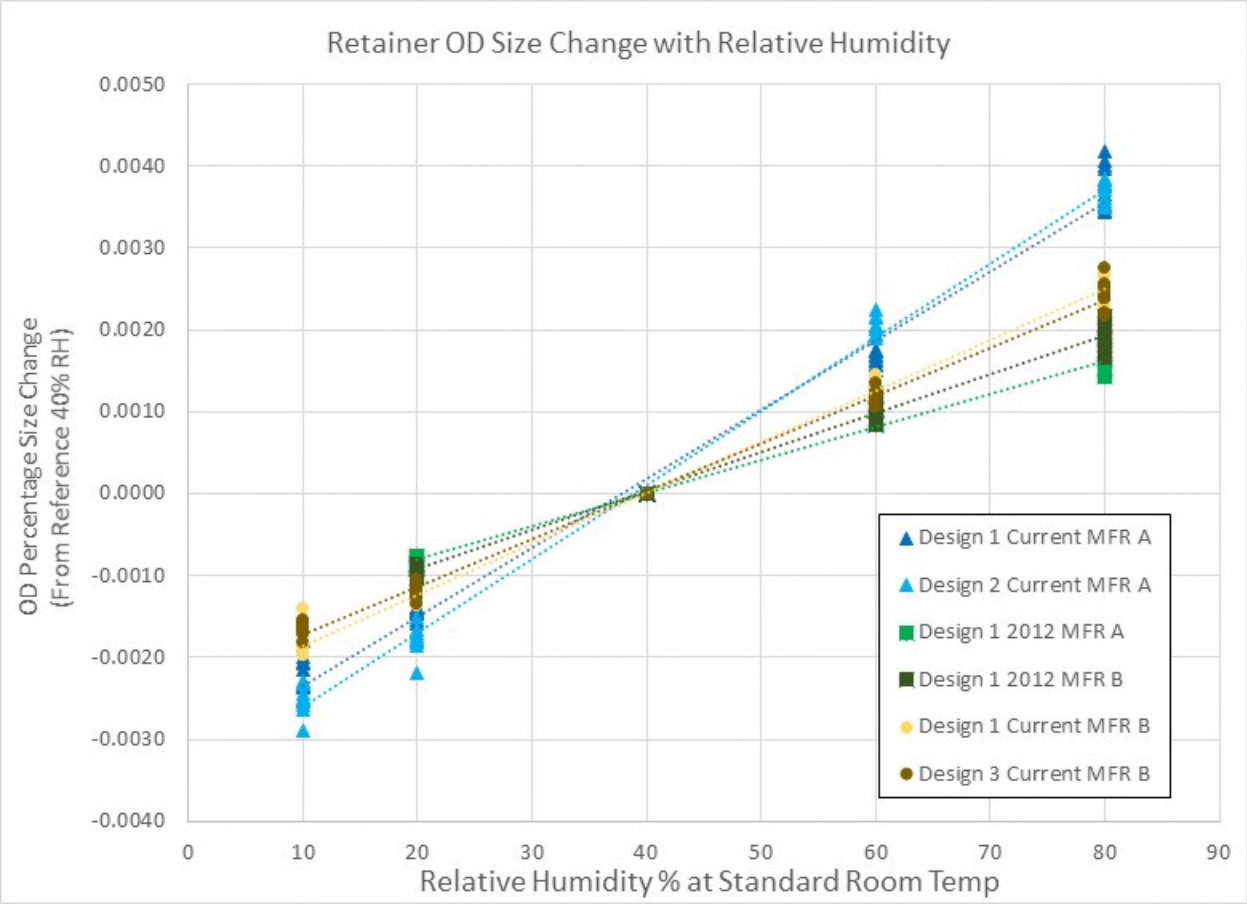

Figure 5: OD size change of phenolic samples with humidity

Data Fitting and Extrapolation

The data from each set appears to follow a linear rate of change. A linear fit can be extrapolated to the design conditions to determine the smallest and largest size the retainer could attain with varying levels of humidity. Linear fits with extrapolation of the expected size changes are listed in Table 2. Included are a fit of each data set as well as combined models for each test set. The size data fits a linear model well, with high correlation coefficients for each individual design and for the combined test data sets.

The underlying purpose of the testing was to determine an adequate phenolic retainer design offset for the as-machined condition when designing for operation in space flight vacuum conditions, assuming 0% relative humidity. This helps to assure the retainers will not shrink onto the inner bearing ring, thereby creating an interference condition in vacuum that could lead to torque increases.

It is not practical to attempt to machine vacuum-dried material to replicate space-like conditions. Vacuum-dried material changes size from moisture absorption at a very fast rate when fully dried at a typical humidity level for manufactured ambient conditions. This has been shown in Manufacturing trials to be less repeatable than machining material at consistent ambient conditions with an offset based on the ambient humidity to account for shrinkage under prolonged vacuum exposure.

Using the combined model of 2012 data, a retainer bore needs to be offset from a reference 40% RH manufactured condition, and the offset would need to account for only a 0.17% reduction in size, on average, to ensure positive clearance of the inner ring at vacuum. The current data for MFR A shows that

a 0.32% reduction in size, on average, would have to be incorporated into the design and the reduction would be 0.21%, respectively, for MFR B. The OD size change for a high-humidity condition is also different. Current test data shows that the ODs could vary up to 0.87% over a full theoretical range of humidity, although this is less of a concern for space flight bearing applications.

Table 2: Linear bore/OD size change models for each data set

	Linear Regression			**Extrapolation**	
	Data Set	**Feature % Rate of Change with RH**	**R^2**	**0%-40% RH**	**Total 0%-100% RH**
Bore	Design 1 MFR A 2012	3.88E-05	0.97	-0.0016	0.0039
	Design 1 MFR B 2012	4.53E-05	0.99	-0.0018	0.0045
	Design 1 MFR A Current	7.91E-05	0.99	-0.0032	0.0079
	Design 2 MFR A Current	8.00E-05	0.96	-0.0032	0.0080
	Design 1 MFR B Current	5.17E-05	0.98	-0.0021	0.0052
	Design 3 MFR B Current	5.32E-05	0.99	-0.0021	0.0053
OD	Design 1 MFR A 2012	4.02E-05	0.99	-0.0016	0.0040
	Design 1 MFR B 2012	4.78E-05	0.99	-0.0019	0.0048
	Design 1 MFR A Current	8.43E-05	0.99	-0.0034	0.0084
	Design 2 MFR A Current	9.00E-05	0.99	-0.0036	0.0090
	Design 1 MFR B Current	5.86E-05	0.99	-0.0023	0.0059
	Design 3 MFR B Current	5.73E-05	0.97	-0.0023	0.0057
Combined Data Sets					
Bore	Combined MFR A/B 2012	4.22E-05	0.97	-0.0017	0.0042
	Combined MFR A Current	7.96E-05	0.97	-0.0032	0.0080
	Combined MFR B Current	5.37E-05	0.98	-0.0021	0.0054
OD	Combined MFR A/B 2012	4.41E-05	0.98	-0.0018	0.0044
	Combined MFR A Current	8.72E-05	0.99	-0.0035	0.0087
	Combined MFR B Current	5.84E-05	0.99	-0.0023	0.0058

Test Minimum Size Extrapolation

The minimum measured humidity condition was 10% RH. Using the linear models, the minimum size can be extrapolated from the minimum measured condition to the fully dry 0% RH vacuum condition. A verification test was performed to review the linear model for accuracy of the minimum expected vacuum dry bore sizes, which are the main areas of concern for bearing function and the risk being reviewed.

Retainers from the current MFR A group were vacuum-dried and test-fit with a set of available gage pins immediately after removal from the vacuum. This is similar to the method Bertrand used with the tapered arbor immediately out of vacuum. An assortment of gage pins both above and below the expected retainer bore sizes were obtained to assess whether the model was adequate at predicting the vacuum-dried condition. The 0% RH model predicted minimum bore sizes using the “Combined MFR A Current” bore size model from Table 2 applied to each individual retainer’s 40% RH reference condition bore measurement to create a 0% RH bore prediction for the functional evaluation.

Tested retainers were vacuum-baked to a fully dry state validated by comparing the retainer mass to values obtained in test step 1. The retainers were cooled to room temperature 20°C at vacuum overnight for size comparison, and at room temperature aligned with the previous Visio measurement conditions. Retainers were removed from the chamber and immediately tested with the assortment of pins. The pin results listed as “go” indicate the retainer easily fits on the pin with minimal force and slid easily, and would slide off under its own weight.

The second outcome of “tight” indicates the retainer went on the pin but with resistance and would not fall off the pin under its own weight. This result assumes a line-to-line/light interference fit. The third outcome, “no,” indicates the retainer would not slide on the pin because the bore was smaller than the pin size being used. Results of pin checks for MFR A Design 2 retainers are shown in Table 3 with the expected modeled 0% RH size for each numbered retainer. This design was used as the verification example as it had the largest available set of pin sizes near the expected minimum size value.

Table 3: Retainer Design 2, MFR A, vacuum-baked minimum size verification

Retainer Sample	**Test Pin Diameter**						**0% RH Model Prediction**
	37.06 mm (1.459 in)	**37.11 mm (1.461 in)**	**37.16 mm (1.463 in)**	**37.21 mm (1.465 in)**	**37.24 mm (1.466 in)**	**37.31 mm (1.469 in)**	
1	go	go	tight	no	no	no	37.16 mm (1.463 in)
2	go	go	go	no	no	no	37.16 mm (1.463 in)
3	go	go	go	no	no	no	37.13 mm (1.462 in)
4	go	go	go	no	no	no	37.16 mm (1.463 in)
5	go	go	go	tight	no	no	37.16 mm (1.463 in)
6	go	go	go	no	no	no	37.16 mm (1.463 in)
7	go	go	go	no	no	no	37.16 mm (1.463 in)
8	go	go	go	no	no	no	37.13 mm (1.462 in)
9	go	go	go	no	no	no	37.19 mm (1.464 in)
10	go	go	go	no	no	no	37.19 mm (1.464 in)

Pin verification aligned with the predicted model in all but one example. Retainer 5 measured slightly larger than the expected model prediction, fitting tightly on a bore pin 51 µm (0.002 in) larger than the model expectation. Given the variation of the bore change in the data set shown in Figure 4, this is not unexpected. Design 1 of the MFR A material was tested similarly but with less resolution of pin sizes. All predicted minimum sizes followed the model prediction.

The variation in the measured retainer parameters for each completed set of test samples highlights an important factor when using phenolic material for bearing retainers in thin section bearings for use in vacuum. The composite structure of the material, along with the variation between production lots, presents risk if a size variation model is used exclusively. Simple design offsets work for most retainer designs; however, some designs inherently result in a higher risk of loss of retainer piloting clearance. In higher-risk applications such as thin section ball bearings, the most conservative approach when applying phenolic retainers is to perform a functional minimum retainer clearance test in serial production either after a vacuum bake cycle or as part of the lubricant vacuum impregnation process.

Lessons Learned / Conclusions

Historical assumptions for phenolic ball bearing retainer size change due to humidity may not be conservative enough for all retainers using currently available materials. This is of the most significant concern in thin section ball bearing designs commonly used in space flight applications Retainer diameters that are larger in proportion to the bearing retainer clearances represent a higher risk for loss of retainer clearance around the inner bearing ring, and loss of retainer piloting clearance can result in excessive bearing torque.

In high-risk bearing applications utilizing continuous (non-segmented) phenolic bearing retainers, design review for operation at full vacuum is recommended. Functional pin testing immediately following vacuum drying or the vacuum impregnation process can be used as a further risk mitigation method. There is a surprising amount of variation reported in the material's response to humidity. It is unknown if this is the result of changes to the material being supplied to the industry or is characteristic of the typical lot-to-lot variation that comes with the composite manufacturing process.

Acknowledgments

The author would like to thank the Timken Company for support of this work, permission to publish and for providing equipment used in testing. The author thanks JPM of Mississippi for providing the additional test samples that were used to finalize the test set.

Reference

[1] Bertrand, P.A. and Sinsheimer, J.D., "Humidity-Induced Dimensional Changes in Cotton-Phenolic Ball-Bearing Retainers," *ASME Journal of Tribology*, Vol. 124 p. 474-479, July 2002
[2] MIL-I-24768/13

Preventing the "Brown Sugar" Lubricant Phenomenon: The Relationship Between PFPE Chemical Compositions and their Susceptibility to Lewis Acid-Catalyzed Degradation

Amanda W. Stubbs* and Jason T. Galary*

Abstract

Lubricants play a critical role in ensuring that mechanisms perform reliably under the demanding operating conditions found in space. Known for their chemical inertness, broad operating temperature range, and low volatility, perfluoropolyethers (PFPEs) are attractive lubricants for space applications. The one Achilles Heel of PFPEs is their susceptability to Lewis acid-catalyzed degradation, also known as the "Brown Sugar" effect, which can negatively impact the wear life of a lubricant.

However, not all PFPEs have the same chemical structure, making some PFPEs more susceptible to Lewis acid-catalyzed degradation than others. In this study, two greases were examined, the legacy Braycote® 601EF and the recently launched NyeTorr® 6350EL, as well as their respective base oils. The greases and oils were subjected to thermal treatments in both the absence and presence of Lewis acids found in space applications.

Samples were monitored for thermal degradation via Thermogravimetric Analysis (TGA) during treatment, and grease samples were subjected to antiwear testing on the SRV® test system and Vacuum 4 Ball Wear Tribometer after treatment. These results provide fundamental insight into the impacts that Lewis acid exposure has on the performance of different PFPE chemistries.

Our preliminary findings suggest that products made with PFPEs classified as "Z fluids", like Braycote® 601EF, are inherently susceptible to Lewis acid-catalyzed degradation. Z fluids also exhibit inferior wear performance after exposure to Lewis acids at high temperatures when compared to PFPEs of different chemical structures. The data collected demonstrates the cause of the Brown Sugar effect and enables engineers to make informed decisions when selecting lubricants for space mechanisms.

Introduction

Background

PFPE-based oils and greases have been go-to solutions for lubrication in space applications for over fifty years [1]. The inherent properties of these fluids make them a good fit for the space environment; their attributes include low vapor pressures and outgassing, broad operating temperature range, and chemical inertness. Their broad operating temperature range is especially important for lubricants in space, not only due to extreme sweeps in ambient temperature conditions, but also due to limited opportunities for heat transfer and dissipation in a vacuum environment. PFPEs offer the highest thermal stability of available base oils and thus are best equipped to withstand the localized high temperatures generated at frictional contacts [1–3].

While PFPE fluids check many of the "must-have" boxes when selecting lubricants for space applications, there are some areas where they fall short. In particular, despite representing some of the most inert lubricants available, in the presence of Lewis acids PFPEs are subject to degradation. When this failure-inducing phenomenon occurs, it is sometimes referred to as the "Brown Sugar" effect due to the resulting residue resembling the color and texture of brown sugar. This phenomenon has been well documented and

* Nye Lubricants, Inc., Fairhaven, MA (member of the FUCHS Group), amanda.stubbs@fuchs.com

studied. At this point, our understanding of the conditions that cause the brown sugar phenomenon is quite good; we know that it is caused by the Lewis acid sites that exist on metal surfaces and that it is more likely to occur under boundary lubrication conditions – presumably due to a combination of elevated localized temperatures at asperity contacts and wear debris that are generated. It is also known that the degradation reaction products exacerbate the problem and promote even more rapid degradation of the fluid [2,4–10]. Available mitigation strategies on the other hand, are more limited. Beyond avoiding conditions that are known increase the chance of degradation occuring, by using ceramic coated balls in bearings for example, it hasn't been possible to prevent Lewis acid-catalyzed degradation of PFPE fluids.

To better understand this problem, we need to look at what is happening on a molecular level. All PFPE fluids are polymers; they are long chain molecules that are made up of repeating units called "monomers" that are chemically linked together. All PFPE monomers are fully fluorinated (no hydrogen atoms – this is what imparts their incredible inertness) and the monomers are linked together by oxygen atoms. The identity of the monomers largely dictates the fluid properties; there are a variety of different PFPE fluids commercially available in varying viscosities. For the purposes of this discussion it should be noted that some fluids contain acetal linkages (-O-CF_2-O-), and others do not. Figure 1 depicts the structures of four different commercially available PFPE fluids; Fomblin® Z, Fomblin® Y, Krytox®, and Demnum™. Shown in red, Fomblin® Y and Fomblin® Z both contain acetal linkages in their structures, with the Fomblin® Z fluid containing the much higher proportion of acetal linkages between the two. In contrast, the Krytox® and Demnum™ fluids do not have any acetal linkages in their structures at all. There is evidence that acetal linkages in PFPEs are especially susceptible to Lewis acid-catalyzed degradation; wih Fomblin® Z fluids known to be the most degradation-prone fluids [10]. Despite this shortcoming, Fomblin® Z fluids are still a popular lubricant selection due to their unrivalled high viscosity index, low evaporative loss, and wear protection.

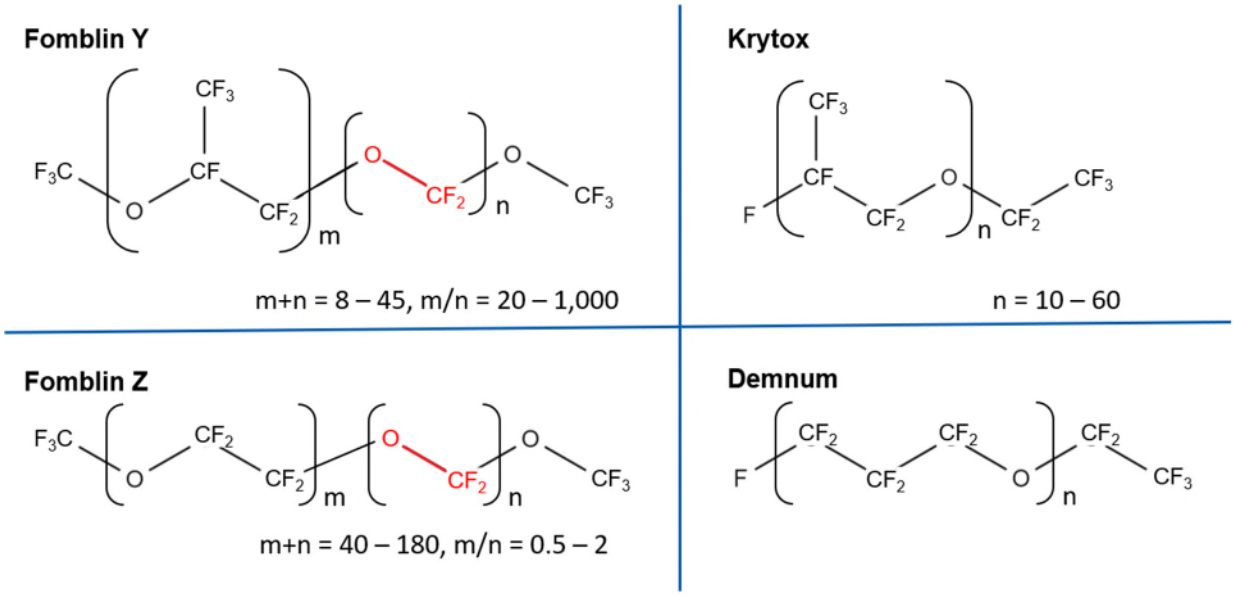

Figure 1. Representation of different PFPE fluid structures

A "Lewis acid" is broadly defined as a species that can accept electrons [11]. In space lubricant applications, a relevant example of a Lewis acid is iron (III) oxide (Fe_2O_3), which is found on stainless steel surfaces. The iron (III) oxide plays a fleeting role in the PFPE degradation process; it temporarily accepts some electron density from the polymer chain, enabling a fluorine atom to transfer from one -CF_2- unit to another, ultimately causing the chain to break in two, as shown in Figure 2. In PFPEs containing acetal units, this transfer is especially easy to do, making them among the most susceptible fluids. Some of the by-products

from PFPE chain destruction are highly reactive species such as carbonyl fluoride (COF_2) that can interact with iron (III) oxide and convert it to iron (III) fluoride (FeF_3), an even stronger Lewis acid.

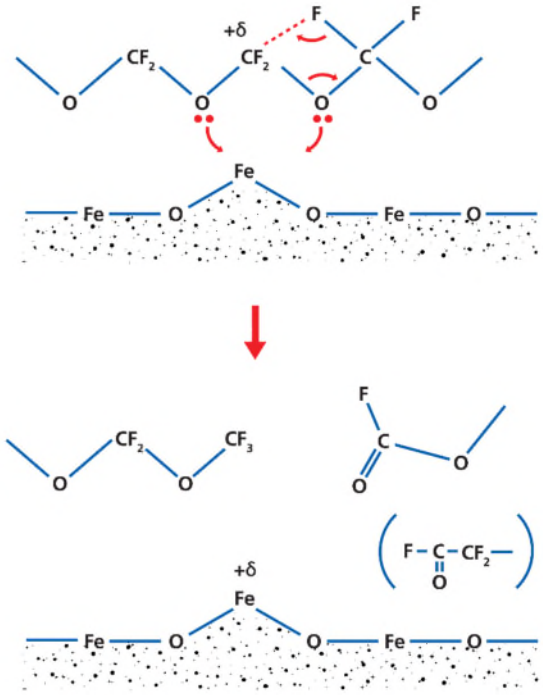

Figure 2. Depiction of a Lewis acid site interacting with an acetal group in a PFPE chain, resulting in chain scission. Adapted from Kasai et. al.[10]

In this work, the heritage space lubricant Braycote® 601EF, which is based on a Fomblin® Z fluid [3], is compared to NyeTorr® 6350EL, which utilizes a proprietary blend of PFPE fluids in its formulation. Both greases and their respective base oils (Brayco® 815Z, NyeTorr® 6351) were subjected to thermal treatments in the presence and absence of the Lewis acids Fe_2O_3 and FeF_3. Additionally, a "booster" additive was added to NyeTorr® 6350EL experimentally to enhance its Lewis acid-catalyzed degradation resistance. Sample masses were monitored during treatment as an indicator of degradation, and after treatment samples were subjected to wear testing on the SRV and Vacuum 4 Ball Tribometer.

Sample Preparation

Neat samples of commercial lubricants were used as received. Lewis acids used in this study were Iron(III) Oxide, (Strem, Hematite, 99.8% Fe) and anhydrous Iron(III) Fluoride (Strem, 99%+). For TGA testing, Lewis acid spiked samples were prepared by combining 9 grams of lubricant with 1 gram of the specified Lewis acid and speedmixing to ensure homogeneity. Spiked samples were prepared immediately before testing to limit the amount of degradation allowed to occur at room temperature prior to starting the TGA test. For wear tribometer tests, Lewis acid spiked samples were prepared by combining 2.7 grams of lubricant with 0.3 gram of the specified Lewis acid. Samples were mixed with a spatula in a Petri dish and placed in an oven at 200°C for 24 hours. Samples were allowed to cool to room temperature prior to testing. Heat treated samples were prepared in a similar manner, without the addition of Lewis acid.

Experimental Methods

Using a TA Instruments TGA Q50 Thermogravimetric Analyzer, thermal stability testing was performed in an air-filled environment. In the method utilized the temperature was ramped at a rate of 100°C/min to 230°C and then held there for 24 hours. Using the precise balance built into the instrument, the weight of the sample was monitored as the temperature was held. The amount of mass loss the sample exhibited

was used as an indicator of degradation; samples that demonstrated greater mass losses are considered more prone to degradation.

Wear testing on the SRV® was used to determine a lubricant's ability to protect against wear when subjected to high-frequency, linear oscillation motion. In this work, conditions included a 52100 steel ball on disc contact, a test load of 100 N (yielding a contact pressure of 2.1 GPa), a frequency of 50 Hz, a stroke amplitude of 1.00 mm, a duration of 1 h and a temperature of 50°C. Specimens used were of hardness Rockwell C60, and met surface roughness and topography criteria as specified in ASTM D 5707 (Standard Test Method for Measuring Friction and Wear Properties of Lubricating Grease Using a High-Frequency, Linear-Oscillation (SRV) Test Machine) section 7.1-7.2. To protect the instrument, a maximum coefficient of friction cutoff was set where the test was terminated if it was exceeded. After the conclusion of a test, the total distance travelled by the specimens was calculated and the wear volume of the scar on the disc was measured using a Taylor Hobson 3D Optical Profilometer. With this information a wear rate was calculated and expressed in $\mu m^3/mm$; this method of data analysis enables the evaluation of even samples that are unable to complete the entire test method, allowing for greater resolution when ranking relative sample performance.

Wear testing on the Vacuum 4 Ball Tribometer (a custom built rig controlled with a LabView DAQ system) was used to evaluate lubricants' performance under conditions more closely resembling the environment in space. In the test method used for this work, a vacuum level of $6.7x10^{-4}$ Pa was achieved before initiating the test, typically by the end of the test the vacuum level had further dropped to $1.3x10^{-4}$ Pa. Selection of other parameters was based off of ASTM D2266 (Standard Test Method for Wear Preventive Characteristics of Lubricating Grease) with some modifications, largely made to reduce the amount of sample needed to a volume of 4 mL. For specimens, 7.9375 mm (5/16 inch) 52100 Alloy Steel balls were used with a hardness of Rockwell C60. An applied load of 290 N was used for testing, resulting in an initial contact pressure of 4.2 GPa. The test was run for one hour at room temperature and a speed of 600 rpm. After completion of the test, wear scar diameters on the lower three balls were measured using a microscope and the average reported. Each sample was run in triplicate.

Results and Discussion

In thermal degradation testing, each commercial base oil and its spiked samples were heated to 230°C and held at that temperature on the TGA, with the total mass loss of the sample after 24 hours of treatment recorded. Each sample was run in duplicate, the average mass losses are displayed in Table 1. Both the NyeTorr® 6351 and Brayco® 815Z exhibited minimal mass loss when run as neat oils, both less than 5% loss but with NyeTorr® 6351 exhibiting the least mass loss with only a 0.12% reduction over the course of 24 hours. When mixed with a Lewis acid prior to heating, both oils exhibited mass loss, which is an indicator of degradation. For each oil the identity of the Lewis acid (Fe_2O_3 vs. FeF_3) didn't have a significant impact on the extent of degradation. The two oils did differ in the extent of mass loss demonstrated, the Brayco® 815Z exhibited a 90% mass loss in each of its runs. Given that 10% of the sample size was the spiked Lewis acid that was not expected to volatilize at this temperature even if degraded, it can be assumed that 100% of the oil in the sample was broken down and volatilized. In contrast, NyeTorr® 6351 only exhibited about 45% mass loss in the presence of Lewis acids; presumably some oil was left intact and hadn't degraded (Figure 3). It is worth noting that for both Brayco® 815Z and NyeTorr® 6351 nearly all degradation occurred within the first 45 minutes of the experiment, the change in mass from hour 1 to hour 24 of the test was negligible. While the identity of the Lewis acid didn't significantly impact the amount of degradation, the identity did impact how long it took for degradation to begin; samples treated with Fe_2O_3 typically didn't have degradation onset until approxiamtely 30 minutes into the run, whereas samples treated with FeF_3 exhibited onset of degradation within the first 15 minutes of the run. This observation is consistent with other experiments reported in the literature where it was found that Fe_2O_3 was converted to FeF_3 during PFPE degradation, and that FeF_3 is an even stronger Lewis acid catalyst [2].

An additional experiment was performed to test the efficacy of a new additive hypothesized to impart resistance to Lewis acid-catalyzed degradation on susceptible base oils. For this experiment pure Fomblin®

Z25 was studied, which is known to degrade rapidly in the presence of Lewis acids at elevated temperatures [5,10]. Consistent with the literature, neat Fomblin® Z25 exhibited minimal mass loss when heat treated (4.44%) but when heat treated in the presence of FeF_3 it underwent complete and rapid degradation. A sample spiked with the "booster" additive at a 1% treat rate was prepared and subjected to the same heat treatment in the presence of FeF_3. Indeed, this sample exhibited stability comparable to that of the neat base oil, with only a 5.12% mass loss over the course of the 24 hour test, in contrast to the 90.36% mass loss exhibited by Fomblin® Z25 in the presence of FeF_3 without the booster additive (Figure 4).

Table 1. Total Mass Loss of Oil Samples Test on TGA

Lubricant	Lewis Acid	Total Mass Loss (wt%)*
Brayco® 815Z	--	3.12%
Brayco® 815Z	Fe_2O_3	89.11%
Brayco® 815Z	FeF_3	90.59%
NyeTorr® 6351	--	0.12%
NyeTorr® 6351	Fe_2O_3	45.19%
NyeTorr® 6351	FeF_3	45.40%
Fomblin® Z25	--	4.44%
Fomblin® Z25	FeF_3	90.36%
Fomblin® Z25**	FeF_3	5.12%

*average of 2 runs
** spiked with booster additive

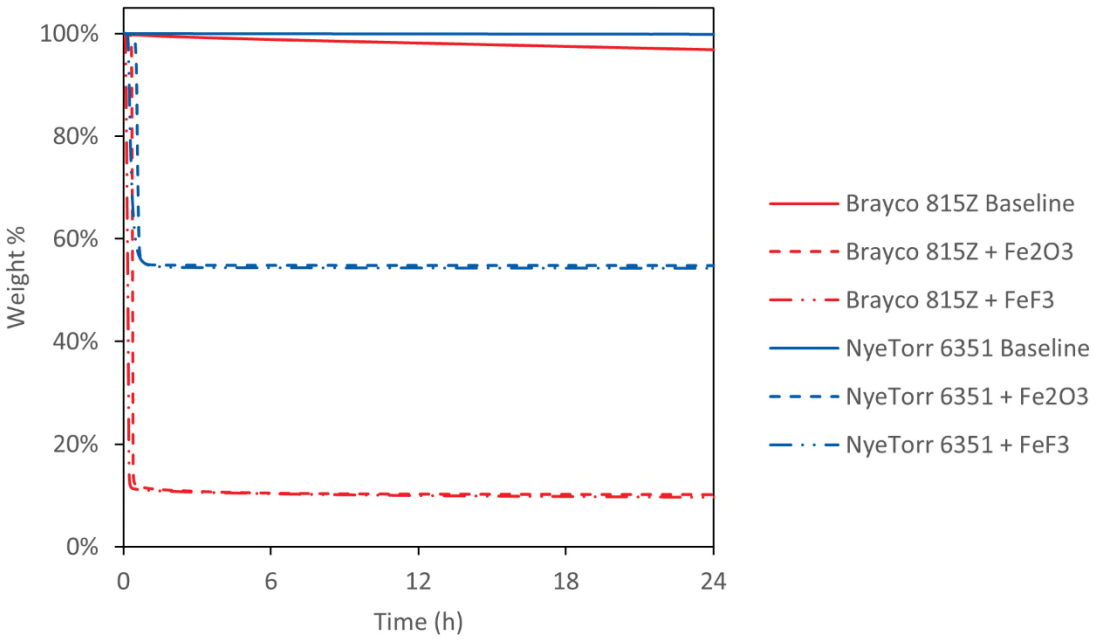

Figure 3. TGA traces of commercial oils in the presence and absence of Lewis acids

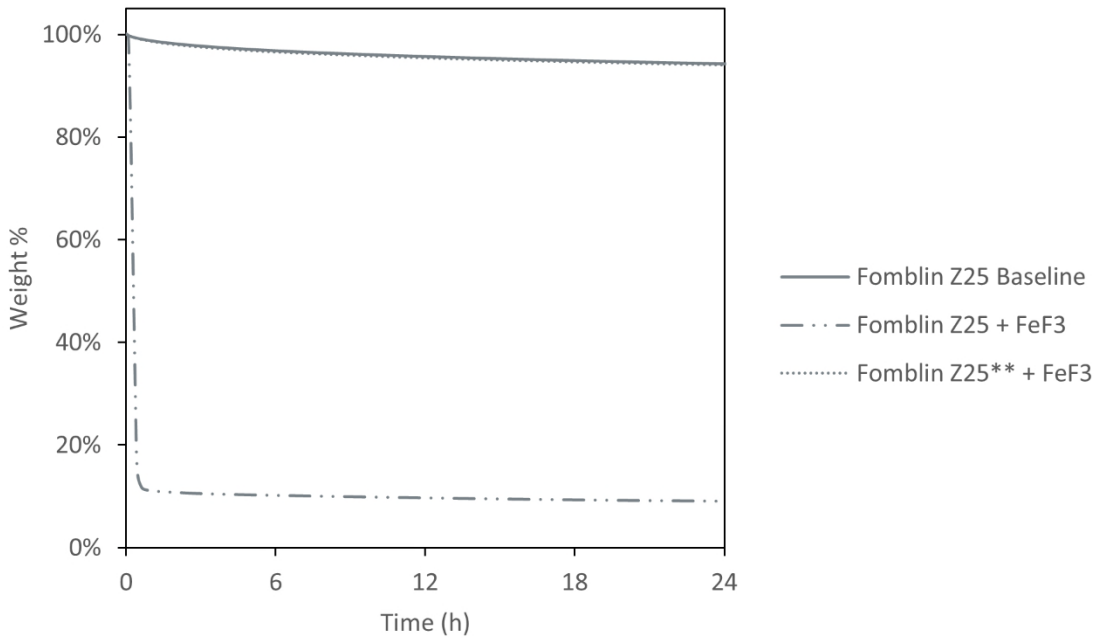

Figure 4. TGA traces of Fomblin® Z25 in the presence and absence of Lewis acids and booster additive

Grease samples were treated in a manner similar to oils on the TGA, results are displayed in Table 2. For both Braycote® 601EF and NyeTorr® 6350EL, mass loss exhibited by the neat greases was minimal, comparable to what was observed for their neat base oils. In the presence of Lewis acids, the story becomes more convoluted. This is perhaps due in part to the fact that greases are more complex formulations with a greater number of components than typically seen in oils, perhaps the most impactful of which is the thickening system. In the neat oils it is feasible that some mixing of the sample and interaction with the Lewis acid would occcur *via* convection currents; with the presence of the thickener network in greases, mixing would be inhibited – this could cause greater variability in performance. In the case of Braycote® 601EF, exposure to Fe_2O_3 resulted in an average mass loss of 11.42%, while exposure to FeF_3 had a more drastic impact with an average mass loss of 30.80%. In contrast, NyeTorr® 6350EL was less affected by the presence of Lewis acids, with merely an average 1.55% mass loss in the presence of Fe_2O_3 and 3.51% mass loss average in the presence of FeF_3 (Figure 5). The improved resistance to degradation in NyeTorr® 6350EL is likely due to the greater inherent resistance demonstrated by its base oil, NyeTorr® 6351 discussed above, as well as impacts from the thickener and other components in its formulation. Inspired by the results of our experimentation with Fomblin® Z25 and the booster additive, an experimental sample of NyeTorr® 6350EL was prepared with this booster (referred to as NyeTorr® 6350EL Plus) to see if its performance could be enhanced even further. As expected, the NyeTorr® 6350EL Plus demonstrated baseline performance comparable to that of NyeTorr® 6350EL, and in the presence of Lewis acids its mass losses were the lowest observed in the study, all less than 1.5% (Figure 6).

Table 2. Total Mass Loss of Grease Samples Tested on the TGA

Lubricant	Lewis Acid	Total Mass Loss (wt%)*
Braycote® 601EF	--	3.60%
Braycote® 601EF	Fe_2O_3	11.42%
Braycote® 601EF	FeF_3	30.80%
NyeTorr® 6350EL	--	0.52%
NyeTorr® 6350EL	Fe_2O_3	1.55%
NyeTorr® 6350EL	FeF_3	3.51%
NyeTorr® 6350EL Plus	--	0.83%
NyeTorr® 6350EL Plus	Fe_2O_3	0.78%
NyeTorr® 6350EL Plus	FeF_3	1.07%

*average of 2 runs

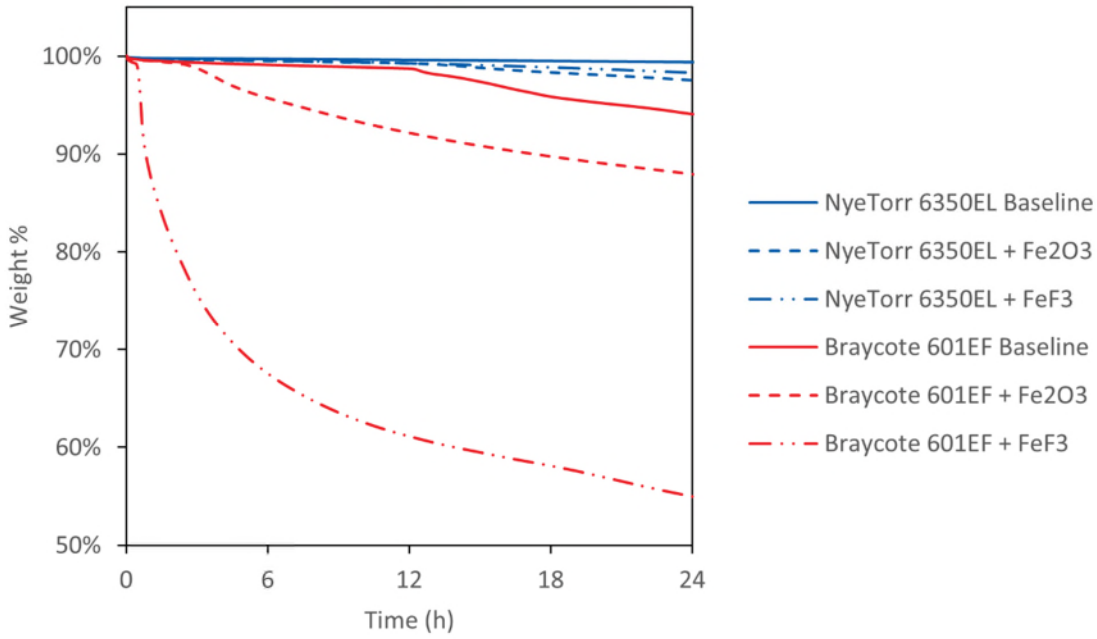

Figure 5. TGA traces of commercial greases in the presence and absence of Lewis acids

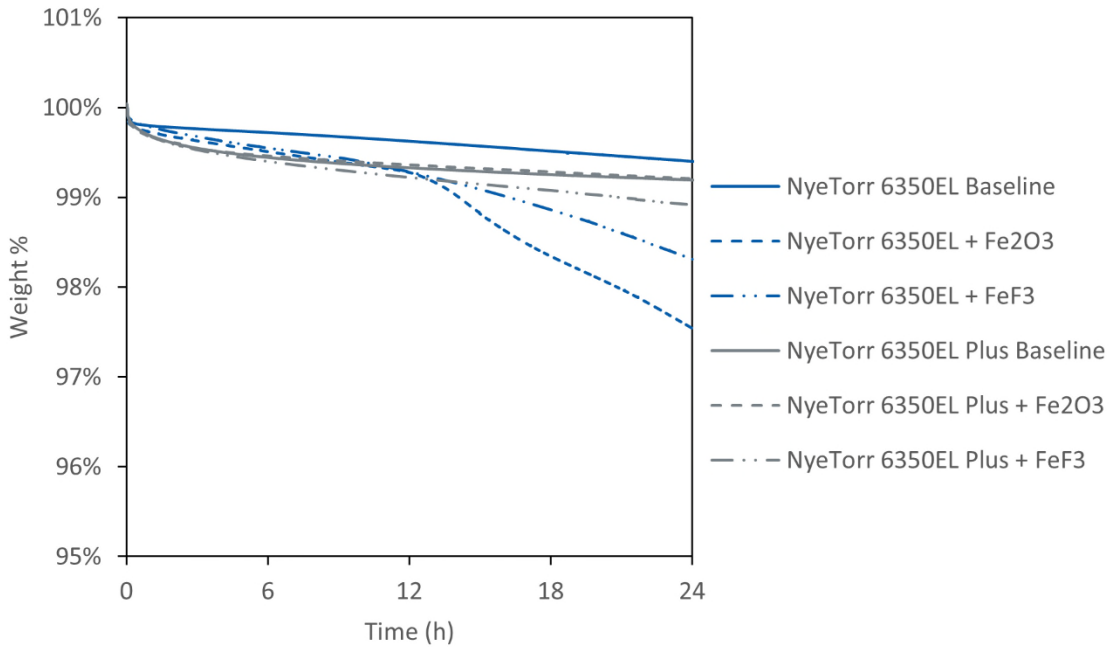

Figure 6. TGA traces of NyeTorr® 6350EL and the experimental NyeTorr® 6350EL Plus in the presence and absence of Lewis acids

Grease samples that were treated with Lewis acids and then heated in an oven were tested on the SRV to evaluate their wear performance. Additional controls were performed including neat, untreated samples as well as greases subjected to heat alone without Lewis acids present. Figures 7-9 show images of Braycote® 601EF, NyeTorr® 6350EL, and the experimental NyeTorr® 6350EL Plus samples as they appeared before and after heat treatment in the presence and absence of Lewis acids. Note that all greases appeared more brown or orange after being heated in the presence of FeF_3, which is likely due to the FeF_3 reacting with the air to form other inorganic, oxidized compounds – reactions happening alongside and in addition to any interactions with the PFPE fluid.

Figure 7. Images of Braycote® 601EF under different treatment conditions

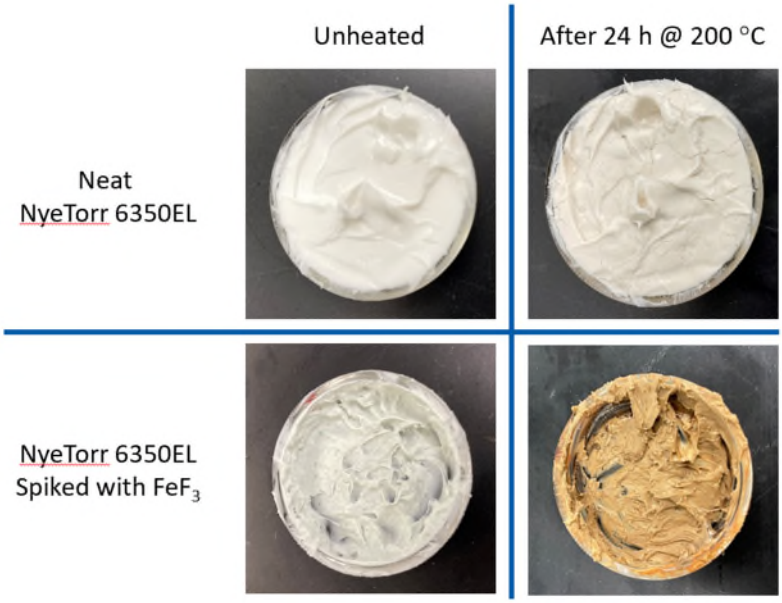

Figure 8. Images of NyeTorr® 6350EL under different treatment conditions

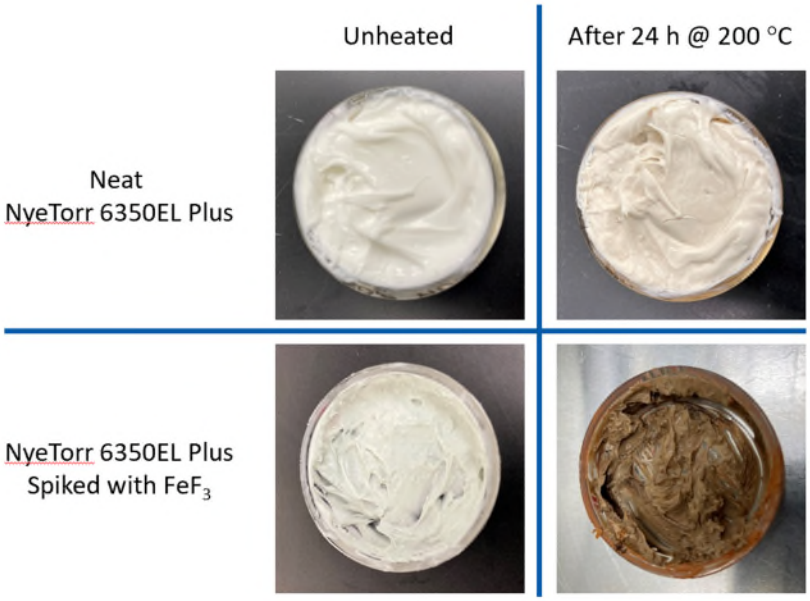

Figure 9. Images of NyeTorr® 6350EL Plus under different treatment conditions

Since none of the samples evaluated on the SRV ran to completion, wear rates were calculated and reported for each so that fair comparisons could be made, these results are displayed in Figure 10. Predictably, each grease had the best performance (lowest wear rate) when not subjected to heat or Lewis acid exposure. Heat treatment resulted in slightly higher wear rates, but the highest wear rates observed were after exposure to Lewis acids. Braycote® 601EF and NyeTorr® 6350EL performed comparably; after exposure to Fe_2O_3 NyeTorr® 6350EL performed better than Braycote® 601EF, but after exposure to FeF_3 the Braycote® 601EF offered the slightly lower wear rate when compared to NyeTorr® 6350EL. Of note, wear rates were higher for both greases after exposure to Fe_2O_3 than they were after exposure to FeF_3. This is potentially due to the fact that FeF_3 is itself a good lubricant – one of the things that make PFPEs effective lubricants is a minor amount of breakdown resulting in FeF_3 formation on the metal surface, which itself functions as an excellent solid lubricant [12] It is possible that the Fe_2O_3 spiked samples had artificially

inflated wear rates due to the Fe_2O_3 particles present, which are not effective solid lubricants. Perhaps of greatest note, the NyeTorr® 6350EL Plus sample (containing booster additive) offered superior wear protection even in the presence of Lewis acids. After treatment with either Fe_2O_3 or FeF_3, NyeTorr® 6350EL Plus offered wear rates nearly half of those observed for Braycote® 601EF and NyeTorr® 6350EL. While NyeTorr® 6350EL Plus is still an experimental sample, it appears that it could be an excellent solution for applications where wear protection in the presence of Lewis acids is essential.

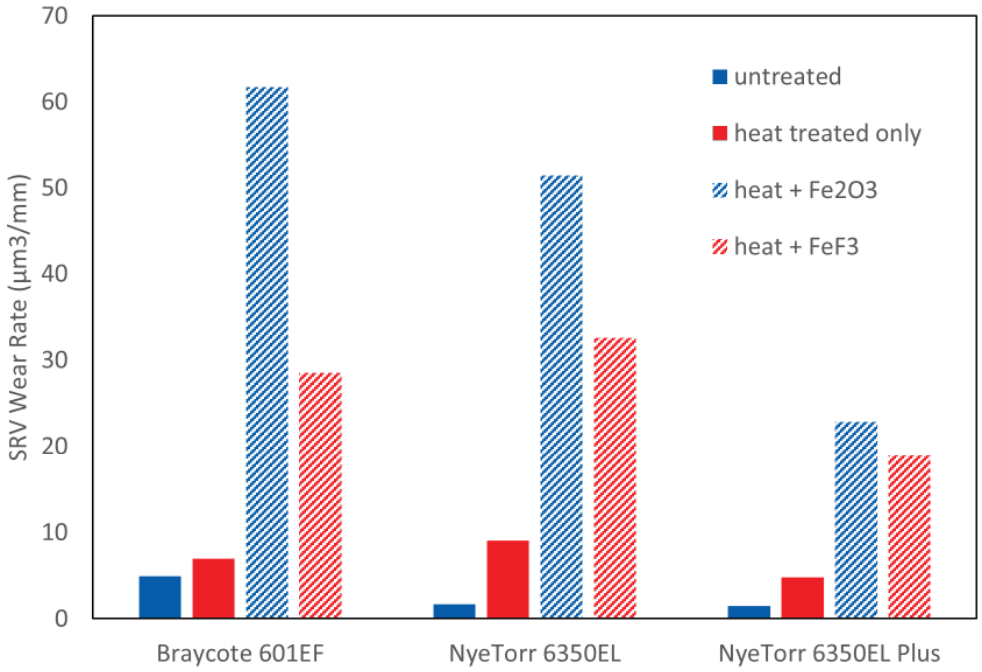

Figure 10. SRV® wear rates for greases subjected to Lewis acid exposure

To evaluate greases' performance in an environment more closely resembling those found in space applications, the Vacuum 4 Ball Wear Tribometer was employed. Similar to the data collected on the SRV, samples were heated in an oven while in the presence of Lewis acids. This testing is still ongoing; currently average wear scar diameters for commercial greases neat and untreated can be reported as a baseline, as well as commercial greases after being subjected to heat in the presence of FeF_3. Preliminary data displayed in Figure 11 indicates comparable performance of Braycote® 601EF and NyeTorr® 6350EL, with Lewis acid treatment having little impact on wear performance. This is in contrast to what was observed in the SRV® testing, where exposure to Lewis acids resulted in significant increases in wear rate of the samples. That being said, it could be that the test conditions used were not harsh enough for us to obtain good resolution in relative performance between the samples studied. This work is ongoing, as performance in a vacuum environment is a critical evaluation for lubricants used in space applications.

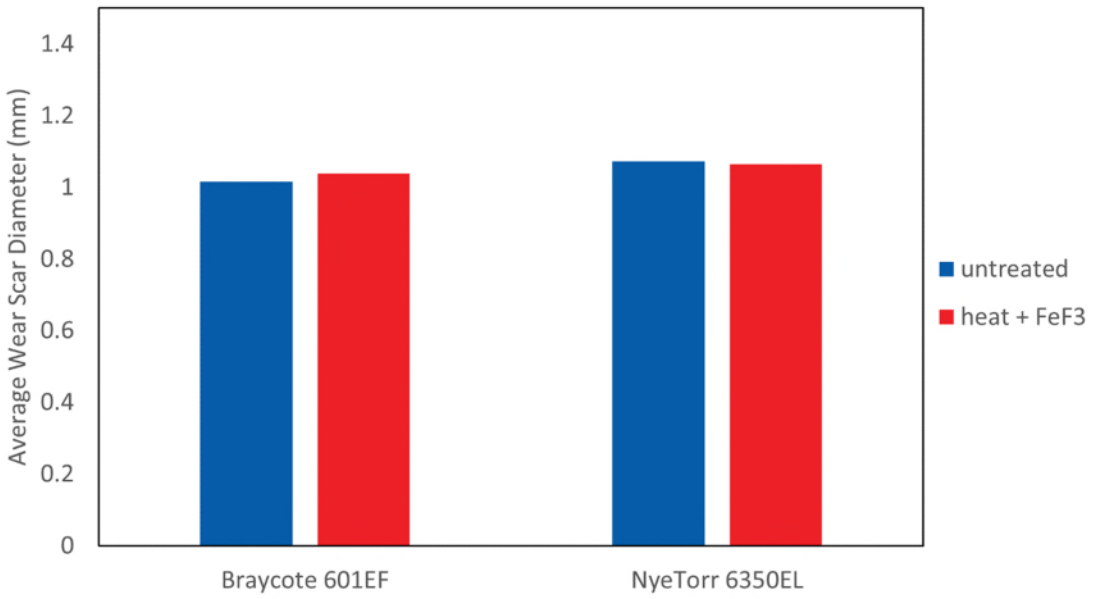

Figure 11. Vacuum 4 Ball Wear average scar diameters for greases before and after Lewis acid exposure

Conclusions

Formulating with raw materials that are inherently resistant to Lewis acid-catalyzed degradation results in lubricants with greater resistance to the phenomenon. NyeTorr® 6351 and NyeTorr® 6350EL offer greater resistance to Lewis acid-catalyzed degradation in thermal studies when compared to heritage products used for space applications. Base oils lacking inherent resistance to Lewis acid degradation can gain resistance with the addition of a “booster” additive; its properites are effective in greases as well as in oils. SRV® wear data after heat treating grease samples in the presence of Lewis acids indicated comparable performance of Braycote® 601EF and NyeTorr® 6350EL. A standout performer was the experimental grease NyeTorr® 6350EL Plus, demonstrating nearly half of the wear rates observed for the commercial products tested. Vacuum 4 Ball Wear Tribometer data indicates that both Braycote® 601EF and NyeTorr® 6350EL offer comparable wear protection in a vacuum environment, regardless of whether treated with Lewis acids or not – this testing will be further refined to gain a better understanding of the impact of Lewis acids on lubrication in the vacuum environment.

Acknowledgements

The work reported in this paper was a highly collaborative effort that was supported by multiple members of the Nye Lubricants R&D lab. All experiments were designed in collaboration with Dr. Jennifer Frias. TGA testing was supported by Paul Moses, Melissa LaRochelle, and Matthew Easterbrooks. All sample preparations for wear performance testing on the SRV® and Vacuum 4 Ball Wear Tribometer were prepared by Paul Moses. The SRV® test method was developed with Robert Mulkern, and SRV testing was performed by Paul Moses. Mason Wood designed and built the Vacuum 4 Ball Wear Tribometer used in this study, he also advised on the test conditions used and performed all of the testing.

References

(1) Jones, W. R. Properties of Perfluoropolyethers for Space Applications. *Tribol. Trans.* **1995**, *38* (3), 557–564. https://doi.org/10.1080/10402009508983442.

(2) Zehe, M. J.; Faut, O. D. Acidic Attack of Perfluorinated Alkyl Ether Lubricant Molecules by Metal Oxide Surfaces. *Tribol. Trans.* **1990**, *33* (4), 634–640. https://doi.org/10.1080/10402009008981999.

(3) Fusaro, R. L.; Khonsari, M. M. *Liquid Lubrication for Space Applications*; Cleveland, 1992.

(4) Mori, S.; Morales, W. Decomposition of Perfluoroalkylpolyethers (PFPE) in Ultra-High Vacuum Under Sliding Conditions. *Tribol. Trans.* **1990**, *33* (3), 325–332. https://doi.org/10.1080/10402009008981962.

(5) Mori, S.; Morales, W. *Reaction of Perfluoroalkylpolyethers (PFPE) with 440C Stainless Steel in Vacuum Under Sliding Conditions at Room Temperature*; Cleveland, 1989.

(6) Carré, D. J. The Performance of Perfluoropolyalkylether Oils under Boundary Lubrication Conditions The Performance of Perfluoropolyalkylether Oils under Boundary Lubrication Conditions. **2008**, *2004*. https://doi.org/10.1080/10402008808981845.

(7) Carré, D. J.; Markowitz, J. A. The Reaction of Perfluoropolyalkylether Oil with FeF_3, AlF_3, and $AlCl_3$ at Elevated Temperatures. *ASLE Trans.* **1985**, *28* (1), 40–46. https://doi.org/10.1080/05698198508981592.

(8) Carré, D. J. Perfluoropolyalkylether Oil Degradation : Inference of FeF_3 Formation on Steel Surfaces under Boundary Conditions Perfluoropolyalkylether Oil Degradation : Inference of FeF3 Formation on Steel Surfaces under Boundary Conditions. **2008**, *8197*. https://doi.org/10.1080/05698198608981668.

(9) Faillard, L.; Mariot, A.; Fotea, C.; Holzbauer, R. FeF_3 Catalytic Influence on PFPE Lubricants Lifetime under Loaded Conditions. In *41st Aerospace Mechanisms Symposium*; Boesiger, E. A., Ed.; 2012; pp 147–154.

(10) Kasai, P. H. Perfluoropolyethers: Intramolecular Disproportionation. *Macromolecules* **1992**, No. 25, 6791–6799. https://doi.org/10.1021/ma00051a011.

(11) Miessler, G. L.; Fischer, P. J.; Tarr, D. A. Acid-Base and Donor-Acceptor Chemistry. In *Inorganic Chemistry*; Jaworski, A., Ed.; Pearson: Boston, 2014; pp 184–197.

(12) Jones, W. R. Properties of Perfluoropolyethers for Space Applications. *Tribol. Trans.* **1995**, *38* (3), 557–564. https://doi.org/10.1080/10402009508983442.

Performance of MoS_2 Coated Gears Exposed to Humid Air During Storage (Study Number Two)

Tysen Mulder*, Timothy Krantz*, Claef Hakun**, Zachary Cameron**, Iqbal Shareef+ and Michael Dube++

Abstract

This work is a follow-on to a prior study on the effect of exposure to humid air on the durability of a molybdenum disulfide (MoS_2) dry film lubricant on spur gears operated in vacuum, motivated by the James Webb Space Telescope (JWST) mission. In this study, MoS_2 dry-lubricating films matching JWST specification were applied to test gears. The gear specimens were subjected to a brief run-in period in vacuum prior to their exposure to humid air, mimicking the sequence of mechanism checkout testing, exposure to air during integration, and then storage prior to launch. Test gear exposure times to humid air ranged from 1 hour to 326 days. After exposure, gear durability tests were conducted as an indication of film lifetime. MoS_2 dry film lubricants that were exposed to humid air (57% RH) exhibited reduced film durability relative to DFLs that were not exposed. On average, the exposed specimens demonstrated 75% shorter film life. The severity of the reduction in film durability did not correlate with the duration of exposure, i.e., long exposures to humid air were not more impactful to film durability than were short exposures.

Introduction

The purpose of this work was to study the effect and exposure to humid air on the durability of a MoS_2 dry film lubricant (DFL) on spur gears operated in vacuum. This study was motivated by the JWST Mission. It is one part of a NASA Engineering Safety Center effort to evaluate potential risks and performance effects to JWST instrument mechanisms and components lubricated with sputtered MoS_2 films. This effort employed both spiral orbit tribometer and gear experiments. Gear teeth experience a unique combination of rolling and sliding friction that differs from pin-on-disk (pure sliding), bearings (mostly rolling), and spiral orbit tribometer testing. The content presented here is limited to results from gear specimens, as a follow-on to a previous publication evaluating the performance of MoS_2 DFL lubricated gears exposed to humid air during storage [1]. The scope of these investigations is detailed in Table 1. Note that durability test results from [1] are included as part of this analysis, referred to as gear set #1. Reference [1] contains additional inspection data from gear set #1 that are not repeated in this publication (i.e., SEM and profilometer data).

The DFLs evaluated in this investigation were sputtered "pure" MoS_2 films matching JWST specifications. The term “pure” does not imply quantification of trace species; the term “pure” is used to differentiate from nanocomposite-type MoS_2 DFL compositions.

Exposure to humid air is known to impact the lubricating performance of MoS_2; changes to the performance and tribological life of a MoS_2 DFL are dependent on the conditions of exposure and the material composition of the film (e.g., co-sputtered or nanocomposite films). The oxidation process of MoS_2 produces molecules of poorly lubricating MoO_3, leading to decreased performance and durability of the DFL. [2,3] However, the practical effects of long-term exposure are not fully understood and experimental data in this area of research is limited. Prior experimental studies have been conducted for many popular space lubricants in a range of exposure conditions and operating environments. This body of knowledge

* NASA Glenn Research Center, Cleveland, OH
** NASA Goddard Space Flight Center, Greenbelt MD
+ Bradley University, Peoria, IL
++ NASA Langley Research Center (NESC), Hampton, VA

has led to the development of best practices for the handling and storage of lubricated parts, but the overall impact of exposure to humid air is highly specific to lubricant type and formulation. [2,3,4]

Table 1. Gear Evaluation Scope and Summary

Test Group	Focus and Work Detail	Work Results Summary
Gear set #1	• Develop criteria to compare lifetimes of unexposed vs. exposed surfaces (condition indicator concept) • Evaluate dry film lifetimes using a set of induction-hardened gears (unexposed vs. exposed) • MoS_2 DFL was supplied by local firm.	• Data was reported at the 44th Aerospace Mechanisms Symposium, May 16-18, 2016 • Commentary from technical community influenced the focus and work detail for evaluation of Gear Set #2
Gear Set #2	• Evaluate dry film lifetimes using a set of case-carburized gears (unexposed vs. exposed) • Adopted a short “running-in” period prior to storage and exposure in constant-humidity chamber • MoS_2 DFL was per JWST flight hardware specification	• Data reported herein

MoS_2 DFLs provide lubrication by the breaking of weak van der Waals bonds between the basal planes of adjacent molecules of MoS_2, allowing layers to "flow" over one another when loaded in shear. This lubricating behavior relies on the layers of a DFL being oriented such that the plate-shaped molecules of MoS_2 are allowed to slide in the desired direction of motion, parallel to the hard substrate material. Luckily, the surface of an MoS_2 film with an undesirable or un-ordered orientation will be realigned during a mechanism's initial cycles of operation ("run-in"), due to the tendency of the molecules to shear together in layers, forming a preferentially ordered surface as the friction between the lubricated components approaches steady state. [3,5]

Preferential orientation of a MoS_2 DFL reduces the film's starting coefficient of friction and can provide additional resistance to oxidation. [6,7,8] The sputtering of MoS_2 produces columnar structures containing crystallites oriented perpendicularly to the substrate material, generally undesirable for lubrication performance and oxidation prevention. Run-in cycles on a MoS_2 DFL lubricated component re-orient the MoS_2 to the preferred basal orientation, but the impact of this effect on the lifetime of MoS_2 DFL subjected to humid air exposure is unquantified, particularly in the case of MoS_2 DFL lubricated gears.

Gear Testing Equipment

Test Rig

The vacuum gear rig will be described with the aid of Figures 1 and 2. The force created by the meshing gear teeth can be described as three orthogonal forces: the tangential force, the separating force, and the thrust force (Figure 1). Each of these forces is measured by a dedicated sensor affixed to the vacuum gear rig’s drive system, as depicted in Figure 2.

The pinion rotation is provided by a variable speed electric motor. A magnetic-particle brake attached to the output shaft imposes torque on the gear. A pressurized air cylinder controls the pinion position (Figure 2a). The air cylinder acts through a pivot axis to rotate the drive motor plate that mounts the driving shaft and drive motor. The rotation of the drive motor plate moves the pinion toward the gear in an arc motion to bring the teeth into mesh. The pressure to the cylinder, and thereby shaft center distance, is adjusted by a hand-operated valve. A linear variable displacement transducer (LVDT) measures the position of the drive motor plate, and this sensor output was used to establish the proper gear center distance (not shown in Figure 2).

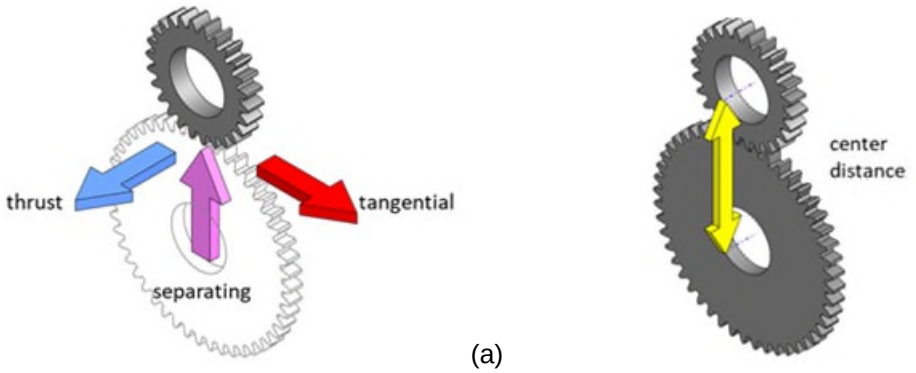

(a) (b)

Figure 1. Depiction of measured gear characteristics. (a) Gear forces: tangential (red), separating (purple) and thrust (blue). (b) Gear operating center distance

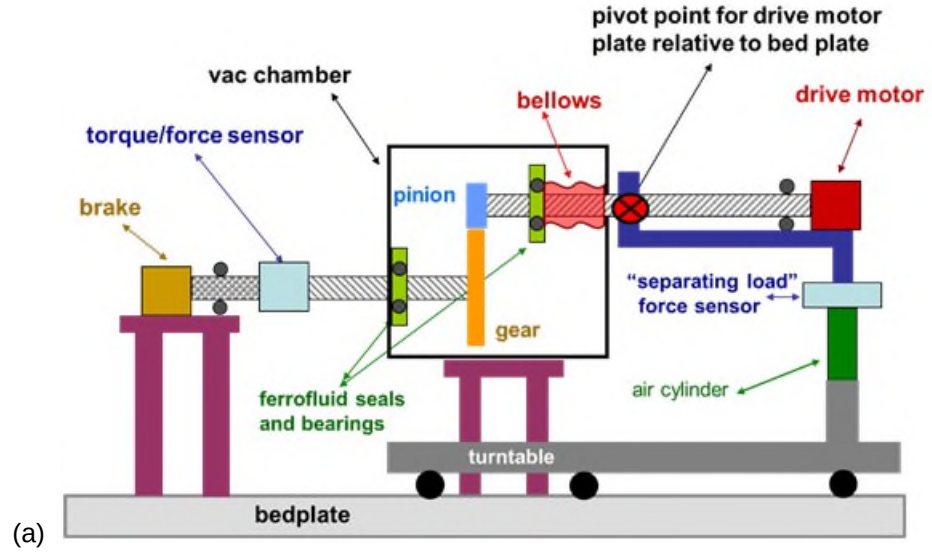

(a)

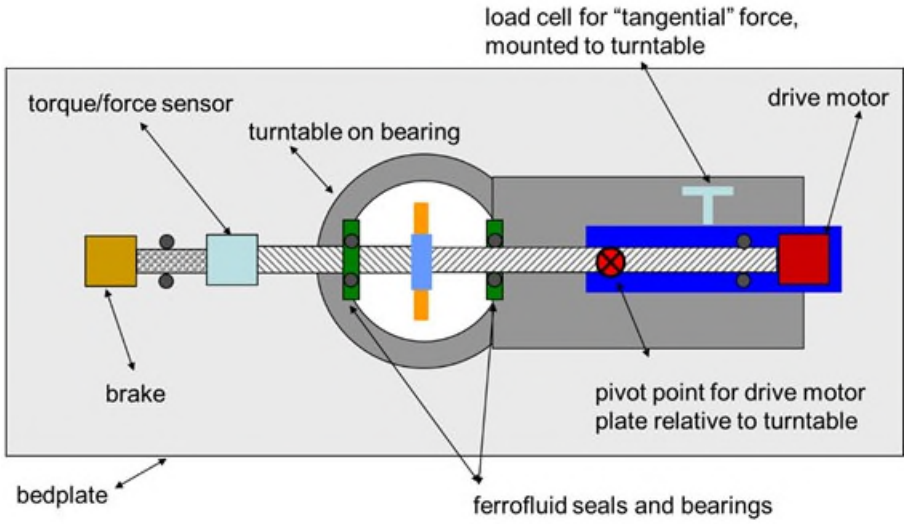

(b)

Figure 2. Schematic representation of vacuum gear rig. (a) Side view. (b) Overhead view.

The rig features a turntable that can be used to impose controlled misalignment of shafts for roller experiments. For gear testing, the turntable was adjusted to align the shaft.

A turbomolecular pump assisted by a scroll pump provides vacuum in the test chamber. Ferrofluid seals maintain the vacuum at the shaft-chamber interfaces. The typical condition in the test chamber is a pressure of 3x10-7 Torr. The most prevalent remaining constituent in the chamber during testing is water vapor as was determined using a residual gas analyzer [9]. Shaft speeds and total number of shaft revolutions were measured using 6000-pulse encoders on each shaft, and the torque on the output shaft was measured by a torquemeter with 22 N-m (200 in-lb) capacity.

The gearing center distance was measured indirectly by an LVDT affixed to a mounting bracket at the base of the drive motor. The LVDT output was related to the operating center distance using calibration results. For each tooth mesh cycle, the friction force reverses direction at the pitch point thereby imparting center distance change that is detected by the LVDT. The friction magnitude influences the magnitudes of the center distance motions, lower friction producing smaller center distance motions.

The gear teeth surface conditions were photographed at regular testing intervals through a viewport using a single-lens reflex camera with a 150 mm micro lens and a 12 million effective pixel image sensor. Lighting conditions and camera settings were consistent between tests.

Humidity Exposure Chamber

Test gear specimens were exposed to humid air in an enclosure (Figure 3) containing a saturated salt solution of water and sodium bromide below the specimens. The sodium bromide solution nominally maintains a relative humidity (RH) of 57% in a closed system. Excursions of relative humidity ranged from 55-60% during transients of the laboratory temperature. This range was deemed acceptable for approximating the 60% RH storage environment matching the maximum level of exposure experienced by the JWST components considered in this investigation.

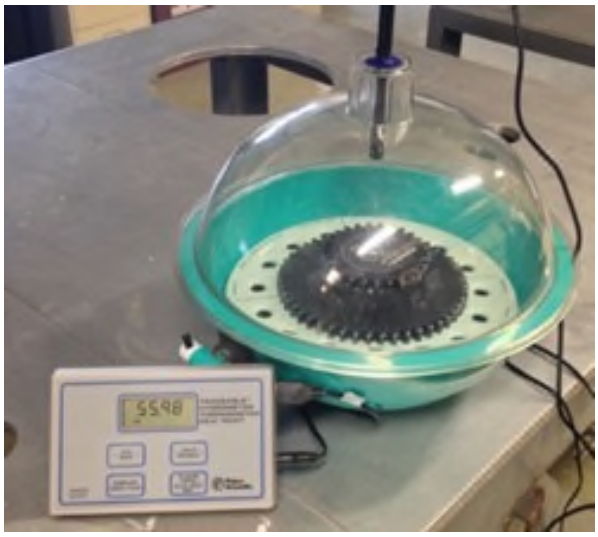

Figure 3. Humidity-exposure chamber for test gears.

Test gears

Readily available stock gears with appropriate center distance were selected and customized for use in this study. The customizations of the stock gear design were the bore diameters, sized for a COTS keyless shaft-locking device, and custom face widths. Design information for the test gears is provided in Table 2.

For gear set #1, there were six pairs of pinions and gears. The material was steel per Japanese material standard S45C (considered equivalent to AISI 1045). The teeth were induction hardened to surface hardness of HRc 50-60 and ground.

Table 2. Gear Design Summary

Parameter	Gear	Pinion
Number of Teeth	48	26
Face Width	10 mm	13 mm
Module	3 mm	3 mm
Pitch Diameter	144 mm	78 mm
Outside Diameter	150 mm	84 mm
Pressure Angle	20°	20°
Surface Hardness	50 to 60 HRc	52 to 60 HRc
Core Hardness	30 to 35 HRc	30 to 35 HRc
Carburization Depth	0.4 to 0.8 mm	0.4 to 0.8 mm

For gear set #2, there were six pairs of pinions and gears of the same geometry as gear set #1, but a different steel was selected. Stainless steel gears (which would have best matched the JWST mechanism gear materials) were not available in a timely manner, resulting in the selection of a case-carburized steel, Japanese material standard SCM415. This steel is considered approximately equivalent to U.S. standard AISI 4115, a low carbon steel (C = 0.15%) commonly used for power transmission gears and having higher strength than AISI 1045. The stock gear specification for surface hardness was 52-60 HRc. The case-carburized condition of gear set #2 was more representative of the subsurface hardness profile of JWST mechanism gears, compared to the relatively shallow case depth of the induction hardened specimens of gear set #1.

DFL for Test Gears

The test gears were coated with a pure MoS_2 DFL by sputtering. While some JWST mechanisms use nanocomposite MoS_2 coatings [i.e., ref. 5], the mechanisms of interest for this work use a pure MoS_2 DFL. Herein the term “pure” does not imply quantification of trace species, but the term “pure” is used to differentiate from nanocomposite-type MoS_2 DFL compositions.

Following the testing and reporting of results for gear set #1, which had a requested coating thickness of 3 to 4 μm, the requested nominal coating thickness for gear set #2 was modified to 2-3 μm to match the JWST specification. The vendor for the coating for gear set #1 was a well-experienced domestic (U.S.-based) vendor. The vendor for gear set #2 was an overseas-based vendor that is the proprietary owner of the specification used for JSWT flight hardware for the mechanisms of interest.

Each gearset required two runs in the sputtering chamber to accommodate the required number of parts. Witness coupons were used to approximate the thickness of the film on the gears and were verified by the vendor to be within the JWST specification. Stylus profilometer measurements taken with gear set #1 indicated that the sputtering process did not change the roughness of the gears’ working flanks [1]. After sputtering, the gears were sealed in bags using a dry inert cover gas. Gears to be tested as unexposed remained in the sealed bags until the start of the installation procedure. The time from the opening of the bag until the gears were in a vacuum condition in the test rig was minimized to all practical extent, typically on the order of 1 hour.

Experimental Method

Test Methods - Common Methodology used for both Gear Set #1 and Gear Set #2

The first step of the testing protocol was to document the specimens for the test (serial numbers and installation orientations) and to note the visual condition of each gear, sometimes including digital photographs. Next, the gear pair was mounted onto the test shafts, the vacuum chamber closed, and then the chamber pressure was stabilized over several hours, and typically overnight, prior to applying torque and motion. The chamber pressure was $7x10^{-7}$ Torr or less at the beginning of each test. Figure 4 shows a pair of the MoS_2 coated test gears out of sealed bags just prior to test and shows the gears in the test chamber just prior to closing the vacuum chamber door.

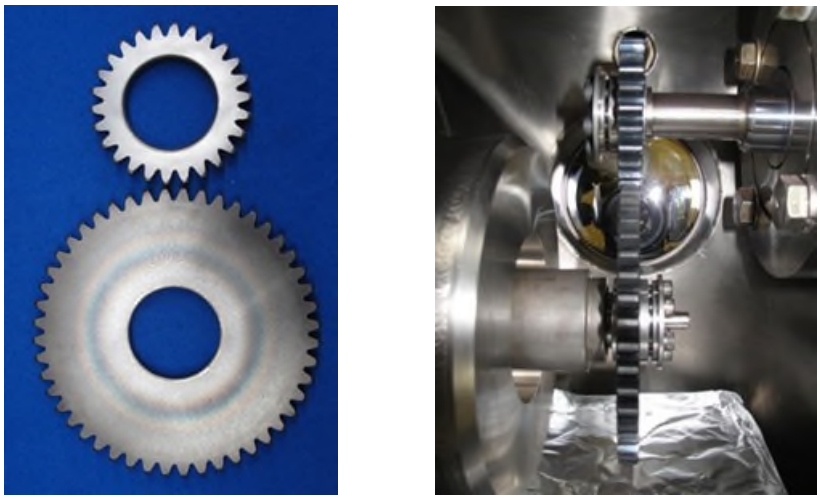

(a) (b)

Figure 4. Test gears. (a) Just prior to testing. (b) Installed in rig just prior to closing of test chamber.

Testing was done at a constant demanded brake torque and motor speed. The demanded torque was 6.8 Nm for the gear, at a test speed of 80 rpm for the pinion (and consequently 43.3 rpm for the gear). The power transmitted was 31 watts. The torque was selected to provide a tooth load intensity (force per unit face width) similar to the tooth load intensity for the mechanisms of interest. The speed was selected to minimize rig dynamic loading and vibration, as determined by previous testing efforts. Testing for endurance of the coatings typically required durations longer than a working day, and unattended testing was not attempted. The testing was paused overnight, as needed, with the test chamber vacuum maintained by continuous operation of the turbopump, and then testing was resumed the following day.

The test progression was monitored by visual inspection of the tooth surfaces through a viewport, aided at times by a strobe light to "freeze" the motion. The visual condition was also recorded by digital photographs illuminated by a short duration flash through a second viewport that provided a view of the gear teeth (but not of pinion teeth). The test progression was monitored by displays of the sensor data plotted as functions of pinion revolutions. Some previous development tests revealed that as wear severity and friction increase, sensor outputs became more erratic even though their mean value remain constant. For example, when friction on the gear teeth increases, the range of the separation force increases even though the mean may still be constant. This phenomenon is the result of the tooth friction force reversing direction as the tooth contact passes through the pitch point. Thereby, the friction force first adds to, and then subtracts from, the magnitude of the separating force during the tooth mesh cycle. With higher tooth friction the excursions from the mean become larger.

Based on prior experiences with health monitoring of geared machines, these observations led to the generation of "condition indicators" to monitor the overall effectiveness of the MoS_2 films. Data for each sensor (output torque, thrust force, tangent force, separating force, gear center distance) was sampled at 1 kHz for a period of 1 second, and the standard deviation of each signal over that period was calculated and catalogued as a "condition indicator". For each 1 second interval throughout a test, the condition indicators for each sensor were plotted as a function of accumulated pinion revolutions. Such condition indicators were reliable indicators of changes in the lubricating performance of the MoS_2 DFL.

Figure 5 provides an example plot of a condition indicator monitored over the duration of a life test (5a), and an example set of data collected in a 1 second period that was used to calculate a single condition indicator (5b). Three regions are marked in Figure 5a: "Region I" is the smooth-running regime, "Region II" the start of MoS_2 compromise, and "Region III" is the significant friction regime. The beginning of Region II is marked, indicating approximately where the performance of the MoS_2 DFL was first compromised. The

example data shown in Figure 5b was collected from the thrust force sensor at an illustrative point of operation in Region III, where relatively high tooth friction generates a varying signal, evident in the last 400 samples.

Film durability was determined using the condition indicator trend plots. The film durability was defined as the number of pinion revolutions until the film compromise started, such as indicated in Figure 5b. The film compromise was defined as the very beginning of a steady degradation of the film's performance regarding friction. A mechanism may continue to perform its intended function for some time after such film degradation begins. The intent was to assess a relative measure of the film durability, with and without exposure to humid air.

For gear set #1, film durability in each test was determined as follows. Lifetimes were determined based on each condition indicator, one at a time, by forming a consensus among four team members. The condition indicators for thrust force, tangent force, and gear center distance were found to be the most sensitive to changes in the lubricating performance of the MoS_2 DFL. Three independent estimates of the film durability were generated for each test, one estimate for each of these condition indicators. These three estimates were then averaged to determine an overall film durability value for each test.

For gear set #2, film durability was determined by a revised procedure. Each of three team members reviewed condition indicator trend plots independently, and each member provided one film durability value for each test, taking all three condition indicators into account for the evaluation. A single overall film durability value was determined for each test by averaging the values provided by each of three team members. This approach tended to reduce sensitivity to outliers in the condition indicator responses and allowed for unbiased estimates from each team member.

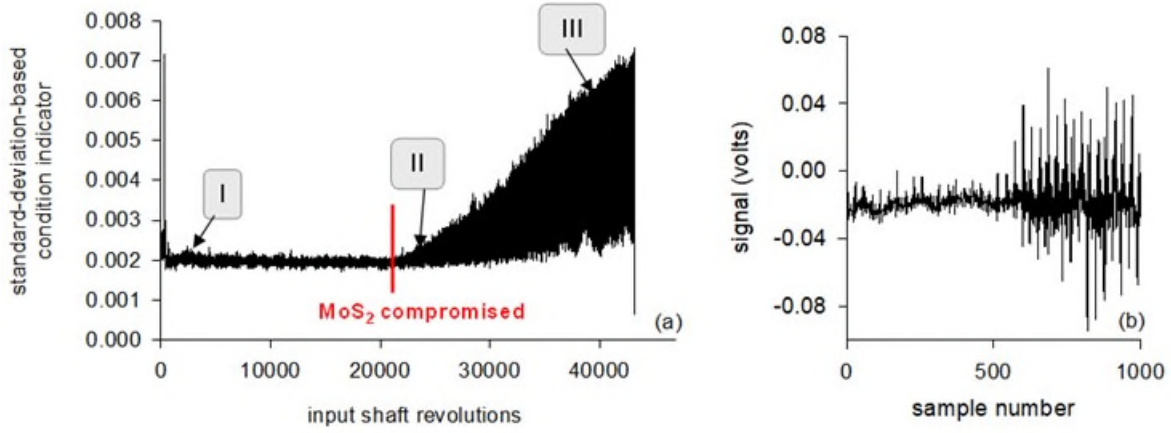

Figure 5. Typical trend and features of a condition indicator of MoS_2 film function. (a) Trend of condition indicator for the center distance (LVDT sensor), for test 1B. (b) Typical data record for calculation of standard-deviation-based condition indicator

Test Methods – Test Set #1

The test matrix used for gear set #1 was per Table 3. A balanced set (equal number of tests for exposed and unexposed surfaces) was planned and executed. For gear set #1, the unexposed surfaces had no run-in cycles prior to exposure to humid air in the constant-humidity chamber.

Table 3. Test Matrix for Gear Set #1

Test Name	Test Article Pairing	Pinion Serial Number	Gear Serial Number	Tooth Side Loaded	Exposed	Total Exposure Duration	Testing Order Sequence
MOS2 1-A	1	P4	G1	A	No	-	1
MOS2 1-B				B	Yes	10 days	3
MOS2 2-A	2	P6	G6	A	No	-	2
MOS2 2-B				B	Yes	28 days	6
MOS2 3-A	3	P2	G2	A	No	-	4
MOS2 3-B				B	Yes	17 days	9
MOS2 4-A	4	P1	G3	A	No	-	5
MOS2 4-B				B	Yes	17 days	10
MOS2 5-A	5	P3	G5	A	No	-	7
MOS2 5-B				B	No	-	8
MOS2 6-A	6	P5	G4	A	Yes	77 days	11
MOS2 6-B				B	Yes	77 days	12

Test Methods – Test Set #2

The test matrix used for gear set #2 was per Table 4. A balanced set (equal number of tests for exposed and unexposed surfaces) was planned. Not all planned tests could be completed because of test rig failures. At one point in time, a shaft seal that allows for the rig's vacuum condition needed to be removed and replaced. The replacement part was a long-lead time item. Therefore, this situation created some constraints on the possible exposure times, and this resulted in the exposure times noted in the table. For gear set #2, the unexposed surfaces have a short running-in period of approximately 100 revolutions of the pinion member prior to exposure to humid air in the constant-humidity chamber.

Table 4. Test Matrix for Gear Set #2

Test Name	Test Article Pairing	Pinion Serial Number	Gear Serial Number	Tooth Side Loaded	Exposed	Total Exposure Duration	Testing Order Sequence
2019-1A	1	19-P1	19-G1	A	Yes	326 days	9
2019-1B				B	No	-	1
2019-2A	2	19-P2	19-G2	A	Yes	296 days	8
2019-2B				B	No	-	2
2019-3A	3	19-P3	19-G3	A	Yes	280 days	7
2019-3B				B	No	-	3
2019-4A	4	19-P4	19-G4	A	Yes	253 days	6
2019-4B				B	No	-	4
2019-5A	5	19-P5	19-G5	A	Yes	213 days	5
2019-5B				B	No	-	*
2019-6A	6	19-P6	19-G6	A	*	*	*
2019-6B				B	*	*	*
* Test equipment problems; test could not be completed.							

Results and Discussion

Observations from Photo Documentation – Tested Gears

The behaviors of the films were also evaluated by studying photographs, profilometry, and SEM inspections. During initial running of each gear pair, it was noted that the tooth surface running-in required very few tooth contact cycles. In other words, the tooth surface appearance changed dramatically, becoming glossier and reflective in appearance after only a few revolutions, and subsequent further visual changes to the tooth surfaces occurred at a very slow and steady rate. Figure 6 illustrates typical results of how the surface visual appearance changed for the gear teeth during a test using gears from gearset #1. The first two images from left to right show the teeth prior to any running and then again after only 1% of the total running time. The other two images in Figure 6 show the teeth after 50% and 99% of the test duration. The last two images show that with further running the visual condition changes less dramatically over the final 98% of running as compared to the first 1% of running durations.

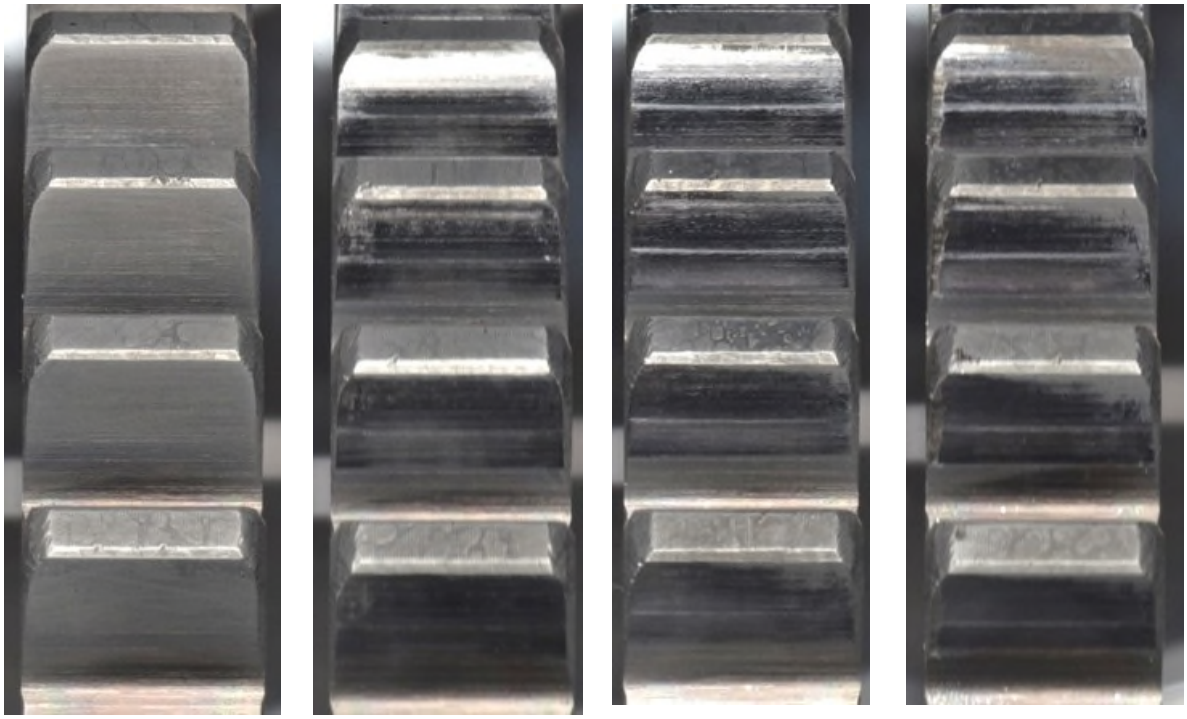

Prior to start | ~1% of test duration | ~50% of test duration | ~99% of test duration

Figure 6. Gear teeth surface appearance for different durations of testing.

For the case of gear set #2, a brief running-in of the gears was performed in vacuum condition, comprising approximately 100 rotations of the input member (pinion) prior to exposing the gear pairs to humid air. Figure 7 shows the appearance of pinion 19-used for test 19-1B (per Table 4), after a 326-day exposure to humid air and just prior to installation for film durability tests. The photos depict the significant change of visual appearance of the gear teeth after only 100 operating cycles (Figure 7a). From a macro-perspective, surfaces with only 100 contact cycles appear like surfaces with more than 40,000 cycles. Gears having had exposure to humidity could show visual signs of iron oxidation, per observed red-brown colorations (Figure 7b) [1]. In general, surfaces from gear set #2 that had a 100-cycle run-in prior to humid air exposure developed more significant regions of red-brown colorations as compared to gears from set #1 that had no run-in prior to exposure. The brief running-in appears to expose the steel substrate at asperity peak features, and/or diminish the MoS_2 film thickness at localized areas (i.e., oxidation is observed visually without the aid of magnification).

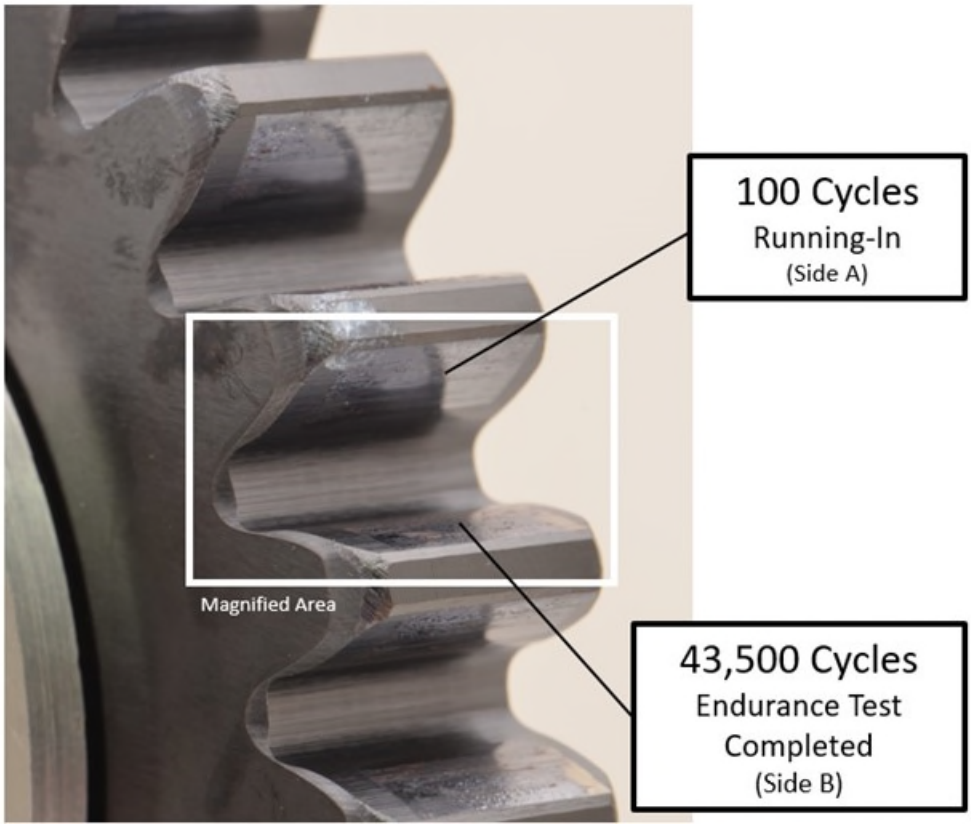

(a)


(b)

Figure 7. Photo of the surface condition of the 26-tooth pinion 19-P1, following completion of endurance test of unexposed surfaces (one side of teeth), 100 cycle run-in (second side of the tooth), and exposure to humidity for 326 days. (a) Overall view. (b) Closeup to capture red-colored oxidation locations.

Note that the test gears were made from a plain carbon steel. The preferred experimental approach would have been to use a stainless steel such as hardened 440C, but such gears could not be obtained within the constraints of this assessment. The best and accepted practice for space mechanisms is to use an appropriate stainless steel for gears and other parts that experience rolling and sliding. The oxidation seen on the plain carbon steel test gears during this assessment may have been enhanced by the presence of MoS_2 while in the humidity of the storage environment.

Dry Film Effective Lifetimes – Gears

During all in-vacuum operation of the test gear specimens, a set of "condition indicators" were calculated from real-time sensor data averaged over a period of one second. Film durability for each test was derived from the condition indicators calculated for three of the measured parameters; the gear center distance, thrust force, and tangent force. For each test, an average film durability was calculated per procedures described in the 'Experimental Method' section above. The results are collected in Tables 5 (for gear set #1, published previously) and 6 (for gear set #2, new data).

The film durability for unexposed gear specimens from set #2 were similar to the results from set #1. The average unexposed film durability from set #1 was 100,200 revolutions, with a median of 83,500 revolutions; set #2 averaged 91,200 revolutions, with a median of 96,800 revolutions for unexposed gears. These values closely replicate the unexposed film durability of set #1, despite differing substrate materials, hardening processes, and applied film thicknesses.

The average film durability of gears exposed to humid air was less than the average durability of unexposed gears, as observed for both gear sets. The average film durability of exposed gears from set #1 was 64,900 revolutions (a 35% reduction relative to the unexposed tests for this set), with a median of 68,800 revolutions (an 18% reduction). The loss in film durability from set #2 was more severe, with an average durability of 24,300 revolutions (a 73% reduction relative to the unexposed tests), and a median value of 24,700 revolutions (a 75% reduction).

Table 5. Test Results of Film Durability, Gear Set # 1

		Film Durability (pinion revolutions)			
Test Name	**Exposure Duration**	**Center Distance**	**Thrust Force**	**Tangent Force**	**Average Value**
MOS2 1-A	0 days	52,000	52,000	56,000	53,333
MOS2 2-A	0 days	59,000	61,000	65,000	61,667
MOS2 3-A	0 days	207,000	184,000	180,000	190,333
MOS2 4-A	0 days	86,000	69,000	94,000	83,000
MOS2 5-A	0 days	125,000	125,000	136,000	128,667
MOS2 5-B	0 days	83,000	80,000	89,000	84,000
MOS2 1-B	10 days	21,000	20,000	22,000	21,000
MOS2 2-B	28 days	69,000	55,000	74,000	66,000
MOS2 3-B	17 days	59,000	65,000	66,000	63,333
MOS2 4-B	17 days	81,000	78,000	95,000	84,667
MOS2 6-A	77 days	84,000	76,000	88,000	82,667
MOS2 6-B	77 days	70,000	71,000	74,000	71,667
* "Average Value" is the average of the 3 durability estimates to the left; Center Distance, Thrust Force, and Tangent Force.					
	Unexposed Group	Average = 100,200		Median = 83,500	
	Exposed Group	Average = 64,900		Median = 68,800	
	Percent Reduction:	**35%**		**18%**	

Table 6. Test Results of Film Durability, Gear Set # 2

		Film Durability (pinion revolutions)			
Test Name	**Exposure Duration**	**Center Distance**	**Thrust Force**	**Tangent Force**	**Average Value**
MOS2 1-A	0 days	52,000	52,000	56,000	53,333
MOS2 2-A	0 days	59,000	61,000	65,000	61,667
MOS2 3-A	0 days	207,000	184,000	180,000	190,333
MOS2 4-A	0 days	86,000	69,000	94,000	83,000
MOS2 1-B	326 days	21,000	20,000	22,000	21,000
MOS2 2-B	296 days	69,000	55,000	74,000	66,000
MOS2 3-B	280 days	59,000	65,000	66,000	63,333
MOS2 4-B	253 days	81,000	78,000	95,000	84,667
MOS2 6-A	213 days	84,000	76,000	88,000	82,667
* "Average Value" is the average of the 3 durability estimates to the left; Center Distance, Thrust Force, and Tangent Force.					
	Unexposed Group	Average = 91,167		Median = 96,833	
	Exposed Group	Average = 24,267		Median = 24,667	
	Percent Reduction:	**73%**		**75%**	

These reductions in film durability attributed to humid air exposure are of similar order of magnitude as compared to the 55 to 20% range of reductions reported by Lince, Loewenthal, and Clark [2] from pin-on-disk evaluations.

The average film durability values are plotted as a function of the duration of exposure to humid air in Figure 8, using data from Tables 5 and 6. While the film durability for exposed surfaces was lower on average than for unexposed surfaces, there is no clear correlation between film durability and the duration of exposure to humid air.

While the range of scatter in film durability is significant, it should be noted that this order of scatter is common for gear wear data. Gear wear experiments for liquid lubrication conditions exhibits similar scatter [10]. Gear wear behavior is influenced by many attributes that can be difficult to control for, such as differing surface textures between specimens, or tooth-to-tooth and gear-to-gear geometric tolerances. Even small variations in the manufacturing process will influence the performance of each individual gear; minute changes in the condition of cutting tools used to form the gear, the exact position of a gear in the heat treatment furnace, etc. Large scatter in performance data can make it difficult to determine quantitative trends, except when very large datasets can be produced.

In spite of the relatively modest number of specimens evaluated in this investigation, the main influencing variables are clear. The most significant of these factors is exposure to humid air; gears that were not exposed to humidity prior to testing exhibited greater film durability than gears that were exposed. The most dramatic reductions occurred in gear specimens that were subjected to a small number of revolutions in vacuum prior to their exposure to humid air. This reduction in film durability does not appear to depend on the duration of a specimens' exposure to humid air; specimens subjected to the shortest exposures and specimens subjected to the longest exposures exhibited comparable reductions in film durability.

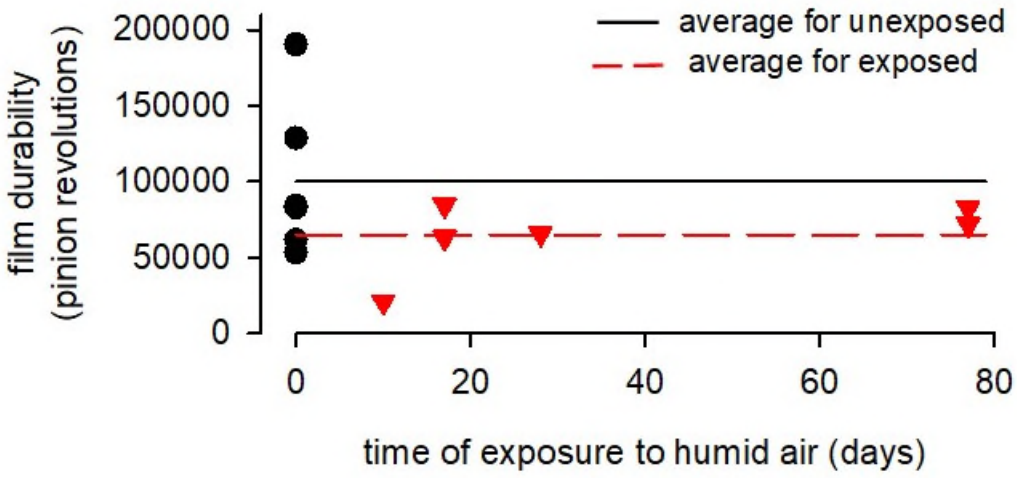

(a)

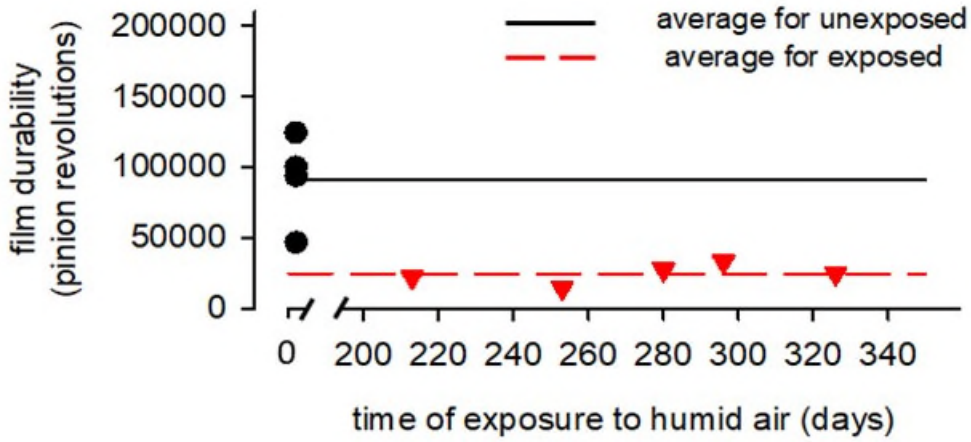

(b)

Figure 8. Film durability as function of time of exposure to humid air. (a) Results for gear set #1. (b) Results for gear set #2.

Summary and Concluding Remarks

This investigation was conducted to study the relative durability of a MoS_2 DFL applied to gear teeth before and after exposure to humid air. The DFLs evaluated in this assessment were applied by a particular overseas vendor as required by a JWST specification for the mechanisms of interest. A previous investigation was conducted using a similar MoS_2 DFL supplied by a domestic vendor [1], referred to as gear set #1. Test specimen gears used in this investigation, gear set #2, were prepared by applying a pure (not nanocomposite-type) MoS_2 DFL to case-carburized steel gears via sputtering. Specimens were then subjected to a brief run-in procedure (100 cycles) in vacuum followed by controlled exposure to a humid air environment at 60% RH for durations ranging from 10 to 326 days.

MoS_2 DFL gear specimens subjected to long-term humid air exposure exhibited lower film durability relative to the baseline unexposed specimens. While the average film durability of unexposed specimens was similar between both studies, the reduction in film durability observed in gear set #2 (75% less life) was more severe than in gear set #1 (35% less life). By visual inspection, the run-in procedure introduced in this investigation appears to have exposed the steel substrate at worn asperity peaks or at localized areas of high MoS_2 wear. Signs of iron oxidation were visible as red-brown colorations on the tooth surfaces of gear specimens after exposure to humid air. More coloration was observed in gear set #2 which had been run-in prior to RH exposure as compared to gear set #1, which had no run-in prior to RH exposure.

The severity of the reduction in film durability after exposure to humid air did not correlate with the duration of exposure. Long exposures to humid air did not reduce film durability more severely than shorter exposures.

References

1. Krantz, T., Hakun, C., Cameron, Z., Shareef, I., & Dube, M. (2018, May). Performance of MoS_2 Coated Gears Exposed to Humid Air During Storage. In *Aerospace Mechanics Symposium* (No. GRC-E-DAA-TN51674).
2. Lince, J. R., Loewenthal, S. H., & Clark, C. S. (2016, May). Degradation of Sputter-Deposited Nanocomposite MoS2 Coatings for NIRCam during Storage in Air. In *Proceedings of the 43rd Aerospace Mechanisms Symposium, (May 2016) pp* (pp. 221-234).
3. Lince, J. R. (2020). Effective application of solid lubricants in spacecraft mechanisms. *Lubricants*, *8*(7), 74.
4. Buttery, M., Lewis, S., Kent, A., Bingley, R., & Cropper, M. (2020). Long-term storage considerations for spacecraft lubricants. *Lubricants*, *8*(3), 32.
5. Lansdown, A. R. (1999). *Molybdenum disulphide lubrication*. Elsevier.
6. Curry, J. F., Argibay, N., Babuska, T., Nation, B., Martini, A., Strandwitz, N. C. & Krick, B. A. (2016). Highly oriented MoS_2 coatings: tribology and environmental stability. *Tribology Letters*, *64*(1), 1-9.
7. Curry, J. F., Wilson, M. A., Luftman, H. S., Strandwitz, N. C., Argibay, N., Chandross, M., Sidebottom, M.A., & Krick, B. A. (2017). Impact of microstructure on MoS_2 oxidation and friction. *ACS applied materials & interfaces*, *9*(33), 28019-28026.
8. Curry, J. F., Ohta, T., DelRio, F. W., Mantos, P., R Jones, M., F Babuska, T. & Chandross, M. (2021). Structurally driven environmental degradation of friction in MoS_2 films. *Tribology Letters*, *69*(3), 1-10.
9. Pepper, S. (2011). Research Note-Characterization of the Test Environment of JWST Roller Wear Evaluation at NASA-GRC.
10. Krantz, T. L., & Kahraman, A. (2004). An experimental investigation of the influence of the lubricant viscosity and additives on gear wear. *Tribology Transactions*, *47*(1), 138-148.

Bearing Starting Torque Measurements Down to -100°C

Kim Aaron*, Duval Johnson*, Shana Worel* and Frank Tao*

Abstract

Starting torque was measured for three different bearings from 0°C down to -90°C and -100°C. These were bearings of the type that will be used in the ice-penetrating radar instrument named Radar for Europa Assessment and Sounding: Ocean to Near-surface (REASON), which is part of the planned science instrument suite for the National Aeronautics and Space Administration (NASA) Europa Clipper mission. This space science mission to Jupiter's moon, Europa, is being led by NASA's Jet Propulsion Laboratory (JPL), which is administered for NASA by the California Institute of Technology. In addition to presenting the starting torque measurements at various temperatures, this paper describes the small test chamber and attachments that allowed the measurements to be made using an existing bearing torque testing machine.

Introduction

Bearings are used in the mechanisms that will deploy the REASON antennas. These antennas use stored strain energy in springs to provide the motive force that deploys the antennas. These antennas are designed, fabricated and tested mechanically by Heliospace Corp. in Berkeley, California under a subcontract to NASA/JPL.

During deployment of the antennas, the temperature may be as low as -70°C. There is a limited amount of data available regarding potential lubricants for operation at such low temperatures. Extrapolation of this data indicated that they could potentially provide the desired lubricating action, but the uncertainty was high so testing was performed to confirm the behavior of the lubricants at these temperatures.

At low temperatures, the viscosity of lubricants can increase by orders of magnitude. Because oil does not crystallize, or solidify, at any temperature, it technically does not freeze. However, at low enough temperatures it will lose its liquid-like properties and not flow enough to provide adequate lubrication. It was possible that the spring force available in the actuators would not be sufficient to overcome the low-temperature bearing resistance. We were confident that if the bearing was able to start turning, the shearing action in the lubricant would warm it locally, decreasing its viscosity, allowing the rolling action of the bearings to continue reliably. Therefore, we focused on measuring just the starting torque at various cold temperatures. These experimental measurements confirmed that the available mechanism torque was well above the measured starting torque even at temperatures that were colder than our expected worst-case cold deployment conditions. In addition, the testing confirmed that the volume of lubricant selected was appropriate for the short-duration one-time operation of the devices containing the tested bearing types.

In the body of this paper, we describe the three bearings tested, indicate the lubricant selected, illustrate the test apparatus, and present the results of starting torque versus temperature.

* California Institute of Technology, Jet Propulsion Laboratory, Pasadena, CA; Kim.M.Aaron@jpl.nasa.gov

Bearings Tested

We tested three bearings of the type selected for use in the design of the mechanism. Our colleague, Mark Balzer, named them Papa Bearing, Mama Bearing, and Baby Bearing because of their relative sizes. We fondly retained this nomenclature.

The three bearings tested are:

1. AST 07150776 (SSRI-1212ZZRA5P25L01 BEARING; MINO: 00585 X 74748)
   Approximate bearing dimensions: 19.05 mm outer diameter (OD) x 12.70 mm inner diameter (ID) x 3.94 mm width (W) (0.750 inch x 0.500 inch x 0.155 inch) (Papa bearing)
2. AST 07366778 (SSR3ZZRA5P25L01 INCH SERIES BEARINGS; MINO: 00585 X 00208)
   Approximate bearing dimensions: 12.70 mm OD x 4.70 mm ID x 4.95 mm W (0.500 inch x 0.185 inch x 0.195 inch) (Mama bearing)
3. AST 07366756 (SSR2ZZRA5P25L01 INCH SERIES BEARINGS; MINO: 00585 X 00187)
   Approximate bearing dimensions: 9.53 mm OD x 3.05 mm ID x 3.96-mm W (0.375 inch x 0.120 inch x 0.156 inch) (Baby bearing)

Manufacturer – New Hampshire Ball Bearing, Inc
Ring material – AISI 440C
Ball material – AISI 440C
Type – Radial
Shields – Double metallic shield, removable
Cage – Ribbon, land piloted
ABEC tolerance – ABEC 5
Radial play – 0.005 mm to 0.013 mm (0.0002 inch to 0.0005 inch)

Prior to testing, the bearings were inspected and passed per the following criteria:

1. Surface Appearance:
   - Lands, faces and mounting surfaces of bearing assemblies shall have a smooth finished appearance.
   - The surfaces shall be free of visible tool marks, chatter and waviness, pits, scratches with raised metal, or other surface imperfections.
   - Metal bearing components shall have a smooth finished appearance and shall be free of burrs, dents and folded material.
   - Non-metallic bearing components, including retainers, cages, and separators, shall be free of delaminations and burrs.
2. Cracks and fractures:
   - All bearing assemblies shall be free of cracks and fractures.
   - All bearing assemblies shall be free of scratches on critical surfaces.
   - All critical surfaces of bearing assemblies shall be free of scratches.
3. Contamination:
   - All exterior surfaces and interior areas of the bearing assemblies shall be free of foreign objects and debris, particles, fibers, grease, oil, fingerprints, etc.
4. Corrosion:
   - All exterior and interior surfaces of the bearing assemblies shall be free of corrosion, rust, and stains.
5. Assembly:
   - The proper number of rolling elements shall be present.
   - Retainers, cages, and separators shall be of the proper type (inner land-/outer land-/ball-guided), made of the proper material, and shall be installed in the proper orientation.

Lubricant

The bearings are commercial off-the-shelf. Their standard lubricant is not suitable for use at the low temperatures possible for this mechanism. After considering the potential operating conditions, we decided to remove the lubricant in the bearings and replace it with Castrol Brayco 815Z Micronic Grade Oil – a clear water white perfluorinated polyether-based fluid. We also selected alternate lubricants, but did not test them because our first choice was demonstrated to operate as desired.

The bearing retainer rings and shields were removed to allow inpsection of the bearing and observation of the meniscus during lubrication. The MIL-PRF-6085 oil was removed from the bearing components using heptane and a low intensity indirect ultrasonic cleaning technique. Previous investigation confirmed that this would not cause brinelling. We did not observe Brinelling using visual inspection at 10x magnification. Figure 1 shows one of the bearings after cleaning and drying.

Figure 1. Clean and Dry Bearing

Following the drying step, oil was injected into the clean bearing using a syringe for which the mass of each oil drop was established. The amount of oil was kept to the barest minimum to avoid making the bearing balls “snowplow” through a thick layer of cold oil.

Oil amounts were initally determined by consulting “A Space Tribology Handbook [2]” which states that a ball bearing with a 10-mm bore diameter takes less than 1 µL of oil to achieve a "starved" lubrication condition, and greater than 10 µL of oil to achieve a "flooded" lubrication condition. Beginning with these values each bearing was lubricated in three steps using the following guidelines:

- Papa Bearing with 2 drops (~6 mg or ~3.2 µL), 4 drops (~12 mg or ~6.4 µL), and 6 drops (~18 mg or ~9.6 µL) of Brayco 815Z oil,
- Mama Bearing with 1 drop (~3 mg or ~1.6 µL), 2 drops (~6 mg or ~3.2 µL), and 3 drops (~9 mg or ~4.8 µL) of Brayco 815Z oil, and
- Baby Bearing with ~2/3 drop (~2 mg or ~1.1 µL), ~4/3 drops (~4 mg or ~2.2 µL), and 2 drops (~6 mg or ~3.2 µL) of Brayco 815Z oil.

During deployment, the bearings operate for just a few seconds, so oil starvation is not a concern.

Oil mass for each bearing was selected iteratively by adding a drop of oil, running in the bearing to distribute the oil, and visually inspecting under magnification for both the presence of an oil meniscus between the

bearing balls and both inner and outer ring raceway grooves, and a thin film of oil fully coating the inner and outer ring raceway grooves. When a thin film and a meniscus was observed, the iterations were stopped and the total mass of oil added was determined and recorded.

The bearings were weighed dry and then again afterwards in order to measure the oil mass. This oil mass for each bearing was as follows:

- Papa Bearing – 13.6 mg
- Mama Bearing – 9.5 mg
- Baby Bearing – 4.3 mg

Figure 2 shows a microscopic view of one of the bearings indicating that the oil formed a meniscus between the ball and the raceway grooves. The view is looking towards the outer ring raceway groove. The body of the retainer crosses the lower right portion of the image. The ball has the curved bright highlight and is towards the upper right of the image. The meniscus is the narrower curved highlight just above that. The curved outer ring raceway groove can be discerned by the circumferential grinding marks extending towards the upper right corner of the photograph. The outer ring face sweeps diagonally across the upper left portion of the photograph.

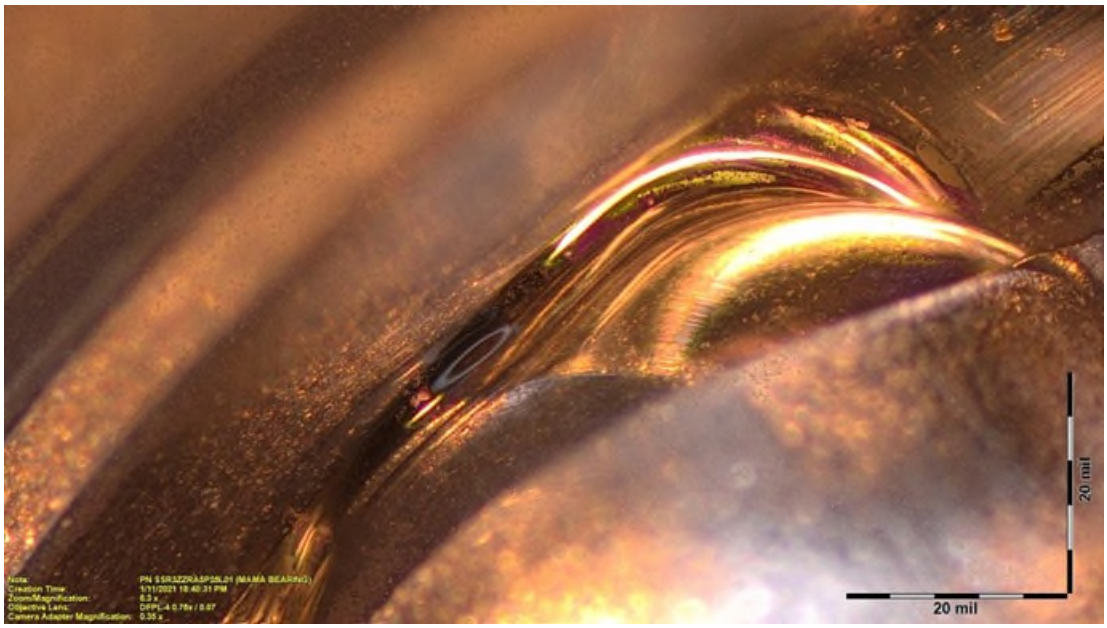

Figure 2. Microscopic View of Bearing Showing Oil Meniscus

Test Apparatus

We chose to use a commercially available VIBRAC BRG-3000 Bearing Inspector II tabletop bearing torque measurement apparatus that we already owned and was readily available. Rather than modifying this apparatus to operate inside a cooled thermal chamber, we elected to design a small insulated chamber that would encapsulate the bearing and provide insulated mechanical connections between the apparatus and the interior of the small chamber. This allowed us to keep the test apparatus at room temperature.

The torque tester has a motor that is controlled by the VIBRAC software to turn a shaft connected to the inner ring of the bearing while the outer ring was restrained by the torque transducer that measures the reaction torque at the outer ring as the inner ring i turned in a controlled manner using the software provided with the testing apparatus.

The experimental setup is shown in Figure 3. The insulated test chamber is the white cylinder with the access door labeled. The torque measurement apparatus consists of the base at the bottom containing the drive motor and the torque transducer near the top of Figure 3. The apparatus includes a structural tower supporting the torque transducer from the base. Just to the right of the torque transducer is a linear displacement sensor used in aligning the upper part of the apparatus to the lower part. On the upper right side of Figure 3 is the thermostatic controller for the liquid nitrogen flow. Below that, you see the plumbing for mixing and controlling the flow of gaseous and liquid nitrogen prior to passing through the wall of the insulated chamber to injection nozzles inside.

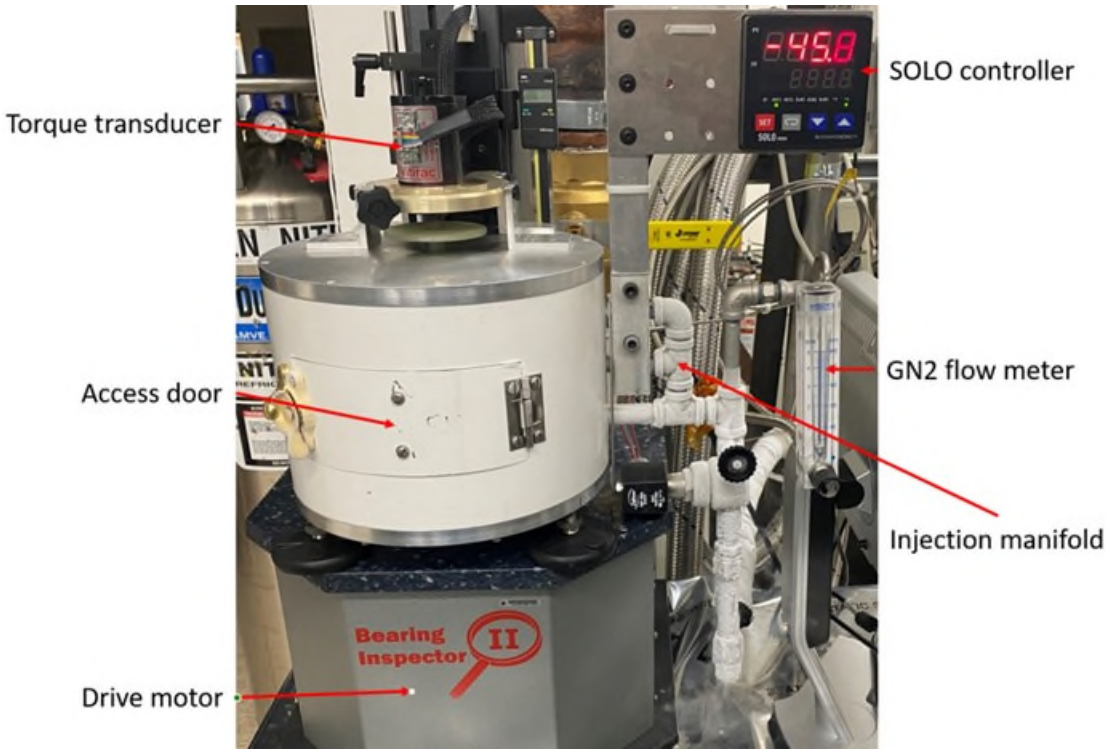

Figure 3. Test Apparatus

The cold chamber was constructed using Schedule 40 polyvinyl chloride (PVC) with 25-cm (10-inch) diameter outer wall and 20-cm (8-inch) diameter inner wall with rigid 80-kg/m^3 (5-lbm/ft^3) PVC foam insulation between the walls. The top and bottom of the inner tube were capped by 3-mm (0.125-inch) thick aluminum discs counterbored into the end of the tube. For the upper and lower caps, 13-mm (0.5-inch) plates of aluminum were used. The plates were separated by a layer of rigid PVC foam 25-mm (1-inch) thick. An access door was cut through the walls and attached using a spring-loaded hinge and a latch.

Figure 4 shows the thermal chamber partway during fabrication. The cold gas manifold is also shown, but without the nozzles to divert the flow laterally.

Figure 4. Cold Chamber During Fabrication

Figure 5 shows the apparatus assembled as it would be inside the thermal chamber. Resting on the right hand side of the baseplate of the testing unit are two of the three bearings along with insulating holders of G10 fiberglass (greenish) and Vespel polyimide (brown). Each bearing has its own customized mounts machined to match the dimensions of the bearing and attach it to the testing machine while providing thermal insulation to allow the testing machine to remain at room temperature. The third bearing is already installed in Figure 5.

Figure 5. Test Appartus Without Thermal Chamber

The large piece of copper is a 2.3-kg (5-lbm) weight that rests on the outer ring of the bearing to provide axial load across the bearing to approximate the loading condition it will experience in the mechanism. The

copper weight rests with its center of mass lower than the bearing to avoid any tendency to topple. The drive motor is inside the base and turns the shaft at the bottom.

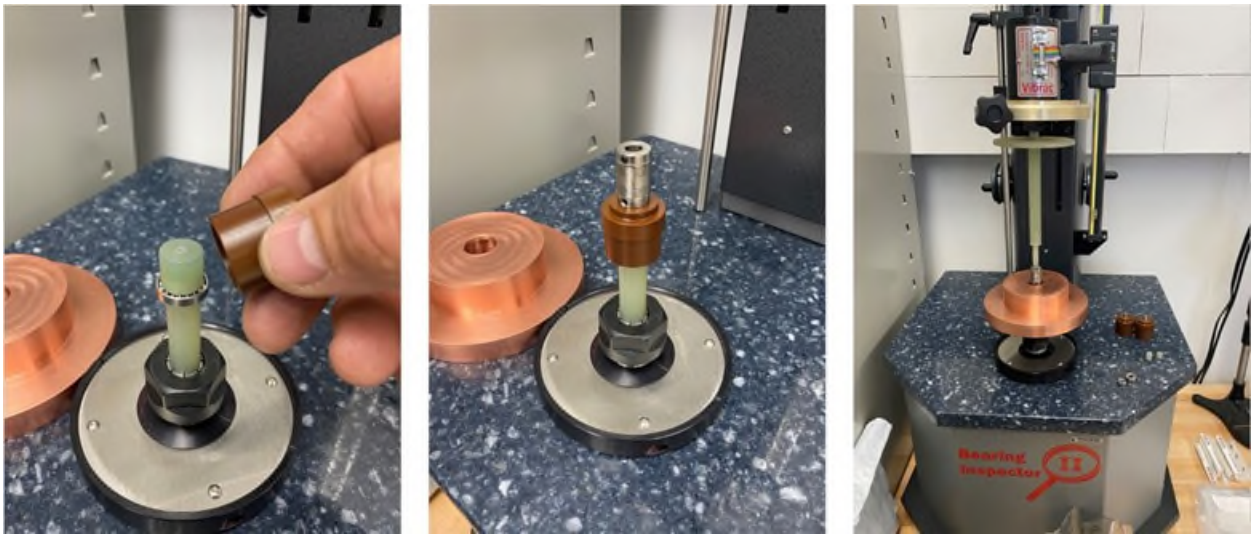

Figure 6. Bearing Support and Connection to Torque Tester

Figure 6 shows a sequence of photographs at successive stages of connection of the elements attaching the bearings to the torque tester. The attachment elements were machined out of G10 (green) and Vespel (brown) to provide mechanical connections while maintaining good thermal isolation. A G10 rod extends from the drive motor collet to the inner bearing ring. The inner bearing ring is captured by a slip fit cap axially clamped by a threaded fastener. The outer bearing ring is then captured using the Vespel cap. The stepped Vespel flange is arranged to support the 2.3-kg copper weight. A bellows-type flexible coupling then attaches the Vespel cap to the G10 rod that extends out the top of the chamber and to the torque transducer. The large G10 disk machined into the shaft protects the torque transducer from the cold nitrogen gas that flows upward around the shaft and out the hole in the top of the chamber. The disk diverts the flow out away from the torque transducer.

Test Operation

During testing, the chamber was cooled using cold nitrogen gas injected tangentially through three nozzles inside the chamber. The cold gas was created by mixing room temperature nitrogen gas with liquid nitrogen. The flow of the room temperature gas was adjusted manually to a desired constant flow rate using a rotameter. The flow of the liquid nitrogen was controlled in an on/off fashion using a solenoid ball valve controlled thermostatically by a SOLO 9696 controller that was also readily available in our lab space. During testing, we found that the flow of gas caused mechanical noise that was picked up by the sensitive torque transducer. Therefore, we temporarily turned off the flow of gas for a few seconds while taking a measurement. This worked quite well and allowed us to acquire reliable measurements of the starting torque.

The test apparatus was programmed to apply an angular acceleration of 0.050°/s^2 up to an angular speed of 0.39°/s for 3° rotation tests and 0.50°/s for 5° rotation tests. This was adequate to measure the starting torque of the bearing as well as to overcome the wind-up in the torque transducer

For each bearing, three measurements were taken in the clockwise direction and three were taken in the counterclockwise direction.

Observations

During early testing, we observed some angular oscillation in the time history as the bearing started to turn. This led us to investigate in more detail how the torque transducer works internally rather than just treating it as a “black box.” Based on a diagram in the manual [4], we learned that the torque transducer principle of operation uses two rods acting collectively as a torsional spring connecting two disks. When torque is applied, one disk rotates a small amount relative to the other disk and the rods bend slightly. This relative rotational deflection is proportional to the applied torque, and is measured optically. It required about 0.5 deg of rotation to wind up this torsional spring before the torque reached the starting torque being measured. The torque transducer was connected to the “fixed” outer ring with its deadweight disk. The small angular displacement of this “fixed” side led to a torsional pendulum action once the starting torque was overcome. For some operating conditions, the angular oscillations would feed back into the motor controller and the oscillations would continue. With a relatively large moment of inertia disk connected to a relatively soft torsional spring, the resonant frequency was just a few Hertz. We learned to test with angular displacements below 5 deg and many tests were programed for 3 deg, so the apparent instabilty never amplified enough to cause any issues. We also learned to keep the commanded angular acceleration very low. This ensured that there were no dynamic effects during the wind-up leading to startup in which the two rings of the bearing started to move relative to one another. The maximum measured torque from the first peak was taken as the measured starting torque even if subsequent peaks were higher. This test apparatus is often used to measure continuous running torque and does not normally have a weight connected with a large moment of inertia, so we did not anticipate this effect prior to our testing. While it was interesting to observe this small dynamic effect, this motion all occured after the measurement of the starting torque.

Figure 7 shows a sample time history of the measured torque during a test. In this case, the total angular displacement applied was 3 deg. The initial rise during the first half second is indicative of the wind-up torque of the torque transducer. Near the top of that first peak, the bearing begins to turn and the measured starting torque is about 0.92 mN·m (0.13 in·ozf). The drop after that is mostly due to release of the strain energy in the torque transducer. The rise back to about 0.64 mN·m (0.09 in·ozf) is more indicative of the running torque of the bearing. We were not making any attempt to measure the running torque, however, as our interest was focussed on the starting torque.

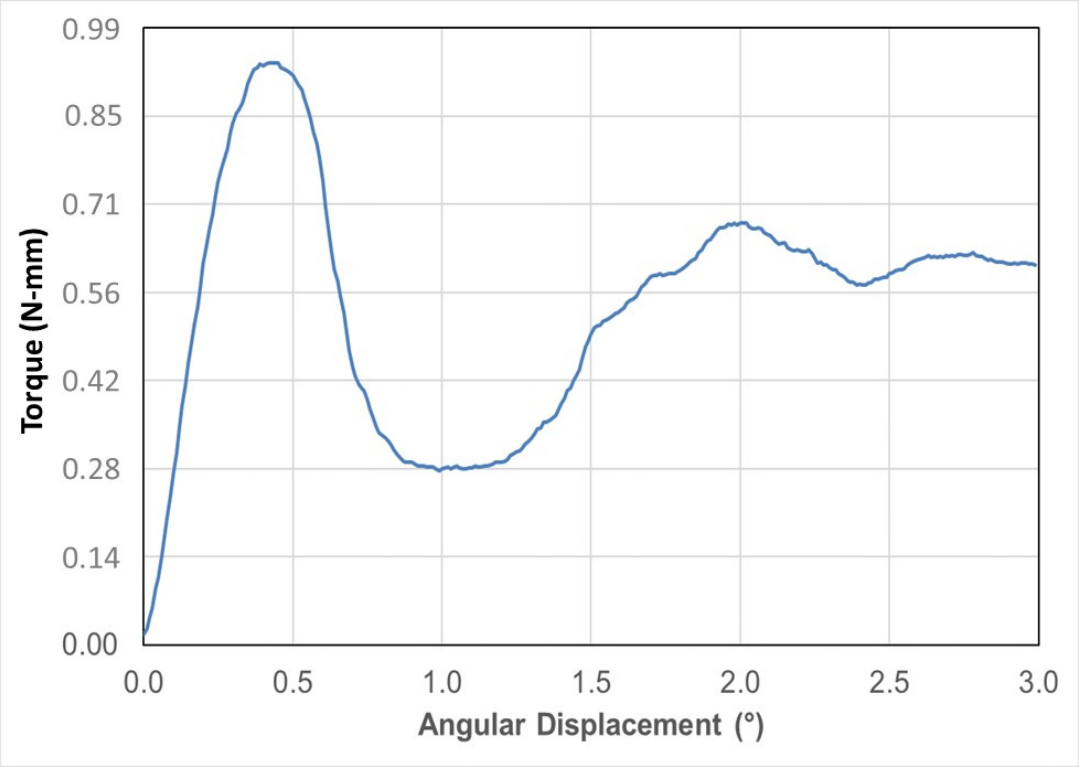

Figure 7. Sample Torque History

Test Results

The results of the testing confirmed that the torque needed to overcome the resistance of the cold lubricant was significantly smaller than the driving torque available from the mechanism. The coldest anticipated operating temperature for the mechanism is -70°C. The qualification testing of the antenna will be performed at a lower temperature of -85°C to demonstrate adequate margin. However, the resisting torque measurements were performed down to -90°C and -100°C. Although it was apparent that the starting torque was increasing rapidly as temperature was lowered, even at -100°C there was still adequate torque margin to overcome the breakaway torque of the bearings.

Figure 8, Figure 9, and Figure 10 show the starting torque for the three bearings. Each point is the average of the six measurements, three clockwise and three counterclockwise. There was no systematic dependence on direction of rotation, and the variability within each set of six measurements was less than ~10% of the average value plotted. As the temperature is decreased, there is a small trend of increasing torque, with a relatively large increase for temperatures below -70°C. This is not surprising since the pour point for the oil is -72°C. These tests also confirmed that the amout of oil applied to the bearings had been selected appropriately for this application. No further developmental testing is needed.

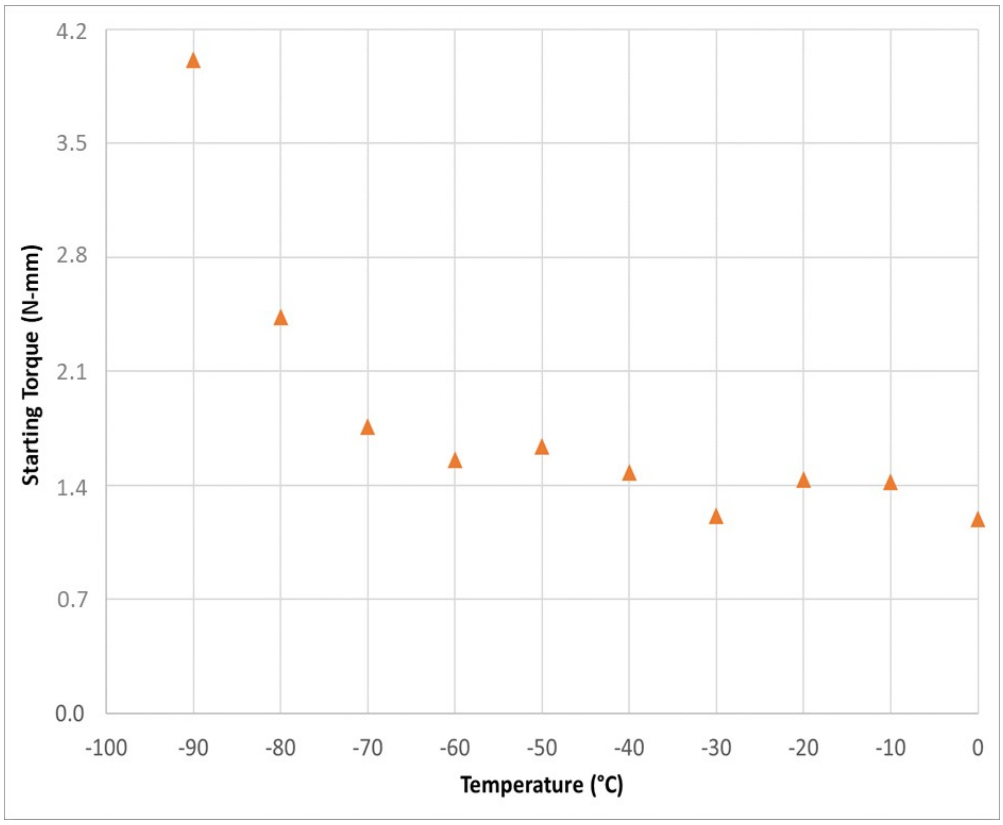

Figure 8. Starting Torque for 19.05 mm OD x 12.70 mm ID x 3.94 mm W (Papa) Bearing

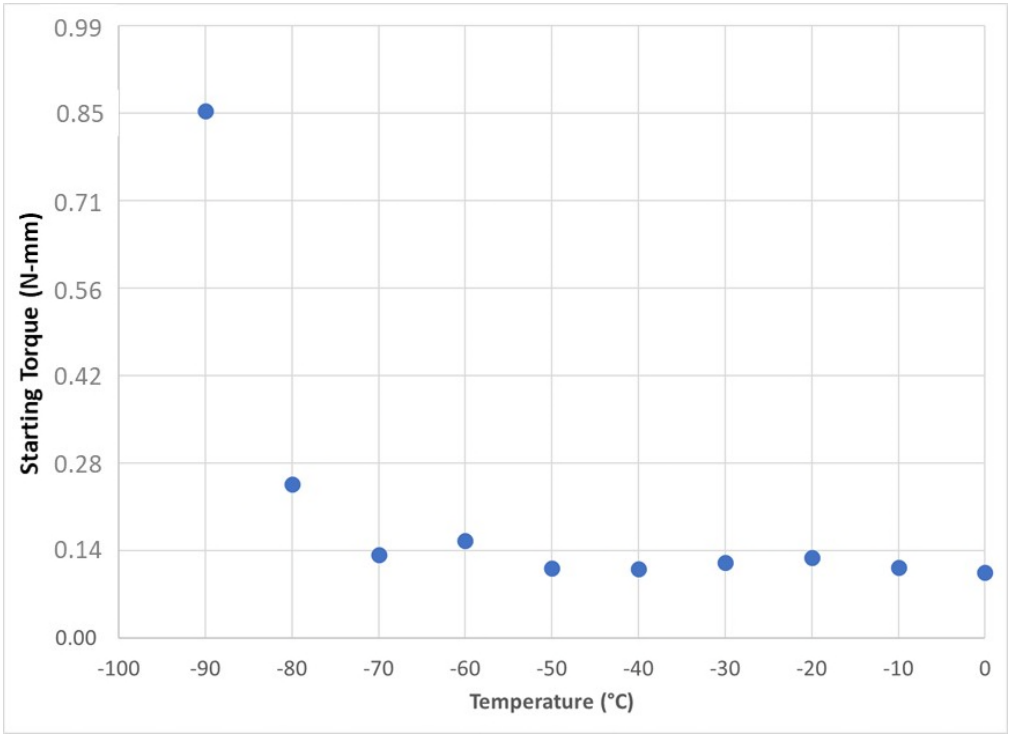

Figure 9. Starting Torque for 12.70 mm OD x 4.70 mm ID x 4.95 mm W (Mama) Bearing

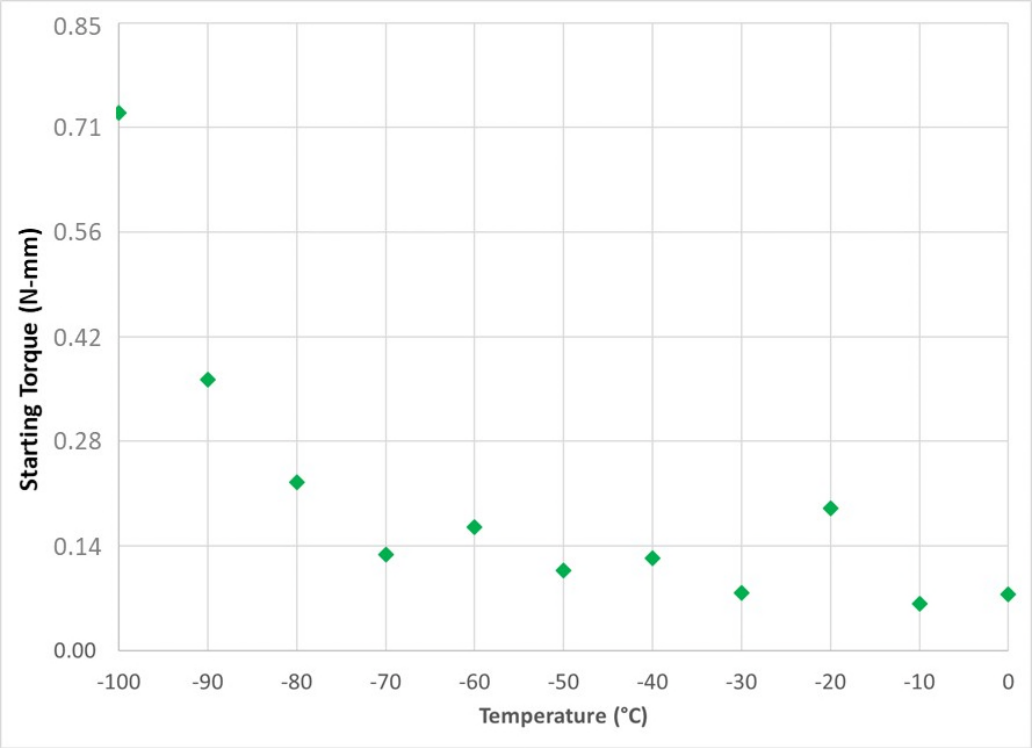

Figure 10. Starting Torque for 9.53 mm OD x 3.05 mm ID x 3.96 mm W (Baby) Bearing

Summary

Starting torque was measured at temperatures from 0°C to -90°C for two bearings and 0°C to -100°C for a third bearing. The oil selected is rated for operation down to -72°C and these measurements confirmed that the starting torque was quite consistent down to this temperature. Since the expected operating temperature of these bearings during deployment of the radar antennas of the REASON instrument could be below the rated temperature, we measured starting torque down to lower temperatures. These measurements retired a risk that the oil might increase in viscosity and cause more bearing drag than the mechanism could overcome at low temperatures. This gives us confidence that the mechanisms will be able to perform as needed during qualification testing as well as in space during the Europa Clipper mission.

Acknowledgement

The research was carried out at the Jet Propulsion Laboratory, California Institute of Technology, under a contract with the National Aeronautics and Space Administration (80NM0018D0004).

References

1. Castrol Brayco® 815Z Data Sheet. Retrieved March 9, 2022. https://msdspds.castrol.com/bpglis/FusionPDS.nsf/Files/C6FBF7AD844E7A6480257796002F8319/$File/Brayco%20815Z.pdf
2. Roberts, E. W., “A Space Tribology Handbook,” 7th European Space Mechanisms and Tribology Symposium, Proceedings of the conference held 1-3 October, 1997 at ESTEC, Noordwijk, the Netherlands. Edited by B. H. Kaldeich-Schürmann. ESA SP-410. Paris: European Space Agency, 1997., p.239, October 1997.
3. Bearing Inspector II Specification. Retrieved March 9, 2022. https://www.vibrac.com/bearing-torque-analysis-systems
4. Vibrac Torque Transducer Mini Series Specification. Retrieved March 9, 2022. https://www.vibrac.com/torque-transducer-mini-series

Project Orion Crew Impact Attenuation System

Dale Kennedy*, Nicholas Williams**, Richard (Rico) Koelsch***, Evan Siracki+
and Charles (Tony) Herrmann++

Abstract

The Project Orion Crew Impact Attenuation System (CIAS) is a structural energy attenuating mechanism that attaches to each crew seat and the backbone structure in the Orion Multi-Purpose Crew Vehicle (MPCV) to protect an Orion crew from excessive g-load during landing. This paper provides an overview of that system and focuses on design issues involving the Energy Absorber (EA) Selector Mechanism within CIAS and the resolution of those issues. The CIAS has two EA selector mechanisms that did not function as intended in their initial design. Operation of the Full-Scale Development (FSD) unit CIAS EA selector mechanisms was very rough and the mechanisms tended to lock up and no longer function without partial disassembly making re-design necessary. The effectiveness of implemented design solutions was verified through additional testing and the lessons learned are summarized. The paper also describes how demanding procurement specification requirements were addressed with an efficient, low weight, straightforward mechanical mechanism design. Finally, the paper includes a discussion on system and subsystem testing accomplished to verify proper operation and performance.

Introduction

To protect the Orion crew from excessive acceleration (g-load) upon landing (primarily off-nominal landings) the Orion MPCV utilizes the CIAS. Figure 1 shows a completed Artemis-2 configuration CIAS flight unit. Each crew seat within Orion (qty 4) independently attaches to a single CIAS (reference Figure 2). During an off-nominal water landing (e.g., one parachute out, high winds/sea state, launch abort), the crew's possible exposure to excessive acceleration (g-load) upon water impact is mitigated by the CIAS which provides crew-mass-specific spinal axis (MPCV Z-axis) energy attenuation at each seat independently.

Figure 1. Artemis-2 Configuration CIAS Ready for Final Packaging and Shipment

* Safe, Inc., Tempe, AZ
** Northrop Grumman, Chandler, AZ
*** NASA Johnson Space Center, Houston, TX
+ Lockheed Martin Space, Denver, CO
++ NASA Glenn Research Center, Cleveland, OH

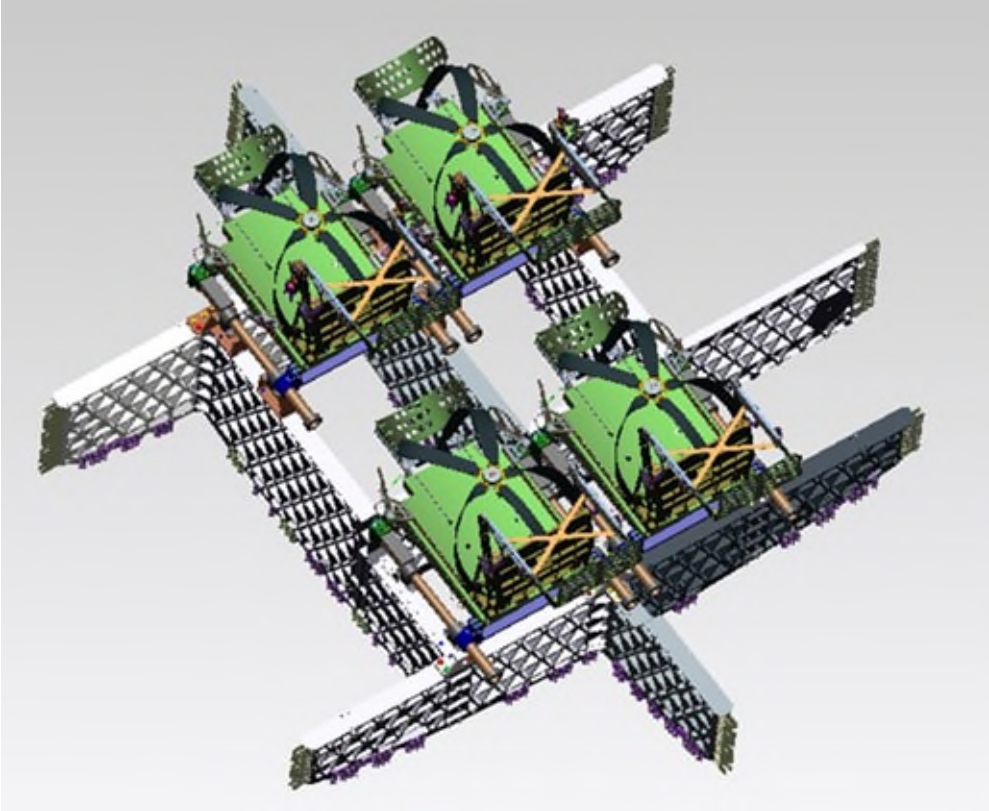

Figure 2. CIAS Attached to MPVC Backbone Structure and Crew Seats Attached to CIAS

CIAS Background

When the landing impact energy exceeds the selected stroking loads for a given crew seat-occupant mass combination, the CIAS limits the load in the Z-axis by stroking along guide rails using controlled material deformation of engaged energy absorber (EA) tubes. CIAS incorporates Safe, Inc.'s Selectable Profile EA technology (U.S. Patent No. 10,543,798) which includes manual EA selector mechanisms to select (i.e., tune) the appropriate amount of energy attenuation based on the total stroking mass. The total stroking mass consists of the crew seat mass, seat occupant mass, and the mass of the stroking portion of CIAS.

Like any aerospace mechanism, size, weight, and power are critical design drivers. In addition to being limited in size and weight, CIAS was required to provide equivalent load attenuation regardless of crew member mass and allow the Orion crew to change seat positions prior to reentry (if necessary) thus requiring the system to be tunable. This was accomplished by two primary means. The first was the performance-driven design of the EA tubes and the second was the ability to mechanically select, on the ground or in flight, various combinations of EA tubes to be engaged/active. This is referred to as tuning the system for a given total stroking mass.

The CIAS design incorporates a total of six crushable EA tubes, three EA tubes on each side of the CIAS. Locating three EA tubes on each side of the CIAS helps to minimize the imbalance of force potentially being applied to the CIAS and seat by the EAs, side to side. The EA force exerted on the seat does not need to be precisely balanced, as the guide rail linear bearings are designed to guide the seat's stroke with significant imbalance; however, good engineering practice suggests minimizing the imbalance to the extent possible without over-complicating the system.

In a landing where the load exceeds the stroking load threshold (typically off-nominal), the EA tubes are deformed (i.e., crushed) by rollers as the seat strokes. The selected EA tubes are engaged by use of the EA selector mechanisms atop each guide rail that are unlocked and rotated to the appropriate setting for the seat occupant. During an impact, the engaged tubes are drawn through precisely placed rollers, deforming the EA tubes in a controlled manner to produce the force profiles necessary to decelerate the occupant at the desired load. Each EA tube is sized to produce a specific load-stroke result that, when added to another engaged EA tube, provides the required composite energy attenuation profile for that occupant's weight range.

This is accomplished by selecting various combinations of EA tubes, appropriate for the entire stroking mass (i.e., seat system, occupant, suit, stroking portion of CIAS), to be engaged (i.e., actively deform) during a high load impact. The guide rails and linear bearings are designed to control the seat motion along the Z-axis and to allow for an adequate amount of off-axis loading. The CIAS is designed to stop stroking within a short distance (reference Figure 3) and can accommodate substantial off-axis, asymmetric loading throughout the stroking.

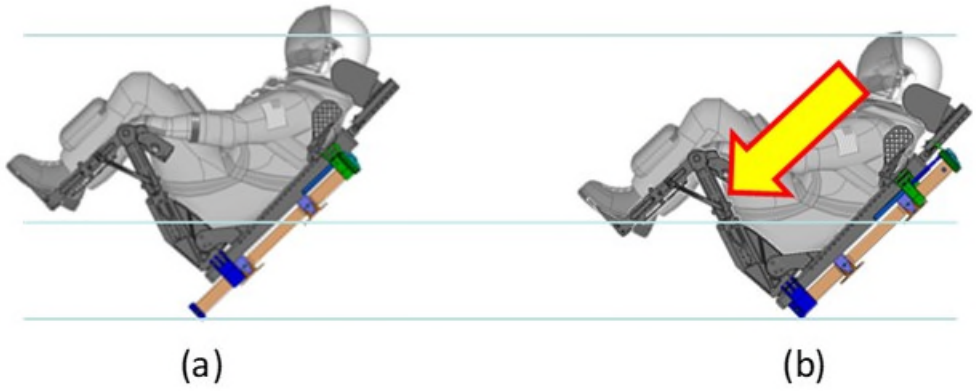

Figure 3. a) Unstroked CIAS and b) Fully Stroked CIAS

CIAS is designed to protect the seated crew occupants by limiting the crew seat accelerations to achieve acceptable Dynamic Response (DR) values for the worst cases of landing impulses (acceleration versus time) most likely to result from off-nominal landing scenarios/cases studied. The requirement is for CIAS to protect seat occupants to the low (deconditioned) DR limits (Reference Table M2.2-2 in [1]) primarily for the Z-axis (i.e., DRz) as that is the direction of travel for CIAS.

CIAS Design

Figure 4 illustrates the primary components of CIAS. Two guide rails control and direct the stroking portion of CIAS. The CIAS components that interface with the spacecraft (i.e., female guide rail supports) bolt to the backbone structure of the crew vehicle. There are four (two upper and two lower) female guide rail supports to which the guide rails are joined thus securing the CIAS into position in the crew vehicle. Two EA selector mechanisms are joined to the top of each guide rail and these mechanisms enable ground and in-flight operations crews to "tune" the CIAS for a specific weight seat and suited seat occupant combination for optimal stroking load should the need arise. The EA tubes are positioned behind the bilateral protective covers that join to the upper seat interface adapters as can be noted by close inspection of the sectioned left-hand side (LHS). The stroking portion of CIAS includes the upper and lower seat interface adapters, lateral braces, EA rollers and axles, protective covers, disengaged EA tubes, and bearings all shown in Figure 4. The EA selector mechanism design will be discussed in more detail.

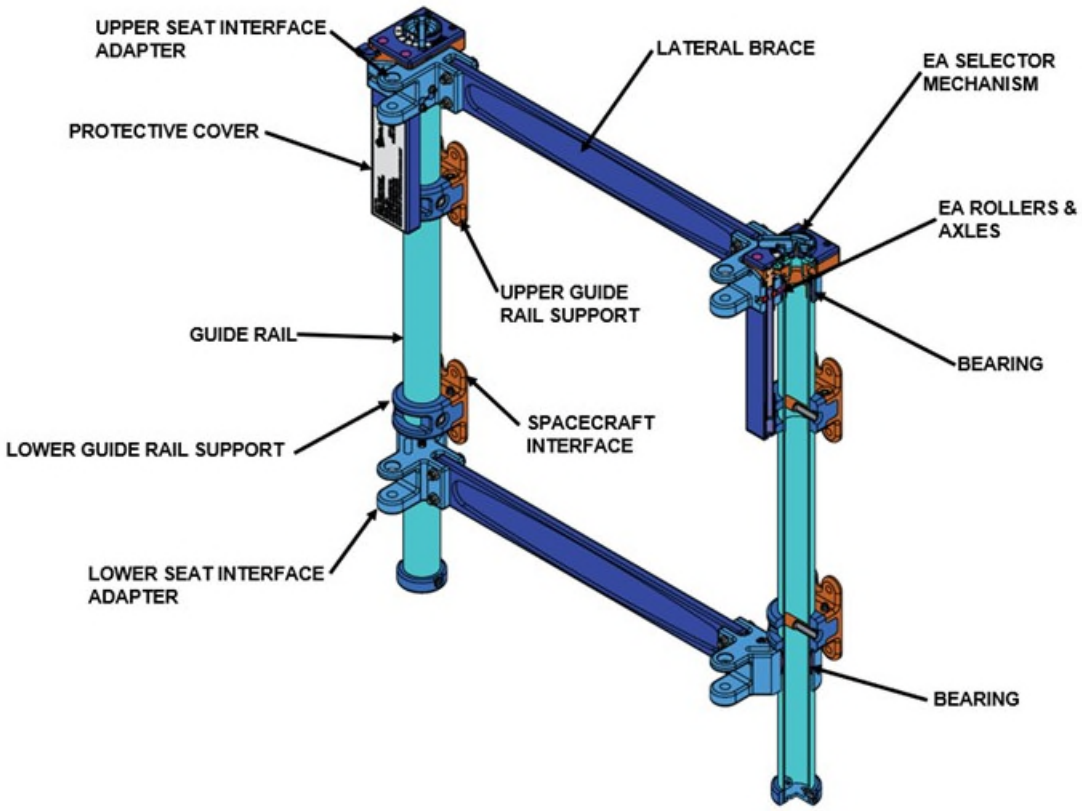

Figure 4. CIAS Primary Components

The center EA tube on each side is always engaged for each CIAS unit and these EA tubes are referred to as “fixed” EA tubes. The other two EA tubes on each side of the fixed EA tube (on each side of the CIAS – left hand side (LHS) and denoted “left” in Table 1 and right-hand side (RHS) and denoted “right” in Table 1 all with respect to the seated occupant) are referred to as “selectable” EA tubes that are selectively engaged via the EA selector mechanisms. The various combinations of these “outer” and “inner” selectable EA tubes along with the fixed EA tubes provide the appropriate energy attenuation for eight different stroking mass ranges (reference Table 1) that are subsets of the overall stroking mass range that must be accommodated by CIAS. Note the increasing number of tubes selected as the stroking mass range increases. This is necessary to adequately attenuate the higher loads associated with the greater stroking masses. This can also be noted in Figure 5 which provides a notional reference for the load versus stroke profile of the various EA tubes as the actual y-axis load and x-axis stroke distance data are redacted to protect intellectual property. Figure 6 illustrates the composite load versus stroke profile for each of the eight profiles (stroking mass ranges) noted in Table 1. Note that the composite profiles are all increasing in load per unit of stroke as stroking mass increases.

Careful inspection of Table 1 shows more EA tubes engaged on one side of CIAS as opposed to the other in several instances. Also, the load-stroke profiles of the EA tubes vary. Thus, the aforementioned significant asymmetric loading that can occur from one side of CIAS to the other must be accommodated in the structural design. In addition to the structural design strength of CIAS, the design also incorporates specially configured linear bearings in the upper and lower seat interface adapters that provide the necessary bearing support throughout the range of asymmetric load.

Table 1. Eight Stroking Mass Range Profiles with Corresponding EA Selector Lever Settings and EA Tube Engagements (Note: "Left" refers to the seated occupant's left shoulder and "Right" refers to the seated occupant's right shoulder.)

Profile	Stroking Mass Range (lb)	Left Selector Setting	Right Selector Setting	Tubes Selected					
				LF	RF	LI	RI	LO	RO
1	204 – 223	7	1	X	X	X			
2	224 – 240	8	2	X	X		X		
3	241 – 262	8	4	X	X				X
4	263 – 288	7	2	X	X	X	X		
5	289 – 310	7	4	X	X	X			X
6	311 – 340	5	4	X	X			X	X
7	341 – 365	6	2	X	X	X	X	X	
8	366 – 402	5	3	X	X		X	X	X

1, 8 = Neither
2, 7 = Inner
3, 6 = Both
4, 5 = Outer

LF = Left Fixed
RF = Right Fixed
LI = Left Inner
RI = Right Inner
LO = Left Outer
RO = Right Outer

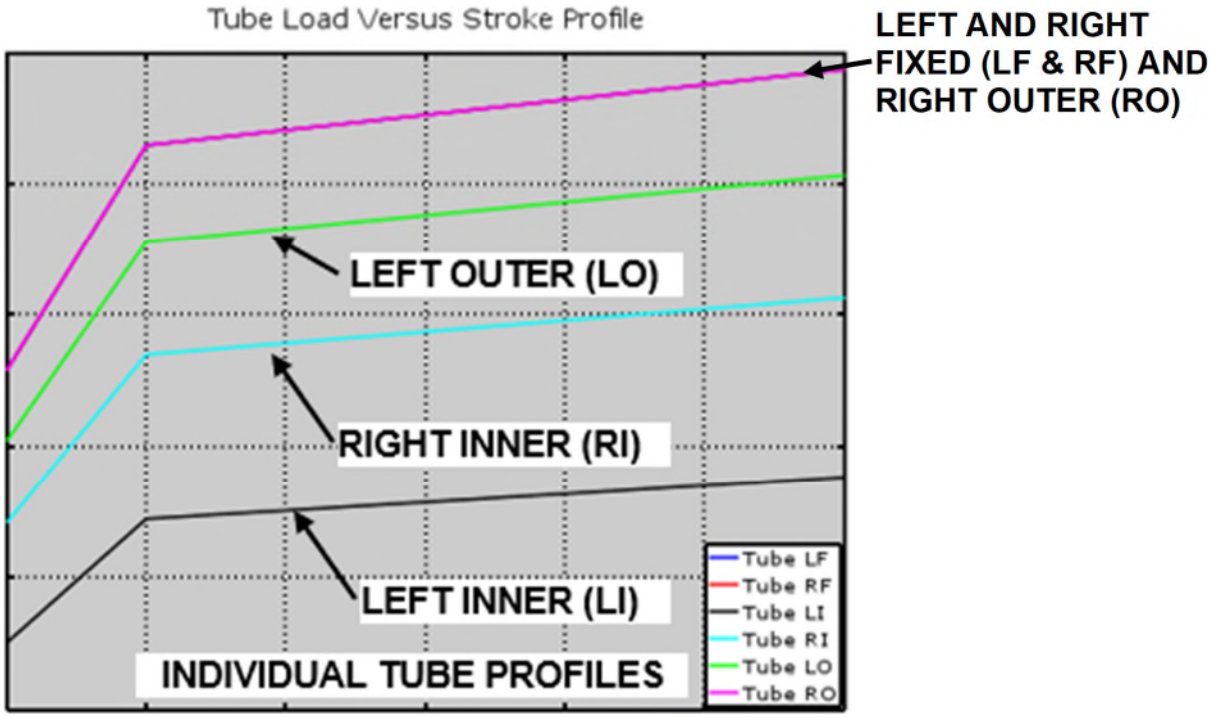

Figure 5. EA tube Load vs. Stroke Profiles Designed to Provide Adequate Range of Protection

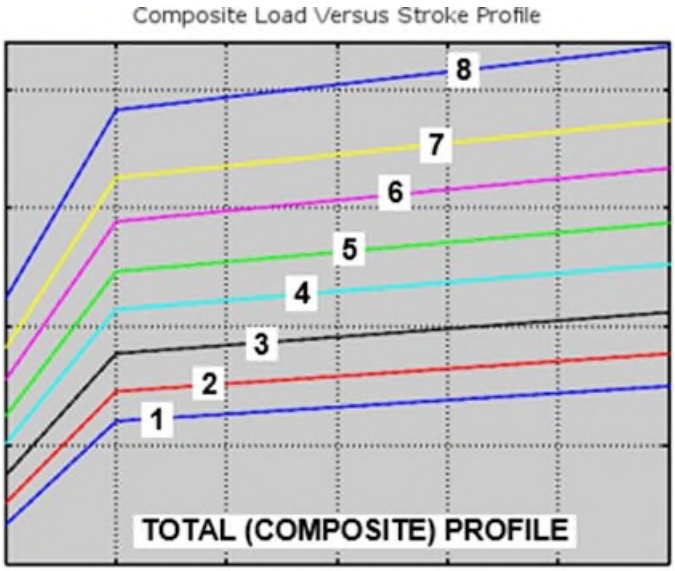

Figure 6. Escalating Load vs. Stroke Profiles for the Eight Selectable Ranges Shown in Table 1

Figure 7 illustrates the improvement in DRz (i.e., DR in the Z-axis) obtained using CIAS to attenuate high landing loads. The reduction in DRz is substantial for the more severe landing cases analyzed.

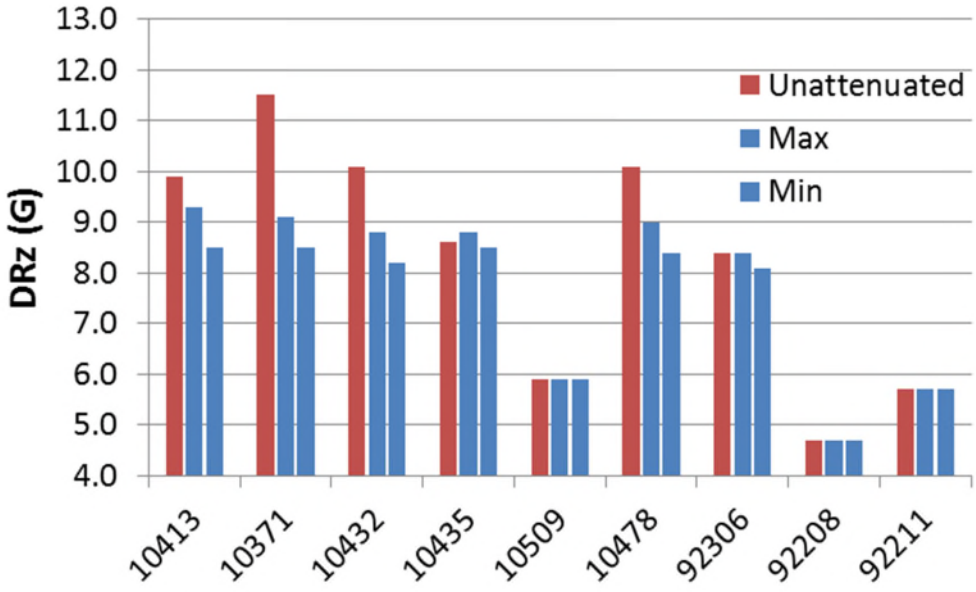

Figure 7. Reduction in DRz for Unattenuated and Attenuated Stroking Masses at Each Range Endpoint for Various Landing Cases

EA Selector Mechanism Design

In order to utilize the composite load stroke profiles and provide tuning capability for all crew member masses, a mechanism was designed to enable selection of EA tube combination in order to provide tunability. The EA selector mechanisms sit atop each guide rail and a close-up photograph of a fully

assembled RHS EA selector mechanism is shown in Figure 8. The two EA selector mechanisms each have four selectable positions. One position does not engage either selectable EA tube, a second position engages only the inner EA tube, a third position engages only the outer EA tube, and a fourth position engages both the inner and outer EA tubes. The EA selector mechanism makes use of engaging (selector) "keys" that either engage a selectable EA or disengage it based on the selector lever's numerically identified position. Table 1 shows the profile selection for eight total stroking mass ranges. It also indicates which EA tubes are engaged for each profile selection. Figure 6 illustrates the increasing load versus stroke capability of the CIAS as increasing numbers of EA tubes are engaged for the total stroking mass range accommodated in the design. Each independent EA selector mechanism includes a two-step manual lock/unlock lever (referred to as a ¼ Turn Lock Pin Assembly). To change a selection (i.e., tailor the load-stroke profile differently – to reset for a different stroking mass), the EA selector must first be unlocked by pushing in on the ¼ turn lock pin assembly compressing the contained spring and then rotating it 90 deg. This disengages the locking pin assembly from the position locating plate (not visible in Figure 8) enabling reselection by manually rotating the lever assembly to a new selection position. After the intended EA engagement selection is made, the unlocking process is reversed to re-lock the EA selector. This locking mechanism is designed to preclude inadvertent, performance degrading EA selection changes. Too high a load selection and too low a load selection are both detrimental to the safety of the seated occupant. The proper EA tube engagement can be visually verified via the EA tube engagement key view ports provided in the EA selector mechanism cover assembly.

Interior EA selector mechanism components also include a dual path cam, the EA engagement keys, and spring plunger assemblies. The dual path cam extends and retracts the EA tube engagement keys to engage/disengage the selectable EA tubes in the inner and outer positions. The spring plunger assemblies provide tactile feedback when each EA selection option position is reached. Then, re-locking the EA selector using the ¼ turn lock pin assembly further confirms the EA selection for the indicated selection number is complete.

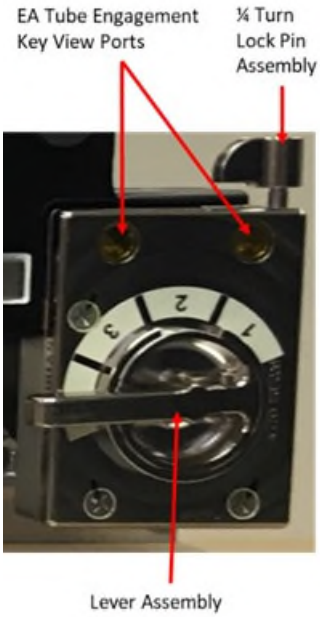

Figure 8. CIAS RHS EA Selector Mechanism Assembly

EA Selector Mechanism Design Evolution

The initial FSD design of the EA selector mechanism did not function as intended. When the FSD test article was initially fabricated and assembled, the EA selector mechanisms jammed when operated and, in some EA selection positions, they tended to lock up. Upon further inspection of the FSD EA selector mechanisms,

it was determined that the original single path cam that was designed to drive both keys simultaneously had poor transition angles at some points along the cam path. The EA engagement keys are pinned to the cams and the pins, that move in the cam path, would bind at these poor transition angles. This is shown in Figure 9.

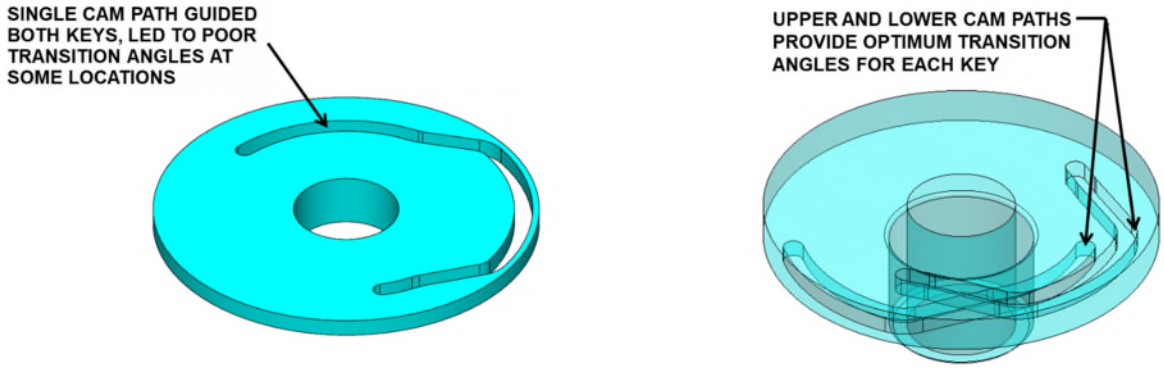

Figure 9. CIAS EA Selector Mechanism Cam FSD Design (left) and Redesign (right)

It was also determined that the original EA engagement key design led to a propensity to jam when sliding in the EA selector housing pockets. The design provided minimal support to one side of each EA engagement key. The revised design altered both the EA selector housing pockets and the EA engagement keys themselves were redesigned to ensure equal support on both sides of the key. Figure 10 shows the EA selector mechanism EA engagement keys for the FSD design and for the redesigned mechanism. Each key in the redesigned mechanism now moves linearly within a corresponding full-walled pocket in the EA selector housing and each is moved in its own cam path with the dual path cam design. Additionally, EA selector mechanism components were coated with dry film lubricant to further reduce operating friction.

Figure 10. CIAS EA Selector Mechanism EA Engagement Key FSD Design (left) and Redesign (right)

The redesigned EA selector mechanism was modeled for a kinematic analysis to determine the functionality of the design prior to fabrication of new components. The model converged on a reasonable torque versus time solution. It is interesting to note that when the initial FSD EA selector mechanism was subsequently modeled for a like kinematic analysis, the model would not converge indicating a problematic design from an operational perspective.

Life Test Results of EA Selection Mechanisms

The EA selector mechanism functionality was life cycle tested during qualification testing to verify performance throughout intended functional life requirements. Each tuning mechanism (i.e., EA selector mechanism) of the qualification test article was fully cycled 200 times to demonstrate adequate service life. Proper EA tube engagement for each tuning mechanism selection was verified for each cycle.

The life test verified that the CIAS EA tuning mechanisms functioned normally over the total number of cycles expected to be put on the mechanism during assembly, test, and in operation with adequate margin. Operational parameters were measured throughout the test to provide quantitative data to assess acceptable and consistent EA selector mechanism operation.

Lock pin force was measured using a force gauge applied to the handle of the lock pin. A light rotation-inducing force was applied to the lever as the force to compress the lock pin was measured. Lever assembly torque was measured with a dial type torque wrench and a purpose-built adapter to interface with the selector mechanism lever. Proper EA engagement key engagement of the applicable EA tube(s) for each EA selector mechanism position was visually verified for each change in selection. Reference Figure 11 for this process.

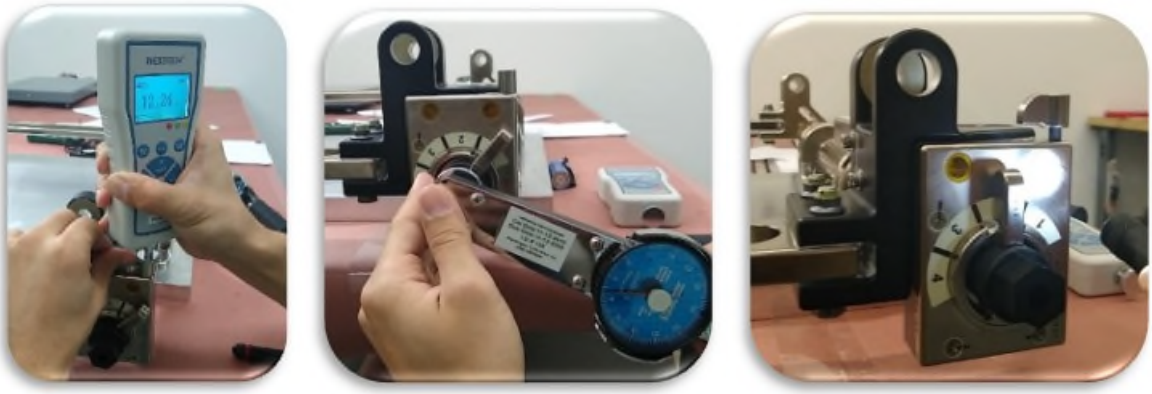

Figure 11. Measuring RHS EA Selector Lock Pin Force (Left) and Selector Torque (Center) and Visually Verifying Proper Engagement of the EA Engagement Keys (Right)

No binding, jamming, or damage was noted during testing nor was there any observed dry film lubricant debris. The maximum lock pin compression force was well below the limit for both the right and left EA selector mechanisms. The maximum lever torque was also well below the limit for both the right and left EA selector mechanisms. Data for the entire 200 cycles of life testing are plotted in Figures 12 and 13. Note that the vertical dashed lines in each graph represent the demarcation between the 15 wear-in/run-in cycles performed as part of acceptance testing and additional life cycle tests subsequently conducted as part of qualification testing. Figure 13 indicates that the RHS EA selector has slightly increasing selector torque until approximately 150 cycles. At approximately 150 cycles, the RHS EA selector torque stabilized and ran at a relatively steady state well below the limit. The higher noted selector torques are associated with the transition from position 3 to position 4 (indicated by a “+” overlay) and from position 1 to position 2 (indicated by a “×” overlay). Both of these transitions are associated with the most aggressive changes in the upper cam path within the applicable EA selector emphasizing the importance of designing in generous transition radii in cam paths.

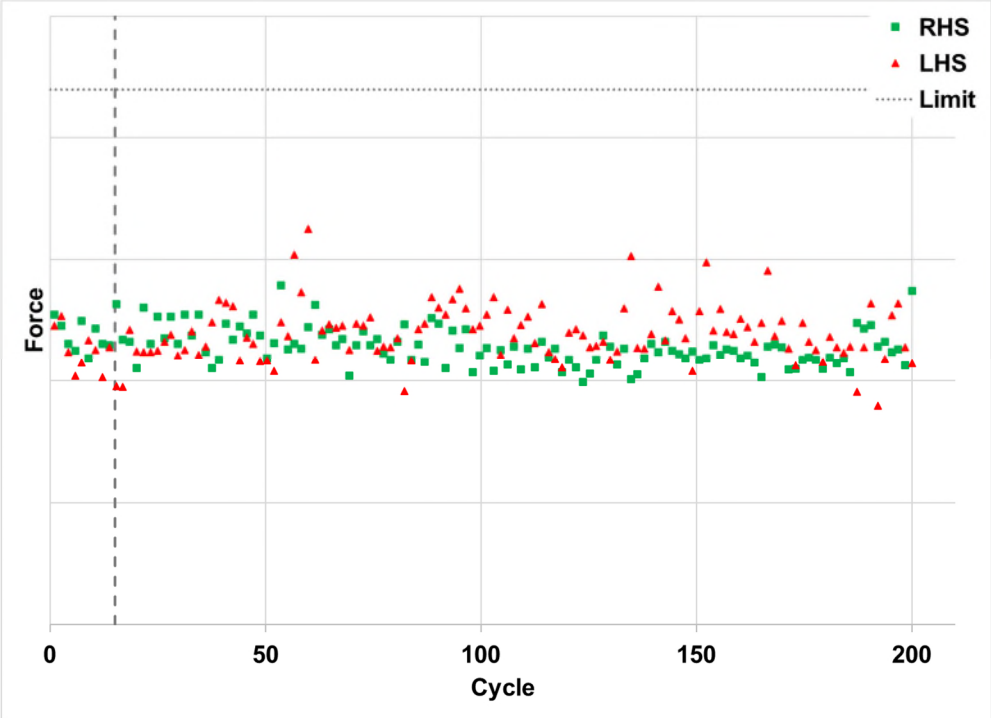

Figure 12. Measured Lock Pin Force

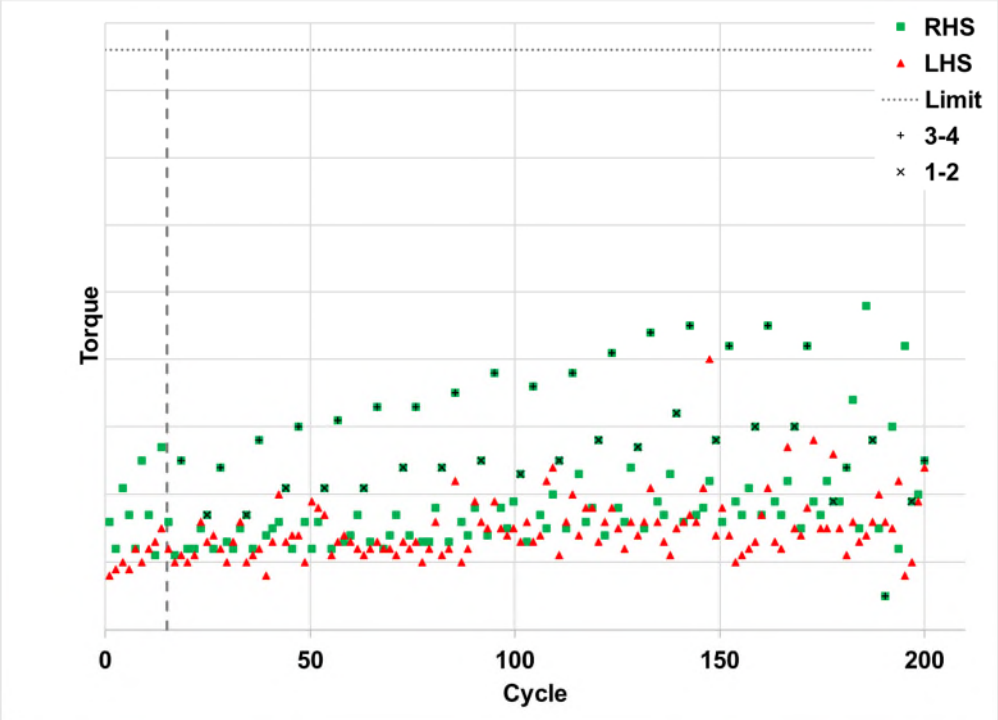

Figure 13. Measured Lever Assembly Torque

The CIAS mechanism was dynamically tested in FSD (reference Figure 14 for test setup) and qualification (reference Figure 15 for test setup for both the 1st-percentile female and the 99th-percentile male mass simulators). This testing was accomplished to verify load-stroke and DR performance. Maximum imbalance was also evaluated and verified acceptable. EA load-stroke was evaluated for each test case and the DR_i values were all verified acceptable. There was some small amount of pre-stroking of the CIAS observed after FSD random vibration testing at launch abort levels was performed. This was just prior to the start of dynamic impact sled FSD testing. This resulted in the design team ultimately deciding to add additional load carrying capability at the neck area of the two fixed EA tubes to reduce the likelihood of pre-stroking in flight under similar conditions. This design revision was included in qualification testing and no pre-stroking was observed post integrated vibration testing.

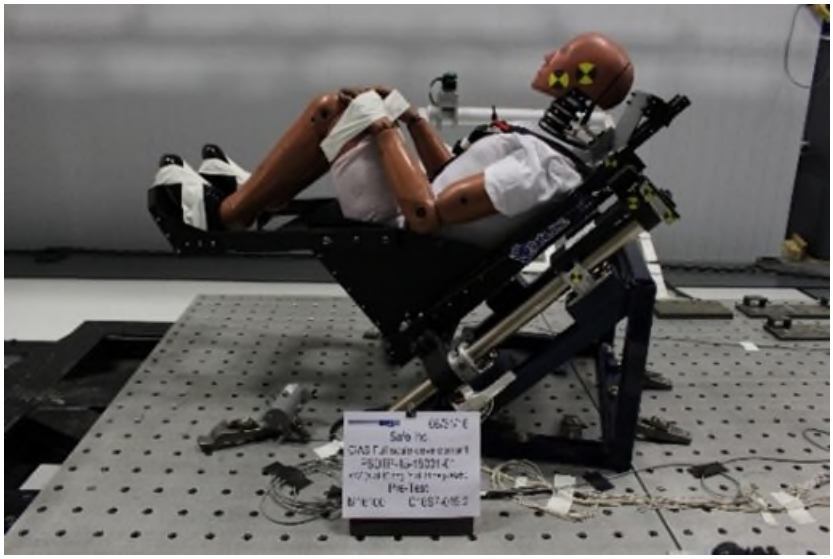

Figure 14. Dynamic Impact Sled Test Setup for CIAS FSD Testing

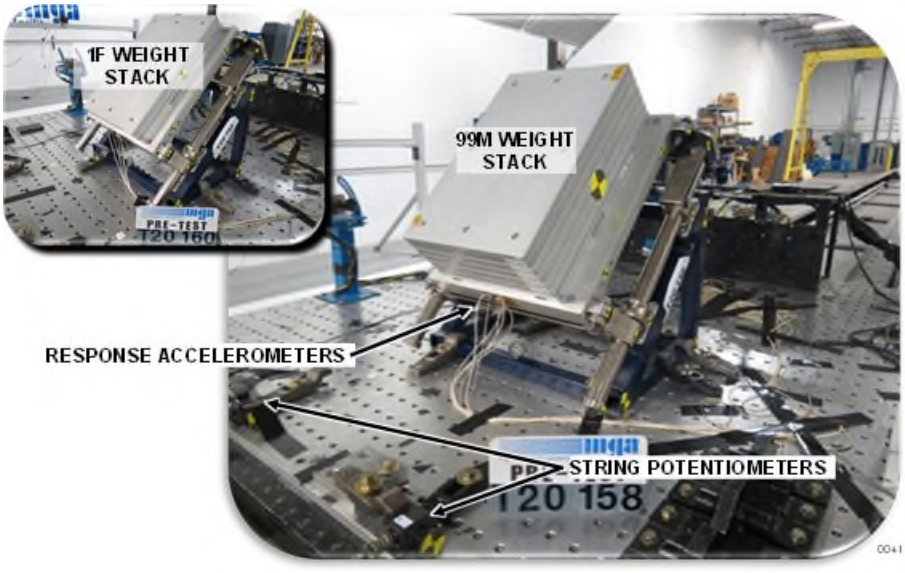

Figure 15. Dynamic Impact Sled Test Setups for CIAS Qualification Testing

Figure 16 shows a close-up of the CIAS qualification test article post-sled test #1 which used a mass simulator for the 99th-percentile male, crew seat, suit and helmet. Figure 16 is a close-up photo of the LHS EA Selector and upper seat interface adapter to provide a visual of the stroked EA tubes.

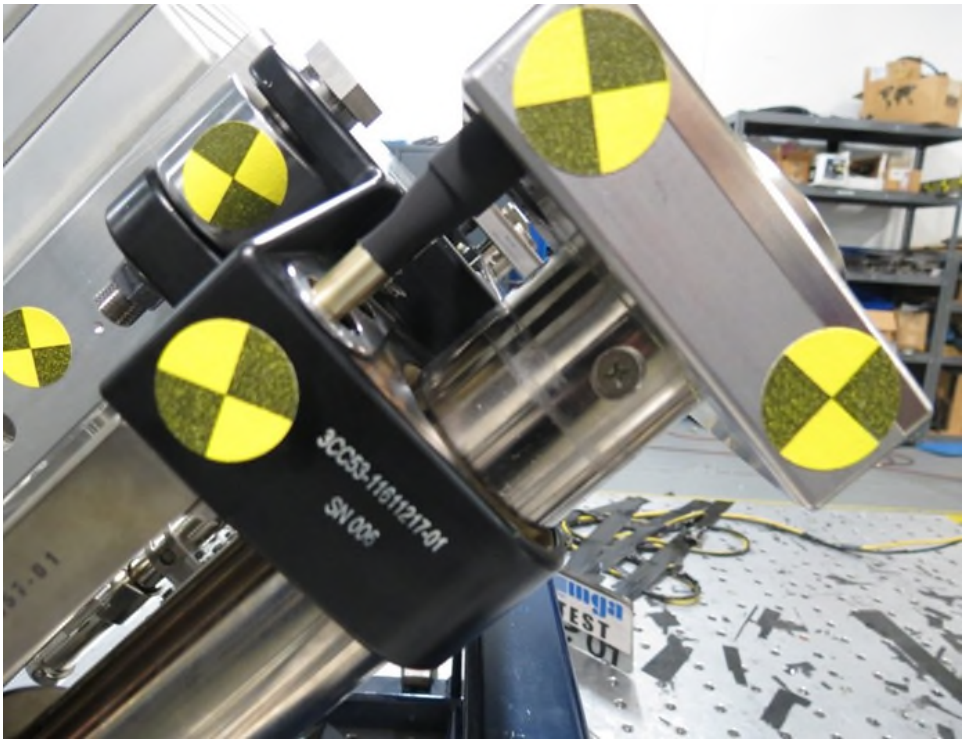

Figure 16. Dynamic Impact Sled Qualification Testing – Post Test #1 Showing Stroked LHS EA Tubes

Conclusion

The available space for CIAS limited both the number of EA tubes that could be incorporated into the CIAS, and it limited the total amount of available stroke distance. It was determined that six EA tubes of varying load-stroke profiles could be designed into the CIAS, and this would provide sufficient energy attenuation throughout the entire required stroking mass range. Two EA tubes, one on each side of the CIAS framework, remain "fixed," meaning that they are always engaged and will stroke given an impact of sufficient energy. The remaining four EA tubes (two each side) are referred to as "selectable." Figure 5 illustrates the load-stroke profiles of the EA tubes (numerical data removed from axes for proprietary reasons). Optimizing load-stroke profiles across the entire expected stroking mass range enables a significant reduction in Dynamic Response Index (DRI), Z-axis (DRz), as illustrated in Figure 7 for unattenuated versus attenuated high energy landing impact cases.

Several lessons learned resulted from the CIAS EA selector mechanism design to improve the likelihood of like systems functioning successfully. First, use generous cam path transition angles and do not overload the cam by attempting to transition multiple components in a single cam path. Second, design for symmetric or near symmetric support of components that must slide in tight housing channels. Third, use kinematic modeling analysis early in the design process to help identify design deficiencies likely to cause problematic/suboptimal functionality.

References

1. MPCV 70024 Revision A dated January 22, 2014, titled "Orion Multi-Purpose Crew Vehicle (MPCV) Program Human-Systems Integration Requirements.

First Steps to Develop a Triboelectric Wind Turbine for Mars Exploration

Borja Pozo*, Iban Quintana*, Ewelina Ryszawa**, Iñigo Muñoz*, Lionel Galliard**
and Erlatnz Fernandez de Gorostiza*

Abstract

The aim of the work has been to develop the trade-off for the first wind turbine which will be an efficient and robust Triboelectric Generator demonstrator that can efficiently operate under Mars environmental conditions, consolidating the technical requirements considering the needs of the past, present, and future space missions. This work has investigated Mars fluidics operation behavior through a turbine, triboelectric materials and has performed a trade-off, with a particular focus on energetic efficiency, robustness, simplicity, scalability, easy mechanical integration, reduction of mass and weight of current turbines, minimization of cost and compatibility to present and future space developments.

Introduction

A consistent and reliable power supply is critical for future Mars missions. The idea is to use Mars winds to produce electrical energy and use it as an auxiliary energy source to solar cells during the Martian storms and continue low electric supply during the storms. However, the usual Electromagnetic Generators (EG) are unsuitable for planetary exploration due to their heavyweight, leading to the high launch costs. The alternative to EG can be the Triboelectric Generator (TEG), which produces more power than an EG when weight and volume are considered as key parameters [1][2]. This paper describes the operation principles, trade-off developments, and results of a first approach to implement the first wind turbine tests based on a TEG for Mars.

Even though on Mars there are wind seasons with high-speed winds, the atmosphere density is very low. It is not obvious that a wind turbine would move under those conditions. According to the power production equation, the extraction potential for wind power is a function of velocity cubed and only proportional to density. This means that the effect of the low density of the Mars atmosphere has less importance than the velocity regarding the power that can be extracted from the winds. In addition, two works of NASA and Houston University [3][4], made theoretical analyses about the possibility to generate energy from the wind with a different type of big size Vertical Axis Wind Turbine. The level of energy estimate was 19 kW in a 29 m/s wind considering a mass of 429 kg. The conclusions were that such a system can work and generate enough energy; however, the generators design must be improved.

Besides the theoretical results that are presented in the mentioned two papers, in another work [5] it was demonstrated that wind power can be used on Mars to produce energy. In this work, several tests in a wind tunnel were performed in the Martian atmospheric environment to duplicate the atmospheric density from Mars. The turbine used in those tests had a quite simple design and the objective was not to maximize the power generation, but to verify that a wind turbine can rotate under Martian condistions and generate energy.

The important point to consider is the effect of Mars atmospheric conditions on the triboelectric principle. As it is described and analyzed in [6], if the TEG is packaged hermetically in CO_2 (pressure inside the package is maintained at 760 Torr), the output performance increases by 157% compared to Earth

* Tekniker, Gipuzkoa, Spain; borja.pozo@tekniker.es
** ESA-ESTEC, European Space Agency - European Space Research and Technology Centre, Noordwijk, The Netherlands; ewelina.ryszawa@esa.int

conditions. This dependence on atmospheric condition can be explained by a charge relaxation model [7]. In this work, this effect has been tested and validated.

Mars Atmospheric Conditions and Winds

The main atmosphere parameters that change on Mars regarding the Earth are the density and velocity. The average atmosphere density on the Earth is 1.217 kg/m^3 and on Mars 0.020 kg/m^3, both at surface level. The wind speeds measured on Mars give a range between 5 and 30 m/s. The work presented in this paper has been developed using real data measured by NASA's Insight mission at the Elysium Planitia to find out how the turbine works in real Martian conditions. Fig.1 shows the measurements from the TWINS instrument used to measure the Mars weather since 2019, which has been used in this work as reference (from Mars InSight Weather Report). Pressure changes due to the seasons and the average, minimum, and maximum wind velocities are shown.

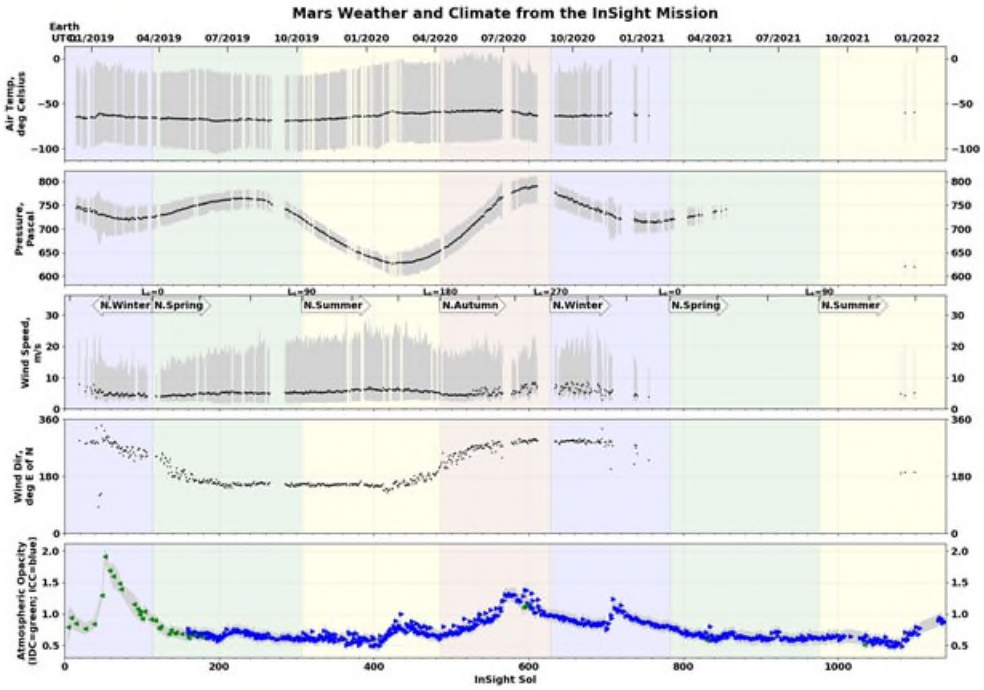

Figure 1. Atmospheric parameters mesuared by Insight in Mars (figure from NASA).

Diurnal and subdiurnal variability on Mars, with its uniquely low average surface pressure, highlights an end-member case of sunlight control of the diurnal cycle, particularly as compared to Earth. This causes on Mars (relative to Earth):

1- Atmospheric thermal tides an order of magnitude stronger, especially in low latitudes.
2- More sustained daytime upslope and night-time downslope flows, especially over steep slopes.
3- A much sharper contrast between the strong daytime, buoyancy driven convective turbulence and the moderate night-time, shear driven mechanical turbulence.

Wind Turbine

Selection of wind turbine type

For the design of the wind turbine, the first aspect that has been studied is the type of turbine that best meets the requirements. The first step for defining a type of wind turbine is to analyze the two principal designs in terms of the orientation of the rotor axis. Wind turbines can be classified as Horizontal Axis Wind Turbines (HAWT) and Vertical Axis Wind Turbines (VAWT). Although VAWTs have fallen significantly behind HAWTs in recent years in terms of technical development and in the number of units manufactured,

they have some advantages that made them suitable for some applications. The main difference between both types of turbines is that VAWTs are crossflow devices and accept wind from any direction while in HAWTs the rotor must be kept perpendicular to the flow of the wind which means that it must be oriented to capture the maximum energy from the wind. Moreover, in VAWTs the components may be connected directly to the rotor shaft and located at the ground level. This eliminates the need for a tower to support the weight of equipment such as the gearbox and other main turbine components. Due to the extreme weather, the Martian dust and the weight limitations, the absence of the orientation mechanism and the ease of operation, maintenance and installation are the key aspects when choosing the type of turbine for this application. Therefore, a vertical axis wind turbine best meets the requirements.

Design of the wind turbine

The main dimensions of the rotor, the number of blades, the airfoil and its chord length, the rotor strength and the pitch angle have been defined. For this purpose, literature references are sought, and Q-blade software was used to simulate the rotor by varying its design parameters. This software is based on the model of moments, and although it does not consider the stall, it allows to obtain very fast results being a very useful tool for the design process. The main dimensions of the rotor are defined, which are height (H) and diameter (D). From these two parameters, both the swept area and the aspect ratio of the rotor are defined and shown in Eq.1 and Eq. 2.

$$Swept\ Area\ (m^2) = H\ x\ D \qquad \textit{Equation 1}$$

$$Aspect\ Ratio\ (-) = \frac{H}{R} \qquad \textit{Equation 2}$$

Considering that the whole system will be tested inside the wind tunnel of the University of Aahrus, there are some dimensional limitations. The wind tunnel is a rectangular cavity of one meter high by two meters wide. It is estimated that the TEG itself will have between 10 and 20 centimeters high, and, in addition, it will be necessary to leave some height in relation to the tunnel ceiling. These two limitations mean that only 0.7 meter of height is available for the rotor. Considering that the larger the swept area the higher the power output and that there is less margin in terms of height, the rotor height has been set to its maximum value, that is H=0.7 m. Then, the diameter has been adjusted, considering the aspect ratio. Reviewing [8][9], it is concluded that if blade tip losses are considered, high aspect ratio values should be used. If the structural aspect is also considered, aspect ratio values between 2.5 and 3 are recommended. By simulating three different diameters that meet this requirement, the diameter is set at D=0.5 m. For the blades definition, the references [10]-[13] indicate that increasing the number of blades decreases the efficiency of the rotor due to interference between the blades. However, the use of more blades balances the turbine and makes the torque generated more constant [14]. Discarding the use of 1 blade (many balancing problems) and 4 blades (very low efficiency), two rotors of 2 and 3 blades respectively were simulated in Q-Blade. The results show higher power coefficients over a wider operating range when three blades are used. As for the aerodynamic profile of the blades, there are several options, many of which have been developed for use in VAWTs [15] [16]. For simplicity it has been decided to use a symmetrical airfoil. After running some simulations, NACA0018 will be used because of its good performance and because it is structurally strong enough. Once the airfoil is known, its dimensions must be defined. The chord length is defined as the distance between the leading edge and the tail of the airfoil. This parameter directly affects the solidity of the rotor which is defined in Eq. 3:

$$\sigma = \frac{Number\ of\ blades\ x\ Chord\ length}{Rotor\ radius} \qquad \textit{Equation 3}$$

The various studies recommend solidities of between 0.2 and 0.5, and it is known that the rotor has a self-starting capability only at solidities greater than 0.4 [17]. Due to the higher power coefficient and a wide operating range and considering other factors such as self-starting capability and cost, the solidity is set at 0.4. This implies that the blades will have a chord length of 0.035 m.The last parameter to configure is the pitch angle. The pitch angle may be positive, if the leading edge of the airfoil points towards the center of the rotor, or negative if it points away from the rotor. From the literature it is concluded that positive pitch angles decrease performance while negative pitch angles increase performance if they are between

0º and 2º [18][19]. After simulating different pitch angles in QBlade the conclusion is that the performance is very similar. In order not to complicate the design, the pitch angle will be left at 0º. Table 1 summarizes the selected values.

Table 1. Main rotor selected parameters.

Parameter	Value	Parameter	Value
Height (m)	0.7	Chrod length (m)	0.035
Diamater (m)	0.5	Solidity	0.4
Number of blades	3	Pitch angle (º)	0
Airfoil	NACA0018		

Finite Element Simulations

The analysis of the wind turbine using the finite element method can be divided into two types of analysis, thermo-fluidic analysis, and mechanical analysis. The thermo-fluidic analysis focuses on obtaining temperature and pressure contours, as well as forces that can be caused by fluids in different solids. The results can be used as input loads to the mechanical analysis where the objective is to study the mechanical behavior of the system by analyzing among other things stresses and deformations. Both analyses have been carried out through several simulations in ANSYS software.

As it is known, wind at a certain speed will impact the blades of the wind turbine, causing a rotational movement around its axis, which will accelerate until it reaches a constant rotational speed. The aim of this analysis is to study the interaction between the wind and the rotor, which will allow us to obtain the performance and the self-starting capacity of the wind turbine itself, as well as the forces exerted on it in different positions and moments. These simulations are all carried out in 2D, as is shown in Fig 2. The geometry for CFD simulations is divided into two parts, a rotating part (rotor domain) and a fixed part (outer domain). The dimensions of the outer domain are those of the wind tunnel, so the width is 2 m while the length is 7 m. The rotor is located 3 m from the tunnel entrance where the velocity inlet boundary condition applies and 4 m from the exit where the pressure outlet boundary condition applies. As for the side walls, when the rotor is simulated inside the wind tunnel, they will have a wall boundary condition while when simulated in the Martian environment they will have a symmetry boundary condition.

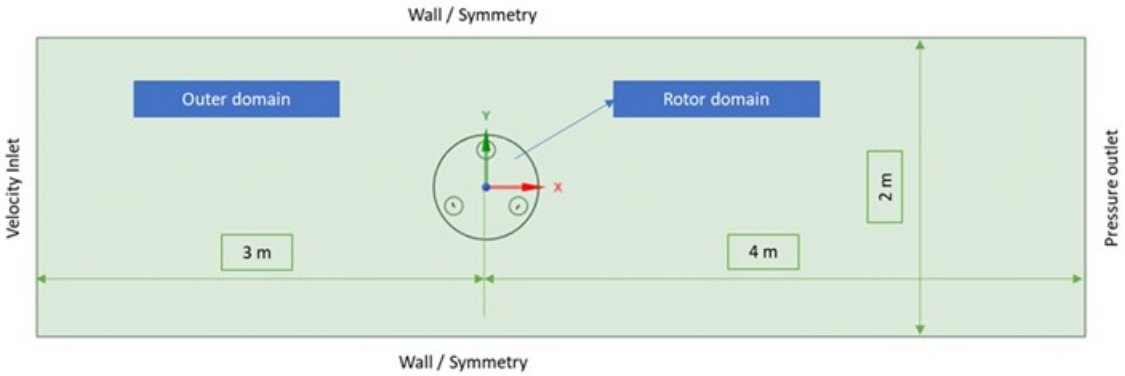

Figure 2.Geometry and boundary conditions for CFD simulations.

To ensure that wind turbulence is well captured in the areas close to the wind turbine blades, it is necessary to mesh these areas more finely. For this purpose, a subdomain is defined around each of the three blades. In this case, the moving part of the mesh, that is, the rotor, moves according to the wind, which in turn is affected by the rotor itself. For this reason, since the rotational velocity of the wind turbine is to be obtained as a function of wind velocity, the 6DOF model must be used. In this model, the inputs have been the mass and moment of inertia of the rotor. To calculate them, the blade material has been selected as carbon fiber. Finally, the CO_2 has been set as a simulation fluid, however, its properties will vary depending on pressure

and temperature, where the data has been obtained from the National Institute of Standards and Technology.

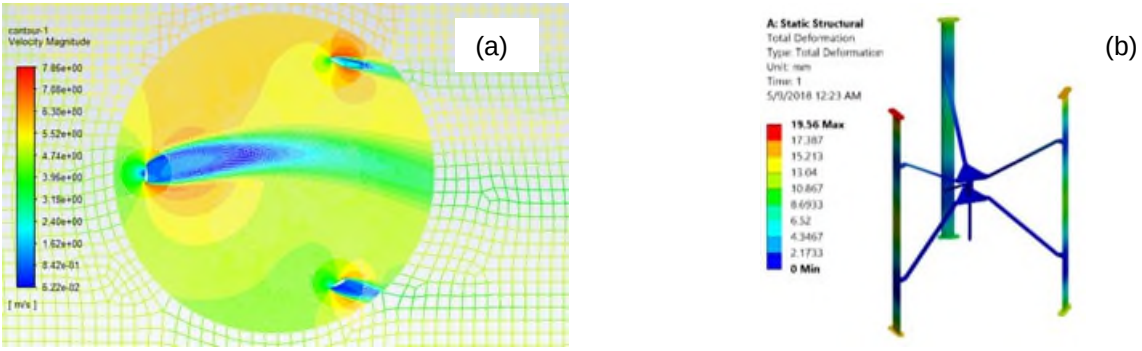

Figure 3. Contour of velocities at two different instants obtained using the 6DOF model. a) Contour of velocities at two different instants obtained using the 6DOF model. b) Structural analysis of the designed turbine.

The CFD simulations have been divided into several packages depending on the results and conclusions to be drawn: Self-starting, Testbench, Mars, and Structural. In the “self-starting” package, the objective has been to determine the minimum necessary conditions that are needed for the wind turbine to operate. The aim is to validate if the turbine is capable of self-starting and generating sufficient torque under the most unfavorable conditions. The objective of the “Testbench” package is to simulate the rotor under test bench conditions, while the “Mars” package is to simulate the rotor under real Martian conditions. Finally, the objective of the “Structural package” is to see if the wind turbine can structurally withstand the loads expected during its operation on Mars (launch loads are not considered within the space of the current work). Therefore, the rotor is subjected to the most extreme conditions both on the test-bench and on Mars to obtain the rotational speeds and the forces exerted by the wind. The table in Figure 4 shows the results obtained in all simulations in terms of rotational speed and self-starting time. In addition, the acceleration graph of the simulation package "Test-bench" is shown in Fig. 4.

Package	ID	Scenery	Angular velocity (r.p.m)	Self-start time (min)
Self-start	Self_01	Mars	12,4	13
	Self_02	Test-bench	10,8	12,2
Test-bench	TB_01	Test-bench	10,8	12,2
	TB_02	Test-bench	40,6	40
	TB_03	Test-bench	78,9	15,7
	TB_04	Test-bench	114,5	12,8
	TB_05	Test-bench	117,7	14,3
	TB_06	Test-bench	138,2	7,5
Mars	InS_01	Mars	264	5,83
	Ins_02	Mars	116	13,3
	Ins_03	Mars	168	5
	Ins_04	Mars	168	5
Structural	SF_01	Mars	384	2,3
	SF_02	Mars	433	2,2
	SF_03	Test-bench	114,5	12,8
	SF_04	Test-bench	138,2	7,5

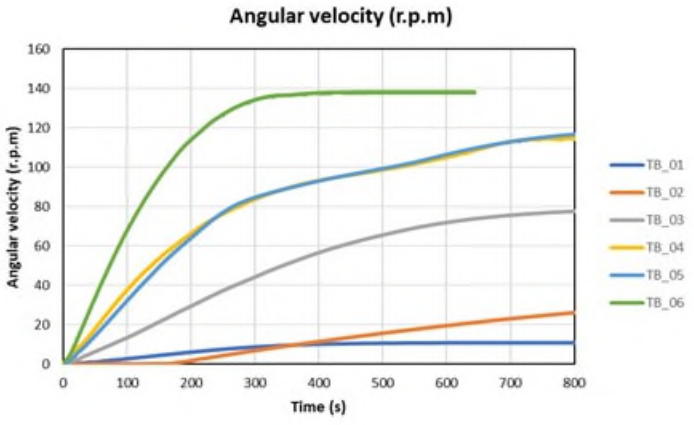

Figure 4. Rotational velocities and self-starting time for all the simulations carried out and acceleration graph for "Test-bench" package.

It is validated, that the turbine accelerates until it reaches a constant speed, the time it takes to accelerate being the self-starting time.

Triboelectric Generator

Triboelectric effect operational princinples

The triboelectric generation consists of the electric charge transfer between two materials by friction. In the triboelectric configuration of this work, the rotor material will be prone to become positively charged, while the stator material will be prone to become negatively charged. Based on their triboelectric properties, their ability to lose or gain electrons, aluminum (Al) and polytetrafluoroethylene (PTFE) can be considered for the rotor and stator, respectively. The functionality of TEGs is based on triboelectrification (or contact electrification) and electrostatic induction phenomena. The TEG architecture involves two materials with different charge affinity during contact. The freestanding TEG has more advantages than a contact separation mode as it does not require attachment to the moving triboelectric layer with an electrode and a lead wire. In this work, a freestanding mode has been selected as generator architecture.

To further assess the effect of the geometry and dimensions of the triboelectric generator on the generation of the electrostatic potential, finite element simulations have been performed using FEMM (Finite Element Methods Magnetic) software. It must be remarked that only the electrostatic induction phenomenon has been simulated, assuming a given charge density generated by the friction between rotor and stator. Parametric variations of the following geometric parameters have been simulated as can be seen in Fig. 5:

- N: Number of poles (blades), affecting the cross-section of each pole
- t: stator conductor thickness
- g: gap between insulated stator conductor sections

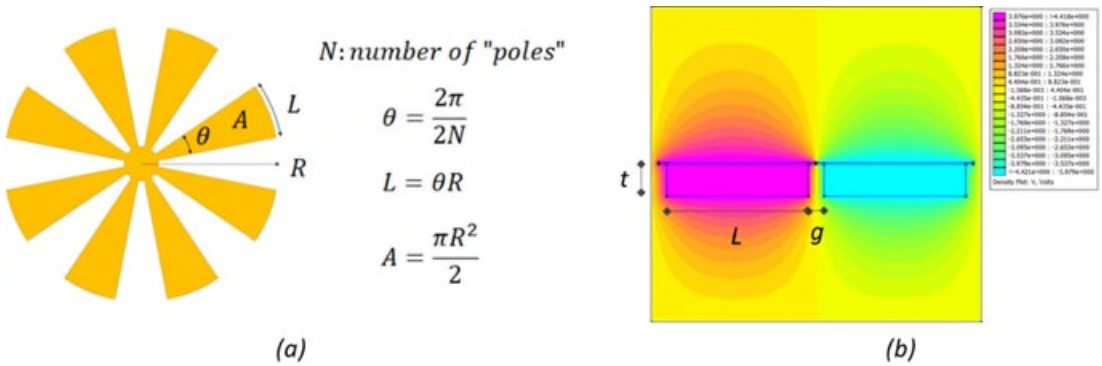

Figure 5. Parameters for electrostatic simulations and simulation example.

In this scenario, a grating structure is manufactured in the rotator and stator where the output power depends on the material selection, contact surface characteristics, grating number and electrode gap.

The simulations gave the results shown in Fig. 6. Fig. 6a shows the simulation results obtained when varying the thickness of the conductors at the stators where the electrostatic potential is induced. Fig. 6b shows the simulation results with further varying of the gap from 5 to 30 mm.

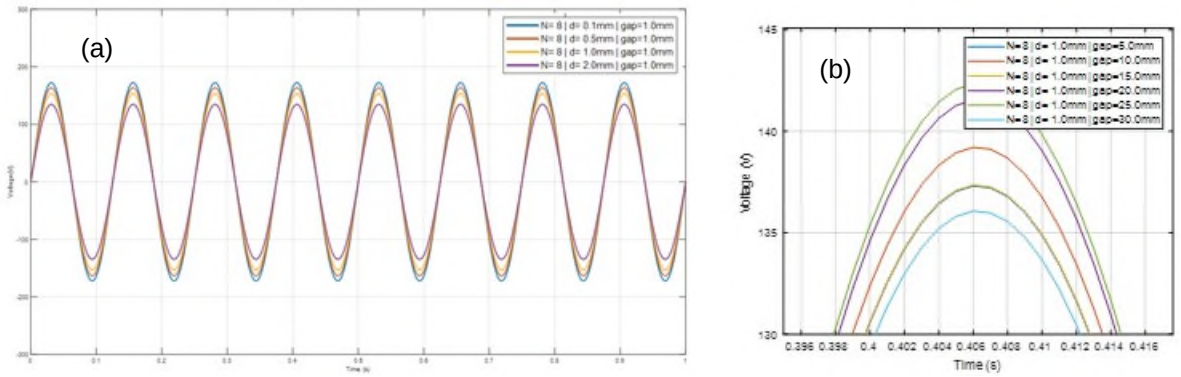

Figure 6. Results achieved with the electrostatic simulations. a) Output voltage vs. conductor width. b) Output voltage vs. gap length.

It has been observed that, for a given charge density, the amplitude of the induced voltage is independent of the number of poles. At the same rotational speed, the frequency of the induced voltage increases with the number of poles. It is assumed that a higher number of poles will result in a more homogeneous charge distribution by friction between the rotor and stator. On the other hand, if a homogeneous charge distribution is assumed for the electrostatic induction simulation, the effect of the number of poles cannot be appreciated. It can be observed that the induced voltage amplitude decreases with increasing conductor thickness. This might be caused by the electric charge concentration on the surface of the conductor (in a very thin layer of the order of nm) and is not affected by the considered conductor The electric field generated by the electric charge on the triboelectric surface decreases with distance and the smaller the thickness of the conductor, the greater the electric field inside the conductor and the greater the induced voltage. It can be observed how the amplitude of the induced voltage starts increasing as the gap between conductors increases, but at a certain point the effect is reversed. On one hand, as the gap between conductors increases, the conductors lie within more intense electric field regions; but on the other hand, the area of the conductors will directly affect the distribution of electric charges inside the conductors. Thus, for the final configuration, the best equilibrium between the gap and conductor area will have to be searched.

Tribopair selection

The TEG concept could harvest both low and high wind speed which made it very attractive for energy harvesting on Mars, with a broadband external wind speed range. It has required the use of advanced triboelectric materials that have a combination of excellent tribological performance (low friction and wear), mechanical (impact resistance), triboelectric properties (triboelectrification and interfacial conductivity), and energy generation density under those extreme conditions, under a freestanding mode.

The pre-selection of these materials, which will be considered as rotor and stator components of the TEG, has been validated by performing pin-on-disc tribological tests under low pressure conditions P=6 mbar and CO_2 environment, as shown in Fig. 7a. The test conditions considered have been: Contact pressure of 11 MPa, a stroke of 3 mm and a sliding velocity of 3 mm/s. Test duration was fixed to 80000 s after preliminary trials which were performed to assure the wear scar detection via optical and confocal microscopy. Friction evolution was also analyzed during the tests. The materials considered for the pin were PTFE and TFM®, a molecularly modified virgin PTFE, which is characterized by a better load carrying capacity, lower gas permeability, and better mechanical properties than the virgin PTFE. For the counterpart (disc), both uncoated and H-DLC (Diamond Like Carbon) coated Al 6082-T4 alloy were considered.

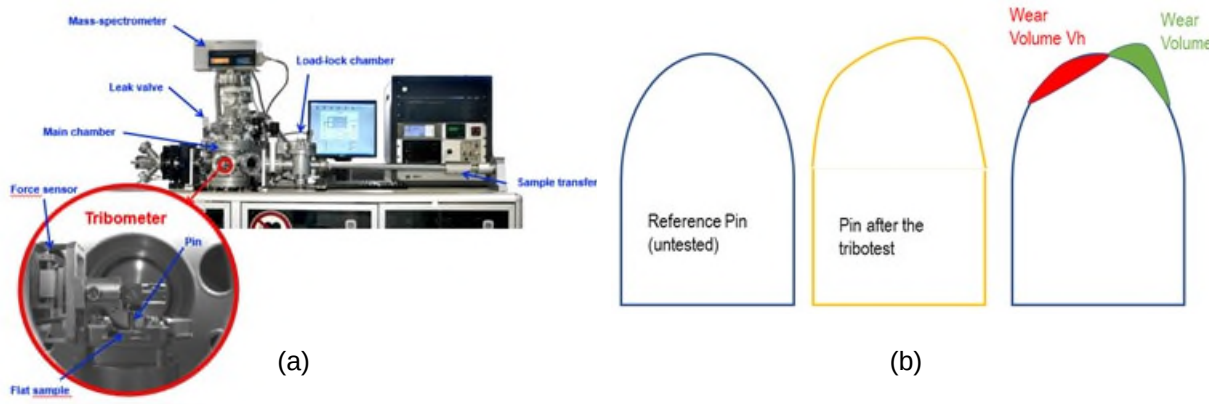

Figure 7. Tribological tests setup. a) Ultra Hight Vacuum tribometer used for tribological tests. b) Representation of the wear volume of the Pins determined via confocal microscopy.

The wear volume of the Pin after the tribological test has been calculated via confocal microscopy, obtaining the hole volume (Vh) and peak volume (Vp), according to the diagram presented in Fig. 7b. The analysis of the wear scars has been carried out via optical and scanning electron microscopy, including compositional analysis by energy dispersive x-ray spectroscopy. The selection of those materials as potential candidates for TEG has been done based on previous research studies where the use of PTFE and a-C:H DLC as dielectric materials provided better tribological and triboelectric behavior than the materials considered as “gold standard” for this application (PTFE and Aluminum) [21][22].

According to previous research studies, high hydrogen content (H>30%) DLC coatings with moderate hardness (5—15 GPa) values might be the best candidates to reach super lubricity and low wear properties against PTFE under Mars environmental conditions [23]. Hence, different a-C:H DLC coatings have been deposited from the PECVD technique by varying C_2H_2 and bias voltage application to obtain high hydrogen content films. 5 Pa pressure and -300V bias voltage process parameters have been selected to achieve the best characteristics in terms of hydrogen contents and mechanical properties of all deposited coatings. Fig. 8a shows the cross-section SEM micrograph of the a-C:H DLC coating selected for tribological tests.

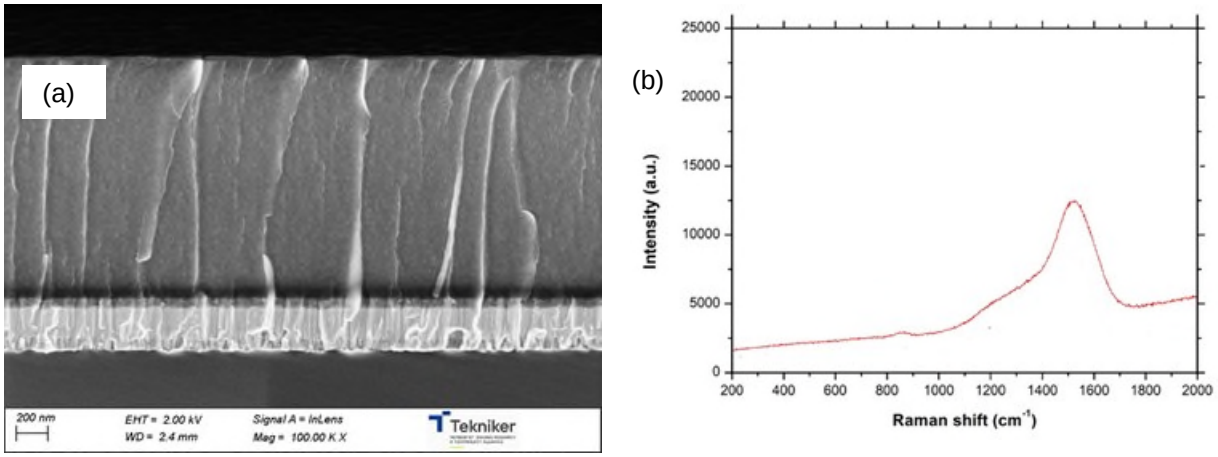

Figure 8. DLC developed for this work. a) Cross section SEM micrograph of a-C:H DLC film by PECVD i4. b) Raman spectra of DLC films developed.

Raman spectroscopy has been considered an indirect tool to measure hydrogen content on the a-C:H DLC film. A higher PL signal and G peak shift towards more negative values is an indication of higher hydrogen contents. If G position lies at 1530 cm^{-1} or lower, it can be concluded that the coating has hydrogen content higher than 35%. Fig. 8b shows the Raman spectra of the DLC produced for the tribological tests. As

indicated in Table 2, the G position lies at 1523 cm-1(corresponding to H%>40%) and a hardness value measured via nanoindentation has been 11GPa.

Table 2. Summary of Raman and Nanoindentation results of the a-C:H DLC considered for tribological tests.

Sample	a-C:H DLC
G peak intensity (a.u.)	>10k
G position (cm^{-1})	1523
Hardness (GPa)	11
Estimated H(at%)	40+

Fig. 9 and 10 show the confocal microscopy characterisation of PTFE pins before and after tribological tests, considering uncoated Aluminum and H-DLC coated Al as counterpart, respectivelly.

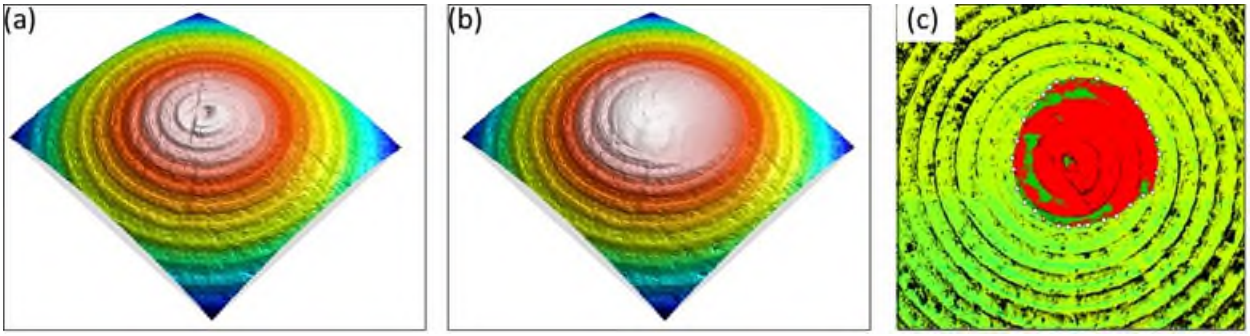

Figure 9: Confocal microscopy characterisaton of the contact surface of the PTFE pin before a) and after b) the tribological test, considering uncoated Aluminum as counterpart. c) wear volume (illustrated in red) of the pin.

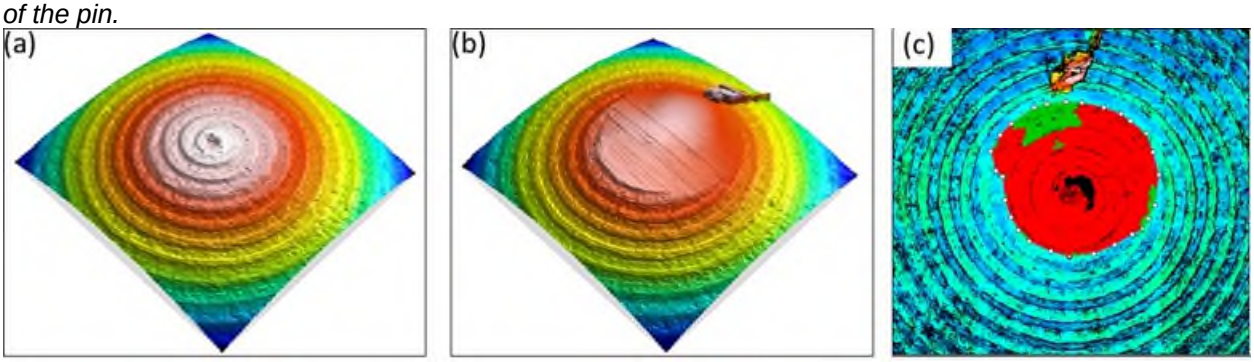

Figure 10. Confocal microscopy characterisaton of the contact surface of the PTFE pin before a) and after b) the tribological test, considering H-DLC coated Aluminum as counterpart. c) wear volume (illustrated in red) of the pin.

Optical microscopy inspection of the PTFE pins after tribological tests showed polymer degradation when uncoated Aluminum is considered as counterpart (Fig. 11c). Thermal degradation of the polymer has been confirmed via EDX showing the lack of Aluminum debris adhesion to the contact surface of the pin. Polymer particle adhesion to the uncoated Al surface is also noticed in Fig. 11a. This adhesion behavior of the PTFE was also observed when H-DLC coated Al is considered as a counterpart. However, no signs of PTFE degradation has been detected (Fig. 12). Hence, in terms of polymer integrity, the use of H-DLC coated Al as a counterpart guarantees better tribological performance.

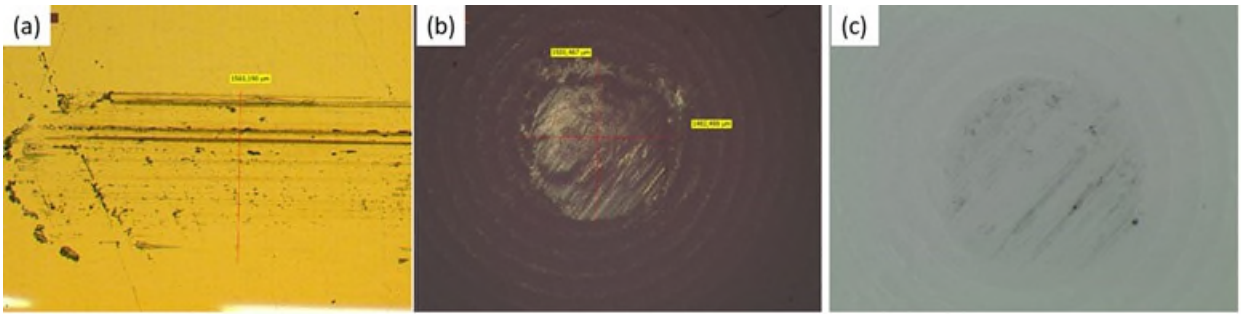

Figure 11. Optical microscopy characterization of the uncoated Al sample (a) and the Pin of PTFE after the tribological test.

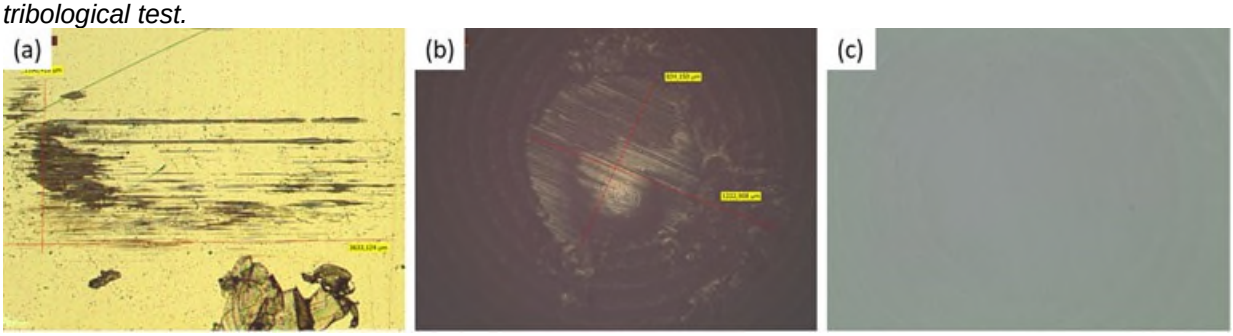

Figure 12. Optical microscopy characterization of the H-DLC coated Al sample (a) and the Pin of PTFE after the tribological test.

Fig. 13 shows the polymeric Pin wear volume after tribological tests as a function of the tribopair selected. According to these results, the selection of TFM® as the polymeric part of the TEG would provide better tribological behavior, characterized by a minimum wear behavior compared to PTFE. The time evolution of the coefficient of friction (COF) also confirms the better tribological performance corresponding to the TFM® + H-DLC coated Al tribopair.

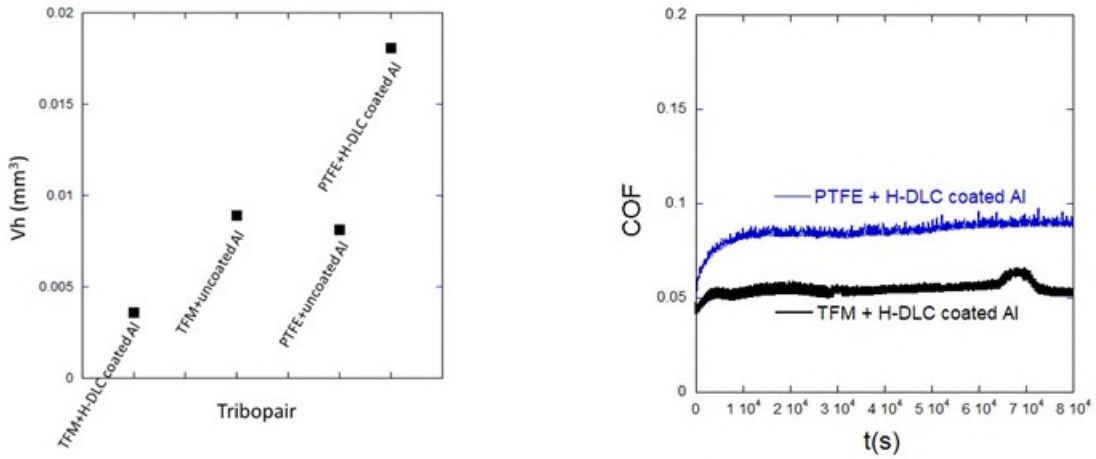

Figure 13. Tribological tests resutls. a) Wear volume after tribological tests (80000 s time duration) for different tribopairs,calculated via confocal microscopy. b) Time evolution of the Coefficient of Friction for selected tribopairs.

The following materials have been selected as the best candidates for experimentation. For polymeric materials: virgin PTFE, TFM® (a molecularly modified virgin PTFE). Then, the Aluminum Al6082 has been chosen as the metallic element for energy generation, and finally, Diamond-like carbon (DLC) coatings have been used as a solid lubricant to improve the lifetime values given by the Aluminum and maintain the

power generation. In this work, 3 DLCs have been developed and tested: a-C:H:W with H> 35 %, a-C:H:W + a-C:H, and a-C:H with H>40%.

Hydrogenated DLC and PTFE have been selected as dielectric pairs due to their highest power density, as well as their potential use as good solid lubricants/films. Abrasion resistance, lubrication ability, durability, and aging effects have been limitations of those materials - these problems have been solved by optimizing the coating architecture (adhesion layer optimization and multilayer architecture to realize residual stresses) and material microstructure (considering PTFE composites) based on lab-scaled tribology test results.

Triboelectrical Tests

After the tribopair selection, the trade-off generator has been designed and manufactured for the triboelectric test to study the performance under different Mars atmospheric conditions (see Fig. 14). To carry out the test, mechanical parts have been manufactured for triboelectric tests. The tribometer has been inserted in a vacuum chamber (called Titan) to carry out the tests.

Tests have been performed for various pressure values, in a sweep from 1000 mbar to 1 mbar with Earth atmospheric composition, vacuum level measurement until 0.2 mbar, and inverted sweep to the first point but in this case with simplified Mars atmospheric composition (CO_2 gas inserted in the chamber).

Figure 14. Test setup. Titan machine to reproduce Mars atmosphere, Falex rotatory tribometer, and manufactured trade-off breadboard to vary the power generation of the TEG.

During the tests, the oxygen ppm have been continuously checked to verify if the atmospheric composition inside the Titan chamber is representative of Mars atmospheric composition conditions. For example, in Earth atmosphere, the O_2 ppm are around 210,000 and at the same pressure but with CO_2 the O_2 ppm are 9419, being CO_2 atmospheric composition 95.51 %. After validation of the test setup, the triboelectrical tests to validate the better operation of the TEG under Mars atmospheric composition and with Earth atmosphetic pressure have been started.

Tests to analyze voltage generation

After the first test, some initial conclusions on the TEG design have been achieved. TEG must be pressurized at least to 1000 mbar pressure with Mars atmospheric composition (95 % CO_2) to ensure a

viable power generation. As is shown in Fig. 15 and Table 3, the improvement at 1000 mbar pressure level is around 30-40 % in comparison with Earth's atmospheric condition. The pressure and the CO_2 are the two main parameters that really affect the output voltage level, which decrease at lower pressure levels (CO_2 effect is also decreased due to the Paschen law). In higher pressure levels, the CO_2 effect on the materials increases the output voltage level (in comparison with air), corroborating the results of the tests with the literature.

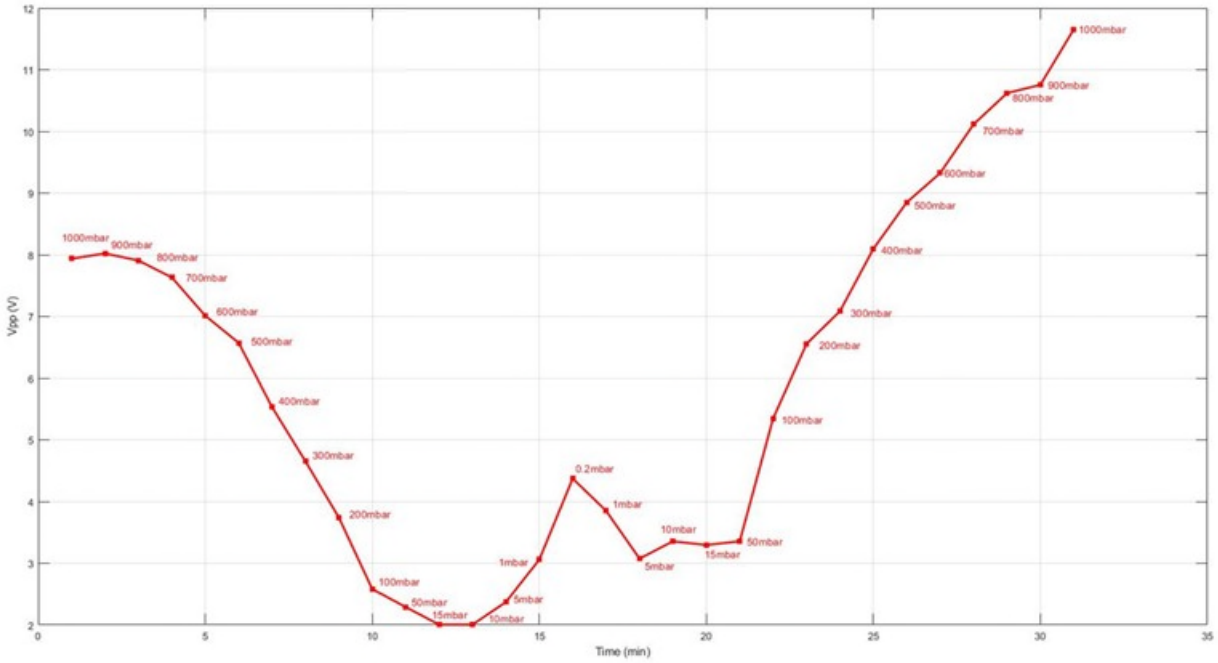

Figure 15. TEG voltage generation with pressure and atmospheric composition changes.

Table 3. Achieved output voltage values and comparison between Earth and Mars atmospheric changes.

Pressure (mbar)	Vpp Earth atm (V)	Vpp Mars Atm (V)	Increase (V)	Increase (%)
1000	7.94	11.65	3.71	31.85
900	8.02	10.76	2.74	25.46
800	7.91	10.62	2.71	25.52
700	7.63	10.12	2.49	24.60
600	7.01	9.33	2.32	24.87
500	6.57	8.85	2.28	25.76
400	5.53	8.10	2.57	31.73
300	4.65	7.09	2.44	34.41
200	3.74	6.56	2.82	42.99
100	2.58	5.35	2.77	51.78
50	2.29	3.35	1.06	31.64
15	2	3.30	1.3	39.39
10	2	3.35	1.35	40.30
5	2.37	3.07	0.7	22.80
1	3.06	3.85	0.79	20.52
0.2	4.37		-	-

The curve in Fig. 15 validates the work hypothesis and sets a roadmap for the generator design (the CO_2 effect is again clearly observed). In this sweep, the output voltage level at 1000 mbar is improved by

31.84%. Thus, to obtain the best working conditions, the generator must be pressurized at 1000 mbar with the Mars atmosphere composition.

In addition, the COF and Torque of the generator have been measured during two tests (Fig. 16). The main goal has been to study if Mars atmospheric composition in Earth atmospheric pressure (CO_2 95%, 1000 mbar) has any significant effect on tribological parameters.

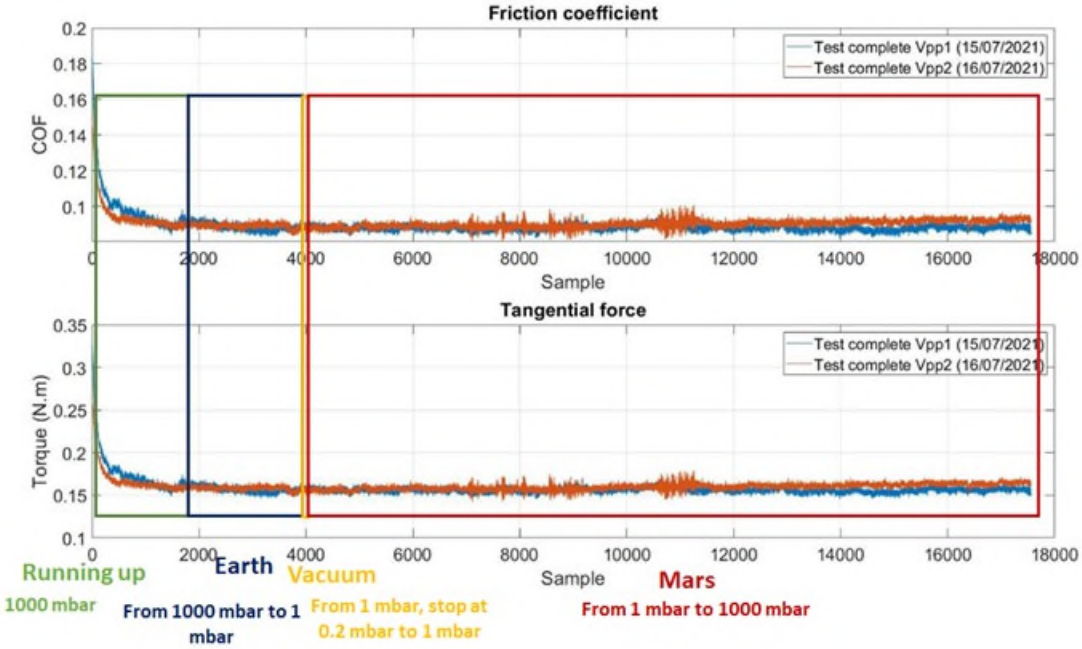

Figure 16. COF and Torque values during two complete sweep tests.

No variation has been observed in these two parameters with the change of pressure, so the conclusion is that the pressure variation doesn't make significant changes in the wear and in the COF of the TEG.

Conclusions

The viability of producing energy with a wind rotary TEG under Mars atmospheric conditions has been demonstrated. The proposed turbine design works properly under Mars wind and atmospheric conditions, with the best tribopair PTFE/DLC (H>40%). The system should be able to work for at least 26 months due to the launch window between Earth and Mars and the tribopair selected should ensure this requirement. In addition, the generator must be pressurized up to 1000 mbar using with Mars atmospheric composition to achieve the higher efficiency in terms of power generation. Based on these results, the wind turbine and the TEG are considered ready for the detailed design phase. The next steps are manufacturing and assembly of the TEG with the turbine, which will then be subjected to testing in a wind tunnel to validate the system under laboratory conditions.

References

[1]. Wang, P., Pan, L., Wang, J., Xu, M., Dai, G., Zou, H., Dong, K., & Wang, Z. L., An Ultra-Low-Friction Triboelectric-Electromagnetic Hybrid Nanogenerator for Rotation Energy Harvesting and Self-Powered Wind Speed Sensor. ACS Nano, 12(9), 9433–9440, 2018. https://doi.org/10.1021/acsnano.8b04654.

[2]. Z.L. Wang et al., Triboelectric Nanogenerators, Hybrid Electromagnetic and Triboelectric Nanogenerator, Chapter 12, Hybrid Cell Composed of Triboelectric Nanogenerator, Green Energy and Technology, Springer International Publishing Switzerland 2016, DOI 10.1007/978-3-319-40039-6_12.

[3]. James, G. H., & Chamitoff, Gregory, D. C. B. (1999). Design and Resource Requirements for successful wind energy production on mars. November 2014.

[4]. Hemmat, A., Nguyen, C., Singh, B., Wylie, K., Zimmerman, D., Kastor, R., & James, G. Conceptual Design of a Martian Power Generating System Utilizing Solar and Wind Energy. Second Annual HEDS-UP Forum, 131–146.

[5]. C. Holstein-Rathlou, P.E. Thomas, J. Merrison , J.J. Iversen, Wind turbine power production under current Martian atmospheric conditions, Mars Workshop on Amazonian Climate 2018 (LPI Contrib. No. 2086).

[6]. Seol, M. L., Han, J. W., Moon, D. Il, & Meyyappan, M. (2017). Triboelectric nanogenerator for Mars environment. Nano Energy, 39(May), 238–244. https://doi.org/10.1016/j.nanoen.2017.07.004.

[7]. T. Matsuyama, H. Yamamoto, Charge relaxation process dominates contact charging of a particle in atmospheric conditions, J. Phys. D. Appl. Phys. 28 (1995) 2418–2423.

[8]. S.Brusca, "Design of a vertical-axis wind turbine: how the aspect ratio affects the trubine's performance," International Journal of Energy and Enviroment Egineering, 2014.

[9]. S. Zanforlin, "Effects of the Reynolds number and the tip losses on the optimal aspect ratio of straight-bladed Vertical Axis Wind Turbines," Energy, no. 148, pp. 179-195, 2018.

[10].X. Sun, "Aerodynamic performance and characteristic of vortex structures for Darrieus wind turbine I. Numerical method and aerodynamic performance.," Journal of Renewable and Sustainable Energy, 2014.

[11].Q. Li, "Effect of number of blades on aerodynamic forces on straight-bladed Vertical Axis Wind turbine," Energy, 2015.

[12].M. Shiono, "An experimental study of the characteristics of a Darrieus turbine for tidal power generation," Electrical Engineering in Japan, vol. 132, 2000.

[13].Blackwell, "Wind tunnel performance data for the Darrieus wind turbine with NACA0012 blades".

[14].G. Bedon, "Computational assesment of the DeepWind aerodynamic performance with different blade and airfoil configurations," Applied energy, 2015.

[15].Klimas, "Tailored airfoils for vertical axis wind turbines," 1984.

[16].Kadlec, "Characteristics of future vertical axis wind turbines," 1982.

[17].J. H. Strickland, "Darrieus turbine: a performance prediction model using multiple streamtubes".

[18].Klimas, "Effgects of blade preset pitch/offset on curved-blade Darrieus vertical axis wind turbine performance," 1981.

[19].T. Friedler, "Blade offset and pitch effects on a high solidity vertical axis wind turbine," Wind Engineering, vol. 33, 2009.

[20].S.H. Ramaswamy et al. “Investigation of diamond – like carbon films as a promising dielectric material for triboelectric nanogenerator” Nano Energy 60 (2019) 875-885.

[21].S.H. Ramaswamy et al. “Development of Highly Durable Sliding Triboelectric Nanogenerator Using Diamond – Like Carbon Films” Tribology Online V15, No.2 (2020) 89-97).

[22].Andersson, J., Erck, R. A., and Erdemir, A. Frictional behavior of diamondlike carbon films in vacuum and under varying water vapor pressure. Surf. Coat. Technol., 2003, 163–164, 535–540.

Mars Sample Handling End-Effector Breadboarding

Isacco Pretto*, Mario Esposito*, Tharek Mohtar*, Stefano Scutti*, Alessandro Bursi*, Massimo Lucia**, Andrea Rusconi**, Guido Sangiovanni**, Davide Nicolis+ and Philippe Schoonejans+

Abstract

A novel End Effector design is presented, developed in the frame of the Mars Sample Return mission preparation. The End Effector is a mechanism that provides manipulation capabilities to the robotic arm onboard the mission lander, and it enables the collection and handling of the sample tubes containing Martian soil specimens, and the ancillary tools onboard the lander. The developed End Effector mechanism operates through the combination of an original passive grasp architecture, and a grasp locking function, which allow for both soft target capture and handling, and high loads application capability. The design and analysis are presented, followed by the integration and test campaign, demonstrating the End Effector performance effectiveness for sample handling, and insertion, extraction and torque application tasks.

Introduction

In the Mars Sample Return mission architecture [1], a Sample Retrieval Lander [2] is equipped with a Sample Transfer Arm (STA), whose primary function is to transfer Martian soil sample tubes, collected by the NASA/JPL Perseverance rover [3] and ESA Sample Fetch Rover from the rovers themselves onto the Mars Ascent Vehicle. The sample tubes collection from Perseverance will be performed either through a dedicated collection tray or directly from the rover bit carousel, according to the latest scenarios.

The STA End Effector (EE) provides the robotic manipulation capabilities to the STA and it is the subject of this paper and of the development and breadboarding activity performed by OHB Italia S.p.A. The activity was conducted by OHB Italia in the frame of the ESA Program STABLE (Sample Transfer Arm Breadboard and Lander Evaluation), with Leonardo S.p.A. as prime contractor of the STA system.

The EE primary function consists in the manipulation of the sample tube containing the collected Martian soil quantity - the Return Sample Tube Assembly (RSTA) - picking it from different locations such as the mission rovers or at different working stations on the lander itself, and handling it through different grip interfaces. This manipulation has to be performed with care, in order not to exceed the force interface limits of the sample tube; nevertheless, the EE is also capable of providing the higher forces required to extract the sample tubes from their storage locations, and insert them at their target location on the orbiting sample canister.

In addition to the sample tube handling, the EE manipulates secondary tools mechanical interfaces, such as a tube collection tray for retrieval from Perseverance, or the lander orbiting sample lid. As reference tool mechanical interface, OHB Italia proposed a custom-designed grapple fixture, which is compatible with the sample tube grip interfaces, but also allows for the application of higher mechanical loads.

The target capture is performed in cooperation with the Sample Transfer Arm, which provides the positioning and the proximity maneuvers to the EE. In this phase, during the target capture sequence, the EE is able to accommodate residual misalignments, simplifying and supporting the overall operation. For this reason, the EE functionality is provided with a soft-capture capability, inherently passive, and a hard-

* OHB Italia S.p.A., Milano, Italy; isacco.pretto@ohb-italia.it
** Leonardo S.p.A., Nerviano, Italy
+ ESA ESTEC, Noordwijk, The Netherlands

capture configuration, which provides the grasp locking after the misalignments are recovered. The passive stability of the capture conditions, also allows for a secure grasp even in the event of a power loss.

Design and Analysis

The EE layout and the sample tube CAD models are displayed in Figure 1. The interaction of the EE with the sample tube can be performed through two different mechanical interfaces: the end-grip, located at the sample tube head, and the body-grip, located at the tube stem. The EE architecture is organized in two sections: the actuator housing, and the gripper mechanism. The housing intergrates the flange for the mechanical interface with the robotic arm, and hosts internally the servomotor assembly, and externally the mechanism control board. On the outer side, the gripper section is made of the target grasp jaws, the mechanical guides to the jaws motion, and the inner mechanical transmission.

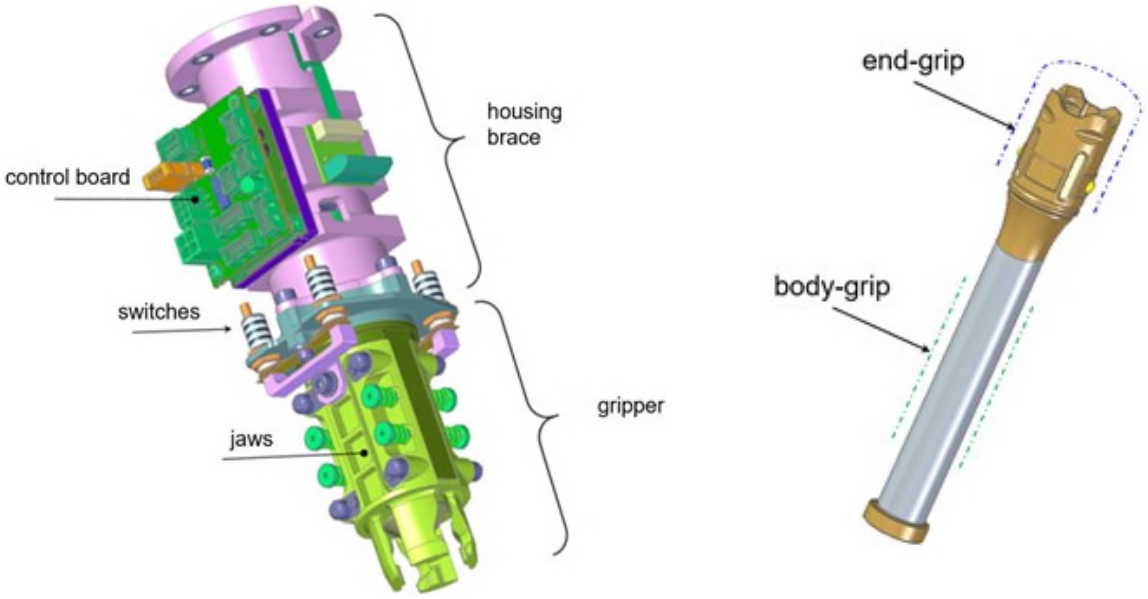

Figure 1. OHB-I End-Effector and JPL RSTA (RSTA model courtesy NASA/JPL-Caltech).

Motor housing.
The EE cross section is displayed in Figure 2. The servomotor actuation and control unit is realized through an aluminum tubular support. The actuator and driver are selected from the Maxon components, and consist of an EC32-flat DC motor, coupled with a GP32 planetary gearhead, 3 stages, controlled through an EPOS4 control board.

The most original setup is embedded in the gripper mechanism section, which core is the cam shaft, providing the opening force actuation to the jaws. A set of 4 microswitches are positioned at the intermediate connection between the two sections, providing the gripper closure signal to the control board. A conical probe element provides the fitting geometry and centering to the sample tube head. The overall envelope of the EE fits in a cylinder of size Ø 70 × 200 mm (0.8 ℓ).

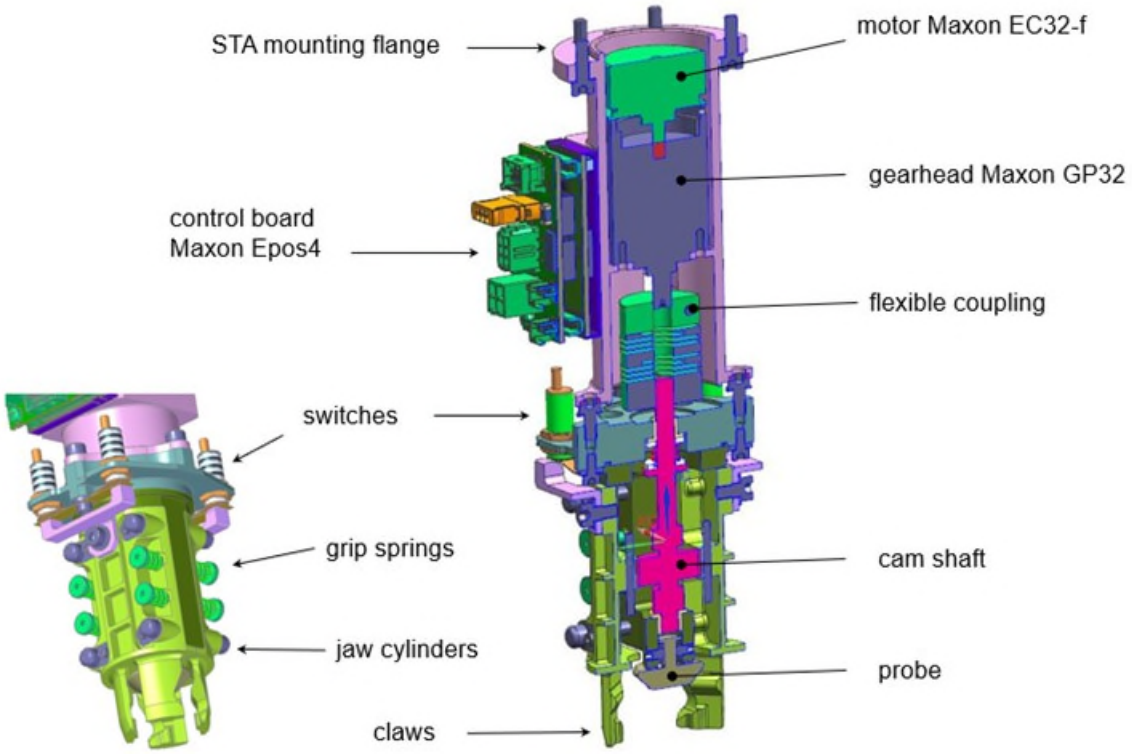

Figure 2. End Effector Cross Section.

Actuation.

The EE actuation and control chain is represented in the block scheme of Figure 3. The control board receives power from the STA electrical interface, commands the motor and receives the motor hall sensors and the microswitches signals. The gearhead reduces the output speed and increases the torque available at the cam shaft.

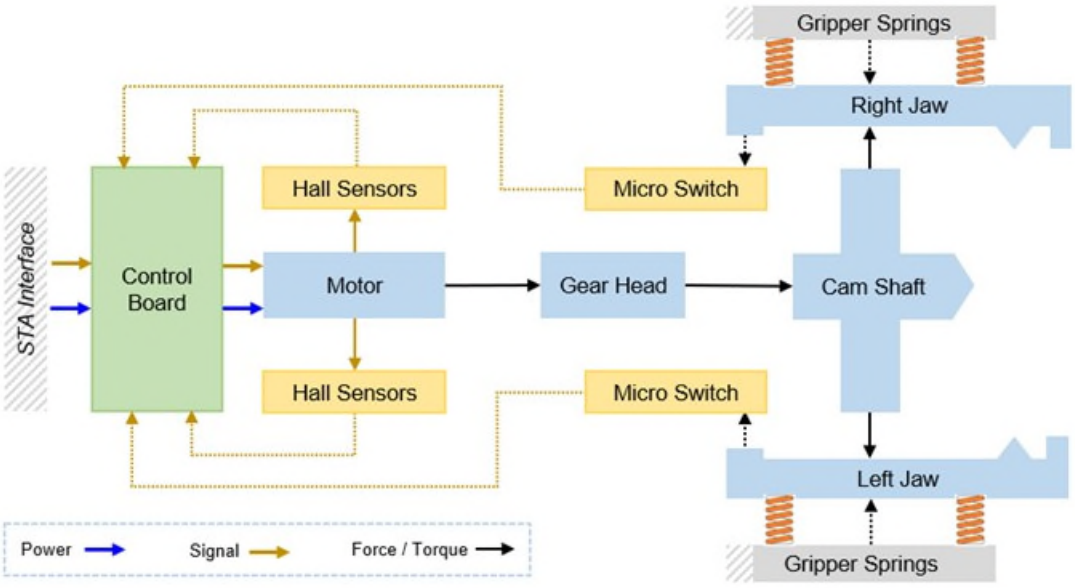

Figure 3. Control, Actuation, and Sensors Chain.

Gripper mechanism.
The gripper mechanism is composed of two grasping stainless steel jaws, which can each displace linearly of 6+6 mm outwards, switching from the closed to the open configuration. The linear displacement is guided by a set of 4 stainless steel pins sliding over PTFE-coated stainless steel bushings (Figure 4).

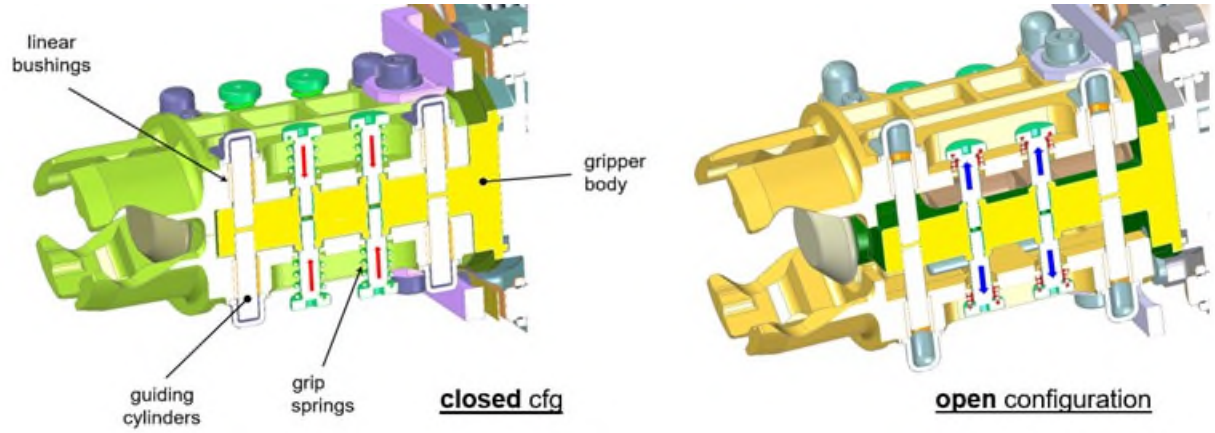

Figure 4. Gripper Springs and Guiding Cylinders.

The jaws are normally closed, thanks to a set of eight helical springs providing the soft compression load between their outer surface and the gripper body part. This load is calibrated in order to provide a contact force below 10 N when manipulating the sample tube. The jaws opening is actuated through a cam profile machined on the cam shaft.

The actuation torque is supplied by the motor gearhead through the interposition of a flexible coupling. The flexible coupling allows for internal misalignments recovery and ensures no undesired bending, normal or shear loads are back transferred to the gearhead.

The stainless steel cam shaft itself is supported in two points through a pair of flanged PTFE-coated stainless steel bushings, and is axially preloaded through a compression wave spring. Diamond-Like Carbon coating is applied to both the cam shaft and the gripper jaws in order to increase the contact hardness for improved cam-contact performance and improved jaws grasping wear resistance.

Laterally to the cam profile, two locking hooks are machined in the cam shaft. The hooks have the function of locking the mechanism at the completion of the grasp.

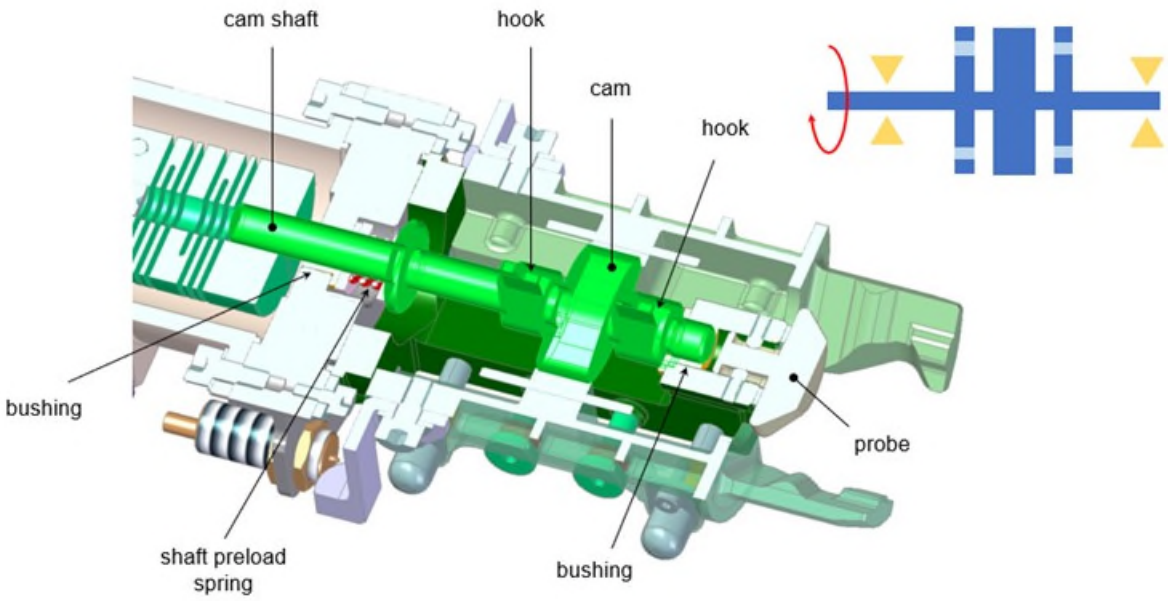

Figure 5. Gripper Cross Section and Cam Shaft Detail.

The jaws opening condition is displayed in Figure 6. The cam profile is rotated up to 90 deg and slides against the flats pushing the jaws internal side; the jaws are then displaced externally sliding along the guiding cylinders, and compressing the gripper retain springs.

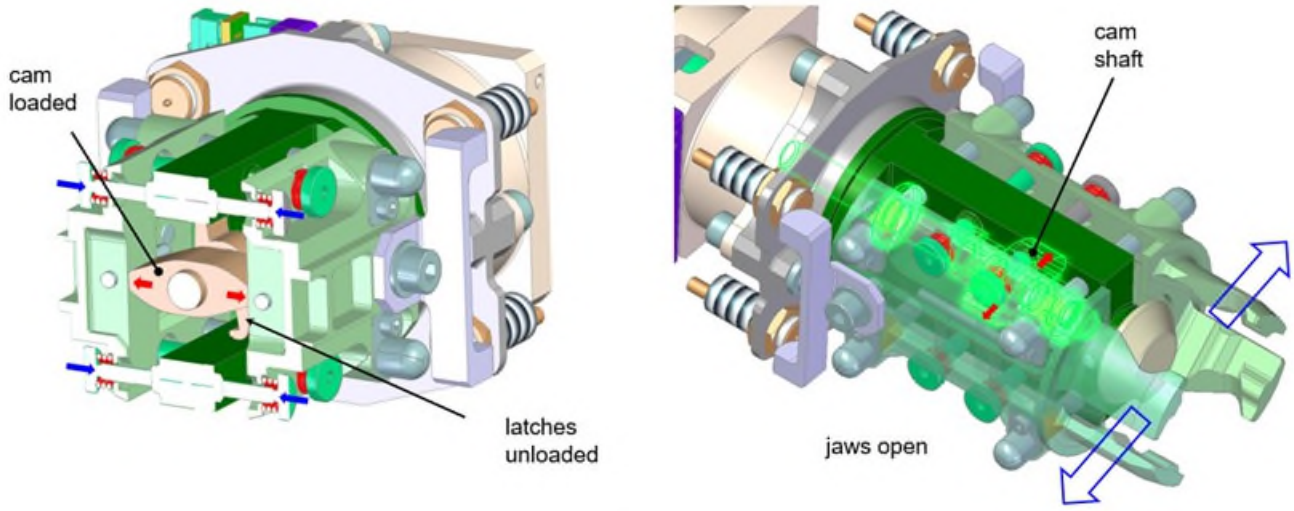

Figure 6. Open Configuration.

In the closure movement (Figure 7), the cam profile is rotated backwards down to 12 deg. At this working angle, the jaws unload the cam profile by reaching their endstops at the gripper body. The grasp closure force is always granted, since it is inherently passive and provided by the gripper springs. Therefore, it does not require electric power and is robust against incidental power losses. The passive closure architecture also allows for the jaws to adapt to the target geometrical constraint, providing roboustness against misalignment and surface uncertainties, such as those due to dust interposition at the grip interfaces. Once the jaws endstop is reached, the microswitches provide the closure signal.

At this moment, the further cam back-rotation can be commanded to the 0 deg homing angle, allowing the engagment of the locking hooks with the two latching stainless steel pins, fixed at the jaws internal side, laterally to the cam flat feature. The engagment of the locking hooks ensures the final secure and rigidized grasp.

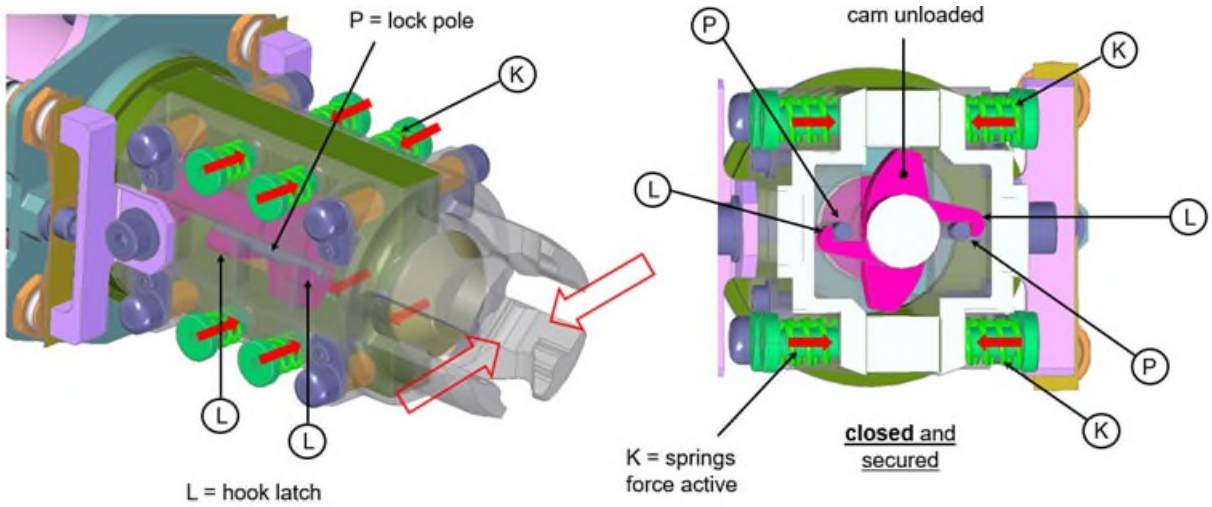

Figure 7. Closed Configuration.

Jaws

The jaws ends are shaped in four claws which comply with the sample tube handling grips (Figure 8). Since both the sample tube body-grip and end-grip present an outer cylindrical shape, the principle of the cylinder-wedge accomodation is implemented, in order to guide the capture of the cylindrical features: a cross-wedge guides the the end-grip capture, while the body-wedge guides the body-grip capture.

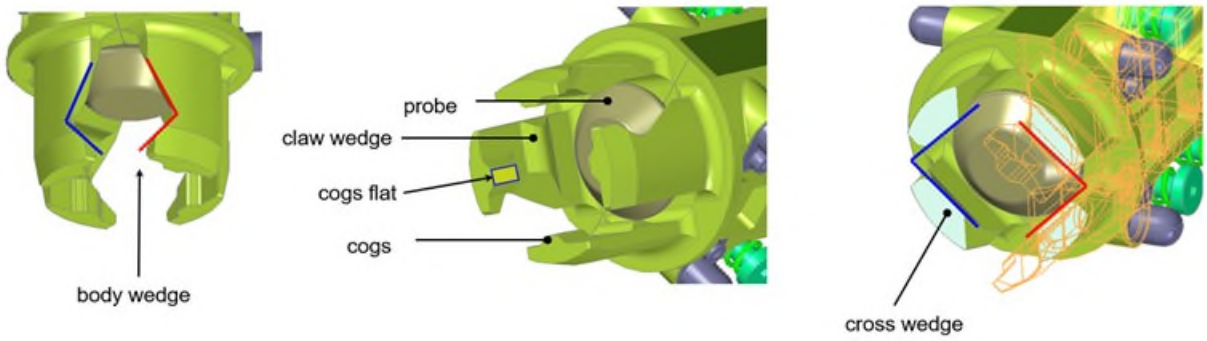

Figure 8. Claws Design.

The sample tube body-grip nominal grasp is displayed in Figure 8. The grasp closes between the jaws body-wedge and the gripper axial probe.

Figure 9. Body-Grip Grasp (RSTA model courtesy NASA/JPL-Caltech).

The grasp of the sample tube body-grip is achieved in subsequent steps (Figure 11). At first the EE is aligned to the sample tube axis through the cross-wedge mating with the tube end-grip cylindrical surface, the axial probe contact provides the alinemnt along the length direction. Only the soft grasp mode is active in these phase, providing the touch of the tube outer surface. Afterwards, the EE is rotated through the arm wrist along the clock direction, until the key protrusions at the claws tips engage with the axial and radial grooves on the sample tube. The engagement is automatic thanks to the action of the gripper soft springs. At this point, the microswitch signals inform of the closure state, and the grasp rigidization can be commanded through the locking hooks engagement.

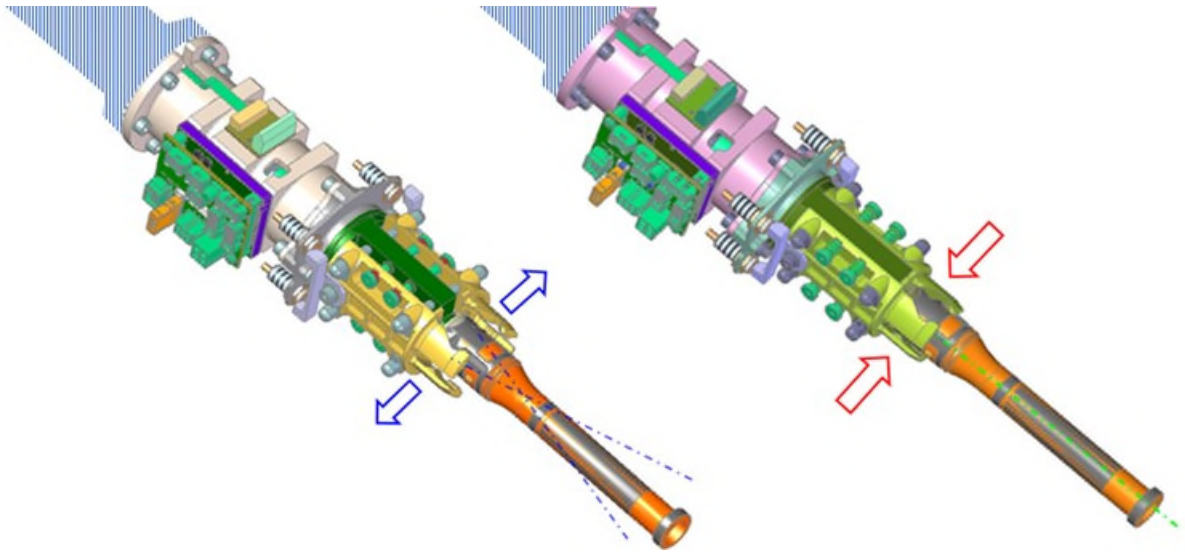

Figure 10. Tilt Alignment (RSTA model courtesy NASA/JPL-Caltech.

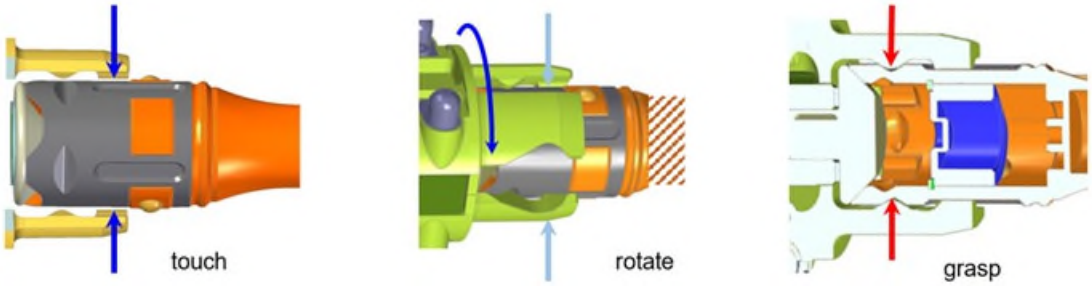

Figure 11. Clock Alignment (RSTA models courtesy NASA/JPL-Caltech)).

Actuation analysis

The actuation torque available at the cam shaft is of 2.3 Nm. This torque guarantees a motorization factor larger than *2* in accordance with the ECSS standards (
Figure *12*).

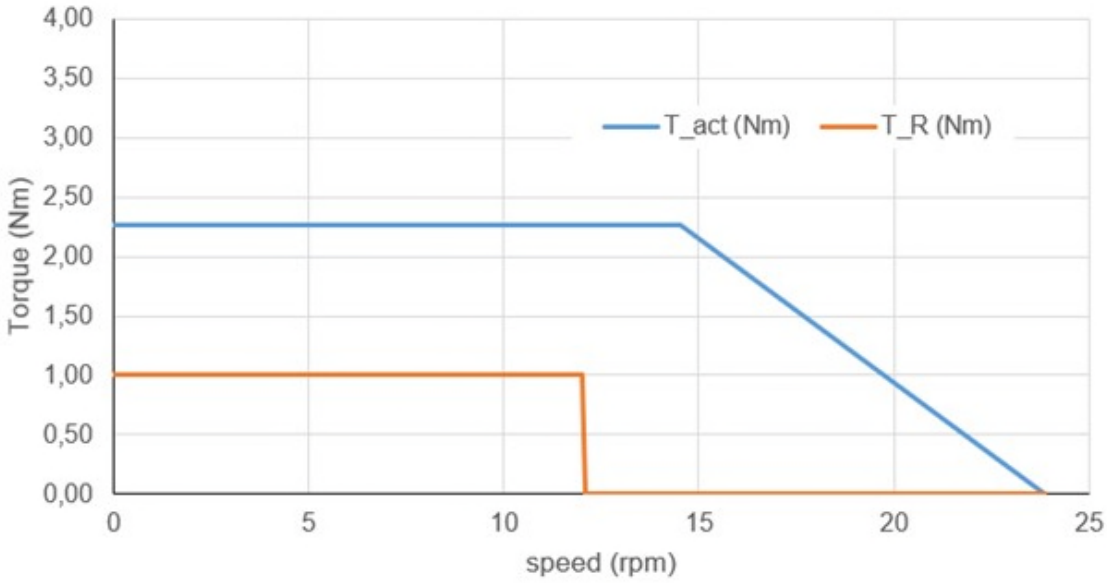

Figure 12. Actuation and Resistant Torques.

Tools Interface

In addition to the sample tube manipulation, the End Effector is capable of handling additional tools which could be adopted in the mission architecture, such as the tube collection tray, and the orbiting sample lid. A design was outlined for the tool interface, named as grapple fixture (Figure 13). The design of the grapple fixture incorporates different grip features for full compatibility with the sample tube grips, and allows for the application of higher mechanical loads. The soft handling is again convenient during the target capture phase, while the full load application can be exerted after grasp rigidization.

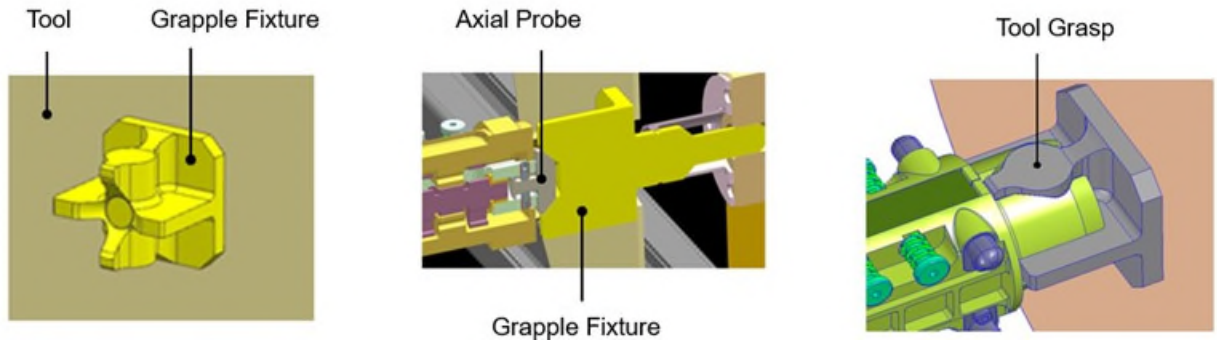

Figure 13. Grapple Fixture Design and Grasp.

It shall be noticed that, once the grasp rigidization is completed, the actuation chain is unloaded, while the load path is absorbed by the EE structural elements.

Integration and Tests

Integration

The integration is carried out in two sub-assemblies. At first the gripper mechanism is integrated, including manual check of the cam operation jaws opening torque measurement through dynamometer read. Then the actuator housing is assembled, including servomotor, microswitches, and control board. Afterwards, the EE is completed by connecting the two blocks (Figure 14). Functional checks are carried out for motor actuation control, and signals acquisition. Motor torque and resistant torque are measured through current acquisition, with confirmation of compliant actuation margins.

The EE overall mass is 1.1 kg, while the peak power absorbed by the motor during the opening maneuver is of 1.40 W. The energy consumption is very low since the torque effort is necessary only for the opening maneuver while the closure and grasp is passively actuated through the gripper springs.

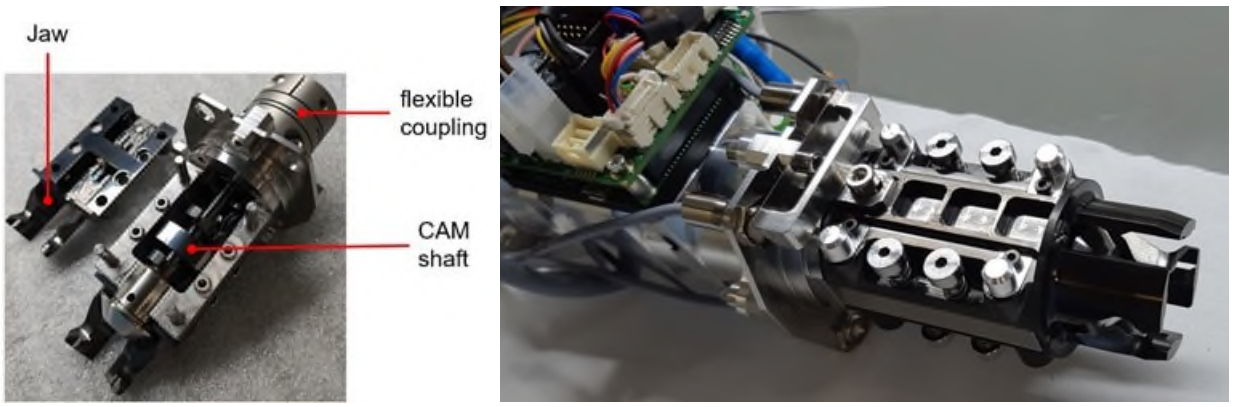

Figure 14. End-Effector at Integration.

Capture tests

Capture tests are performed for the sample tube end-grip and body-grip, and the tools grapple-fixture. The end-grip capture (Figure 15) is carried out considering misalignments up to ±3 mm and ±5 deg. The sample tube dummy is placed in the capture volume of the EE, which grasp soft-closure force aligns the grip to the tube axis. A relative axial displacement allows the axial probe to contact the tube head. Then, a relative

clock rotation is provided until the jaws automatically engage with the tube axial grooves. Microswitch closure signals are detected, and the secure grasp rigidization is commanded to the locking hooks. The correct performance of the end-grip capture and locking operations was verified.

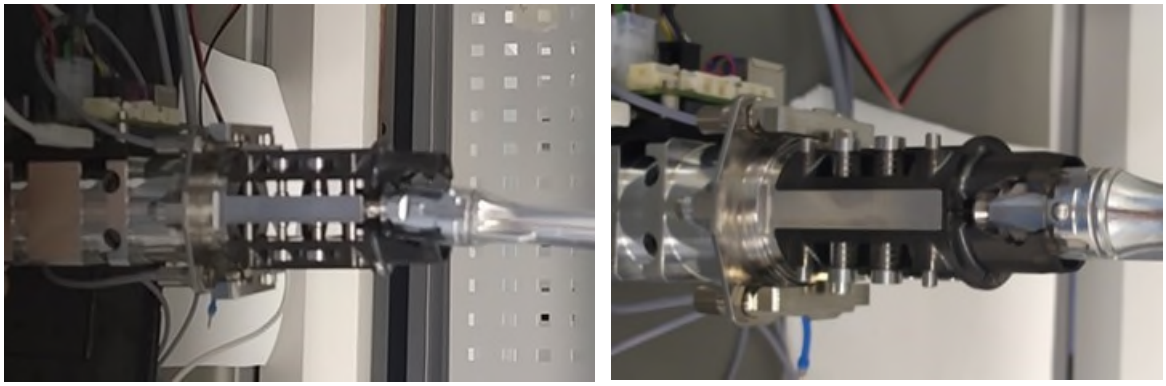

Figure 15. RSTA end-grip capture test (RSTA models courtesy NASA/JPL-Caltech).

The body-grip capture test was then carried out (Figure 16) considering target misalignments up to ±3 mm and ±5 deg. The sample tube dummy is presented to the EE with transverse orientation and residual misalignment; the EE soft-closure then aligns the tube body axis. Microswitches closure signals are detected, and the secure grasp rigidization is commanded to the locking hooks. The correct performance of the body-grip capture and locking operation was verified.

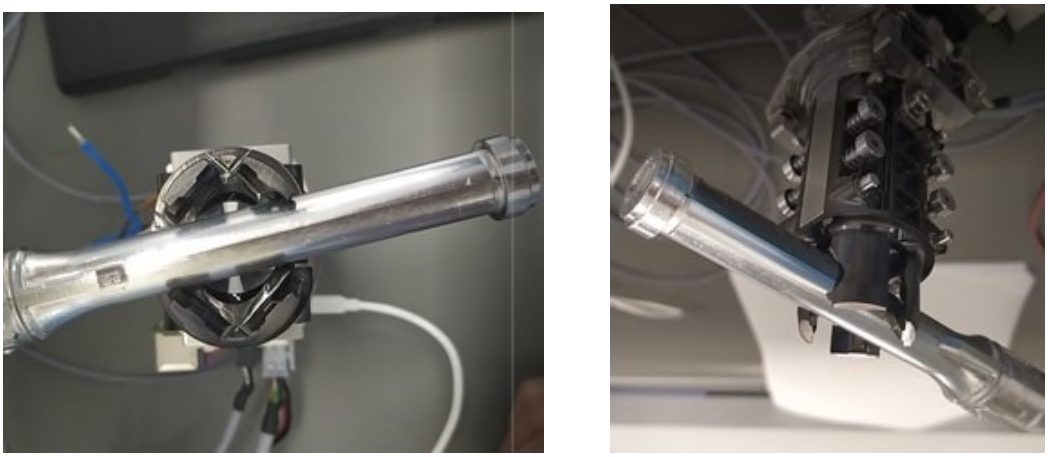

Figure 16. Body-grip capture test (RSTA models courtesy NASA/JPL-Caltech).

Similarly, the grapple-fixture capture was tested (Figure 17), proceeding with the misalignment, capture, and locking sequence. Capture and locking performance were confirmed.

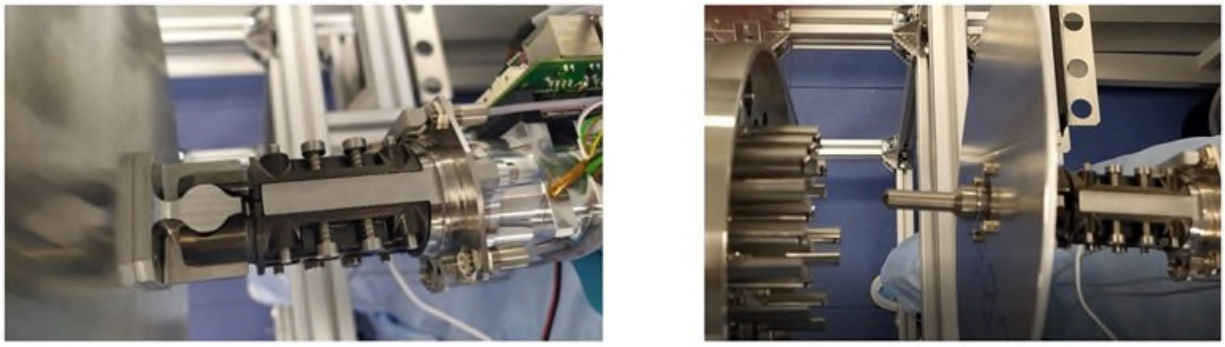

Figure 17. Grapple-Fixture Grasp of the OS-Lid Dummy.

Insertion and extraction tests followed the higher load tests, including: sample tube insertion test, sample tube extraction test, OS-Lid insertion test, and OS-Lid extraction test. The tests were performed against custom-designed ground equipment restaint interfaces. The secure grasp locking confirmed the robust performance of each operation (*Figure 18*).

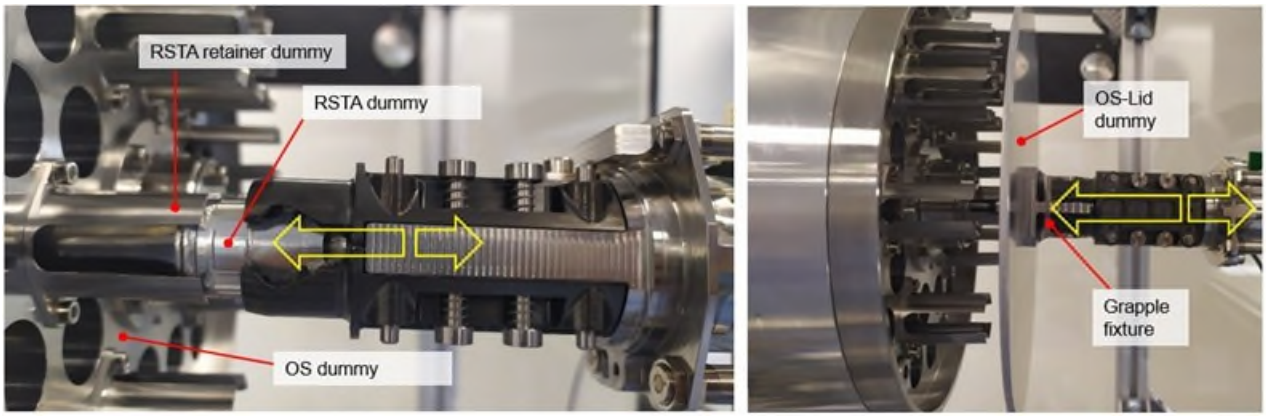

Figure 18. RSTA and OS-Lid Dummy Insertion and Extraction test.

The most significant engineering budget and performance features of the EE breadboard are summarized in Table 1.

Table 1. End-Effector Features.

Quantity	**Value**
EE Envelope	Ø70 mm × 200 mm (0.8 ℓ)
EE Mass	1.1 kg
Peak Power	< 5 W
Soft Capture Grasp	10 N
Secure Grasp Locking	✓
Axial Force Capacity	> 350 N
Shear Force Capacity	> 250 N
Bending Moment Capacity	> 20 Nm
Torque Capacity	> 60 Nm

Conclusions

The sample handling End Effector breadboard design and tests were presented. The system study and development led to a compact End Effector design. The EE is capable of both soft-capture handling and withstanding the higher interaction loads due to insertion, extraction, torque and mass loading operations. The EE is also capable of handling additional tool interfaces, for which a custom design grip interface was designed and tested.

The EE architecture relies on an original passive grasp concept, in which the gripper jaws are normally closed through a set of compression springs. The actuation chain operates a cam shaft opening the gripper jaws against the springs force. The EE architecture is capable of handling target misalignments and is equipped with a mechanical locking feature which secures the grasp once the correct capture is confirmed by the sensor setup.

The design was realized and integrated, and the EE test campaign confirmed the performance with respect to tube sample and the ancillary tools capture, extraction, insertion and release operations.

References

1. B. K. Muirhead, A. K. Nicholas, J. Umland, O. Sutherland, S. Vijendran, “Mars Sample Return Campaign Concept Status”, *Acta Astronautica*, Volume 176, 2020.
2. M. Greco, “Sample Retrieval Lander Concept Overview”, 16th International Planetary Probe Workshop, 2019.
3. M. Silvermann, J. Lin, “Mars 2020 Rover Adaptive Caching Assembly: Caching Martian Samples for Potential Earth Return”, Proceedings of the 45th Aerospace Mechanisms Symposium, 2020.

Lunar Dust: Its Impact on Hardware and Mitigation Technologies

Dorota Budzyń[*], Eóin Tuohy[** ***], Natan Garrivier[**], Timon Schild[**], Aidan Cowley[**], Reuben Cruise[+], Masato Adachi[++], Hossein Zare-Behtash[*] and Andrea Cammarano[*]

Abstract

The finest fraction of Lunar regolith – Lunar dust – has been proven to pose a challenge for surface hardware operations. This paper discusses the impact of Lunar dust particles on various hardware and explains the reasons for such negative influence in order to better understand possible solutions. This work focuses on presenting a classification of viable dust mitigation methods and examples of such technologies. A variety of approaches from active, passive, and implicit dust mitigation solutions are presented to showcase and evaluate available technologies for design engineers working on Lunar hardware.

Introduction

NASA and its international partners are planning to land astronauts on the Lunar surface during the Artemis program. In the Apollo missions, one of the factors heavily affecting Lunar operations was Lunar dust, or regolith [1]. In the words of Apollo 17's mission commander Eugene Cernan in 1973, "…dust is probably one of our greatest inhibitors to a nominal operation on the Moon. I think we can overcome every other physiological or physical or mechanical problems, except dust…" [2]. In this paper we present and analyze some solutions available to fight the Lunar dust problem.

During the Apollo program, researchers discovered negative effects of Lunar dust on almost all equipment it came in contact with [1]. Dirty or scratched surfaces (helmets' visors, thermal surfaces, etc.), mechanisms jammed with the dust (astronaut suits, the Lunar rover, the geological tools, mechanisms of cameras). All of these challenges interfered with the astronauts' work, compounding the difficulty and physical demand of operating in an EVA. Outside of the scope of this paper, it is equally important to mention how exposure to Lunar regolith (e.g., if brought into the habitat) also represents a health hazard for astronauts, impacting their respiratory, cardiovascular, nervous and ocular functions [3].

There are multiple ways that dust can damage a piece of hardware. The first type is dust entering the gaps between elements in rigid-body mechanisms. Such intrusion, due to the characteristics of the regolith, described further in the next section, increases the friction of kinematic pairs and, in some cases, can jam them completely. The traditional approach is to seal the joints from the dusty environment. However, as Apollo's experience showed, the abrasive characteristics of the Lunar dust tend to break seals [1]. This means that traditional seals are prone to damage and are possibly only postponing the inevitable friction increase in the protected kinematic pairs. Dust abrasion also has a negative effect on surfaces that are expected to remain smooth, e.g., spacesuits' visors, solar panels, thermal coatings, sensors' surfaces, etc [4]. Thermal surfaces can be degraded by dust, not only through abrasion but also by dust accumulation as it modifies the thermal emissivity and/or the effective surface of exposure [2]. Finally, conductive elements can be severely damaged by destructive dielectric discharge of the accumulated electric charge, including sensitive microelectronic components. As demonstrated, the mechanisms of dust-related damage differ greatly, and therefore demand bespoke solutions for the challenge of dust mitigation.

[*] University of Glasgow, Glasgow, Scotland, United Kingdom
[**] European Space Agency, European Astronaut Centre, Linder Höhe, Cologne, Germany
[***] Irish Research Council, Dublin, Ireland
[+] Imperial College London, South Kensington Campus, London, United Kingdom
[++] Kyoto University, Nishikyo-ku, Kyoto, Japan

The Lunar Environment and Dust Characteristics

Lunar regolith is the layer of unconsolidated material covering almost the entire surface of the Moon. Even though it also includes larger pebbles, rocks and boulders, this work focuses on the hardware impact from subcentimeter fractions of the regolith. This grey sand-like material is composed of a heterogenous mix of rock fragments, minerals, glass, and glass bonded agregates called agglutinates [5]. The lunar soil is very fine and therefore sometimes referred to as “dust”. Representative samples show a median particle size between 40 µm and 130 µm, and with particles smaller than 20 µm representing 10% to 20% of the weight [6]. In addition, some of the most abundant minerals such as arnorthite, bytownite, labradorite, fayalite or forsterite exhibit Mohs hardness values of 6 or above, making them harder than common engineering materials (e.g., aluminium alloys, titanium alloys, stainless steel). Furthermore, these minerals, together with glass, form grains with sharp and serrated edges due to their brittle nature, and are most present in the smallest size fractions [7], which explains the abrasive nature of the dust. Additionaly, due to constant solar wind plasma bombing, cosmic ray spallation, solar UV, and X-ray radiation, the dust is also electrostatically charged. Certain characteristics of the Lunar environment and regolith (discussed later in this section) lead to a large build-up and retention of charge. This build-up of charge causes particles to adhere easily to surfaces and may also cause the dust to float above the surface having easier access to mission hardware. This carries a significant risk to most hardware.

Further charging of Lunar regolith can also occur as a result of contact, which will be prevalent when it comes to Lunar surface hardware. This method of contact charging is referred to as triboelectric charging.

If two conducting materials are in contact, charge is transferred between them based on their work function difference. A metal’s work function is the energy required to liberate an electron from its surface. The transfer of charge under contact serves to change the material’s work functions and bring them into alignment, effectively equalizing the surface potentials of the two materials. Insulating materials do not have work functions, as they by definition do not have free electrons at their surface. It has been found however that insulators in contact with metals exhibit charge transfer proportional to the work function of the contacting metal [8,9]. This dependence on metal work function implies that an ‘effective’ work function can be assigned to an insulator, which can help determine the direction and magnitude of triboelectric charge transfer for that material. It is important to note however that the effective work function of an insulator is not the same as the work function of a metal. The effective work function simply describes the affinity of an insulator to transfer charge when contacted against metal and is likely determined by a number of factors from hydrophobicity to surface state defects.

When a particle is charged triboelectrically against a conducting surface, it has been shown that the resultant surface charge density is inversely proportional to the particle’s size [10]. This relationship means that smaller dust particles in the Lunar regolith will charge to a very high charge-to-mass ratio (specific charge). The larger specific charge of dust particles compounds the dust adhesion problem for Lunar exploration, making it more difficult to prevent adhesion and/or remove adhered particles.

There are two primary mechanisms for the discharge of materials; these are the conduction of surface charge and electrical breakdown of the surrounding medium. Strong electric fields created by charge build-up can lead to electrical breakdown and thus discharging of the charged surface. The breakdown limit in the air is further decreased when humidity is higher [11]. As the Lunar environment is a high vacuum, an electrical breakdown is unlikely to occur. This means that much greater charges can be reached in the Lunar environment relative to in an atmosphere such as the Earth’s.

Metals will quickly discharge when contacting a grounded surface. Insulators, however, will not tend to lose charge under the same circumstances, and may even gain extra charge depending on the material. Both metals and insulators can passively lose charge over time to the air surrounding them. Since the lunar environment is lacking suitable atmosphere this mechanism of discharge will not occur. This means that dusty regolith which gains charge, be it through environmental effects or physical interaction, will retain that charge over very large timeframes. Therefore, the only way to remove unwanted charges would be to

triboelectrically charge the dust on a material with a similar work function or to introduce it to an atmosphere (i.e., inside of the Lunar module) and use a method such as an ionizing gun.

Classification of Dust Mitigation Methods

To date, there is no single available dust mitigation technique that shows 100% efficacy on all grain sizes and for all possible hardware applications. We agree with the literature suggesting that the Lunar dust problems need to be addressed using multiple dust mitigation solutions combined in a layered engineering defense strategy [12]. In this section, a classification of available dust mitigation technologies is presented.

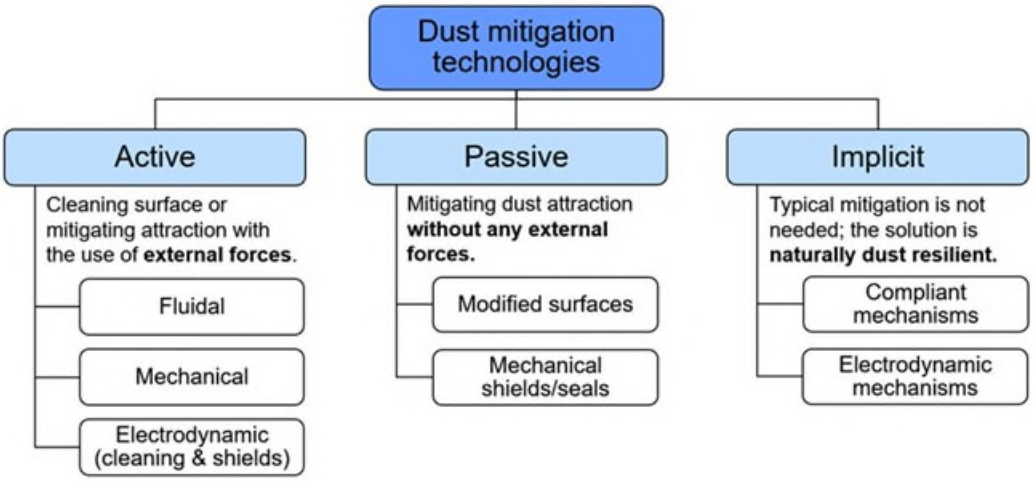

Figure 1. Dust mitigation technologies classification

There are three main approaches to dust protection: active, passive, and implicit – see Figure 1. Active methods are defined by their ability to clean (or sometimes protect – like electrodynamic solutions) surfaces with external force. The external force can be mechanical like in the case of using brushes to dust off surfaces. It can also be any other type of force like such as more advanced electrostatic, magnetic, and vibrational forces. It is important to note that the Lunar dust adhesion is mostly caused by the electrostatic potential gradient, and not by Van der Waals forces which usually play a big role with adhesion. Due to this fact, active methods show different efficacy depending on the attraction forces they target, as such mechanical methods (e.g., brushes) have a low efficacy since they do not break the electrostatic forces between particles. During the Apollo program, brushes were a primary method of cleaning equipment from dust [4]. When used in vacuum they were innefective. Once the equipment was in a pressurized Lunar module, the dust was easier to brush off due to the fact that the atmosphere helps it to discharge [1]. The active group also includes methods that use electrodynamic or vibrating systems. Most active methods focus on removing a dust coating that has already accumulated on a surface. As opposed to that, passive dust mitigation methods decrease dust adhesion or exposure to reduce the contamination before it happens and without the need for any external force. Such methods include sealing and mechanical shielding technologies as well as surface engineering and coatings. Similar to active methods, the efficacy of the types of these solutions differ. For example, microstructured surfaces target Van der Waals forces and present lower efficacy than solutions aiming to minimize the difference in potentials between the Lunar dust particles and equipment surfaces – e.g., work function matching coatings [4]. The last group -the implicit solutions- are designs that, by their nature, are not dust sensitive – e.g., friction-free solutions like compliant mechanisms. Solutions from this group, even when exposed to dust contamination are not affected by it and preserve their functions. This group also includes the usage of mechanisms that are included in active technologies, but as mechanisms themselves – e.g., an electrodynamic system can be used for transporting, size-sorting, and sampling of the dust. Such an approach could potentially be applicable for magnetic and vibrational methods as well.

.

Compliant Mechanisms

In this section, we discuss compliant mechanisms as an alternative to traditional rigid-body mechanisms. Dusty environments are quite challenging for rigid-body mechanisms, specifically for the kinematic pairs connecting their components. Sliders leave exposed areas prone to dust contamination which leads to jamming. Hinges are less exposed than sliders but unfortunately can still get contaminated as hinges have gaps that can be penetrated by fine dust. It should be considered to avoid both of them (where possible), especially if other types of protection are hard to achieve. The alternative to mechanisms based on rigid-body kinematic pairs is the use of compliant mechanisms. There is a general rule related to mechanisms that some mechanisms designers refer to, and it says: “prefer pivots to sliders, flexures to either” [13]. This rule may be highly applicable on the Moon to make sure the hardware is dust resilient.

Rigid body mechanisms perform their functions by the relative motion of separate components connected by kinematic pairs. Compliant mechanisms provide motion by elastic deformation [14,15]. As such, they can be designed as monolithic pieces – see an example of compliant hinges compared to rigid body hinge in Figure 2. When designed this way, compliant mechanisms require little to no assembly. Since compliant mechanisms deflect elastically, the work supplied to a compliant mechanism is partially stored as elastic energy in the material of the mechanism. In this sense, they are spring-loaded mechanisms. Once the input force is removed the mechanism releases stored energy and returns to its original shape.

Figure 2. Left: rigid-body hinge; middle: butterfly design of compliant hinge; right: cartwheel compliant hinge

The lack of inter-element gaps in compliant mechanisms eliminates backlash and makes them well-suited for high-precision applications. It also makes them naturally dust resilient by eliminating the gaps prone to dust intrusion, and by eliminating friction between relative moving components. As opposed to rigid-body mechanisms, compliant mechanisms do not require any additional dust protection and therefore using compliant mechanisms can be considered a design level dust mitigation approach which is classified as implicit method, Figure 1. This approach might not be useful for every type of hardware, e.g., applications that require multiple revolutions have to be designed in the traditional way. With compliant mechanisms, the range of motion is also highly dependent on their designs. For example, cartwheel compliant hinge and butterfly hinge, visible in Figure 2, are usually designed to deflect ±20 deg. [16,17]. Designs capable of more significant revolution with up to ±90 deg. are presented in Figure 3. Compliant revolute joints could be used instead of hinges in applications where multiple revolutions are not needed.

Figure 3. Compliant revolut joints; left: Flex-16, right: cross-axis flexure, designed at BYU [18]

Designing compliant mechanisms as whole systems can be more challenging than designing traditional mechanisms and requires careful material and geometry selection to fulfill the kinematic requirements. Nonetheless, there are some standardized analytical designing methods like Rigid-Body Replacement Method or Freedom And Constraint Topology (FACT) as well as numerical methods like topology optimization. An example of a compliant gripper designed by using topology optimization is presented in Figure 4.

Figure 4. 3D printed compliant gripper from opened (on the left) to closed (on the right) position.

Electrostatic Mitigation Systems

Electrostatic mitigation systems consist of high-voltage amplifiers with an electric circuit and electrodes which cover cleaning-target surfaces. The power supply unit applies several types of high-voltage waveforms on the electrodes, generating electrostatic fields nearby to remove charged dust particles. Since electrostatic systems do not require any mechanical drives nor intermediate fluid for handling regolith particles, they have several advantages for use in Lunar and Martian environments, such as simple and low-weight design, low power-consumption and heat-generation, and high dust tolerance. Here, we present some promising techniques that have been developed.

Electrodynamic Dust Shield

Electrodynamic active dust mitigation technologies appear today as the most promising solutions in terms of dust removal efficiency. The most efficient electrodynamic technology existing up to now is the Electrodynamic Dust Shield system (EDS). This concept was mentioned in Tatom's report of NASA [19] but was not manufactured. The first prototype was developed in 1970 by Masuda's group (*University of Tokyo*) [20], initially as a solution for the confinement and transportation of charged aerosol clouds [21]. Since then, many applications have been developed to clean dust in space environments as well as on Earth, e.g., cleaning spacesuits and optical lenses on the Moon, and cleaning solar panels in desert areas [22-29].

The EDS system is based on the electrodynamic field generated by parallel electrodes activating alternately in a sweeping motion. This technology consists of a set of parallel conductive electrodes integrated onto a substrate; each electrode is linked to one of multiple independent power channels. Those channels are driven by a microcontroller which sends a high-voltage (1 kV to 5 kV), alternating current, multiple-phase sequenced signal to each of those electrodes. The electrostatic field generated around each electrode serves as carrier for the dust particles – whether they are charged (positively or negatively) or not, in a sweeping motion, thanks to the alternating nature of the current and the sequenced signal. The general operation of an EDS system is described in Figure 5 [26].

Several methods can be employed to integrate the electrodes on the substrate. The most straightforward one is to make use of a commercial polyamide or PCB board, on which copper electrodes are printed. This allows for quick prototyping, as well as reliably precise manufacturing and integration onto already existing systems.

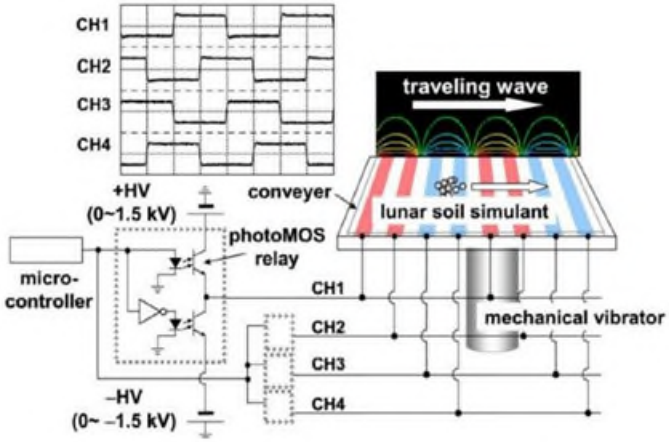

Figure 5. Diagram of the general operation of an EDS system [26]

This technology was originally proposed for dust mitigation operation on rigid surfaces, especially radiators or solar panels, on which the coverage of dust particles has a significant impact. For this particular application, the use of transparent Indium Tin Oxide (ITO) substrates have been suggested. Kawamoto's group [26] reported cleaning rates of Lunar dust simulant ranging from 80% to 90% in air conditions and almost 100% removal in high vacuum conditions. Calle's group [30] also reported cleaning rates ranging from 75%-90%. They further demonstrated the efficiency of the technology by implementing a 20x25 cm EDS substrate on the exterior wall of a Lunar Habitat Demonstration Unit [31].

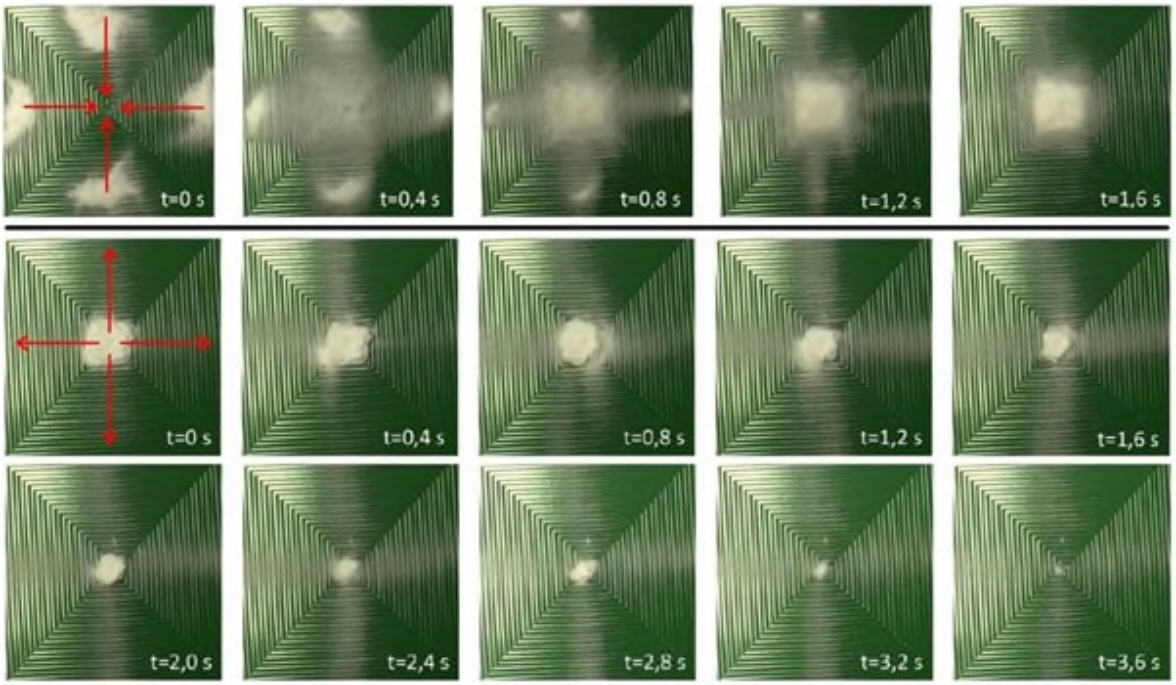

Figure 6. EDS system in 2 different modes of operation. Copper electrodes on PCB substrate, spacing between electrodes = 1 mm, travelling wave frequency = 20 Hz, operating voltage = 2000 V

Figure 6 displays the results of two different sets of qualitative experiments conducted with polyamide powder particles with a particle size distribution of 50 to 100µm. These pictures are successive frames of two different videos: in the first row, the electrostatic travelling wave is pointing inwards; in the second to third row, it is pointing outwards. It is possible to observe the effective displacement of the powder in both cases within a few seconds, even with an important initial dust load.

The EDS technology has recently benefited from development of advanced materials manufacturing, specifically in the domain of spinnable carbon nanotubes (CNTs), allowing the production of “endless” linear networks of CNTs. Originally, the EDS integrated to a spacesuit was developed by Kawamoto [32]. Copper electrodes were then considered because of copper’s superior conductivity (16.78 nΩ·m at 20°C, IACS data). The first use of CNTs as electrodes for an EDS system has been proposed by Manyapu [33], under the name SPIcDER (for Spacesuit Integrated CNT Dust Ejection/Removal system). This choice stems from the observation that CNT yarns, although less conductive than most metals, are able to conduct electricity to the point where it generates an electric field that is powerful enough to operate an EDS system; albeit slightly less conductive (1-2 orders of magnitude less than copper), they present a far higher flexibility and mechanical strength (resistance in fatigue), as well as a much lower density, allowing for a reduced weight when integrated to the spacesuit. This combination of factors makes them a better candidate when it comes to integrate the EDS technology to any sort of flexible, mobile piece of equipment requiring dust mitigation when operated on the Lunar surface, including Lunar exploration spacesuits.

CNT yarns as electrodes have proven to be almost as effective as copper electrodes, with similar dust removal rates under the same operating conditions (Figure 7a). However, the use of a flexible substrate brings forward a new set of challenges and limitations, amongst which dielectric breakdown occuring at high operating voltages between neighbouring electrodes (Figure 7b). This phenomenon is, as of today, the main limitating factor for a standardised use on relevant systems. While working well under high vacuum (<100 mPa), using this technology in Earth atmosphere (10^5 Pa) and low-to-medium vacuum is difficult. Research on ways of mitigating the electric arc generation is ongoing, and has already brought forward solutions such as polymer encasing of the electrodes and conductivity enhancement of the material through ionic doping and densification of the CNT structure [34]. The adaptation of the EDS technology to flexible substrates is an active research topic, and it is a safe bet that it will one day be implemented by space agencies in Lunar exploration spacesuits and Lunar dust-sensitive equipment.

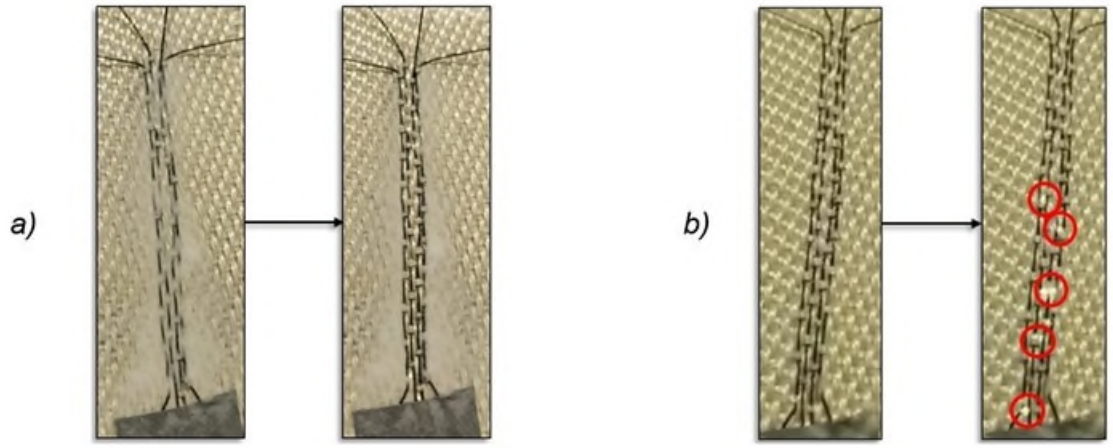

Figure 7. a) CNT EDS sample sweeping Ø60µm PMMA microparticles away with ~100% efficiency at 1200V; b) Dielectric breakdown arcing occurring between uninsulated CNT electrodes at 2000V

Other Electrostatic Mitigation Systems

The electrostatic dust shield system was invented to prevent the Lunar regolith from intruding into a mechanical gap of extravehicular equipment [35] (Figure 8). The system utilizes a standing wave of high voltage applied to electrodes attached to the mechanical gap. The generated electrostatic field can attract

particles close to the gap and then repel them outward. The performance of the electrostatic dust shield was evaluated in the lab experiments, and it was confirmed that the system can remove a majority of the particles, approximately 90% of them, compared with the case when they get inside of the gap with no countermeasure (Figure 9).

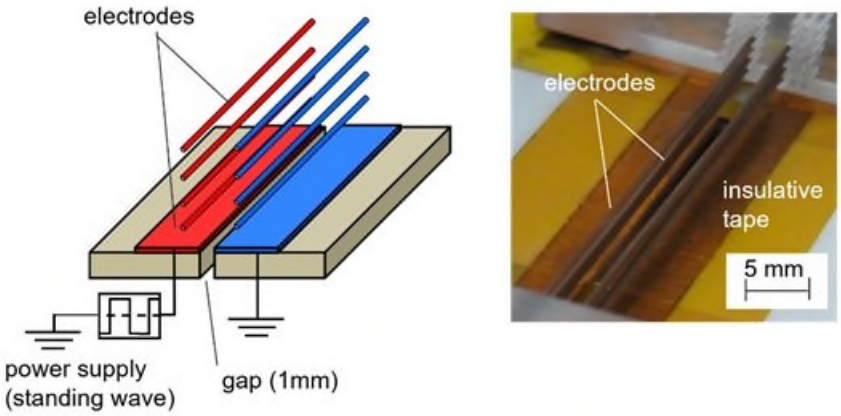

Figure 8. Configuration of the electrostatic dust shield system. Wire and plate electrodes are placed just above a gap. A standing wave of high voltage is applied to electrodes on one side, while other electrodes are grounded, generating an electrostatic field to capture and repel dust particles

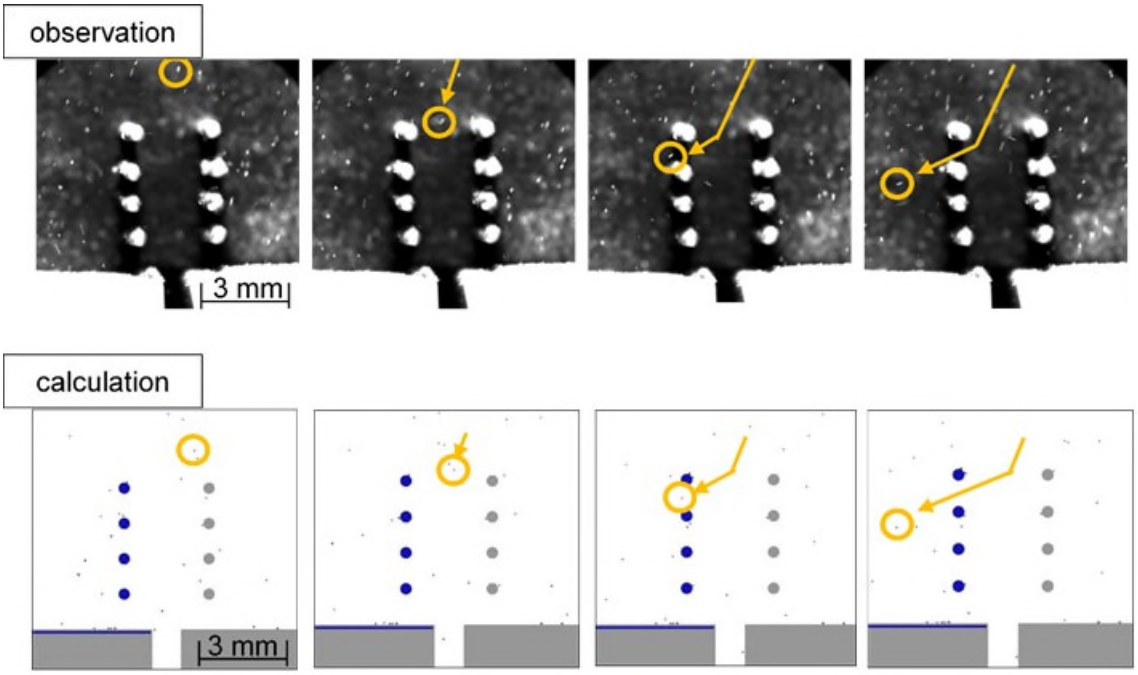

Figure 9. Observed and simulated motions of particles that are supplied to the electrostatic dust shield system from the top. The falling particles are captured and then repelled outwards by the electrostatic force [36]

In addition to the EDS system for spacesuit, a handheld cleaning tool using an electrostatic force was developed for assisting astronaut's cleaning tasks [35]. The tool consists of screen electrodes, a tube with printed parallel electrodes, and a collection bag, as shown in Figure 10. When a standing wave of high voltage is applied to the screen electrodes, the resultant electrostatic field captures the dust on spacesuits, and then the particles are transported to the collection bag by a traveling wave applied to the parallel

electrodes. Astronauts can use this device inside or outside of Lunar bases easily and quickly for cleaning spacesuits and even other systems. Figure 11 shows the technology demonstrator.

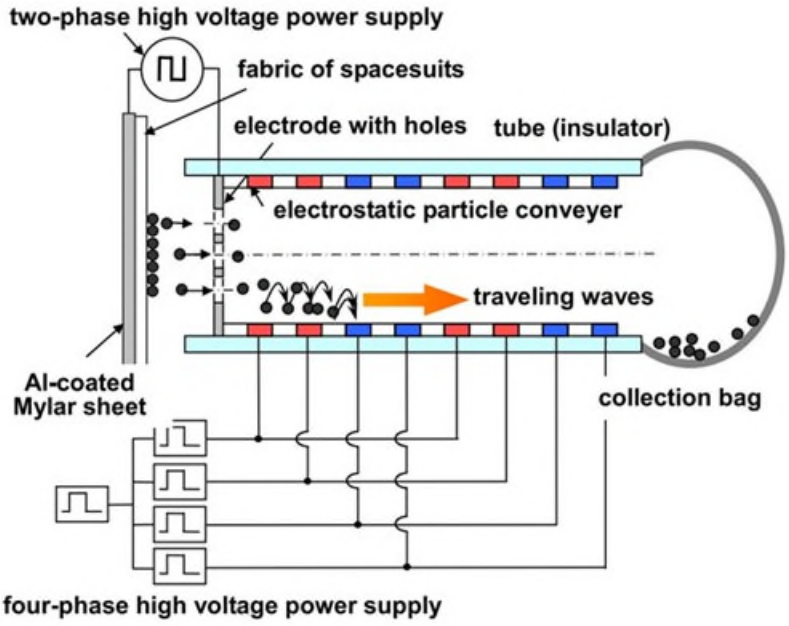

Figure 10. Configuration of the electrostatic handheld cleaning tool for spacesuits. A standing wave of high voltage is applied to screen electrodes, capturing the dust on spacesuits. The captured particles are transported by a traveling wave supplied to electrodes printed on a tube [35].

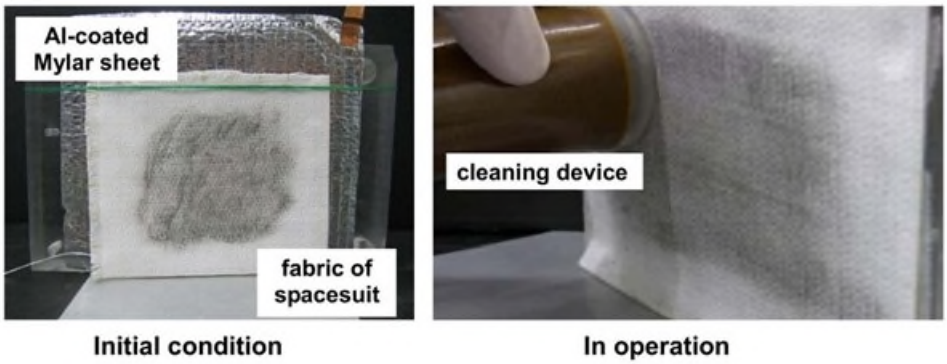

Figure 11. Demonstration of the electrostatic handheld cleaning tool for spacesuits. Astronauts can use this device for quick cleaning for themselves [36].

Moreover, such mechanisms using an electrostatic force for cleaning can also be applied for handling particles as an implicit method. The capturing process of the electrostatic handheld cleaning tool can be used for sampling of the regolith. As shown in Figure 12, the Lunar regolith simulant can be sampled by using an electrostatic force in low gravity environment [37,38]. Another example is the electrostatic size-sorting system [39] (Figure 13). When the regolith simulant particles are transported by using an electrostatic traveling wave, the particles can be sorted by employing a balance between the electrostatic and gravitational forces, which corresponds particle size. The demonstration showed that particles less than 20 μm in diameter can be sorted from the bulk of the regolith simulant efficiently.

While some examples of electrostatic mitigation systems and implicit handling techniques are introduced here, other non-mechanical mitigation systems are also available, such as magnetic, vibration, and the

mixing of methods [32,40,41]. Since they also do not rely on mechanical drives nor fluid, the same advantages as electrostatic systems can be achieved for the magnetic and vibration methods.

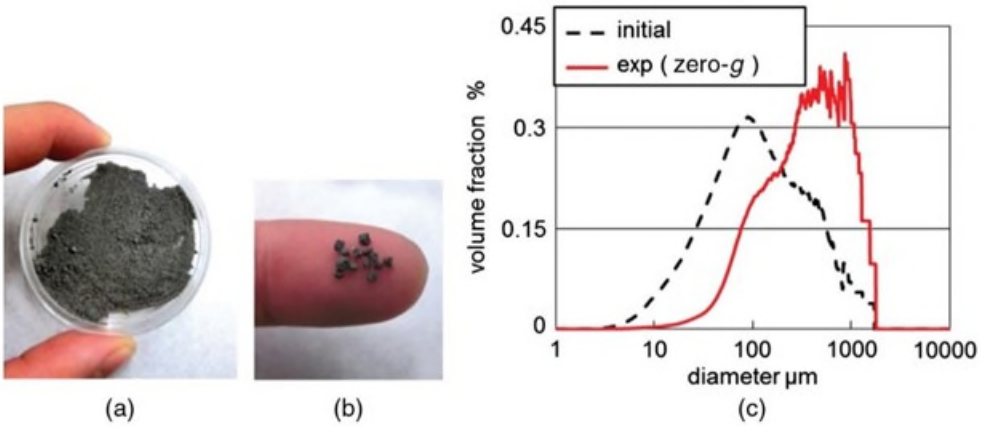

Figure 12. Sampled Lunar regolith simulants using an electrostatic force. (a) (b) approximately 900 mg of the simulant can be collected in one low-gravity experiment. (c) size distributions of initial and captured particles, showing that the electrostatic force can manipulate even larger particles in low gravity [37].

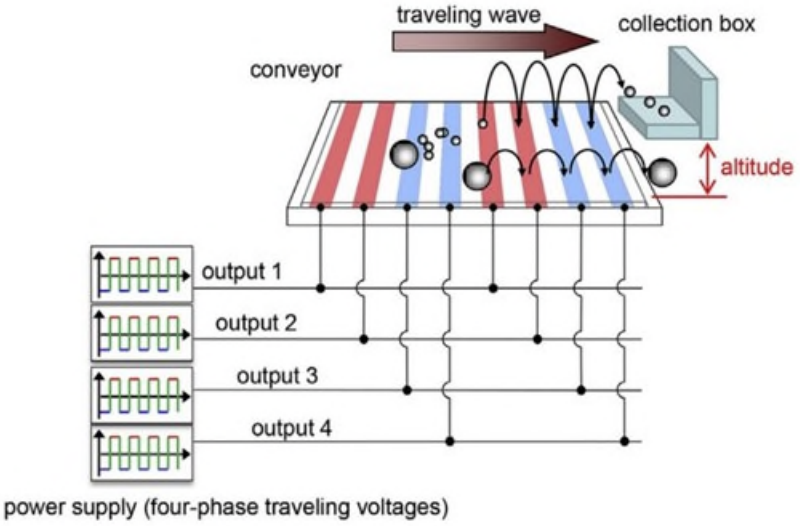

Figure 13. Experimental setup of the size-sorting system using an electrostatic traveling wave. The regolith particles can be transported, while smaller particles can be extracted by utilizing a force balance between electrostatic and gravitational forces [39].

Work Function Matching Coatings

The magnitude and direction of charge transfer between two materials when they are in contact is dependent on the difference between their work functions. As mentioned, the work function is the energy needed to remove an electron from the surface of a material, and it is relatively constant for metals, but not as consistent for insulators which do not have mobile surface electrons. When materials come into contact, charge is transferred such that their work functions are altered and come into equilibrium. This means that if two materials with the same work function come into contact with each other, there will be no charge transfer. Sternovsky, et al., conducted studies to estimate the work function of Lunar regolith simulant. It provided insight into which materials have a similar work function to that of Lunar regolith [42]. Of course, the closest match to the work function of Lunar regolith is the Lunar regolith itself. Therefore, the dust

resistance effectiveness of a surface coating made from Lunar regolith simulant has been assessed and, as demonstrated in literature [43], such coating reduces the adhesion of Lunar simulants to thermal control surfaces. In the mentioned tests the coating was applied via ion beam sputter deposition using an argon ion beam source. This resulted in a 100nm thick coating.

Another method of coating materials with a Lunar regolith relies on using the Marangoni effect. This phenomenon is well understood but was first reported with Lunar regolith simulant by Dominguez and Whitlow [44]. They observed the upward migration of molten Lunar regolith in a crucible. The movement was driven by temperature gradients in the melt's bulk and along the crucible wall which created a surface tension strong enough to overcome the forces of gravity. The authors of this paper also observed the same phenomena while conducting experiments. A thin 0.5-mm Lunar regolith simulant coating was repeatedly produced by heating the simulant to its melting point under vacuum conditions. The coating's characteristics could be controlled by altering the amount of regolith used, the heating profile, and by doping the simulant. Three samples with varying coating heights can be seen in Figure 14.

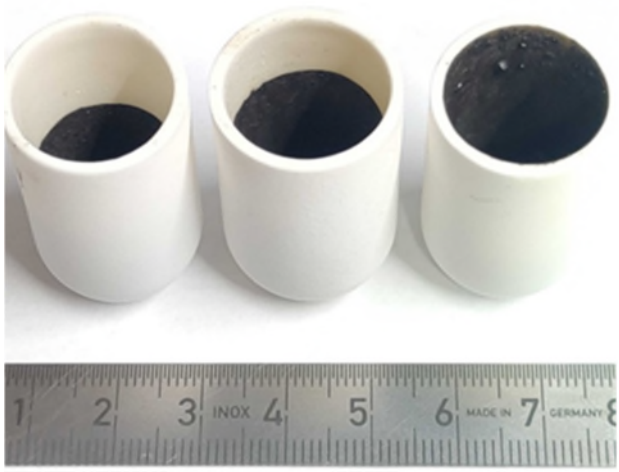

Figure 19. Marangoni effect coating with JSC-2A simulant.

This coating method is yet to be further tested for its dust mitigation effectiveness but based on the work of Gaier, et al. [43], it could lead to promising results. In addition, this process could lend itself to producing coatings for surfaces in-situ as the Lunar regolith is in abundance and the vacuum environment only needs heating to produce the ideal conditions. Furthermore, the process of coating could provide itself useful as a wear resistant coating against the abrasive Lunar dust. Again, this is yet to be tested but if the coating showed positive results, it would provide a double protection against both the Lunar dust adhesion and abrasion.

The method mentioned above aims at reducing the potential difference of hardware surfaces. But for extended contact with regolith another important factor is also the discharge mechanism. In a case where the charge on Lunar regolith is to be discharged, this is unlikely to work consistently if it is contacted against an insulating material or ungrounded conductor. This is because charge is conserved in triboelectric charge transfer. Negatively charged regolith in contact with neutral charging material of similar work function may lose some charge and the charging material will gain electrons. In this process the work function of the charging material will decrease, while the work function of the regolith will increase. In this case, the discharged regolith will begin to gain electrons back from the charging material, or any other regolith that encounters the charger will not discharge due to the saturation of electrons on the charging material.

To sustain discharging of Lunar regolith over long time periods, charge building up on the charging material gained from the regolith must be removed in order to make way for further charge. In an atmosphere it is possible to neutralize any material's charge using an ionizer. Using an ionizer is not possible in the Lunar vacuum however, since the working principle of an ionizer is to strip electrons from air molecules, yielding

mobile charges that are attracted to and neutralize charged surfaces. The best way to ensure constant work function of a charging material is to use a conducting material and to ground it, keeping its electrostatic potential at zero. If a conducting material with similar work function to neutrally charged regolith is grounded, then any amount of charged regolith can be continuously contacted against the conductor and the regolith's charge will approach zero.

In addition to grounding a conducting material with a similar work function to Lunar regolith, it is possible to alter the work function of any conducting material in order to match it with that of the bulk regolith. This is done by applying a constant voltage to the conductor, raising, or lowering its Fermi level, and hence its work function. This can be tuned so that the charge on any contacting material (Lunar dust in this case) will gain net neutral charge when continuously charged against the biased conductor.

This work function altering process is displayed through the schematic in Figure 20. In Figure 20 a) an insulator and a grounded metal are shown, along with their work functions ϕ_I and ϕ_M respectively. These materials are contacted multiple times, leading to the transfer of electrons from the metal with a lower work function to the insulator, until their surface potentials come into equilibrium as shown in Figure 20 b). Figure 20 c) shows the case where a voltage V_{Apl} is applied to the metal, increasing its work function to ϕ_{Alt}. This in turn reduces the work function difference between the metal and the insulator, and hence reducing any charge transfer. If the polarity of V_{Apl} was switched, then the metal's work function would be decreased, and the insulator would gain extra charge compared to the grounded case.

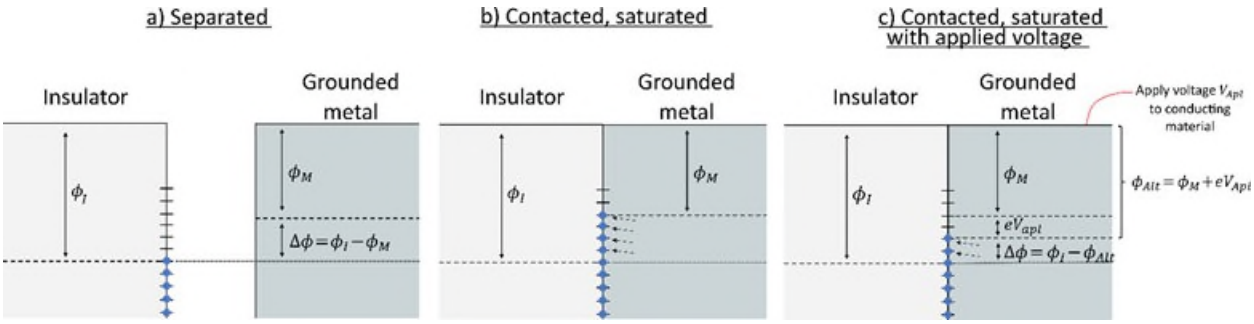

Figure 20: Schematic of the triboelectric charge transfer between an insulator and a metal based on their work functions when the metal is grounded (b) and when the metal has a voltage applied to it (c). The application of a voltage in order to alter the work function of a metal can be used in order to reduce the saturation charge of a contacting insulator.

This method of applying a voltage to a conductor charging an insulator has already been tested for triboelectric nanogenerator applications [45]. A parylene film was rubbed with a platinum coated tip, with applied voltages ranging from $-10\,V$ to $+10\,V$. They found that with an applied voltage of $\sim 3\,V$ the saturation charge of the parylene film was zero. For voltages $< 3\,V$ the film gained a negative charge, while at $> 3\,V$ the film gained positive charge. This proof of concept for neutralizing the charge on insulators contacting a conductor by applying a voltage is very promising, and points towards a potential method for the neutralization of charge on Lunar regolith.

Conclusions

Lunar dust has proven to be a challenging characteristic for surface missions. Since the Apollo missions, new technologies have been developped and some are ready to be further tested or even applied to flight hardware. We also demonstrated that the nature of the regolith adhesion is mainly electrostatic and therefore some traditional cleaning methods are not particularly useful. Nevertheless, in this paper, we presented different approaches to dust mitigation as well as examples of promising solutions. As shown, the available technolgies differ significantly and one should take them into careful consideration when designing Lunar hardware. Since there is no standard approach yet to the Lunar dust mitigation, the engineering community should be open to the implementation of novel solutions in future missions.

References

1. J. R. Gaier, The Effects of Lunar Dust on EVA Systems During the Apollo Missions, Nasa/TM-2005-213610, 2005
2. J. S. Levine, D. Winterhalter, and R. L. Kerschmann, The Impact of Lunar Dust on Human Exploration, Cambridge Scholar Publishing, Texas, 2020.
3. M. Braddock, Hazards of Lunar Regolith for Respiratory, Central Nervous System, Cardiovascular and Ocular Function, in M. B. Rappaport and K. Szocik, The Human Factor in the Settlement of the Moon (pp. 141-157), Springer, 2021
4. S. Pirrotta, D. Lefebvre, M. W. Co-chair, H. Wong, J. Buffington, and J. J. Gaier, Dust mitigation gap assesment report, 2016
5. D. S. McKay, G. Heiken, A. Basu, G. Blanford, S. Simon, R. Reedy, B. M. French, and J. Papike, The Lunar Regolith, in G. Heiken, D. Vaniman, and B. M. French, Lunar sourcebook: A user's guide to the moon (pp. 285-356), Cambridge University Press, England, 1991
6. W. D. Carrier III, G. R. Olhoeft, and W. Mendell, Physical Properties of the Lunar Surface, in G. Heiken, D. Vaniman, and B. M. French, Lunar sourcebook: A user's guide to the moon (pp. 285-356), Cambridge University Press, England, 1991
7. D. Rickman, and K. W. Street, Expected Mechanical Characteristics of Lunar Dust: A Geological View, Proceedings of the Space Technology and Applications International Forum, Albuquerque, 2008
8. J. Cross, Electrostatics: Problems, Principles, and Applications, IOP Publishing, Oxford, 1987
9. W.R. Harper, Contact and Frictional Electrification, Laplacian Press, Morgan Hill, CA, 1998.
10. R. D. Cruise, K. Hadler, S. O. Starr, and J. J. Cilliers, The effect of particle size and relative humidity on triboelectric charge saturation, J. Phys. D. Appl. Phys., 2022
11. S. Matsusaka, H. Maruyama, T. Matsuyama, and M. Ghadiri, Triboelectric charging of powders: A review Chem. Eng. Sci., 2010
12. S. Wagner, Asteroid, Lunar and Planetary Regolith Management: A Layered Engineering Defense, 2014
13. A. Chakrabarti, Engineering Design Synthesis: Understanding, Approaches and Tools, London: Springer, 2002
14. L. L. Howell, Compliant Mechanisms, Wiley, 2001
15. X. Zhang, and B. Zhu, Topology optimization of compliant mechanisms, Springer, 2018
16. B. Shusheng, Z. Hongzhe, and Y. Jingjun, Modeling of a cartwheel flexural pivot, J. Mech. Des. Trans. ASME, 2009
17. D. F. Machekposhti, N. Tolou, and J. L. Herder, A review on compliant joints and rigid-body constant velocity universal joints toward the design of compliant homokinetic couplings, J. Mech. Des. Trans. ASME, 2015
18. BYU CMR, Compliant Mechanisms Research Group models available on thingiverse website: https://www.thingiverse.com/byu_cmr/designs, acces 20/02/2022
19. F. B. Tatom, J. G. Adams, B. L. Cline, N. A. Contaxes, R. D. Johnson, H. Seaman, V. Srepel, Lunar Dust Degradation Effects and Removal/prevention Concepts, NASA, 1967
20. S. Masuda, Electric Curtain for Confinement and Transport of Charged Particle Clouds, Adv. Static Electr., 1970
21. S. Masuda, K. Fujibayashi, K. Ishida, and H. Inaba, Confinement and transportation of charged aerosol clouds via electric curtain, Electr. Eng. Japan, 1972
22. H. Kawamoto, Electrostatic Transport and Manipulation of Lunar Soil and Dust, AIP Conference Proceedings, Albuquerque, 2008
23. C. I. Calle, J. L. Mcfall, C. R. Buhler, S. J. Snyder, and E. E. Arens, Dust Particle Removal by Electrostatic and Dielectrophoretic Forces with Applications to NASA Exploration Missions, ESA Annual Meeting on Electrostatics, p. 1, 2008.
24. C. I. Calle, E. E. Arens, J. M. McFall, C. R. Buhler, S. J. Snyder, J. K. Geiger, R. A. Hafley, K.M. Taminger, and C. D. Mercer, Reduced gravity flight demonstration of the dust shield technology for optical systems, IEEE Aerospace conference, 2009
25. C. I. Calle, The electrostatic environments of Mars and the Moon, Journal of Physics: Conference Series, vol. 301, 2011

26. H. Kawamoto, M. Uchiyama, B. L. Cooper, and D. S. McKay, Mitigation of Lunar dust on solar panels and optical elements utilizing electrostatic traveling-wave, Journal of Electrostatics, vol. 69, 2011
27. M. N. Horenstein, M. Mazumder, and R. C. Sumner, Predicting particle trajectories on an electrodynamic screen – Theory and experiment, Journal of Electrostatics, vol. 71, 2013
28. M. Mazumder, M. N. Horenstein, J. W. Stark, P. Girouard, R. Sumner, B. Henderson, O. Sadder, I. Hidetaka, A. S. Biris, R. Sharma, Characterization of electrodynamic screen performance for dust removal from solar panels and solar hydrogen generators, IEEE Transactions on industry applications, 2013
29. B. Guo, W. Javed, C. Pett, C.-Y. Wu, and J. R. Scheffe, Electrodynamic dust shield performance under simulated operating conditions for solar energy applications, Solar Energy Materials and Solar Cells, vol. 185, 2018
30. C. I. Calle, C. R. Buhler, M. R. Johansen, M. D. Hogue, and S. J. Snyder, Active dust control and mitigation technology for Lunar and Martian exploration. Acta Astronautica. 2011
31. C. I. Calle, C. D. Immer, J. Ferreira, M. D. Hogue, A. Chen, M. W. Csonka, S. J. and Snyder, Integration of the electrodynamic dust shield on a Lunar habitat demonstration unit, In Electrostatics Society of American Annual Meeting, 2010
32. H. Kawamoto, and N. Hara, Electrostatic Cleaning System for Removing Lunar Dust Adhering to Space Suits, Journal of Aerospace Engineering, vol. 24, 2011
33. K. K. Manyapu, Spacesuit Integrated Carbon Nanotube Dust Mitigation System for Lunar Exploration, PhD Thesis Dissertation, 2017
34. N. Garrivier, Novel Materials and Approaches for Lunar Exploration Spacesuits, Université de Lorraine, 2021
35. M. Adachi, Dynamics of Electromagnetic Particles and Its Application for Mitigation and Utilization Technologies of Regolith on Moon, Mars, and Asteroids, Waseda University, 2016
36. H. Kawamoto, Electrostatic Cleaning Device for Removing Lunar Dust Adhered to Spacesuits, J. Aerosp. Eng., vol. 25, 2012
37. M. Adachi, H. Maezono, and H. Kawamoto, Sampling of Regolith on Asteroids Using Electrostatic Force, Journal of Aerospace Engineering, vol. 29, 2016
38. M. Adachi and H. Kawamoto, Electrostatic Sampler for Large Regolith Particles on Asteroids, Journal of Aerospace Engineering, vol. 30, 2017
39. M. Adachi, H. Moroka, H. Kawamoto, S. Wakabayashi, and T. Hoshino, Particle-size sorting system of Lunar regolith using electrostatic traveling wave, Journal of Electrostatics, vol. 89, 2017
40. H. Kawamoto, and H. Inoue, Magnetic Cleaning Device for Lunar Dust Adhering to Spacesuits, Journal of Aerospace Engineering, vol. 25, 2012
41. H. Kawamoto, Handheld Cleaning Tool for Lunar Dust Adhered to Spacesuits Using Magnetic and Electrodynamic Forces, Journal of Aerospace Engineering, vol. 34, 2021
42. Z. Sternovsky, S. Robertson, A. Sickafoose, J. Colwell, M. Horányi, Contact charging of Lunar and Martian dust simulants. Journal of Geophysical Research: Planets, 2002
43. J. Gaier, D. Waters, B. Banks, R. Misconin, M. Crowder, Evaluation of surface modification as a Lunar dust mitigation strategy for thermal control surfaces, In 41st International Conference on Environmental Systems, 2011
44. J. A. Dominguez, J. Whitlow, Upwards migration phenomenon on molten Lunar regolith: New challenges and prospects for ISRU, Advances in Space Research, 2019
45. Y. S. Zhou, S. Wang, Y. Yang, G. Zhu, S. Niu, Z. H. Lin, Y. Liu, Z. L. Wang, Manipulating nanoscale contact electrification by an applied electric field, Nano Letters, 2014

The Standardization of In-space and Surface Docking Systems

James L. Lewis* and Stanley R. Donahoe*

Abstract

The International Docking System Standard (IDSS) was developed and establish to aid on-orbit crew rescue and joint operations between different spacecraft. For the International Space Station (ISS), the IDSS has successfully enabled global interoperability for commercial crew and it is now being extended to the Artemis campaign. Similarly, as more companies, agencies, and nations announce their intentions to explore and occupy Low Earth Orbit (LEO) and Cis-Lunar space, including the Lunar surface, it is a natural supposition that new, vehicle interface standards will be required to support the build-up of infrastructure for campaign-based exploration or permanent occupation by national and multi-national agencies, industries, and companies.

A surface version of the IDSS, a.k.a. IDSS-Surface (IDSS-S), is under consideration at the NASA Johnson Space Center (JSC) by the docking discipline leads responsible for the leadership of technical development and negotiation of the original IDSS over a decade ago. The IDSS-S, like its predecessor, will ultimately detail the physical geometric mating interface and design load requirements to ensure physical interoperability and to support a broad set of design reference missions which, if accommodated, increases the probability of successful Lunar surface docking between different modules enabling the accessibility and inclusivity required for multi-national, sustainable Lunar exploration.

Introduction

For many years, NASA and JSC have been critically involved in activities leading to the development and establishment of standards. One such standard, the International Docking System Standard (IDSS), was born out of joint collaborative docking mechanisms development work which began under the JSC X-38 Program. Despite the X-38 Programs cancellation, the efforts of the two principal collaborating partners, NASA and ESA, caught the attention of Senior NASA Manager Bill Gerstenmaier who set forth in motion the action for JSC Engineering, along with the existing ISS International Partners, develop the framework for creating and establishing the first in-space docking system standard. This paper does not delve too much into the background of the development of the IDSS. However, the experience of developing, implementing, and managing the IDSS as a standard provides valuable insight and lessons learned which would be applicable to the creation of a Surface IDSS, or IDSS-S, as future Lunar surface element providers pursue the development of modules, systems, and infrastructure that require the mating and assembly necessary to enable a permanent, sustainable Lunar capability. The in-space docking standard IDSS can be viewed as a success; demonstrated by the fact that several commercial vehicles are now able to dock to the ISS, and that new commercial LEO platforms, as well as, the Lunar Gateway, are all using the IDSS to drive their critical interface specifications and enable their interoperability and compatibility.

While there will always be naysayers, including those within the spacefaring community of practice, who have expressed doubts about the inevitability of successfully achieving a crew rescue mission, events over recent years have highlighted the real potential for the most basic form of spacecraft interoperability by, as a minimum, ensuring first vehicles are equipped with the basic fit and form necessary to enable a crew rescue function. While we have never yet performed an in-space crew rescue mission, it is only a matter of time as more entities, nations, agencies, and commercial partners, develop and fly more vehicles supporting more missions, there will eventually come a time that a rescue, or even worse case a recovery

* NASA Johnson Space Center, Houston, TX; james.l.lewis@nasa.gov; stanley.r.donahoe@nasa.gov

mission, could be attempted to aid the distressed. To accentuate this point it wasn't that long ago during the inaugural unmanned demo flight of the Boeing Starliner crew transport vehicle, the unmanned craft failed to make orbit and according to published accounts very nearly reached the point where it could not reenter either. Had this vehicle been crewed and outfitted with a fully compliant IDSS interface, it is conceivable that a second vehicle, similarly outfitted could have been launched to rendezvous and provide whatever assistance could have been delivered. Harkening back to the ill-fated Columbia mission, it could be possible that at some point in the not too distant future that had a prepositioned rescue vehicle could provide agencies more options when dealing with critical situations. The primary lesson here is that with the proper planning and implementation, in the future it will be more possible that aid can delivered in time to impact mission outcomes, or to simply aid in recovery. This lesson has not been lost on the submariners community as there are also interface and operations standards in place to aid in rescue and recovery globally even for aiding those who are traditionally not our ally. A simple internet search on the acronym ISMERLO will lead you to information highlighting an highly analogous, world-wide, ocean-based emergency rescue capability and community of practice.

Beyond basic crew rescue interoperability, there is a larger level of interoperability which entails both pre-planned as well as impromptu mission planning yielding permanent, semi-permanent, or temporary element-to-element docking with prescribed resource transfer connectivity for the sharing of things like fluids, power, and data. As activities for exploration, colonization, and occupation of the Lunar surface by an ever-growing list of participants increases, it seems practical to begin the dialog concerning the continued development of standard interfaces and operations enabling both nominal and off nominal capabilities.

History and Evolution of the IDSS

As mentioned earlier the IDSS evolved out of the interaction between NASA and ESA while pursuing the development of docking mechanism for the X-38 Vehicle. However, the real roots of international docking go further back to the 1970's during the Apollo Soyuz Test Program (ASTP), where the United States (US) and Russia demonstrated that it was possible with the right interface design and requirements for two independent developers to design, test, and execute in-space docking of two vehicles from different sources (Figure 1). A key point worth highlighting is that prior to the ASTP, in-space docking mechanisms were of designs which relied on prescriptive male and female geometry (e.g., probe/cone), meaning that mating pairs of vehicles always had to have the right combination of geometry to achieve docking. In as much as ASTP was geopolitical historical event between the two cold war powers, it also showcased that a more universal geometric interface arrangement demonstrating equality was possible by the selection of a 3-petal androgynous interface. The benefit of an androgynous docking interface layout is it bypasses the physical limitation of always having to have the correct pair of docking interface geometry.

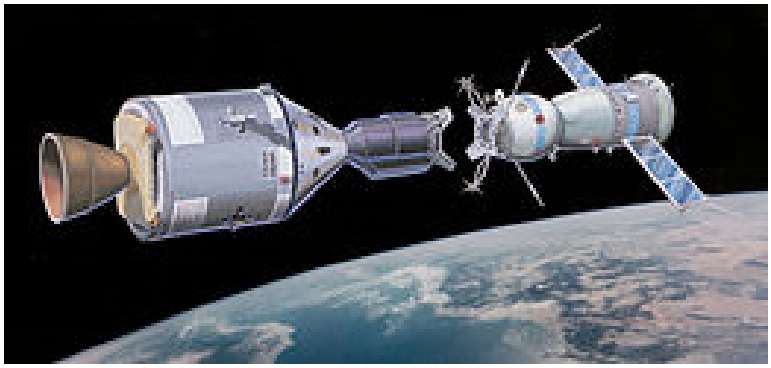

Figure 1. A 1973 artist's conception of the docking of the two spacecraft using 3-petal androgynous interface (source http://spaceflight.nasa.gov/gallery/images/apollo-soyuz/apollo-soyuz/html/s73-02395.html)

Fast forwarding through the 1980's, 1990's and into the 2000's, both the U.S. and Russia had retained the androgynous geometric interface layout in docking systems developed or in development. For the Russians, who had gotten farther along in their development than the U.S., they had already certified their androgynous docking system - Androgynous Peripheral Assembly System (APAS). So when the call to action came to develop the first international docking standard, the basic groundwork for true docking interoperability had already been set in motion decades earlier. The real challenge at that point was to establish a basic detailed design specification and the critical dimensions necessary to base the standard interface definition on. While recent NASA efforts in the development of new docking system used modern technology, it was ultimately decided that the IDSS be based on the NASA ISS-Shuttle docking system which had been procured from Russia and used for the Shuttle-Mir Program. Having a flight-proven, certified, design made selecting a design baseline easier for NASA Managers. While the APAS was chosen, there have been slight tweaks made to improve the IDSS design over the last decade to address changes needed to accommodate an expanding set of missions and environments, although the basic core design of the standard has not changed. Likely the biggest overall change from the original APAS design was a recent change to require recessing the power resource umbilical/connector below the mating sealing interface plane; which will be discussed more in a section below.

Basic Geometry and Keep Out Zones

While the term androgyny is used to describe the actual geometric arrangement of the interfacing features, in terms of physical implementation this means a circular docking ring with 3 equally spaced guide petals as depicted in Figure 2. During initial docking contact, in what is generally referred to as "docking soft capture", two 3-petal ring interfaces are guided into alignment with each other. Each petal on one ring is guided between the edges of two petals on the opposing ring very effectively provides a means of guiding the two 3-petal interfaces from a completely unconstrained state to a precisely aligned, fully constrained state. At the point of maximum meshing a trip latch similar to a simple door latch is used to hold the two rings together.

Given human spacecraft are typically larger in volume with significant masses, it is difficult to precisely control them in-space primarily due the precision and magnitude of thruster control authority coupled with real-time knowledge and accuracy of relative position and state vectors. To overcome this, the standard IDSS mechanism design requires one of the two 3-petal soft capture rings to be mounted on a 6 degree-of-freedom mechanism which when extended enables capture ring orientation compliance for matching the orientation of the second mating guide ring; as well as providing "stroke for attenuation" when fully meshed after capture. After this compliant "soft capture system" achieves soft capture and motion is attenuated, the active ring is fully retracted into final alignment bringing the two docking structural and sealing interface together, which is called "hard latching". Hard latching nominally involves inserting large diameter close tolerance "guide pins" which provide both the final precise positioning required for the high strength hook latching as well as an interface shear load reacting feature. The action of fully latching and preloading these two structural interfaces compresses the docking seals which are required for pressurization of the vestibule/passageway to enable crew and logistics transfer after hatch opening. These high-strength latch hooks and the docking tunnel are designed to hold the two docking interfaces together and resist the forces trying to separate them (e.g., internal cabin pressure or any external loads applied be either of the two mated vehicles result from thruster firing or from internal disturbance like crew exercise).

Since docking results in a finally controlled and aligned state, it enables locating very precisely secondary docking interfaces; such as resource transfer connectors or umbilicals which can be used to share power, data, and fluid resources between spacecraft. The IDSS IDD prescribes keep out zones around the circular docking interface like the numbers arranged around the edge of a clock face to further aid with docking resource standardization. While there is currently not much in the way of standardization of the "connectors" themselves between the various existing NASA Programs, by specifying and controlling the keep out zones, mission planners are able to use these zones for mating of connectors and transferring of resources across a mated interface meeting the specifications of their specific Program needs. Although, today there is little commonality of resource transfer technology across the industry, as the industry grows it is expected that further standardization will occur over time. Until this occurs, the IDSS IDD implementation will use the keep

out zones and the requirement that all spacecrafts umbilical connectors remain retracted below the seal plane out of the way and unable to prevent the primary functions of docking which is the minimum required for crew rescue. After docking is complete, resource connectors/umbilicals can be actuated to extend and mate with connectors mounted on the other side and conversely retracted prior to undocking..

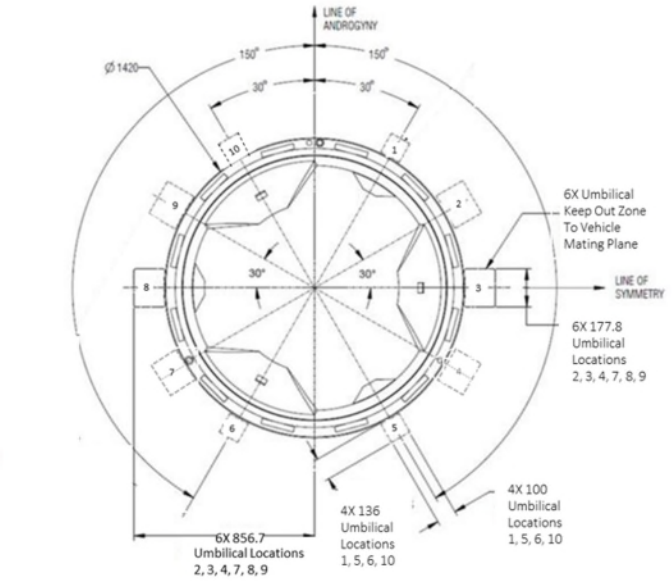

Figure 2. IDSS umbilical connector Keep-Out Zones

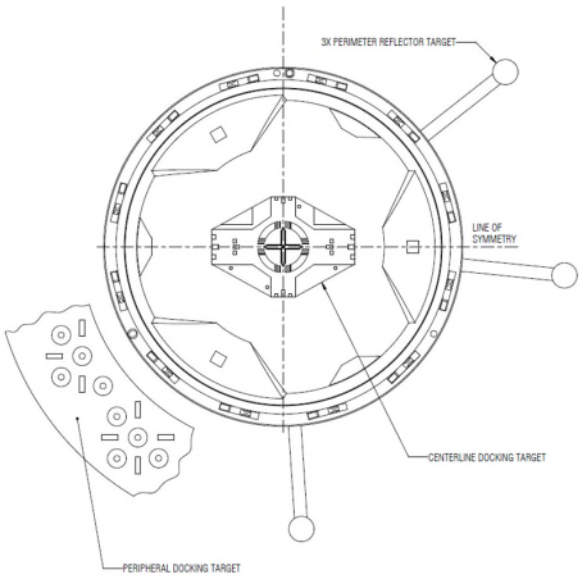

Figure 3. The 3 Types of IDSS Navigation aids (CDT-Cenerline Docking Target, PDT-peripheral Docking target, PRT- peripheral Reflector Targets) combination of which provide navigation support for active vehicle operations at long, mid, and short ranges

In Space Docking Challenges

Besides resource transfer connectors, there are two other related capabilities that also may influence the primary function of docking/mating. One is the placement of rendezvous navigation aids in or around the periphery of the docking interface. These are required by the active spacecraft to be able see/sense their alignment and positional accuracy as the spacecraft move closer and closer into proximity with each other for docking. Currently there are difference types of technologies, (e.g., cameras, lidar), each with its strengths and weaknesses and while industry continues to improve and promote various technologies in this area, like resource connectors, there is still not any consensus on the navigation target and aids required to enable rendezvous, proximity operations, and docking (RPOD). However there are separate standards in-place or in development by both Human Space Flight and satellite refueling spacecraft developers and is a discipline where things are evolving quickly.

Another factor which offers challenges for the design of docking systems and their operations is the use of docking systems/interfaces for “berthing” operations. Berthing is another category of spacecraft attachment which differs from docking in that instead of two “free flying” spacecraft, a robotic manipulator system (RMS) or robotic “arm” is used to reach across from one craft to grapple the other. This robotic arm then provides the positional and closing initial contact conditions for mating. For example, after the now retired Space Shuttle had docked with the ISS, the Shuttle RMS could retrieve large modules from its payload bay and plug them into specialized “berthing ports” on the ISS. Another example of this is the ISS Cygnus resupply vehicle when fly’s up close the ISS and “station keeps” (i.e., floats within a small navigation box) as the Station RMS reaches, grapples, and berths the craft to a Common Berthing Mechanism port. Since the beginning of the IDSS there have been efforts to improve commonality between docking and berthing mechanisms, and the primary way for docking to not preclude berthing is to ensure that the force/velocity requirements for docking system to achieve compliance and capture are such that they don’t exceed the capabilities of a robotic arm.

Like navigation aids and resource umbilicals, berthing compatibility is an area where further definition and standardization needs definitization to better ensure all of these RPOD and berthing disciplines work together rather than have incongruous or competing requirements. Standards like the IDSS IDD are intended to enable cooperation and collaboration between space agencies, industry, and programs and highlight that it is important to consider a broader view of envisioned architectures in a functioning space infrastructure and the benefits of further standardization on global collaboration.

The Case for Surface Docking Interoperabilty

As human space exploration continues to mature and expand, mission planners and architects have already turned their attention to the eventual occupation and exploitation of other Solar System surface destinations, like the Moon and Mars. Once initial Lunar-return missions get beyond the Apollo-style ‘visit and live out of your lander’ paradigm, focus will turn to long-term, sustainable, infrastructure emplacement, and just like was demonstrated for the ISS assembly, long term Lunar or Mars surface occupation will require an equivalent of rendezvous, docking and resource transfer connectivity. As attention has returned to surface missions in recent years, so has the attention of NASA docking system discipline organization to begin to understand what it will take to develop the systems and capabilities to docking of grounded surface vehicles. At first glance it may seem this is easier than in-space docking but that is not necessarily the case. In the case of the Moon, lunar dust presents a formidable challenge when it comes to sealing and mechanisms. For any surface mission, the mass constraints for landing every ounce of mass are more stringent meaning systems need to be designed to be even more mass efficient. Also, unlike its in-space equivalent, surface docking will be “constrained” due to surface elevation variations as most likely any two surface modules will never be able to be brought into perfect final alignment like they can easily be done in-space. This is called “fixed-fixed” connectivity and is a challenge to existing docking system designs. A potential solution for dealing with the “fixed-fixed” challenge of surface docking of two pressurized elements involves the use of a pressurized tunnel to extend the reach of the docking interface between misaligned vehicles. In effect, this is like elongating the soft capture system of its in-space equivalent and forgoing the action of bringing the two mating halves together into perfect alignment with no gap. Besides overcoming misalignment, a connecting pressure tunnel can also aid in meeting potential “planetary protection” requirements of a future

Mars missions. Enabling surface mating and pressurized transfer tunnel would minimize exposure to the planetary surface and mitigate the potential of human and Martian biological/hazardous cross-contamination between internal and external environments.

The current NASA Mars reference mission publicly available shows the crew descending to the Mars surface on a Mars Descent Vehicle, along with a Pressurized Rover which serves as the crew habitat for their mission. Nominally the Mars crew would perform Extra-Vehicular Activities (EVAs) via Suitport which is a special EVA suit-sized docking interface with the Pressurized Rover. However crew and cargo transfer can be enabled by using a pressurized tunnel pre-positioned Mars Ascent Vehicle (MAV) for their surface departure and ascent to the Mars Transit Vehicle for their return to Earth (Figures 4 and 5). This pressurized transfer capability, also known as “shirt-sleeve transfer”, would be great aid between the Mars Pressurized Rover and the MAV. The MAV will also likely need a deployable tunnel with a standard docking interface extending from the higher MAV elevated deck height down closer to the surface for the Pressurized Rover to dock with.

Figure 4. Mars Rover docked to Mars Ascent Vehicle utilizing Pressurized Transfer Concept (source is JSC in-house modeling/rendering)

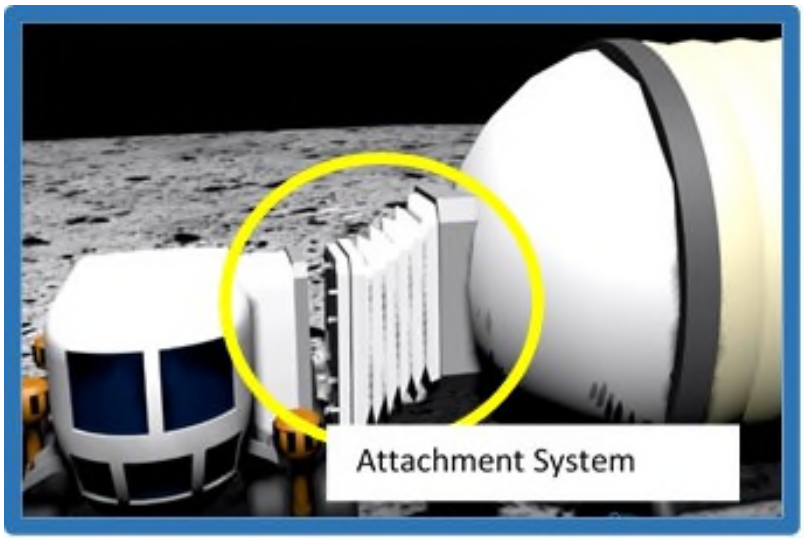

Figure 5. Illustration Depicting Lunar Rover Docked to Surface Module Active - Active Docking Adapter utilizing Pressurized Transfer Concept with misalignment (source is JSC in-house modeling/rendering)

The surface docking capability for Mars could be demonstrated on the Lunar surface as part of a certification process and lessons learning experience. In addition to lunar proving ground demonstration benefits there are additional advantages for lunar sustained operations including efficiencies gained for shirt-sleeve crew and cargo transfer and the possibility of a large logistics carrier that can be landed and then docked to the habitat for use as a cupboard, closet, or even for trash management. Having such a capability in a sustained lunar environment would help minimize lunar EVAs for housekeeping and logistics transfer activities, while conversely increasing the percentage of EVA time for science and maintenance, and/or reducing the overall frequency of EVA suit maintenance and the effort and time required to do so.

Overcoming Surface Docking Challenges - Study Activities to Date

As previously described, for surface missions involving multiple modules and rovers, vehicle and element misalignments will require a mating systems and tunnels which will help accommodate some residual final alignment offsets due to the presence of lunar gravity and uneven terrain. At JSC, some low-fidelity, non-flight hardware is currently under study for use in helping develop requirements; and to help buy down future risks to surface docking articulation, latching, and sealing which are the essential elements required to enable a pressurized, shirt-sleeve, transfer passageway between vehicles and elements.

The docking discipline team at JSC has on-going development activities exploring docking and shirt sleeve transfer capabilities on planetary surfaces. Articulating variants that will perform the docking function for two pressurized elements are being developed and tested. A primary objective for the NASA team is to explore and document the features and requirements of a potential international interface standard. It is a goal in the next year to create a draft of this new surface docking standard as well as begin collaboration with commercial and international stakeholders towards baselining this standard in the next few years. The timing of this is critically important to support anticipated surface mission development activities leading to sustainable lunar operations. While it would be best to implement the right standard early on, timing, funding, and maturity may limit this from happening. A fall back strategy would be to scar early elements/vehicles for potential retrofit of a docking interface or system in the future for later implementation.

Figure 6 shows images of concept hardware currently under development at JSC intended to feed most notional lunar surface architectural roadmaps and near-term timely development activities for future commercial development and deployment. Efforts are currently underway by JSC Engineering seeking substantial active partnering with Industry with the expectation to accelerate work in this area to the benefit of enabling lunar surface sustainability sooner and with less cost.

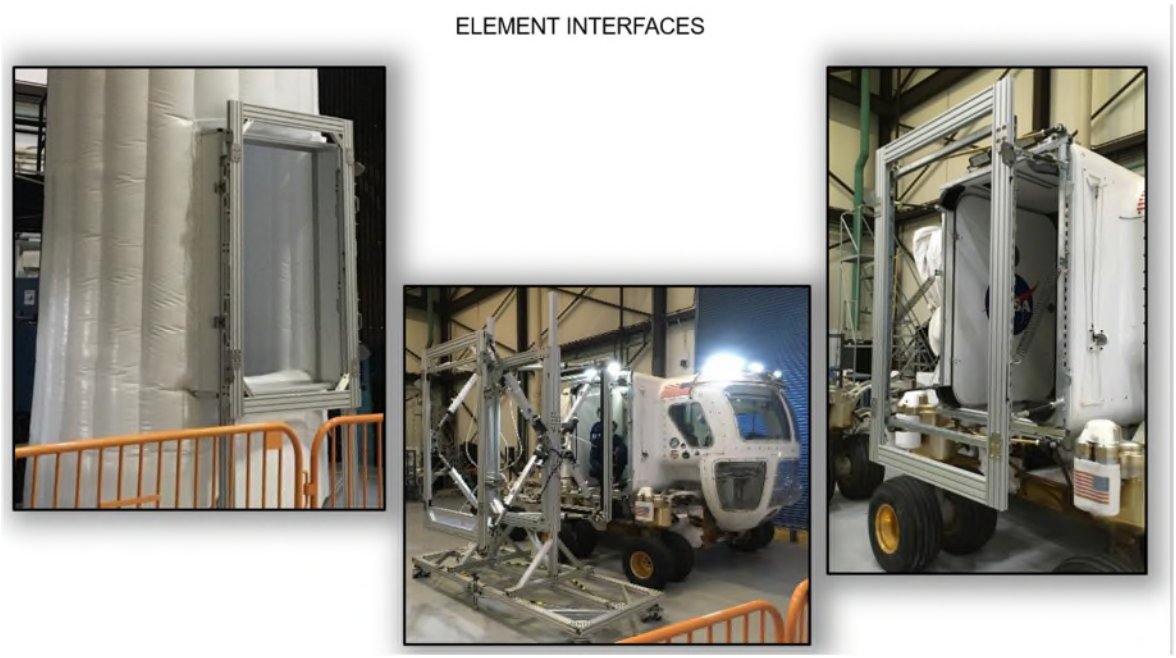

Figure 6. Proof of Concept Surface Docking and Pressurized Transfer Concept Hardware

Conclusion

This paper has intended to highlight the significance of in-space and surface docking standardization in hopes of conveying the importance of standardization which in turn enables interoperability, crew rescue, more sustainable crew and logistics transfer, and planetary protection. Careful consideration of exploration architectures as well as implementation of interface standards can support not only the planned but the unplanned, providing greater flexibility to reconfigure and sustained operations over time.

As new platforms and vehicle are developed for LEO, deep space, and surface activities, it is critical for space agencies, programs, and commercial developers to recognize the great benefits of standardization but be committed to compliance to implementation and be willing to overcome any disadvantages that may come with less optimized solutions. A true world view of space exploration, docking standardization supports a greater efficiencies, encourages global cooperation, and enables inherently safer and sustainable missions and operations.

Remote Diagnosis and Operational Response to an In-Flight Failure of the Drill Feed Mechanism Onboard the Mars Science Laboratory Rover

Ryan Kinnett*, Thomas Green*, Douglas Klein* and Megan Richardson Lin*

Abstract

On November 30, 2016 (Sol 1536 of the mission), the Mars Science Laboratory (MSL) flight operations team commanded the Curiosity rover to drill into a Martian rock to acquire the mission's 16th rock powder sample. The drilling operation was halted when the drill feed mechanism unexpectedly stalled shortly after disengaging its magnetically-actuated friction brake at the start of a long move to extend the drill bit into contact with the target rock. The drilling campaign was put on hold and later abandoned as diagnostic data revealed a tendency for the actuator to transition in and out of a high-drag state in which the mechanism could not actuate. In the subsequent months, the team conducted a variety of in-flight and ground-based investigations to determine root cause and identify mitigation strategies for continued operation. Mechanism reliability continued to degrade and, by June 2017, it became clear that the mechanism could not be relied upon to support drilling operations. The team identified a workaround that enabled collecting samples without the mechanism. This workaround utilized the drill feed in an extended configuration. The first feed-extended drilling sample was successfully collected on Sol 2057, 521 sols after the initial feed stall. This paper discusses the anomaly investigation process, failure analysis, and feed mechanism operation mitigation strategies. It concludes with key lessons learned about mechanism design, mission architecture, and operational best practices.

Background

The Mars Science Laboratory mission seeks to understand the past climatological and geophysical history of Mars in order to determine whether Mars might once have been habitable[1]. Of prime importance to this objective is the rover's subsurface sampling capability afforded by its rotary-percussive drill system. The drill system is an integral part of the rover's turret at the end of its robotic arm.

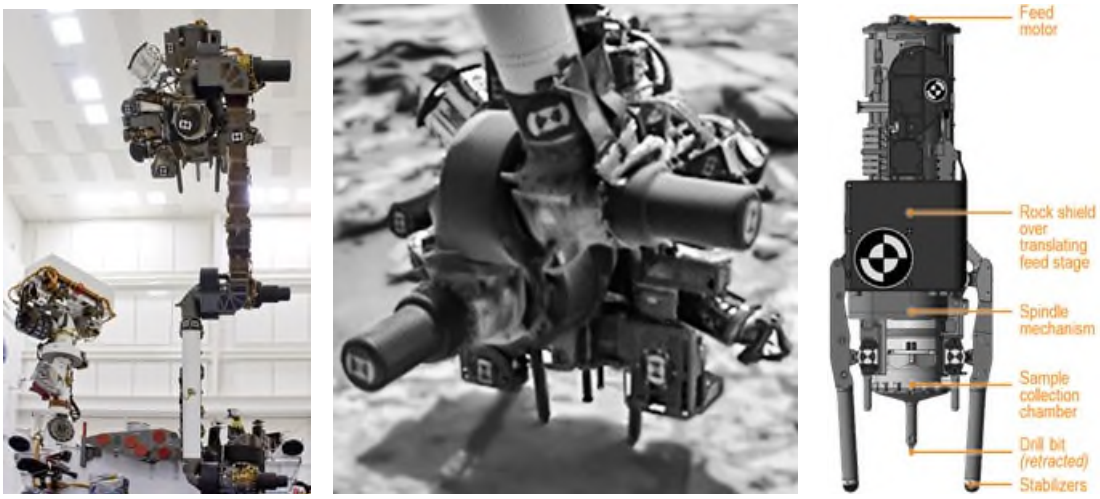

Figure 1. Left: MSL robotic arm and turret extended during pre-launch robotic arm deployment testing. Center: drill deployed against a Martian rock with stabilizers preloaded in the original drilling configuration and bit retracted prior to the start of drilling on mission Sol 170. Right: MSL drill system overview.

* Jet Propulsion Laboratory, California Institute of Technology, Pasadena, CA

The MSL Rover Drill System

The drill system design includes a pair of cross-linked stabilizers which, when preloaded against a rock by the robotic arm, serve to maintain axial orientation and position of the drill while drilling (see Figure 1). The tungsten carbide masonry drill bit penetrates rocks by simultaneously rotating and percussing while a linear feed mechanism maintains pressure and advances the bit. The drill's rotary motion draws pulverized rock powder into a collection chamber in the drill bit assembly via a set of spiral channels along the shaft of the drill bit. After drilling, the drill feed retracts to a stowed position which aligns an output port from the drill bit sample collection chamber with an inlet port to the CHIMRA (Collection and Handling for *In situ* Martian Rock Analysis) system for further processing and distribution to science instruments inside the rover[2,3,4].

A linear feed stage provides 110 mm of travel of the drill bit relative to the drill housing and stabilizers. This feed stage consists of a rotary actuator coupled to a 625:1 planetary gear set which drives a ball screw linear translation carriage. The feed carriage translates a percussion mechanism, a spindle mechanism, a ball-lock chuck mechanism, and a drill bit assembly. A toroidal force sensor measures axial force transmitted from the drill bit, through the chuck, spindle, and percussion mechanisms. During drilling operations, a control algorithm maintains roughly constant bit pressure by gradually feeding forward while sensing pressure against the drill bit.

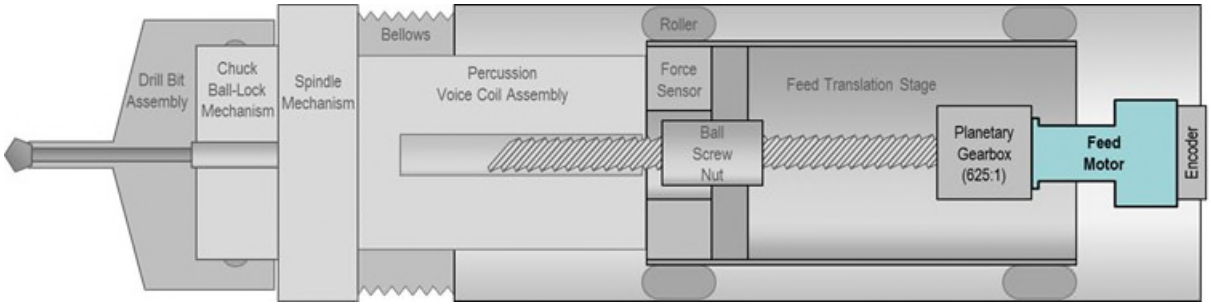

Figure 2. MSL drill system internal functional overview (not to scale)

The drill feed motor consists of a brushless DC motor fitted with a magnetic encoder and an electromagnetically-actuated disk brake. When the brake solenoid is unpowered, a set of springs preload an annular ferrous brake disk against a brake rotor that is attached to the motor shaft. To disengage the brake, the rover's motor control system drives current through one or both of the actuator's redundant brake solenoids, pulling the ferrous disk out of contact with the brake rotor. The brake plate translates axially along a set of guide pins (not shown in Figure 3). A magnetic encoder indicates the motor shaft angle to the motor controller for commutation.

Remote Drill Operation

Drilling campaigns span many sols from target selection and triage to sample delivery to the analytical instruments. The target selection process begins with the science team identifying rock(s) of interest and specific parts of a rock to be sampled. Candidate targets are first studied by turret-mounted instruments prior to contact. Rover Planners then perform various triage techniques to evaluate stability before committing to full-depth drilling.

The drilling process as designed consisted of setting the drill stabilizers against a rock target and pressing against the target with 300 N generated by the weight of the turret and torque from the robotic arm. Once stable, the drill feed mechanism began translating the bit forward until the drill force sensor detected contact against the rock. The drilling sequence then performed a hole-start routine and proceeded to continuous rotary-percussive drilling, progressively ramping up and backing off percussion levels as needed to maintain steady rate of progress. The sequence nominally concluded when the drill bit reached the target depth (65 mm) or the algorithm detected that progress had slowed below a threshold level.

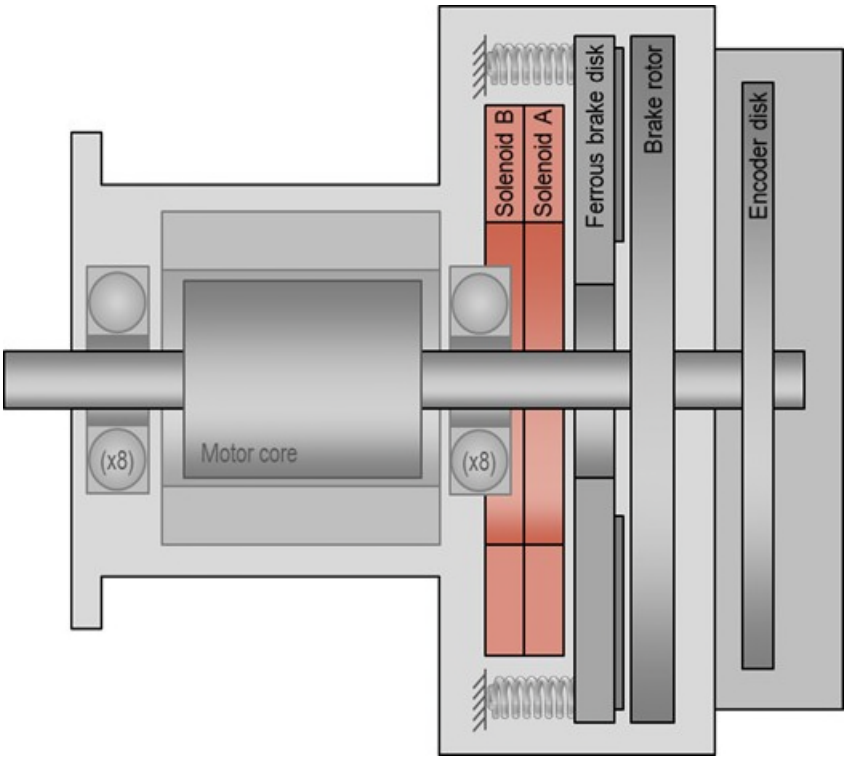

Figure 3. Drill Feed motor, brake, and encoder schematic (not to scale)

Rover Engineering Telemetry

The rover autonomously curates and prioritizes telemetry according to onboard selection rules and autonomous fault responses. Rover activities are generally optimized to generate just enough telemetry for the downlink team to declare success or investigate failures. Command sequences and autonomous fault responses can trigger creation of more detailed telemetry for planned critical events and autopsy data leading up to detected faults.

Engineering data for rover mechanisms is typically recorded with an 8-Hz sampling frequency, while parts of the drilling operation record specific events at 32 Hz and 64 Hz. Additionally, the rover's motor control system maintains a limited history buffer of detailed motor control telemetry sampled at 512 Hz. This history buffer is not normally downlinked to preserve data volume for science. However, the rover autonomously dumps this buffer to a data product following any motor fault. The high-rate motor control telemetry buffer has proven invaluable throughout the mission, most notably during the first drill percussion short event on Sol 911 [3], as well as during the drill feed fault described herein.

Upon indication of activity failures or motor faults, the downlink team performs an initial assessment to gauge the scope and severity of the problem. If there is any chance that the fault poses risk to the next sol's plan, the downlink team alerts the tactical planning team of the situation and may opt to introduce planning constraints. Anomaly records are written for new, emergent issues, and for major issues, an Anomaly Response Team is formed. This team is headed by the Engineering Operations team and draws on expertise from other parts of the mission team as well as relevant subject matter experts. Some anomalies can be solved rather quickly, restoring full rover capability within hours or days. Other investigations can persist for months, as iterations of ground and flight diagnostics are performed to better understand the behavior and if necessary, alternative capabilities are developed.

Drill Feed Anomaly Investigation Overview

On November 30, 2016, the MSL tactical planning team assembled a plan for the main drilling sol for the drilling campaign on a target named Precipice within the Murray Formation on the lower slopes of Mount Sharp. The following morning, the downlink team received telemetry indicating the drilling sequence had terminated prematurely due to the drill feed motor stalling.

The Sol 1536 drill feed stall anomaly presented an immense challenge to the engineering team. It imminently prevented drill sampling and posed a serious long term threat to sampling operations. The investigation unfolded and evolved over several months. Table 1 provides a high level overview of the phases and key events associated with the drill feed anomaly investigation.

Table 1. Timeline of Drill Feed anomaly investigation

Date	Sol	Event
Dec 2016	1536	Initial feed stall
Dec 2016 - Mar 2017	1537-1650	Early flight diagnostics focused on root cause investigation and understanding motion reliability with respect to various factors
Mar 2017	1627	Discovered similar failure signatures on the drill's chuck mechanism actuator
Apr 2017	1651	Regolith sample acquisition including significant amounts of turret dynamic activities
Apr 2017 - Jul 2017	1653-1753	Late flight diagnostics focused on mitigation techniques and achieving reliable motion. Observed accelerating degradation of performance. Began developing contingency feed-extended drilling technique.
Jul 2017	1754-1780	Permanent feed extension to enable potential development of feed-extended drilling
May 2018	2057	First feed-extended drilling on Mars

Sol 1536 Drill Feed Stall Fault

Telemetry from the rover indicated that the robotic arm had successfully deployed the drill against the rock and preloaded the stabilizers, but the motor controller detected that the drill feed motor stalled at the start of a long move to extend the drill bit into contact with the rock. Rover flight software autonomously terminated the drilling operation and dumped a high-rate (512 Hz) motor control history buffer to a high-priority data product. The robotic arm unloaded the stabilizers and lifted the drill away from the rock.

Upon receipt of initial telemetry from the Sol 1536 drill feed anomaly, it was immediately clear that this incident was not a simple commanding error or other easily recoverable fault. Engineers had not previously experienced a feed stall fault during normal operations in testbeds or in flight. The drilling campaign was suspended and an Anomaly Response Team consisting of subject matter experts and the operations engineers was formed to direct the anomaly investigation.

Early Diagnostics

Within the Sol 1536 high-rate motor telemetry, downlink engineers observed that the feed motor encoder indicated no change whatsoever in the motor shaft position. The closed-loop rate controller ramped up current through the motor in an effort to recover nominal rate, but quickly reached the motor's current limit without any indication of motor shaft motion from the encoder, thus triggering the stall declaration.

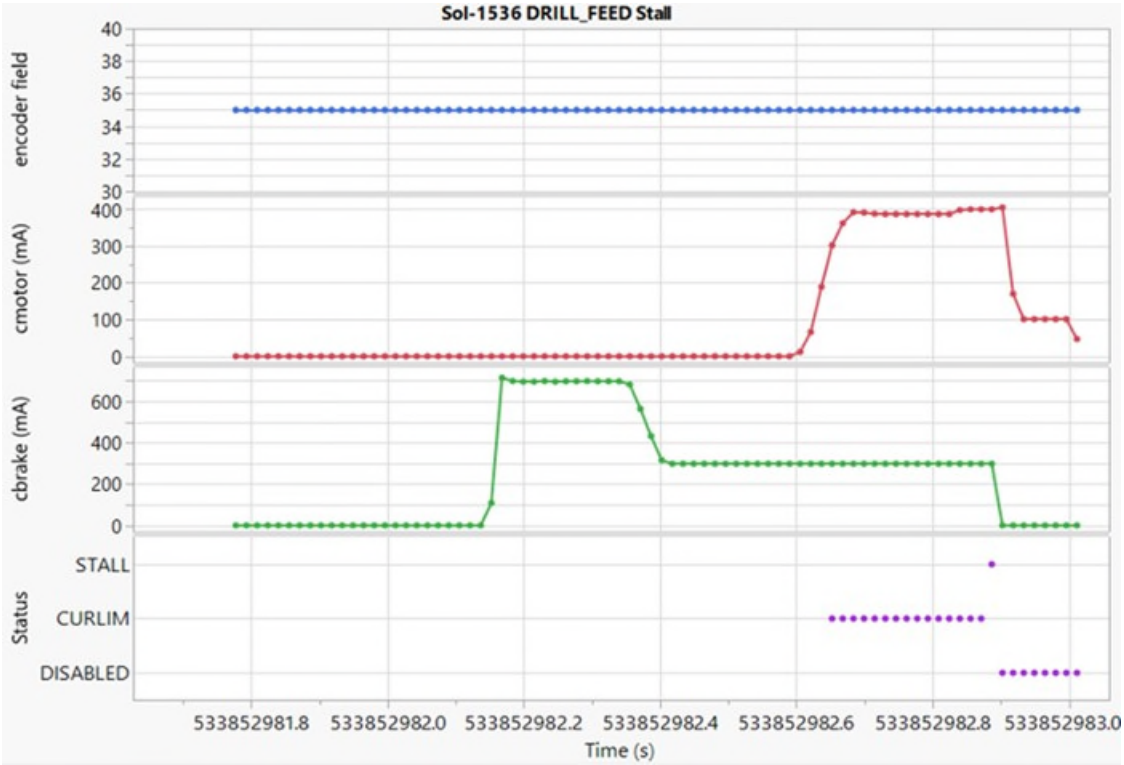

Figure 4. Sol 1536 drill feed stall motor telemetry. From top to bottom: encoder field number (between 0 and 144 DN); sensed motor current, brake current; control state. Brake current tracked the standard profile which started with a 0.2-second "pull-in" period then reduced to 300 mA during motor commutation. The closed-loop rate controller began commutating at time 533852982.6. Sensing no change in motor shaft position, the controller ramped up motor current, reached current limit, and declared stall.

The motor windings appeared to be healthy, indicated by a routine conductance check performed prior to first feed motion and corroborated by voltage and current telemetry during the attempted feed motion. This observation effectively ruled out potential problems with the motor windings and harness.

Several initial hypotheses were formed to explain the apparent lack of motor shaft rotation, including:

- encoder electrical or mechanical failure, or harness failure
- mechanical obstruction in the motor assembly
- gearbox failure
- brake disengagement failure
- control system electrical or logical failure

These initial hypotheses informed a first round of follow-up diagnostics designed to incrementally bifurcate the problem space. While these diagnostics were executed, the anomaly response team placed operational constraints against changing the drill's orientation or performing any activities that would vibrate the turret. The team wanted to perform initial diagnostics in the exact same configuration as the initial fault so that results would be less ambiguous if changes were observed.

Sol 1537 Diagnostics: Blind Commutation

The anomaly response team recommended attempting a short, standalone feed motion command to check if the problem was persistent across thermal cycles and power states, followed by a second motion using a blind commutation mode which could potentially differentiate between an encoder signal problem vs mechanical. Engineers devised and tested a sequence to command the prescribed diagnostic feed moves and incorporated this sequence into the next sol (1537) plan. The following day, the downlink team reported that the feed motor had stalled again, both during the initial feed motion command with normal commutation, and during the later command using blind commutation. This result reduced the likelihood that the problem originated from the encoder.

Sol 1541 Diagnostics: Increasing Brake Hold Current

The standard brake control profile starts with a brief pulse of “pull-in” current prior to the start of active motor commutation, then drops the brake current to a more thermally sustainable “hold” current level for the duration of motor motion. The next experiment raised the hold current to match pull-in current to check if the brake might be reengaging during the transition from pull-in to hold. This diagnostic sequence started by repeating the blind commutation method, first with nominal 2-step brake pull-in and hold current values, then with hold current increased to match pull-in current. Both operations failed. The encoder signal appeared to deflect by three counts opposite the commanded direction, but these signal deflections could not be definitively attributed to physical motion.

Sol 1543 Diagnostics: Combinations of Primary and Redundant Brake Solenoids

Similar to the previous plan, the plan on Sol 1543 started with another attempt to move the motor using standard brake current settings and blind commutation to confirm the problem had not spontaneously cleared since the previous attempt. Unsurprisingly, this first move stalled as before. Next, the sequence reconfigured controller settings to energize the backup brake solenoid rather than the primary. This yielded another motor stall result. This helpfully reduced the likelihood of a possible open-circuit condition local to the primary brake control circuit. The same move was retried, using the backup solenoid, but increasing hold current to match pull-in current. This again resulted in a stall.

The Sol 1543 diagnostic sequence then enabled both the primary and redundant brakes simultaneously, effectively doubling the force used to disengage the brake. The anomaly response team was pleasantly surprised to find that this worked. After reading a home pulse on the encoder, the motor controller exited the blind commutation mode (denoted as STARTUP status in Figure 5), and the feed motor appeared to operate nominally with no obvious signs of physical resistance or other anomalous behavior.

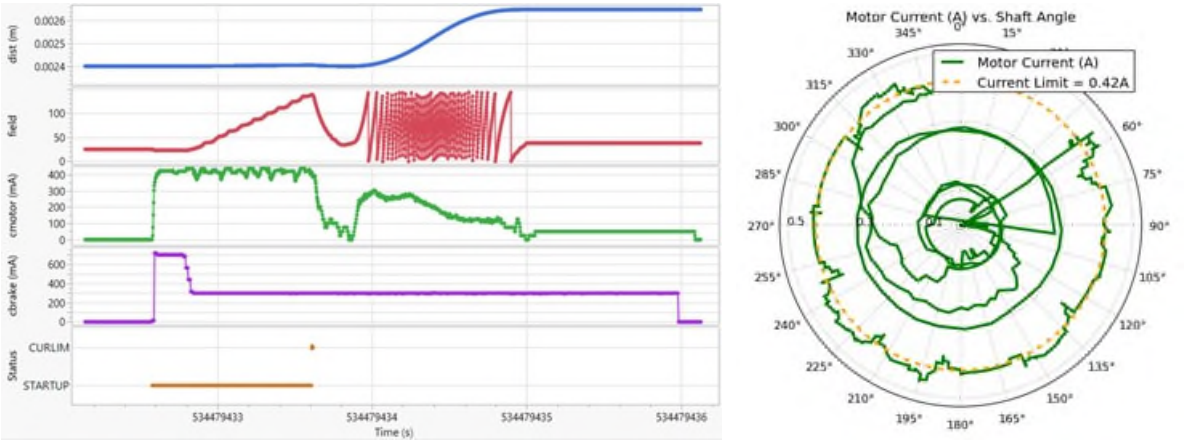

Figure 5. Sol 1543 drill feed diagnostic motion with primary and redundant brake solenoids energized. Brake current (per-coil “cbrake”, violet) tracked the standard 2-step profile. Motor control started in blind commutation (“STARTUP”) mode, then transitioned to normal closed-loop rate control just before time 534479434. Motor current (“cmotor”, green) appeared normal. Right: motor current vs shaft angle.

Sols 1544 - 1573 Diagnostics: Early Exploration of Dynamic Sensitivities

Following the first successful post-anomaly motion on Sol 1543 with both brakes energized, the team attempted 7 feed motions, all using the primary brake solenoid with standard current settings. All 7 moves completed successfully with no signs of resistance.

The anomaly response team and project management then lifted operational constraints against activities, allowing robotic arm motion, driving, and CHIMRA sample processing operations. The anomaly response team requested that planning teams execute short forward and back drill feed motions following the first instance of each of these physically dynamic activity types to gauge sensitivity to turret dynamics.

A sample processing activity on Sol 1545 utilized CHIMRA vibration and was followed by the drill feed diagnostic sequence containing commands to drive the feed a short distance forward and then back. In this experiment, the feed motor stalled after nearly reaching its goal. Telemetry inspection revealed a new signature and new insight into the behavior inside the feed actuator. Distinct, repeating current spikes were observed with frequency equal to the rotation rate of the motor (one spike per motor revolution).

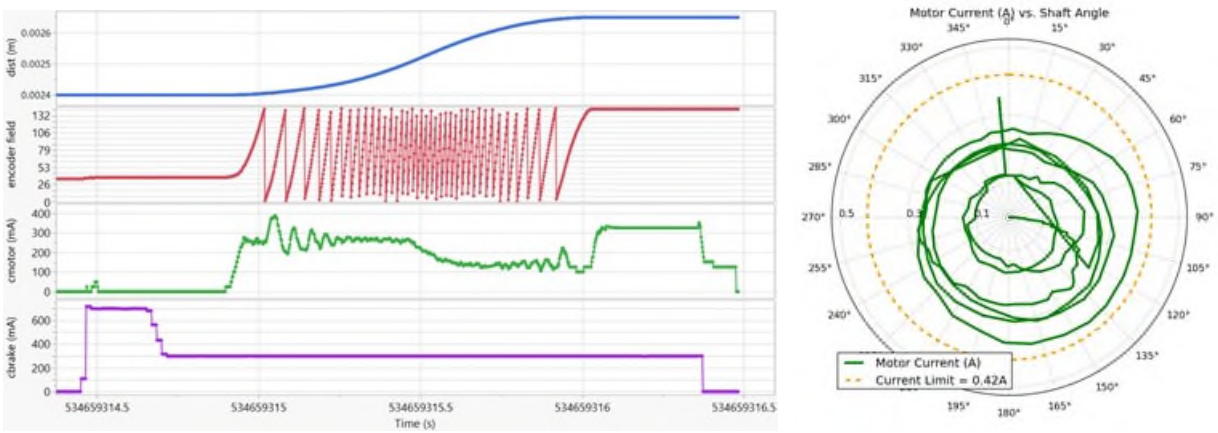

Figure 6. Sol 1545 drill feed diagnostic motion following turret vibration from a sample processing operation. Left: Oscillations in motor current ("cmotor", green) correlate to encoder-indicated motor shaft angle (red), indicating presence of a clocking-dependent disturbance. Right: motor current plotted versus motor shaft angle indicating asymmetric torque disturbance.

Motor current reflects the closed-loop rate controller's reaction to sensed torque disturbances. Plotting motor current vs shaft angle (as shown in Figure 6) provides a rough indication of mechanical resistance within the motor assembly, correlating to shaft position. Nominally, motor current should not significantly vary with motor shaft position during steady state control, in which case the motor current polar plot should appear roughly axially symmetric, as exemplified on Sol 1543 in Figure 5. Asymmetric skew depicted in Figure 6 indicates higher mechanical resistance within a limited fraction of the motor shaft's range of motion. This method of polar plotting motor current vs shaft angle proved invaluable throughout this investigation for tracking the evolution of an apparent "high friction zone".

The small forward and back motion was attempted again three days later, on Sol 1548. These instances completed successfully, but exhibited current spikes similar to those seen on Sol 1545.

A more advanced diagnostic activity was developed, involving several small forward and back motions at normal and slow speeds, and with one or both brake solenoids energized. In addition to gathering data to help identify root cause, these diagnostics were also intended to build confidence in (and experience with) feed stall recovery methods in anticipation of needing to redesign drilling algorithms to autonomously recover from intermittent feed stalls.

The new diagnostic sequence first executed on Sol 1552 with promising results. The first forward and back motions stalled; the first near the end of motion, and the second at the start of motion. A third motion reached its goal but exhibited worsening current spikes and nearly stalled toward the end. The next move energized both brake solenoids. Encouragingly, this move succeeded with no clear periodic current spikes. Further, the next pair of standard feed moves also executed cleanly, adding another data point suggesting that energizing both brakes simultaneously seemed to clear the periodic elevated mechanical resistance signature.

Failure Analysis

The anomaly response team divided and managed tasks to maintain steady progress toward understanding the nature of the persistent drill feed stall anomaly through flight diagnostic activities while also pursuing other lines of investigation. The team generated a fishbone failure diagram to organize hypotheses and evidence for and against each, shown in Figure 7.

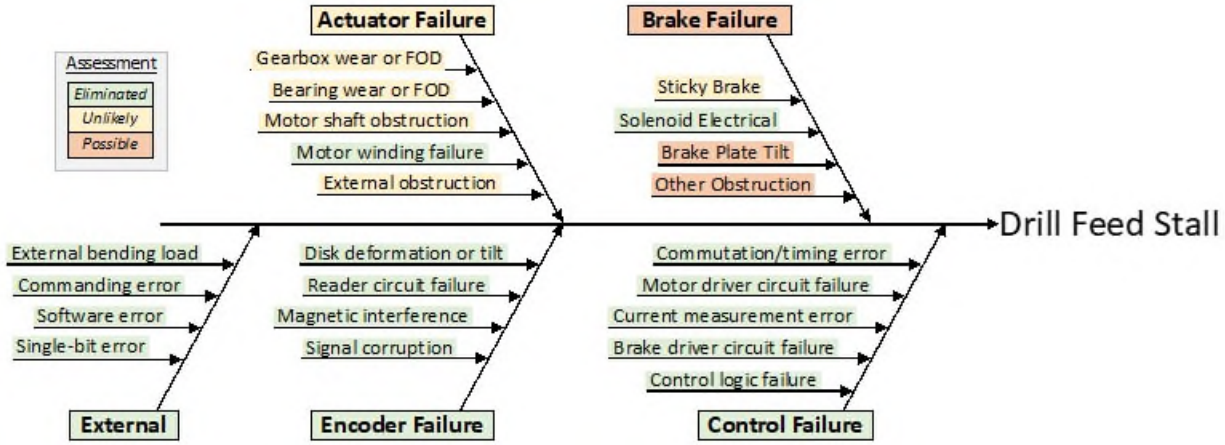

Figure 7. High-level anomaly fishbone failure diagram based on initial flight diagnostics

Telemetry and other observables from the rover were used to rule out whole branches of the fishbone. Once flight diagnostic activities regained motion of the actuator, the team quickly narrowed in on the brake being the most likely branch that caused the anomaly due to the telemetry collected. One key observation ruled out a significant number of potential root causes. Specifically, the impediment to the feed actuating was observed as a “high friction zone” that occurred at a consistent clocking angle with respect to the motor output, and was roughly one third of a motor revolution wide. This meant that obstructions within the gearbox, bearings, or external to the actuator, were highly unlikely. In addition, all other actuator telemetry from the encoder, PRTs, and motor controllers appeared to be otherwise nominal. This telemetry ruled out root cause options related to avionics and control software. Additionally, it was discovered that applying higher brake disengagement force by energizing both brake solenoids simultaneously reduced the magnitude of the drag on the motor through this zone. Repeatedly “clapping” the brake open several dozen times in between motor rotations could achieve a similar effect.

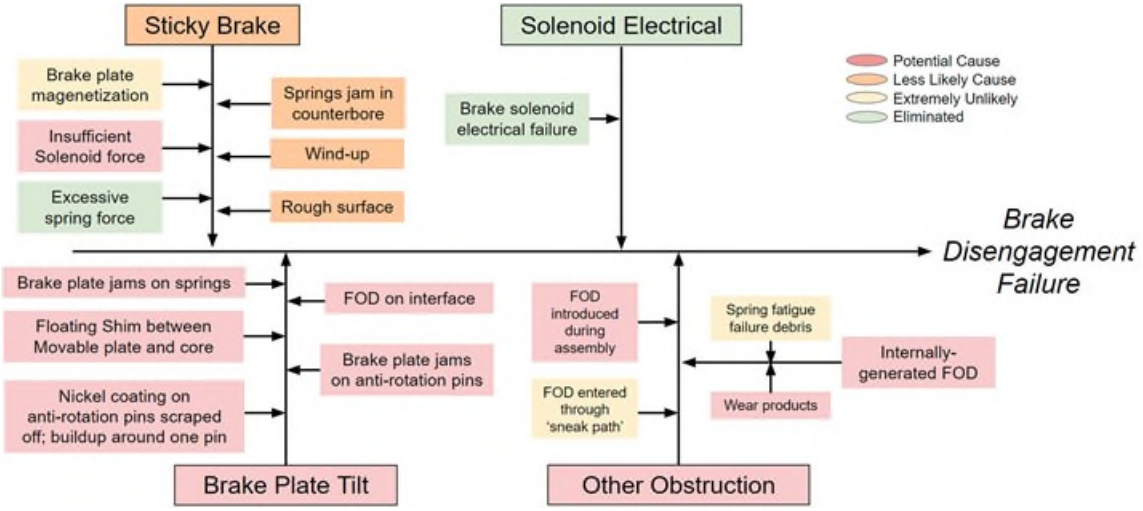

Figure 8. Detailed fishbone failure diagram focusing on potential brake-related problems

The anomaly response team was unable to rule out root causes related to the brake plate failing to disengage creating a high friction zone when the motor turned. Mechanically, this could be explained by the ferrous brake disk not being able to fully retract with a foreign object or piece of debris (FOD) or other obstacle preventing it. This would lead to the ferrous brake disk being tilted with respect to the brake rotor, which is also not perfectly perpendicular to the rotor axis due to assembly tolerances, resulting in a once per motor revolution interference. However, some signatures in the telemetry were not explained by this model. For example, the friction zone appeared to be more difficult to pass through moving in one direction than the other, and would increase in magnitude over time as it was driven through repeatedly, but could be reset by clapping the brake several times. A reduced fishbone diagram focusing on the Brake Failure branch is shown in Figure 8.

At the conclusion of this investigation, the leading theory was that the feed actuator brake was only partially disengaging in a titled state. This was supported by all telemetry from initial diagnostics conducted on the rover. The sub-branches of the anomaly fishbone detailed in Figure 8 show the family of root causes that could lead to a disengagement failure. The most likely causes were either related to parts within the motor shifting within their tolerances (Brake Plate Tilt), or debris building up behind the brake plate (Other Obstruction), or potentially a combination of these causes. The next sections of this paper summarize investigations that were done in parallel with the flight diagnostics in an attempt to narrow down the root cause further.

Review of Feed Actuator Life Qualification Testing and Flight Usage

During development, a qualification model unit of a similar motor type underwent qualification testing involving representative thermal cycling for the duration of the prime mission and rotary life testing with representative mechanical load and 2x total motor and brake cycles. Typical wear products were found inside the qualification model unit during inspection after the life test. No signs of functional or physical degradation were observed during the life test or post-test inspection.

Representative qualification model and flight units were also subjected to limited vibration and shock profiles primarily representing launch and landing dynamic loads. Some limited vibration exposure testing was conducted with representative turret vibration (4-g), but not in a high-fidelity flight-like configuration and not for prolonged periods representing anticipated 1x surface life exposure time. This is in part due to the fact that sample processing and handling routines were developed in parallel with or after the motor development program through systematic characterization of sample processing performance.

At the time of the Sol 1536 feed stall anomaly, the mission overall had surpassed the prime mission surface duration (669 sols) by a factor of 2.3 and had completed 15 successful drilling campaigns out of 27 in the reference mission description. Due to late development of target rock triage routines which added many full-length feed extension cycles, the feed actuator usage rate turned out to be higher than anticipated. Prior to Sol 1536, the flight unit had traversed 97% of its 1x life cumulative travel requirement. This alone was not overly concerning given that the actuator type had been qualified to 2x life. As will be explained in later sections of this report, this accelerated usage profile is not believed to have been a primary driver of the apparent premature failure of the drill feed mechanism.

Investigation of Ground Spare Units

An engineering model actuator from a development chuck mechanism was CT scanned, disassembled, and analyzed for potential signs of wear. No abnormalities were observed, though particle analysis showed signs that small amounts of debris was being generated from the brake plate and other hardware within the motor. None of the qualification model units that went through multiple life cycles, and are frequently used in ground-based testing far beyond 1x life requirements, have shown any anomalous behavior to date.

Benchtop Recreation of Anomaly Signature

In parallel with the on-going flight diagnostics, additional ground testing was executed to support the anomaly investigation. The objective was to re-create the anomalous behavior using an engineering model actuator to aid in determining potential mitigation steps beyond what had already been discovered. The tests were successful in recreating a once per motor revolution friction zone with approximately the correct torque by using stainless steel shims with different thicknesses, widths, and positions. This confirmed the viability of the brake tilt hypothesis as the probable root cause. It also demonstrated that either “clapping” (repetitively cycling) the brakes open and closed or increasing the brake solenoid current could reduce the drag even with an incompressible steel shim. Lastly, it was discovered that clapping the brake was producing axial displacement of the motor shaft within its slop which potentially explained why the benefit was only temporary.

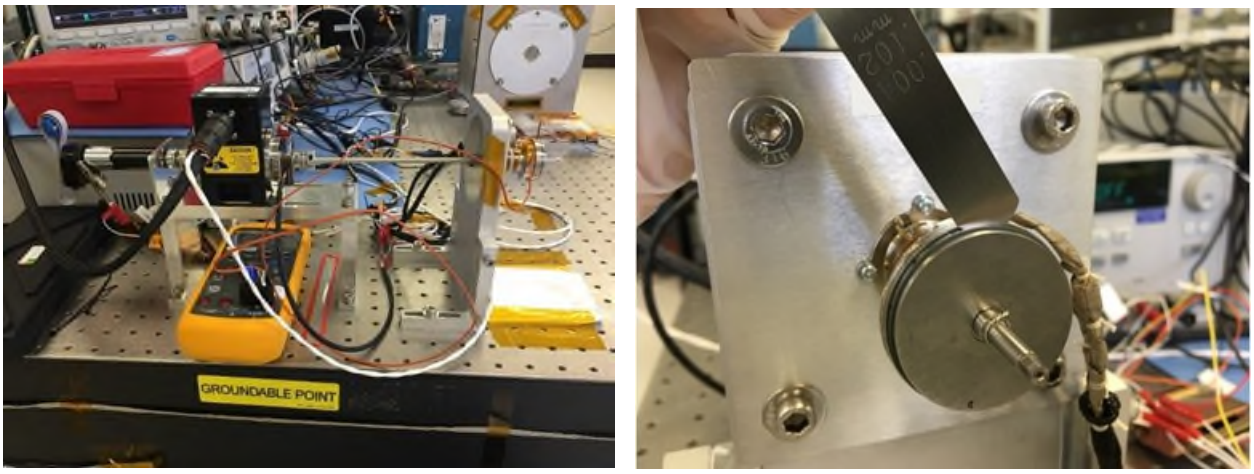

Figure 9. Test setup for benchtop motor investigation (left) with shim manually inserted behind ferrous brake disk to recreate anomaly conditions (right)

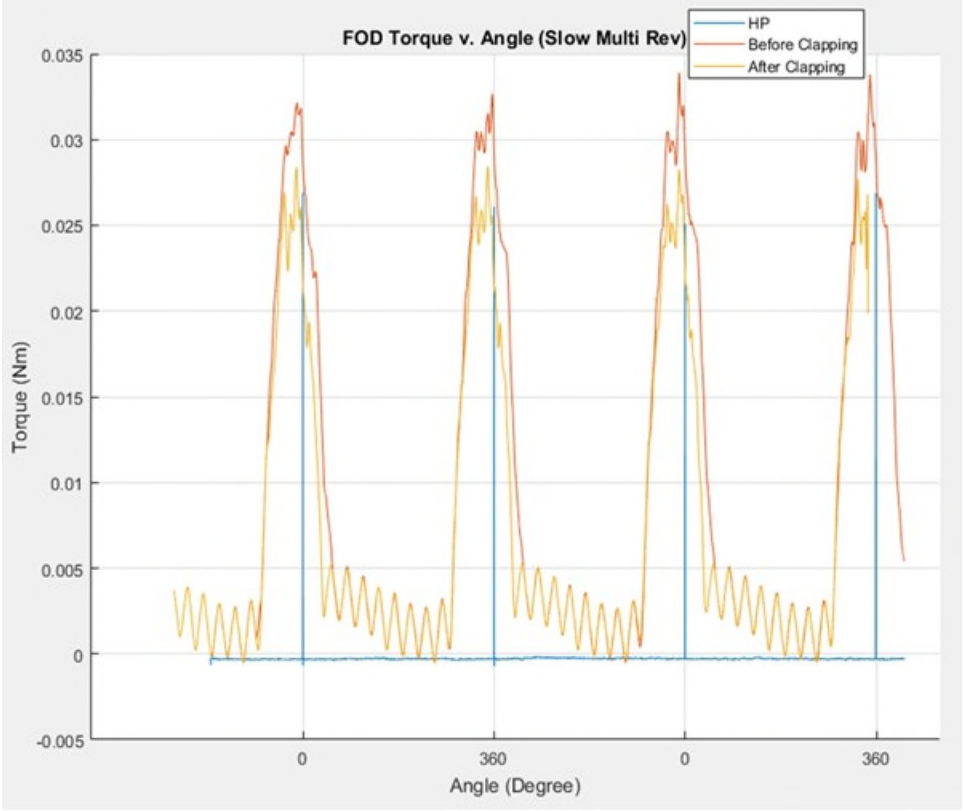

Figure 10. Benchtop motor test sample results. Inserting a shim behind the brake disk to prevent full disengagement yielded a 0.025 N-m torque disturbance spanning approximately one third of a motor revolution, roughly matching flight observations. Furthermore, "clapping" the brake reduced the torque disturbance (yellow).

Late Diagnostics

The Mars Science Laboratory mission continued its scientific investigation of Mars, albeit without a rock sampling capability, in parallel with the ongoing feed anomaly investigation. Over the subsequent months after the initial fault, the team executed a number of diagnostics investigating not only the root cause, but also exploring techniques to overcome the motor drag and conditions that impact mechanism operation reliability. In addition to the aforementioned mitigations, diagnostics explored techniques to begin commanding far from the friction zone, to generate inertia prior to entering the friction zone. The impact of mechanism orientation with respect to gravity, motion directionality, motor velocity, and mechanism heating were also explored, generally with marginal results or statistically insignificant improvement indicators. Repeatable diagnostics continued to be inserted before and after activities imparting turret dynamics. Lastly, increasing motor current limits, effectively allowing the motor controller to request more current, also improved reliability, however there were hardware safety implications with this mitigation. Maximum allowable stall torque limited the amount that motor current could be increased and thermal considerations limited the duration of elevated current operations.

In addition, the Project performed diagnostics on mechanisms similar to drill feed, some of which were used rarely in operations. Through the course of the investigation, it was discovered that the actuator for the drill chuck mechanism showed similar symptoms (but to a lesser severity), and a prior intermittent in-flight stall of the CHIMRA tunnel actuator is suspected to also have had the same root cause. The drill chuck actuator had never been used in flight, so the fact that it was symptomatic indicated the root cause was not related to lifetime usage of the actuators. This implicated other external factors such as turret dynamics, thermal cycles, and other environmental impacts.

Four months after the initial fault, the Project began a regolith sampling campaign at Bagnold Dunes. Regolith sampling did not use the drill and only required CHIMRA actuators to scoop sand, process the material, and deliver instrument portions[3]. This activity included 20 minutes of vibrating the CHIMRA mechanism while rocking the scooped sample back and forth across a 150 micron sieve to separate particles small enough for instrument delivery from the rest of the bulk material. This represented significantly longer duration dynamics than had been executed since the discovery of the feed anomaly. Given the scientific importance of sampling regolith at this site, and the uncertainty in the operation's likelihood to negatively impact the feed mechanism, the Project made the decision to continue with regolith sampling on Sol 1651. As had become routine, dynamic activities associated with regolith sampling were interleaved with feed diagnostics.

Feed diagnostics following the sieving operations yielded no feed motion. The anomaly response team used the subsequent week to re-attempt techniques that had previously been successful, failing to achieve any motion. Finally, the team began combining mitigations that were previously independently successful as well as strategies that anecdotally seemed to improve reliability without strong statistical evidence. On Sol 1659, the feed completed some successful motions, relying on elevated brake and motor currents, energizing both brake solenoids, increased commanded acceleration, and additional mechanism heating. This week completely changed the tone of the anomaly investigation, as the team shifted from root cause investigation and strategies for improving motion reliability to long term preservation of sampling capabilities.

Path Forward

As the team began to conclude that feed motor performance was not reliable enough to be utilized within the dynamic environment of a full drill campaign and normal rover operations risked a complete loss of functionality, efforts were diverted to sampling capability preservation. In the nominal feed stowed position, the drill bit is unable to contact most surfaces due to its positioning behind the contact stabilizer hardware. The stabilizers were designed to contact and preload against any surface in order to stabilize the arm in preparation for drilling activities. Despite all currently available drilling methods first depending on the use of the stabilizers prior to drill bit extension, the Project decided to fully extend the feed mechanism. This action would retain access to the drill bit, thus preserving the possibility of future sampling capability developments.

The process to extend the feed was carefully planned and executed. Long duration and repeated use of the feed motor had been shown to worsen the overall anomaly state. To reduce risk of irreversible binding, motions were conducted using an open-loop commutation mode with moderate brake and motor current limits to ensure that any worsening state of the actuator could be recovered using previously developed mitigation strategies. A thermal watchdog strategy was developed to avoid excessive self-heating due to non-standard, elevated, brake and motor currents that could result in motor heating not easily detectable by conventional thermal fault protection. Brake cycling was inserted after each attempt at extending the feed to reduce the magnitude of the friction zone. The full activity required 4 sols of motion to reach an extension of 58mm, about half way. At that point, Mars and Earth entered solar conjunction, halting communication with the vehicle for several weeks. During this period, the mechanism was placed in what the team believed to be the most beneficial gravity vector with the drill bit pointing up. Following conjunction, the remainder of the activity was performed in a single sol and was successful in moving the feed to its fully extended position of 110 mm. Figure 11 shows the drill bit location at its fully extended position. Without reliable use of the feed mechanism, the team needed to develop a new technique to preload directly on the drill bit and use the robotic arm's 5 degree of freedom capability to safely drill, retract, and deliver samples.

Figure 11. Left: Sol 1780 MastCam verification of the drill feed in its extended position, placing the drill bit beyond the drill stabilizers and preserving the possibility of later development of feed-extended drilling. Right: Sol 2057 drill bit placement at start of first feed-extended drilling operation. (Image Credit: NASA/JPL-Caltech/MSSS)

Conclusion

While MSL's drill feed anomaly investigation never yielded a clear root cause, a family of root causes related to the alignment or obstruction of the ferrous brake plate emerged as a likely source of the behavior. Causes impacting alignment and obstructing the brake were proven to potentially result in the observed behavior and such an issue arising late in MSL's extended missions was deemed credible. Additionally, most alternative suspects were eliminated or determined to be unlikely.

Reliable feed motion has not been achieved since fully extending the feed mechanism. Diagnostics after the feed extension confirmed the engineering team's fears; the mechanism had reached end of life. However, MSL was successful in developing feed extended drilling and sample transfer techniques. After over a year of being unable to sample, Curiosity collected the first feed extended sample on Sol 2057. Curiosity has now collected the majority of its samples using feed extended sampling techniques and continues to conduct a productive and fully capable scientific investigation on Mars.

This investigation exposed several valuable lessons. Paramount to all aspects of the investigation was mechanism performance visibility. The ability to record motor telemetry at a rate significantly higher than the motor turn rate was crucial to understanding the behavior and evaluating mitigation strategies. Additionally, the system's ability to autonomously write higher rate mechanism data in the event of a failure provided key visibility, and saved sols by eliminating the need for additional diagnostics. This lesson was carried forward to the Mars 2020 and Europa Clipper projects, among others. Additionally, several dimensional changes were made to actuators on the Mars 2020 rover to mitigate the most likely causes related to jamming of the brake plate.

An adaptable flight software command architecture coupled with flexible avionics also proved to be an invaluable diagnostic tool. The software preserved the capability to modify motor current limits, commanded brake currents, simultaneously command both brakes, and modify the motor controller commutation mode. All of this was within the existing avionics system's design capability. This exposed uncommonly used functionality that provided operators with an arsenal of diagnostic options, immediately available to the operations team.

This experience exemplified the need for routine mechanism health checks to detect behavioral changes and establish performance baselines for reference when anomalies occur. In the case of the MSL drill chuck mechanism, early detection allowed the team to put into place periodic monitoring and mitigations which are believed to have extended its life. The MSL Project has adopted routine trending activities that provide enhanced visibility into mechanism health beyond nominal use. The Mars 2020 Project intends to repeat

critical mechanism health checkout activities performed after landing periodically to monitor system performance.

Lastly, engineers gained an appreciation for *planning for all potential outcomes*. The Project's decision to extend the feed while it was still semi-operable proved invaluable to restoring drilling capability at the heart of Curiosity's scientific mission and furthering humanity's understanding of the history of Mars[5].

Acknowledgements

The work described in this paper was performed by the Jet Propulsion Laboratory, California Institute of Technology, under contract with the National Aeronautics and Space Administration.

The drill feed anomaly response was an enormous team effort. The authors were only a small part of the anomaly response team consisting of operations engineers and subject matter experts. We would like to thank the following members of the anomaly response team for tirelessly working long nights and weekends for more than a year. Without their contributions to diagnose and extend the feed, it would not have been possible to re-establish the core mission sampling capability: Kobie Boykins, Andrew Kennett, Carolyn Brennan, Alex Bielawiec, Taryn Bailey, Avi Okon, Daniel Limonadi, Jeffrey Biesiadecki, Joseph Carsten, John Michael Morookian, Charles Bell, Steven Lee, Daniel Levine, Anna Boettcher, Kenneth Glazebrook, Ronald Kruid, Kevin Davis, and Daniel Zayas.

References

1. Abbey, William, et al. "A Look Back: The Drilling Campaign of the Curiosity Rover during the Mars Science Laboratory's Prime Mission." *Icarus*, vol. 319, 2019, pp. 1–13., https://doi.org/10.1016/j.icarus.2018.09.004.
2. Okon, Avi B. "Mars Science Laboratory Drill." *Proceedings of the 40th Aerospace Mechanisms Symposium,* (May 2010).
3. Sunshine, Daniel. "Mars Science Laboratory CHIMRA: A Device for Processing Powdered Martian Samples." *Proceedings of the 40th Aerospace Mechanisms Symposium*, (May 2010).
4. Jandura, Louise. "Mars Science Laboratory Sample Acquisition, Sample Processing and Handling: Subsystem Design and Test Challenges." *Proceedings of the 40th Aerospace Mechanisms Symposium*, (May 2010).
5. Abbey, William, et al. "A Look Back, Part II: The Drilling Campaign of the Curiosity Rover during the Mars Science Laboratory's Second and Third Martian Years." *Icarus*, vol. 350, 2020, p. 113885., https://doi.org/10.1016/j.icarus.2020.113885.

Radial Loading of Hydrodynamic Bearings due to Magnetic Variation

Warrick Leigh*, Flora S. Mechentel*, Sehyun Oh* and Michael Underhill*

Abstract

Anomalies during integration of a small-scale hydrodynamic pump motor prompted an investigation into all sources of radial loading on the motor shaft bearings and revealed that, overall, loads were insufficiently characterized. Experimental measurements demonstrated that magnetic forces in the pump motor contributed to significant amounts of radial loading on the bearings, potentially causing wear over long periods of operation and premature failures. The magnitude of these magnetic forces was determined for the rotor and stator separately, as well as for the rotor-stator combination by designing various experimental setups able to recreate the pump motor without hydrodynamic bearings. Characterization of these magnetic forces led to changes in manufacturing processes and enabled selective choices of components, improving the pump motor hardware in order to meet NASA's Europa Clipper project requirements.

Introduction

Mechanically pumped fluid loops have been successfully implemented on various NASA space missions, including the Heat Rejection Systems of the Mars Science Laboratory (MSL) Rover[1], *Curiosity*, and Mars 2020 Rover, *Perseverance*, to control vehicle temperatures by managing waste energy generated by heat sources such as electronic components. In these systems, the working fluid (CFC-11, trichlorofluoromethane) is circulated in a closed loop with at least one compact, 3-phase brushless DC centrifugal pump. This small-scale pump motor utilizes a 6-pole rotor and a 15-pole stator, packaged in a housing of roughly 25-mm diameter and 50 mm in length. The pump operation had been successfully demonstrated in flight, and spare units dedicated to long-term testing on Earth[2,3] (up to 12 years) were still in operation and had shown no indication of abnormal performance. Nevertheless, when operational testing of newly manufactured pumps for the Europa Clipper Heat Redistribution System (HRS)[4] resulted in electrical anomalies and premature failures, expectations of an uneventful integration were replaced with causes for concern. An immediate root-cause investigation and recovery strategy was conducted to meet the manufacturing schedule and ensure the pumps would meet the 12-year life requirements of NASA's Europa Clipper mission.

The investigation started with inspecting the operational life-test pumps to quantify any differences in manufacturing with the newly received pumps. Subsequent disassembly of these units revealed an unexpected discovery: the pumps had been operating in a mixed lubrication regime, with rotors exhibiting extensive surface damage at the bearing interfaces. As a result, a quantification of all potential sources of radial loading present in the original pump design was carried out. The radial magnetic forces imparted by the rotor and stator were determined to be major contributors to bearing wear and had not been considered in the hydrodynamic bearing analysis for the pump design. The experimental characterization and quantification of the radial loading due to magnetic forces in small-scale, surface-mounted permanent magnet motors is the focus of this paper.

Hydrodynamic Bearings

Hydrodynamic bearings differ from radial ball bearings in that there are no rolling elements mechanically restraining a rotating shaft. Hydrodynamic bearings rely on a fluid film between the shaft (or journal) and bearing sleeve for load transfer and lift. A pump using this type of bearings is illustrated in Figure 1. The hydrodynamic bearing geometry allows for fluid pressure to be generated as the shaft rotates, which creates

* Jet Propulsion Laboratory, California Institute of Technology, Pasadena, CA

a fluid boundary that lifts the shaft and is intended to prevent contact with the inner walls of the bearing sleeve. The viscosity of the working fluid, the rotational speed of the shaft, and the geometry of the bearing sleeve are all considerations in designing a hydrodynamic bearing with appropriate lifting force to counteract radial loading on the shaft. When properly designed and running at the designed rotational speed, hydrodynamic bearings ideally have no physical contact between the outer diameter of the shaft and inner diameter of the bearing sleeve, which results in a theoretically infinite life. Shaft-to-bearing sleeve contact should only be present during start and stop cycles, where acceleration from, and deceleration to a no-rotation state results in insufficient film thickness to lift the shaft away from the inner surfaces of the bearing sleeve. In this mixed lubrication regime, the resulting contact can lead to wear on the shaft and bearings and reduce the service life of the pump.

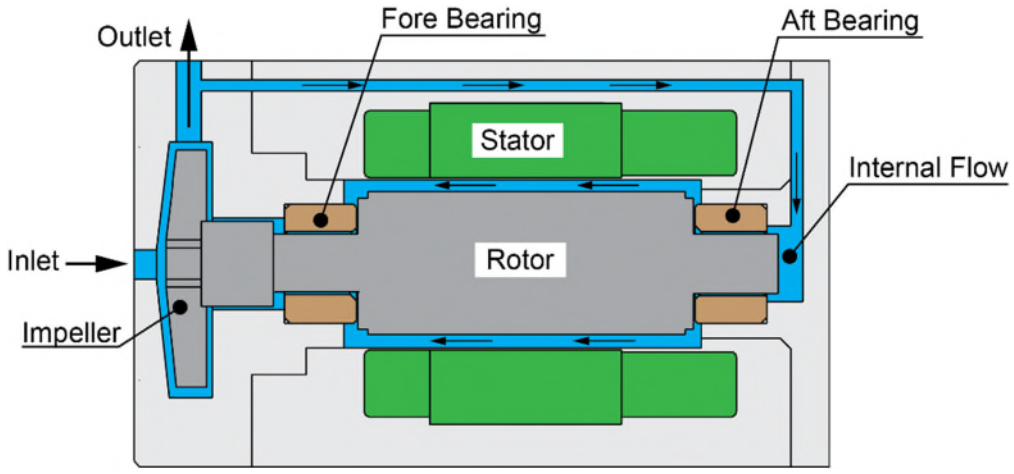

Figure 1. Cross Section of a Hydrodynamic Pump

A pump used in a fluid loop system is a prime candidate for hydrodynamic bearings, as the working fluid in the system can also be utilized for the pump motor bearings. This creates competing design interests as the working fluid must be able to fulfil multiple roles, such as the heat transfer and bearing lubrication requirements. In the case of the Europa Clipper HRS, CFC-11 is a low-viscosity refrigerant—ideal for heat transfer, but not ideal for bearings—which further increases the importance of understanding the radial loading of the pump in order to meet the 12-year life requirement for the Europa Clipper mission.

Life-test Pump Observations

Operation of this pump had been demonstrated over a 12-year period as part of the Mars Exploration Rover/MSL cooling fluid loop life testbed and showed no abnormal behavior prior to removal from the testbed. After disassembly, the hydrodynamic pump components were thoroughly inspected. As shown in Figure 2, shaft wear was evident on the bearing surfaces of the rotor, indicating that the radial loading was significant enough to cause the shaft to contact the inner diameter of the bearing during operation. This provided strong evidence that the pump bearings were operating in a mixed lubrication regime rather than the assumed fully hydrodynamic state and prompted the need for further investigation on what forces could be causing mixed lubrication operation.

Sources of Radial Loading

The hydrodynamic bearing analysis had originally considered two main sources of radial loading on the fore and aft bearings. The first was from dynamic unbalance, which stems from uneven mass distribution of the rotor, and generates a force perpendicular to the axis of rotation; the second is produced by the reaction forces at the centrifugal impeller from interaction with the working fluid. A more detailed investigation suggested that forces from variations in magnetic field of the rotor and the stator, a subject not originally considered, could be an order of magnitude greater than forces caused by the rotor's dynamic

unbalance and impeller operation. The different sources of radial loading in the hydrodynamic bearing are illustrated in Figure 3, and listed in order of increasing magnitude:

1. Reaction force from the impeller's interaction with the working fluid
2. Dynamic unbalance
3. Magnetic unbalance

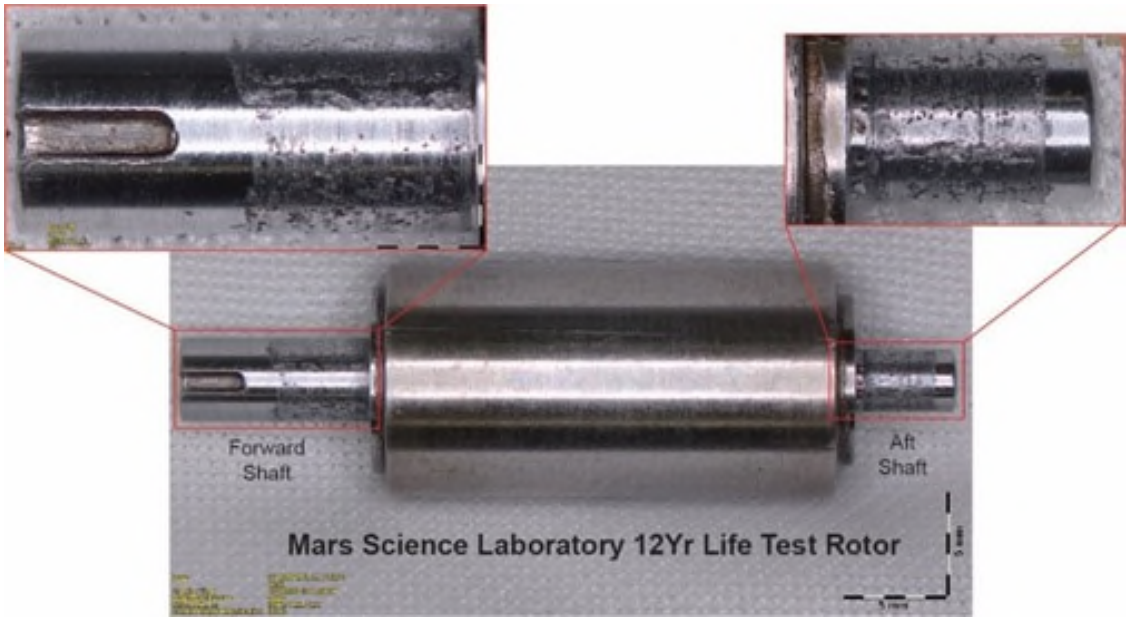

Figure 2. Shaft Wear on Life-test Pump Rotor

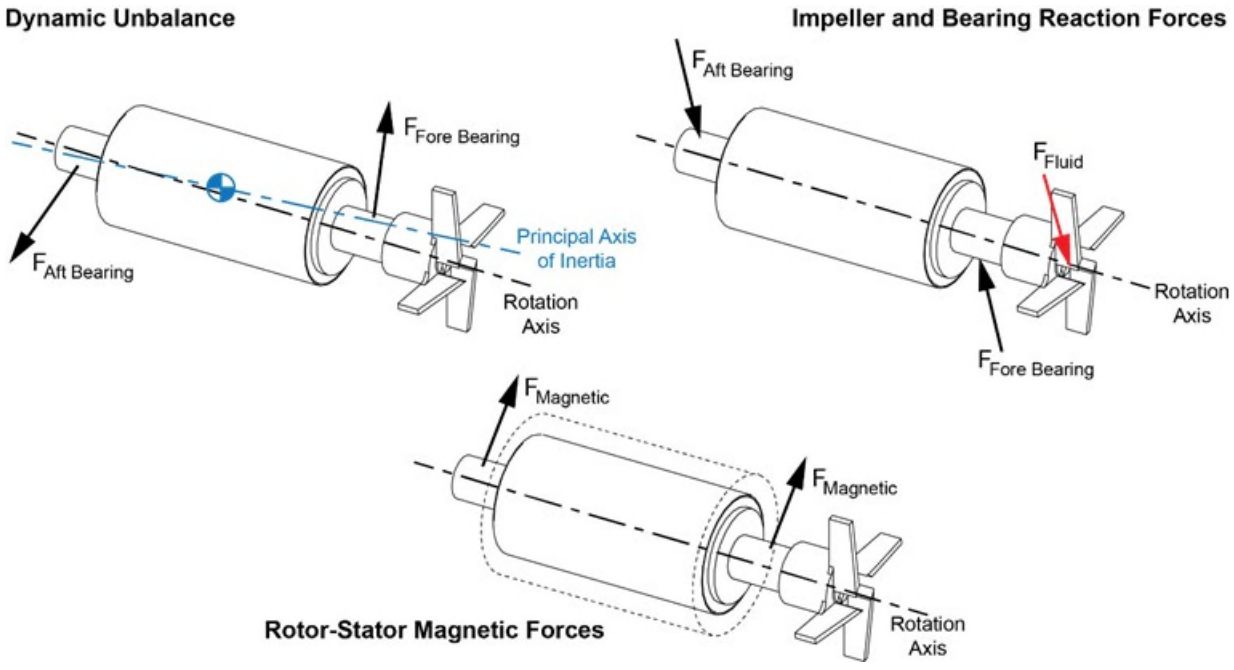

Figure 3. Sources of Radial Loading in the Hydrodynamic Pump

Radial Loads due to Impeller Forces

The pump design features a cantilevered impeller that is mounted on the end of the rotor shaft. During pump operation, the fluid imparts a radial force on the rotor as each blade pushes the fluid into the outlet of the pump. This action induces a force and moment on the shaft that is reacted by the two bearings. A Computational Fluid Dynamics analysis was carried out to determine the magnitude and characterize the varying nature of this force as a function of flow rate. In the operational regime of the pump for the Europa Clipper mission, the average radial load reacted from the impeller was estimated to be 0.2 N for the fore bearing and 0.06 N for the aft bearing.

Radial Loads due to Mass Unbalance

To reduce vibrations and bearing wear, dynamic balancing of rotating parts is common practice in industrial machines. Dynamic unbalance of the rotors was measured on two planes at 5000 rotations per minute using a dynamic balancing machine. The maximum unbalance of newly manufactured rotors was 2.3e-7 kg.m per plane. To reduce the unbalance, component tolerances were reviewed across the manufacturing of rotors at different stages of assembly. In addition, a dynamic balancing step was added to the existing manufacturing process, aimed at correcting unbalance introduced during the early phases of rotor fabrication. The method of material removal, shown in Figure 4, was chosen to work within the existing pump motor design. It required drilling out a small amount of material from underneath the magnets on the rotor.

The dynamic balancing step reduced the rotor unbalance to a maximum value of 7.6e-9 kg.m per plane. Using $F_{Unbalance} = U * \omega^2$ (with U the measured unbalance, and ω the rotational speed of the rotor), the radial bearing forces were calculated to be up to 0.1 N per bearing at the maximum rotation speed of the pump.

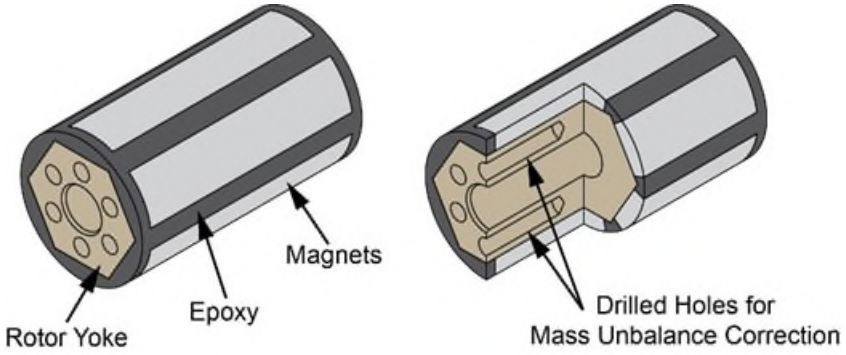

Figure 4. Rotor Construction and Mass Unbalance Correction Through Mass Removal

Radial Loads due to Magnetic Forces

Variations in magnetic forces between the rotor and the stator can have significant contributions to bearing radial load. Magnetic field deviation in the radial direction of a cylindrical component is characterized as magnetic runout. Furthermore, the interaction of the two magnetic fields is affected by any physical radial offset of the stator from the rotation axis of the rotor, which will create a non-uniform air gap between the rotor and stator. The magnitudes of these magnetic forces were determined experimentally for the rotor and stator separately, as well as for the rotor-stator assembly using variations of a test setup which was able to recreate the rotation of the rotor inside the stator without the use of hydrodynamic bearings.

Experimental Setup Validation

To reconstruct the pump motor without the presence of the fluid loop or fluid bearings, a mandrel was inserted into the center bore of a rotor and installed in between two radial ball bearings as part of the test setup shown in Figure 5. The mandrel was connected to a dynamometer in order to apply a variable load

to the motor during operation. Linear stages were used to adjust the radial position of the stator relative to the rotor, and the axial position of the rotor relative to the stator. The forces acting on the stator were measured with several high-stiffness load cells.

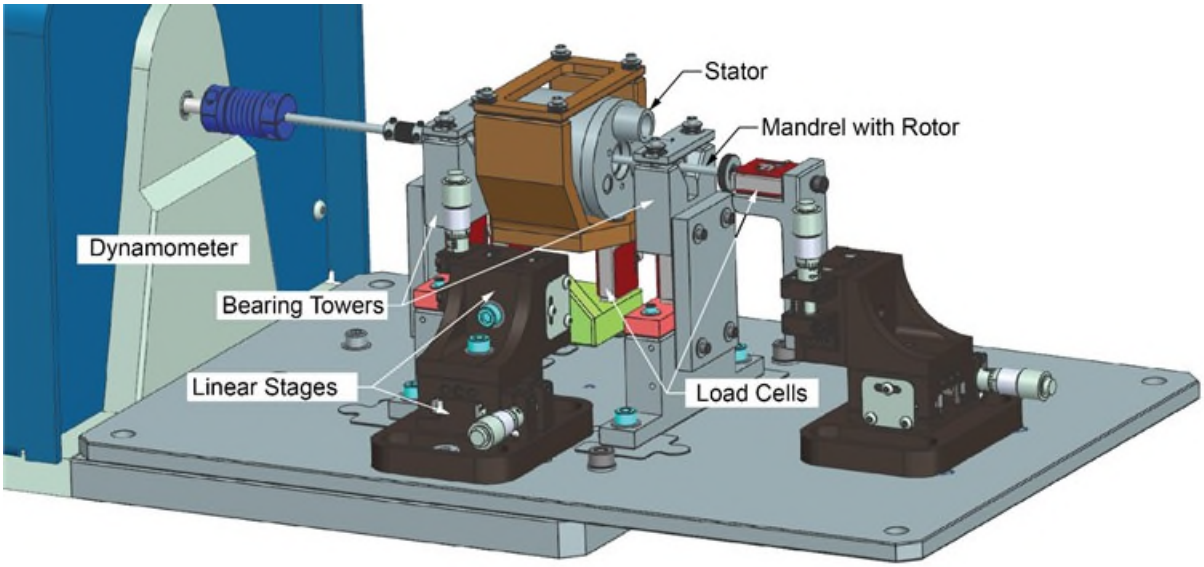

Figure 5. Pump Motor Dynamometer Test Setup for Magnetic Load Characterization

Operational testing of the pump motor was successfully demonstrated using the test setup shown in Figure 5. The results showed that the current draw of the motor as a function of torque resistance was consistent with the manufacturer specification, proving that the test setup would produce reliable results for subsequent investigations. The dynamic balancing process using material removal directly beneath the magnets on the rotor was cleared for production use by demonstrating that a rotor with a maximum allowable amount of material removed still met the pump operational specifications.

Magnetic Runout Characterization of Rotors

Magnetic runout of the rotor is the result of differences in the strength and placement of the magnets on the rotor yoke. Differences in magnet adhesive gap thickness, magnet material property variation, and physical runout of the rotor shaft are all factors that can change the magnetic field and shift the magnetic center radially away from the axis of rotation. The combined effect of these individual errors is a net radial attractive force in the direction of the highest magnetic field. Investigating this force required the development of a method for measuring the magnetic runout of the rotor.

A dedicated test setup, shown in Figure 6, was designed to gain an understanding of the magnetic runout present in the pump rotor. The rotor was installed in a mandrel, and a surrogate magnetically attractive component (in this case, a carbon steel flat head bolt) created the necessary attractive force with the rotor permanent magnets. The attractive force was measured by the supporting load cells providing a measurement range of ±36 N. A stepper motor was coupled to the mandrel, allowing a slow, controlled rotation at 3 rpm above the surrogate bolt. The air gap, or distance between the rotor and the magnetic element, was adjusted by varying the height of the platform supporting the surrogate bolt and the load cells. A first iteration of the test setup led to relatively large variations in air gap (≈0.13 mm) during the rotation of the rotor due to material deflections. Improvements in the stiffness of the components and the load cells led to a reduction in air gap variation by a factor of 10, thus highly improving the magnetic characterization of the rotors.

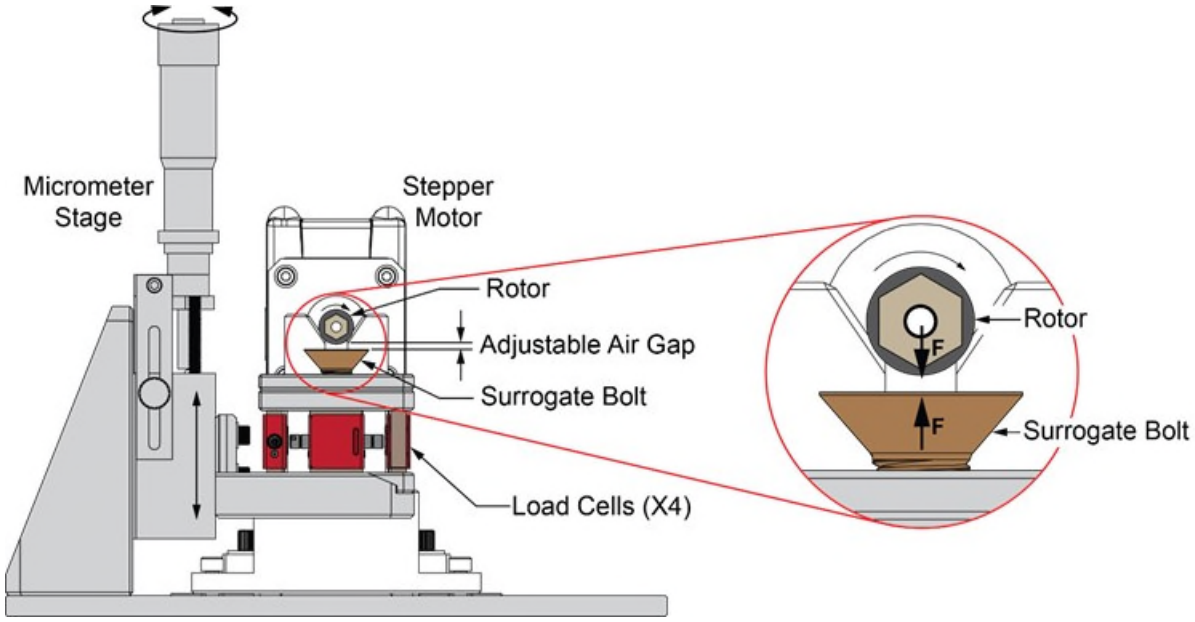

Figure 6. Test Setup for Magnetic Runout Characterization of the Rotors

Force data in the vertical direction was collected over a full rotation of the rotor for different air gaps, as shown in Figure 7. Maximum forces were found to occur between adjacent pole (magnet) pairs, with six pole pairs per rotation (Figure 9). Minimum forces were found to occur at the pole locations. The magnitude of the force profile increased quadratically as the air gap between the rotor and magnetic surrogate was reduced. This observation is important when characterizing magnetic runouts of various rotors, since any comparison between units needs to done at the same air gap. Figure 8 is a representation of the same force data on a polar plot, and the red dot locates the centroid of the magnetic field of the rotor—the radial distance of the magnetic center. The magnetic runout of the rotor is directly correlated to the offset between this centroid and the axis of rotation.

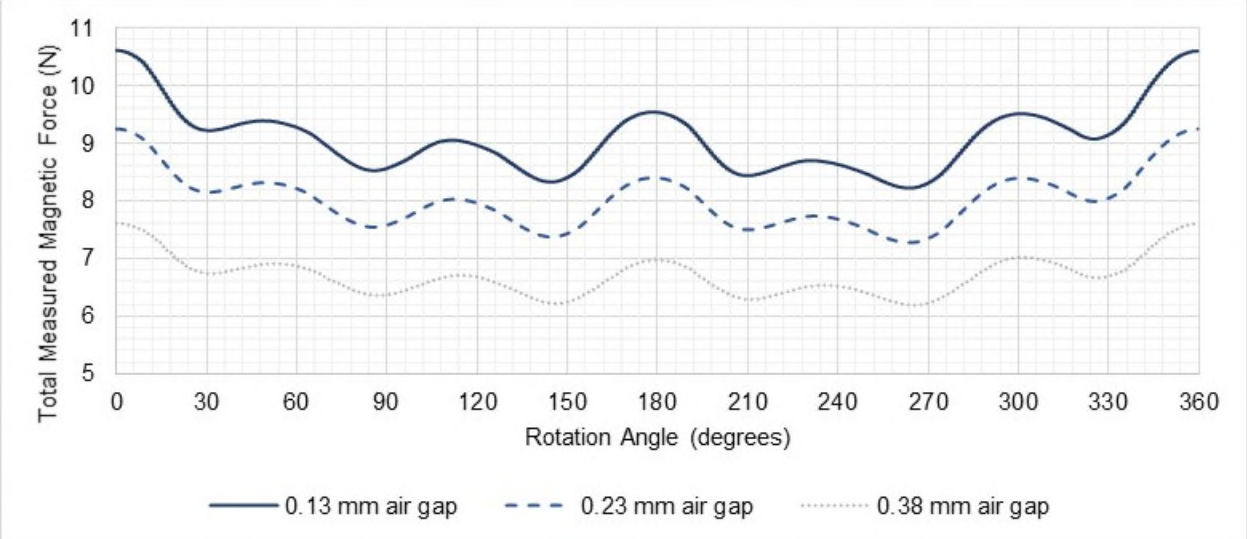

Figure 7. Measured Magnetic Forces of a Rotor and Surrogate Magnetic Element as a function of Rotor Rotation Angle at Various Air Gaps

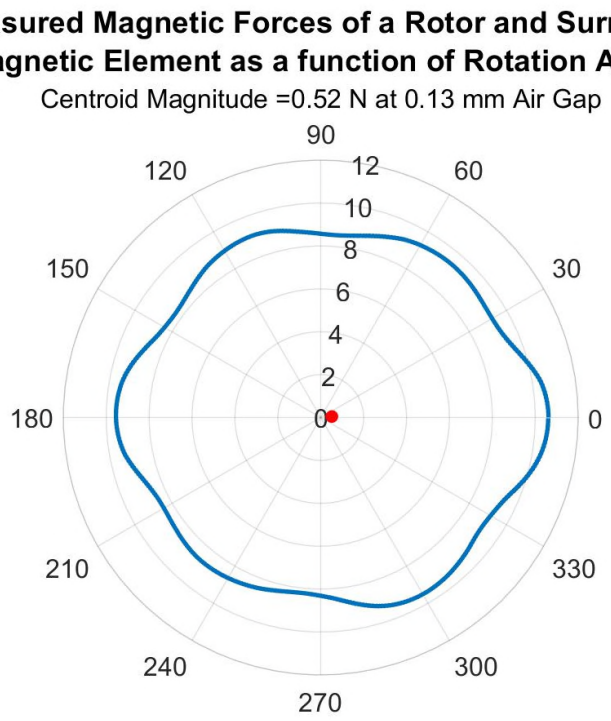

Figure 8. Magnetic Field of a Rotor Measured with a Surrogate Magnetic Element Represented on a Polar Plot. The Magnetic Centroid is shown in Red.

From the magnetic force measurements, it was determined that an ideal rotor with no physical or magnetic runout would have a six-per-revolution period force profile corresponding to the number of pole pairs present in the rotor, as illustrated in Figure 9. However, the rotor's axis of rotation is not necessarily coincident with the magnetic center of the rotor. Two components contribute to this effect: the physical runout of the rotor, and the physical runout of the mandrel. In an effort to remove the physical runout of the mandrel, the magnetic characterization of the rotor was performed with the mandrel press fit at four different clocking positions with respect to the rotor, and the four datasets were averaged. The magnetic and physical runout impose a longer, once-per-revolution period sinusoidal force profile on top of the six-per-revolution sinusoidal force profile and shifts the magnetic center away from the axis of rotation.

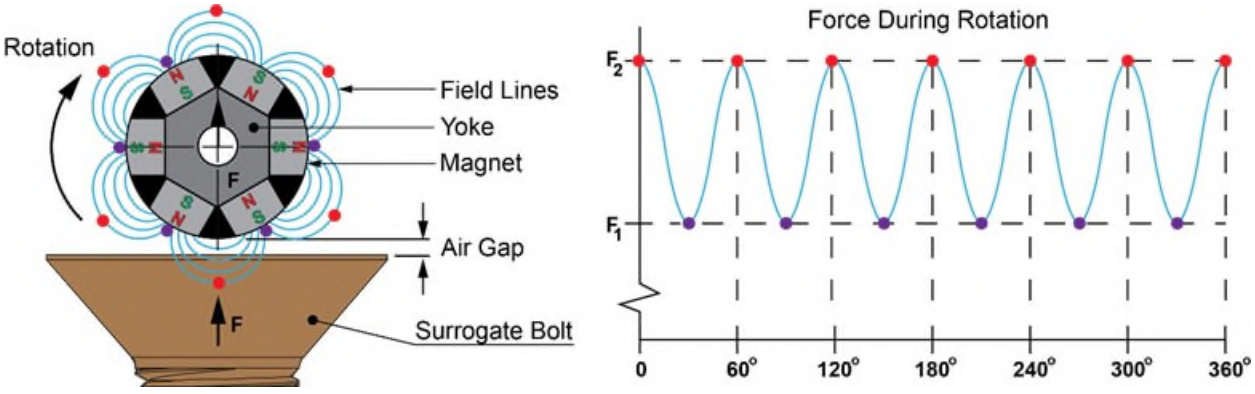

Figure 9. Schematic of a Rotor's Magnetic Field without Magnetic Runout

To investigate the effects of magnetic runout of the rotor on the radial loading of the bearings, a numerical model was developed to simulate the rotor inside an ideal stator. This model assumes that an ideal 15-pole stator can be modeled as 15 fixed magnetic elements surrounding the rotor. The experimental measurement of the radial force of the rotor with respect to a single magnetic element (the surrogate bolt) as a function of rotation angle is used as input, and the sum of the 15 radial forces is computed to determine the total magnetic force. The total resultant force, which contributes to the radial loading of the pump motor bearings, is then calculated over a complete rotation of the rotor.

Two numerical test cases were used to validate this 15-pole stator model. The first assumes a rotor without magnetic runout. In this case, the magnetic force versus rotation angle between the rotor and a single fixed magnetic element is represented by a cosine function with six periods per revolution (Figure 9). When taking the sum of the radial forces from 15 fixed elements, the resultant force is zero for all angles of rotation. In other words, a 6-pole rotor without magnetic runout will produce no net radial force in an ideal 15-pole stator. The second test case assumed some magnetic runout of the rotor, represented by additional cosine and sine functions with one period per revolution. In this scenario, the magnetic centroid is not coincident with the axis of rotation (Figure 10). When taking the sum of the radial forces from 15 fixed elements, the resultant load over a full revolution of the rotor is constant, and larger than zero. The magnitudes of the two orthogonal components of the radial load (F_y, F_z), and the resultant force as a function of rotation angle are shown in Figure 10. Furthermore, an interesting correlation was made: the ratio between total resultant force and magnitude of the magnetic centroid was exactly 7.5.

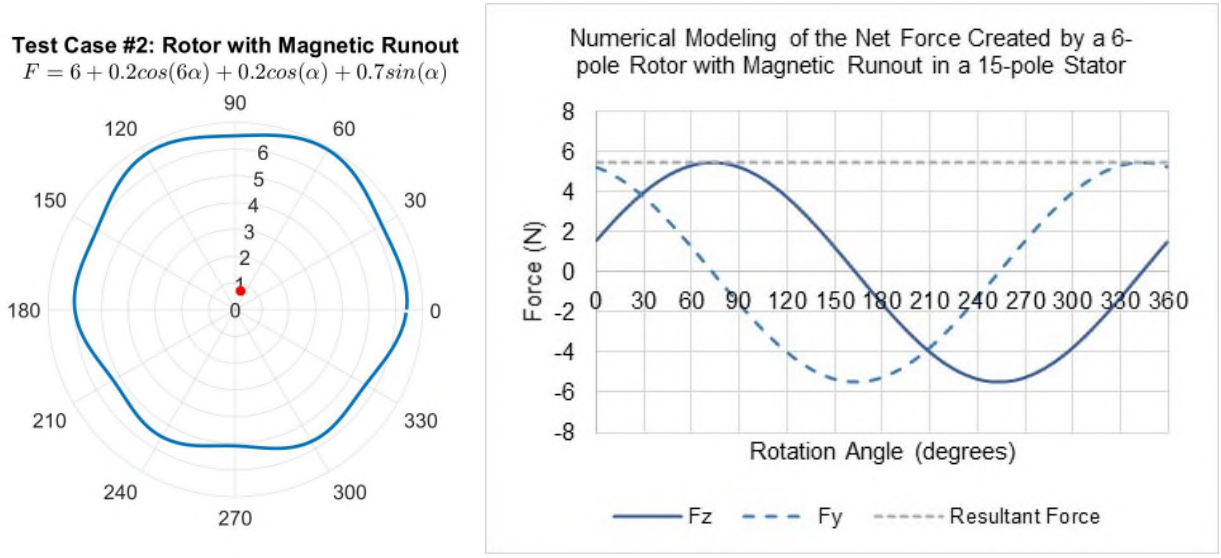

Figure 10. Forces Computed with the 15-pole Numerical Stator Model using a Numerical Model for a Rotor with Magnetic Runout (Left) as a function of Rotation Angle (Right)

The magnetic runouts of 27 newly manufactured rotors were experimentally characterized using the surrogate bolt setup, and the data was used as input for the 15-pole numerical model to calculate the resultant radial loading in the pump motor assembly. Confirming the result from the ideal test case, the resultant radial force and the magnetic centroid of the rotor were linearly correlated with a factor of 7.5, as shown in Figure 11. Consequently, the magnitude of the magnetic centroid of a rotor, measured with a single surrogate magnetic element over a full rotation of the rotor at a given air gap, was selected as the parameter to characterize and perform relative comparisons of the magnetic runout of the rotors.

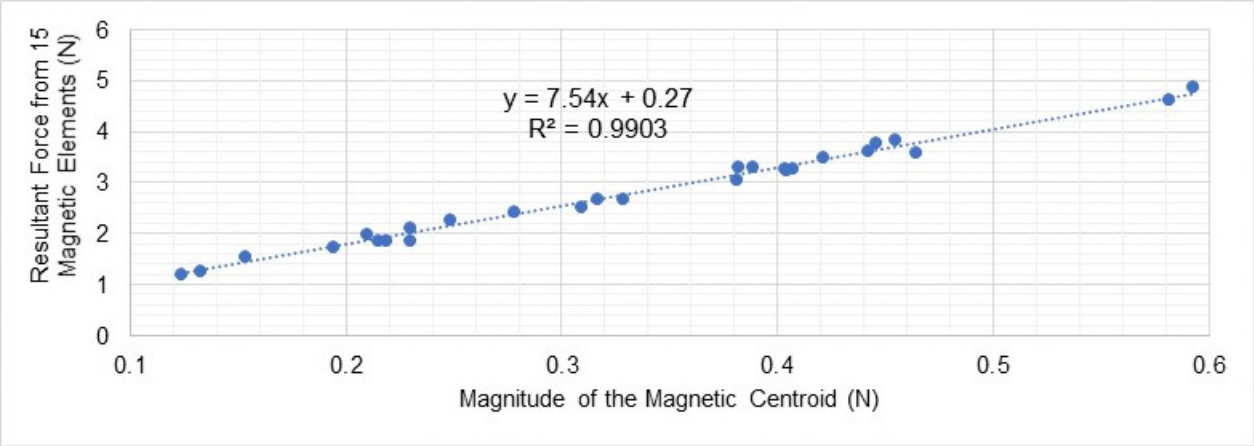

Figure 11. Resultant Force Calculated with the 15-pole Numerical Model as a Function of the Experimentally Measured Magnetic Centroid of 27 Rotors

Magnetic Runout Characterization of Stators

A similar test setup was designed to characterize the magnetic runout of the stators (Figure 12). In this case, a strong neodymium magnetic element was adhered to a carbon steel mandrel placed inside the stator and acted as a single magnetic element creating a vertical attractive force with a localized portion of the stator. The air gap between the magnetic element and the stator could be adjusted with linear stages. The stator was not energized in this case and was rotated around the magnetic element with the use of a stepper motor to establish the magnetic characterization at all angles. In practice, the rotor rotates inside the stator, but in the test setup, rotating the single magnetic element would have also required a rotation of the load cells to measure the radial force in line with the magnet. Instead, the magnetic element was kept stationary, and the vertical magnetic force was measured with a stack of four load cells. Figure 13 shows the total magnetic force as on a polar plot, where the 15 poles of the stator can be identified. The magnetic centroid can thus be measured using this type of setup to characterize, and relatively compare the magnetic runout of the stators.

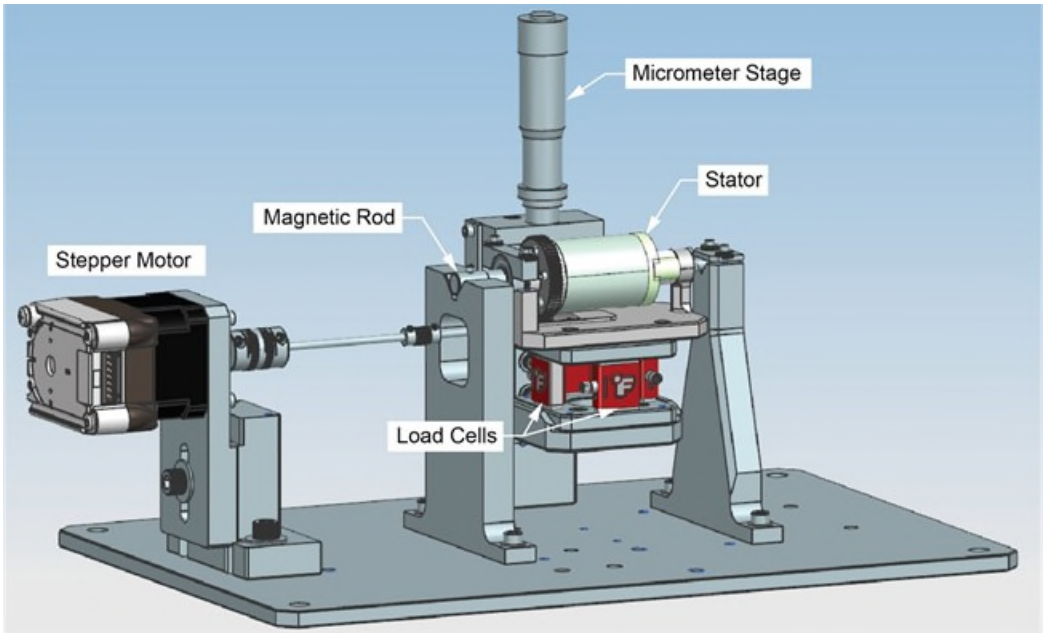

Figure 12. Test Setup for Magnetic Runout Characterization of the Stators

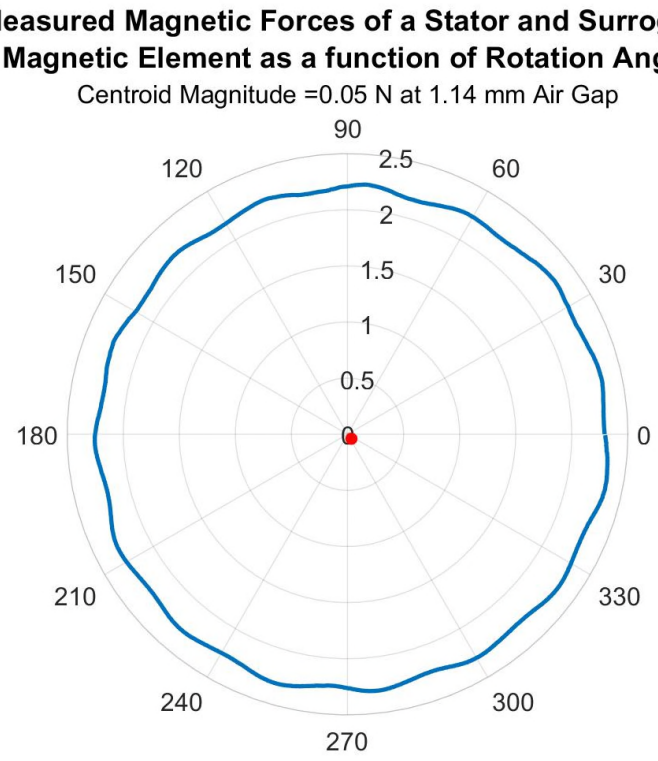

Figure 13. Magnetic Field of a Stator Measured with a Surrogate Magnetic Element Represented on a Polar Plot. The Magnetic Centroid is Shown in Red.

Radial Magnetic Force as a Function of Rotor-Stator Offset in the Pump Motor Assembly

Following the magnetic characterization of the rotor and stator separately, various measurements were made at the pump motor-assembly level. First, the stator was translated vertically with the rotor remaining in a fixed position. Because magnetic forces increase with a reduction in distance between sources, the offset generates a greater radial magnetic attractive force in the area of least air gap between the rotor and stator. As shown in Figure 14, the starting point for the stator was chosen to be at a hard limit, with the upper portion of the stator bore contacting the outside diameter of the rotor. The stator was then translated upward, allowing the rotor to pass through the center of the stator until coming into contact with the opposite side of the stator bore. Neither rotor nor stator were rotated during this translation.

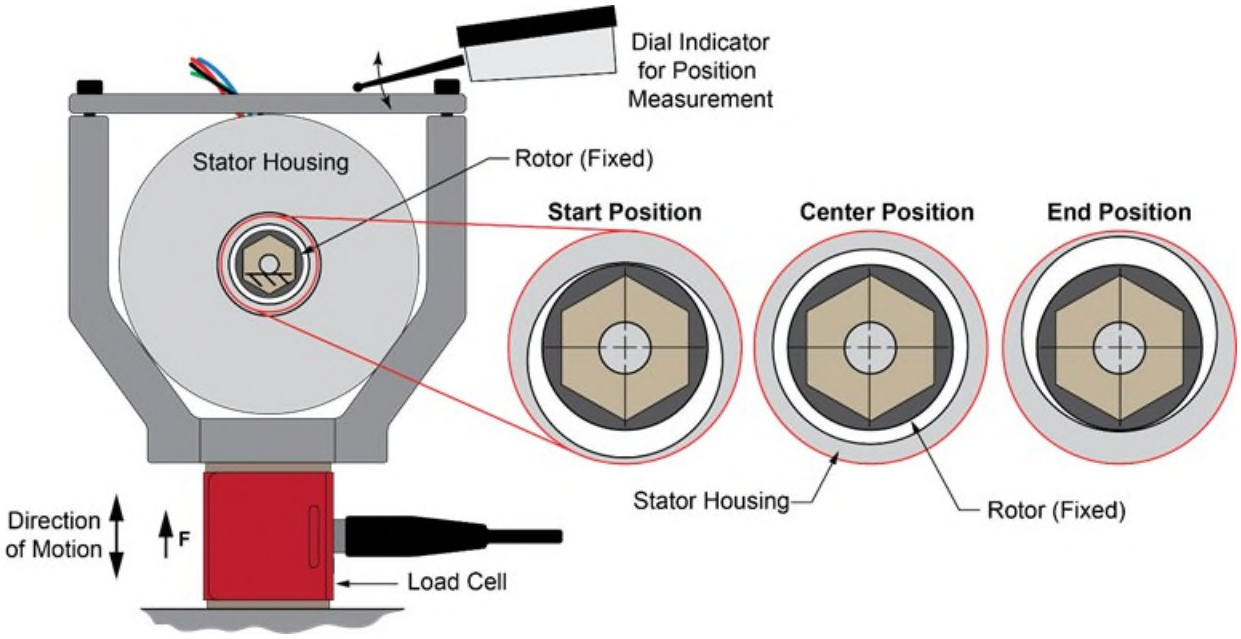

Figure 14. Pump Motor Radial Offset Test Setup

Force results are given in Figure 15. Different datasets were obtained by rotating the position of the stator in 45 degree increments to capture the magnetic force as a function of radial position in different locations around the circumference of the stator bore. A combined average (dotted line) was then used to characterize the rotor-stator assembly. In the starting position, the maximum attractive force occurs at the top of the stator, pulling it downwards, and therefore putting the load cells in compression, creating a negative force. At the final position, the stator is being pulled upwards, putting the load cells in tension, and creating a positive force. However, the measured data needed to be corrected for the stiffness of the mandrel mounted through the rotor, contributing to an uncertainty in the vertical position of the rotor inside the stator in the test setup. Because the data in Figure 15 was fairly linear over small displacements, the correction was made by modeling the magnetic load as a linear spring of constant k_1, using the mandrel material stiffness k_2, and calculating an equivalent spring constant k_{eq} using Equation 1 for two springs in series. The experimental data demonstrated that the magnetic runout of the rotor and the stator would play a large part in the static radial loading of the bearings, and a displacement of only 14 microns could create as much as 1 N of radial load, largely exceeding the dynamic unbalance and impeller loads.

$$\frac{1}{k_{eq}} = \frac{1}{k_1} + \frac{1}{k_2} \tag{1}$$

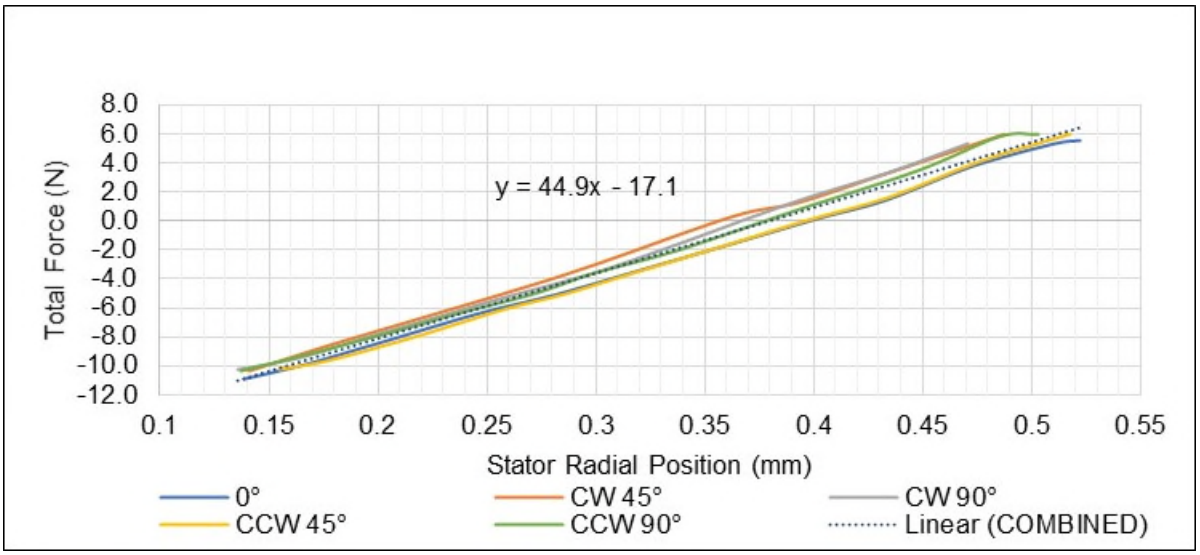

Figure 15. Experimental Measurement of the Radial Magnetic Force as a Function of Rotor-Stator Offset

Radial Magnetic Force in the Rotor-Stator Assembly

In order to further quantify potential loads on the bearings at the pump motor-assembly level, the setup was modified to read the force on the stator during rotation of the rotor (Figure 16). The same stack of four load cells was used to measure the vertical force (F_z) by using the sum of the four measurements. As shown in Figure 17, the two load cells located on both sides of the mandrel (off axis) could also be used to recover the shape—but not the magnitude—of the horizontal force (F_y) using a moment balance.

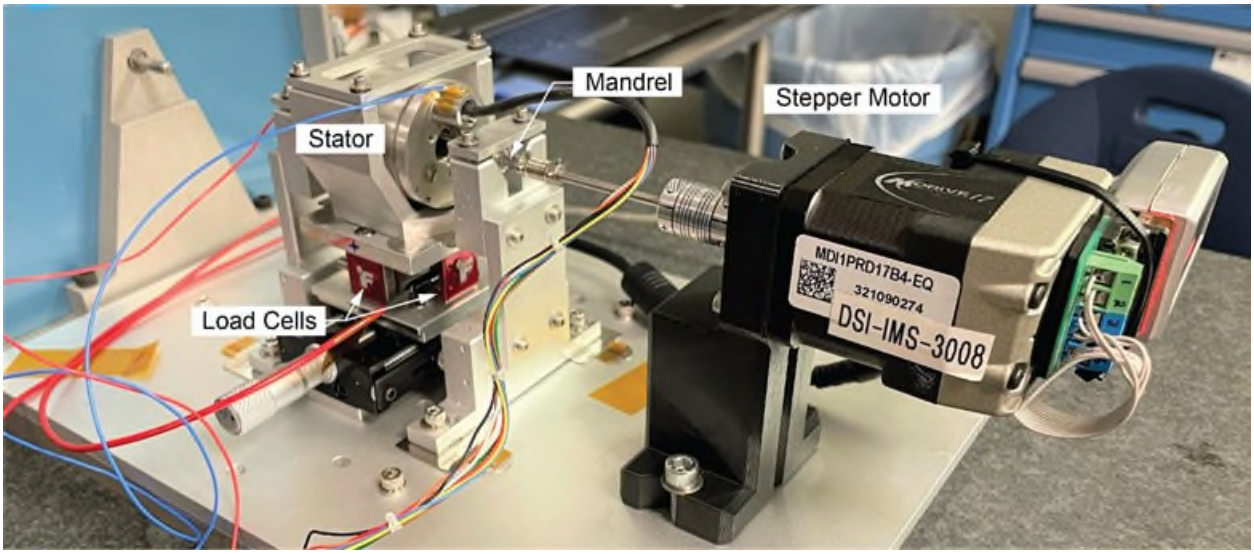

Figure 16. Test Setup for Measuring Bearing Forces using Rotor and Stator

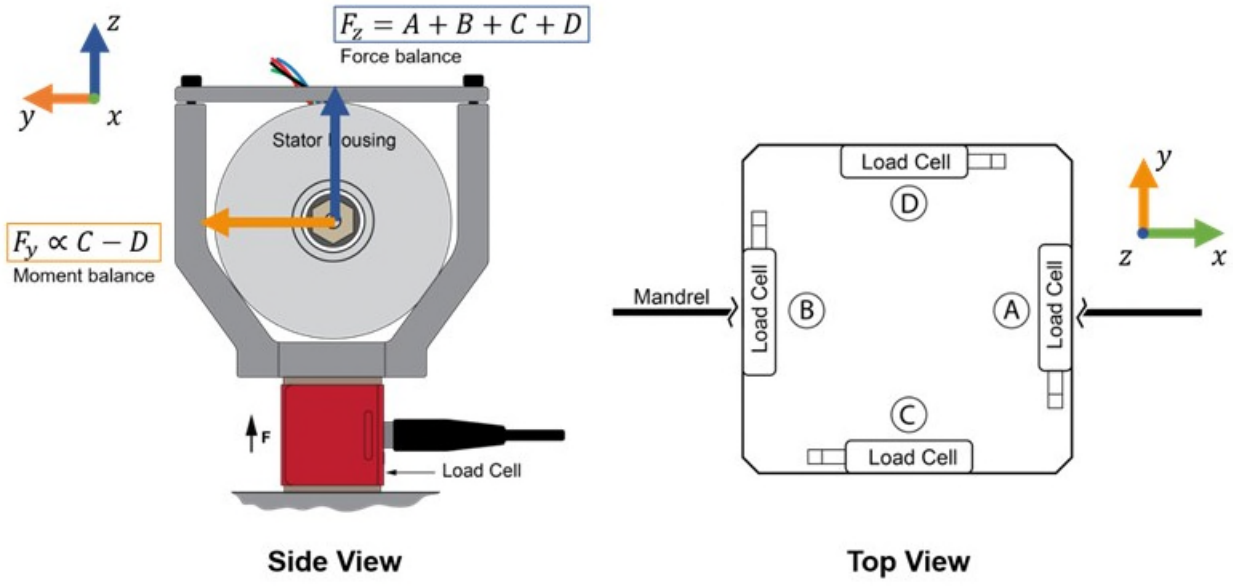

Figure 17. Load Determination from the Four Load Cell Measurements

The experimental measurements of these two forces (proportional to F_y and F_z) for a rotor-stator assembly are given in Figure 18. The numerical 15-pole stator model described in an earlier section had demonstrated that the magnitude of the radial load was ideally constant over a full rotation of the rotor. From Figure 18, at 110 and 290 degrees, the force is vertical ($F_{y=0}$), corresponding to when the stator is being pulled directly downward and the rotor is being pulled directly upward, or similarly, when the stator is being pulled upward and the rotor being pulled downward. The curve of F_z is shifted in the vertical direction and not centered around zero due to the radial offset between the rotor and the stator. The difference between maximum and minimum values (8 N) is the value of interest. At 110 and 290 degrees, F_z is equal to the magnitude of the resultant radial load, which is on the order of ±4 N. As a result, the radial loading due to magnetic forces from the rotor and the stator during pump motor operation clearly eclipse the radial loads due to dynamic unbalance (≈0.1 N per bearing) and the impeller (≈0.2 N and 0.06 N) by an order of magnitude.

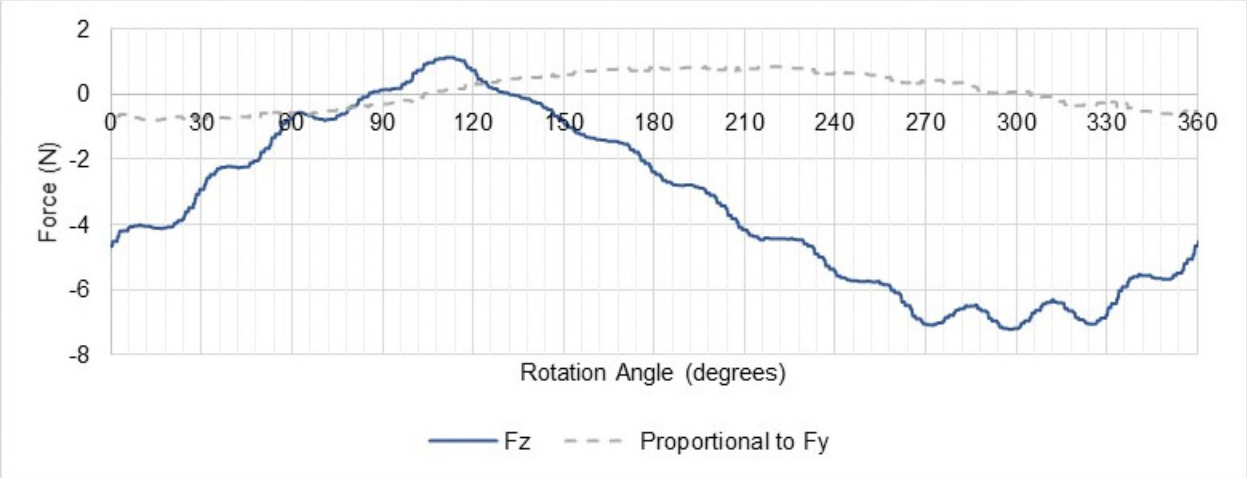

Figure 18. Vertical and Horizontal Radial Magnetic Forces Measured in the Rotor-Stator Assembly as a Function of Rotation Angle of the Rotor

Conclusions

When considering the radial bearings loads in a small-scale hydrodynamic pump, the internal magnetic forces between the rotor and the stator were found to be a major contributor. Loads due to the impeller and dynamic unbalance were small compared to these magnetic forces, which are fundamental to the operation of the motor. The final estimate of loads in the pump were large enough to potentially shorten the life of hydrodynamic bearings.

Magnetic forces could be attributed to the magnetic runouts of both the rotor and stator and were measured experimentally with different variations of a test setup utilizing a single magnetic element to characterize the magnetic field over a full rotation of the component. Measurements were also made at the rotor-stator assembly level and demonstrated that the interaction of the magnetic fields was also affected by any physical radial offset of the stator from the rotation axis of the rotor. In all of these experimental setups, selecting sufficiently stiff components was critical to reducing measurement uncertainty.

Understanding how the radial magnetic forces change as a function of radial offset can assist in defining manufacturing tolerances that can limit bearing loads from rotor or stator positional errors. Furthermore, collecting magnetic runout data for rotors and stators can enable methods for screening components for particular final assemblies. While the heritage Mars missions have outlived the original life expectancy using this pump design, these magnetic measurements will help retire risks associated with future pump motor operation and help meet NASA's Europa Clipper mission life requirement.

Acknowledgements

This work was performed at the Jet Propulsion Laboratory, California Institute of Technology, under a contract with the National Aeronautics and Space Administration. Reference herein to any specific commercial product, process, or service by trade name, trademark, manufacturer, or otherwise does not constitute or imply its endorsement by the United States Government or the Jet Propulsion Laboratory, Pasadena, California. © 2022. California Institute of Technology. Government sponsorship acknowledged. The authors wish to acknowledge AMETEK, for their work on developing the long-life pump technology, and Michael R. Johnson for his invaluable guidance and feedback.

References

1. Bhandari, Pradeep. Birur, Gajanana. Paris, Anthony. Novak, Keith. Prina, Mauro. Ramirez, Brenda. Bame, David. "Mars Science Laboratory Thermal Control Architecture" *35th International Conference on Environmental Systems*, (July 2005).
2. Bhandari, Pradeep. Birur, Gajanana C. "Long Term Life Testing of a Mechanically Pumped Cooled Loop for Spacecraft Thermal Control." *AIAA 32nd Thermophysics Conference,* (June 1997). AIAA 97-2470.
3. Furst, Benjamin I. Birur, Gajanana C. Carroll, Brian. Yavrouian, Andre. Warner, William N. Lewis, Donald F. "Life Testing of an Irradiated Mars Flight Heritage Mechanically Pumped Fluid Loop for the Planned Europa Mission" *47th International Conference on Environmental Systems*, (July 2017).
4. Ochoa, Hared A. Hua, Jenny. Lee, Raymond. Mastropietro, A. J. Bhandari, Pradeep. "Europa Clipper Thermal Control Design." *48th International Conference on Environmental Systems*, (July 2018).

Conceptual Design of an Extendable Rope-Inspired Module Space Orbit Arm for Maneuvering: ERM-SOA

Bhivraj Suthar* and Seul Jung*

Abstract

The space orbit arm comprises rigid links with long length and a fixed working volume that limits its maximum reachable distance. Due to a rigid and long arm structure, the transfer of the contact impact momentum to a floating Space Orbit Arm (SOA) system causes the collision between the arm end-effector and the target object. To mitigate the limitation of the space orbit manipulator, we proposed the conceptual design of a deployable and extendable rope-inspired modular space orbit arm (ERM-SOA). The arm has a radius and the humerus link with 7 DOF like a human arm. The arm links are designed as a rope-inspired structure incorporated with a multi-strand parallel twisted-scissor mechanism to make it extendable. The twisted structure enhances its strength with flexibility. The arm is designed modular by introducing several metamorphic modules for easy scalability without affecting conventional scissor fundamentals. The arm is designed and tested for its functionality in 3D modeling software. The proposed design and fundamental simulation results have shown that the arm can change its working volume according to the applications. The proposed arm may minimize the transfer of contact impact momentum caused by the contact between the end-effector and the target object due to the structure variable stiffness. The ERM-SOA acts like a soft arm due to its variable stiffness. Furthermore, the ERM-SOA also has a protective soft hose cover like human skin to protect the arm itself from debris collision, high temperature, and radiation. We developed a prototype to check its feasibility and it shows extendability without mechanical singularity. Overall, the proposed design concept of ERM-SOA may help to develop an extendable soft space orbit arm for present and future NASA missions and applications.

Introduction

Space manipulator robotics has played a significant role on the International Space Station (ISS) used for many operations, including berthing spacecraft, space station assembly, astronaut positioning, payload transfer, satellite deployment, and spacecraft inspection before reentry. In addition, new missions and applications are being considered, such as asteroid retrieval and redirection, asteroid mining, satellite servicing, and small payload delivery to space stations that can benefit from long-reach manipulators. Three manipulator systems have been deployed in space: the Canadian Mobile Servicing System (MSS), the Japanese Experiment Module Remote Manipulator System (JEMRMS), and the European Robotic Arm (ERA) [1-3]. The MSS includes the 17-m long with 7 degrees-of-freedom Space Station Remote Manipulator System, JEMRMS 10-m long with 6 degrees-of-freedom and ERA is 11-m long with 7 degrees-of-freedom.

The state-of-the-art in long-reach space traditional manipulators incorporates rigid links connected by rotary joints that include motors, gearboxes, and brakes. The rotary joints account for 85 to 90 percent of the manipulator mass and compliance in response to an applied load [4]. The long booms result in restrictive packaging options and adding joints to improve packaging would incur an extremely high mass penalty. The high mass associated with the joints also results in practical limits to reaching, packaging, stiffness and tip force that can be achieved with the conventional architecture.

Recently, an invention of a novel modular space robotic manipulator, Tendon-Actuated Lightweight In-Space MANipulator (TALISMAN) has been developed [5-9]. TALISMAN has a combination of lightweight

* Chungnam National University, Korea; bhivrajiitd@cnu.ac.kr and jungs@cnu.ac.kr

truss links, a novel hinge joint, tendon-articulation and passive tension stiffening that the new robotic manipulator architecture achieves compact packaging, high strength, stiffness and dexterity while being very lightweight compared to conventional manipulators. It is easy to scale for different reach, load and stiffness requirements, enabling customization for a diverse set of applications. TALISMAN uses several actuators for tendon actuation that are installed in a semi or fully antagonistic fashion. These actuated cables provide a variable stiffness structure to minimize the arm's collision impact with a floating spacecraft. However, many actuators lead to complex design, bulky structure, control issues, high cost, and working volume fixed once deployed in space, limiting its workspace. Compared to other space manipulators, such as the Shuttle Remote Manipulator System and the Space Station Remote Manipulator System, a TALISMAN with equivalent stiffness in the plane of the cables provides an order of magnitude reduction in mass and nearly an order-of-magnitude reduction in a packaging volume. However, it has variable stiffness only in one plane due to the several cables. So, it can not resist the transfer of contact momentum to the floating space station in the 3-dimensional space. The SOA requires variable stiffness in all planes also. Therefore, these SOA design problems need to be solved for present and future NASA missions and applications.

In order to enable a long-reach SOA to minimize the impact of the contact forces on the arm and floating spacecraft, it is desirable to improve the SOA by significantly increasing the manipulator’s reach, packaging efficiency, and stiffness while reducing manipulator mass and complexity.

In this paper, an extendable rope-inspired module space orbit arm (ERM- SOA) is proposed as a new space manipulator architecture with a twisted scissor mechanism inspired by a rope structure. The arm has seven DOF like a human arm (shoulder-3DOF, Elbow-1DOF, and wrist-3DOF) to perform manipulation. The arm links (Radius and Humerus) are made of the twisted scissor mechanism called metamorphic module and connected several metamorphic segments in series. These metamorphic module structures are twisted like a rope for introducing structure strength with foldbility. The metamorphic segment structure achieves longer moment arms by changing the link lengths of Radius and Humerus. The arm can change its expansion and contraction length due to the twisted scissor structure. As a result, the arm can increase and decrease its maximum reach with variable compliance.

Conceptual Design of an Extendable Rope-Inspired Module Space Orbit Arm (ERM-SOA)

In this section, we describe a proposed rope-inspired parallel twisted-scissor mechanism (PTSM) and its fundamental components. This design is based on the linkage design approach.

In this section, a parallel twisting of scissor strands in scissor mechanism like ropes, as shown in Fig. 1 is proposed. The separate thin strands are weak, and it can be bent easily. If strands twisted over each other, then a rope may be vital. Suppose the twisting of scissor strands is possible using a single actuator with small bending deformation. In that case, this mechanism may have space applications, such as extendable space arm, debries collecting space robot, etc. It may reduce robot weight and cost as well. Borrowing this concept to the conventional scissor mechanisms leads to redesigning the scissor mechanism without affecting the scissor's fundamental.

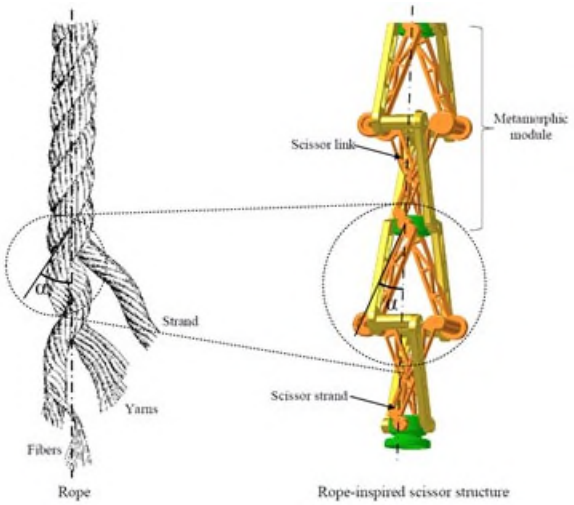

Figure 1. Rope-inspired scissor structure

S-shape linkage design approach

A core aspect of the PTSM design philosophy is the use of two scissor structures in such a way to twist on each other by redesigning links and revolute joints. An S-shaped linkage and a circular connecting node having multiple revolute joints were designed. The S-shape link has a connecting pin with a V-notch passive self-locking feature, as shown in Fig. 2. One side of the link has a revolute joint with a ball bearing, and another end has an extruded revolute joint for connecting S-shape links in series.

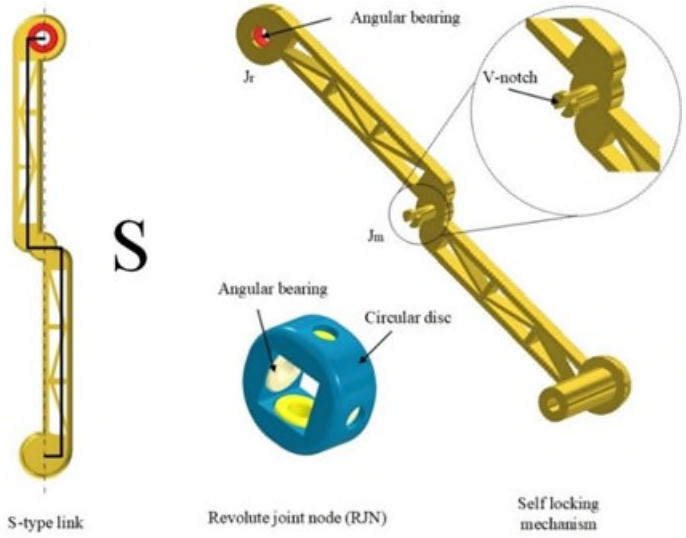

Figure 2. S-shape linkage design approach

Construction of a metamorphic segment

The metamorphic segment consists of multiple S-shape links, connected through revolute joints on the circular node by pressing the link. Metamorphic segments are shown in Fig. 3 for two and four S-shape links. Every segment has multiple S-shape links (see Fig 3(a), prismatic view) in a cross fashion (see Fig 3(b), top view) and is placed orthogonally in X-Y and Y-Z planes. The numbers 1, 2, 3, and 4 in the circle stand for the number of S-shape scissor links. This segment is symmetrical about the center of an axis passing through the circular node, and each link has a variable angle of α, called a scissor angle (see Fig 3(c), side view). The scissor angle decreases as the structure unfolding increases. The S-shape link and circular node are easily connected in series.

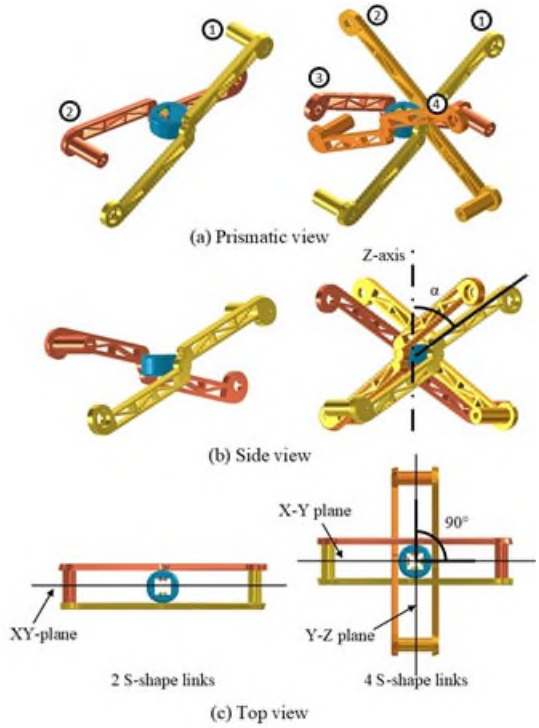

Figure 3. Single metamorphic segment of multiple strands rope-inspired twisted-scissor mechanism

Construction of multi-strands metamorphic link of the space arm

We designed a metamorphic link in such a way that allows multiple scissor links to twist on each other like a rope. The proposed design has a strand-like rope. The multi-strands extendable link has a train of metamorphic segments. The segment has S-shape links connected to the revolute joint node. These are connected through revolute joints, as shown in Fig. 4. In the figure, a 4-strand parallel twisted-scissor mechanism is presented. Every scissor strand has a chain of S-shape links, so we called it a scissor strand.

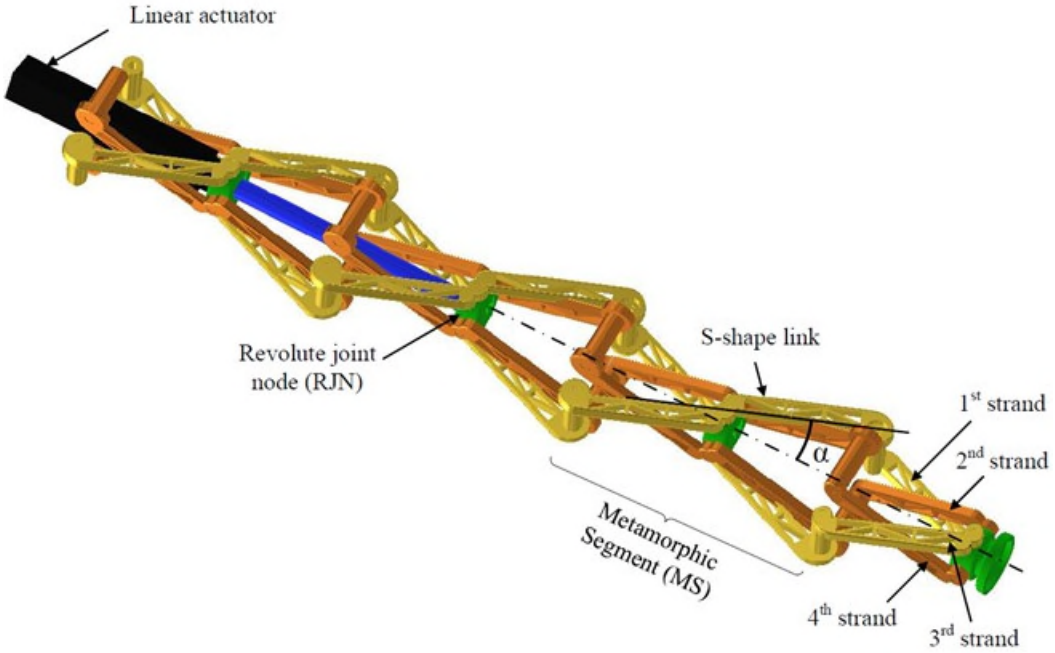

Figure 4. Rope-inspired extendable robot link with scissor angle (α)

This scissor strand is twisted along the axis' center. The proposed design has four scissor strands placed in parallel and twists like a helix. This mechanism is symmetrical about the center of an axis passing through the circular node, and each link has a variable angle of α called a twist angle. The twist angle increases as the structure unfolds and decreases as folding by a linear actuator. A foldable arm's design with longer reachability based on metamorphic link can easily be achieved by adding the metamorphic segments in series also.

Construction of 7 DOF ERM-SOA

- Conceptual design

An entire ERM-SOA motivation is shown in Fig. 5(a) that is inspired by a human arm. The whole structure is like a rope-inspired scissor structure. A long twisted scissor structure is possible to actuate using a single actuator. We propose a 7-DOF foldable rope-inspired space robot arm (shoulder 3 DOF, elbow 1 DOF and wrist 3 DOF) like a human arm for maneuvering, as shown in Fig. 5(b). The proposed foldable arm may improve the end-effector reachability by changing the twisted scissor angle (alpha). The radius and humerus structure has a resistive property against contact momentum transfer. The modular design allows extending the arm's working volume and can be used for multiple applications. It may reduce arm weight, maintenance and cost as well.

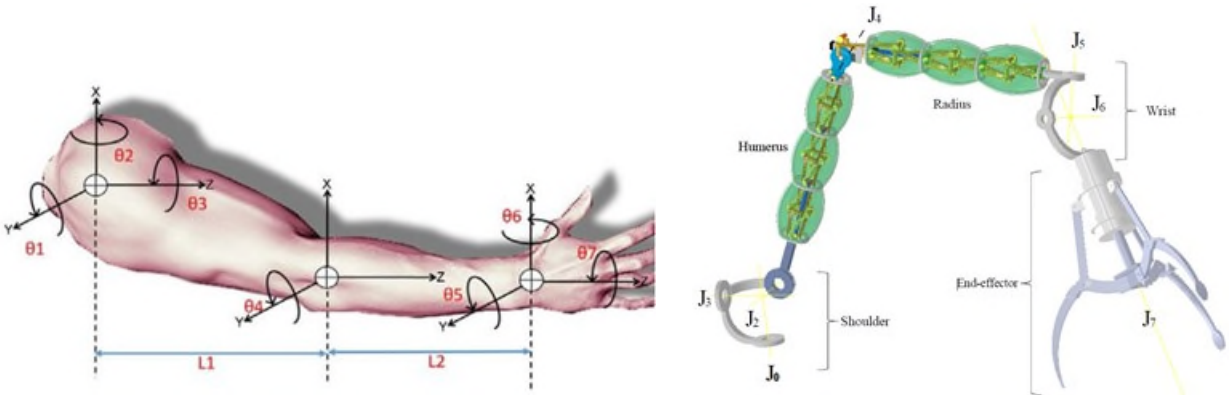

(a) Anatomy of a human arm *(b) Concept of an extendable arm*

Figure 5. Conceptual design of an extendable rope-inspired Module Space Orbit Arm for maneuvering

- Functionality

The basic functionality of the extendable rope-inspired space orbit arm (ERM-SOA) is shown in Fig. 6. The arm has the unique functionality of an adjustable working volume. The arm can be used for small-reach and long-reach maneuvering according to the application. When the radius and the humerus length are fully folded, the arm has a small working volume and small reach (see Fig. 6 (a)). It can be used for close maneuvering to the space station, for example, astronaut positioning on the International Space Station (ISS) for maintenance. If the arm is fully unfolded, it has a large working volume and long reach (see Fig. 6 (b)). It can be used to maneuver far from the space station to avoid collision. For example, to capture a dead satellite or asteroid far away from the International Space Station due to collision avoidance can be done. When the arm is entirely extended, it behaves like a cantilever. The arm has a variable stiffness, and it behaves like a rigid body when it is entirely folded and acts as a soft body when it is entirely unfolded. Due to the variable stiffness, the contact momentum transfer caused by the collision between the arm end-effector and the target object can be minimized. The arm can extend its long reach and capture the moving satellite to avoid the contact momentum transfer to the space station and reduce its reach for precise maneuvering.

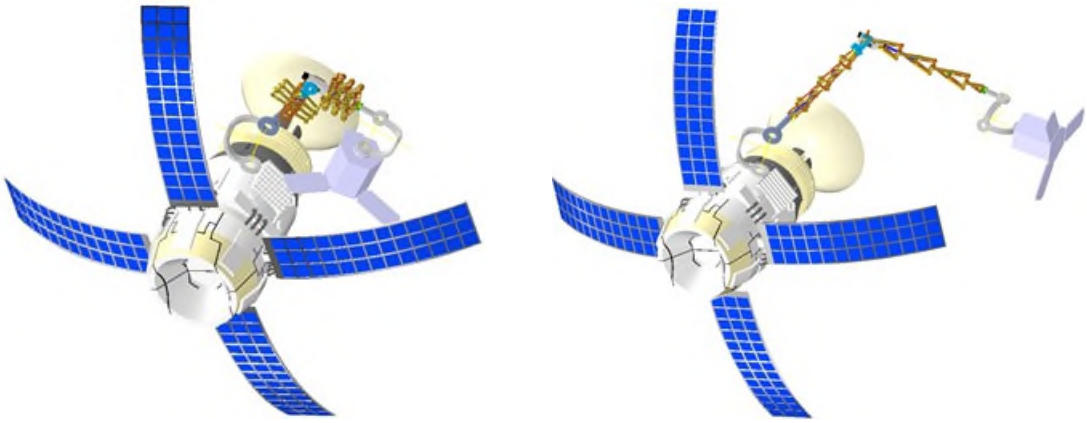

(a) Fully folded ERM- SOA (small-raech) *(b) Fully unfolded ERM-SOA (long-reach)*

Figure 6. Functionality of the extendable rope-inspired modue space orbit arm: ERM-SOA (adjustable space arm working volume)

- Protective cover

The proposed arm is covered by a soft hose which is resistive to provide the ability to protect the arm from being damaged due to debris collision, high temperature, radiation, etc. A soft and resistive hose covers each segment module of the arm (see Fig. 7) and the cover is connected to the sequential module by connecting rings that allow us to add or remove the module according to the application. The cover is soft enough to allow the arm's basic functionality, resistive enough to provide the protection against outer debris, and strong enough to increase rigidity in an extended direction. The connection ring with soft cover may increase the strength of the arm.

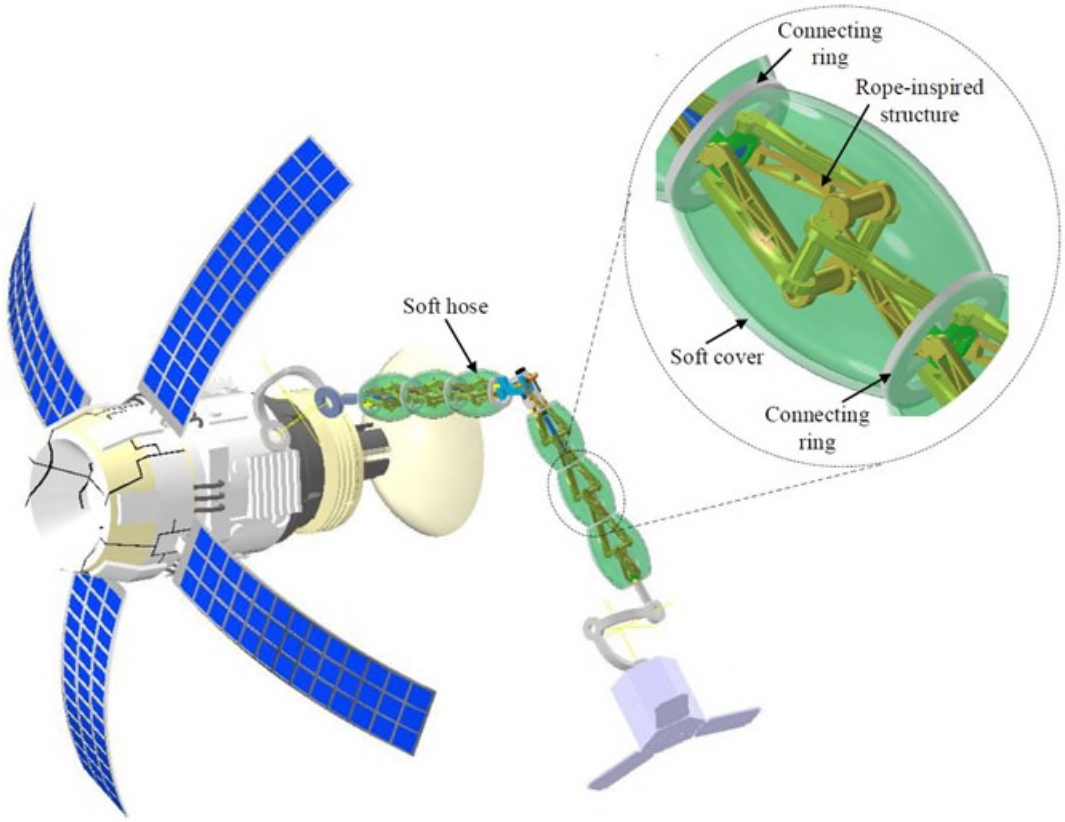

Figure 7. ERM-SOA with a soft protective cover (soft hose cover)

Preliminary Results and Analysis

Extendable maximum reach and working volume

Figure 8 (a) shows the working volume of the ERM-SOA. This is the typical workspace of a robot arm with seven degrees of freedom like a human arm. Three revolute joints intersect at the same point and make a spherical joint like a shoulder joint in a human arm. The arm has two spherical joints one at the shoulder and another at the wrist. The arm has a Humerus and Radius like a human arm with extending capability and extends its working volume as shown in Fig. 8 (b). Therefore, the arm can change its length according to the maximum reach. The arm has the capability to make multiple maximum reach lengths in the space.

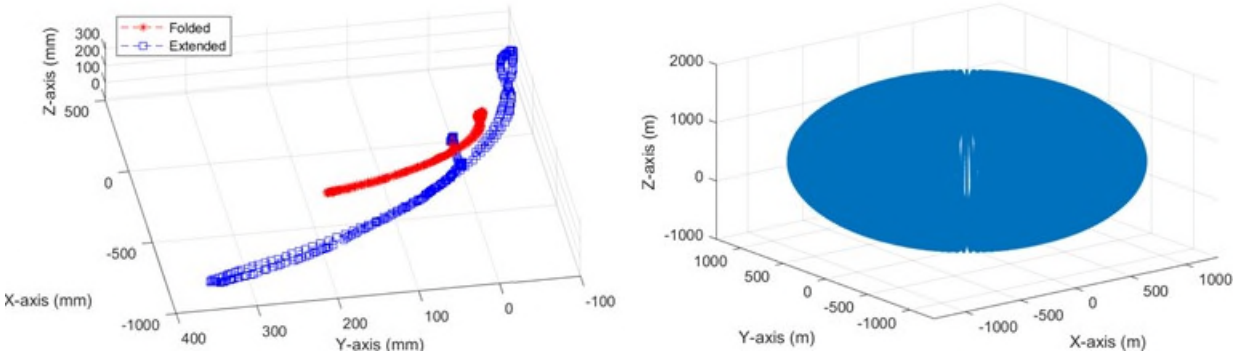

(a) variable maximum reach of end-effector (b) Working volume of arm when it was fully extended

Figure 8. Extended working volume and maximum reach of a ERM-SOA in the space

Variable elbow pose during tracking

This simulation is performed to check the feasibility of various elbow pose to reach a particular point in the space. Sometimes traditional robots can not reach the target point due to fixed link length. However, the extendable length of humerus and radius length may help to achieve this target. In this subsection, we aim to achieve compliance of a robot manipulator along a predefined path, giving the robot the ability to change its elbow pose while tracking a circular path. Figure 10 illustrates this objective, where the desired path is a fixed circle, the links humerus and radius change their length to keep tracking circular path. In the simulation we change the simulated three cases: first for the same Humerus and Radius length (see Fig. 9 (a)); second is when the Radius length is greater than Humerus length (see Fig. 9 (b)) and third is when the Humerus length is higher than radius length (see Fig. 9 (c)). However, in all three cases, the circle path position is fixed (5, 6). The results show that the arm can reach the target point by changing its elbow pose. this capability may use for developing a next-generation space arms with enhanced reaching capability.

Impact analysis

The impact force propagation in the structure is a significant problem in developing long space arms. The impact force may destroy the long space structure and floating station. In order to see the impact effect on the proposed space arm, We created a simulation environment in Autodesk Inventor design software, as shown in Fig. 10. The impact force of 10 N was applied to the structure and observed the deformation. The deformation is small (in X-axis 6.91 mm, Y-axis 3.78 mm and Z-axis 7.75 mm) for long extension (700 mm). The proposed twisted scissor structure behaves like a foldable cantilever so that deformation behavior makes the structure compliant and soft in nature. The simulation results show it has the capability to withstand the impact force and compensate the impact force. The overall simulation results suggest that rope-inspired scissor links may help for making large space structures in the future.

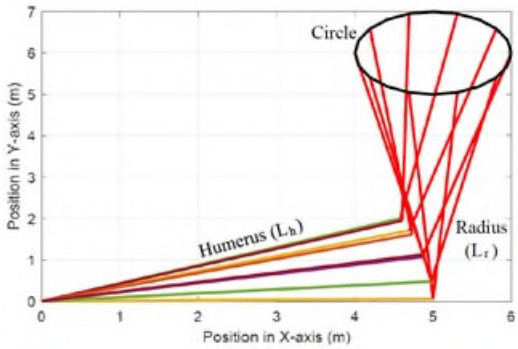

(a) Circle tracking with same length of Humrus and radius length of the ERM- SOA

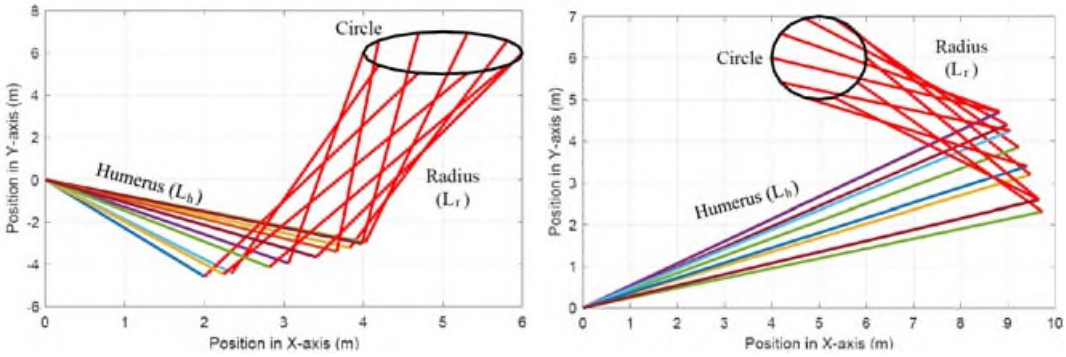

(b) when Radius length is greater then Humrus (c) when Radius length is greater then Humrus

Figure 9. Simulation of a variable pose of ERM-SOA while tracking fixed circle

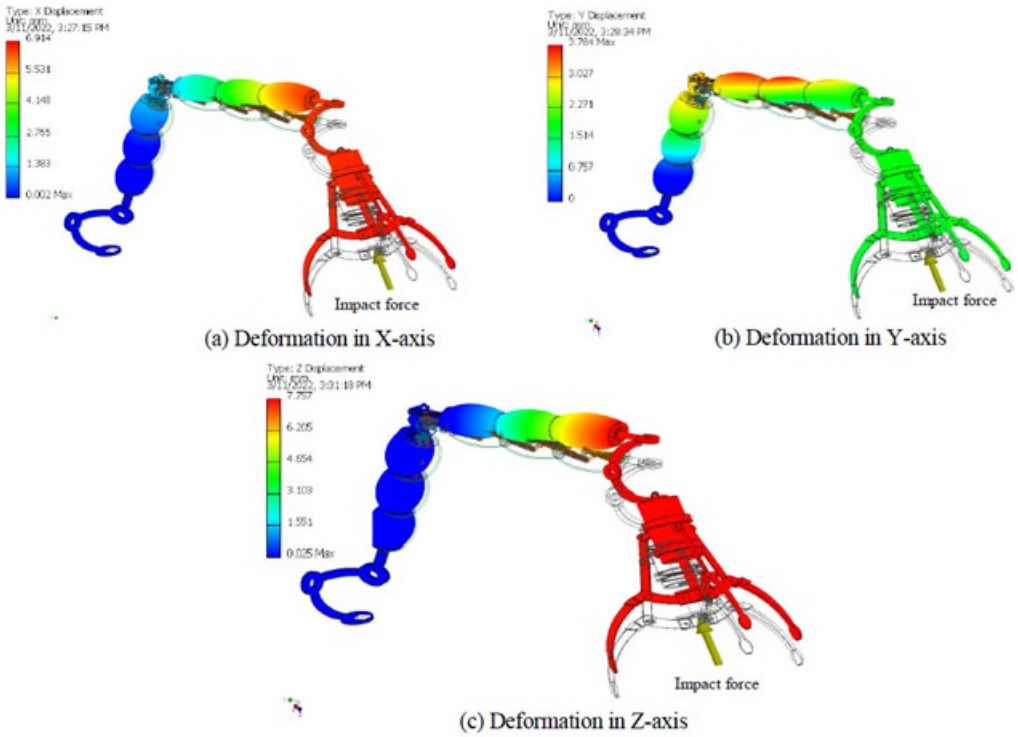

Figure 10. Deformation of a ERM-SOA due to impact force of 10 N at the end effector

Prototype development

We developed a prototype of a rope-inspired extendable link to check its feasibility and functionality as shown in Fig. 11. The scissor strands are twisted on each other and align with the central axis. The black strand is printed in black to observe its basic feasibility. We observed that the extendable rope-inspired structure was able to extend and contract using a single actuator. When it extended, it shows bending under gravity. However, the bending is pretty low as compare with the traditional extandable scissor structure (see Fig. 11). In case of a space application, due to the absence of gravity this structure may be useful. Therefore, the preliminary results shows the capability to use it as a foldable link in space robot arm. We also tested introducing multiple metamorphic segments to make it more longer. The most exciting finding was that our proposed design has a unique feature of several self-locking feature to avoid singularity without using additional sensors or mechanism or control. All links automatically locked themselves to each other and the structure cannot extend further (see the prismatic and front view in Fig.12). Each link's end is connected uniformly in a square shape, which is a hollow square beam. The PTSM allows smooth full extension and full contraction. The good news is that PTSM never gets a bending singularity due to the symmetrical structure along the central axis. In our experiment, we observed that it does not depend on the metamorphic segment. We used four metamorphic segments and fully extended. If we increase the number of metamorphic scissor segments, it bends more but never gets the bending singularity.

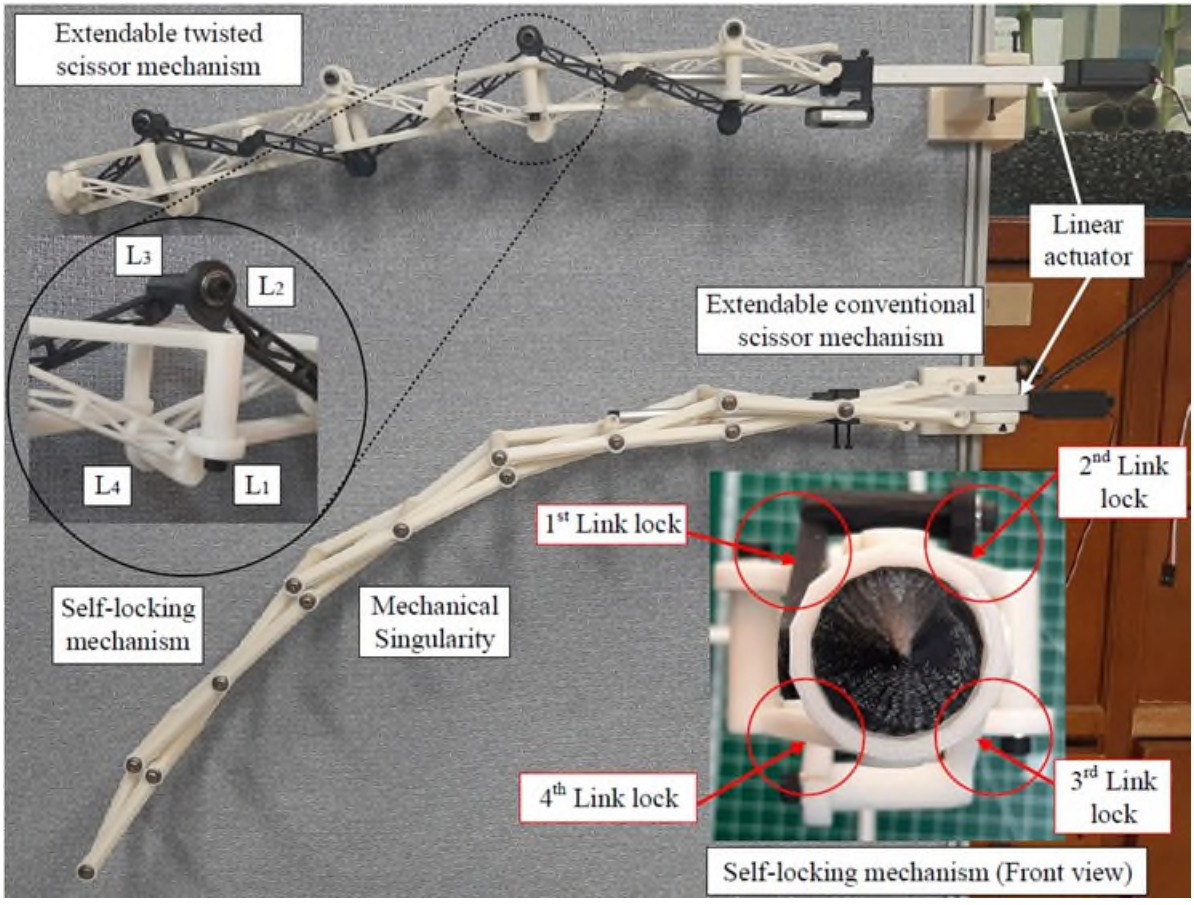

Figure 11. Propotype development and feasibility test of rope-inspired structure

Advantages of the ERM-SOA and Applications

Advantages

The key features of the new ERM-SOA are:

- Extendable links (radius and humerus) due to twisted-scissor structure with major components being the lightweight link, truss and connectors,
- A single actuation actuates the deformable structure (radius or humerus),
- Extendable working volume; arm has a variable working volume due to foldable links,
- Modularity; arm length and working volume are easy to scale due to metamorphic modules without adding any additional actuators,
- Self-locking structure without a mechanical singularity,
- Protective soft hose protects the arm from the external environment and increases manipulator's stiffness,
- Lightweight and hollow structure allows optimized packaging efficiency, range-of-motion, dexterity, etc.,
- Structure has a variable stiffness that decreases as structure grows and act as a soft link,
- Structure may reduce impact momentum transfer from end-effector to floating station due to decrease in the stiffness,
- Arm requires small space in the launching rocket due to folding capability.

Applications

- Present applications

The proposed extendable space arm has enormous potential for present and future space applications due to adjustable long-reach maneuvering such as astronaut positioning, payload transfer, berthing spacecraft, space station assembly, satellite deployment, and spacecraft inspection before reentry. The space manipulator reach can be adjustable according to the application requirement. For example, the proposed arm can grab a payload and drop it into spacecraft.

- Future applications

Future NASA missions and applications are being considered, such as an asteroid collision avoiding system, asteroid retrieval, redirection, asteroid mining, dead and active debris capturing that can benefit from long-reach manipulators with its momentum transfer resistive property.

- Asteroid collision avoiding system

A new application of space manipulators has emerged in the future mission as an asteroid collision avoiding, retrieval, and redirection system for International Space Station. This structure may helpful for developing extendable single and multiple space arms, as shown in Fig. 12. The long-reach based on the proposed concept may deploy on the ISS for large asteroid capturing and diverting it before the collision occurs with the ISS or any space station.

- Space debris collection at ISS

Currently, active debris removal has become a more urgent application, so the proposed extendable arm may be helpful to track, capture and collect debris. The major problem of capturing active debris is the momentum transfer to the floating capturing system due to collision between arm end-effector and target debris, which may cause losing tracking path itself. Due to the variable arm stiffness, the proposed space arm may minimize the momentum transfer to the floating capturing system.

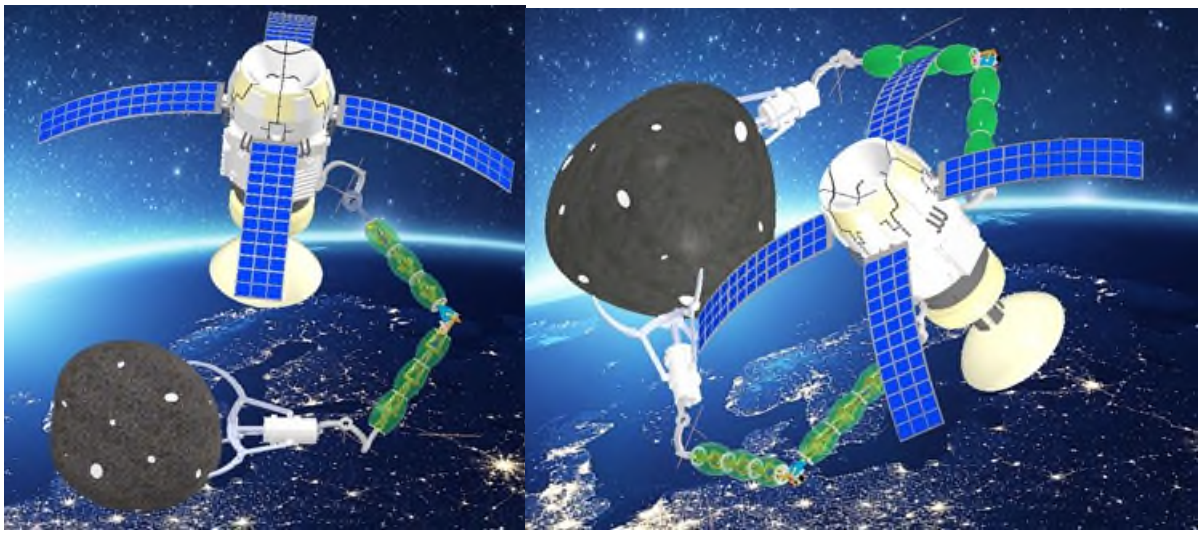

(a) Single space arm for capturing dead debris (b) Multiple space arms for capturing dead debris

Figure 12. ERM-SOA-based debris collection space robot system

- Dead debris capturing

The earth is surrounded by a lot of debris, and it is a crucial issue of capturing and dumping them. The proposed extendable space arm can capture debris before reaching enough close to the floating satellite due to its unique feature of extendability. In addition, the proposed arm is module-based, so the maximum reach can be increased simply by adding more modules in the space arm. Therefore, the floating capturing satellite may be safe and out of risk of debris collision, as shown in Fig. 13.

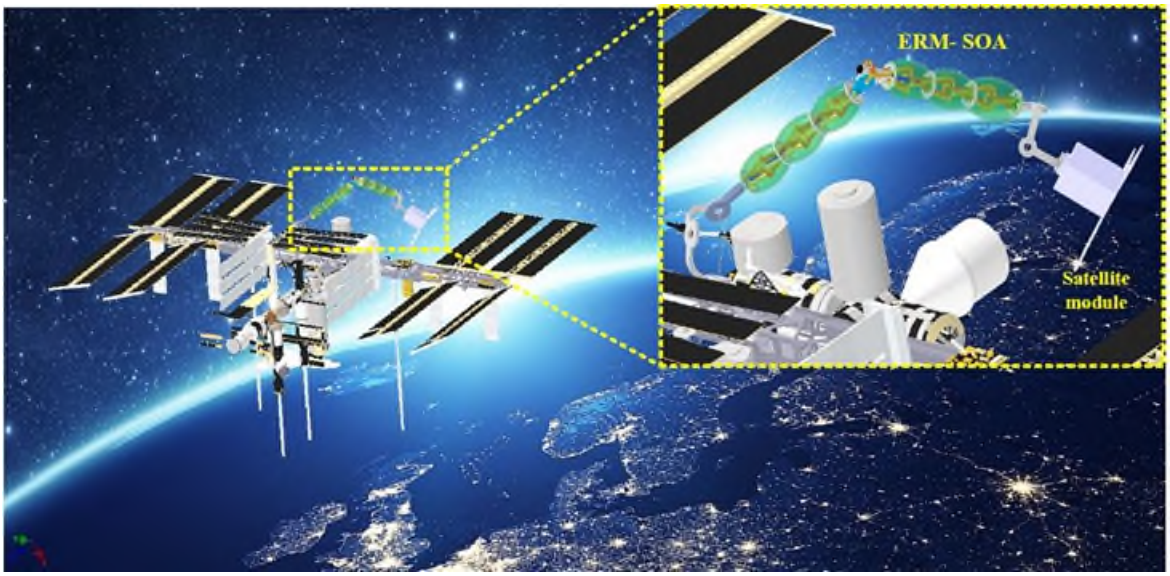

Figure 13. Space debries capturing and diverting from ISS using an ERM-SOA

- Manipulation in space for maintenance and assembling operation

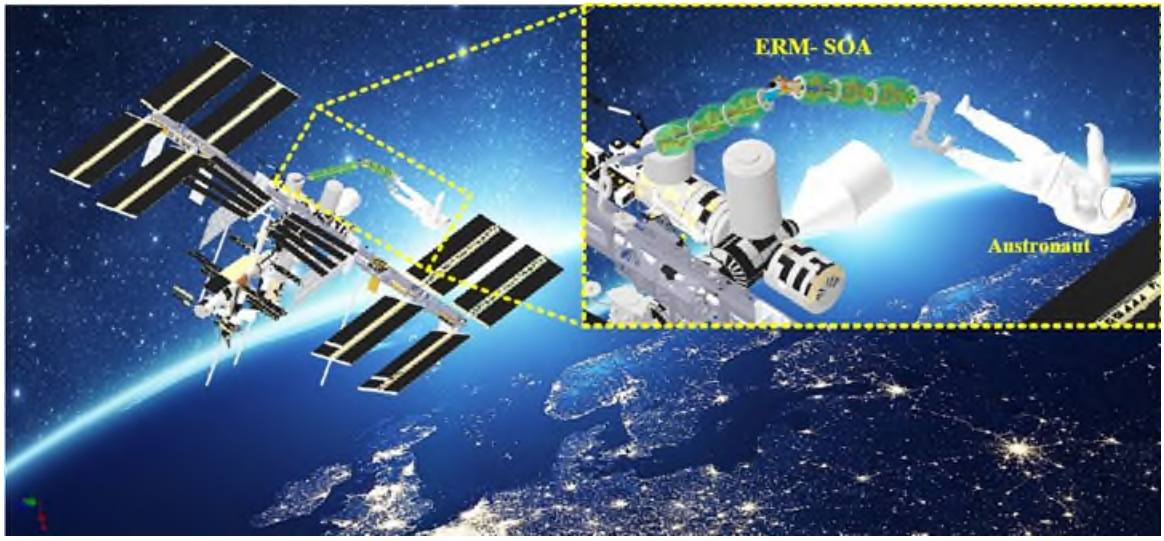

Figure 14. Astronauts with ERM-SOA for inspection and maintenance of solar panels.

At the International Space Station, the space robot arm performs several operations such as inspection, observation, maintenance, assembling, etc. In these operations, the working volume is the key requirement to perform these operations in the space. The traditional space robot arm has limited working volume and it can not enhance it after installation. Therefore, traditional space arms can perform space operations in a limited working volume. For reaching every point of ISS, one needs to install multiple space robot arms, which make the system more complex, require large maintenance, and increases mission cost.

To solve these challenges, we propose an extendable space arm and install it on the ISS at the optimal location from which the space arm is able to cover maximum ISS outer space for performing space operations (see in Fig. 14). During the space operation contact between two bodies, that contact geometry is characterized as three cascade peg-in-hole pairs (one rectangular peg/hole and two cylindrical pegs/holes). This is just one of many batteries of different sizes and designs on ISS, which have been maintained by either EVAs or the dual arm ISS robot Special Purpose Dexterous Manipulator.

Generally, space operations like maintenance and assembling create contact impact between the robot boom and ISS surface. The insertion or removal of such a battery into or from its housing worksite was one of the most difficult operations of the ISS robot. All capture and some manipulation operations involve physical contact between the robot arm and an external object or the environment. Contact operations are among the most difficult operations for a space arm, whose contact behavior is governed by contact dynamics. The proposed arm has the capability to change its stiffness with the extension of the arm. It behaves like a cantilever when it is fully extended which absorbs the vibration due to contact between two bodies. This may help to allow performing operations more accurately. It may enhance the maintenance cycle of the robot itself.

Conclusion and Future Work

This work presented a novel mechanism design approach for the preliminary design of an extendable rope-inspired module space orbit arm for maneuvering in space. The arm has 7 degrees of freedom like a human arm. The metamorphic segments were designed using the S-shape linkage design approach to develop a module-based arm using multiple twisted parallel scissor strands like a rope. This metamorphic parallel twisting mechanism has been introduced in the scissor mechanisms, called rope-inspired scissor mechanism. The arm can contract and extend its maximum reach of the end-effector. This linkage design approach does not affect conventional scissor fundamentals. However, it enhances the strength and

modularity of the structure. It has shown better performance than a conventional scissor. It does not get a bending singularity in the fully unfolded configuration and is independent from the number of metamorphic segments. Considering all of this evidence, it seems that a rope-inspired scissor mechanism is a suitable candidate for deployable and reconfigurable mechanism. Another significant result is that it requires only a single actuator for multiple strands, making the rope-inspired scissor mechanism lightweight and cheap. The arm behaves like a cantilever while fully extended. The extendable compliant structure may absorb and compensate the impact forces during contact between end-effector and object. The approach was applied to the design of an extendable space robot for maintenance, inspection, and assembly on the ISS.

In future work, we will develop the hardware of 7 DOF rope-inspired arm and perform manipulation operation in zero gravity environment. Future work also includes experimental evaluation of the impact forces on the proposed space arm.

References

1. Laryssa, Patten, Evans Lindsay, Oshinowo Layi, Ochisor Marius, Kazuharu Nara, Lodewijk Aris, and T. Ed., "International space station robotics: a comparative study of ERA, JEMRMS and MSS," *7th ESA Workshop on Advanced Space Technologies for Robotics and Automation*, pp. 19-21, 2002.
2. Evans, W. M., "The Canadian Space Program—Past, Present, and Future (A history of the development of space policy in Canada)," *Canadian Aeronautics and Space Journal, vol.* 50(1), pp. 19-31, 2004.
3. HUNTER, J., T. USSHER, and D. GOSSAIN, "Structural dynamic design considerations of the shuttle remote manipulator system," In *23rd Structures, Structural Dynamics and Materials Conference*, pp. 762. 1982.
4. Aikenhead, Bruce A., Robert G. Daniell, and Frederick M. Davis. "Canadarm and the space shuttle." *Journal of Vacuum Science & Technology A: Vacuum, Surfaces, and Films*, vol. 2, pp. 126-132, 1983.
5. Doggett, William R., John T. Dorsey, Thomas C. Jones, and Bruce King, "Development of a tendon-actuated lightweight in-space MANipulator (TALISMAN)," In *Proceedings of the 42nd Aerospace Mechanisms Symposium*, vol. 405, pp. 14-16. 2014.
6. Altenbuchner, Cornelia, John Dorsey, and Thomas C. Jones, "Flexible Multi-Body Dynamic Modeling of a Tendon-Actuated Lightweight In-Space MANipulator (TALISMAN)," *AIAA SPACE 2015 Conference and Exposition*, pp. 4629, 2015.
7. Jones, Thomas C., John Dorsey, and William R. Doggett, "Structural sizing methodology for the Tendon-Actuated Lightweight in-Space MANipulator (TALISMAN) system," *AIAA SPACE 2015 Conference and Exposition*, pp. 4627, 2015.
8. Mahlin, Matthew, Robert L. Wagner, John Dorsey, and Thomas C. Jones, "Tendon-Actuated Lightweight In-Space MANipulator (TALISMAN) Hinge Joint Structural," In *ASCEND 2020*, pp. 4251, 2020.
9. Doggett, William R., John Dorsey, and Thomas C. Jones, "Improvements to the Tendon-Actuated Lightweight In-Space MANipulator (TALISMAN) system," *AIAA SPACE 2015 Conference and Exposition*, pp. 4682, 2015.

SWOT and NISAR Boom Ground Deployment Test Challenges & Resolution

Paul D. Lytal*, Jeff Waldman* and Kyle C. Waters*

Abstract

NASA's Jet Propulsion Laboratory is developing two new spacecraft that use radar instruments to characterize temporal changes in the Earth's surface with unprecedented precision (Figure 1). Both the Surface Water Ocean Topography (SWOT) and the NASA-ISRO Synthetic Aperture Radar (NISAR) spacecraft utilize large, precision flight deployable booms to properly position and support their instrument reflectors. The SWOT spacecraft includes two nearly identical reflector booms, each of which have similar flight deployable hinge designs. The NISAR spacecraft has a single reflector boom, with four unique hinge designs. These booms each undergo a multi-staged flight deployment sequence on orbit to transition from the launch stowed configuration to the science configuration within days of launch (Figure 2).

Figure 1. Artist's Renderings of Deployed SWOT (Left) and NISAR (Right) Spacecraft On-Orbit

The SWOT and NISAR projects faced significant challenges relevant to requirement verification as well as hardware safety in their approach to ground testing these large flight deployables. This report summarizes flight deployable system design decisions that contributed to ground testing challenges. The report also summarizes the architecture trade study conducted for ground deployment testing.

A summary of key issues encountered during flight deployable ground testing with the chosen common gravity offload system ensues, with discussion of the issues and mitigation measures implemented by both projects that ultimately enabled successful flight subsystem-level full range of motion ground tests. Recommendations and lessons learned are offered to facilitate ground testability of future analogous large scale flight deployables.

* Jet Propulsion Laboratory, California Institute of Technology, Pasadena, CA;
Paul.D.Lytal@JPL.NASA.gov; Jeffrey.D.Waldman@JPL.NASA.gov; Kyle.C.Waters@JPL.NASA.gov

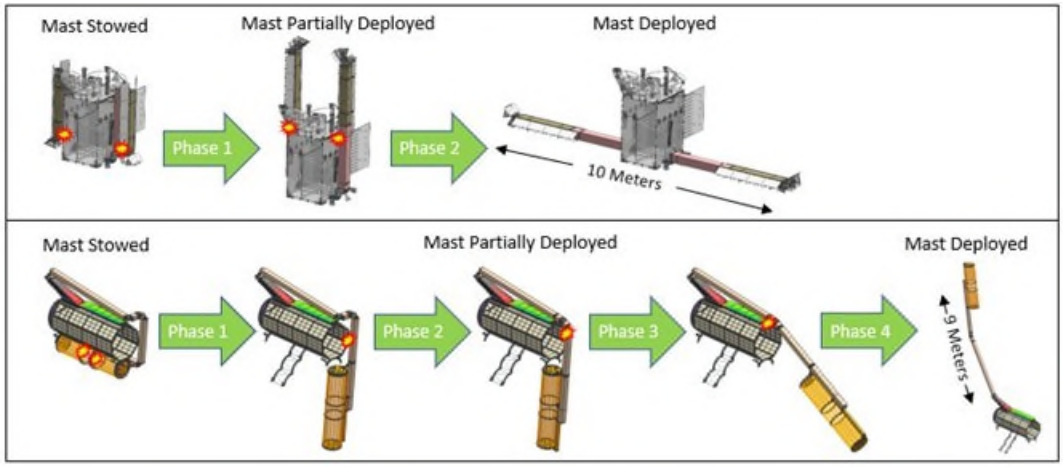

Figure 2. On-Orbit Boom Deployment Sequence for SWOT (Top) and NISAR (Bottom)

Flight Hardware Design for Testability

Deployable Structure Architecture Decisions

Both the SWOT and NISAR deployable boom designs faced significant technical challenges to meet project performance requirements while also stowing to fit within tight launch vehicle constraints and deal with loads from an over-constrained system. Priority was given to overcoming these technical challenges and several decisions were made early on to enable the primary on orbit mission success while sacrificing ease of testability during ground integration and test activities.

The NISAR project had a very complicated configuration to fit within an extremely tight launch vehicle (Figure 3). The radar feed and the stowed reflector were located on opposite sides of the payload structure, requiring the composite boom to wrap around the aluminum structure resulting in additional complexity for the design. The boom required four hinges to meet the stowed launch configuration volumetric constraints while still meeting the deployed optical prescription and with some consideration given for ground testability. Configurations utilizing three hinges all resulted in two hinges deploying in a common plane with the third hinge deploying in a challenging-to-test orientation. The four hinge configuration selected enabled three hinges to deploy in a common plane with the fourth hinge deploying in an orthogonal plane. While this configuration was chosen to improve the deployment test program feasibility, the orthogonal out of plane hinge deployment still proved to be exceedingly challenging to implement. For this hinge, offload weight errors and offloader friction became direct sources of deployment drag in contrast to the other hinges with hinge axes nominally oriented parallel to gravity for testing.

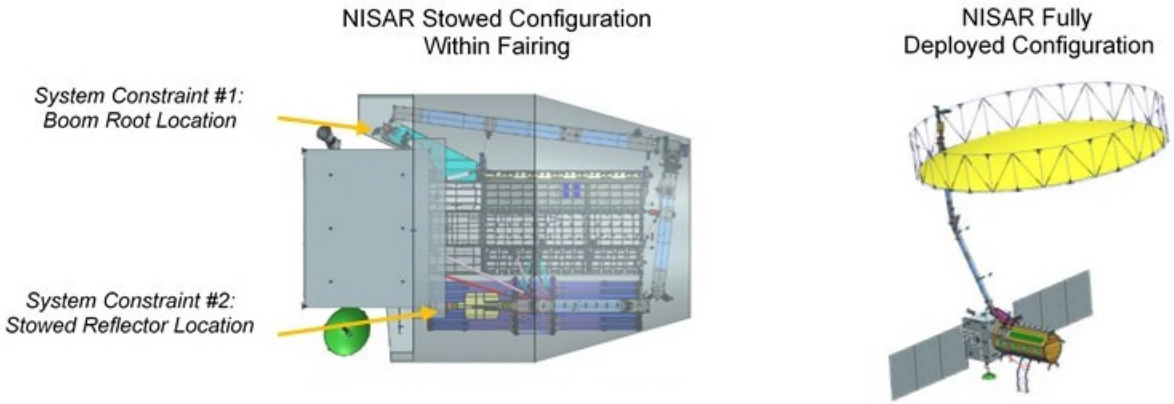

Figure 3. NISAR Boom Stowed Versus Deployed Key and Driving Configurational Constraints

For both the SWOT and NISAR missions, deployment mechanism architectures were selected to only deploy a single hinge at a time through serial launch restraint releases. This was done to achieve the highest confidence in full deployment success, as each phase could be deployed and telemetry reviewed to confirm success before proceeding with subsequent hinge deployments. Other programs such as Soil Moisture Active Passive (SMAP) have taken alternate approaches where two hinges deploy back-to-back and use a syncronization gear to avoid scenarios where contact or undesired motion could occur. The staged approach of SWOT and NISAR simplified the technical design of the deployment mechanisms and was lower in flight mass, however, it resulted in a significant increase in the number of deployments to set up and test on the ground. While the SMAP deployable boom had two deploying hinges, it only required a single offloaded test set up to fully deploy both hinges. SWOT and NISAR required a unique setup and reconfiguration for each one of their hinges and sometimes even a separate set up for the deploy direction verses the stow direction. This resulted in a significant increase in the complexity of the design of the test program, offload Mechanical Ground Support Equipment (MGSE), and duration of ground test activities. NISAR added further configurational complexity to the design of the GSE with the out-of-plane hinge deployment, a unique motion compared to the other hinges where the center of gravity (cg) changed vertical height by 0.6 m (2 feet) where all other deployments swept in an arc parallel to the ground. The decision to build a one size fits all deployment offload GSE system for both projects resulted in a very challenging design space to be able to accommodate all of the different configurations required.

The ground deployment tests were elected to be carried out on a fixed immovable ground constraint rather than offloading all components in a free-free test condition. This decision stemmed from the complicated over-constrained launch stowed configurations and the need for the launch restraints that reach back to the payload structure to stage the various hinge deployments in a flight-like manner. Ideally, the entire boom would be disconnected from the payload and offloaded in a free-free state. In a free-free configuration, errors in the offload weight would be observable in test as the structure sinks or rises, enabling the offload force to be tuned even with imperfect a priori mass properties knowledge. It was not feasible to offload the entirety of the payloads for either SWOT or NISAR, therefore the fixed root architecture had to be employed. This resulted in much tighter requirements in offload weight accuracy and center of gravity location knowledge as well as increased risk to hardware safety if an incorrect counterweight was applied. This prioritization of the design of the deployable booms for mission performance over ground test simplification enabled the projects to close on technical issues earlier, however, it came with the penalty of a significantly more complicated integration and test program.

Hinge Deploy & Latching Mechanism Handling Constraints

For both SWOT and NISAR, a torsion spring / viscous damper mechanism was used to deploy each boom hinge on orbit (Figure 4). Ground deployment test related requirements were not well-defined prior to completion of the detailed design of these flight mechanisms. Key flight mechanism design decisions were made that created challenges for full range of motion ground deployment testing.

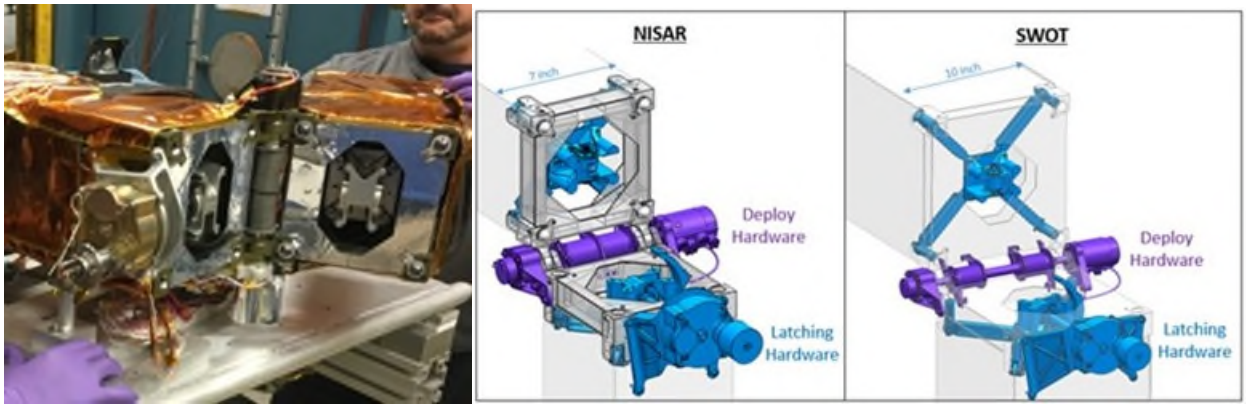

Figure 4. Hinge Deploy and Latch Mechanisms

Both SWOT and NISAR selected a flight deployable hinge architecture in which the deployment mechanisms included hinge pins that doubled as the primary structural load paths. For their function as a mechanism, the hinge pins were coated in a thin, life limited dry film lubrication. The flight configuration of the mechanism made recoating or replacing hinge pins after deployment testing impractical and would engender a hardware safety risk. Similarly, replacing the interfacing press-fit bushings carried non-trivial hardware safety risk and Verification and Validation (V&V) implications. As a result, restrictive allowable loads on the hinge pins for hardware safety during ground deployment testing were levied as requirements on the gravity offload system, which were particularly challenging to meet with the large mechanical advantage present in the flight configuration.

The interfacing bushings for these hinge pins were integral to large bonded composite structures. Large deployable full motion deployment testing was impractical to conduct in the relevant temperature and vacuum environment, and the flight architecture did not include sufficient mechanical field joints to enable lower level subassembly V&V in the flight configuration as these field joints would have necessitated a non-trivial mass increase. Therefore, each matched set of flight deployable mechanisms with flight deployable hinge harness was first installed on a flight-identical test fixture for environmental conditioning and thermal vacuum performance testing and then removed and reinstalled on the flight deployable structure with identical bushings per the same procedure. Part of the verification plan involved demonstrating correlation between the ambient torque performance of each mechanism and deployable harness set between the test fixture and flight installed configurations. Tight requirements relevant to deployment interference torques from the gravity offload system were needed to enable this approach to V&V.

In addition, volume constraints on the flight spring / damper mechanisms responsible for deploying the hinges resulted in low net deployment torque available for deployment. Non-trivial uncertainty in the resistance torque associated with deployable hinge-crossing electrical harness resulted in relatively large bounding allocations, which further limited the torque available to overcome ground deployment system torque losses. Given the small net deployment torque available from the flight mechanisms, modest gravity offload system alignment errors and offload force magnitude errors would result in violation of the bounds of the acceptable deployment torque test profile.

Similarly, while the hinge latch mechanism design had sufficient capability to withstand all on-orbit deployment and post-deployment load cases, this flight latch mechanism design created highly challenging design constraints on the ground deployment test system. Due to the large mechanical advantage of the gravity offload points on the boom and the relatively low latched hinge preload, small errors in offload force and offload alignment with the center of gravity of the deployable hardware would cause latched hinges to gap, potentially damaging the flexures in the latching mechanism. Hardware safety handling constraints for ground testing were levied restricting maximum allowable moments on latched hinges to approximately half of the minimum gapping threshold loads. This necessitated multiple offload points on each boom segment, tight tolerances on target offload forces at each offload point, and continuous monitoring of these offload forces at each location during deployment for hardware safety. A whippletree system was employed to attempt to achieve the target offload force distribution between the multiple offload interface points.

Ground Deployment Test Architecture Trade Study

To identify the appropriate gravity offload methodology that could be used for all six types of deployable hinges for SWOT and NISAR ground deployment testing, the following heritage JPL approaches were evaluated in a trade study (see Figure 5):

1. Helium Balloon Offload System
2. Overhead Swing Arm Offload System
3. 2-Axis Overhead Trolley Offload System
4. Caster / Air Bearing Support from Below Offload System

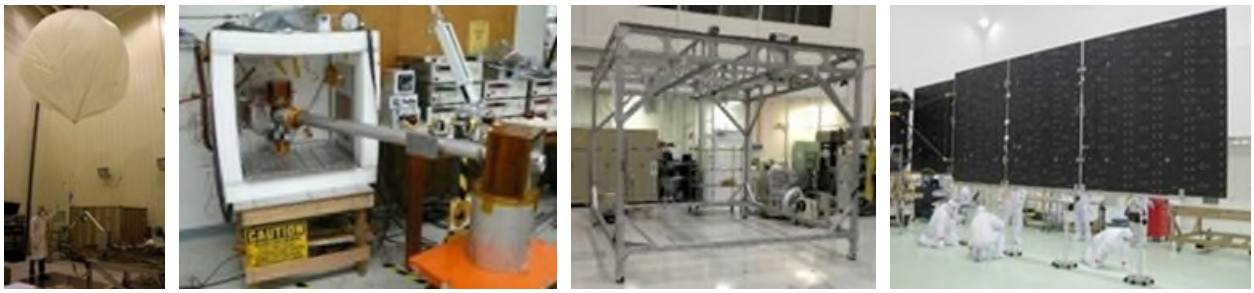

Figure 5. (From Left to Right) Insight Robotic Arm Balloon Offload, Aquarius Boom Deploy Device, SMAP Boom Overhead Trolley, JUNO Solar Array Castered Offload System

The primary metrics used for evaluation included the following:

1. Hardware and Personnel Safety
2. Estimated Cost of Offload System Development
3. Test Facility Needs

Results of the trade study are summarized in Figure 6. Additional metrics including deployment performance impacts and offload system setup / characterization time were considered but not assigned an appropriately high priority, given the fact that dozens of setups were required in the SWOT and NISAR integration flows. The overhead swing arm architecture with whippletree system was selected for both SWOT and NISAR, and an MGSE design implementation team took over the design-through-delivery of the offload system henceforth referred to as the Deploy Fixture (DF).

Category	Criteria	Balloon Offload	Double Swing Arm	2-Axis Overhead Trolley	Support from Below
Hardware Safety	Boom in GCF Testing	• 0.5x to 1.8x of boom inertia during deployment • Relatively constant offload force • Minimal drag effects	• 0.5x to 1.3x of boom inertia during deployment • Constant offload force	• 0.4x to 5.0x of boom inertia during deployment • Constant offload force	• 2.3x to 4.1x of boom inertia during deploy • Each cart will be between 40-170 lbs • Very friction/slope sensitive
	Boom in GCF Failure	• Negligible risk • Balloon catch system • Spreaders above flight hardware	• Negligible risk • Spreaders above flight hardware	• Negligible risk • Spreaders above flight hardware	• Negligible risk • No suspended loads above flight hardware
Cost and Schedule	Total ROM Cost (Eng. Dev + ME + Fab + Assembly + Proof Test)	• $270k • Minimal structure & mechanism count relative to other options	• $300k • More engineering effort for structure and mechanisms than balloon option	• $350k • More engineering effort for structure and mechanisms than other options	• $225k • Floor: ~$120k • Medium structure & mechanism development required
	Schedule Impacts & Cost Risks	• Lowest impact on schedule, most researched option • JPL experience • Vendor quotes ready	• High-level conceptual diagrams complete • No heritage MGSE • No detailed design work complete	• Heritage MGSE but 7-yr ago • No detailed design work complete	• Rowcena & Thompson are in the loop • Large variation in cost estimates due to leveling requirements
Facility Needs	Facility Constraints during Testing	• Floor space: 30' x 30' (42' for NISAR) • SWOT 94' ceiling • NISAR 22' ceiling	• Floor space: arc length of deployment (3' to 12') • Height: ~15'	• Floor space: 21' x 15' • Height: ~15'	• Floor space: 20' x 16' • No ceiling height req. • Highbay 2 floor requires more effort
	Facility Constraints during Storage	• 22 ft^3 • Can be folded into box, easy shipping	• Can be designed to fold simply against wall • Arms removable	• Large fixture in cramped highbay • Must be disassembled between tests	• Requires time consuming assembly, alignment, and tear down

Figure 6. Gravity Offload Architecture Trade Study Summary

Gravity Offload System Challenges

An initial set of requirements were communicated to the DF design team to assure boom flight hardware safety as well as acceptable deployment performance to support correlation to analytical model predictions and subassembly-level ambient deployment performance testing. These requirements covered the following topics:

1) Maximum suspended flight hardware mass and center of gravity offset from the DF swing arm hinge axis
2) Interface locations on the flight hardware for offloading
3) Keep out zone for the swept volume of flight hardware
4) Maximum allowable deployment resistance torque from the DF
5) Repeatability tolerance for the DF resistance torque in a given setup
6) No deployment assistance torque from the DF permitted for performance tests
7) Maximum permissible moment loading on latched hinges
8) Maximum permissible inertia of the moving GSE
9) Maximum allowable overshoot force from the moving GSE at the end of deployment
10) The ability to offload all four NISAR hinges and all SWOT hinges multiple boom configurations
11) The ability to be taken apart for shipment

Many of these requirements were fully satisfied in the implemented design of the DF. However, some requirements, such as the total drag torque, were only met under nearly perfect setup conditions. Little was understood at the time of delivery about the alignment and positioning tolerances needed to obtain acceptable drag torques, nor the challenges of the setup process necessary to achieve them. Another example was the lack of understanding of the tolerances on knowledge of mass properties needed during testing to stay within the not-to-exceed hinge moment loads.

To make matters worse, several driving requirements on the offload MGSE became substantially tighter as knowledge of flight deployable hardware sensitivities matured; flight hardware development was progressing in parallel with the design of the DF. It was identified in the initial DF requirements set not to apply a moment to an open hinge that violated static proof loads, resulting in a handling constraint of 389.8 N•m (3,450 in•lbf). This was later revised down to 54 N•m (480 in•lbf) based on the need to prevent gapping of latched hinges during deployment testing. A third revision, intended to reduce the risk of damaging the dry lubricant on the flight deployable hinge pins, was identified much later in the DF development, restricting the maximum moment to hinges to only about 11.3 N•m (100 in•lbf). After understanding the implementation challenges associated with compliance with this 11.3 N•m limitation, the requirement was later relaxed to 28.25 N•m (250 in•lbf) through additional qualification model hinge testing that demonstrated no significant hinge pin coating damage occurring at this loading. Nevertheless, it still remained a tight, driving requirement for the test system which, if identified earlier in the gravity offload MGSE development, could have been a driving consideration in the MGSE offload architecture trade study.

Both projects had varying cg distances depending on the hinge being deployed that ranged from 63.5 to 165 cm (25 to 65 in) from the swing arm and varying total offload weights of 46 to 136 kg (101 to 300 lbm). Errors in either the total offload, cg location, or verticality of the hinge line could all produce moments on the moving hinge, and had to be carefully managed (Figure 7). The suballocated test setup tolerances were on the order of ±1.25 kg (±2.75 lbm) for offload error (0.9% of total offload) and ±0.6 cm (±0.25 in) of cg offload location error to stay within the 28.25 N•m (250 in•lbf) not-to-exceed moment requirement. This forced the team to not rely on CAD estimates for mass, and rather to weigh all flight components and GSE components and perform very careful configuration tracking to stay within these bounds. Mass properties testing of the assembled flight components generated very accurate initial mass and cg for each boom tube segment. This was followed on by individual piece part measurement of all additional flight components and GSE added to the moving hardware, including mass and cg location. Procedures were generated to track all configuration changes with quality assurance verifications implemented to ensure the hardware configuration matched the calculations. If it had been feasible, a free-free test configuration (or reduced flight hardware sensitivity) could have eliminated the need for this tedious process and greatly simplified

the integration and testing process, not to mention reducing the risk to the flight hardware associated with human error in this extensive analytical tracking effort.

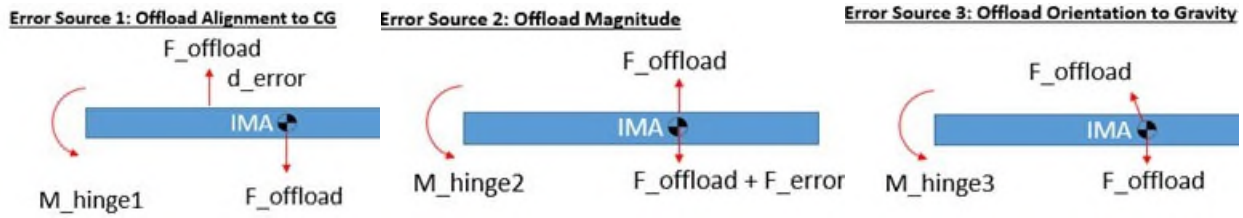

Figure 7. Offload Errors Causing Moments on Moving Hinge Pins & Deployment Resistance Torque

One additional complicating factor for the offload approach selected was the use of a series of four pulleys to route the offload cable from the flight article to the counterweight in order to reduce the inertia of the system. The combined drag force through all four pulleys at the maximum offload weight of 125 kg (275 lbm) was 2.25 kg (5 lbm). If the moving boom did not sweep through a perfectly level arc, its cg would move up or down and the offload weight would similarly need to move with it. With the drag in the system of pulleys alone, this would generate up to 2.25 kg (5 lbm) of error in the offload force on the deploy hardware, which violated the ±2.75 lb requirement. This was managed in several ways. First, the moving hinge pin is intentionally loose fitting, allowing for roughly ±0.1 deg of free angular movement. The verticality of the moving hinge was measured to make sure it was within ±0.2 deg of perfectly vertical prior to each deployment. Therefore the looseness of the hinge pin could correct for some of the initial angular misalignment and allow the boom to deploy through a more level arc with respect to gravity. Second, the pulley diameters were changed from 15.25 cm (6 in) to 50.8 cm (20 in) while keeping the same ball bearing sizes (Figure 8). This allowed for similar load carrying capability through each pulley but drastically reduced the total pulley system drag force from 2.25 kg (5 lbm) to 0.9 kg (2 lbm).

Figure 8: Deployment Fixture with 15.25-cm Diameter Pulleys Upgraded to 50.8-cm Pulleys to Reduce Drag

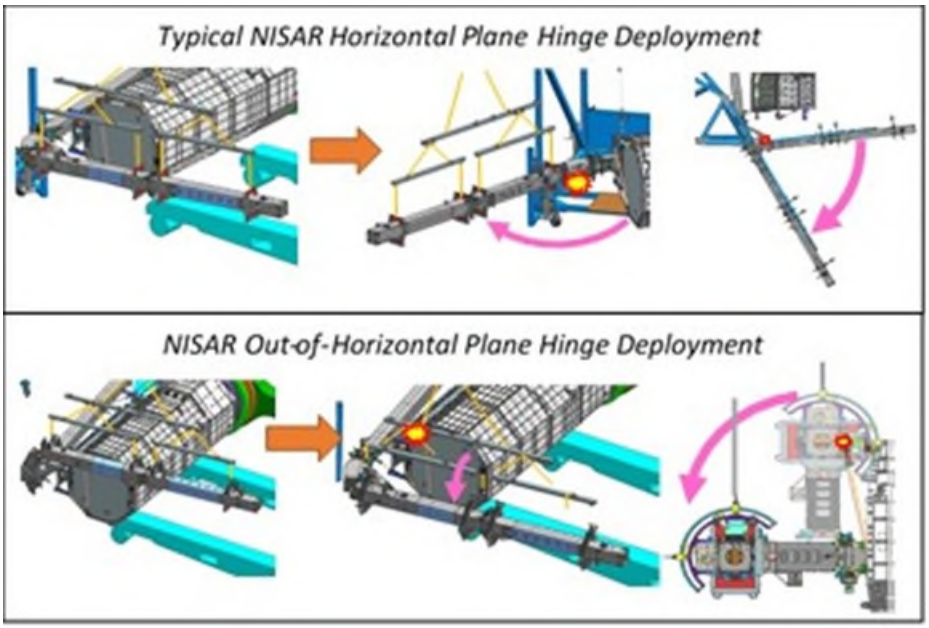

Figure 9: Horizontal-Plane versus Out-of-Horizontal-Plane Hinge Deployments

The offload error due to mass properties uncertainty or friction in the pulleys was especially critical for NISAR's out-of-horizontal-plane hinge deployment as it directly opposed deployment motion (Figure 9). Therefore, the driving constraint was not 28.25 N•m (250 in•lbf) for hardware safety, but only 4.5 N•m (40 in•lbf) to stay within allowable deployment torque performance requirements. At a distance of 63.5 cm (25 in) between the cg and hinge line axis, the maximum offload error could only be zero to 0.7 kg (1.6 lbm). Prior to each out-of-plane NISAR hinge deployment, a dummy weight was attached to the Deploy Fixture and a measurement of the system friction was taken. During the deploy test, the offload mass was intentionally adjusted to account for pulley drag and result in a near nominal offload force.

Even with the care taken to measure all flight hardware and GSE masses, account for frictional effects, and rigorously track the configuration, it was extremely difficult to get consistent deployment results for the NISAR out-of-horizontal-plane hinge deployment. Subtle changes in deployable mass (for example, the routing of test cables or the addition of thermal blankets) significantly effected the measured deployment profiles. Figure 10 shows a spread of deployment profiles taken over a year with multiple reconfigurations in between each data set for both a typical horizontal plane NISAR hinge deployment and the out-of-plane hinge deployment. The deployment profile shapes for each horizontal plane deployment were roughly consistent and deploy times matched ±20% between all tests. The out-of-plane hinge deployment profile data shows very different profiles for each deployment, with total deployment times ranging from 110 seconds on the fastest to 2400 seconds for the slowest. The difference between the fastest deploy time of 110 seconds and the middle deploy time of 740 seconds was determined to potentially be caused by a difference in offload of 0.34 kg (0.75 lbm) and a lateral cg difference of 0.5 cm (0.2 in) between the two runs. This extreme sensitivity of deployment performance due to minor test setup errors led the project to eliminate deployment profile consistency as a metric for test success for this hinge. Instead, the criteria for success was changed to safely deploy the hardware from launch to deployed configurations, with a thorough visual inspection of the mechanisms pre- and post- deployment to confirm their health.

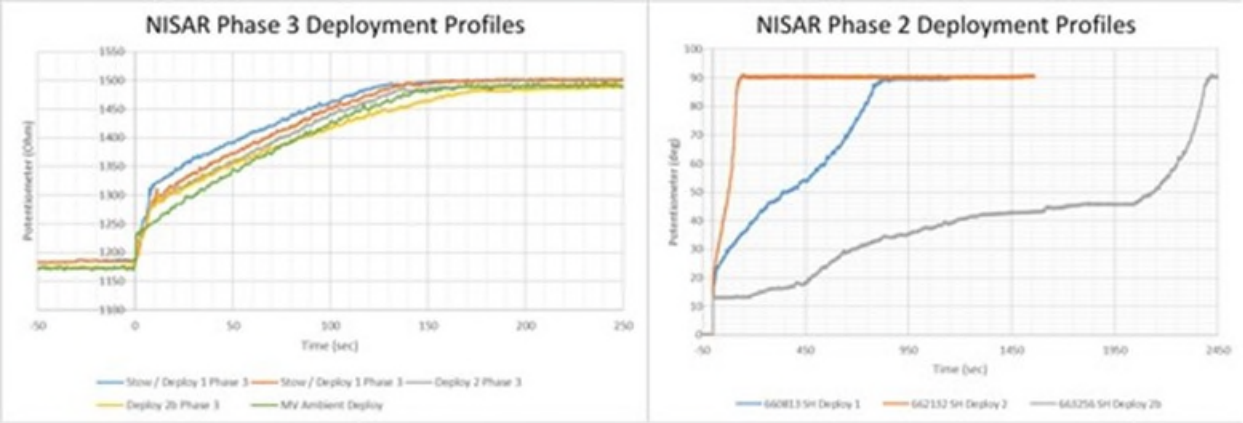

Figure 10: Variation in Hinge Angle Verses Time Telemetry Data for a Typical NISAR Horizontal Plane Hinge Deployment and the NISAR Out-of-Plane Hinge Deployment

A final set of requirements that was not well understood until after delivery of the deploy fixture pertained to the required stiffnesses for this MGSE. The implemented design had a low-stiffness support structure for the swing arm axis. This meant the DF swing arm rotation axis changed orientation and positioning under load throughout the flight deployable range of motion. Torque error and flight hinge loads associated with this phenomenon needed to be addressed by appropriately pre-biasing the DF orientation during setup to minimize the peak magnitude of these contributions to remain within allowable limits. In addition, the clocking of the DF support structure was carefully selected for each hinge range of motion to minimize the contributions to torque error from swing arm support structure deflection. There was a clear need for pre-characterization of offload fixture performance in each setup prior to usage with the flight deployables.

Characterizing Gravity Offload System Performance

Shortly after delivery of the DF to the Integration and Test team, it was recognized that the DF would be a challenging system to use to meet the precision and consistency of offload needed for SWOT and NISAR boom ground deployment testing. The teams operating the DF in conjunction with the flight hardware needed to develop and utilize consistent procedures for the set-up, characterization, and pre-test analysis of DF performance to ensure each setup was safe for the flight hardware and would enable successful verification of performance requirements. A tedious but workable process was developed, but the methodology evolved significantly as the teams learned the nuances of large-scale gravity offload operations throughout the test campaigns.

Before any setup and characterization of the DF took place, the flight hardware was secured to a stable fixture with its deployable hinge axis sufficiently well aligned to the gravity vector. The maximum permissible angular error between the flight hinge axis and the gravity vector was 0.2 degree to limit cg vertical translation (and associated deploy torque impacts) throughout the deployment range of motion.

In regard to DF setup challenges, the DF consisted of a massive support structure with very limited and coupled degrees of freedom. The available degrees of freedom proved insufficient to allow for efficient setup for testing. The DF swing arm hinge axis had to be sufficiently aligned to the flight hardware hinge axis. To achieve this, two self-leveling lasers were projected, perpendicular to each other, onto the flight hinge axis (Figure 11). The DF was rolled into position such that the DF hinge axis coincided with the flight hardware hinge axis (defined by projected lasers) to within 5 cm (2 in) in plane projected distance. Because the DF swing arm was about 6 m (20 ft) above the flight hardware, the lasers had to be moved and projected onto to the DF axis in order to measure the offset to the flight hinge axis on the ground. Projecting lasers between two axes separated by a height of two stories, and then measuring the offset to the visually estimated centerline of the flight hinge axis had non-trivial measurement uncertainty. When accounting for the stackup of measurement uncertainties, the remaining allowable offset from nominal concentricity was

determined to be 1.9 cm (0.75 in). In other words, the 1360 kg (3000 lbm) DF structure had to be rolled across an uneven floor on its four casters, and its swing arm hinge had to be aligned to the flight hinge axis 6 m (20 ft) below it, to within 1.9 cm (0.75 in). Once the two axes were aligned, the levelness of the DF swing arm axis with respect to gravity had to be characterized to ensure it did not impart any deployment assistance torques or unacceptably large resistance torques onto the flight hinge. Four jacks positioned at the four corners of the base structure provided only coarse adjustment capability to the levelness of the swing arm. Due to the large distance between the jacks and the swing arm, small adjustments at the base mapped to large changes in swing arm rotation axis levelness and position. Oftentimes, the levelness adjustments would put the hinge axes alignment out of the allowable 1.9 cm (0.75 in) positioning tolerance. As a result, the huge structure would need to be lowered back onto the casters to make small adjustments to the concentricity. And then the leveling process would need to be repeated. Many time-consuming iterations were typically needed to achieve an acceptable levelness in conjunction with an acceptable hinge axes co-alignment.

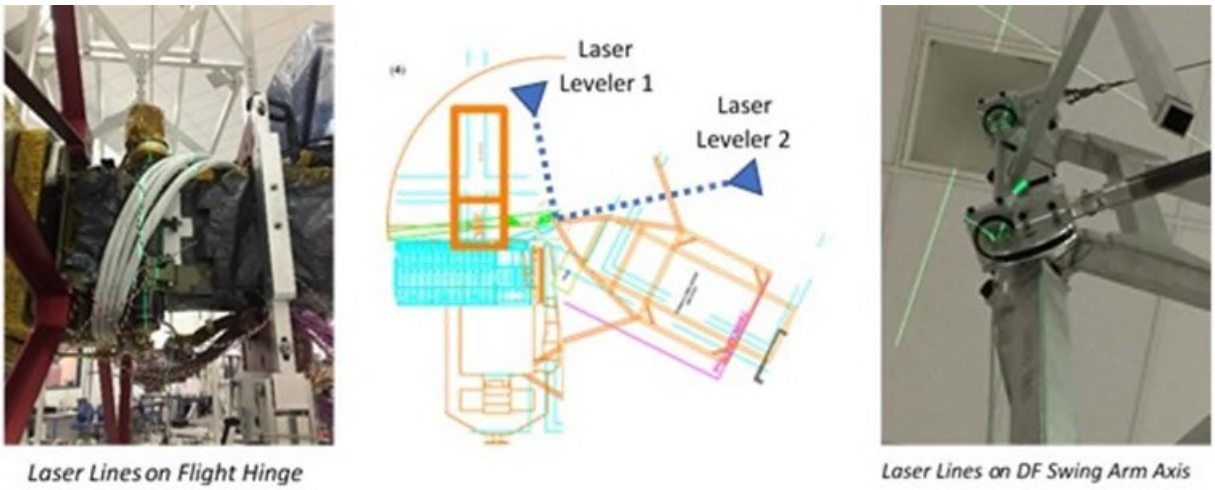

Figure 11: Laser Levelers Positioned Orthogonally for Alignment of Deploy Fixture Swing Arm Hinge Line to Flight Hinge Line

To characterize DF induced deployment interference torques in each setup, a test mass representative of the moving hardware was suspended from the DF offload cable while an operator manually rotated the swing arm at a constant rate using a T-handle wrench with extension. To record this characterization data, a torque transducer with angle encoder were placed in series with the load path of the T-Handle wrench and the adapter on the DF swing arm, capturing data while the operator rotated the swing arm and hanging mass. The transducer and encoder data were recorded on a nearby laptop. It was assumed this method of monitoring the drag torque would be sufficient in verifying that the DF was not assisting the rotation of the swing arm with hanging mass, and also not exceeding the resistance torque requirement. This characterization method was also used prior to stowing the flight hardware hinges pre-deployment test; however, the resistance/assistance torque requirements were significantly looser as only hardware safety requirements had to be met, rather than the more strict deployment performance correlation requirements.

For the NISAR project, this manual characterization method proved to be sufficient to meet their hardware safety and deployment performance requirements. This stemmed primarily from the fact that the flight deployment mechanism minimum net torque available at the end of the deployment sweep was significantly higher for NISAR than for the SWOT booms, and hence the deployment resistance torque requirements were higher for the NISAR deployment fixture. But inconsistent results from this manual characterization scheme from different operators (and even from different characterization runs done by the same operator) resulted in more torque characterization variability than could be used to demonstrate requirements compliance for SWOT booms. The SWOT project's booms also had a higher mass and rotational inertia than the NISAR boom segments during ground testing (given the stowed reflector needed to be included

at the end of the SWOT booms, but not on NISAR's). The increased inertia of the hanging mass on the swing arm made it more difficult for an operator to maintain consistency through manual characterization. One of the major difficulties that became hard to avoid in manual characterizations were inconsistent human interference loads in the torque data. These were caused by the operator accidentally rotating the swing arm too fast and then attempting to correct by slowing down (not necessarily rotating in the opposite direction, but just reducing the speed of rotation). When combined with small pendulous swinging motion of the test weight under the swing arm, this would sometimes show up as assistance torque in the data. Operator manual interference torques proved very challenging to decouple from DF torques in the measured data, resulting in high uncertainty in characterization runs and preventing deployment performance requirements from being able to be verified conclusively for SWOT.

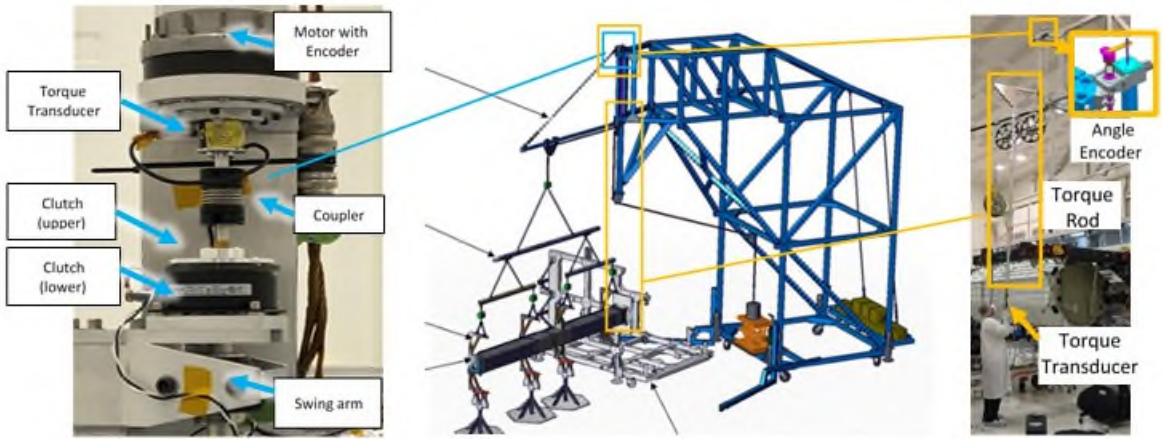

Figure 12: SWOT Motorized Torque Characterization Tool (Left), Full Swing Arm Offload System (Center), NISAR Manual Torque Characterization Tool (Right)

In the pursuit of sufficiently repeatable and accurate characterization runs, the SWOT project reworked the DF after initial testing. A motor with torque transducer and encoder was used to rotate the swing arm at a constant rate (selected to match the predicted average deployment speed) while recording the resistance torque / angle characterization data over the applicable deployment range of motion during characterization runs, with a clutch to disengage the system for flight deployment testing (Figure 12). The integration of this system to the top of the DF was a difficult undertaking, requiring weeks of iterations to align, test, and verify that the rotational axes of the motor and swing arm were sufficiently aligned as to not impart an additional drag torque into the characterization data that would not have existed during flight hinge deployments. While the time spent integrating this device caused a brief testing schedule delay, it resulted in higher characterization accuracy and consistency, which ultimately reduced the frequency of performance requirement violations in test. Despite the increased characterization fidelity, some performance requirement violations still occurred and more characterization challenges remained to be addressed.

In the course of investigation of one performance requirement violation, a concern was identified that DF deployment interference torques may be changing between pre-test characterization and actual deployment testing (or during deployment testing). A system had not been developed to directly measure DF deployment interference torques during flight deployment tests. To investigate this concern area, DF characterization runs were completed both pre-deployment and post-deployment. For some deployment tests, both the average torque value and even the shape of the measured DF torque curve were observed to change significantly between the pre- and post-characterizations (Figure 13). The exact root cause of the change was not conclusively determined, but there are two prevailing theories.

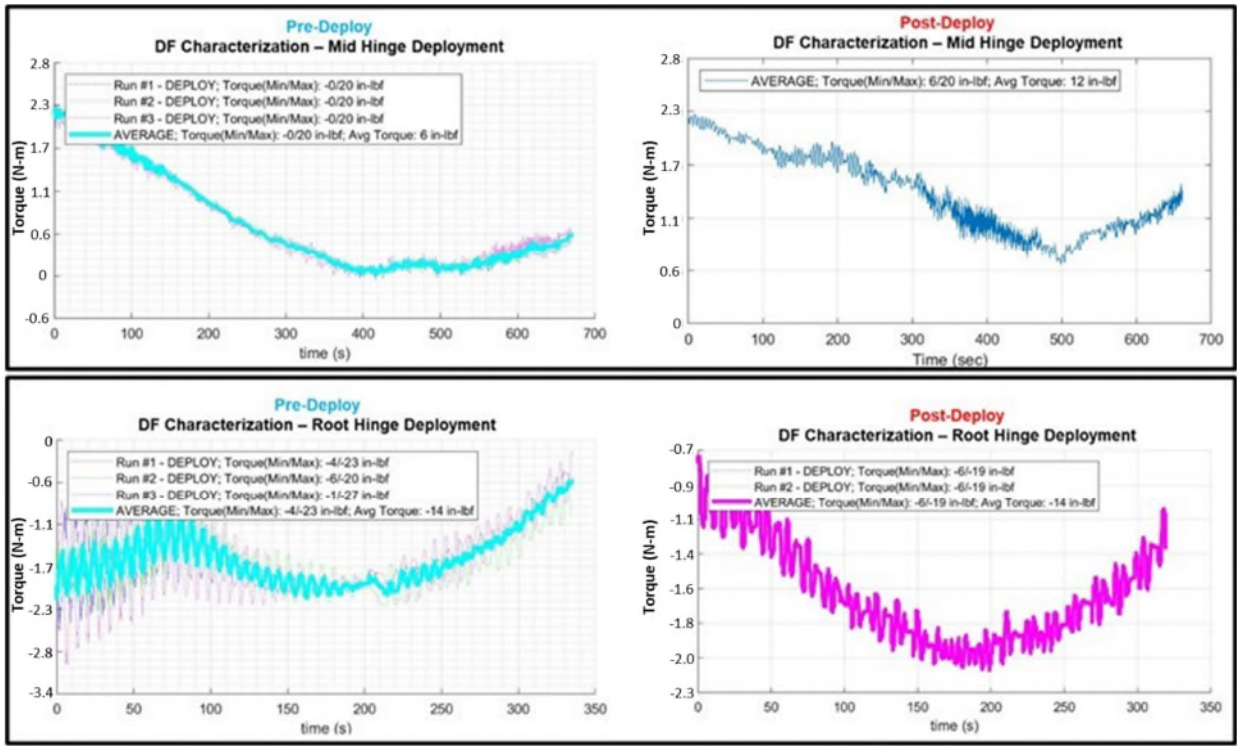

Figure 13: Top Row - Pre-vs-Post DF Characterization Data for SWOT 180 Degree Sweep Angle Hinge. Bottom Row – Pre-vs-Post DF Characterization Data for SWOT 90 Degree Sweep Angle Hinge

During characterizations and deployments, the DF would sometimes make a creaking / popping sound that generally occurred in the same regions within the angular range. The DF support structure with all of its welds were thoroughly inspected and ruled out as a potential source of the audibles. It is expected that the swing arm radial bearings and thrust bearing may have shifted within their bores during deployment tests, causing an audible sound during the slip events. This bearing position change would result in swing arm rotation axis changes, with corresponding changes in parasitic torque. Another potential root cause identified was that the DF was supported by 4 points of contact to the floor via manually cranked jacks. It was observed during characterizations, where the jacks were used as the mechanisms for leveling, that the DF would sometimes rock about 2 opposing jacks—similar to an imbalanced 4-legged stool. Depending on which combination of three jacks supported the DF, the resulting torque curve / average would change. It is believed this phenomenon could have occurred across characterization tests, as well as during deployment tests, resulting in resistance torques that varied by a non-trivial amount, even in the “same setup” of the DF. The free hanging mass during characterization runs did not perfectly represent the loads on the DF when offloading a partially constrained boom as well as kickoff dynamics in deployment testing; hence the potential for rocking in deploy testing but not in pre-characterization. In response to these findings, both pre- and post-test characterizations were conducted for each deployment test and additional quality assurance verifications were implemented after this investigation to ensure all four jacks were well seated on the floor prior to the pre-test characterization runs.

Another late breaking realization was that the speed at which the swing arm rotated during characterization had an effect on the torque curve. Generally, the slower the swing arm was rotated, the higher the average measured parasitic torque. Once this effect was identified, the new process for characterization included pre-characterization of DF performance to ensure sufficient setup for hardware safety, and post-test re-characterization at the average measured speed of the flight hardware during deployment for performance requirement verification. While this methodology also helped improve the correlation of test results to predictions, more performance requirement violations and associated investigations ensued--further improvement in the process was still needed.

One of the major features the DF lacked was the ability to record real-time resistance torque contributions from the DF with the Flight Hardware rigged to the deployment cable. There was a fundamental difference between articulating the swing arm with a free hanging mass and articulating the swing arm with a partially constrained boom suspended. DF pre-characterization measurements with a free suspended mass simulator did not fully account for any of the error sources referenced in Figure 7.

A detailed ground support equipment deployment performance modeling effort was undertaken to analytically bound additional error sources based on additional alignment and weight measurements taken in each setup; this enabled analytical post-processing of test data to demonstrate compliance with hardware safety limits and adequate correlation of flight deployable performance with lower level ambient test results.

Through this additional deployment modeling, it became apparent that the simplistic approach of specifying a maximum average resistance torque requirement across the range of motion did not ensure compliance with the deployment performance duration requirement. DF interference torque near the end of the deployment range of motion had a far more significant, non-linear impact on total deploy duration than interference torque near the start of the range of motion. Therefore, the maximum allowable resistance torque imparted by the DF needed to be reduced further towards the end of the boom's deployment sweep, posing even tighter constraints on the already-challenging task of aligning and leveling the DF swing arm axis to the boom hinge axis.

To further reduce discrepancies between deployment duration model predictions and as measured performance in test, actual measured DF test characterization data was also input into the deployment model. When accounting for the as-measured characterization data in the model, this method proved to be quite accurate, predicting durations within 5% of actuals for the final two deployments on SWOT for which it was implemented.

Conclusions, Lessons Learned, and Recommendations for Future Large Deployables Testing

The lessons learned following completion of the SWOT and NISAR boom deployment testing campaigns fall into several broad categories.

The first category is to carefully consider ground test needs for large-scale flight deployables early on in the mission planning phase. Flight design teams can have a tendency to "optimize" flight hardware designs for the flight system with little to no consideration for ground testing. A more balanced approach would likely be of best value to the project. Several costly issues encountered during the SWOT and NISAR ground deployment test campaigns stemmed from flight hardware design decisions made very early in the planning, and it was too late to reverse these decisions once the impacts to the MGSE and testing teams were better understood. Involving integration and test and MSGE engineers at the earliest stages to work through the ground test program even at a conceptual level could have uncovered many of the issues that were discovered only after the DF was delivered. Generating flight mechanism designs that were outside of the main structural load paths and flight configurations that are able to be tested in free-free offloaded states also would have greatly reduced the risk to the hardware and simplified the overall test setups. Separable field joints should be included for all deployable hinges to allow flight acceptance testing at the lowest levels of assembly and simplify higher level system tests except under the most mass constrained programs. Where possible, self-supporting deployable structures or structures with less sensitivity to reasonable parasitic loads can greatly simplify testing operations and requirements verifications.

The second category of lessons learned applies during the concept generation and down selection of MGSE gravity offload architectures. Invest effort to achieve an adequate understanding of flight hardware sensitivities and requirements early in the development, and identify and push back on overly challenging / constraining requirements from the flight system as early as possible. In generating concepts, a good understanding of the architecture's sensitivity to misalignments and how it effects deployment performance as well as the degree of difficulty to achieve the required alignments needs to be a key metric for down selection. For flight designs requiring a very high level of offload precision, self-aligning deployment systems

such as balloons or balance beams should be utilized to reduce complexity (and cost and schedule implications) during I&T. GSE architectures should be evaluated with preference toward minimizing setup, reconfiguration, and characterization time needed on the project critical path—for example, a single configuration of GSE applied at the start of the test campaign for all phases of deployment. The overall I&T plan and flow should also give consideration to minimizing the amount of reconfigurations and repeat setups / recharacterizations of GSE and gravity offload systems, including facility considerations to enable offload systems to remain in place.

The final category of lessons learned revolves around items specifically relevant to swing arm gravity offload systems. While these systems can function well for a variety of applications, care must be taken during the initial design phases to understand the detailed requirements and needs of the specific mechanism being tested. Swing arms are sensitive to the alignment of the swing arm with respect to gravity. Direct alignment features / degrees of freedom for the swing arm should be incorporated into the design to allow for any necessary tuning of the swing arm alignment and positioning independent of global support structure positioning / leveling capabilities. And the support structure must be designed to be stiff enough and rigidly assembled to prevent unacceptable levels of deflection or shifting of this swing arm axis during usage.

The SWOT and NISAR projects ultimately achieved their needs for safely verifying functionality and performance requirements for the boom deployment systems. However, there was a long and arduous path to figure out how to use the as-delivered MGSE to meet these needs. Application of the above lessons learned throughout the entire lifecycle of a future project will significantly reduce risks and challenges encountered in meeting the needs of large scale deployable test programs.

Acknowledgement

This research was carried out at the Jet Propulsion Laboratory, California Institute of Technology, under a contract with the National Aeronautics and Space Administration (80NM0018D0004).

Flatness Adjustment in the Design and Integration of a 35-m^2 Space Deployable Synthetic Aperture Radar Antenna.

Leonel Garategaray*, Juan Casais*, Alberto Martin Ghiselli**, Horacio Quiroz**
and Gustavo Di Pasquale**

Abstract

This paper presents the process carried out to achieve the flatness requirement requested in orbit for the Synthetic Aperture Radar (SAR) antennas of the Satélite Argentino de Observación Con Microondas (SAOCOM) mission. It describes the main design characteristics, integration and test processes in line with the mission requirements and the possibility to verify it on ground due to the test constraints. The results of the Structural Qualification Model integration process and flatness measurements are described, showing the improvements and modifications that were implemented in the measurement strategy in order to guarantee the success of the flight models, mainly in the measurement strategy.

The results of the tests performed on the Flight Models showed that the flatness requirement was met with margin and confirmed the design robustness.

Introduction

The SAOCOM Mission is defined, managed and operated by CONAE (Comisión Nacional de Actividades Espaciales), Argentine Space Agency. It is composed of a twin satellite constellation, SAOCOM 1A and SAOCOM 1B, carrying each one a polarimetric L-band SAR instrument. The main driver of the mission is to operatively generate soil moisture maps. Both satellites were launched in 2018 and 2020 respectively and now are in full operating mode in a polar sun synchronous frozen orbit at 619 km with a 98° mean inclination.

The SAR Antenna structure and its mechanisms were designed and manufactured by the Comisión Nacional de Energía Atómica (CNEA), while the assembly, integration and tests were conducted together with CONAE.

The SAR Antenna consists of seven panels whose structure is made of a sandwich structure with an aluminum honeycomb core and carbon fiber facings, where all units are mounted (mechanisms, the electronic boxes and RF front end). In the short sides of the panels, two reinforcements are bonded, forming a “U-shape”. With all these hardware mounted, each panel weights approximately 200 kg; the smaller panels are 1.5 meters long and 4.0 meters wide. The whole SAR Antenna has a radiant surface of 35 m^2 with a 10 meters long by 4.0 meters high envelope. The SAR Antenna has a structural configuration with one central panel fixed to the Service Platform (SP) and two symmetrical wings with three panels each that unfold in a spiral way from center to extremes. The central panel is fixed to the SP by means of a tube-reticulated assembly, composed of 16 carbon fiber cylindrical cross section tubes with aluminum end fittings. This interface structure (IS) is fixed to the SP on 6 points connecting the cylindrical trusses by means of titanium fittings and allows the differential thermal displacements between the aluminum SP and the carbon fiber antenna minimizing the distortion of the radiant surface.

During launch, each wing is folded and retained with a dedicated mechanism, once in space each wing is released and deployed by stepper motors in a controlled way by ground commands, reaching its final

* National Commission for Space Activities, Buenos Aires, Argentina (CONAE)
** National Atomic Energy Commission, Buenos Aires, Argentina (CNEA)

position after six deployment steps. Figure 1 shows general views of the SAR Antenna in folded and deployed configurations.

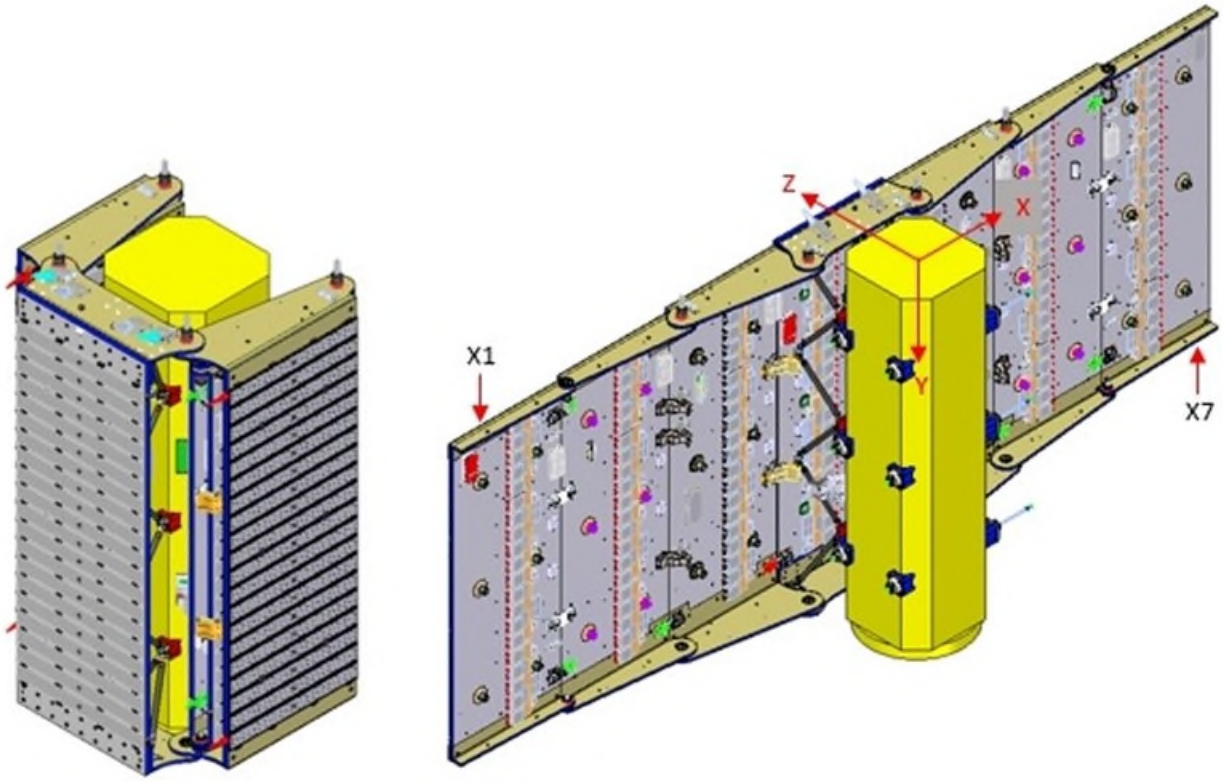

Figure 1. Launch and Flight Configuration of the SAR Antenna.

To assure the operational performance of the instrument, the flatness of the radiant surface must be controlled. The analysis of the flatness of the radiating surface of the deployed SAR Antenna in space should include several error sources such as geometric error sources known and characterized on ground (antenna panels mechanical flatness deviations, mechanism misalignment, stiffening truss errors) and unknown error sources in space (thermo-elastic deformations induced by sun-eclipse cycles, spacecraft maneuvers and instrument OFF-ON transition, dynamic coupling, induced deformation by attitude control perturbations, other movable mechanisms dynamics and the 1G to 0G unloading deformations).

In early phases of the project, an alignment budget was established in order to design the structure, the mechanisms, and the integration process according to this budget. This requirement was so demanding that in order to achieve it, complex integration processes had to be developed and verified.

Key Requirements

Many requirements were derived from SAR System to SAR Antenna in order to achieve the desired performance. In addition to these performance requirements, manufacturing, assembly, integration, test and transportation requirements were added, making it difficult to reach a balance between them.

For alignment purposes, an ideal plane was defined by the external faces of the Radiating Modules in Flight Configuration (SAR Antenna Deployed): Overall Antenna Radiating Plane (OARP). The Geometric Center of OARP was located at the intersection of the two ideal diagonals of the OARP, as shown in Figure 2.

The analysis of the deployed SAR Antenna distortions in space, related to the OARP and containing all error sources should be less than 24 mm or λ/10 (where λ is the wavelength of the instrument) and should

have 20% positive margin. This value shall be evaluated between two points located anywhere over the radiating area.

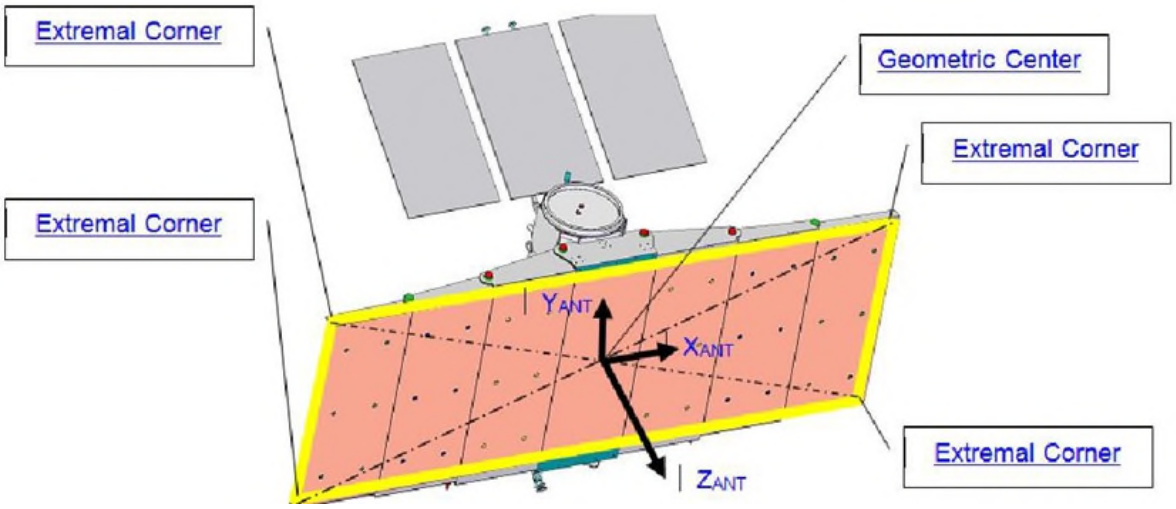

Figure 2. SAR Antenna OARP and coordinate system.

As it was said before, in order to reach final flatness requirements, a budget that considered all the possible geometric error sources that affected the flatness and could be characterized on ground was established in order to control it during the manufacturing and integration processes, the in-orbit flatness requirement was extrapolated to ground and additional security margin was applied to the result. The evaluation resulted in a requirement of a maximum of 12.7 mm RMS value for the flatness of the entire radiant surface when measured on the ground.

A detailed alignment strategy had to be determined in order to align of the SAR Antenna Panels during their integration to minimize the misalignments of the whole SAR Antenna. Considering that the requirement was given on the radiating surface of the antenna, and that it is a sensitive surface, since it is completely coated with white paint, a non-contacting measurement methodology had to be determined.

In addition to flatness requirements, SAR Antenna mechanisms were not designed to support the complete antenna weight on ground, so all the integration had to be supported by a zero-gravity offload device that was designed and used for the integration and deployment on ground and which had to compensate at least 85% of the SAR Antenna deployable panels weight.

In addition to the rigorous design requirements, the integration policies adopted by CONAE added critical constraints to the assembly and integration and test strategy, consequently, the SAR Antenna had to be assembled in vertical position, in a clean room without crane on a dedicated support structure, functionally tested and characterized and then had to be transported to the main contractor facilities, where the SAR Antenna had to be integrated to the spacecraft SP in folded configuration, maintaining the shape and flatness when deployed, with a mounting residual antenna pointing error that should not exceed 0.014 degrees in both azimuth and elevation.

Mechanisms Development

The following mechanisms were designed to accomplish the requirements of keeping the antenna safe during transportation and launch, release it once in orbit, allow the deployment and keep it in that configuration until end of life:

- Restrain-Release (RR)
- Hinges
- Latches

Mechanisms Description and Main Features

Restrain-Release mechanism (RR):

The main function of the RR is to give support to the Antenna while it is in folded configuration for transport and launch and to release it once the satellite is in orbit. To accomplish this task a total of 12 RR are distributed, 6 to each wing of 3 panels. Each RR mechanism consists of the following sub-assemblies: three tubes attached to inserts potted to the sandwich panels; a flange fastened to the SP through four4 calibrated stem bolts and a rod which provides the preload to hold the tubes tightened, as shown in Figure 3.

The six RR mechanisms have the capacity to compensate the misalignments between panels' inserts that arise from the integration process described above, as well as the alignment of the entire wing with respect to the fixing points of the SP or mounting structure.

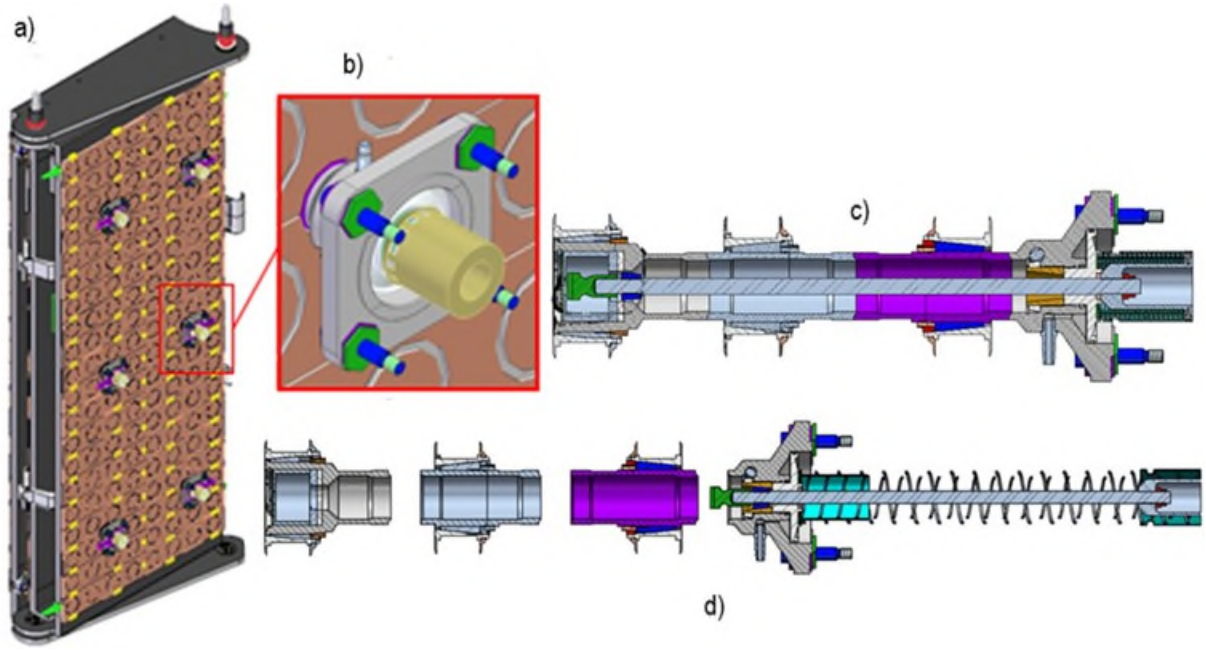

Figure 3. Restrain-Release mechanism a) Distribution in the -X wing b) Flange details c) Mechanism in preloaded configuration d) Mechanism in released configuration.

Hinge mechanism:

The hinges link two adjacent panels, forming the joint axis between them. Furthermore, they provide the active torque needed for deployment by means of a stepper motor installed in one of the two hinges which form each joint; the other hinge is not motorized and features a potentiometer to provide telemetry of the position of the panel. The hinges have the capability to move the rotation shaft in two directions perpendicular to the shaft (flatness adjusting device); the axial position can be adjusted by means of calibrated shims in the motorized hinges. The angular displacements can also be regulated by differential adjustment between opposite hinges. To avoid over constraints and distortion in the panels, the non-motorized hinges allow the shaft to slide axially. INVAR 36 was selected for most of the parts in hinges to minimize thermal-induced distortion propagating to the antenna, see Figure 4.

A total of 12 hinge mechanisms are installed to form the 6 rotational joints of the antenna.

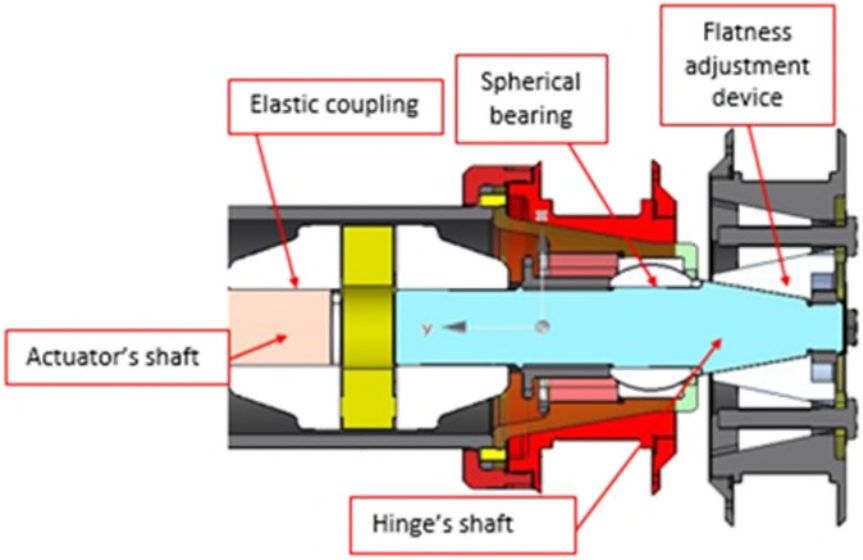

Figure 4. Motorized hinge cross section

Latch mechanism:
Latch mechanism is composed of the base and the pawl sub-assemblies. Positive latching is achieved with a lock bolt that slides down a notch in the pawl that prohibits the pawl retraction. Once deployed, the latches constitute two contact points with no movement and no gap, and along with the regulation capabilities of the hinges, allow the longitudinal, transversal and warping adjustment of each panel, therefore modifying the flatness of the antenna. INVAR 36 was selected for base and pawl to minimize thermal-induced distortion propagating through the antenna, as shown in Figure 5.

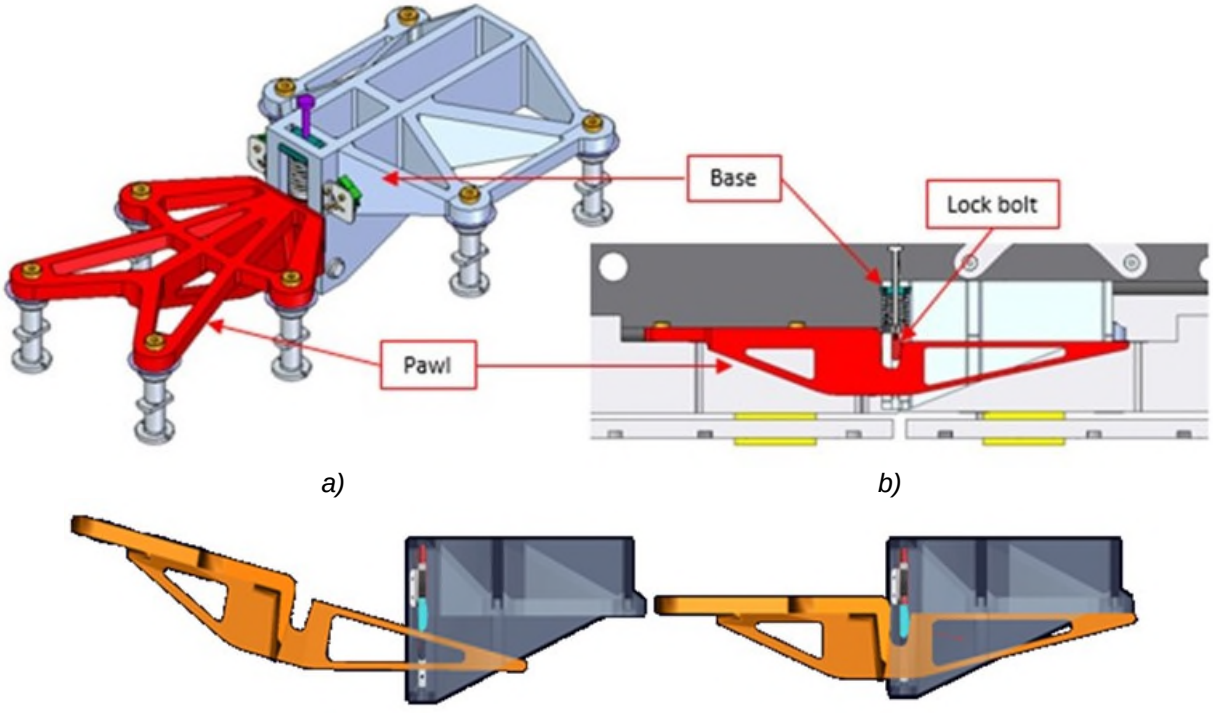

Figure 5. Latch mechanism a) Isometric view b) Cross section c) Latching kinematics

Structural Model Campaign

The models adopted by the SAOCOM mission to verify deployment, flatness and alignment requirements were a structural qualification model (SQM), a proto-flight model (SAOCOM 1A) and a flight model (SAOCOM 1B).

The SQM is a full-scale model composed of the SP fully representative and the SAR Antenna composed of the central panel X4 with the IS, a structural flight-like wing (panels X5, X6 and X7) and dummy wing simulating panels X3, X2 and X1; this dummy wing did not have deployment capabilities.

In order to decouple SAR Antenna assembly from SP integration, a dedicate Mechanical Ground Support Equipment (MGSE), called Mounting Structure which simulated the SP was developed. This MGSE has the same interfaces as the SP.

The SAR Antenna structural model integration

The IS was mounted on central panel X4, and both were integrated to the mounting structure standing in vertical position. This integration was done using a dedicated MGSE which hangs the panels from the RR inserts, allowing slow motion movements, in order to reach the mounting structure interface. This assembly was placed with minimum position restrictions, since the integration criteria were height, level and perpendicularity with respect to the mounting structure, which were achieved taking advantage of the articulated and adjustable ends fittings of the IS.

Once the central panel was positioned and fixed, the next adjacent panel (X5) was assembled and handled via the RR inserts with the same integration device mentioned above. The integration objectives were the hinges inserts were aligned; the hinges could be assembled without introducing any loads to the structure (no panel deformation); and the correct actuation of the latch mechanisms. Once these objectives were met, the 0-g device was integrated; the hinges were assembled with calibrated shims when necessary; and the integration device was released.

After reaching the final position of the panel, the partial flatness is measured without contact using a laser theodolite. Corrections can be made using the regulation capabilities of the hinges until this partial value is accepted. Same steps were performed to achieve the integration of the other two panels, X6 and X7.

All measurements made with position regulation purposes were performed with a laser theodolite and several dial indicator gauges.

After the Antenna wing was assembled, the 6 Restrain-Release mechanisms were integrated. No measurement methodology was considered necessary, so their regulation was achieved through an iterative process of folding one panel on the following, measuring the alignment of the tubes, unfolding, regulating and all over again.

The integration of the dummy wing was performed with the same MGSE in a simpler way since it did not require RR integration and regulation, no flatness nor deployment requirements were applicable, no latch mechanisms were present, the only restriction was that all dummy wing hinges needed to be integrated.

In order to complete the SQM integration process, the antenna SQM needed to be transferred to the main contractor facility, where it had to be re-assembled and joined with the SP SQM instead of the mounting structure. For the transportation, the SAR Antenna was separated in 3 main sub-assemblies: central panel (X4), +X wing (panels X5, X6 & X7) and dummy wing. Before disassembling the antenna, some key parameters were measured, in order to try to reproduce the integration condition on the SP. These measurements were relative positions between interface flanges, latch components and hinges.

Once in the integration facilities, the Antenna and the SP were meant to be integrated all together conforming the whole satellite structural model. In this opportunity, due to the level of integration in the wings and the advantage of having a crane bridge, the procedure was different:

The first step was the integration of the central panel X4 with IS to the SP, which was placed in horizontal position. The central panel was hoisted and lifted onto the SP by means of a bridge crane; once positioned the IS was fastened and secured to the platform. In a similar way, the measurements required for regulating the position were initiated with dial indicator gauges and adding the assistance of a 3-D coordinate measurement arm. The central panel final position was established with the relative positions taken when it was vertical, which means that the latch base was in the same relative position with respect to the RR flange interface of the SP.

The second stage consisted of rotating the SP, leaving the central panel pointing sideways and a lateral face upwards. The 3-panel assembly, or +X wing, was hoisted onto the SP with the crane, after measurements and position regulation, was fastened in place through the Restrain-Release flanges. In this stage, the desired position was one that could meet integration requirements, meaning the hinges should be aligned and the 24 calibrated stem bolts (shear bolts) of the RR flange should be able to be placed using the allowable regulation systems (hinge alignment mechanisms and adjustable shear pins concentric with the bolts). After several interactions, the desired position could not be reached so some of the shear calibrated bolts were replaced by standard bolts. Finally, when all bolts were placed, both hinge mechanisms in the joint between the central panel and X5 panel were re-assembled and regulated.

Finally, the SP was rotated 180° and a similar procedure was executed to integrate the dummy wing. In this case, no RR mechanisms were present but hinges between the central panel and the dummy were. At this moment we noticed that central panel was tilted so it was not possible to integrate the dummy wing as planned because the hinges axis could not be aligned. This was solved by doing some modification of the dummy hinge, but this method was not acceptable for flight.

The first deployment of the antenna was not successful, since the latch mechanisms of the joint between the central panel and the X5 panel did not make it to the final position. A lack of alignment and a shift in position were confirmed through a number of measurements. A procedure to adjust the +X wing (without de-integrating it) was developed and performed; the issue was solved, and the antenna did perform all the following deployments correctly. Nevertheless, the integration measurements and instruments had been proven inaccurate to guarantee the success criteria of the deployment.

Flatness was measured after 3 deployments, 2 before the mechanical tests campaign and 1 after it. The instrument used was the laser theodolite and a 40 dots matrix. As it was a partial antenna (4 panels), the flatness requirement budget established a peak-to-peak value equal or less than 10.7 mm. Table 1 shows these results.

Table 1. Flatness results in SAR Antenna SQM for 3 different deployments

	Deployment #1	**Deployment #2**	**Deployment #3**
Flatness, peak-to-peak (mm)	7.83 ±2	7.43 ±2	7.11 ±2
Pass criteria (mm)	≤ 10.70	≤ 10.70	≤ 10.70

Due to the limited accuracy in the relative position of the sub-assemblies of the SQM (platform, central panel, +X wing and dummy wing), some deviations to the design needed to be included:

- Not all the bolts in the RR flanges could be of calibrated stem. Some had to be replaced for reduced stem ones, increasing the clearance with the bore.

- The dummy hinge mechanisms between the central panel and the dummy wing had to be modified to make their integration possible. A modification to enlarge the regulation capabilities was chosen as a time-saving solution.

Adopting a standard policy regarding alignment measurement, it had been requested that the central panel of the antenna should have two alignment cubes, so that it could be referenced to the SP. These cubes were placed in the lateral beam of the panel, and were not used throughout the integration process, but they were used to determine if there were variations in their relative position after environmental qualification campaign, giving satisfactory results. However, these cubes did not give information regarding the SAR Antenna radiating plane position and it was determined that their alignment was very sensitive to truss tensioning and hinge loading. This last condition occurred every time we preload the RR mechanisms.

This integration process was done with high confidence in mechanisms and structure design criteria, without taking into account integration process restrictions that could arise (technical and programmatic). This led to a difficult and long integration.

Design Changes to Improve Results

After the qualification campaign some changes were implemented in the hardware and in the integration procedures, with the aim to improve and facilitate the integration of the flight models and to reduce the time required for the task (limit the iterative operations). These changes are summarized as follow:

Modifications to the hardware:

- The size and tolerances of the Platform bores were incremented, to slightly increase the clearances. These bores were finished with reamer to improve roughness and verified with go/no go gauges, as well.

- The use of a number of bolts with reduced stem were allowed. The nominal diameter of the stem was between 15.842 mm (max) and 15.799 mm (min) and was reduced by 0.2 mm.

- The pieces used to regulate and adjust the position of the bolts in the RR flanges (named “eccentrics”) were modified to avoid blind spots in the regulation.

- Calibrated shims were added to fill gaps between flanges and platform and avoid distortions in the panels.

- 8 inserts with calibrated bore were potted in each one of the 7 panels of the antenna (near corners, 4 in the radiating face and 4 in the back). These inserts allowed an accurate and repetitive positioning (and quick removal) of measuring devices for the photogrammetry and laser tracker equipment.

Modifications in procedures and MGSE:

- New measuring equipment that facilitated control during both integrations, vertical and horizontal were acquired. This equipment was composed of a real-time 3D coordinate measurement system composed of a FARO Vantage laser tracker [1] and a photogrammetry V-STARS D System configured with two high-speed DynaMo D12 cameras [2]. These systems are complementary to each other, since the first one allows direct measurement of the desired surface, measuring one point at a time with high precision, while the second requires placing magnetic or adhesive targets on the desired surface, allowing the entire cloud of points to be measured in the same acquisition. This measurement equipment showed its results in a 3D model of the antenna and its MGSE, which identify the points measured in the real model, indicating their deviations from the desired position.

- During the antenna integration in vertical position, the regulation of the RR was changed, adding more measurement and characterization and reducing the iterative trial-and-error process.

- A complete mechanical characterization of all assemblies was performed before starting the integration (central panel, wings and platform were measured with laser tracker and photogrammetry equipment). Results were gathered and analyzed with a software tool. Based on this, the most convenient position (target position) for each assembly was defined.

- Related to the previous bullet, for the integration of each main assembly, two bolt holes were selected as most convenient and guidance pins were installed to facilitate reaching the target position.

- The order of integration of the 3 main assemblies of the antenna to the SP was altered: from central panel, then +X wing, finally dummy wing in the SQM to +X wing, then -X wing, finally central panel in both Flight Models.

- The integration of the IS was modified. For the flight models the integration to the central panel was partial: 12 out of 16 tubes were integrated when the central panel was hoisted on the SP. The remaining 4 were integrated after the central panel was already positioned and fixed.

All these modifications were verified with the SQM before being implemented in the flight models. After the structural qualification campaign was complete, the antenna was removed from the SP and re-integrated.

To verify the integration, flatness and repeatability, 9 deployments were performed, yielding the results shown in Table 2. The instrument used was the photogrammetry equipment, with a PRO-SPOT [3] which allows a grid of 5600 light dots in each projection. In addition to substantially increasing the amounts of dots, a great improvement in precision was also achieved.

Table 2. Flatness results in deployments after the SQM was re-integrated implementing the proposed changes.

	Deployment #								
	1	**2**	**3**	**4**	**5**	**6**	**7**	**8**	**9**
Flatness, peak-to-peak (mm)	7.3 ±0.3	7.4 ±0.3	6.7 ±0.3	7.5 ±0.3	7.2 ±0.3	7.2 ±0.3	8.0 ±0.3	8.0 ±0.3	6.9 ±0.3
Pass criterion for one wing (mm)	≤ 10.70								

Flight SAR Antenna Integration in Vertical Position

The first step of the integration was to characterize the mounting structure using the laser tracker and photogrammetry measurement systems in order to know the position of the actual fixation points, and the more relevant parts. This characterization will then be used across the whole assembly process, because it was the reference for alignment and folding as it will be explained later.

In parallel to this characterization, the central panel without the IS was characterized using both measurement systems. This characterization includes the four structure calibrated reference points located at the corners of the panel, the position of the latch mechanisms, which was needed for reference for next panels integration, and the hinges axis position, as is shown in Figure 6.

Once the initial characterization was done, the points of each component measured from the real model were fitted to the 3D model using a best-fit criterion that minimized the dispersion of the points. Once the measured points were related to the ideal locations, the central panel 3D model was placed in the best position with respect to the mounting structure 3D model. The SAR Antenna alignment with respect to the SP was very sensitive to the central panel position, but not SAR Antenna flatness, which could be corrected with the mechanisms provided for the integration of the panels. The resulting 3D model positions defined where the reference points should be (nominal position), and in order to reach that position, how the IS had to be assembled in order to fit the panel to the mounting structure.

Then the IS was assembled and aligned to the desired position with a dedicated auxiliary frame, in order to enable mounting of the central panel to the mounting structure. The IS together with the frame ware stiff enough to guarantee that the central panel position would be maintained. Then, central panel together with

the IS was hoisted vertically, using the dedicated MGSE described above, in order to reach mounting structure interface. Once the IS reached the final position, screws were adjusted and all MGSE was removed. A new characterization was done using the system, where the final position of the panel was compared with the desired one, in order to reach a position which met alignment and flatness requirements, antenna panels' integration, and subsequent folding. In the event that small corrections were necessary, they could be accomplished by tensioning the IS, guided in real time with the photogrammetry system. Otherwise, the central panel would have had to be removed, restarting the entire process. Fortunately, this did not happen. The resulting position was measured and taken as a baseline for SAR Antenna Integration. The most critical points were final hinge axis and latch mechanisms positions as shown in figure 7.

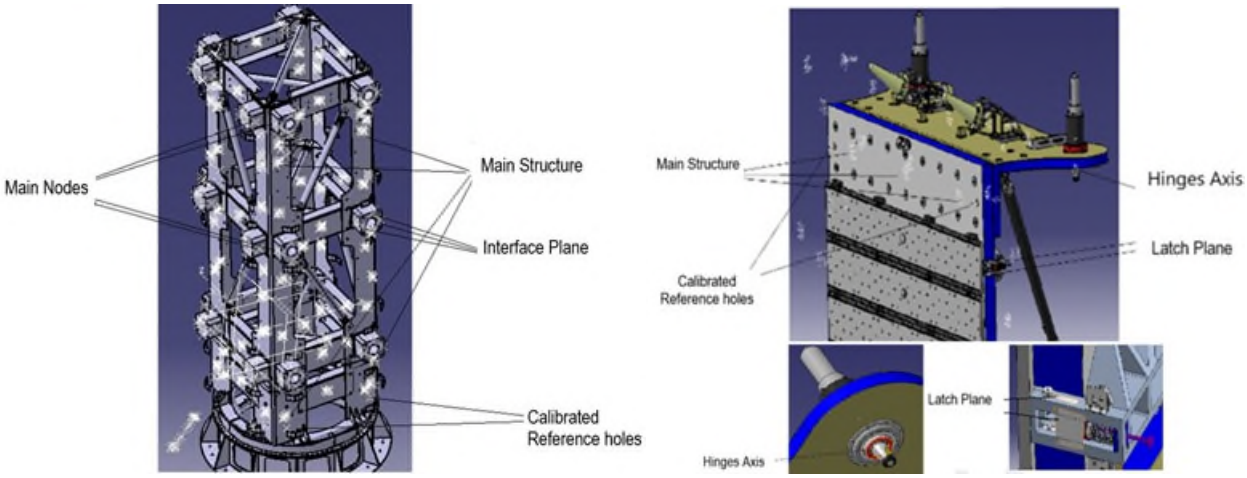

Figure 6: Mounting structure characterization - Central Panel Characterization

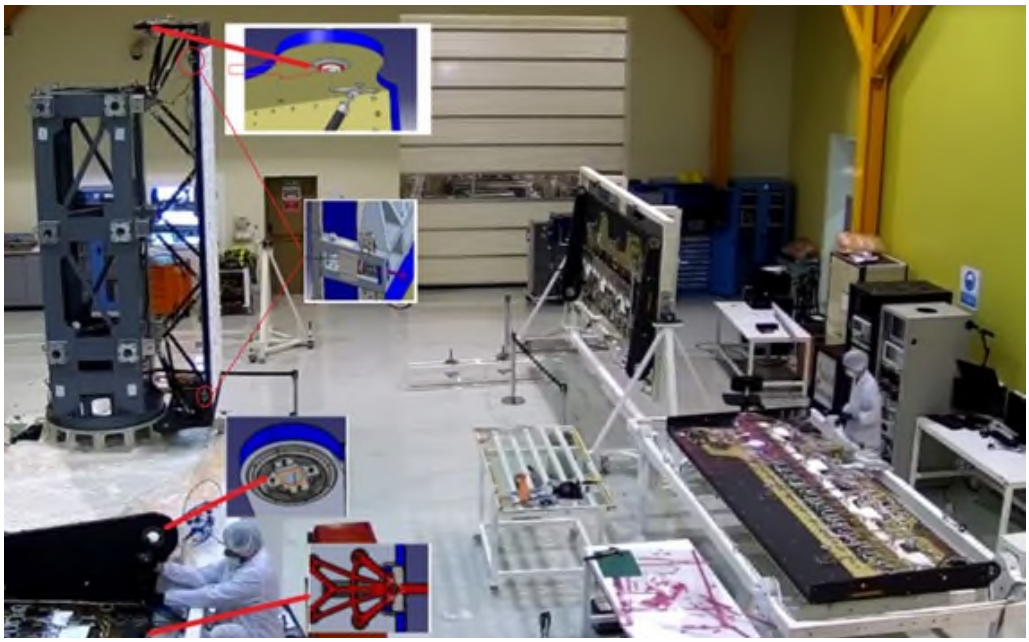

Figure 7. Hinges and latches characterization in central panel and in X5 panel.

Once the central panel was placed and characterized, the next step was to start with the integration of the adjacent panel. The procedure was similar for all panels. Before mounting, each panel was characterized using a laser tracker and the photogrammetry system as described above, and the measurement included the same critical points, similar to the central panel.

Once the panel to be mounted was characterized, the best fit to the 3D model was established and was virtually integrated in the position necessary to meet the flatness and alignment requirements. This desired position normally required some calibrated shims installed on the hinge shaft to align the panel on Y axis. This position was called the nominal position, being the position that would achieve a perfect plane. This nominal position established the desired positions of the four structure reference points of each panel to achieve an acceptable accuracy.

Then the panel was positioned using the same dedicated integration device used for the central panel, which supports the panels from the RR inserts. The position of the panel was monitored in real time with the photogrammetry system, which showed the residual value between the desired and current position of the structure reference points, so the integration conductor could lead the maneuver until these residuals met the integration requirement. Once this objective was met the hinges were assembled with the shims defined before, without forcing the structure, and then the 0-g device was integrated in order to support the panel weight and to release it from the integration device. Then the added panel was folded, the pawls of the latch mechanisms were integrated, and then it was deployed again to evaluate repeatability and final position once latched. In case it was necessary, the panel alignment could be corrected with precision by means of the regulation capabilities of the hinges. If necessary to raise or lower the panel, calibrated shims could be placed on the hinge shafts. After reaching the final position of the panel, the partial flatness was measured without contact using a dense array of high-contrast targets projected [3] onto the radiating surface. If this partial value was accepted, then this new configuration was characterized and same process was repeated for the next panel, see Figure 8.

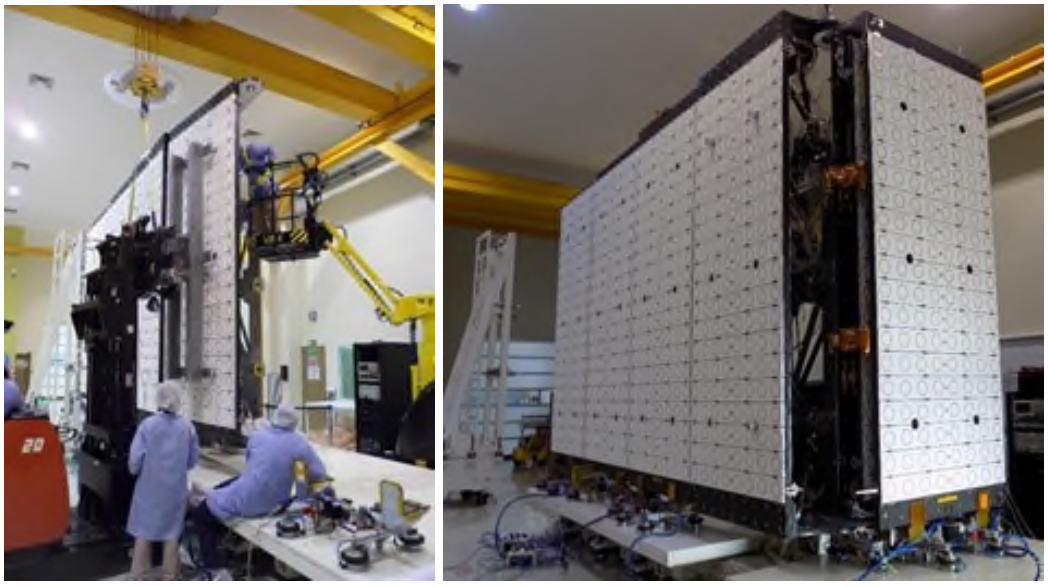

Figure 8. SAR Antenna during integration in vertical position, one panel at the time.

Once one wing was assembled, a complete folding was done in order to evaluate repeatability and start with the restrain release mechanisms integration and alignment in order not to introduce distortions -therefore loads- to the antenna structure. Once the mechanisms were aligned with respect to the panels, their positions were fixed, leaving only the possibility of adjusting the interface in a circle with a 4mm radius, in order to absorb differences when mounted to the SP.

After the SAR Antenna was completely integrated, the flatness and alignment were verified, and the radiation pattern was characterized in an anechoic chamber. Following that, it was disassembled into three main sub-assemblies: central panel with the IS, and the two wings. These sub-assemblies were sent to the main contractor where they were integrated again in a folded configuration, together with the hinges that were removed during the partial disassembly process.

SAR Antenna Assembly in Horizontal Position

As described during the SQM integration, the integration of the SAR Antenna to the SP was performed in horizontal position and making use of a bridge crane. The main differences implemented in the integration of flight models were the measurement systems and the sequence of integration.

Before the integration itself, a series of geometric characterizations using laser tracker and photogrammetry were performed. In the SP, the planar contact surface and the 4 holes of each node were characterized (6 nodes for +X wing, 6 nodes for -X wing and 4 nodes for IS). Likewise, similar characterizations were made in the antenna sub-assemblies, the planar contact surfaces and bolt holes of the RR flanges and those of the IS. Also, the hinge axes and selected surfaces of the latches were characterized as well.

The measured components were best fit to their 3D model and the nominal position for each sub-assembly was defined and transformed in the target position to be accomplished during the integration. This position was defined not only taking into account the integrability in the current folded position but the final deployed position, in order to guarantee flatness and alignment requirements. As a result of this analysis, 2 bolt holes were defined as integration reference points and guidance pins were installed in order to facilitate the position of the sub-assemblies.

The first stage of final integration was the +X wing. The SP was installed on the integration trolley with the +X face oriented upwards. The +X wing sub-assembly was hoisted and guided onto the SP. When the wing was in an approximate position, the photogrammetry measuring system was initiated, taking advantage of its real-time and multi-point information, enabling the wing to reach its target position. Once the positioning was completed, achieving the pre-defined tolerances, the shear calibrated bolts were installed (but not torqued) in the RR flanges to assess whether standard-size bolts could be used throughout. A final measurement of predefined points was made with the laser tracker, using its greater accuracy to verify an acceptable integration. Once the position was accepted, the interface bolts were tightened.

Figure 9. SAR Antenna during wing integration (left) and central panel integration (right) in horizontal position.

A similar procedure was followed to integrate the -X wing, adding the actual position of the +X wing to adjust the analysis determining the target positions of the -X wing and central panel.

Finally, the central panel and the IS (partially integrated with 12 out of 16 tubes) was hoisted and positioned onto the SP (Figure 9). The positioning was guided using the guidance pins and the photogrammetry equipment; the final position was verified with the laser tracker. To complete the IS assembly, the interface bolts were tightened; and the 4 hinge mechanisms were assembled without introducing deformation to the panels, confirming the first success criteria of the integration. The second success criterion were flatness and alignment, which were verified in the deployed configuration.

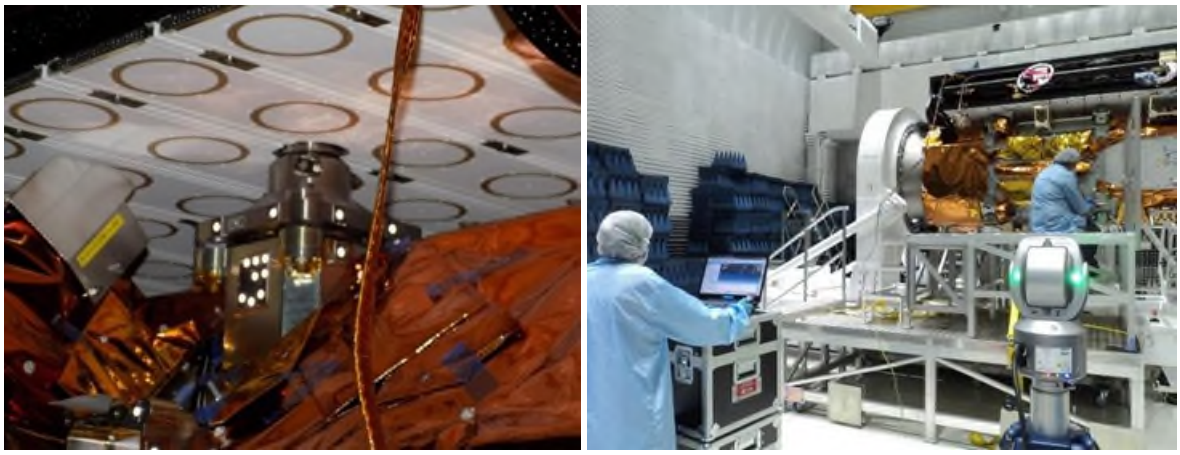

Figure 10. Reflective targets for photogrammetry measurement (left) and measurement with laser tracker during central panel integration (right).

Flatness Measurement

Once the SAR Antenna was completely integrated, a workflow similar to the structural model was followed: the satellite was positioned in vertical position and atop the corresponding trolley; the MGSE for deployment was installed (0-g device and deployment tables), leaving the antenna ready for its first deployment.

Along the AI&T campaign, a total of 3 mandatory deployments were planned, including a system validation test (several extra deployments were performed but for operational convenience and with no requirement-verification purposes). Flatness was measured each time (see Figure 11)

- Deployment #1 after antenna integration was completed
- Deployment #2 prior to the mechanical environment test campaign
- Deployment #3 after the mechanical test campaign

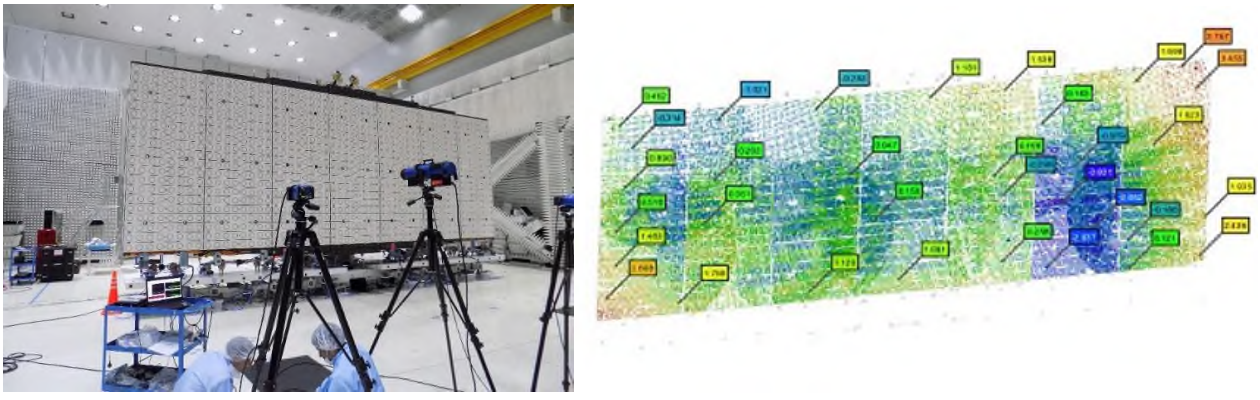

Figure 11. SAR Antenna flatness verification. Measuring set-up (left) and data visualization (right)

The SAOCOM 1A and 1B achieved similar flatness and repeatability values. Table 3 summarizes the flatness measurement results obtained during SAOCOM 1A and 1B AIT campaigns.

Table 3. Flatness results in deployments pre and post dynamic tests campaign, for SAOCOM 1A/B.

	SAOCOM 1A		SAOCOM 1B	
	Pre dyn. test	**Post dyn. test**	**Pre dyn. test**	**Post dyn. test**
Flatness, peak-to-peak (mm)	8.7 ±0.3	8.6 ±0.3	8.0 ±0.3	7.0 ±0.3
Pass criterion (mm)	≤ 12.70			

Conclusions

A short summary of the mechanism's design and its contribution to flatness regulation were introduced. Integration and measurements strategies along the lifecycle of the project were described, including the improvements.

As was indicated, at the very beginning the best way to meet the flatness and alignment requirements from the design and manufacturing point of view were established, without considering the problems that the integration and assembly of the antenna could arise. Trying to use standard alignment criterion (such as the use of cubes) in such complex, flexible and large structures was not possible, and it would not have allowed the radiating plane of the antenna to be measured relative to the satellite reference system. These inconveniences were detected early, thanks to the model philosophy adopted by the project, and the pertinent design modifications that accounted for integration requirements in the design and manufacture of the structure. The reference points calibrated on the structural panels were key to the success of the integration.

The acquisition of modern measurement equipment and great metrology and engineering teams made the integration successful in both satellites, fulfilling the desired requirements with sufficient margin. Also, this methodology allowed not only a significant reduction in the integration time but a minor uncertainty in their predictions, since the iterative, trial-error procedures are by nature uncertain and they were reduced.

It was also a good decision to implement the MGSE mounting structure. This allowed decoupling of the integration of the antenna from the SP, dealing with a great part of the tasks (flatness and RR regulation, for instance) in parallel, thus, optimizing the schedule.

The commissioning of both satellites also showed very good results for the instrument performance, thus confirming that the flatness requirements were also compliant to design requirement after the in-orbit deployment allowing the mission to start its operational phase successfully.

References

[1] https://www.geodetic.com/products/systems/v-stars-d/
[2] https://www.faro.com/Products/Hardware/Vantage-Laser-Trackers
[3] https://www.geodetic.com/wp-content/uploads/2019/07/GSI_PS-A_Brochure_2019_print.pdf